FACULTY
OF MATHEMATICS
AND PHYSICS
Charles University

DOCTORAL THESIS

Helena Žlebčíková

Anisotropic tomography of the European upper mantle

Department of Geophysics

Supervisor of the doctoral thesis: RNDr. Jaroslava Plomerová, DrSc.
Study programme: Physics
Specialization: Geophysics

Prague 2018

I declare that I carried out this doctoral thesis independently, and only with the cited sources, literature and other professional sources.

I understand that my work relates to the rights and obligations under the Act No. 121/2000 Coll., the Copyright Act, as amended, in particular the fact that the Charles University has the right to conclude a license agreement on the use of this work as a school work pursuant to Section 60 paragraph 1 of the Copyright Act.

In Prague October 28, 2018

Helena Žlebčíková (born Munzarová)

I would like to express my sincere gratitude to Jaroslava Plomerová, my supervisor, who has introduced me to the fascinating topic of the Earth's lithospheric structure and to the methods revealing its various aspects. She has always been determined to help me with emerging problems, to discuss them and to give me inspiring guidance. Furthermore, I am very grateful for the opportunity to attend various conferences and workshops, which have always pushed me forward. I greatly thank Prof. Eduard Kissling (ETH Zürich) for sharing tomography code Telinv with us and for many and many hours of thought-provoking discussions. I also thank Jaroslava Plomerová, Petr Jedlička and Josef Kotek, and all the related working groups for operating passive seismic experiments BOHEMA, RETREAT and LAPNET. Next, I would like to thank Vladislav Babuška and Luděk Vecsey for their help during my whole studies, for their inspiring ideas and useful comments. Furthermore, I thank Luděk Vecsey for preprocessing of the seismic data. I also appreciate a helpful and friendly atmosphere at the Institute of Geophysics and at the Department of Geophysics of the Faculty of Mathematics and Physics. Special thanks go to my dear mum Helena and to my beloved husband Radek for their support, love and care. I also would like to express deep respect to my dad Nuri whose life has been and always will be a source of encouragement for me. The research was supported particularly by grant no. 210/12/2381 of the Grant Agency of the Czech Republic, by grant no. 111-10/253101 of the Grant Agency of Charles University, by grant no. M100121201 of the Czech Academy of Sciences, by SCIEX Scholarship Fund, by research infrastructure CzechGeo/EPOS LM2015079 funded by the Ministry of Education, Youth and Sports, and by project CzechGeo/EPOS-Sci, no. CZ.02.1.01/0.0/0.0/16_013/0001800, financed from the Operational Programme Research, Development and Education within ERDF.

Title: Anisotropic tomography of the European upper mantle

Author: Helena Žlebčíková

Department: Department of Geophysics, Faculty of Mathematics and Physics, Charles University

Training institution: Institute of Geophysics of the Czech Academy of Sciences (IG CAS)

Supervisor: RNDr. Jaroslava Plomerová, DrSc., IG CAS

Consultants: RNDr. Vladislav Babuška, DrSc., IG CAS

RNDr. Luděk Vecsey, Ph.D., IG CAS

Abstract: Large-scale seismic anisotropy of the continental mantle lithosphere derived from joint inversion/interpretation of directional variations of P-wave travel-time residuals and SKS-wave splitting calls for orientation of the symmetry axes to be treated generally in 3D. Nevertheless, most of the tomography studies neglect the anisotropy of the body waves completely or they are limited to either azimuthal or radial anisotropy. Therefore, we have developed a code called AniTomo for coupled anisotropic-isotropic travel-time tomography of the upper mantle. The novel code allows inversion of relative travel-time residuals of teleseismic P waves simultaneously for 3D distribution of P-wave isotropic-velocity perturbations and anisotropy of the upper mantle. We assume weak anisotropy of hexagonal symmetry with either the 'high-velocity' *a* axis or the 'low-velocity' *b* axis. The symmetry axis is allowed to be oriented freely in any direction. Model parameters are perturbations of isotropic component of the anisotropic velocity, strength of anisotropy, and azimuth and inclination of the symmetry axis. We have tested the new code thoroughly, involving both simple methodological tests to find out basic characteristics of the method and tests mimicking real tomographic inversions as to the target structures and the station-event distribution. Regarding the well-known trade-off between P-wave anisotropy and isotropic heterogeneities, the inversion with code AniTomo can successfully distinguish the isotropic and the anisotropic components of the velocity, depending, of course, on data quality. For the first application of the novel code, we opted for data from international passive seismic experiment LAPNET (2007 – 2009) deployed in a tectonically stable region of northern Fennoscandia. The resulting tomographic model shows that the strongest anisotropy and the largest isotropic-velocity perturbations concentrate at the mantle-lithospheric depths while in the deeper parts their amplitudes decrease significantly. The anisotropy derived in the mantle-lithospheric part of the model enables us to delimit regions of laterally and vertically consistent anisotropy. These regions are compatible with the domains inferred from the joint interpretation of directional variations of P-wave travel-time residuals and SKS-wave splitting parameters. We associate the domain-like anisotropy with fossil fabrics of blocks of the Archean mantle lithosphere, preserved probably from the time of the lithosphere origin.

Keywords: Seismic tomography, Velocity anisotropy, Body waves, Upper-mantle structure, 3D fabrics of mantle-lithosphere domains, Fennoscandia

Název: Anizotropní tomografie svrchního pláště pod Evropou

Autor: Helena Žlebčíková

Katedra: Katedra geofyziky, Matematicko-fyzikální fakulta, Univerzita Karlova

Školící pracoviště: Geofyzikální ústav Akademie věd České republiky (GFÚ AV ČR)

Vedoucí: RNDr. Jaroslava Plomerová, DrSc., GFÚ AV ČR

Konzultanti: RNDr. Vladislav Babuška, DrSc., GFÚ AV ČR
RNDr. Luděk Vecsey, Ph.D., GFÚ AV ČR

Abstrakt: Výzkum seismické anizotropie kontinentální plášťové litosféry odvozené ze společné inverze/interpretace směrových variací odchylek v časech šíření teleseismických vln P a parametrů štěpení vln SKS naznačuje, že orientaci os symetrie anizotropie je potřeba uvažovat obecně ve 3D. Mnohé tomografické studie nicméně anizotropii objemových vln zanedbávají zcela nebo se omezují pouze na azimutální nebo radiální anizotropii. Proto jsme vyvinuli kód AniTomo pro sdruženou anizotropní-izotropní tomografii svrchního pláště. Kód AniTomo modeluje 3D rozložení anizotropie a perturbací izotropních rychlostí vln P ve svrchním plášti inverzí relativních odchylek v časech šíření teleseismických vln P. Předpokladem je slabá anizotropie s hexagonální symetrií. Kód připouští oba typy hexagonální symetrie, tj. s „rychlou“ osou *a* a „pomalou“ rovinou (*a,c*) nebo s „pomalou“ osou *b* a „rychlou“ rovinou (*a,c*). Navíc osa symetrie může být orientována libovolně ve 3D. Modelové parametry jsou perturbace izotropní složky anizotropní rychlosti, síly anizotropie a azimutu a inklinace osy symetrie. Důkladné testování nového kódu zahrnuje jak jednoduché, metodologicky zaměřené testy, které odhalují základní vlastnosti metody, tak testy napodobující skutečné tomografické inverze, tj. zohledňující reálné rozložení seismických stanic a jevů a realistickou strukturu svrchního pláště. Pokud jde o dobře známý „trade-off“ mezi anizotropií vln P a izotropními heterogenitami, inverze spočítaná kódem AniTomo dokáže úspěšně rozlišit izotropní a anizotropní složky rychlosti s ohledem na kvalitu dat. Pro první aplikaci nového kódu jsme vybrali data z mezinárodního pasivního seismického experimentu LAPNET, který probíhal v tektonicky stabilní oblasti severní Fenoskandie mezi roky 2007 a 2009. Výsledný tomografický model ukazuje, že nejsilnější anizotropie a největší perturbace izotropní složky rychlosti se nacházejí v hloubkách odpovídajících plášťové litosféře, zatímco hlouběji oboje vykazuje výrazně nižší amplitudy. Anizotropie v hloubkách odpovídajících plášťové litosféře nám umožňuje vymezit oblasti s laterálně a vertikálně jednotnou anizotropní strukturou. Tyto oblasti jsou kompatibilní s doménami odvozenými ze společné interpretace směrových variací odchylek v časech šíření teleseismických vln P a parametrů štěpení vln SKS. Oblasti s jednotnou anizotropií interpretujeme jako bloky archaické plášťové litosféry, které si pravděpodobně uchovaly anizotropní strukturu z doby svého vzniku.

Klíčová slova: Seismická tomografie, Anizotropie rychlostí, Objemové vlny, Struktura svrchního pláště, 3D anizotropní struktura domén plášťové litosféry, Fenoskandie

Contents

1. Introduction

1.1 Investigations of seismic anisotropy of the upper mantle

Anisotropy of seismic-wave velocities of the Earth's upper mantle is a key source contributing to deciphering tectonic history of the lithosphere-asthenosphere system (e.g., Babuška & Cara 1991; Šílený & Plomerová 1996; Silver 1996; Savage 1999; Park & Levin 2002; Fouch & Rondenay 2006; Mainprice 2007; Maupin & Park 2007; Long & Silver 2009; Long & Becker 2010). Large-scale anisotropy, detectable by seismic waves passing through the Earth, occurs as a consequence of lattice-preferred orientation (LPO) of the intrinsically anisotropic minerals, particularly olivine and pyroxene, constituting the upper-mantle rocks. The LPO reflects the stress field acting when the rocks were ductile, i.e., the stress field in the time of a mantle-lithosphere origin (e.g., Babuška & Plomerová 1989) or a current stress field in the case of asthenosphere (e.g., Silver & Chan 1991; Savage 1999). The effective strength of the large-scale upper-mantle anisotropy is lower than the intrinsic anisotropy of the individual minerals (e.g., Christensen 1984).

While sub-horizontally propagating surface waves can provide us with integral and long-wavelength variations of the upper-mantle anisotropy, body waves, i.e., shear waves and particularly P waves, are sensitive to smaller-size structures due to their shorter wavelengths and broad angles of steeper propagations. Thus, the P waves can supply us with relatively detailed information on the upper-mantle fabrics (e.g., Babuška & Plomerová 1992; 2006). Nevertheless, most of the standard teleseismic body-wave tomography studies neglect the P-wave anisotropy although such a simplification is incongruous with the current understanding of the upper-mantle dynamics. Moreover, ignoring the seismic anisotropy can produce artefacts in the resulting purely isotropic-velocity models (e.g., Sobolev *et al.* 1999; Menke 2015; Bezada *et al*. 2016).

Various tomographic approaches that do not fully neglect anisotropy appeared in the past and their number has been increasing recently (e.g., Hirahara & Ishikawa 1984; Eberhart-Phillips & Henderson 2004; Ishise & Oda 2005; 2008; Wang & Zhao 2008; 2012; Tian & Zhao 2013; Ishise *et al.* 2015; Koulakov *et al.* 2015; Liu & Zhao 2016; 2017). However, they are mostly limited to the crust, using local-earthquake datasets and searching for azimuthal anisotropy only. On the other hand, e.g., Hua *et al.* (2017) or Gou *et al.* (2018) evaluate also radial anisotropy from merged local-earthquake and teleseismic datasets, i.e., travel times or travel-time residuals of P waves, but the separation of the radial and azimuthal anisotropy yet represents a significant simplification of the true anisotropic structure of the Earth.

Confining orientation of the symmetry axis to horizontal (in azimuthal anisotropy) or vertical (in radial anisotropy) directions does not conform to path-integrated anisotropic characteristics inferred from teleseismic body waves observed in tectonically different continental provinces (e.g., Babuška *et al.* 1984; 1993; Babuška & Plomerová 2006; Plomerová & Babuška 2010; Plomerová *et al.* 2011; 2012). The authors demonstrate dependence of SKS-wave splitting parameters and P-wave travel-time residuals on direction of wave propagation, taking into account both azimuth and incidence angles. Such characteristics with a general 2π periodicity imply a need to treat anisotropy in 3D. Self-consistent anisotropic models of continental mantle lithosphere usually document that derived symmetry axes of the anisotropic domains are oriented generally in 3D, i.e., inclined from horizontal (e.g., Plomerová *et al.* 2012).

To contribute to studies of the large-scale anisotropy of the upper mantle, we have developed a novel code called AniTomo for regional coupled anisotropic-isotropic tomography. The AniTomo code inverts travel-time residuals of teleseismic P waves simultaneously for 3D distribution of the isotropic-velocity perturbations and anisotropy assuming weak anisotropy with hexagonal symmetry oriented generally in 3D. The code represents a step further from modelling homogeneously anisotropic blocks of the mantle lithosphere (e.g., Plomerová *et al.* 2002; Vecsey *et al.* 2007; Plomerová *et al*. 2011) towards modelling anisotropy arbitrarily varying in 3D.

1.2 Preparation for the coupled anisotropic-isotropic tomography – Upper-mantle anisotropy of the Northern Apennines and isotropic tomography of the Bohemian Massif

In the beginning of this work, we studied separately the methods that reveal a path-integrated anisotropy (Munzarová *et al.* 2013; Supplement 1) and the isotropic-velocity tomography (Plomerová *et al.* 2016; Supplement 2). This approach helped us to gain a more thorough knowledge on seismic anisotropy and tomography, and to decide how we would include the P-wave anisotropy into the tomography. We briefly summarize the outcomes of the two publications in this Section.

International passive seismic experiment RETREAT (2003 – 2006; Margheriti *et al.* 2006) provides data to study the upper mantle beneath the Northern Apennines with different methods such as analysis of directional terms of relative P-wave travel-time residuals, i.e., P-wave anisotropy, and SKS-wave splitting (Plomerová *et al.* 2006; Salimbeni *et al.* 2008), receiver functions (Miller & Piana Agostinetti 2012), estimation of depth of the lithosphere-asthenosphere boundary (LAB) from static terms of relative P-wave travel-time residuals (Plomerová & Babuška 2010), or teleseismic tomography (Benoit *et al.* 2011). Munzarová *et al.* (2013; Supplement 1) suggest a model (Fig. 1.1) of the lithosphere-asthenosphere system for the Northern Apennines by complementing and jointly interpreting the previous investigations, particularly the P-wave anisotropy, estimates of the LAB depths and SKS-wave splitting.

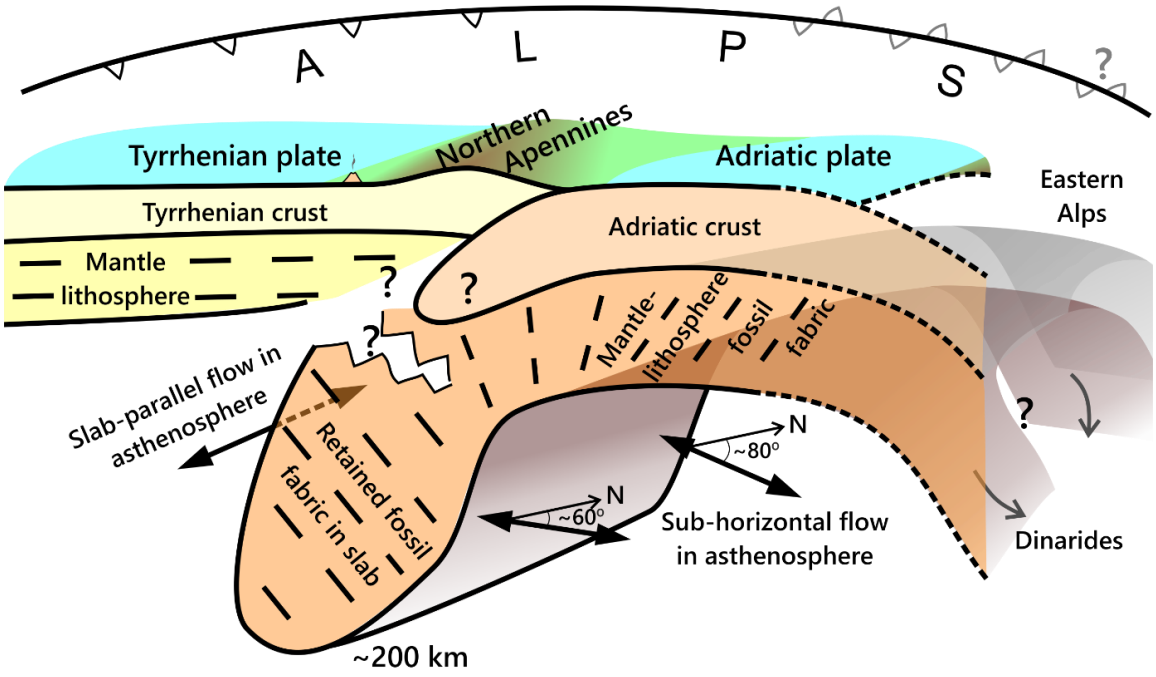

Figure 1.1 Cartoon of the lithosphere-asthenosphere system beneath the Northern Apennines and the surrounding area (Munzarová *et al.* 2013). The front of the cartoon is approximately orogen perpendicular. Fossil fabrics, both in the Adriatic mantle lithosphere and in the subducted slab, in a combination with the asthenospheric flow, are interpreted as sources of the evaluated anisotropic signal in seismic body waves. The slab-parallel flow in the sub-lithospheric mantle beneath the Tyrrhenian plate and almost slab-orthogonal flow on the Adriatic side indicate a ceased slab roll-back. The north-eastern flow beneath the Adriatic plate might result from its blocking within a limited space by surrounding subductions.

We identify two sources of anisotropy in the upper mantle beneath the RETREAT seismic array. One of the sources is in the mantle lithosphere, which can be separated into regions characterized by different anisotropy interpreted as fossil fabrics of the individual lithospheric blocks. The other source lies in the sub-lithospheric mantle, where the anisotropy probably reflects recent flows of the asthenosphere (Fig. 1.1). A slab-parallel flow prevails in the sub-lithospheric mantle beneath the thin Tyrrhenian plate, i.e., westward from the Northern Apennines, while nearly slab-perpendicular orientation of the high-velocity directions dominates on the Adriatic side of the region. Such a pattern excludes a simple corner-flow in the mantle wedge to fit the fabric of the sub-lithospheric mantle in the syn-convergent extensional tectonics and suggests the end of the subduction roll-back. We map fossil anisotropy with inclined symmetry axes within two domains of the thick Adriatic lithosphere. We estimate the lithosphere thickness of the Tyrrhenian and Adriatic plates at ~50 km and ~80 km, respectively, the latter being subducted down to no more than ~200 km with indications of an inherited frozen-in anisotropic fabric.

Despite a complexity of the lithosphere-asthenosphere system beneath the Northern Apennines and the fact that the applied method was developed for tectonically stable regions, it worked well and led to a self-consistent model of the upper mantle thanks to combination of different datasets and approaches and permitting the anisotropy to be oriented generally in 3D. The assumption of a general orientation of anisotropy might seem reasonable for a region where a 3D dynamics is evident. Nevertheless, limiting the research to either azimuthal or radial anisotropy is a common simplifying practice.

The second publication (Plomerová *et al.* 2016; Supplement 2) focuses on the isotropic-velocity structure of the upper mantle beneath the western part of the Bohemian Massif (BM). The BM upper mantle appears as a part of an extensive low-velocity region beneath central Europe detected in various large-scale tomographic studies (e.g., Goes *et al.* 1999; Wortel & Spakman 2000; Piromallo & Morelli 2003; Amaru 2007; Koulakov *et al.* 2009). However, the resolution of such tomographic images, based on travel times of body waves measured only at permanent observatories in the area, is not sufficient to infer the upper-mantle structures at scales smaller than 100 km. Therefore, passive seismic experiment BOHEMA I was organized in the western part of the BM between 2001 and 2003 (Plomerová *et al.* 2003). One of the main questions behind this experiment is whether a small mantle plume exists beneath the western BM as Granet *et al.* (1995) hypothesized for all Variscan Massifs in a context of the European Cenozoic Rift System (ECRIS).

We evaluate tomographic models of P- and S-wave isotropic-velocity perturbations in the upper mantle separately for teleseismic P waves (17 776 measurements) and S waves measured on the Q (1 943 measurements) and T (1 464 measurements) components (Fig. 1.2). All the three tomographic models show a 200km-broad zone of relatively low velocities suggesting rather an upwelling of the asthenosphere than a narrow sub-vertical mantle plume for an interpretation. The broad zone of the low-velocity perturbations extends particularly along the Eger Rift, i.e., a Cenozoic rift, in the vicinity of which an abundant volcanic activity took place during the Cenozoic. The Eger Rift roughly follows a Variscan suture between the Saxothuringian and Teplá-Barrandian tectonic units, representing a weak zone in the otherwise rigid continental mantle lithosphere. The zone can channel upwelling of a hot mantle material accompanied by thinning of the lithosphere (e.g., Plomerová *et al.* 2007; Babuška & Plomerová 2013).

In spite of different wavelengths, directions of propagation and volume coverage of the P and S waves, i.e., different resolutions, the three isotropic-velocity tomography models exhibit similar large-scale features. Differences between them might possibly originate from neglecting seismic anisotropy. The independent investigations of seismic anisotropy of the BM reveal domains of mantle lithosphere with consistent anisotropy oriented generally in 3D (e.g., Babuška *et al.* 2008; Plomerová *et al.* 2007; Babuška & Plomerová 2013). Therefore, application of new code AniTomo to data from various passive experiments carried out in the Bohemian Massif is one of our plans for the near future.

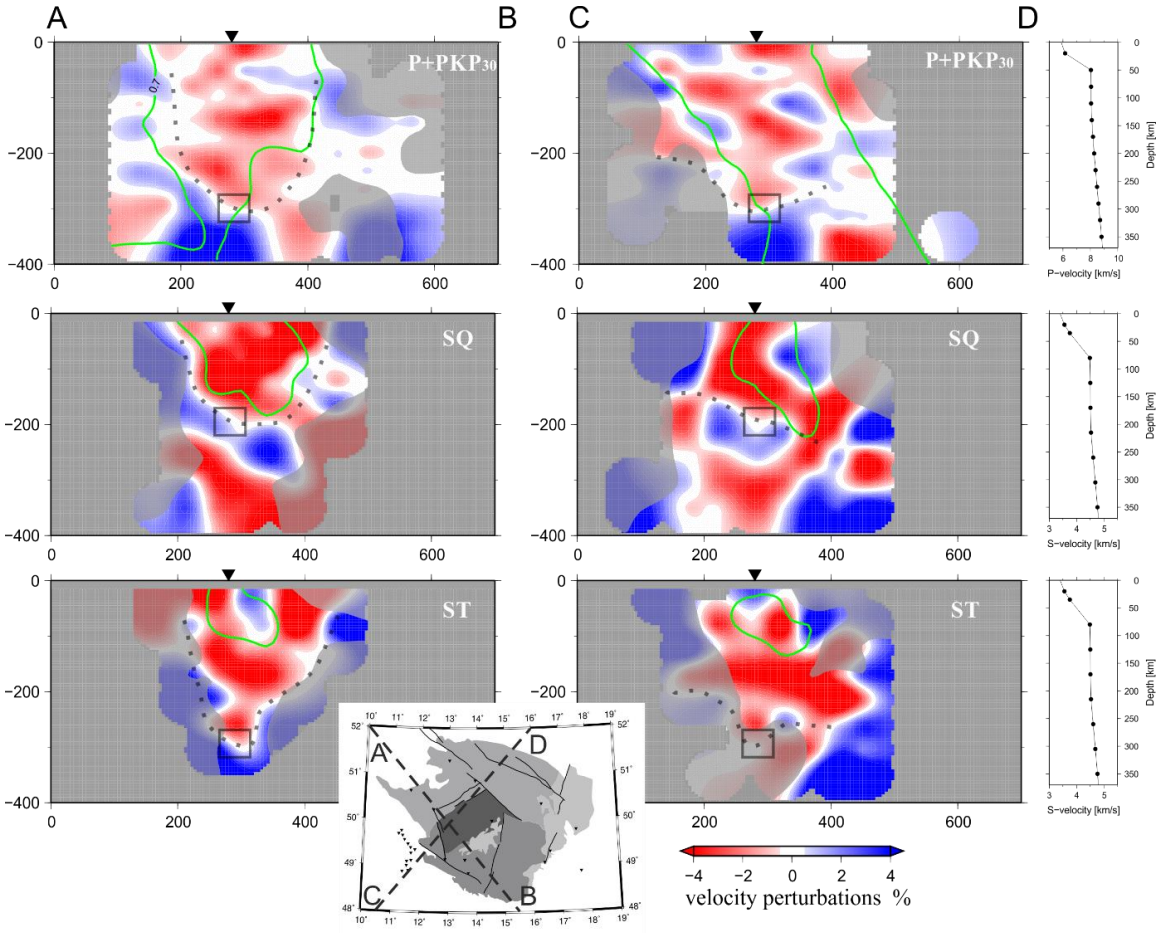

Figure 1.2 Cross sections through the P- and S-wave models of isotropic-velocity perturbations along the AB and CD profiles cutting the most distinct anomalies. We calculate the S-wave models separately for the arrival-time measurements on the T and Q components. Perturbations with hit-count larger than 30 and 10 are plotted for the P and S models, respectively. Regions with diagonal elements of the resolution matrix (RDE) lower than 0.5 are dimmed and with RDE larger than 0.7 contoured (green). The continuous relatively low-velocity perturbations are schematically marked by dotted curves. Rectangles mark their depth extent beneath the point of profile crossing (triangles at the zero depth).

We used Fortran code Telinv to evaluate the P- and S-wave isotropic-velocity models of the BM upper mantle (available at http://www.ig.cas.cz/en/research-teaching/software-download/). Code Telinv was originally developed by J. Taylor, E. Kissling, U. Achauer, C. M. Weiland and L. Steck. It has been modified by many authors and applied to various regions (see, e.g., Weiland *et al.* 1995; Arlitt *et al.* 1999; Lippitsch *et al.* 2003; Sandoval *et al.* 2004; Shomali *et al.* 2006; Eken *et al.* 2007; Karousová *et al.* 2012; 2013; Karousová 2013; Plomerová *et al.* 2016; Silvennoinen *et al.* 2016; Chyba *et al.* 2017).

1.3 Development of code AniTomo and the structure of the Thesis

We have developed code AniTomo for the coupled anisotropic-isotropic tomography as a modification of the Telinv code (see previous paragraph). We have kept the overall framework and the subroutines solving the individual steps as they are in Telinv, but we have allowed for the anisotropic propagation of the P waves. Code AniTomo inverts travel-time residuals of teleseismic

P waves for parameters describing the P-wave anisotropic velocity within a volume of the upper mantle beneath a regional array of seismic stations. We assume weak anisotropy with hexagonal symmetry oriented generally in 3D. Both the high-velocity *a* and low-velocity *b* axis of the hexagonal symmetry are admitted. The model parameters searched during an iterative inversion are perturbations of isotropic component of the anisotropic velocity, strength of anisotropy, azimuth and inclination of the symmetry axis. The derivation of all the equations used in the code is described in detail in **Chapter 2**. The code enables us to limit the search for anisotropic parameters only to a well-resolved part of the volume studied and to run the isotropic-velocity inversion simultaneously in the remaining part of the volume.

The primary target of the AniTomo code is to invert travel-time residuals for coupled anisotropic-isotropic model parameters, but the forward mode of the code is not of less significance. We took advantage of the possibility to calculate P-wave travel times for a given arbitrarily heterogeneous anisotropic model and we have evaluated synthetic P spheres, which display directional variations of the travel-time residuals at a station (e.g., Babuška & Plomerová 2006), for various examples of the upper-mantle structures (**Chapter 3**; unpublished results). There is also a model of the Eger Rift and the adjacent Teplá-Barrandian and Saxothuringian tectonic units among the synthetic upper-mantle structures.

A careful testing focused on functionality, strengths and weaknesses should be an inseparable part of development of any new code. We started the synthetic testing of code AniTomo from very simple, unrealistic models targeted purely on checking of the methodology and on learning basic principles of our anisotropic-tomography approach (**Chapter 4**; unpublished results).

The subsequent series of synthetic tests (**Chapter 5**; published by Munzarová *et al.* 2018 - Part I) mimics tomographic inversions with realistic parameterization of the upper-mantle volume. This part includes many synthetic tests of resolution, separation of the isotropic and anisotropic model parameters, their convergence to the true values and effects of the inversion setup on the results. Furthermore, we derive and show an example application of so-called ray density tensors (RDT; Kissling 1988) - a tool to represent coverage of the parameterization cells by rays in 3D, which we have implemented into AniTomo.

The extensive testing of the new code allowed us to proceed smoothly to inversion of a real dataset. For the first application of AniTomo, we opted for a dataset from northern Fennoscandia, where international passive seismic experiment POLENET/LAPNET was deployed between 2007 and 2009. The resulting 3D model of P-wave isotropic-velocity perturbations and anisotropic parameters of the upper mantle is presented in **Chapter 6** (published by Munzarová *et al.* 2018 - Part II).

We include references at the end of each chapter.

References

Amaru, M.L., 2007. Global Travel Time Tomography with 3-D Reference Models, *PhD thesis*, Utrecht University, Utrecht.

Arlitt, R., Kissling, E. & Ansorge, J., 1999. Three-dimensional crustal structure beneath the TOR array and effects on teleseismic wavefronts, *Tectonophysics*, **314**, 309–319.

Babuška, V. & Cara, M., 1991. *Seismic Anisotropy in the Earth*, Kluwer Academic Publishers, Dordrecht, Boston, London.

Babuška, V. & Plomerová, J., 1989. Seismic anisotropy of the subcrustal lithosphere in Europe: another clue to recognition of accreted terranes?, in *Deep structure and past kinematics of accreted terranes*, edited by J. W. Hillhouse, pp. 209-217, Geophys. Monograph 50, IUGG 5, Washington, D. C.

Babuška, V. & Plomerová, J., 1992. The lithosphere in central Europe—seismological and petrological aspects, *Tectonophysics*, **207,** 141–163.

Babuška, V. & Plomerová, J., 2006. European mantle lithosphere assembled from rigid microplates with inherited seismic anisotropy, *Phys. Earth Planet. Inter.* **158,** 264–280.

Babuška, V. & Plomerová, J., 2013. Boundaries of mantle-lithosphere domains in the Bohemian Massif as extinct exhumation channels for high-pressure rocks. *Gondwana Res.*, 23, 973-987.

Babuška, V., Plomerová, J. & Šílený, J., 1984. Spatial variations of P residuals and deep-structure of the European lithosphere, *Geophys. J. R. astr. Soc.*, **79,** 363–383.

Babuška, V., Plomerová, J. & Šílený, J., 1993. Models of seismic anisotropy in the deep continental lithosphere, *Phys. Earth Planet. Inter.*, **78**, 167–191.

Babuška, V., Plomerová, J. & Vecsey, L., 2008. Mantle fabric of western Bohemian Massif (central Europe) constrained by 3D seismic P and S anisotropy, *Tectonophysics*, **462**.

Bezada, M.J., Faccenda, M. & Toomey, D.R., 2016. Representing anisotropic subduction zones with isotropic velocity models: A characterization of the problem and some steps on a possible path forward, *Geochem. Geophys. Geosyst.*, **17**, 3164–3189, doi: 10.1002/2016GC006507.

Benoit, M. H., Torpey, M., Liszewski, K., Levin, V. & Park, J., 2011. P and S wave upper mantle seismic velocity structure beneath the northern Apennines: New evidence for the end of subduction, *Geochem. Geophys. Geosyst.*, **12**, Q06004, doi:10.1029/2010GC003428.

Christensen, N.I., 1984. The magnitude, symmetry and origin of upper mantle anisotropy based on fabric analyses of ultramafic tectonites. *Geophys. J. R. Astron. Soc.* **76**, 89-111.

Chyba, J., Plomerová, J., Vecsey, L. & Munzarová, H., 2017. Tomography study of the upper mantle around the TESZ based on PASSEQ experiment data, *Phys. Earth planet. Inter.*, **266**, 29-38. doi.org/10.1016/j.pepi.2017.01.002

Eberhart-Phillips, D. & Henderson, C.M., 2004. Including anisotropy in 3-D velocity inversion and application to Marlborough, New Zealand, *Geophys. J. Int.*, **156** (2), 237–254.

Eken, T., Shomali, H., Roberts, R. & Bödvarsson, R., 2007. Upper mantle structure of the Baltic Shield below the Swedish National Seismological Network (SNSN) resolved by teleseismic tomography, *Geophys. J. Int.*, **169,** 617–630.

Fouch, M.J. & Rondenay, S., 2006. Seismic anisotropy beneath stable continental interiors, *Phys. Earth planet. Inter.*, **158,** 292–320.

Granet, M., Wilson, M. & Achauer, U., 1995. Imaging a mantle plume beneath the French Massif Central, *Earth Planet. Sci. Lett.*, **136**, 281-96.

Goes, S., Spakman, W. & Bijwaard, H., 1999. A lower mantle source for central European volcanism, *Science*, **286**, 1928-1931.

Gou, T., Zhao, D., Huang, Z. & Wang, L., 2018. Anisotropic 3-D ray tracing and its application to Japan subduction zone. *J. Geophys. Res. Solid Earth*, **123**, https://doi.org/10.1029/2017JB015321.

Hirahara, K. & Ishikawa, Y., 1984. Travel time inversion for three-dimensional P-wave velocity anisotropy, *J. Phys. Earth*, **32**, 197-218.

Hua, Y., Zhao, D. & Xu, Y., 2017. P wave anisotropic tomography of the Alps, *J. Geophys. Res. Solid Earth*, **122**, 4509–4528, doi:10.1002/2016JB013831.

Ishise, M. & Oda, H., 2005. Three-dimensional structure of P-wave anisotropy beneath the Tohoku district, northeast Japan, *J. Geophys. Res.*, **110**, B07304, doi:10.1029/2004JB003599.

Ishise, M. & Oda, H., 2008. Subduction of the Philippine Sea slab in view of *P*-wave anisotropy, *Phys. Earth planet. Inter.*, **166,** 83–96.

Ishise M., Miyake, H. & Koketsu, K., 2015. Dual subduction tectonics and plate dynamics of central Japan Shown by three- dimensional P-wave anisotropic structure, *Phys. Earth planet. Inter.*, **244**, 49-68, http://dx.doi.org/10.1016/j.pepi.2015.03.008.

Karousová, H., Plomerová, J., & Babuška, V., 2013. Upper-mantle structure beneath the southern Bohemian Massif and its surroundings imaged by high-resolution tomography, *Geophys. J. Int.*, **194**, 1203–1215, doi:10.1093/gji/ggt159.

Karousová, H., Plomerová, J. & Vecsey, L., 2012. Seismic tomography of the upper mantle beneath the north-eastern Bohemian Massif (central Europe), *Tectonophysics*, **564–565,** 1–11.

Kissling, E., 1988. Geotomography with local earthquake data, *Rev. Geophys.*, **26**, 659-698.

Koulakov, I., Kaban, M.K., Tesauro, M. & Cloetingh, S., 2009. P- and S- velocity anomalies in the upper mantle beneath Europe from tomographic inversion of ISC data. *Geophys. J. Int.*, **179**, 345-366.

Koulakov, I., Kukarina, E., Fathi, I., Khrepy, S. & Al-Arifi, N., 2015. Anisotropic tomography of Hokkaido reveals delamination-induced flow above a subducting slab, *J. Geophys. Res.*, **120**, 3219–3239.

Lippitsch, R., Kissling, E. & Ansorge, J., 2003. Upper mantle structure beneath the Alpine orogen from high-resolution teleseismic tomography, *J. Geophys. Res.*, **108**, 2376.

Liu, X. & Zhao, D., 2016. Seismic velocity azimuthal anisotropy of the Japan subduction zone: Constraints from P and S wave traveltimes, *J. Geophys. Res.*, **121**, 5086–5115.

Liu, X. & Zhao, D., 2017. P-wave anisotropy, mantle wedge flow and olivine fabrics beneath Japan, *Geophys. J. Int.*, **210**, 1410-1431, doi:10.1093/gji/ggx247.

Long, M.D. & Becker, T.W., 2010. Mantle dynamics and seismic anisotropy, *Earth Planet. Sci. Lett.*, **297**, 341–354.

Long, M.D. & Silver, P.G., 2009. Shear-wave splitting and mantle anisotropy: measurements, interpretations, and new directions, *Surv. Geophys.*, **30,** 407–461.

Mainprice, D., 2007. Seismic anisotropy of the deep Earth from a mineral and rock physics perspective, in *Treatise on Geophysics*, pp. 437--491, ed. Schubert, G., Elsevier, Oxford, U. K.

Maupin, V. & Park, J., 2007. Theory and observations–Wave propagation in anisotropic media, in *Treatise on Geophysics*, vol.1, Seismology and the Structure of the Earth, pp. 289--321, ed. Romanowicz, B. & Dziewonski, A., Elsevier, Boston, Mass., doi:10.1016/B978-044452748-6.00007-9.

Margheriti, L., Pondrelli, S., Piccinini, D., Agostinetti, N.P., Giovani, L., Salimbeni, S., Lucente, F.P., Amato, A., Baccheschi, P., Park, J., Brandon, M., Levin, V., Plomerová, J., Jedlička, P., Vecsey, L., Babuška, V., Fiaschi, A., Carpani, B. & Ulbricht, P., 2006. The subduction structure of the Nothern Apennines: results from the RETREAT seismic deployment, *Annals of geophysics*, **49**, 1119-1131.

Menke, W., 2015. Equivalent heterogeneity analysis as a tool for understanding the resolving power of anisotropic travel-time tomography, *Bull. Seism. Soc. Am.*, **105**, 719–733.

Miller, M.S. & Piana Agostinetti, N., 2012. Insights into the evolution of the Italian lithospheric structure from S receiver function analysis, *Earth Planet. Sci. Lett.*, **345**, 49-59, doi:10.1016/j.epsl.2012.06.028.

Munzarová, H., Plomerová, J., Babuška, V. & Vecsey, L., 2013. Upper-mantle fabrics beneath the Northern Apennines revealed by seismic anisotropy, *Geochem. Geophys. Geosyst.*, **14**, 1156–1181, http://dx.doi.org/10.1002/ggge.20092.

Munzarová, H., Plomerová, J. & Kissling, E., 2018. Novel anisotropic teleseismic body-wave tomography code AniTomo to illuminate heterogeneous anisotropic upper mantle: Part I – Theory and inversion tuning with realistic synthetic data, *Geophys. J. Int.*, **215** (1), 524-545, http://dx.doi.org/10.1093/gji/ggy296.

Munzarová, H., Plomerová, J., Kissling, E., Vecsey, L. & Babuška, V., 2018. Novel anisotropic teleseismic body-wave tomography code AniTomo to illuminate heterogeneous anisotropic upper mantle: Part II - Application to data of passive seismic experiment LAPNET in northern Fennoscandia, *Geophys. J. Int.*, 215 (2), 1388-1409, http://dx.doi.org/10.1093/gji/ggy327.

Park, J. & Levin, V., 2002. Seismic anisotropy: Tracing plate dynamics in the mantle, *Science*, **296**, 485-489, doi:10.1126/science.1067319.

Piromallo, C. & Morelli, A., 2003. P wave tomography of the mantle under the Alpine-Mediterranean area, *J. Geophys. Res.*, **108(B2)**, 2065.

Plomerová, J. & Babuška, V., 2010. Long memory of mantle lithosphere fabric-European LAB constrained from seismic anisotropy, *Lithos*, **120,** 131–143, doi:10.1016/j.lithos.2010.01.008.

Plomerová, J., Achauer, U., Babuška, V., Granet., M. & BOHEMA W.G., 2003. Passive seismic experiment to study lithosphere-asthenosphere system in the western part of the Bohemian Massif, *Stud. Geophys. Geod.*, **47**, 691-701.

Plomerová, J., Achauer, U., Babuška, V. & Vecsey, L., 2007. Upper mantle beneath the Eger Rift (Central Europe): plume or asthenosphere upwelling?, *Geophys. J. Int.*, **169(2)**, 675-682.

Plomerová, J., Babuška, V., Vecsey, L., Kouba, D. & TOR working group, 2002. Seismic anisotropy of the lithosphere around the Trans-European Suture Zone (TESZ) based on teleseismic body-wave data of the Tor experiment, *Tectonophysics*, **360**, 89-114.

Plomerová, J., Margheriti, L., Park, J., Babuška, V., Pondrelli, S., Vecsey, L., Piccinini, D., Levin, V., Baccheschi, P. & Salimbeni, S., 2006. Seismic Anisotropy beneath the Northern Apennines (Italy): Mantle Flow or Lithosphere Fabric? *Earth Planet. Sci. Lett.* **247,** 157-170.

Plomerová, J., Munzarová, H., Vecsey, L., Kissling, E., Achauer, U. & Babuška, V., 2016. Cenozoic volcanism in the Bohemian Massif in the context of P-and S-velocity high-resolution teleseismic tomography of the upper mantle, *Geochem. Geophys. Geosyst.*, **17** (8), 3326–3349, http://dx.doi.org/10.1002/2016GC006318.

Plomerová, J., Vecsey, L., Babuška, V. & LAPNET working group, 2011. Domains of Archean mantle lithosphere deciphered by seismic anisotropy – Inferences from the LAPNET array in northern Fennoscandia, *Solid Earth*, **2**, 303–313, doi:10.5194/se-2-303-2011.

Plomerová, J., Vecsey, L. & Babuška, V., 2012. Mapping seismic anisotropy of the lithospheric mantle beneath the northern and eastern Bohemian Massif (central Europe), *Tectonophysics*, **564–565,** 38–53.

Salimbeni, S., Pondrelli, S., Margheriti, L., Park, J. & Levin, V., 2008. SKS splitting measurements beneath Northern Apennines region: A case of oblique trench-retreat, *Tectonophysics*, **462**, 68-82.

Sandoval, S., Kislling, E., Ansorge, J. & SVEKALAPKO Seismic Tomography working Group, 2004. High-resolution body wave tomography beneath the SVEKALAPKO array - II. Anomalous upper mantle

structure beneath the central Baltic Shield, *Geophys. J. Int.*, **157**, 200-214, doi:10.1111/j.1365-246X.2004.02131.x.

Savage, M.K., 1999. Seismic anisotropy and mantle deformation: what have we learned from shear wave splitting?, *Rev. Geophys.*, **37,** 65–106.

Shomali, Z.H., Roberts, R.G., Pedersen, L.B. & the TOR Working Group, 2006. Lithospheric structure of the Tornquist Zone resolved by nonlinear P and S teleseismic tomography along the TOR array, *Tectonophysics*, **416,** 133–149.

Šílený, J. & Plomerová, J., 1996. Inversion of shear-wave splitting parameters to retrieve three-dimensional orientation of anisotropy in continental lithosphere, *Phys. Earth planet. Int.*, **95**, 277–292.

Silvennoinen, H., Kozlovskaya, E. & Kissling, E., 2016. POLENET/LAPNET teleseismic *P* wave travel time tomography model of the upper mantle beneath northern Fennoscandia, *Solid Earth*, **7**, 425-439, doi:10.5194/se-7-425-2016.

Silver, P.G., 1996. Seismic anisotropy beneath the continents: Probing the depths of geology, *Annu. Rev. Earth Planet. Sci.*, **24**, 385–432, doi:10.1146/annurev.earth.24.1.385.

Silver, P.G. & Chan, W.W., 1991. Shear wave splitting and subcontinental mantle deformation, *J. Geophys. Res.*, **96**, 16429-16454, doi:10.1029/91JB00899.

Sobolev, S., Gresillaud, A. & Cara, M., 1999. How robust is isotropic delay time tomography for anisotropic mantle?, *Geophys. Res. Lett.*, **26** (4), 509–512.

Tian, Y. & Zhao, D., 2013. Reactivation and mantle dynamics of North China Craton: Insight from P-wave anisotropy tomography, *Geophys. J. Int.*, **195**, 1796–1810.

Vecsey, L., Plomerová, J., Kozlovskaya, E. & Babuška, V., 2007. Shear-wave splitting as a diagnostic of varying upper mantle structure beneath south-eastern Fennoscandia, *Tectonophysics*, **438**, 57–77, doi:10.1016/j.tecto.2007.02.017.

Wang, J. & Zhao, D., 2008. P-wave anisotropic tomography beneath Northeast Japan, *Phys. Earth planet. Inter.*, **170**, 115–133.

Wang, J. & Zhao, D., 2012. P wave anisotropic tomography of the Nankai subduction zone in Southwest Japan, *Geochem. Geophys. Geosyst.*, **13**, Q05017.

Weiland, C.M., Steck, L.K., Dawson, P.B. & Korneev, V.A., 1995. Nonlinear teleseismic tomography at Long Valley caldera, using three-dimensional minimum travel time ray tracing, *J. Geophys. Res.*, **100**, 20379–20390.

Wortel, M.J.R. & Spakman, W., 2000. Subduction and slab detachment in the Mediterranean-Carpathian region, *Science*, **290**, 910–917.

2. Theory

The primary target of this Chapter is to derive an equation for velocity of P waves propagating through weakly anisotropic medium with hexagonal symmetry that is oriented generally in 3D. The derivation of the equation, for which we use a first-order approximation of the equation of motion for plane waves, follows in general Backus (1965), but with consideration of different assumptions on anisotropy and direction of wave propagation (Sections 2.1 – 2.3). Then we establish a linearized relation between the P-wave travel-time residuals and perturbations of the model parameters related to their reference values (Section 2.4). Finally, we show an application of the derived equations to a given set of elastic parameters approximating peridotite aggregates, i.e., typical rocks of the Earth's upper mantle (Section 2.5).

2.1 P-wave velocity in weakly anisotropic media

Following common notations, we introduce density-normalized fourth-order tensor of elastic parameters for a weakly anisotropic medium

$$\Gamma_{ijkl} = \frac{C_{ijkl}}{\rho}, \tag{1}$$

where C_{ijkl} are elements of the stiffness tensor and ρ is density. The density-normalized elastic parameters of a weakly anisotropic medium can be decomposed into

$$\Gamma_{ijkl} = \Gamma^{iso}{}_{ijkl} + \gamma_{ijkl}, \tag{2}$$

where γ_{ijkl} represent small variations from the isotropic elastic parameters to adjust for weak anisotropy. The density-normalized elastic parameters for an isotropic medium are

$$\Gamma^{iso}{}_{ijkl} = \frac{1}{\rho}\left[\lambda\delta_{ij}\delta_{kl} + \mu\left(\delta_{ik}\delta_{jl} + \delta_{il}\delta_{jk}\right)\right], \tag{3}$$

where λ and μ symbolize Lamé coefficients and δ_{ij} is Kronecker delta.

Equation of motion for a plane wave in homogeneous anisotropic medium has a form of eigensystem

$$B_{il}g_l = Bg_i, \tag{4}$$

where B_{il} is Christoffel matrix, B represents an eigenvalue and g_i is a corresponding unit eigenvector. Specifying the Christoffel matrix for a weakly anisotropic medium according to relation (2), we get

$$B_{il} = \Gamma_{ijkl}n_j n_k = \left(\Gamma^{iso}{}_{ijkl} + \gamma_{ijkl}\right)n_j n_k = B^{iso}{}_{il} + b_{il}, \tag{5}$$

where $\vec{n} = (n_1, n_2, n_3)$ is a unit vector characterizing a direction of wave propagation. The isotropic part of Christoffel matrix is, thus, defined as

$$B^{iso}{}_{il} = \frac{\lambda + \mu}{\rho} n_i n_l + \frac{\mu}{\rho} \delta_{il} \tag{6}$$

and the anisotropic part of Christoffel matrix as

$$b_{il} = \gamma_{ijkl} n_j n_k \,. \tag{7}$$

From (4), we express the eigenvalue as

$$B = B_{il} g_i g_l \,. \tag{8}$$

Let's write the eigenvalue and the eigenvector as

$$B = B^{(0)} + B^{(1)} + B^{(2)} + \ldots, \tag{9}$$

$$g_i = g_i{}^{(0)} + g_i{}^{(1)} + g_i{}^{(2)} + \ldots \,. \tag{10}$$

$B^{(0)}$ and $g_i{}^{(0)}$ represent solution of (4) for the isotropic medium, i.e., for $B_{il} = B^{iso}{}_{il}$, while $B^{(n)}$ and $g_i{}^{(n)}$ are the terms of n^{th} order. Inserting (5), (9) and (10) into (4), the 1st order perturbation $B^{(1)}$ of the eigenvalue of Christoffel matrix is

$$B^{(1)} = b_{il} g_i{}^{(0)} g_l{}^{(0)} \,. \tag{11}$$

In the case of P waves, for which $g_i{}^{(0)} = n_i$, we get

$$B^{(1)} = b_{il} n_i n_l = \gamma_{ijkl} n_i n_j n_k n_l \,. \tag{12}$$

Then the square of the anisotropic P-wave velocity, expressed to the same order as $B^{(1)}$, is

$$B = v^2 = c^2 + B^{(1)}, \tag{13}$$

where v is P-wave velocity for the weakly anisotropic medium and c is P-wave velocity for a background isotropic medium, i.e., $B^{(0)} = c^2 = \frac{\lambda + 2\mu}{\rho}$. Since $B^{(1)} << c^2$, let us approximate the anisotropic velocity with the use of $(1 + x)^p \approx 1 + px$, where x and p are real numbers, as

$$v = c + \frac{B^{(1)}}{2c} \,. \tag{14}$$

Term $B^{(1)}$ gets form according to the symmetry of the weak anisotropy.

2.2 Hexagonal symmetry of anisotropy

An anisotropic medium with hexagonal symmetry, where the axis is parallel with the x_3-axis, can be described by 5 elastic coefficients A, C, F, L, and N, which in matrix notation is

$$\begin{pmatrix} A & A-2N & F & 0 & 0 & 0 \\ A-2N & A & F & 0 & 0 & 0 \\ F & F & C & 0 & 0 & 0 \\ 0 & 0 & 0 & L & 0 & 0 \\ 0 & 0 & 0 & 0 & L & 0 \\ 0 & 0 & 0 & 0 & 0 & N \end{pmatrix}. \tag{15}$$

Thus, non-zero variations of the density-normalized elastic parameters adjusting for the weak anisotropy defined in equation (2) are only

$$\begin{aligned} &\gamma_{1111} = \gamma_{2222}, \\ &\gamma_{3333}, \\ &\gamma_{1122}, \\ &\gamma_{1133} = \gamma_{2233}, \\ &\gamma_{1313} = \gamma_{2323}, \\ &\gamma_{1212} = \frac{1}{2}(\gamma_{1111} - \gamma_{1122}). \end{aligned} \tag{16}$$

Considering an isotropic medium with elastic parameters

$$\begin{pmatrix} \lambda+2\mu & \lambda & \lambda & 0 & 0 & 0 \\ \lambda & \lambda+2\mu & \lambda & 0 & 0 & 0 \\ \lambda & \lambda & \lambda+2\mu & 0 & 0 & 0 \\ 0 & 0 & 0 & \mu & 0 & 0 \\ 0 & 0 & 0 & 0 & \mu & 0 \\ 0 & 0 & 0 & 0 & 0 & \mu \end{pmatrix}, \tag{17}$$

we can express the small variations γ_{ijkl} as

$$\begin{aligned} \gamma_{1111} &= \frac{1}{\rho}[A - (\lambda + 2\mu)], \\ \gamma_{3333} &= \frac{1}{\rho}[C - (\lambda + 2\mu)], \\ \gamma_{1122} &= \frac{1}{\rho}[(A - 2N) - \lambda], \\ \gamma_{1133} &= \frac{1}{\rho}(F - \lambda), \\ \gamma_{1313} &= \frac{1}{\rho}(L - \mu). \end{aligned} \tag{18}$$

Introducing coefficients γ_{ijkl} into equation (12) and employing $n_i n_i = 1$, we get

$$B^{(1)} = \gamma_{1111} + 2(\gamma_{1133} + 2\gamma_{1313} - \gamma_{1111}){n_3}^2 + (\gamma_{1111} + \gamma_{3333} - 2\gamma_{1133} - 4\gamma_{1313}){n_3}^4. \tag{19}$$

Substituting $n_3 = \cos\alpha$, where α is angle between the vector of propagation direction and the symmetry axis, we get

$$B^{(1)} = \gamma_{1111} + 2(\gamma_{1133} + 2\gamma_{1313} - \gamma_{1111})\cos^2\alpha + (\gamma_{1111} + \gamma_{3333} - 2\gamma_{1133} - 4\gamma_{1313})\cos^4\alpha \,. \quad (20)$$

A 2π-periodic real function $s(x)$ of real variable x that can be integrated on interval $[-\pi, \pi]$ can be expressed as a Fourier series

$$s_N(x) = \frac{a_0}{2} + \sum_{n=1}^{N}[a_n \cos(nx) + b_n \sin(nx)], \quad (21)$$

where $N > 0$ and n are integer numbers. The Fourier coefficients are computed as follows

$$\begin{aligned} a_n &= \frac{1}{\pi}\int_{-\pi}^{\pi} s(x)\cos(nx)dx, \quad n \geq 0, \\ b_n &= \frac{1}{\pi}\int_{-\pi}^{\pi} s(x)\sin(nx)dx, \quad n > 0. \end{aligned} \quad (22)$$

By evaluating Fourier coefficients for $B^{(1)}(\alpha)$, we obtain only three non-zero coefficients

$$\begin{aligned} a_0 &= \frac{1}{\pi}\int_{-\pi}^{\pi} B^{(1)}(\alpha)d\alpha = \frac{1}{4}[3(\gamma_{1111} + \gamma_{3333}) + 2(\gamma_{1133} + 2\gamma_{1313})], \\ a_2 &= \frac{1}{\pi}\int_{-\pi}^{\pi} B^{(1)}(\alpha)\cos(2\alpha)d\alpha = \frac{1}{2}(\gamma_{3333} - \gamma_{1111}), \\ a_4 &= \frac{1}{\pi}\int_{-\pi}^{\pi} B^{(1)}(\alpha)\cos(4\alpha)d\alpha = \frac{1}{8}[\gamma_{1111} + \gamma_{3333} - 2(\gamma_{1133} + 2\gamma_{1313})]. \end{aligned} \quad (23)$$

Formula (20) can be thus written as a finite Fourier series

$$B^{(1)} = P + Q\cos 2\alpha + R\cos 4\alpha, \quad (24)$$

where the coefficients are

$$\begin{aligned} P &= \frac{a_0}{2} = \frac{1}{8}[3(\gamma_{1111} + \gamma_{3333}) + 2(\gamma_{1133} + 2\gamma_{1313})], \\ Q &= a_2 = \frac{1}{2}(\gamma_{3333} - \gamma_{1111}), \\ R &= a_4 = \frac{1}{8}[\gamma_{1111} + \gamma_{3333} - 2(\gamma_{1133} + 2\gamma_{1313})], \end{aligned} \quad (25)$$

or with the use of the isotropic and anisotropic elastic coefficients as in equations (18)

$$P = \frac{1}{8\rho}\left[3(A+C)+2(F+2L)\right] - \frac{\lambda+2\mu}{\rho}, \tag{26a}$$

$$Q = \frac{1}{2\rho}(C-A), \tag{26b}$$

$$R = \frac{1}{8\rho}\left[A+C-2(F+2L)\right]. \tag{26c}$$

Formula (24) is an exact expression of (20), which we can prove by expanding the multiple-argument cosines in (24).

Then, anisotropic velocity (14) is expressed as follows

$$v = c + \frac{P}{2c} + \frac{Q}{2c}\cos 2\alpha + \frac{R}{2c}\cos 4\alpha . \tag{27}$$

According to Ishise & Oda (2005): "Observations of azimuth variations of the P_n velocity suggested that in the upper mantle the $\cos 4\alpha$ term is negligibly small in comparison with other terms (e.g., Raitt *et al.* 1969)." We will come to a similar conclusion in Section 2.5, where we evaluate coefficients Q and R for elastic parameters of hexagonal-symmetry approximations of originally orthorhombic peridotite aggregates (Ben Ismail & Mainprice 1998). Thus, neglecting the $\cos 4\alpha$ term, equation (27) becomes

$$v = c + \frac{P}{2c} + \frac{Q}{2c}\cos 2\alpha . \tag{28}$$

In general, we can separate the anisotropic velocity into a sum of isotropic component $\bar{v}$ and directional component δv

$$v = \bar{v} + \delta v, \tag{29}$$

where we define the isotropic component as $\bar{v} = \frac{v^{\max} + v^{\min}}{2}$.

Comparing (28) and (29), it is obvious that

$$\bar{v} = c + \frac{P}{2c} \tag{30}$$

and

$$\delta v = \frac{Q}{2c}\cos 2\alpha . \tag{31}$$

Considering relation (24) and $B^{(1)} << c^2$, we see that $P << c^2$ and $Q << c^2$ is valid as well. Hence, raising (30) to the second power, neglecting the P^2 term and comparing the result with (26a), we get relation for $\bar{v}^2$

$$\bar{v}^2 = \frac{1}{8\rho}\left[3(A+C)+2(F+2L)\right]. \tag{32}$$

Similarly, because of $P \ll c^2$ and $Q \ll c^2$, the isotropic velocity c in the denominator of (31) can be substituted with the isotropic component of velocity $\bar{v}$ without a loss of accuracy

$$\delta v = \frac{Q}{2\bar{v}}\cos 2\alpha\,. \tag{33}$$

Defining an absolute value of strength of anisotropy as

$$k = \frac{v^{\max} - v^{\min}}{\bar{v}} \tag{34}$$

and taking into account the form of directional component (33) of the P-wave velocity in the weakly anisotropic medium with hexagonal symmetry, we can express the strength of anisotropy as

$$k = \frac{Q}{\bar{v}^2}\,, \tag{35}$$

or

$$k = \frac{4(C-A)}{3(A+C)+2(F+2L)}\,. \tag{36}$$

The value of strength is $k \geq 0$ for $C \geq A$, corresponding to a hexagonal symmetry with the high-velocity *a* axis, or $k < 0$ for $C < A$, corresponding to the low-velocity *b* axis. Thus, we may write the anisotropic velocity (28) as

$$v = \bar{v}\left(1+\frac{k}{2}\cos 2\alpha\right) \tag{37}$$

using the isotropic component of velocity and the strength of anisotropy.

2.3 Orientation of the symmetry axis generally in 3D

The following step is to relate angle α with the angles defining a direction of wave propagation and an orientation of the hexagonal-symmetry axis (Fig. 2.1). Let us define unit propagation vector $\vec{n}$ as

$$\begin{aligned}\vec{n} &= (n_1, n_2, n_3) = (\sin(\pi - i)\sin(\varphi - \pi), \sin(\pi - i)\cos(\varphi - \pi), \cos(\pi - i)),\\ \vec{n} &= (-\sin i \sin\varphi, -\sin i \cos\varphi, -\cos i),\end{aligned} \tag{38}$$

where i and φ are wave incidence angle, measured upward from the positive *z*-axis (downward vertical) to the incoming ray, and wave back-azimuth, measured clockwise from the positive *y*-axis (to the north) to the horizontal projection of the incoming ray, respectively.

We describe the symmetry-axis orientation with unit vector $\vec{s}$

$$\vec{s} = (s_1, s_2, s_3) = (\sin\theta\sin\lambda, \sin\theta\cos\lambda, \cos\theta),\ \theta \in \left\langle 0, \frac{\pi}{2} \right\rangle, \tag{39}$$

where θ and λ are axis inclination, measured upward from the positive *z*-axis to the symmetry axis, and azimuth, measured clockwise from the positive *y*-axis to the horizontal projection of the symmetry axis, respectively.

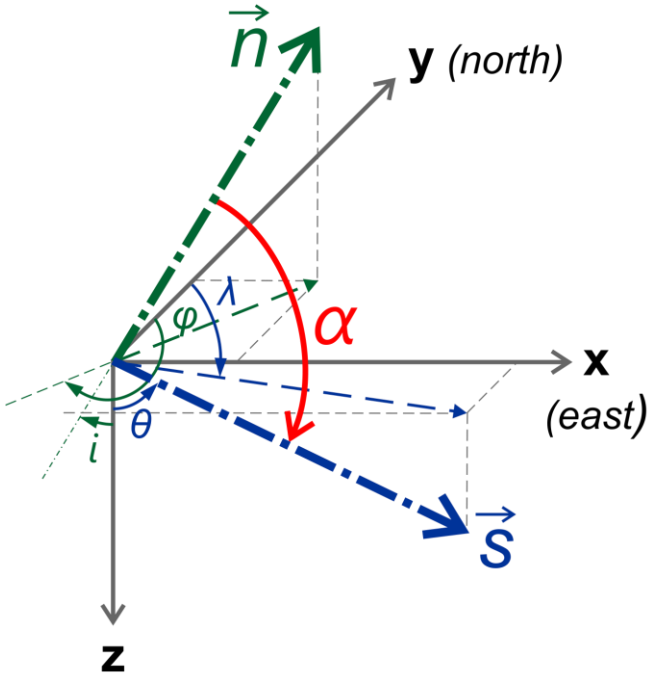

Figure 2.1 Definition of the Cartesian coordinate system for the purpose of the anisotropic tomography. The *x*, *y* and *z* axes are oriented eastward, northward and downward, respectively. Angles λ and θ determine azimuth and inclination of hexagonal-symmetry axis vector $\vec{s}$, respectively. The wave-propagation direction is represented by unit vector $\vec{n}$. Angles φ and i mark back-azimuth and angle of propagation of the wave, respectively. Angle α represents an angle between the symmetry axis and the wave-propagation direction.

Cosine of angle α, i.e., angle between vectors $\vec{n}$ and $\vec{s}$ (Fig. 2.1), is equal to the scalar product of these two vectors

$$\begin{aligned} \cos\alpha &= \vec{n}\cdot\vec{s} = -\sin i\sin\varphi\sin\theta\sin\lambda - \sin i\cos\varphi\sin\theta\cos\lambda - \cos i\cos\theta, \\ \cos\alpha &= -\sin i\sin\theta\cos(\varphi-\lambda) - \cos i\cos\theta. \end{aligned} \tag{40}$$

Introducing (40) into (37) and using $\cos 2\alpha = 2\cos^2\alpha - 1$, we obtain the equation for velocity of a P wave propagating in a weak anisotropic media with hexagonal-symmetry axis oriented generally in 3D

$$v = \bar{v}\cdot\left\{1 + k\left[(\sin i\sin\theta\cos(\varphi-\lambda) + \cos i\cos\theta)^2 - \tfrac{1}{2}\right]\right\}. \tag{41}$$

Expression (41) is valid without any further assumption, e.g., whether anisotropic medium has the symmetry axis along the high-velocity of low-velocity direction.

2.4 Linearized relation between the P-wave travel-time residuals and the anisotropic-velocity parameters

The integral evaluating travel time of a wave within a volume studied is usually approximated by a sum of partial travel times corresponding to relatively short segments of the ray path in seismic travel-time tomography

$$t = \int_{ray} \frac{ds}{v} \quad \rightarrow \quad t = \sum_{segments} t^{seg} = \sum_{segments} \frac{s^{seg}}{v^{seg}}, \tag{42}$$

where s^{seg} is a ray segment and v^{seg} is anisotropic velocity (41) representative for the segment.

The teleseismic travel-time tomography employs travel-time residuals as input data

$$\Delta t = t_{obs} - t_{cal}, \tag{43}$$

where t_{obs} is the observed travel time and t_{cal} is the travel time calculated according to a reference velocity model.

Similarly, as the travel time in (42), also the travel-time residual of a given wave can be expressed by a sum of residuals for the individual ray segments

$$\Delta t = \sum_{segments} \Delta t^{seg}. \tag{44}$$

In the following part, we associate a travel-time residual created along a segment of the ray path with the perturbations of the anisotropic parameters that are representative for that segment. For the sake of simplicity, we omit the superscript "*seg*" in the following equations. The linearized relation between the data and the model parameters is

$$\Delta t = \frac{\partial t}{\partial \bar{v}} \Delta \bar{v} + \frac{\partial t}{\partial k} \Delta k + \frac{\partial t}{\partial \theta} \Delta \theta + \frac{\partial t}{\partial \lambda} \Delta \lambda. \tag{45}$$

The individual partial derivatives of the travel time fixed to the reference values are

$$\frac{\partial t}{\partial \bar{v}} = \frac{\partial t}{\partial v} \cdot \frac{\partial v}{\partial \bar{v}} = -\frac{s}{{v_0}^2} \cdot \left\{ 1 + k_0 \left[(\sin i \sin\theta_0 \cos(\varphi - \lambda_0) + \cos i \cos\theta_0)^2 - \frac{1}{2} \right] \right\} =$$

$$= -\frac{s}{v_0 \cdot \bar{v}_0} \tag{46}$$

for the isotropic component of velocity,

$$\frac{\partial t}{\partial k} = \frac{\partial t}{\partial v} \cdot \frac{\partial v}{\partial k} = -\frac{s}{v_0} \cdot \left[(\sin i \sin\theta_0 \cos(\varphi - \lambda_0) + \cos i \cos\theta_0)^2 - \frac{1}{2} \right] \tag{47}$$

for the strength of anisotropy,

$$\frac{\partial t}{\partial \theta} = \frac{\partial t}{\partial v} \cdot \frac{\partial v}{\partial \theta} = -\frac{s}{v_0} \cdot 2k_0(\sin i \sin\theta_0 \cos(\varphi - \lambda_0) + \cos i \cos\theta_0) \cdot$$

$$\cdot (\sin i \cos\theta_0 \cos(\varphi - \lambda_0) - \cos i \sin\theta_0) \tag{48}$$

for the azimuth of symmetry-axis orientation,

$$\frac{\partial t}{\partial \lambda} = \frac{\partial t}{\partial v} \cdot \frac{\partial v}{\partial \lambda} = -\frac{s}{v_0} \cdot 2k_0(\sin i \sin\theta_0 \cos(\varphi - \lambda_0) + \cos i \cos\theta_0) \cdot$$

$$\cdot \sin i \sin\theta_0 \sin(\varphi - \lambda_0) \tag{49}$$

for the inclination of symmetry-axis orientation, and with $v_0 = v(\bar{v}_0, k_0, \theta_0, \lambda_0)$ as a reference anisotropic velocity

$$v_0 = \bar{v}_0 \cdot \left\{1 + k_0 \left[(\sin i \sin\theta_0 \cos(\varphi - \lambda_0) + \cos i \cos\theta_0)^2 - \frac{1}{2}\right]\right\}. \tag{50}$$

Equation (45) established for all the station-event P-wave travel-time residuals forms a system of linearized equations that we iteratively solve with the damped least-square method (Menke 1984)

$$\boldsymbol{m} = \left(\mathbf{A^T W_D A} + \varepsilon^2 \mathbf{W_M}\right)^{-1} \mathbf{A^T W_D} \boldsymbol{d}, \tag{51}$$

where $\boldsymbol{m}$ is a vector of model parameters $\Delta\bar{v}$, Δk, $\Delta\lambda$ and $\Delta\theta$ at all grid nodes. Data vector $\boldsymbol{d}$ contains travel-time residuals Δt and matrix $\mathbf{A}$ stores the partial derivatives from equation (45). Observation errors are considered in weighting matrix $\mathbf{W_D}$. Damping factor ε^2 and horizontal smoothing $\mathbf{W_M}$ stabilize the ill-posed problem. All these matrices have a block structure. During the calculations, the inverse in equation (51) is approximated by truncated singular value decomposition and for the ray-tracing, 3D bending technique Simplex (Steck & Prothero 1991) is applied.

2.5 Anisotropic velocity for aggregates of the upper-mantle peridotites

In this Section, we evaluate isotropic component of velocity (32) and strength of anisotropy (36) for elastic parameters characterizing peridotite aggregates, a typical rock of the upper mantle. Ben Ismail & Mainprice (1998) examined 110 samples of peridotites gathered, e.g, from fast spreading ridges or regions of subduction volcanism and they showed that the orthorhombic symmetry with the following stiffness parameters expressed in GPa

$$\begin{pmatrix} 195.45 & 71.11 & 72.08 & 0 & 0 & 0 \\ 71.11 & 236.91 & 72.37 & 0 & 0 & 0 \\ 72.08 & 72.37 & 205.92 & 0 & 0 & 0 \\ 0 & 0 & 0 & 71.37 & 0 & 0 \\ 0 & 0 & 0 & 0 & 62.99 & 0 \\ 0 & 0 & 0 & 0 & 0 & 69.77 \end{pmatrix}$$

well represents the fabric of the upper-mantle peridotite aggregates.

As the highest and the lowest velocity for this anisotropy differ about less than 10 % (Fig. 2.2), an approximation of the orthorhombic symmetry by a hexagonal symmetry with either high-velocity *a* or low-velocity *b* symmetry axis appears useful for real applications with respect to the number and distribution of seismic rays available (e.g., Šílený & Plomerová 1996; Babuška & Plomerová 2006). The stiffness parameters measured in GPa for a hexagonal symmetry with the high-velocity *a* symmetry axis (direction of lineation) and the low-velocity plane (foliation) are

$$\begin{pmatrix} 200.42 & 72.34 & 71.74 & 0 & 0 & 0 \\ 72.34 & 200.42 & 71.74 & 0 & 0 & 0 \\ 71.74 & 71.74 & 236.91 & 0 & 0 & 0 \\ 0 & 0 & 0 & 70.57 & 0 & 0 \\ 0 & 0 & 0 & 0 & 70.57 & 0 \\ 0 & 0 & 0 & 0 & 0 & 64.04 \end{pmatrix}$$

and for the case with the low-velocity *b* symmetry axis and the high-velocity plane, the parameters are

$$\begin{pmatrix} 220.78 & 73.00 & 71.60 & 0 & 0 & 0 \\ 73.00 & 220.78 & 71.60 & 0 & 0 & 0 \\ 71.60 & 71.60 & 195.45 & 0 & 0 & 0 \\ 0 & 0 & 0 & 66.38 & 0 & 0 \\ 0 & 0 & 0 & 0 & 66.38 & 0 \\ 0 & 0 & 0 & 0 & 0 & 73.89 \end{pmatrix}.$$

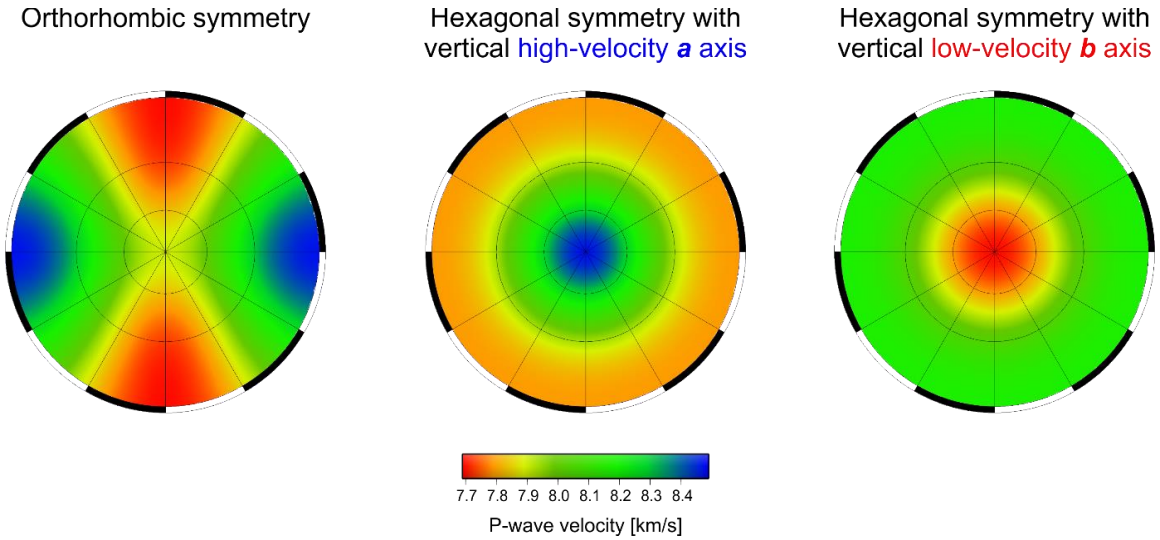

Figure 2.2 P-wave velocity for peridotite aggregates approximated with different types of symmetry of anisotropy and evaluated according to Christoffel equation (4). The elastic parameters of the orthorhombic symmetry follow Ben Ismail & Mainprice (1998) and the parameters for the two types of hexagonal symmetry with a vertical symmetry axis, approximating the orthorhombic symmetry, are according to Babuška & Plomerová (2006).

Let's evaluate coefficients Q (26b) and R (26c), isotropic component of velocity $\bar{v}$ (32) and strength of anisotropy k (36) and the dependence of anisotropic velocity (37) on the direction of wave propagation (Figs. 2.3 and 2.4) for the two sets of elastic parameters presented above and for density $\rho = 3.3$ g/cm^3.

***a*-type hexagonal anisotropy**:

$$Q = \frac{1}{2\rho}(C - A) = 5.53 \text{ km}^2/\text{s}^2$$

$$R = \frac{1}{8\rho}\left[A + C - 2(F + 2L)\right] = 0.44 \text{ km}^2/\text{s}^2$$

$$\bar{v} = \sqrt{\frac{1}{8\rho}\left[3(A + C) + 2(F + 2L)\right]} = 8.11 \text{ km/s}$$

$$k = \frac{4(C - A)}{3(A + C) + 2(F + 2L)} = 8.4\ \%$$

Amplitudes of the $\cos 2\alpha$ and $\cos 4\alpha$ terms, respectively, are

$$\frac{Q}{2\bar{v}} = 0.34 \text{ km/s},$$

$$\frac{R}{2\bar{v}} = 0.03 \text{ km/s}.$$

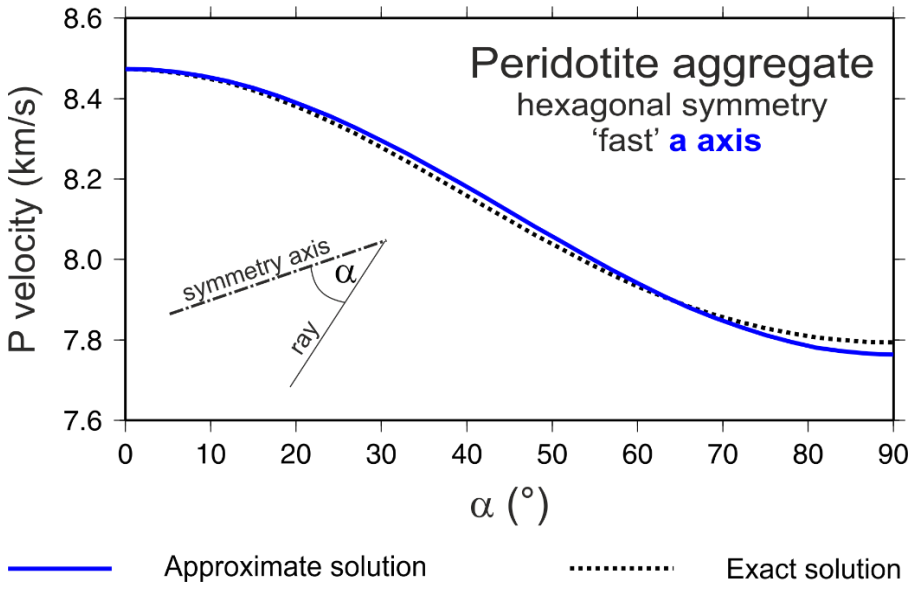

Figure 2.3 Comparison of P-wave velocities calculated according to approximate equation (37) assuming a weak anisotropy and those evaluated as the exact solution of Christoffel equation (4). The elastic coefficients chosen for this example of a hexagonal model with the *a* symmetry axis

correspond to peridotite aggregate, the most abundant mantle material (see, e.g., Ben Ismail & Mainprice 1998; Babuška & Plomerová 2006).

***b*-type hexagonal anisotropy**:

$$Q = \frac{1}{2\rho}(C - A) = \text{-3.84 km}^2/\text{s}^2$$

$$R = \frac{1}{8\rho}\left[A + C - 2(F + 2L)\right] = \text{0.28 km}^2/\text{s}^2$$

$$\bar{v} = \sqrt{\frac{1}{8\rho}\left[3(A + C) + 2(F + 2L)\right]} = \text{7.92 km/s}$$

$$k = \frac{4(C - A)}{3(A + C) + 2(F + 2L)} = \text{-6.1 \%} \quad \Rightarrow \quad \text{6.1 \%}$$

Amplitude of the $\cos 2\alpha$ and $\cos 4\alpha$ terms, respectively, are

$$\frac{Q}{2\bar{v}} = \text{-0.24 km/s} \quad \Rightarrow \quad \text{0.24 km/s,}$$

$$\frac{R}{2\bar{v}} = \text{0.02 km/s.}$$

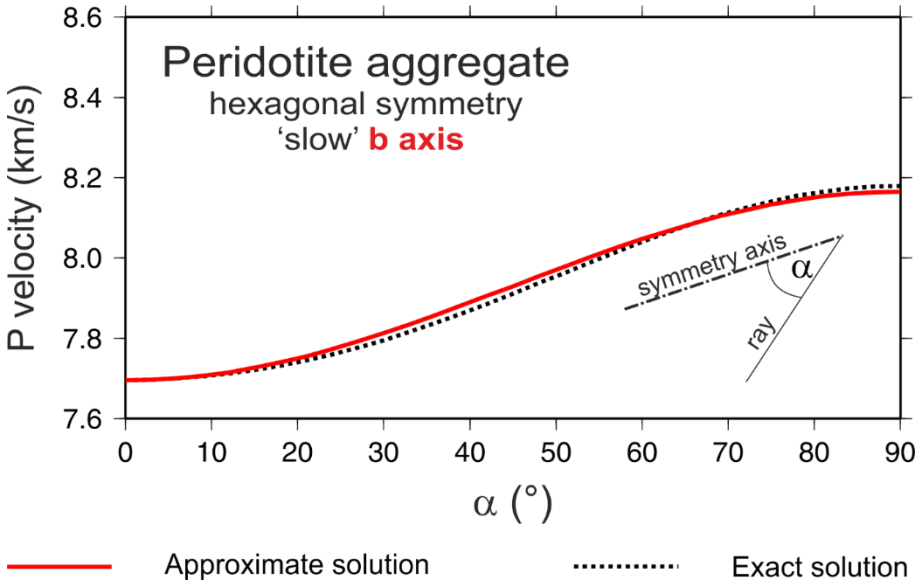

Figure 2.4 Comparison of P-wave velocities calculated according to approximate equation (37) assuming a weak anisotropy and those evaluated as the exact solution of Christoffel equation (4). The elastic coefficients chosen for this example of a hexagonal model with the *b* symmetry axis correspond to peridotite aggregate, the most abundant mantle material (see, e.g., Ben Ismail & Mainprice 1998; Babuška & Plomerová 2006).

Application of the equations derived in previous Sections to the elastic parameters characterizing peridotite aggregates shows that the approximate relation for P-wave velocity in weakly anisotropic media is sufficiently close to the exact solution, especially when we take accuracy of the seismic tomography into account.

References

Babuška, V. & Plomerová, J., 2006. European mantle lithosphere assembled from rigid microplates with inherited seismic anisotropy, *Phys. Earth Planet. Inter.* **158,** 264–280.

Backus, G.E., 1965. Possible forms of seismic anisotropy of the uppermost mantle under oceans, *J. Geophys. Res.*, **70**, 3429-3439.

Ben Ismail, W. & Mainprice, D., 1998. An olivine fabric database: an overview of upper mantle fabrics and mantle anisotropy, *Tectonophysics*, **296**, 145-157.

Ishise, M. & Oda, H., 2005. Three-dimensional structure of P-wave anisotropy beneath the Tohoku district, northeast Japan, *J. Geophys. Res.*, **110**, B07304, doi:10.1029/2004JB003599.

Menke, W., 1984. *Geophysical Data Analysis: Discrete Inverse Theory*, 1st edn, Academic Press, Inc., Orlando.

Raitt, R.W., Shor, G.G., Francis, T.J.G. & Morris, G.B., 1969. Anisotropy of the Pacific upper mantle, *J. Geophys. Res.*, **74**, 3095-9109.

Šílený, J. & Plomerová, J., 1996. Inversion of shear-wave splitting parameters to retrieve three-dimensional orientation of anisotropy in continental lithosphere, *Phys. Earth planet. Int.*, **95**, 277–292.

Steck, L.K. & Prothero, W.A., 1991. A 3-D ray-tracer for teleseismic body-wave arrival-times, *B. Seismol. Soc. Am.*, **81**, 1332-1339.

3. Directional variations of P-wave travel-time residuals due to anisotropy of the upper mantle – Modelling with the forward mode of AniTomo

Code AniTomo uses equations (41) and (42) (see Chapter 2) to calculate travel times of teleseismic P waves propagating through a given arbitrarily heterogeneous anisotropic model of the upper mantle. In this Chapter, we focus on the forward mode, during which the program evaluates the travel times without performing the inversion for model parameters. The forward mode is commonly used for a generation of data for synthetic tests of the inversion. We take advantage of the possibility to trace the rays and to evaluate anisotropic velocities to investigate how a specific heterogeneous anisotropic upper-mantle structure projects into the directional variations of the P-wave travel-time residuals. For that purpose, we design various models of the upper mantle consisting of homogeneous anisotropic blocks or layers, for which we calculate travel times for a set of P waves propagating from 24 regularly distributed teleseismic events (12 at epicentral distance of 40˚ and 12 at 80˚) to 11 stations arranged in a line with 20 km inter-station distance.

Subsequently, we follow the procedure for evaluation of directional terms of relative travel-time residuals (e.g., Babuška *et al.* 1993; Babuška & Plomerová 2006; Plomerová *et al.* 2011; 2012; Munzarová *et al.* 2013; Supplement 1). The procedure evaluates the relative travel-time residuals, i.e., normalized differences between the observed travel times (for the target model in our case) and the travel times for reference velocity model IASP'91 (Kennett & Engdahl 1991). The normalization minimizes the effects coming from outside the volume studied from the residuals. In a synthetic case, there are no sources of travel-time variations outside the volume studied. Then, we extract the directional terms from the travel-time residuals by subtracting the station directional mean, representing an average velocity beneath the station. The directional terms at a station express azimuth-incidence angle dependent parts of the relative residuals. Imaging the directional terms in the lower-hemisphere stereographic projection, we obtain so-called P spheres. P-sphere patterns of the early- and delayed-wave arrivals (relatively to a station average) reflect the path-integrated anisotropy beneath each station. For the real data, the stations with a similar P-sphere pattern delimit regions of a homogeneous anisotropy, often related to large-scale tectonic units. For details of the method, we refer to, e.g., Babuška & Plomerová (1992; 2006).

3.1 Block structure of the mantle lithosphere with different anisotropy

The forward mode of AniTomo enables us to investigate directly the causes of different P-sphere patterns, including the role of a trade-off between anisotropy and lateral variations of isotropic velocities. In the first test series, the models consist of homogeneous blocks of different anisotropy or variable isotropic component of velocity. The blocks extend from 30 km down to 110 km depth mimicking units of continental mantle lithosphere. With such models, we can investigate not only the effects of the individual homogeneous blocks but also the influence of their boundaries.

We start with a model consisting of one isotropic block and one anisotropic block (Fig. 3.1). The anisotropy has a hexagonal symmetry with the high-velocity *a* axis dipping eastward, i.e., toward the neighbouring isotropic-velocity block, and the low-velocity (*b*,*c*) plane dipping westward. The strength of anisotropy is 5 %. The isotropic velocities correspond to reference velocity model IASP'91 (Kennett & Engdahl 1991). At the surface, there are eleven stations in a line lying symmetrically above the blocks. We evaluate the P spheres, showing the directional terms of P-wave travel-time residuals for each station, as it is described above. We can see in Fig. 3.1 that a distinct bipolar P-sphere pattern occurs at the stations above the anisotropic block. The waves propagating from the east arrive relatively earlier (negative directional terms) to the stations, compared to the waves coming from the west (positive directional terms). There is a difference in

arrival times of ~ 0.8 s for the waves propagating from the east and from the west, close to the directions of the maximum and minimum velocities caused by the anisotropy. The absolute values of the directional terms decrease toward the isotropic block, but the bipolar character of the P spheres remains distinct at all the stations above the anisotropic block. On the other hand, the stations above the isotropic block do not exhibit any notable directional variations of the P-wave travel-time residuals. It is possible to clearly detect and separate the two blocks according to the P-sphere patterns.

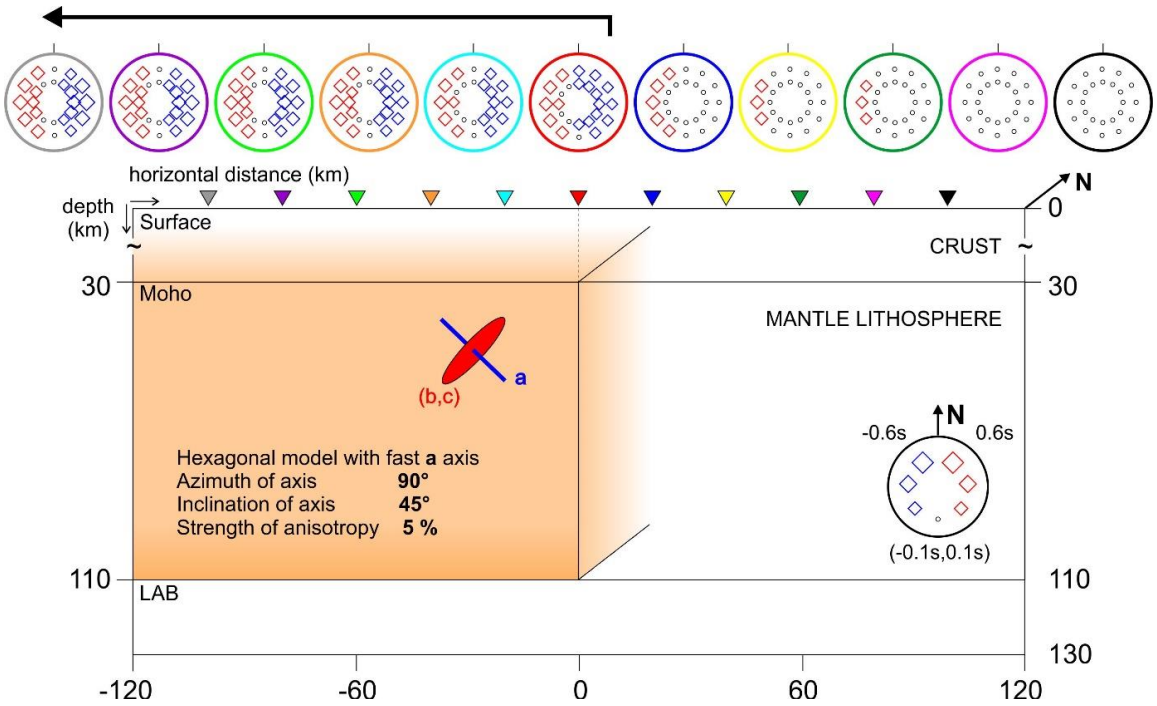

Figure 3.1 P spheres generated by a synthetic model of blocks with different anisotropic velocities mimicking continental mantle lithosphere (schematically displayed below the spheres). The block in the west is anisotropic (see the description in the figure for the particular properties of the anisotropy), while the block in the east is isotropic. Each P sphere is linked by colour of its frame to the respective station (triangles at the surface, interstation distance is 20 km). The anisotropic block with inclined symmetry axes produces a bipolar P-sphere pattern at all the stations located above the block (marked with the thick black arrow at the top of the figure).

One can ask whether it is possible to create a bipolar P-sphere pattern with a purely isotropic large-scale heterogeneity. Therefore, the next tested model consists of two isotropic blocks with velocities differing by 5 % (Fig. 3.2). The only directional variations of the travel-time residuals are due to the jump of velocities at the block interface. The waves arriving from the east are relatively faster than those coming from the west, which gives rise to a bipolar P-sphere pattern, but only around the block boundary. The bipolar pattern does not persist to distances larger than ~ 20 km from the boundary. Thus, we can conclude that purely isotropic large-scale heterogeneities cannot be responsible for a bipolar P sphere pattern that remains unchanged over areas as large as hundreds of kilometres.

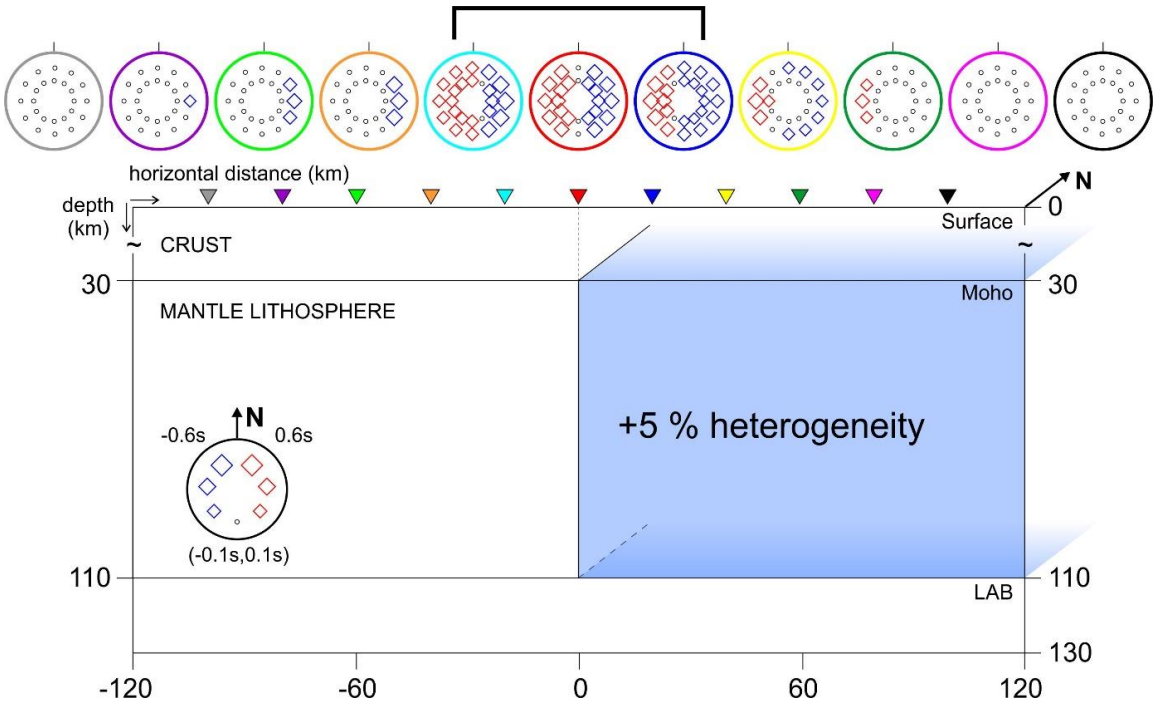

Figure 3.2 P spheres generated by a synthetic model of blocks with different isotropic velocities. The block in the east has a velocity higher by 5 % compared to the block in the west, which follows the IASP'91 velocity model. There is a distinct bipolar P-sphere pattern only in a 40 km wide band above the boundary of the two blocks.

The last example shows the P spheres evaluated for two anisotropic blocks with opposite orientations of the symmetry axes (Fig. 3.3). For this test, we choose hexagonal symmetry with the low-velocity *b* axis for the target anisotropy in both blocks. Similarly as in Fig. 3.1, clear bipolar P spheres oriented in agreement with the directions of the high- and low-velocities due to the anisotropy appear above the blocks. An influence of the distinct anisotropic structure of the neighbouring block is evident to a distance of 40 km from the boundary. Regarding the hexagonal symmetry with the low-velocity *b* axis, the bipolar patterns are effectively the same as those for the model with the high-velocity *a* axis dipping to the opposite azimuth (compare the patterns of, e.g., the black station in Fig. 3.3 and the grey station in Fig. 3.1). The teleseismic P waves cannot discriminate between the two types of hexagonal symmetry with dipping axes. The directions of relatively high and low velocities are decisive for the P-sphere pattern (see also Fig. 5a in Chapter 6).

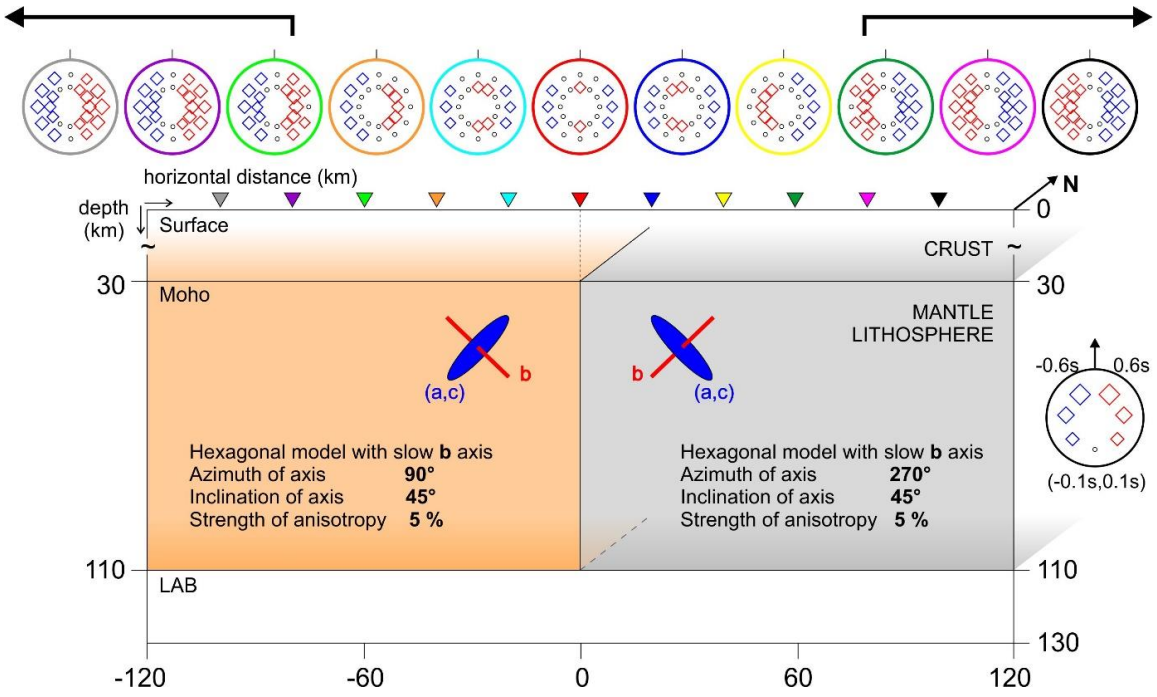

Figure 3.3 P spheres generated by a synthetic model of blocks with divergently dipping foliations. The bipolar P-sphere pattern caused by the anisotropy weakens toward the boundary.

We have demonstrated in this Section that a laterally persistent bipolar P-sphere pattern reflects a large-scale anisotropy of the mantle lithosphere when the symmetry axes are inclined. On the contrary, purely isotropic heterogeneities can hardly be responsible for a bipolar P-sphere pattern consistent over large distances.

3.2 Dipping anisotropy in the mantle lithosphere and sub-horizontal anisotropy in the asthenosphere

Sub-lithospheric mantle is also a source of large-scale anisotropy potentially influencing propagation of teleseismic waves. Present-day flow in the asthenosphere results mostly in a large-scale anisotropy with a sub-horizontal orientation of the high-velocity axis. To test the influence of such anisotropy on the travel-time deviations of teleseismic P waves, we construct double-layer models where the anisotropy of the lower layer has a horizontal high-velocity symmetry axis (Fig. 3.4). First, we keep the upper layer purely isotropic and the anisotropy is only in the lower layer (Fig. 3.4a). The resulting P-sphere pattern is very weak. Notable directional variations appear only at its outer part, i.e., for the waves with a large angle of incidence (epicentral distance ~30˚-50˚), and the pattern tends to be quadrupolar.

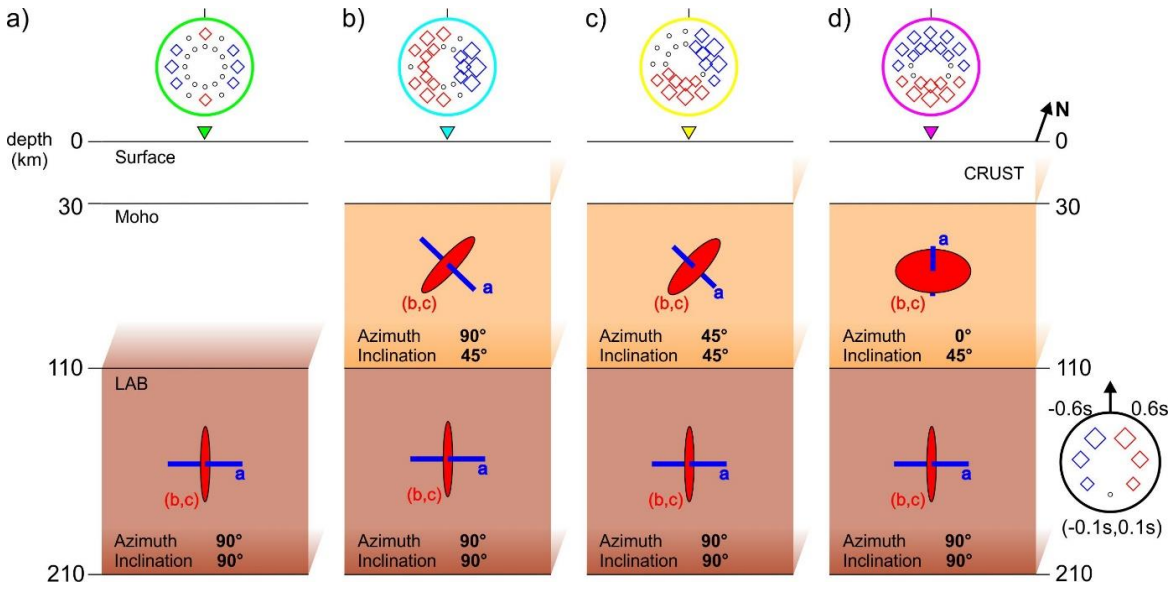

Figure 3.4 P spheres created by synthetic double-layer models, where the lower layer is always anisotropic with a horizontal high-velocity symmetry axis, mimicking a horizontal flow in the asthenosphere. Anisotropy in the upper layer changes. The strength of anisotropy is 5 %.

When we add an inclined anisotropy into the upper layer, the P-sphere pattern is again distinct and bipolar, but with some minor distortions depending on a mutual orientation of azimuths of the high-velocity axes of the two layers (Fig. 3.4b-d). When the two azimuths are at the angle of 45˚, there is a range of directions, for which the directional terms are around zero (Fig. 3.4c). On the other hand, when the azimuths of the high-velocity symmetry axes are either parallel or perpendicular, the P-sphere pattern is clearly bipolar (Fig. 3.4b and d). Thus, we can conclude that even if there is an anisotropy with a sub-horizontal high-velocity axis at the sub-lithospheric depths, the inclined anisotropy located in the mantle lithosphere has a dominant impact on the directional variations of the travel-time residuals of teleseismic P waves.

3.3 Model mimicking upper-mantle structure of the Eger Rift and mantle-lithosphere domains of the Teplá-Barrandian and Saxothuringian tectonic units

The forward mode of AniTomo can be also used to generate synthetic P spheres for a proposed velocity model in order to compare the synthetics with P spheres evaluated for the real data. We show such an example for a western part of the Bohemian Massif, where the Eger Rift developed above a contact of the Saxothuringian and Teplá-Barrandian tectonic units (Fig. 3.5a). The mantle lithosphere of the Bohemian Massif has been studied intensively (see, e.g., Babuška & Plomerová 2013, for a review) with the use of data from passive seismic experiments that have been gathering data for this region for already more than two decades (e.g., BOHEMA, PASSEQ, AlpArray). Several representative P spheres evaluated for selected long-term operating stations located in a band crossing the Eger Rift are shown in Figs. 3.5 a) and b). The P-sphere patterns typical of the Saxothuringian and Teplá-Barrandian tectonic units are bipolar with the relatively early arrivals in the north and the southeast, respectively (Babuška *et al.* 2008). These clearly bipolar patterns persist yet at the stations that are ~ 100 km far away from the rift, within the respective unit. The patterns at the stations above the Eger Rift itself show relatively delayed arrivals for the waves coming from the northeast and southwest, which corresponds to a propagation within the thinned and transitional mantle lithosphere beneath the Eger Rift.

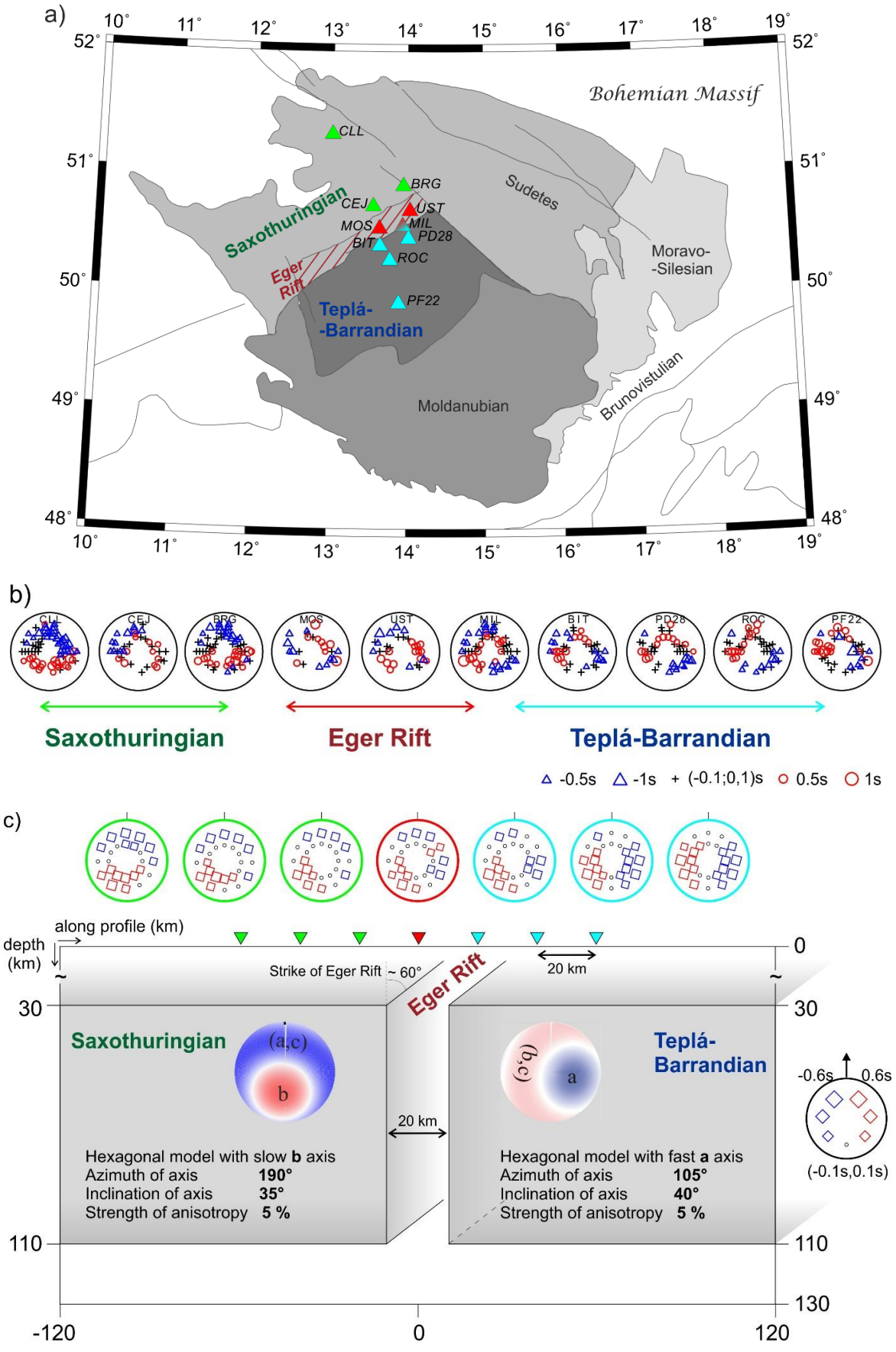

Figure 3.5 (a) Tectonic units of the Bohemian Massif with locations of stations deployed in a band crossing the Eger Rift. (b) Observed P spheres evaluated for the stations imaged in (a) from data of

various passive seismic experiments. See, e.g., Babuška & Plomerová (2013). (c) Synthetic P spheres for the imaged schematic model of the Eger Rift and two adjacent mantle-lithosphere tectonic units - Saxothuringian and Teplá-Barrandian. The anisotropic models are adopted from Babuška *et al.* (2008).

For the purpose of the forward modelling, we design a schematic model, where two 80 km thick anisotropic blocks are separated by a 20 km wide zone of isotropic velocities (Fig. 3.5c). We adopt anisotropic models for these two mantle-lithospheric domains from Babuška *et al.* (2008), who infer 3D orientation and strength of anisotropy by joint interpretation of directional variations of P-wave travel-time residuals and SKS/SKKS-wave splitting. The Saxothuringian unit is characterized by anisotropy with the low-velocity *b* axis dipping to the south, while the high-velocity *a* axis is dipping roughly to the east in the Teplá-Barrandian unit.

We calculate synthetic P spheres for seven stations arranged in a line across the Eger Rift (Fig. 3.5c) and for the same set of 24 regularly distributed events as in the previous tests. There are no isotropic-velocity heterogeneities in the synthetic model. The P-sphere patterns at the stations apart from the rift reflect the dipping anisotropy. Closer to the rift, the patterns are influenced by the laterally variable structure. In general, the synthetic P-sphere patterns resemble to those from the real data (Fig. 3.5b). This is an independent confirmation that the models of large-scale anisotropy with dipping symmetry axes in the mantle-lithosphere domains suggested by Babuška *et al.* (2008) can be responsible for the observed P-sphere patterns.

The presented tests devoted to modelling of the P-residual spheres with the forward mode of code AniTomo confirm that a large-scale anisotropy is a significant source of directional variations of P-wave travel-time residuals. Anisotropy with inclined symmetry axes can be responsible for an often observed bipolar P-sphere pattern that is consistent over regions of hundreds of kilometres. On the other hand, this is not the case of purely isotropic-velocity structures.

References

Babuška, V. & Plomerová, J., 1992. The lithosphere in central Europe—seismological and petrological aspects, *Tectonophysics,* **207**, 141–163.

Babuška, V. & Plomerová, J., 2006. European mantle lithosphere assembled from rigid microplates with inherited seismic anisotropy, *Phys. Earth Planet. Inter.* **158**, 264–280.

Babuška, V. & Plomerová, J., 2013. Boundaries of mantle-lithosphere domains in the Bohemian Massif as extinct exhumation channels for high-pressure rocks. *Gondwana Res.*, 23, 973-987.

Babuška, V., Plomerová, J. & Šílený, J., 1993. Models of seismic anisotropy in the deep continental lithosphere, *Phys. Earth Planet. Inter.*, **78**, 167–191.

Babuška, V., Plomerová, J. & Vecsey, L., 2008. Mantle fabric of western Bohemian Massif (central Europe) constrained by 3D seismic P and S anisotropy, *Tectonophysics*, **462**.

Kennett, B. & Engdahl, R., 1991. Travel times for global earthquake location and phase identification, *Geophys. J. Int.*, **105,** 429–465.

Munzarová, H., Plomerová, J., Babuška, V. & Vecsey, L., 2013. Upper-mantle fabrics beneath the Northern Apennines revealed by seismic anisotropy, *Geochem. Geophys. Geosyst.*, **14**, 1156–1181, http://dx.doi.org/10.1002/ggge.20092.

Plomerová, J., Vecsey, L., Babuška, V. & LAPNET working group, 2011. Domains of Archean mantle lithosphere deciphered by seismic anisotropy – Inferences from the LAPNET array in northern Fennoscandia, *Solid Earth,* **2**, 303–313, doi:10.5194/se-2-303-2011.

4. Simple methodological tests of the inversion mode

Careful testing of AniTomo is necessary before we apply the new code to real datasets. Synthetic tests allow us to see directly the impact of a specific inversion setup on the solution, unlike in a real case. Therefore, we have performed various synthetic tests to shed light on some aspects that arise with the approach of anisotropic travel-time tomography. In this Chapter, we investigate two fundamental questions:

1) How much does the incorporation of azimuths and inclinations of the symmetry axis among the unknown parameters influence stability of the inversion?

2) Does a search for only a subset of the model parameters make the inversion more stable?

Furthermore, we complement this Chapter with a test devoted to quality of the ray coverage (Section 4.3).

We design a uniform distribution of rays for these methodological tests, respecting the range of possible incidence angles of teleseismic P waves in order not to bias the results by any directional irregularities (see Fig. 14a in Chapter 5 for the ray coverage of the volume studied). We consider 66 equally distributed teleseismic events (Fig. 4.1a) and an array of 12 x 12 receivers regularly spread above a target volume of 240 x 240 x 120 km. The total number of rays is 9 504. A very simple parameterization of only 2 x 2 x 1 grid nodes is sufficient at this stage of testing of the inversion mode (Fig. 4.1b). The grid nodes are located in the centre of 120 x 120 x 120 km large orthogonal grid cells.

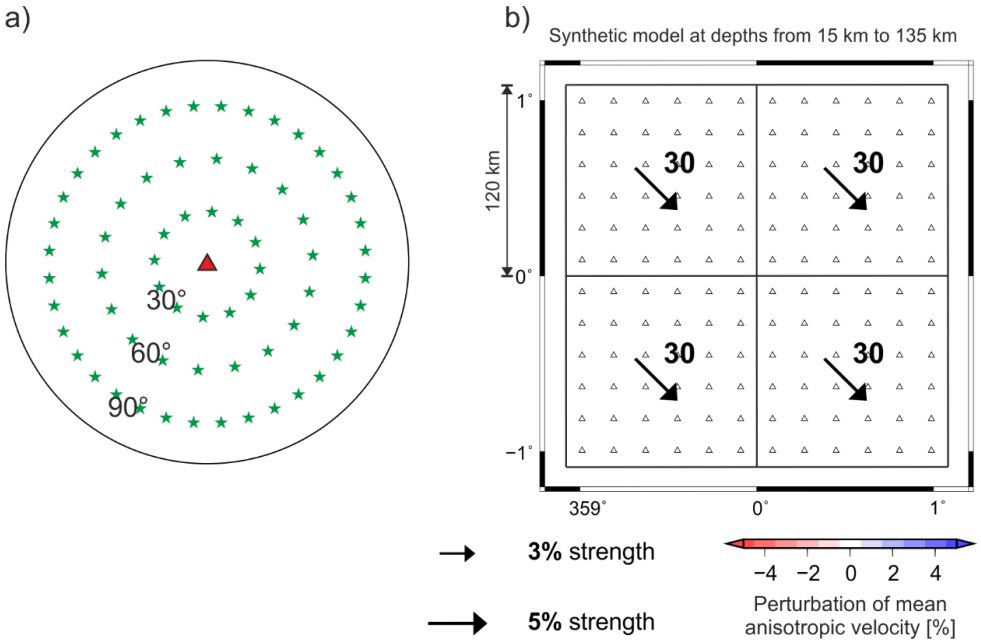

Figure 4.1 Distribution of the synthetic sources of the teleseismic P waves (a) and the target model of dipping anisotropy proposed for the synthetic methodological tests (b). The arrows represent anisotropy of the grid cells. Arrow length indicates strength of anisotropy, which is 5 % in this case. We plot the arrows only for anisotropy stronger than 1 %, in general. Orientation of the arrows marks azimuth of the symmetry axis. The numbers next to the arrows mean inclination of the symmetry axis measured in degrees upward from the vertical direction. Symmetry is characterized by the high-velocity *a* axis, triangles represent receivers located at the surface.

An anisotropy with hexagonal symmetry with the high-velocity *a* axis and with strength of 5 % is assigned to each of the four grid nodes of the target synthetic model. We have to notice that the type of hexagonal symmetry is indicated by the sign of strength of anisotropy in AniTomo, i.e., the positive sign for symmetry with the high-velocity *a* axis and the negative sign for symmetry with the low-velocity *b* axis (see eq. 36 in Chapter 2). The symmetry axis of the target model inclines toward the south-east in an azimuth of 135° and the inclination is 30° measured upward from the vertical (Fig. 4.1b). The isotropic component of the velocity is equal to the IASP'91 reference model (Kennett & Engdahl 1991).

We start all the inversions from a homogeneous initial model. The isotropic-velocity component of the initial model is equal to those of the IASP'91 reference model. The initial strength of anisotropy is 1 % and azimuth and inclination of the symmetry axis are 180° and 45°, respectively. We let all the inversions run for eight iterations, which is enough to evaluate the character of convergence of the model parameters toward the correct solution. Smoothing of the model parameters is turned off if not stated otherwise.

The travel-time residuals are calculated as differences between the "observed" P-wave travel times, i.e., the travel times of the P waves propagating through the target model, and the theoretical travel times calculated for the IASP'91 reference model. We mimic the observation errors by adding synthetic errors with a Gaussian distribution with a standard deviation of 0.05 s to the "observed" travel times.

4.1 Damping of azimuth and inclination of the symmetry axis

Damping factor is a regularization parameter that helps to stabilize the inversion by minimizing a combination of prediction error and solution length (e.g., Menke 1984). The damping factor controls how much the model parameters change from one iteration to the other. Linearization of the travel-time equation (see eq. 45 in Chapter 2) requires short steps to assure relatively slow changes towards the correct solution.

A particular attention must be paid to damping of the angles defining the orientation of the symmetry axis, because of the non-linearity between the axis orientation and the anisotropic velocity (see eq. 41 in Chapter 2). This test shows that well-tuned damping factors of the azimuth and inclination of the axis are essential for stability of the inversion (Fig. 4.2). We run the inversion first with damping factor of the angles equal to 10 (blue triangles) and second with 0.001 (red triangles). The damping factors of the isotropic-velocity component and of the strength of anisotropy are set constantly to 0.001 and the remaining inversion configuration is unchanged as well. We can see that the higher damping factor of the angles guarantees a steady and stable convergence of all the model parameters toward the correct solution (Fig. 4.2), because it successfully prevents the azimuths and inclinations to move unpredictably from one iteration to another.

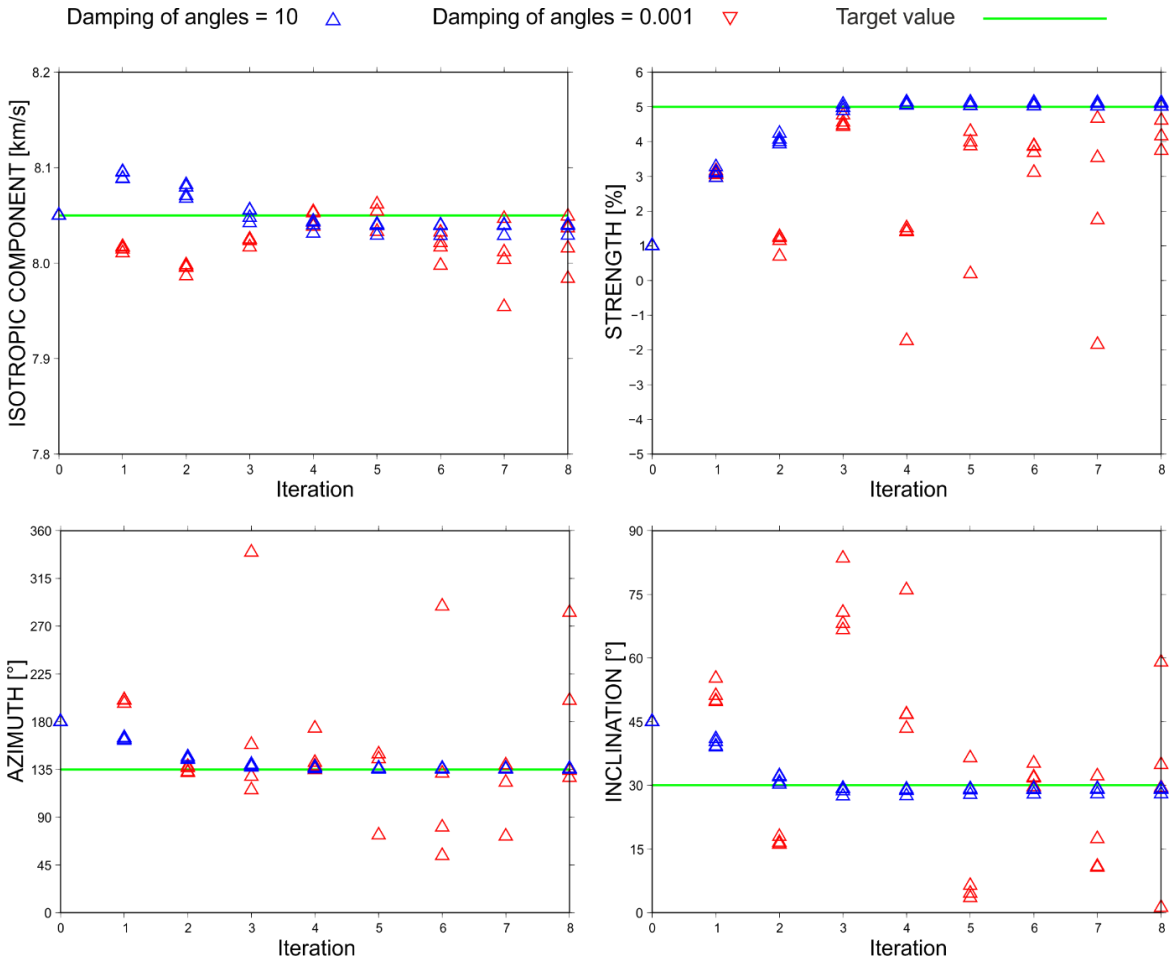

Figure 4.2 Evolution of model parameters for all the grid nodes in dependence on number of iteration for an inversion with damping factors of the azimuths and inclinations equal to 10 (blue triangles) or 0.001 (red triangles). Each graph is dedicated to one of the four model parameters, i.e., isotropic component of the velocity (top left), strength of anisotropy (top right), azimuth (bottom left) and inclination (bottom right) of the symmetry axis.

4.2 Inversion for a subset of the model parameters

Inverting only for some of the model parameters, e.g., the azimuths and inclinations, while keeping the other parameters fixed, might be suitable for decreasing the overall number of model parameters. Nevertheless, we show in Fig. 4.3 that the convergence to the correct solution is better when we allow the inversion also for the strength of anisotropy (red triangles). When we invert only for the angles and keep the strength fixed at an incorrect value (blue triangles and blue dashed line), the inclinations are not able to converge to the target value.

We usually run the testing inversions once with and next time without the lateral smoothing of the model parameters. In general, the results of the tests are better when the smoothing is turned off (cf. grey and red triangles in Fig. 4.3). The smoothed inversion possibly needs more iterations to converge.

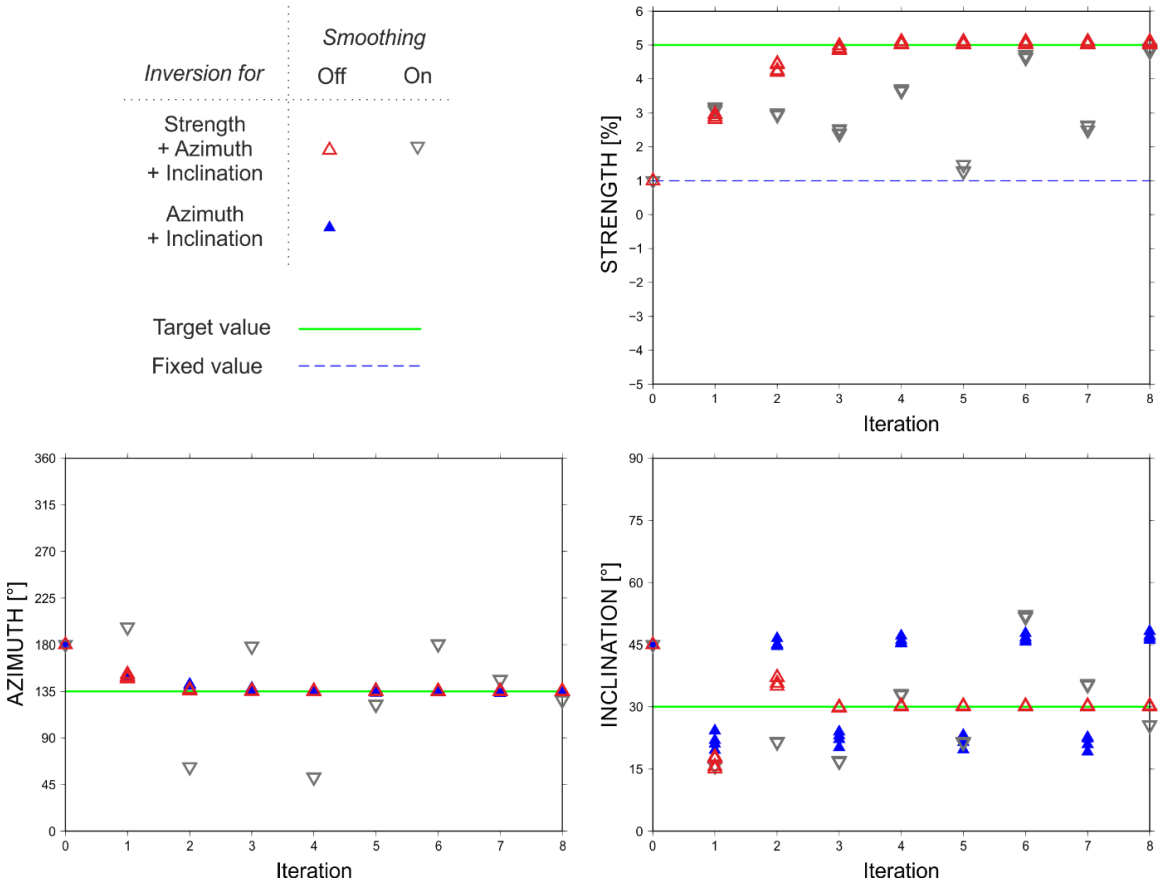

Figure 4.3 Evolution of the model parameters in dependence on number of iteration in the case of inversion for only azimuths and inclinations (blue triangles), and when we extend the model parameters by the strength of anisotropy (red triangles – smoothing turned off, grey triangles – smoothing turned on). We fix the isotropic component of velocity in this testing series at the target value of the IASP'91 reference model.

4.3 Inversion of datasets with different quality

The set of 9 504 equally distributed rays is optimum for the methodological testing of the new code. To see how the anisotropic inversion succeeds with a dataset of a lower quality, we decrease the number of the rays at the stations located in the western half of the array to one quarter of the original set and to one eighth at the stations in the eastern half of the array.

The anisotropic part of the synthetic model for this test is still characterized by the 5 % strength and the high-velocity axis dipping south-eastward, but we modify the isotropic part in this case. We assign +1 % isotropic-velocity perturbation relative to the IASP'91 model (Kennett & Engdahl 1991) to the north-western and south-eastern grid nodes and -1 % perturbation to the north-eastern and south-western nodes (Fig. 4.4). The isotropic component of the target structure forms a checkerboard pattern.

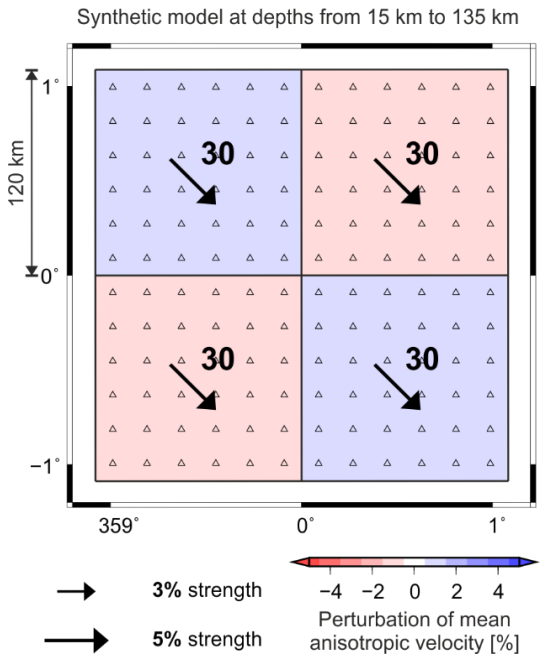

Figure 4.4 Synthetic model of the homogeneous dipping anisotropy and checkerboard isotropic-velocity structure. The arrows represent anisotropy of the grid cells. Arrow length indicates strength of anisotropy, which is 5 % in this case. We plot the arrows only for anisotropy stronger than 1 %, in general. Orientation of the arrows marks azimuth of the symmetry axis. The numbers next to the arrows mean inclination of the symmetry axis measured in degrees upward from the vertical direction. Symmetry is characterized by the high-velocity *a* axis. Triangles represent receivers located at the surface.

The convergence of the model parameters toward the target values is as good at the grid nodes located in the western part of the volume as for the inversion with the original dataset (Fig. 4.5). In the eastern part of the volume, where the number of rays is one half of the rays covering the grid cells in the west, the convergence is slower, but correct.

The very basic and simple testing series proves that the new AniTomo code works and retrieves the anisotropic structures sufficiently well. In next Chapter, we proceed to explore the functionality of the code for more realistic but still synthetic cases. We focus mainly on the damping factors of the individual model parameters in a greater detail and on the choice of an initial anisotropic model.

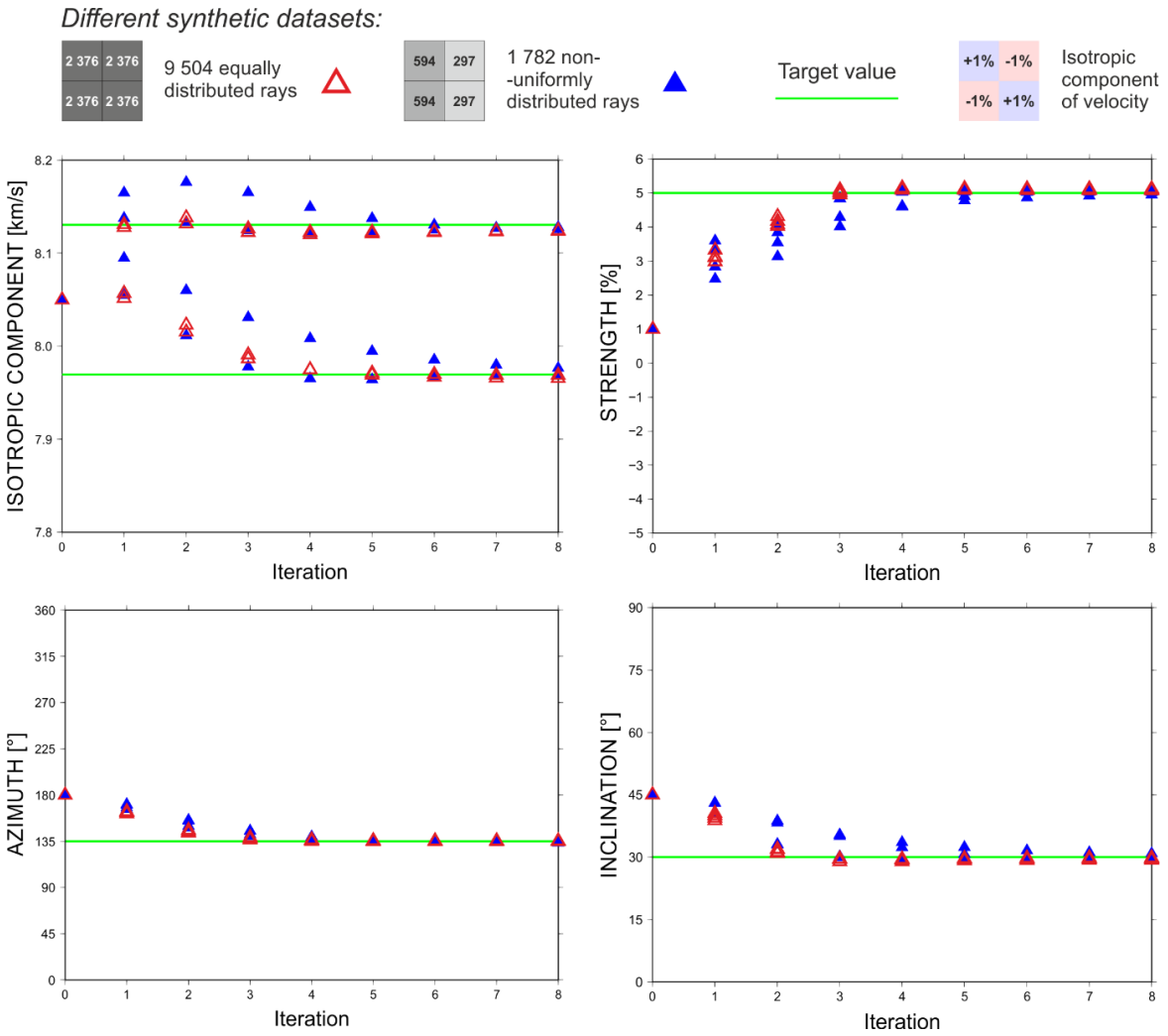

Figure 4.5 Evolution of the model parameters in dependence on number of iteration during the inversion of the original dataset (red triangles) and the inversion of the reduced non-uniform dataset (blue triangles).

References

Kennett, B. & Engdahl, R., 1991. Travel times for global earthquake location and phase identification, *Geophys. J. Int.*, **105,** 429–465.

Menke, W., 1984. *Geophysical Data Analysis: Discrete Inverse Theory*, 1st edn, Academic Press, Inc., Orlando.

5. Novel anisotropic teleseismic body-wave tomography code AniTomo to illuminate heterogeneous anisotropic upper mantle: Part I - Theory and inversion tuning with realistic synthetic data

Helena Munzarová[1], Jaroslava Plomerová[1], Eduard Kissling[2]

Geophysical Journal International, Volume **215**, Issue 1, October 2018, Pages 524-545, doi:10.1093/gji/ggy296

[1] Institute of Geophysics, Academy of Sciences, Prague, Czech Republic
[2] Institute of Geophysics, Department of Earth Sciences, ETH Zürich, Zürich, Switzerland

Geophysical Journal International

Geophys. J. Int. (2018) **215,** 524–545
Advance Access publication 2018 July 19
GJI Seismology

doi: 10.1093/gji/ggy296

Novel anisotropic teleseismic body-wave tomography code AniTomo to illuminate heterogeneous anisotropic upper mantle: Part I — Theory and inversion tuning with realistic synthetic data

Helena Munzarová,[1] Jaroslava Plomerová[1] and Eduard Kissling[2]

[1]*Institute of Geophysics, Academy of Sciences, Prague, Czech Republic. E-mail: helena@ig.cas.cz*
[2]*Institute of Geophysics, Department of Earth Sciences, ETH Zürich, Switzerland*

Accepted 2018 July 18. Received 2018 July 16; in original form 2018 February 15

SUMMARY

Considering only isotropic wave propagation and neglecting anisotropy in teleseismic tomography studies is a simplification obviously incongruous with current understanding of the mantle–lithosphere plate dynamics. Therefore, we have developed a code for anisotropic–teleseismic tomography (AniTomo), which allows to invert relative traveltime residuals of teleseismic *P* waves simultaneously for coupled anisotropic–isotropic *P*-wave velocity models of the upper mantle. Due to a more complex anisotropic propagation of *S* waves, the AniTomo is applicable only to *P*-wave data. Weak hexagonal anisotropy together with isotropic velocity heterogeneities are interpreted as a cause of the observed *P*-wave traveltime residuals. Moreover, the axis of the hexagonal symmetry can be oriented freely in all directions, which represents a unique approach among recent approaches that usually incorporate only azimuthal or radial anisotropy into the body-wave tomography.

Apart from outlining the theoretical background of AniTomo, we examine various aspects coming along with anisotropic tomography such as choice of a set of initial anisotropic models and setup of parameters controlling the inversion. Synthetic testing furthermore allows investigation of the well-known trade-off between effects of *P*-wave anisotropy and lateral variations of isotropic velocity. The target synthetic models are designed to schematically represent different heterogeneous anisotropic structures of the upper mantle. Considering realistic distributions of stations and events at teleseismic distances, a separation of seismic anisotropy and isotropic velocity heterogeneities is plausible and a stable output model can be achieved within a few iterations. Careful testing of the new code on synthetics, concentrating on its functionality, strength and weaknesses, is a necessary step before AniTomo is applied to real data sets.

Key words: Body waves; Seismic anisotropy; Seismic tomography.

1 INTRODUCTION

Seismic anisotropy of the Earth's upper mantle is a key source contributing to deciphering tectonic history of the lithosphere–asthenosphere system (e.g. Babuška & Cara 1991; Šílený & Plomerová 1996; Silver 1996; Savage 1999; Park & Levin 2002; Fouch & Rondenay 2006; Mainprice 2007; Maupin & Park 2007; Long & Silver 2009; Long & Becker 2010). Smooth and long-wavelength variations of large-scale anisotropy are usually studied from propagation of surface waves (e.g. Anderson 1961; Aki & Kaminuma 1963; Anderson & Dziewonski 1982; Montagner & Nataf 1986; Montagner 1994, 1998; Bruneton *et al.* 2004; Becker *et al.* 2012). Resulting shear-velocity models include azimuthal and/or radial anisotropy of the mantle prevailingly (e.g. Panning & Romanowicz 2006; Kustowski *et al.* 2008; Fichtner *et al.* 2010, 2013; Auer *et al.* 2014; French & Romanowicz 2014; Yuan *et al.* 2014; Zhu *et al.* 2014; Chang *et al.* 2015; Debayle *et al.* 2016; Ho *et al.* 2016; Nita *et al.* 2016).

In an effort to map structural variation in finer scales, one has to view the Earth with shorter wavelength optics and at different angles. Body waves, shear waves and particularly *P* waves, are sensitive to smaller-size structures due to their shorter wavelengths and broad angles of propagation in comparison with the surface waves. Thus they supply us with much more detailed information on the upper-mantle fabrics (e.g. Babuška & Plomerová 1992, 2006). However, most of standard teleseismic body-wave tomography studies neglect *P*-wave anisotropy, despite the fact that such significant simplification is incongruous with current understanding of the upper mantle–lithosphere plate dynamics. Moreover, neglecting seismic anisotropy can produce artefacts in tomographic models, both as to

amplitude and localization of heterogeneities (Sobolev *et al.* 1999; Menke 2015; Bezada *et al.* 2016).

Since the time that Backus (1965) has formulated an approximate but explicit formula for body-wave velocity of weakly anisotropic medium with a general symmetry, various methodologies incorporating anisotropy into *P*-wave traveltime tomography have been developed. Relatively complex and unique assumptions on anisotropy were introduced by Hirahara & Ishikawa (1984) in their pioneering traveltime inversion for anisotropic velocity structure beneath southwest Japan. These authors determined anisotropic perturbations by a two-step inversion, in which they combined hexagonal symmetry with horizontal axis and spheroidal *P*-wave velocity surface in order to approximate orthorhombic symmetry. However, the amount of data available at that time was not sufficient to exploit advantage of the inversion for such a complex anisotropy.

Nowadays, the amount of data suitable for exploration of seismic-wave velocity anisotropy has substantially increased. Therefore, isotropic images of the Earth or those considering only azimuthal anisotropy appear incomprehensible. Such tomography models of the crust and shallow subcrustal lithosphere were calculated from traveltimes of local *P* waves for various regions, for example in Japan (Ishise & Oda 2005, 2008; Wang & Zhao 2008, 2012; Yu & Wang 2013; Ishise *et al.* 2015; Koulakov *et al.* 2015), New Zealand (Eberhart-Phillips & Henderson 2004), or Alaska (Tian & Zhao 2012). Incorporating teleseismic *P*-wave traveltime residuals into the local data sets improved the ray coverage and depth extent of the volumes studied, for example for southeastern Tibet (Wei *et al.* 2013), the United States (Huang & Zhao 2013) or the North China Craton (Tian & Zhao 2013). Recently, new codes considering radial anisotropy of body-wave propagation have been developed, for example for the Alps (Hua *et al.* 2017) or for Japan (Wang & Zhao 2013; Huang *et al.* 2015; Gou *et al.* 2018). The radial and azimuthal anisotropy are usually modelled separately. Liu & Zhao (2017a) assume orthorhombic symmetry with a vertical symmetry axis, which leads to a simultaneous determination of azimuthal and radial anisotropy.

Another recent approach is to include not only *P* waves but also *S* waves into the anisotropic tomography. Liu & Zhao (2016, 2017b) invert *S*-wave traveltimes from local earthquakes together with relative traveltime residuals of teleseismic *S* waves for isotropic shear-wave velocities and azimuthal anisotropy of the crust and upper mantle beneath Japan. A joint inversion of the *P*- and *S*-wave data sets results in distribution of isotropic *P*- and *S*-wave velocities and azimuthal anisotropy.

Confining orientation of the symmetry axis to horizontal (in azimuthal anisotropy) or vertical (in radial anisotropy) directions, however, does not conform to anisotropic characteristics inferred by single-station methods from teleseismic body waves, generally observed in tectonically different continental provinces (e.g. Babuška *et al.* 1984, 1993; Babuška & Plomerová 1993, 2006; Plomerová & Babuška 2010; Plomerová *et al.* 2011, 2012). These authors demonstrate dependence of SKS-wave splitting parameters and *P*-wave traveltime residuals on direction of wave propagations, taking into account both azimuth and incidence angles. Such characteristics with a general 2π periodicity imply a need to treat anisotropy in 3-D. This allows us to evaluate fabrics of the upper mantle, in particular within the mantle lithosphere, without any limiting assumption on orientation of symmetry axes. Self-consistent anisotropic models of continental mantle lithosphere usually document (e.g. Plomerová *et al.* 2011) that derived symmetry axes of the anisotropic domains are oriented generally in 3-D, that is inclined from horizontal.

In this methodological paper, we present a novel and unique tomographic code called AniTomo that allows us to invert relative traveltime residuals of teleseismic *P* waves for 3-D distribution of both isotropic and anisotropic *P*-wave velocities in the upper mantle. This code represents a step further from modelling 3-D self-consistent homogeneously anisotropic blocks of mantle lithosphere (e.g. Babuška *et al.* 1993; Šílený & Plomerová 1996; Vecsey *et al.* 2007), towards modelling the upper mantle with anisotropy arbitrarily varying in 3-D. The AniTomo code for coupled anisotropic-isotropic tomography assumes weak anisotropy with hexagonal symmetry typical for upper mantle, either with high-velocity *a*-axis or low-velocity *b*-axis, oriented generally in 3-D. An important option of the code is the possibility to decide whether anisotropic, or isotropic, or both inversions will be performed in each node. Of course, ray coverage controls in which part of a model the coupled anisotropic-isotropic inversion is feasible. Apart from deriving the equations for this specific type of tomography, we document, with a series of synthetic tests, effects of the inversion setup on the results. The tests mimic realistic tomographic inversions in terms of target synthetic model representing anisotropic structures of the upper mantle, particularly the anisotropic domain-like structure of the mantle lithosphere, and also in terms of amount and incidence angles of teleseismic *P*-wave data. On the other hand, we keep the azimuthal coverage uniform not to bias the tests of, for example regularization of the inversion, by any directional asymmetry. Testing carefully the new code on synthetics, concentrating on its functionality, strengths and weaknesses, represents a necessary step before an application of AniTomo to real data sets. First, we apply the new AniTomo code on data from northern Fennoscandia (Munzarová *et al.* 2018, revision submitted), where also real non-uniform ray distributions are tested.

2 THEORY

We aim at modelling anisotropic upper-mantle structures with the use of teleseismic *P*-wave tomography. The crucial part of the theory is derivation of an explicit formula for *P*-wave velocities in weakly anisotropic medium with hexagonal-symmetry axis oriented generally in 3-D. Then, linearization of the relation between data (traveltime residuals) and model parameters describing the anisotropic medium is straightforward.

2.1 *P*-wave velocity in weakly anisotropic medium with hexagonal-symmetry axis generally oriented in 3-D

Backus (1965) applied first-order expansion of Christoffel equation for propagation of plane waves in homogeneous anisotropic elastic medium and he found an approximate but explicit formula for body-wave velocity v in weakly anisotropic medium with a general symmetry

$$v = c + \frac{B^{(1)}}{2c}, \tag{1}$$

where c is wave velocity in isotropic medium and $B^{(1)}$ is the 1st-order perturbation of the non-degenerated eigenvalue of Christoffel tensor. Particularly for *P* waves, $B^{(1)}$ can be expressed as

$$B^{(1)} = \gamma_{ijkl} n_i n_j n_k n_l, \tag{2}$$

where γ_{ijkl} are small variations of isotropic density-normalized elastic coefficients adjusting for the weak anisotropy. Vector $\mathbf{n}$ represents the *P*-wave propagation direction.

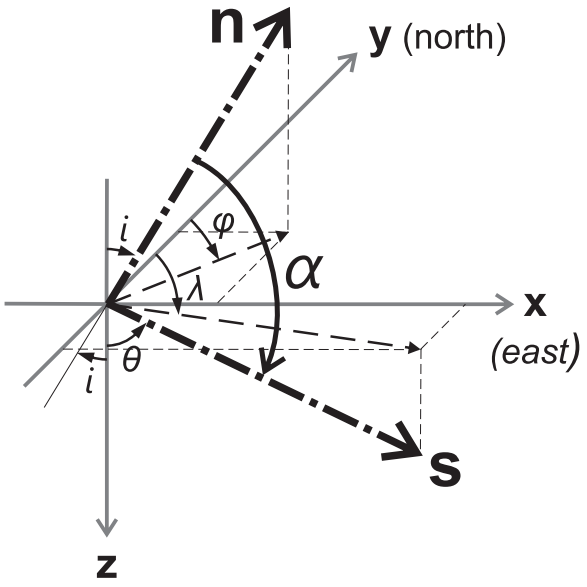

Figure 1. Definition of the Cartesian coordinate system used in AniTomo. Angles λ and θ label azimuth and inclination of the hexagonal-symmetry axis (unit vector **s**), respectively. Wave-propagation direction is represented by unit vector **n**. Angles ϕ and i mark backazimuth and angle of propagation of the wave, respectively. α is angle between the symmetry axis and the wave-propagation direction.

We present a detailed description of implementing hexagonal symmetry into eq. (2) and derivation of anisotropic velocity (eq. 1) in Appendix A. Then, the velocity for this specific symmetry is

$$v = \bar{v}\left(1 + \frac{k}{2}\cos 2\alpha\right), \tag{3}$$

where $\bar{v}$ is isotropic component of anisotropic velocity, k is strength of anisotropy and α is an angle between the symmetry axis and wave-propagation direction (Fig. 1).

As AniTomo employs only P wave and no S wave traveltimes, we cannot recover the five elastic coefficients of the anisotropy with assumed hexagonal symmetry individually, but only their combinations. We translate these combinations into isotropic component of velocity $\bar{v}$ and strength of anisotropy k (Appendix A), which we express as

$$\bar{v}^2 = \frac{1}{8\rho}\left[3\,(A + C) + 2\,(F + 2L)\right], \tag{4}$$

$$k = \frac{4\,(C - A)}{3\,(A + C) + 2\,(F + 2L)}, \tag{5}$$

where ρ is density. Positive values of strength of anisotropy correspond to hexagonal symmetry with axis a in direction of high velocity (call high-velocity a-axis), perpendicular to low-velocity plane (b,c), and vice versa—negative values correspond to hexagonal symmetry with axis b in direction of low velocity (call low-velocity b-axis), perpendicular to high-velocity plane (a,c) (Fig. S1).

Fig. S1(b) documents that the cosine function (eq. 3) is a sufficient approximation of P-wave velocities in the upper mantle in the case of weakly anisotropic medium with hexagonal symmetry. The maximum difference between the P-wave velocities calculated according to approximate eq. (3) and evaluated as the exact solution of the Christoffel equation is only ∼0.5 per cent for an anisotropic upper-mantle approximated by peridotite aggregate (Ben Ismail & Mainprice 1998; Babuška & Plomerová 2006).

In order to transform angle α into ray-parameter coordinate system, we define orientation of the symmetry axis by unit vector **s** and propagation direction of the wave by unit vector **n** (Fig. 1) as

$$\mathbf{s} = (\sin\theta\sin\lambda, \sin\theta\cos\lambda, \cos\theta), \tag{6}$$

where λ and θ are azimuth and inclination (measured upward from vertical) of the symmetry axis and

$$\mathbf{n} = (-\sin i\sin\phi, -\sin i\cos\phi, -\cos i), \tag{7}$$

where ϕ and i are backazimuth and incidence angle of the wave propagation. After substituting $\cos 2\alpha = 2\cos^2\alpha - 1$ and $cos\alpha = \mathbf{n}\cdot\mathbf{s}$ in eq. (3), the P-wave velocity in weakly anisotropic medium with hexagonal symmetry and a general orientation in 3-D can be expressed as

$$v = \bar{v}\left\{1 + k\left[(\sin i\,\sin\theta\cos(\phi - \lambda) + \cos i\,\cos\theta)^2 - \frac{1}{2}\right]\right\}. \tag{8}$$

This equation relates anisotropic velocity v of a P-wave propagating in direction given by angles ϕ and i with isotropic component $\bar{v}$ of anisotropic velocity and directionally variable velocity perturbation, that is the term with strength of anisotropy k.

2.2 System of linearized equations

Similarly to the isotropic tomography, AniTomo needs a linearized relation between traveltime residual Δt and model parameters, that is perturbations of the parameters describing the medium $\Delta\bar{v}$, Δk, $\Delta\lambda$ and $\Delta\theta$,

$$\Delta t = \sum_j \left(\frac{\partial t}{\partial \bar{v}}\right)_j \Delta\bar{v}_j + \sum_j \left(\frac{\partial t}{\partial k}\right)_j \Delta k_j + \sum_j \left(\frac{\partial t}{\partial \lambda}\right)_j \Delta\lambda_j + \sum_j \left(\frac{\partial t}{\partial \theta}\right)_j \Delta\theta_j, \tag{9}$$

where index j denotes contribution to the traveltime residual from the jth ray segment. The traveltime t of a P wave in the anisotropic medium is

$$t = \frac{s}{v\,(\bar{v}, k, \lambda, \theta)}, \tag{10}$$

where $v(\bar{v}, k, \lambda, \theta)$ stands for the anisotropic velocity (eq. 8). Partial derivatives of the traveltime with respect to the anisotropic parameters in eq. (9) are then

$$\frac{\partial t}{\partial \bar{v}} = -\frac{s}{v_0\cdot\bar{v}_0}, \tag{11}$$

$$\frac{\partial t}{\partial k} = -\frac{s}{v_0}\cdot\left[(\sin i\,\sin\theta_0\cos(\phi - \lambda_0) + \cos i\,\cos\theta_0)^2 - \frac{1}{2}\right], \tag{12}$$

$$\frac{\partial t}{\partial \lambda} = -\frac{s}{v_0}\cdot 2k_0\,(\sin i\,\sin\theta_0\cos(\phi - \lambda_0) + \cos i\,\cos\theta_0) \times \sin i\,\sin\theta_0\sin(\phi - \lambda_0), \tag{13}$$

$$\frac{\partial t}{\partial \theta} = -\frac{s}{v_0}\cdot 2k_0\,(\sin i\,\sin\theta_0\cos(\phi - \lambda_0) + \cos i\,\cos\theta_0) \times (\sin i\,\cos\theta_0\cos(\phi - \lambda_0) - \cos i\,\sin\theta_0). \tag{14}$$

As the partial derivatives depend on anisotropic parameters, the problem is still non-linear. Thus, we fix the anisotropic parameters in eqs (11)–(14) to the reference values (marked with index 0) and solve the problem iteratively. The reference values come from the initial model during the first iteration and from the model resulting after the (n–1)th iteration during the nth iteration.

Eq. (9) established for individual station-event P wave traveltime residuals form a system of linearized equations that is solved with the damped least-square method (Menke 1984). During the nth iteration, we obtain vector of model parameters updating the solution from the previous iterations at all the grid nodes

$$\mathbf{m}^{(n)} = \left(\boldsymbol{A}^T \boldsymbol{W}_D \boldsymbol{A} + \epsilon \boldsymbol{W}_M\right)^{-1} \boldsymbol{A}^T \boldsymbol{W}_D \mathbf{d}^{(n-1)}. \quad (15)$$

Vector $\mathbf{d}^{(n-1)}$ contains traveltime residuals evaluated for the reference model equal to the solution from the (n–1)th iteration. The partial derivatives (eqs 11–14) are stored in matrix $\boldsymbol{A}$. Errors of arrival-time measurements can be reflected in weighting matrix $\boldsymbol{W_D}$. Stabilization of the ill-posed problem can be achieved through damping factor ε^2 and smoothing matrix $\boldsymbol{W_M}$. Damping factor controls prediction error versus solution length (Menke 1984).

To assess reliability of the model parameters for a given ray distribution and inversion setup, we evaluate an approximation of the resolution matrix as

$$\boldsymbol{R} = \left(\boldsymbol{A^T W_D A} + \varepsilon^2 \boldsymbol{W_M}\right)^{-1} \boldsymbol{A^T W_D A}. \quad (16)$$

Diagonal elements of resolution matrix (RDE) represent how well an estimate of model parameters can fit the true solution based on the ray geometry within the parametrization cells (Menke 1984). We parametrize the volume studied by an orthogonal grid of nodes. Off the nodes, the isotropic component of velocity is determined by a linear interpolation and strength of anisotropy and symmetry-axis orientation are assumed constant in each cell surrounding the grid node.

3 ANITOMO–TOMOGRAPHY CODE WITH IMPLEMENTED 3-D ANISOTROPY

The developed coupled anisotropic–isotropic tomography code (AniTomo) has been created as a modification of widely used code Telinv for high-resolution regional isotropic tomography of the upper mantle from residuals of traveltimes of teleseismic body waves. Telinv is a Fortran code originally developed by J. Taylor, E. Kissling, U. Achauer, C. M. Weiland and L. Steck. It has been used and modified by many authors (e.g. Weiland *et al.* 1995; Arlitt *et al.* 1999; Lippitsch *et al.* 2003; Sandoval *et al.* 2004; Shomali *et al.* 2006; Eken *et al.* 2007; Karousová *et al.* 2012, 2013; Karousová 2013; Plomerová *et al.* 2016; Silvennoinen *et al.* 2016; Chyba *et al.* 2017). Actual updated version of the Telinv code can be downloaded from http://www.ig.cas.cz/en/research-teaching/software-download/.

In order to step from isotropic (Telinv) to P-wave anisotropic tomography (AniTomo), we have implemented equations derived in Section 2 into the original code. The coupled anisotropic–isotropic code AniTomo allows to run both isotropic and/or fully 3-D anisotropic inversions. We have kept the overall framework and the subroutines solving the individual steps especially of linear algebra as they were in Telinv. This chapter focuses on key attributes of the AniTomo anisotropic-tomography code. For more information on specific procedures related already to Telinv, we refer the reader to the publications dedicated to isotropic tomography mentioned in above paragraph.

AniTomo is a new and unique code for regional traveltime anisotropic tomography of the upper mantle. Traveltime residuals of teleseismic P waves are inverted for anisotropy velocity model described by parameters of weak anisotropy with hexagonal symmetry. These model parameters are perturbations of isotropic component of anisotropic velocity, strength of anisotropy and general orientation of the symmetry axis in 3-D defined by its inclination and azimuth. Directionally dependent velocities of wave propagation are evaluated according to eq. (8) whenever it is required, for example during ray tracing or calculation of the partial derivatives of traveltimes. Eq. (8) is valid only for P waves in weakly anisotropic media with hexagonal symmetry and axes oriented generally in 3-D. Thus AniTomo can not be used for S waves, for which anisotropic propagation is more complex.

The inversion starts from an anisotropic initial model, in which starting parameters have to be specified in each parametrization node. Final model is obtained after iterative updating of the initial model. We can either start the inversion from a homogeneous very weak (∼1 per cent) anisotropic model or involve some a-priori information on anisotropy, for example from previous studies, into the initial model. Sections 4 and 5 survey the choice of initial model.

To adapt the original isotropic code for its anisotropic version, we enlarge number of unknown parameters, because we iteratively search for up to four model parameters at each node of a 3-D orthogonal grid. Thus, total number of model parameters is four times larger compared to the isotropic tomography. Due to the increased complexity, good ray coverage of the model in terms of number and directional distribution of the rays is crucial for a reliable inversion. The code is written in such a way that we can fix any parameter when it is not well determined. Thus, we can limit anisotropic inversion only to a well-resolved part of the volume studied and run isotropic inversion in the remaining volume simultaneously. Purely isotropic inversion is also possible with AniTomo.

Further step, adapting the inversion for anisotropy, was an extension of matrix $\boldsymbol{A}$ (eq. 15) to include partial derivatives of traveltime with respect to each of the four anisotropic parameters (eqs 11–14). Matrix $\boldsymbol{A}$ is now a block matrix containing up to four blocks. The size of the blocks depends on number of unknowns for each of the four anisotropic parameters. Smoothing matrix $\boldsymbol{W_M}$ (eq. 15), which enables horizontal Laplacian smoothing of any of the four types of model parameters, is of the same block structure. Any of the blocks is set to identity when the respective smoothing option is switched off. Damping factor ε^2 is assigned separately to each type of the model parameters (see Section 4). The inverse of matrix in eq. (15) is computed by truncated singular value decomposition.

Resolution matrix (16) is also made up of one block for each of the four types of model parameters. As the resolution matrix contains partial derivatives, resolvability of azimuth and inclination of the symmetry axis directly depends on strength of anisotropy (eqs 13–14). Thus, in the case of relatively low strength of anisotropy we obtain a very low RDE for axis orientation despite a very good ray coverage. It simply means that for a too low value of anisotropy, orientation of the symmetry axis is not resolved reliably (see Section 4.4).

Attention should be paid to quality of directional coverage of the volume studied by rays. In order to express 3-D distribution of the rays within the parametrization cells, we implemented in AniTomo calculations of ray density tensor (Kissling 1988; Sandoval 2002; Sandoval *et al.* 2004). Detailed theoretical background of evaluation of the ray density tensors (RDT) is presented in Appendix B.

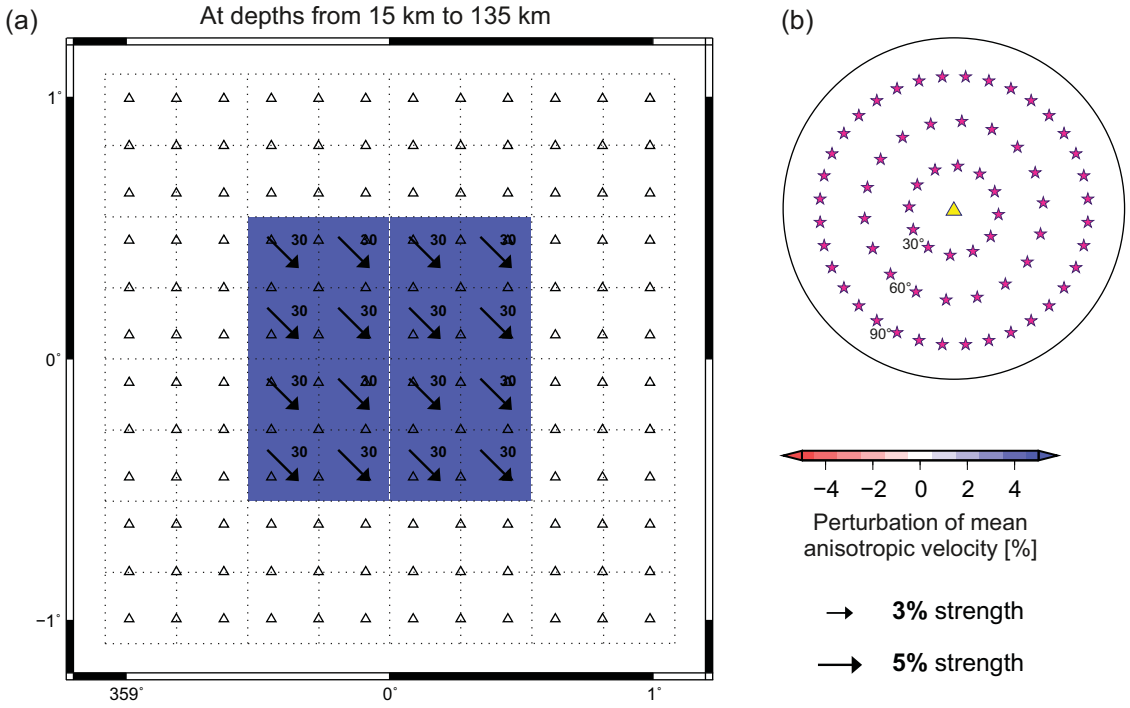

Figure 2. Model of high-velocity heterogeneity with dipping anisotropy designed for synthetic tests of influence of damping and initial model on the solution (a). The velocity perturbation of the heterogeneity is 5 per cent relative to IASP'91. The strength of anisotropy with dipping symmetry axis towards southeast is also 5 per cent. The arrows indicate strength of anisotropy and azimuth of orientation of the symmetry axis at the parametrization nodes. In general, we plot the arrows only for anisotropy stronger than 1 per cent. Axis inclination measured upward from vertical is marked with a number next to the arrow. A case of a low-velocity symmetry axis would be marked with b, otherwise the axis is high-velocity. The horizontal distribution of pparametrization cells, each of which is centred around an inversion node, is marked with dotted lines. Stations located at the surface with 20 km spacing are represented by triangles. Locations of events regularly distributed in teleseismic distances are in (b).

4 SYNTHETIC TESTS I—EFFECTS OF DAMPING AND INITIAL MODEL SETUP ON THE FINAL OUTPUT MODEL

Power of synthetic tests results from a possibility to compare the final output model with the original input model. Thus, one can directly see the impact of a specific inversion setup on the solution, unlike in a real case. Synthetic tests are useful to become familiar with any new code, to explore its strengths and weaknesses before applying it routinely as well as to establish a proper model-volume parametrization, find optimum control parameters and explore capability of the given ray coverage to resolve the model parameters, always when a new data set is to be processed. In the case of the new anisotropic code AniTomo, it is essential to examine various aspects of this unique approach. In this chapter, we demonstrate how the choice of damping (eq. 15) and of the initial anisotropic model influence the resulting model. The synthetic model designed for this methodological purpose is very simple. Tests with a more complex synthetic structure are in Section 5. Effects on non-uniform ray distribution in real data are tested in the accompanying paper (Munzarová *et al.* 2018, revision submitted).

4.1 Setup of methodological synthetic experiments

In order to mimic a setup of a regional teleseismic tomography of the Earth's upper mantle, particularly the continental mantle lithosphere, we consider a volume of 240 km × 240 km × 120 km with a synthetic anisotropic heterogeneity of 120 km × 120 km × 120 km in the middle (Fig. 2). The heterogeneity is characterized by an isotropic velocity component that is 5 per cent higher than the IASP'91 reference model (Kennett & Engdahl 1991). Furthermore, we assign anisotropy of 5 per cent strength to the synthetic heterogeneity. The anisotropy has hexagonal symmetry with high-velocity *a*-axis. We note that the type of symmetry axis is determined in AniTomo only by the sign of strength of anisotropy, that is by positive strength for high-velocity *a*-axis and by negative sign for low-velocity *b*-axis (Section 2). The inversion, in principle, does not favour any type of the symmetry. Orientation of the symmetry axis of the synthetic anisotropic heterogeneity is defined by azimuth of 135° and inclination of 30°, measured upward from vertical.

We parametrize the volume studied by an orthogonal 3-D grid of 8 × 8 × 4 nodes, in which the model parameters are searched. Grid spacing is 30 km both horizontally and vertically. Synthetic set of 9504 rays corresponds to *P* waves propagating from 66 equally distributed teleseismic events to 144 stations located at the surface above the volume studied (Fig. 2b). Input data set for the synthetic tests of AniTomo consists of traveltime residuals calculated as differences between the traveltimes of *P* waves passing through the synthetic structure described above and the traveltimes calculated for the IASP'91 reference model. Gaussian errors with standard deviation of 0.05 s are added to the calculated traveltimes mimicking the observation errors. Smoothing of the model parameters is switched off. All the inversions run for eight iterations in order to evaluate both the stability of the inversion and the character of convergence of the model parameters in dependence on number of iterations. In the following parts, we test influence of damping and initial anisotropic model on inversion stability and development of model parameters.

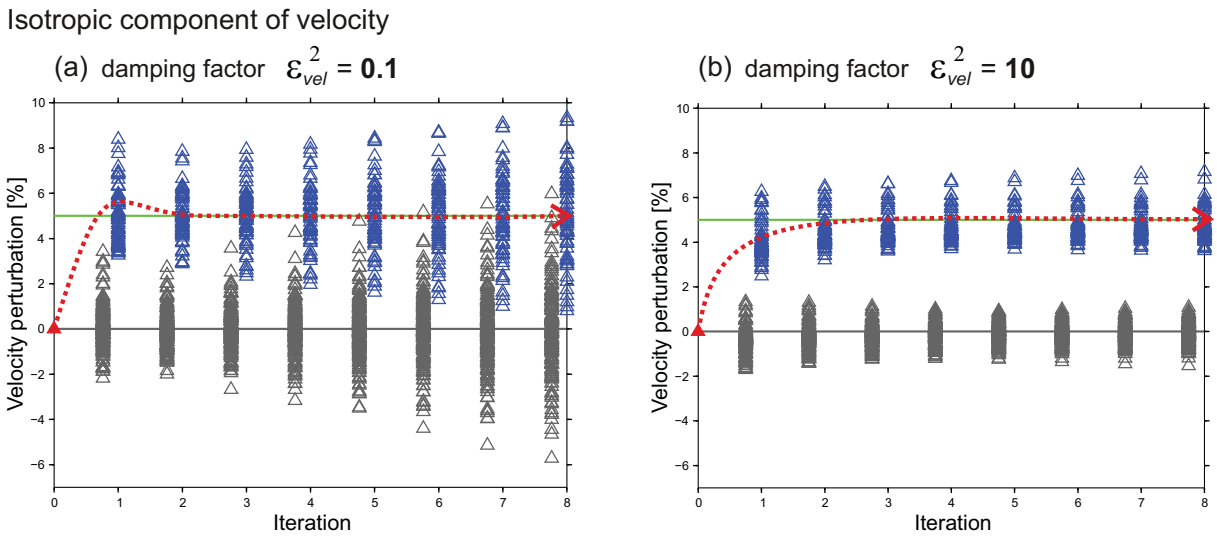

Figure 3. Perturbations of isotropic components of velocity for damping factor of 0.1 (a) and 10 (b). To show evolution of the model parameters with increasing iteration number, we plot them for all the nodes and all the iterations in one graph. The model parameters of the nodes with the high-velocity anisotropic heterogeneity in the synthetic model (Fig. 2) are distinguished with blue colour from the model parameters of the surrounding nodes (grey). Green and grey lines indicate the target model values of the nodes with and without the synthetic heterogeneity, respectively. Red triangle marks the initial value assigned to all the nodes before the inversion. Red dotted curve tracks the overall trend of the model parameters belonging to the nodes with the synthetic heterogeneity. The damping factors strongly influence the rate of convergence and the scattering in the results for all model parameters. See Fig. S2(b) for an example with a higher value of damping.

4.2 Effect of damping factor on the solution

Damping is a regularization parameter that helps to stabilize inversion of underdetermined problems by minimizing a combination of prediction error and solution length (eq. 15; Menke 1984). The choice of damping factor affects rate of convergence of the model parameters, their overall amplitude and scatter in dependence on number of iterations. A well-selected damping factor suppresses small or even single-cell anomalies, coming mostly from data errors, or large perturbations in less resolved nodes. Different values of damping have to be assigned to each of the four types of model parameters, which are isotropic component of anisotropic velocity, strength of anisotropy and azimuth and inclination for orientation of the symmetry axis. Therefore, the damping factors defined as follows:

$$\left[\varepsilon^2_{\mathrm{vel}}\right] = \left[\frac{\Delta t^2}{\Delta \bar{v}^2}\right] = \frac{\mathrm{s}^4}{\mathrm{km}^2}, \tag{17}$$

$$\left[\varepsilon^2_{\mathrm{stren}}\right] = \left[\frac{\Delta t^2}{\Delta k^2}\right] = \mathrm{s}^2, \tag{18}$$

$$\left[\varepsilon^2_{\mathrm{azim}}\right] = \left[\frac{\Delta t^2}{\Delta \lambda^2}\right] = \frac{\mathrm{s}^2}{\mathrm{rad}^2}, \tag{19}$$

$$\left[\varepsilon^2_{\mathrm{incl}}\right] = \left[\frac{\Delta t^2}{\Delta \theta^2}\right] = \frac{\mathrm{s}^2}{\mathrm{rad}^2}, \tag{20}$$

have different physical meaning. Though it is necessary to treat each damping factor as an individual quantity, they are related among themselves. The proper values differ for individual data sets and inversion settings.

The most common way of displaying effects of different inversion setups, apart from plotting the output model itself, is to draw trade-off curves, that is model- and data-variance pairs. In order to get a more detailed insight into the influence of a given inversion setup, we investigate evolution of the model parameters with increasing number of iterations. In such a way, we can examine how fast and how precisely the output model parameters reach the correct values in dependence on different factors of damping (Figs 3–5 and Fig. S2). During these synthetic tests, we always change only one of the four damping factors, while the three others as well as other settings remain fixed. Below, we evaluate effects of intensity of damping on the convergence rates and scatter of isotropic component of velocity, anisotropy strength and axis inclination for Synthetic model I (parameters see above).

Quite a wide range of damping factors leads to a stable inversion for perturbations of isotropic component of anisotropic velocity. The retrieved model velocities converge fast to the correct values of the target model (Fig. 3). On the other hand, different values of damping distinctly affect scatter of the perturbations. The scatter around the target velocities increases with increasing number of iterations of the inversion with low damping of 0.1, while the model velocities for damping of 10, chosen as the appropriate one, form a narrow band of a constant scatter around the target value. Damping of 100 is, on the contrary, too high and it evidently slows down the convergence of the isotropic-velocity perturbations (Fig. S2b). Fig. 4 and Fig. S2(d) show the same kind of plots for low, medium and high damping of strength of anisotropy with factors of 0.1, 100 and 1000. Damping of 100 significantly reduces the scattering of anisotropy strength but it also slows down the convergence.

In the case of azimuth and inclination, which define the orientation of the symmetry axis, well-tuned damping factors are essential for stability of the inversion because of non-linearity between the angles and the anisotropic velocity (eq. 8). Damping controls step length for each iteration of the model parameters. Linearization requires the step length to be short enough to assure relatively slow changes of azimuths and inclinations towards the correct solution. In the case of low damping factor (Fig. 5a), the model inclinations overshoot the correct values after the first iteration. However, despite that the inclinations converge fast to the target values and the

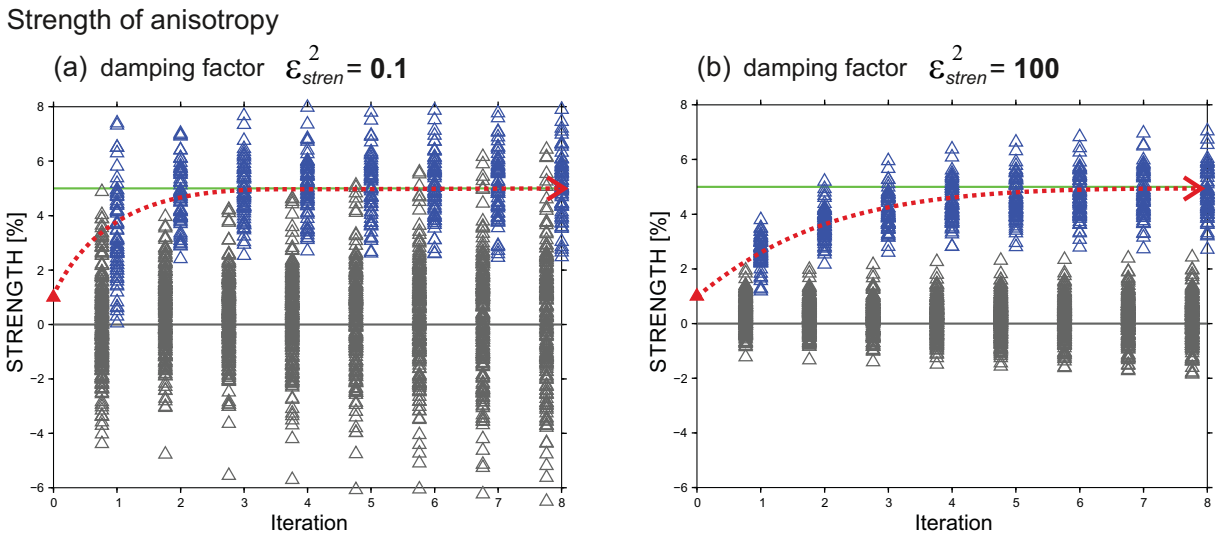

Figure 4. Resulting model parameters corresponding to strength of anisotropy after individual iterations for damping factor of 0.1 (a) and 100 (b). See Fig. S2(d) for an example with a higher value of damping. See also caption of Fig. 3.

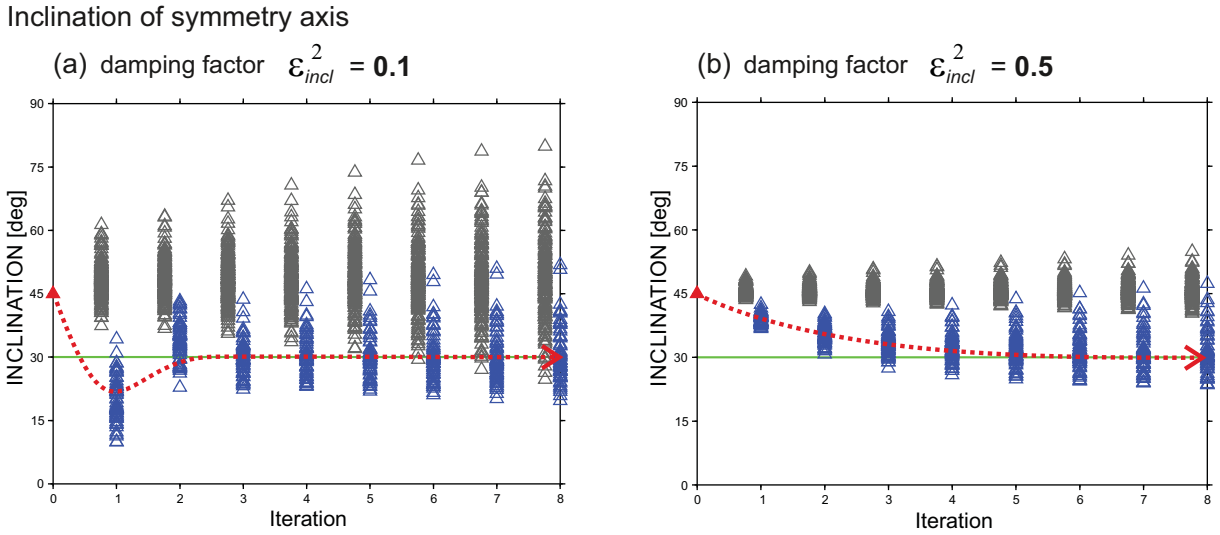

Figure 5. Resulting model parameters corresponding to inclination of symmetry axis after individual iterations for damping factor of 0.1 (a) and 0.5 (b). See Fig. S2(f) for an example with a higher value of damping. See also caption of Fig. 3.

inversion remains stable. On the contrary, the higher damping factor results in a slow steady convergence of the model inclinations (Fig. 5b).

According to rate of convergence and scatter of the model parameters we choose 1, 100, 0.1 and 0.5 damping for isotropic component of velocity, strength of anisotropy and azimuth and inclination of the symmetry axis, respectively. This combination of damping factors leads to fluently converging model parameters and it minimizes their scatter. In this series of synthetic tests, we have demonstrated how damping of anisotropic inversion affects the resulting model. Well-tuned factors of damping of all the model parameters are essential for a stable inversion. On the other hand, testing different inversion settings is appropriate not only for anisotropic tomography but generally.

4.3 Effect of initial model setup on the solution

Another aspect of anisotropic inversion, which is relevant to be tested on synthetics, is setting up an initial anisotropic model. The inversion should start from a model that is relatively close to the target one to satisfy conditions of linearization of the traveltime equation (eq. 9). This is a well-known assumption also from isotropic tomography, which is generally fulfilled in the upper mantle for standard reference earth models, for example IASP'91 (Kennett & Engdahl 1991) or ak135 (Kennett *et al.* 1995; Montagner & Kennett 1996), or a minimum 1-D model in local earthquake tomography (e.g. Kissling 1988; Spakman *et al.* 1993; Kissling & Spakman 1996). Nevertheless, what does it mean for anisotropic tomography and what limitations does it introduce? Attention must be paid particularly to orientation of the symmetry axis, whose the relation

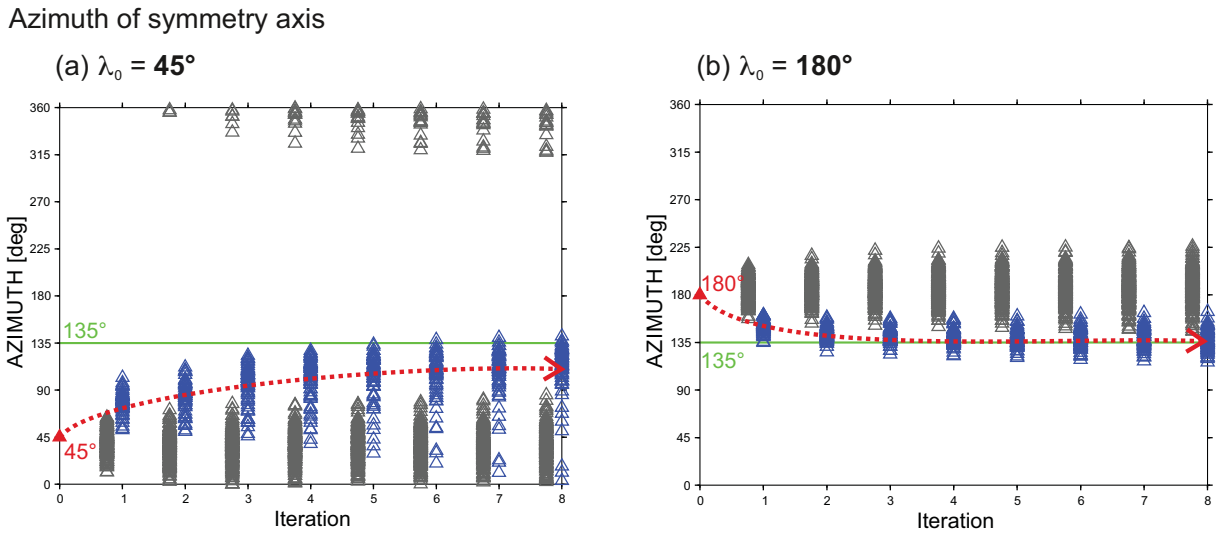

Figure 6. Resulting model parameters corresponding to azimuth of the symmetry axis after individual iterations for the initial values of 45° (a) and 180° (b). See also caption of Fig. 3.

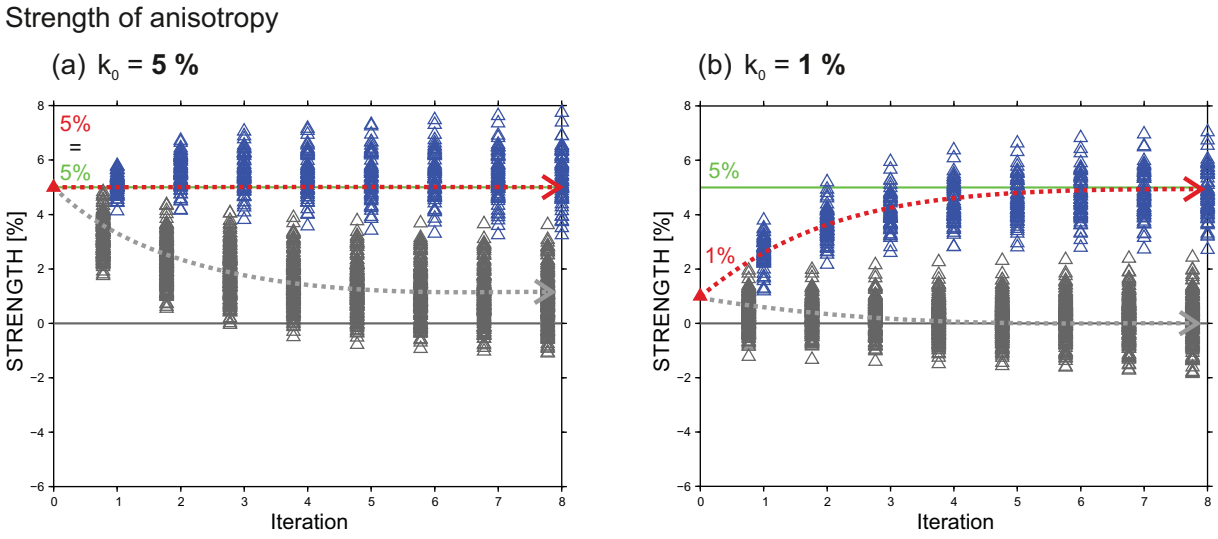

Figure 7. Resulting model parameters corresponding to strength of anisotropy after individual iterations for the initial values of 5 per cent (a) and 1 per cent (b). See also caption of Fig. 3.

to anisotropic velocity (eq. 8) is not linear. In the following tests, we prescribe different initial models containing non-zero homogeneous anisotropy in all the grid nodes, where the model parameters are searched, to investigate effect of the initial setup on the output model.

Fig. 6 shows evolution of model parameters in relation to number of iterations for initial models with differently oriented axis of hexagonal symmetry. In the first model we assume initial azimuth of 45° and in the second one the initial azimuth is 180°, whereas the target azimuth is 135° at the nodes with the synthetic anisotropic heterogeneity. Despite the 90° difference between the first initial and the target azimuths, most of the model azimuths tend to approach the target value (blue triangles in Fig. 6a). There is no surprise that the iterative model azimuths converge better and faster in the case of initial model with azimuth of 180°, which is closer to the target value of 135° (Fig. 6b). We can conclude that the closer the initial model parameters are to the target ones, the faster the iterative model parameters converge to the correct values. It is evident that the choice of the initial orientation of the symmetry axis influences the resulting model. Therefore, we advocate necessity of an appropriate and systematic scanning of the volume with a set of initial orientations. We discuss that in Sections 5.1 and 5.2.

Fig. 7 shows influence of the initial value of strength of anisotropy on the results. Starting the inversion with 5 per cent anisotropy, which might be considered as an approximation of peridotitic upper mantle, it is difficult to eliminate anisotropy artificially assigned to the boundary nodes of Synthetic model I, where only isotropic velocities were prescribed (a). On the contrary, a better recovery of both the isotropic and anisotropic parts of the model is obvious in the case of iterative inversions initiated from weak anisotropy strength of 1 per cent (b). However, we avoid starting the inversion with anisotropy strength set to 0 per cent, because it is equivalent to fixing the azimuth and inclination of the symmetry axis during the first iteration (eqs 13–14). These tests have shown that a very week initial strength of anisotropy does not impose artificial anisotropy into the isotropic part of the model and that it enables a fluent convergence

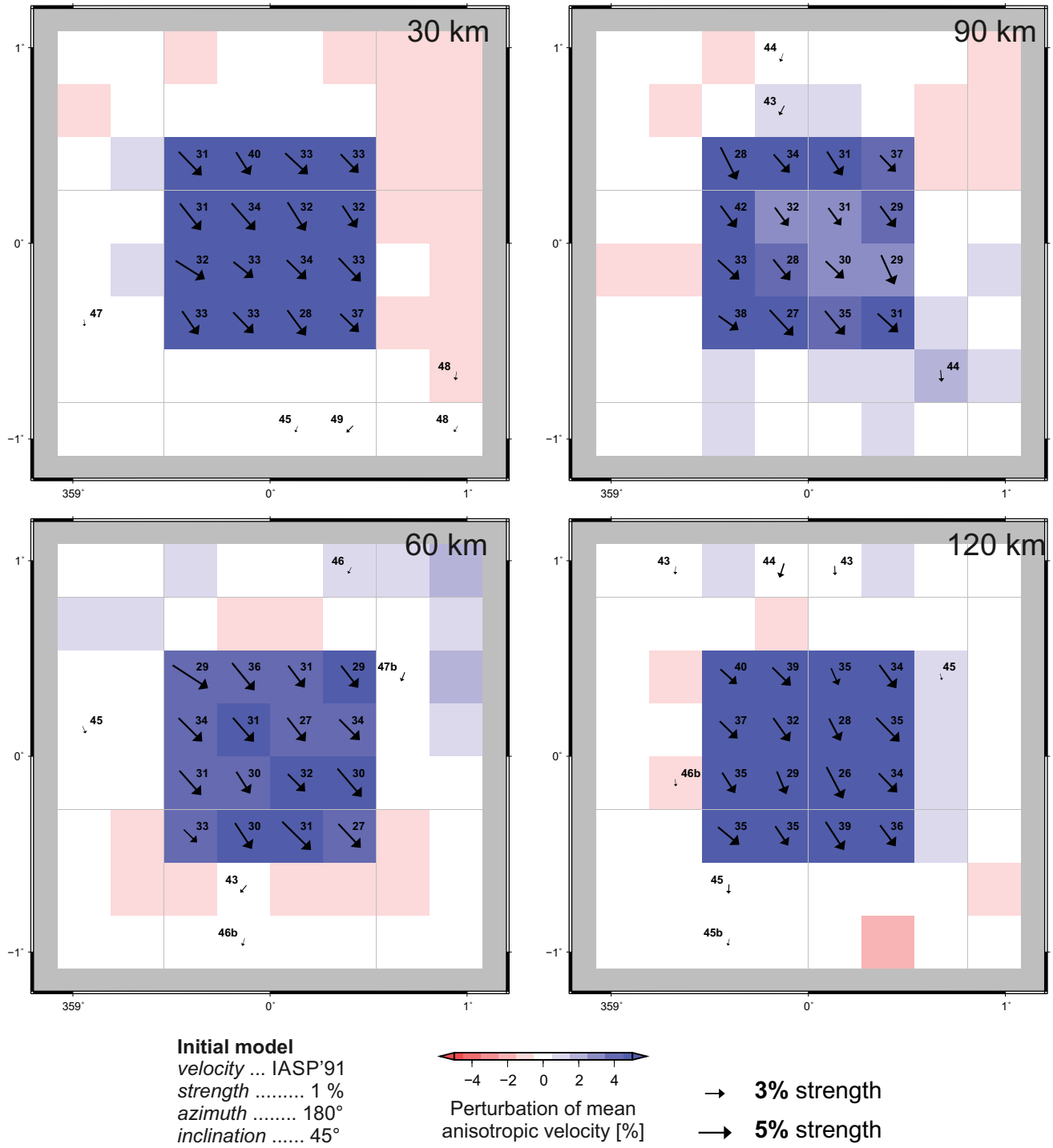

Figure 8. The entire model resulting after four iterations of the synthetic inversion with well-tuned damping factors and the initial model close to the target model (Fig. 2). See caption of Fig. 2 for description of visualization of the anisotropic parameters.

of the iterative strength parameters within the anisotropic part of the model.

4.4 Resulting model of the methodological synthetic experiment

Finally, we present the model (Fig. 8) that comes out from the 4th iteration of the inversion with well-tuned damping factors (Section 4.2) and with the initial model as follows: isotropic velocity equal to the IASP'91 velocities, strength of anisotropy of 1 per cent, and azimuth and inclination of the symmetry axis of 180° and 45°, respectively. 3-D shape of the heterogeneity is perfectly restored for all anisotropic parameters. No lateral deformation of the heterogeneity occurs. An area of negative-velocity perturbations with low amplitudes, particularly at 30 km depth, neighbours the high-velocity heterogeneity in the centre. It might be due to the general incapability of teleseismic tomography to recover the absolute velocities. The reduction of data variance is 98 per cent

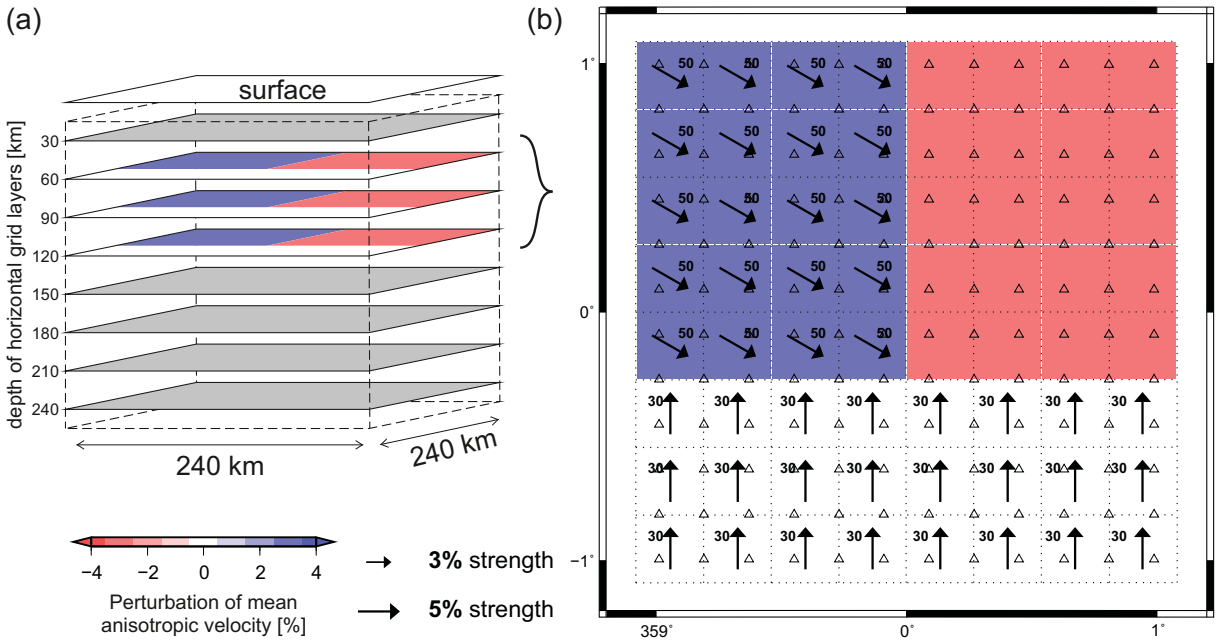

Figure 9. Scheme of synthetic model mimicking a realistic anisotropic structure of the mantle lithosphere (a). Three blocks with different mean velocities and anisotropy (b) are put between depths of 45 km and 135 km. Both the northwestern high-velocity and the northeastern low-velocity blocks exhibit 3 per cent amplitude of the isotropic-velocity perturbations. Strength of anisotropy in the northwestern and in the southern blocks is 5 per cent. See caption of Fig. 2 for description of visualization of the anisotropic model and the synthetic station-event distribution.

Table 1. Anisotropic parameters of three anisotropic blocks between 45 and 135 km depths of the synthetic model mimicking domains of continental mantle lithosphere (see Fig. 9).

	Vel. pert. from IASP'91 (%)	Strength of anisotropy (%)	Azimuth of symmetry axis (°)	Inclination of symmetry axis (°)
Northwestern b.	3	5	120	50
Northeastern b.	–3	0	NA	NA
Southern b.	0	5	0	30

Shortcut vel. pert. stands for velocity perturbation and b. for block.

and the remaining traveltime residuals are at the level of noise of 0.05 s.

As a matter of interest, we plot diagonal elements resolution matrix (RDE; eq. 16) for the model investigated in this section in Fig. S3. While resolution of the isotropic component of velocity and strength of anisotropy is perfect everywhere, the image of RDE for azimuth and inclination of symmetry axis follows shape of the anisotropic heterogeneity. RDE are high enough in the central part, where the anisotropic heterogeneity is in the input model, but outside of the anisotropic region, the RDE are low. As there is no anisotropy in this part of the model, the axis might turn arbitrarily there. This is in agreement with eqs (13) and (14).

5 SYNTHETIC TESTS II—ASSESSING POTENTIAL TRADE-OFF BETWEEN ANISOTROPY AND ISOTROPIC HETEROGENEITY

5.1 Setup of the synthetic experiment representing domain-like structure of continental mantle lithosphere

Series of synthetic inversions presented in this chapter focus on setting initial models for anisotropic tomography of the mantle lithosphere and the sublithospheric mantle. The Synthetic model II, mimicking a domain-like structure of continental mantle lithosphere, occupies 240 km × 240 km × 240 km, that is it is twice as deep as the Synthetic model I in Section 4. We enlarge the thickness of the model, in order to examine depth resolution of the method. We keep spacing between the nodes at 30 km both horizontally and vertically, resulting in 8 × 8 × 8 grid nodes, in which the unknown model parameters are searched. We use the same synthetic quasi-equal distribution of 9504 teleseismic *P* waves as in Section 4. The Synthetic model II consists of three blocks, two of which are anisotropic (northwestern and southern) and one (northeastern) is purely isotropic. The blocks differ in their shapes as well. All the three blocks extend from 45 km down to 135 km and they are characterized by different isotropic components of anisotropic velocity (Fig. 9 and Table 1). The anisotropic blocks possess 5 per cent anisotropy with different orientations of the symmetry axes. The isotropic velocities are non-perturbed above and below the three blocks. Such a synthetic model of sharply bounded anisotropic blocks is motivated by a concept of continental mantle lithosphere being formed as an assemblage of lithospheric domains, preserving their mean velocities and fossil fabrics (e.g. Plomerová & Babuška 2010).

During the inversion, damping factors are the same as those adopted as optimum for the methodological synthetic test I (Section 4.4), because we keep the parametrization grid, the ray coverage and the synthetic-data error. We demonstrated in Section 4.3 that

the output model depends on the angular deviation between the orientation of symmetry axes of the initial and the searched model due to the non-linear relation between anisotropic velocity and orientation of the symmetry axis (eq. 8). Therefore, we keep the IASP'91 velocities and strength of anisotropy of 1 per cent in the initial model and we repeat the inversion for regularly changing setups of initial azimuths and inclinations. We invert twelve times with all combinations of initial azimuths (0°, 90°, 180° and 270°) and inclinations (10°—subvertical axis, 45°—dipping axis and 80°—subhorizontal axis) in order to systematically cover the range of initial orientations of the hexagonal-symmetry axis. By this procedure we minimize a danger that the resulting model will be affected by the initial setup of anisotropy orientation.

5.2 Resulting model of the synthetic experiment representing domain-like structure of continental mantle lithosphere

Fig. 10 shows output model parameters at depth of 90 km from three types of inversions according to initial inclination: with initial symmetry axis inclined at 45° successively at azimuths of 0° (a), 90° (b), 180° (c) and 270° (d), with a subvertical axis orientation of 10° inclination and azimuth of 0° (e) and a subhorizontal orientation of 80° inclination and azimuth of 90° (f). For results in other depths we refer to Fig. S4. Anisotropy in the northwestern block characterized by axis inclining 50° from vertical in azimuth of 120° (Fig. 9 and Table 1) is well recovered for the initial models with inclined initial axis in azimuth of 90° (Fig. 10b) or 180° (Fig. 10c) and also for the initial model with the subhorizontal axis gently dipping in azimuth of 90° (Fig. 10f). In the case of the other two initial orientations of inclined axes (at azimuth of 0° and 270°) the recovered model is more complex and does not capture well the anisotropy of the Synthetic model II. At some nodes, even solutions with low-velocity *b*-axis occur despite the fact that the target anisotropy is of a high-velocity *a*-axis (Figs 10a and d). Such a solution appears when the initial orientation of the symmetry axis is far from the true high-velocity *a*-axis of the synthetic model and it is thus closer to the low-velocity (*b,c*) plane of the prescribed hexagonal anisotropy. In the southern block, anisotropy inclined at 30° in azimuth of 0° is recovered well by inversions with the initial inclined or subvertical symmetry axes both in azimuth of 0° (Figs 10a and e).

The sensitivity of resulting models on initial anisotropic parameters calls for being careful when setting the initial parameters for anisotropic tomography. To minimize any potential bias, while modelling the *a priori* unknown anisotropic structure of the Earth's upper mantle, we have looked for a way how to evaluate and present a whole family of anisotropic model parameters retrieved in each node for the set of initial setups. Fig. 11 combines all the output models in such a way that the isotropic components of velocity resulting from all the inversions are averaged in individual nodes, while the output strength of anisotropy, the azimuth and inclination of the symmetry axis are displayed individually for each inversion and every grid node. To present the retrieved anisotropy in each node, we plot its strength in stereographic projection on the lower hemisphere, where the two angles represent orientation of symmetry axis.

Fig. 11 displays the combined resulting model at depths of 90 and 150 km (for the whole combined model see Supplementary Fig. S5). We concentrate on distinct features and general trends of the resulting parameters from inversions with different initial models that are consistent over relatively large regions. The three blocks of the Synthetic model II can be easily distinguished at the depth of 90 km according to all parameters. The red-white-blue background in Fig. 11 expresses the velocity perturbations, whereas the blue and red symbols reflect orientation of the high-velocity and the low-velocity anisotropy axes, respectively. This way of presentation of the results is complex, but allows us to consider all four basic model parameters jointly.

The resulting orientations of the high-velocity *a*-axis (blue symbols) tend to concentrate in roughly southeastern inclined directions in the northwestern block of the model (within dashed green curve, Fig. 1), which is in agreement with the target anisotropy in the northwestern block. On the other hand, there are also low-velocity *b*-axes (red symbols) that incline in approximately opposite, that is in the northwestern directions. These secondary solutions with the low-velocity *b*-axis have a very similar distribution of directions of relatively high and low velocities for teleseismic *P* waves as the target anisotropy with high-velocity *a*-axis. Preference of the models with *b*-axis is a consequence of a large angular deviation between the corresponding initial axes and the target symmetry axis. Moreover, distribution of the solutions with a low-velocity *b*-axis complements at each node the solutions with a high-velocity *a*-axis, confirming thus self-consistency and stability of the anisotropic part of the model.

In the south (within dotted green curve), the resulting high-velocity *a*-axes concentrate in directions steeply inclined towards the north. On the other hand, the northeastern region does not exhibit distinct signs of anisotropy. The strength of anisotropy is low there (1–2 per cent) and orientations of the output axes are rather diffuse than localized. This indicates that the coupled anisotropic–isotropic inversion does not create any coherent anisotropy in the isotropic northeastern part of the model. In general, structure of the two anisotropic and one isotropic blocks is well recovered (Fig. S5) and the resulting model captures perfectly sharpness of the block boundaries.

Contrast between the resulting parameters at the depth of 90 km and those at 150 km, representing the topmost isotropic layer below the anisotropic blocks, is evident (Fig. 11). Some leakage of both the isotropic and anisotropic components of velocity below the anisotropic blocks appears due to smearing along the ray paths, which is a typical drawback of teleseismic tomography, but it does not exceed amplitude of 2 per cent of isotropic perturbations and anisotropy strength. Moreover, concentration of symmetry axes towards a particular direction is very limited and it appears only in a few grid cells or at the model edges indicating an artefact. The negative effect of smearing is evident particularly at the 30 km depth, at the upper limit of our model (Fig. S5).

Results of Synthetic test II allows us to conclude that running the anisotropic inversion systematically for different initial orientations of the symmetry axis leads to a robust model of anisotropic velocities.

5.3 Trade-off between isotropic-velocity heterogeneities and anisotropic structure

The previous test shows that the AniTomo code is capable to reveal structures with both anisotropic- and isotropic-velocity components. For further testing of the code, we consider either only the isotropic or only the anisotropic part of the synthetic model imaged in Fig. 9, in order to see how the traveltime residuals from purely isotropic or purely anisotropic structures are interpreted by the coupled anisotropic–isotropic inversion.

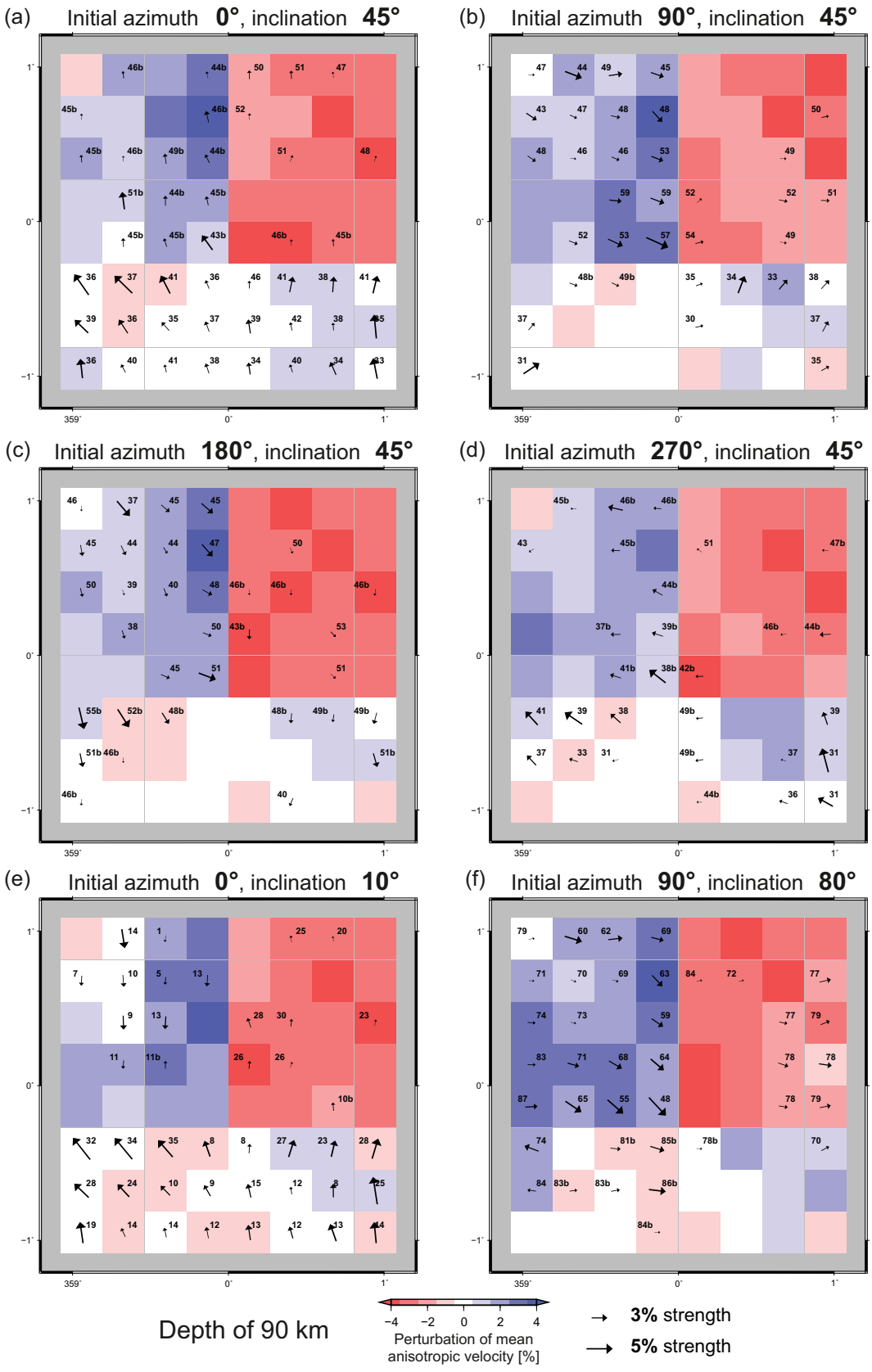

Figure 10. Resulting model parameters at 90 km depth after four iterations of synthetic inversions with different initial orientations of the symmetry axis (the models down to 180 km depth are in Fig. S4; synthetic model is in Fig. 9). See caption of Fig. 2 for description of visualization of the anisotropic parameters. Initiating the inversion from an orientation of the symmetry axis that is not much deviated from the searched orientation, the symmetry axis turns in a correct direction during the inversion.

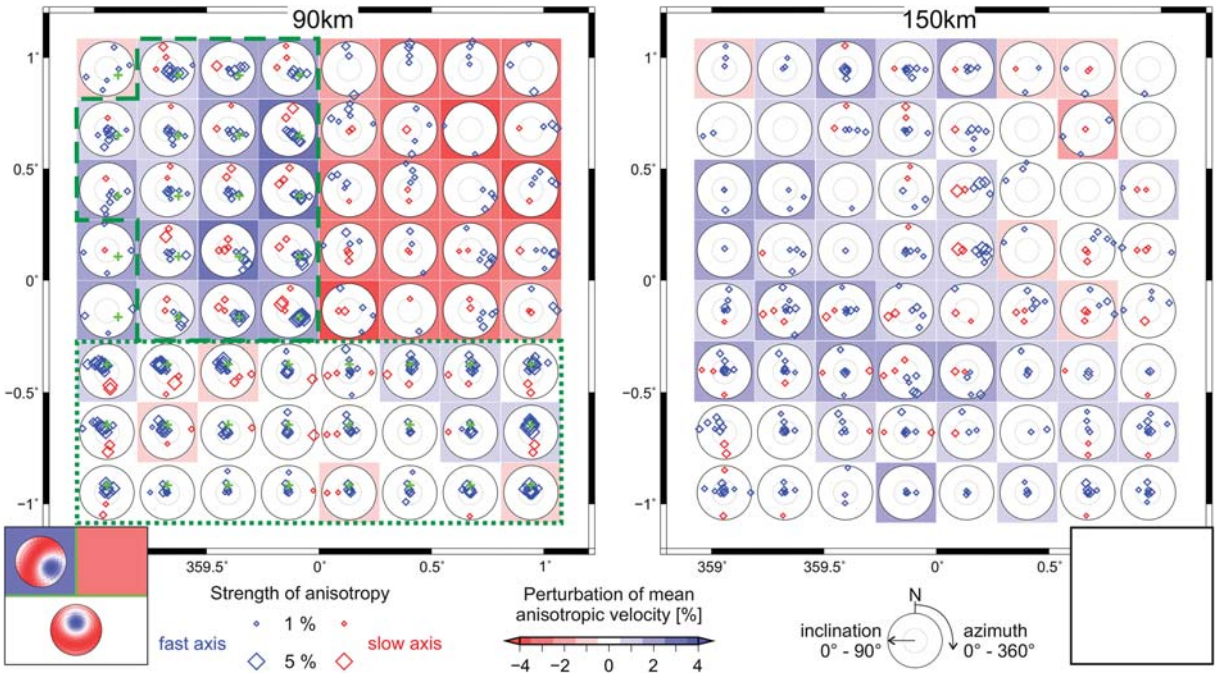

Figure 11. Resulting model parameters after four iterations of synthetic inversions with different initial orientations of the symmetry axis imaged together in the combined output model at 90 km and 150 km depths (the whole combined model is in Fig. S5; synthetic model is in Fig. 9). The isotropic components of velocity from the individual inversions are averaged at each node and displayed as background squares in the combined model. Output orientations from individual inversions are imaged as single points at each node represented by blue or red symbols for high-velocity *a* or low-velocity *b*-axis of hexagonal symmetry, respectively, in lower-hemisphere stereographic projection (white circles). Size of the symbols is scaled by strength of anisotropy and only parameters with strength larger than 1 per cent are plotted, because resolution of symmetry-axis orientation decreases with decreasing strength of anisotropy. The synthetic, that is correct orientations of symmetry axis are marked with green crosses at nodes where non-zero strength is assigned in the synthetic model. The insets also schematically image the input synthetic structure. Dashed, or dotted, green curves delimit regions that exhibit a relatively homogeneous anisotropy associated with the northwestern, or southern, block of the synthetic model, respectively.

First, we perform the coupled anisotropic–isotropic inversion with the purely isotropic-velocity heterogeneities (Fig. 12 for depths of 90 and 150 km and Fig. S6 for all depth layers). The coupled inversion retrieves the synthetic structure very well. Smearing of the isotropic velocities is very weak and no artificial anisotropy is generated. Anisotropy exceeding 1 per cent strength emerges only sporadically.

In the second step, we invert purely anisotropic structures (Fig. 13 and S7). The coupled inversion retrieves the directions of relatively high and low velocities properly in the blocks where anisotropy is prescribed in the input model, that is in the northwestern and southern blocks. However, some signs of artificial, though very weak anisotropy, can be found at the edge of the originally purely isotropic northeastern block. The strongest artefacts occur in the topmost layer at 30 km depth, where neither anisotropy nor isotropic-velocity variations exist in the synthetic model (Fig. S7). The anisotropic patterns in the northwest and south of the 30 km layer meet the orientations of the deeper layers and they result from upward smearing of the strongly anisotropic structures at 60–120 km. On the other hand, the low-velocity perturbations in the central and northeastern parts of the 30 km layer, together with the highly spread high-velocity axes of anisotropy in the northeast, are isolated. This structure is a strong artefact, but it is limited to the topmost, less resolved, layer (Fig. 14). The low-velocity heterogeneity possibly arises from upward smearing of accordingly oriented low-velocity directions in the northwestern and southern blocks. The spread high-velocity axes in the northeast emerge possibly to compensate the artificial low-velocity heterogeneity in the central part. The deeper parts of the output model, evaluated for the purely anisotropic input, are contaminated by false isotropic-velocity perturbations reaching mostly 1 per cent and locally 2 per cent amplitude (Fig. S7). This test has shown that isotropic-velocity artefacts can be generated from anisotropic input velocities by the coupled anisotropic–isotropic inversion, particularly in the topmost part of the model, where there is not sufficient cross-firing of the rays (see also Fig. 14).

Another test is a standard isotropic-velocity inversion with the same synthetic model consisting of the anisotropic structure of the blocks at depths of 60, 90 and 120 km. Thus, the traveltime residuals caused by anisotropy are forced to be interpreted only as isotropic-velocity perturbations (Fig. S8). Distribution of the low and high isotropic-velocity perturbations is similar to that imaged by the coupled anisotropic–isotropic inversion (Fig. 13 and S7), but the amplitudes are stronger. Reduction of data variance, that is (initial variance—final variance)/initial variance, is 64 per cent for the isotropic-velocity inversion. Evaluation of variance reduction for the coupled anisotropic–isotropic inversion (Fig. 13 and S7) is not as straightforward as in the isotropic case, because we can calculate this measure just for each inversion of the set of anisotropic inversions. Nevertheless, even for the individual anisotropic inversions, the data variance reduction attains values from 71 to 86 per cent and thus increases compared to the isotropic case.

Alternatively, we can fix the isotropic-velocity perturbations and invert only for the strength of anisotropy and orientation of the symmetry axis (Fig. S9). The variance reduction of the individual inversions varies from 66 to 85 per cent. The anisotropic artefacts similar to those in Fig. S7 above and beneath the anisotropic blocks

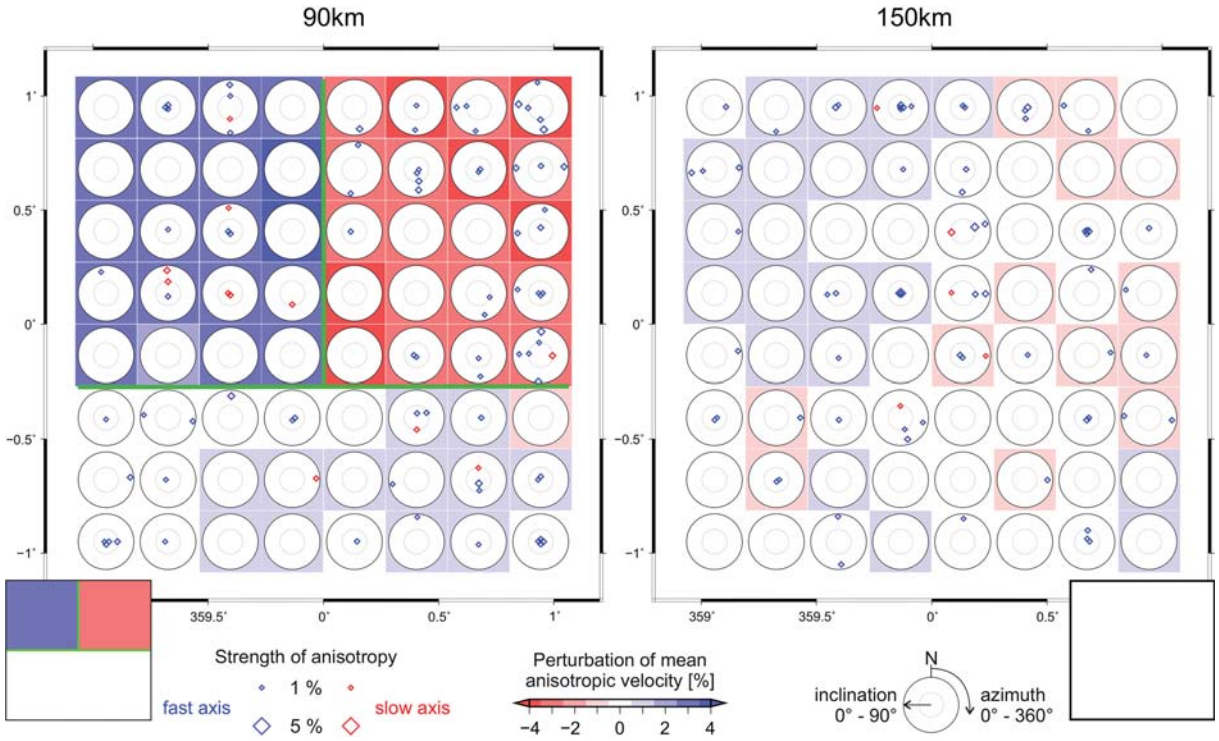

Figure 12. Depth sections at 90 and 150 km of the model of anisotropic velocities resulting from coupled anisotropic–isotropic inversion of synthetic traveltime residuals calculated for *P* waves propagating through the isotropic part of the structure imaged in Fig. 9 (see also the insets at the bottom of each depth section). See Fig. 11 for more details.

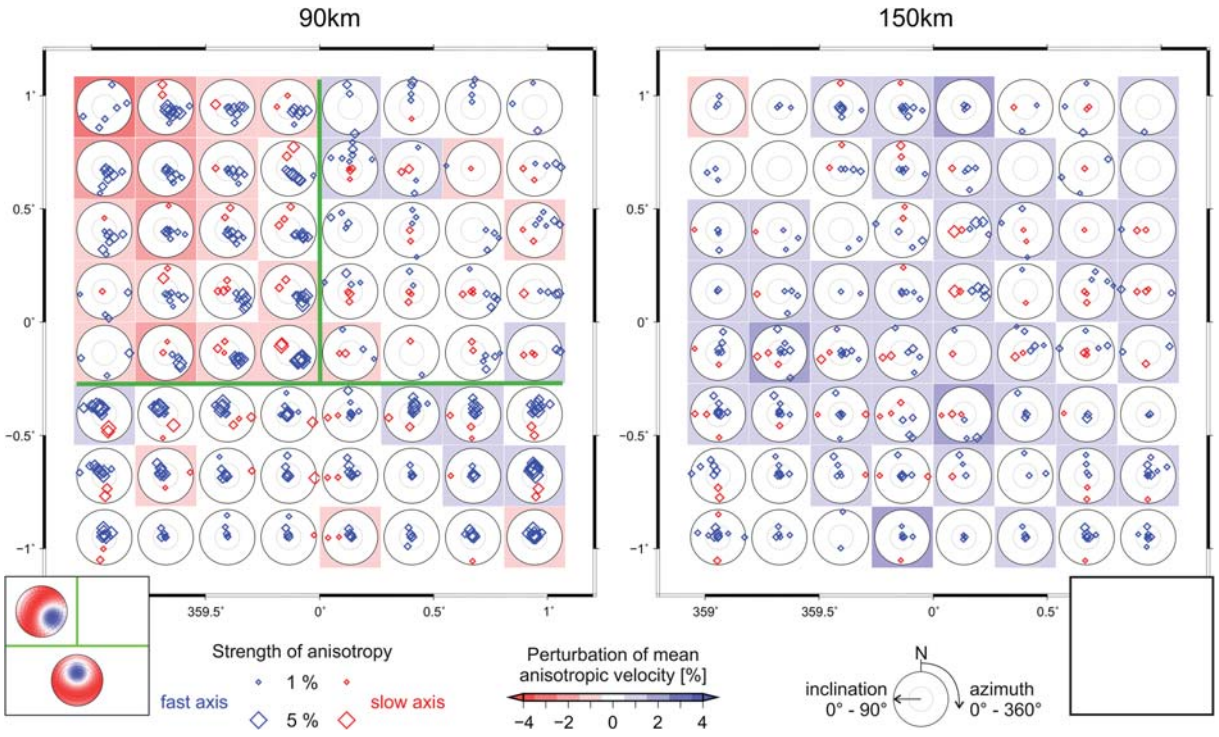

Figure 13. Depth sections at 90 and 150 km of the model of anisotropic velocities resulting from coupled anisotropic-isotropic inversion of synthetic traveltime residuals calculated for *P* waves propagating through the anisotropic part of the structure imaged in Fig. 9 (see also the insets at the bottom of each depth section). See Fig. 11 for more details.

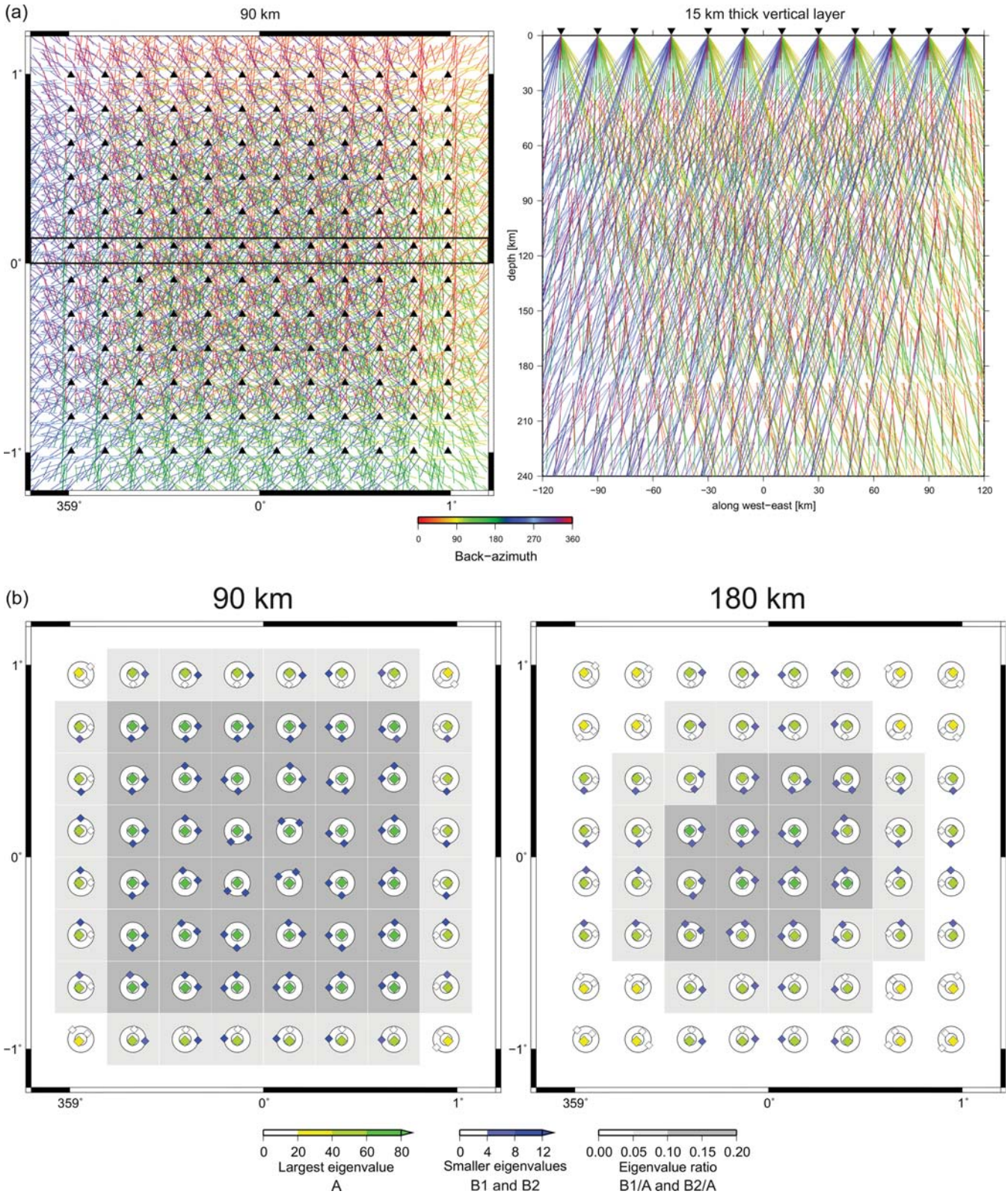

Figure 14. (a) Ray paths of the synthetic set of equally distributed teleseismic events (Fig. 2b) within depth layer of 90 km and within a vertical layer of 15 km thickness oriented west–east (marked with horizontal black lines in the map on the left). The ray paths are coloured according to wave backazimuth. Triangles represent the equally distributed receivers. (b) Ray density tensors (RDT) evaluated for the parametrization nodes of the 90 and 180 km depths for our set of equally distributed synthetic rays. Orientation of three RDT eigenvectors of each node is imaged with points displayed in the lower-hemisphere stereographic projection. Size of the largest RDT eigenvalue of a node is displayed with a different colour scale (marked as A) than size of the two smaller eigenvalues (marked as B1 and B2). Ratios between the smaller eigenvalues and the largest eigenvalue at a node, that is B1 A^{-1} and B2 A^{-1}, are imaged with a background colour. Both the ratios must be larger than the lower limit of a colour band to mark the node with that colour. Such a visualization of RDT eigenvalues and eigenvectors enables to distinguish the nodes according to quality of their ray coverage.

remain, but the structure of the three blocks is imaged correctly and very clearly.

Results of the isotropic-velocity inversion, when the input velocity model is purely anisotropic, depend on distributions and orientations of anisotropy. Some of them are more prone to be misinterpreted as isotropic velocities than others. For example, we perform such a test also with a synthetic model where in the northwestern block the symmetry axis still dips to the southeast, but the type of the axis is changed from high- to low-velocity. It means that the directions of relatively high and low velocities are reversed. After the purely isotropic inversion, data variance for that anisotropic input is reduced only by 40 per cent. In the previous case, in which the high-velocity axis dips to the southeast in the northwestern block, the variance reduction was 64 per cent. This reflects the fact that the convergently oriented high-velocity directions in the two anisotropic blocks favour creation of a high-velocity region beneath them (Fig. S7). Thus, a larger part of the traveltime residuals due to the anisotropic input can be absorbed by the isotropic-velocity perturbations in the output model.

To summarize the last synthetic tests, the coupled anisotropic–isotropic inversion does not tend to create anisotropic artefacts when the real structure is purely isotropic. In the case of anisotropic structure, the situation is more complex. A part of the anisotropic contribution to velocity might be misinterpreted either as an isotropic component or as localized, usually weaker, anisotropy smeared into the isotropic part. Nevertheless, regions of distinct anisotropy and isotropic-velocity heterogeneities are identified correctly. Such findings represent a great benefit of the coupled anisotropic–isotropic inversion compared to a purely isotropic inversion, which misinterprets the anisotropic signal completely.

5.4 Ray density tensor—A tool to investigate distribution of the rays

Quality of directional coverage of the volume studied by rays is crucial to retrieve anisotropic velocities. Fig. 14(a) shows segments of ray paths lying in the horizontal layer at 90 km depth and within a vertical layer of 15 km thickness. The synthetic set of rays used in this paper is realistic for teleseismic *P* waves, but idealistic regarding their uniform distribution. With such an evenly distributed set of rays, we avoid biasing the presented tests, focusing on other aspects of the method by any directional asymmetry (see Munzarová *et al.* 2018, revision submitted, for anisotropic tomography with a real ray distribution). Teleseismic *P* waves propagate within the upper mantle at angles between $\sim 20^\circ$ and $\sim 50^\circ$ and thus the waves are sensitive particularly to anisotropy with inclined symmetry axes.

AniTomo enables evaluation of so-called ray density tensors (RDT; Appendix B) which is a tool to represent directional coverage of a volume studied by a set of rays. Fig. 14(b) shows orientation of eigenvectors and size of eigenvalues of RDT at the nodes of depth of 90 and 180 km of our parametrization grid. The images indicate not only an overall amount of the rays within the parametrization cells (size of the eigenvalues), but they also express directional evenness of the ray distribution (orientation of the eigenvectors and ratio between the eigenvalues). One of the eigenvalues (A) is always much larger than the other two RDT eigenvalues (B1 and B2), which is caused by the limited incidence angles of the teleseismic *P* waves. The more vertical orientation of the eigenvector belonging to the largest eigenvalue (green or yellow dots), the more even azimuthal coverage of the parametrization cell by the teleseismic rays we have. In our case of quasi-equally distributed rays, orientation of the eigenvectors with the largest eigenvalues is vertical for the central part of the individual depth layers and inclines towards the model edges (Fig. 14b). A simplified way how to express evenness of the directional coverage is to investigate ratios of the smaller eigenvalues to the largest eigenvalue, that is B1 A^{-1} and B2 A^{-1}. We can see that ratios B1 A^{-1} and B2 A^{-1} in a range from 0.1 to 0.2 (grey background colours in Fig. 14b) ensure a very good recovery of the anisotropic parameters according to the results of the synthetic tests (Sections 4 and 5).

6 DISCUSSION

We present new code AniTomo for anisotropic teleseismic tomography of the upper mantle, and focus in details on its functionality and potential limitations. Careful tuning of the inversion setup is important in order to get robust and reliable models as we have demonstrated in a methodological series of synthetic tests (Section 4). Damping factors directly affect stability of the inversion, rate of convergence of the model parameters with number of iterations and their scatter. Testing a range of various damping factors before selecting the final values should represent a routine step for any kind of regularized inversion. In the case of anisotropic tomography, different physical meaning of model parameters, that is perturbation of the isotropic component of anisotropic velocity, strength of anisotropy, azimuth and inclination of the symmetry axis, imposes specific demands on the selection of damping. Although regularization of all model parameters decides about success and reliability of the inversion, only little can be found in publications on tomography of azimuthal or radial velocities of the body waves. Huang & Zhao (2013) and Tian & Zhao (2013) show at least a trade-off curve for various damping values of velocity perturbations, but the way of treating the other model parameters remains unspecified.

The general strategy how a complex anisotropic heterogeneous structure can be retrieved with AniTomo is demonstrated in Section 5 on a synthetic block-like structure mimicking domains of the continental mantle lithosphere. The non-linearity of the relation between anisotropic velocity and orientation of the symmetry axis (eq. 8) calls for repeating the inversion several times, starting always from a different initial orientation of the symmetry axis, to systematically cover the whole range of initial conditions. The solution of a particular inversion depends in each node on a deviation between the initial and the searched orientations of the symmetry axis. If the deviation is smaller than about 60°, a distinct anisotropy with a systematic convergence towards the correct orientation easily develops within a few iterations. On the other hand, the parameters converge more slowly when the deviation is large or the searched velocities are isotropic. If the output anisotropic parameters, returned from inversions with different initial axis orientations, tend to create similar pattern, it is an indication of reliability of that anisotropic feature. For a real application of AniTomo, some of the initial models could also be based on *a priori* information on anisotropy in the region if available from other geophysical methods and data sets.

Anisotropy and isotropic heterogeneities affect *P*-wave propagation and it is not simple to discriminate between these two sources of traveltime deviations. But in general, large-scale anisotropy can hardly be fully mimicked by a large-scale isotropic structure, or vice versa. We perform a series of synthetic tests with the coupled anisotropic–isotropic inversion to assess the potential trade-off between effects of isotropic-velocity heterogeneity and seismic anisotropy. Our synthetic tests document that the coupled

anisotropic–isotropic inversion with AniTomo successfully distinguishes both effects, though indistinctive isotropic- or anisotropic-velocity artefacts might occur, particularly at the edges of the structures. Some distortions of the velocities come from well-known subvertical smearing which is a general drawback of teleseismic tomography. On the other hand, running only purely isotropic inversion, when the target structure is anisotropic leads to misinterpretations in the resulting models as we show in our synthetic tests (Section 5.3). Advantage of the developed coupled anisotropic–isotropic inversion is that it does not create anisotropic artefacts when the real structure is purely isotropic.

Although our synthetic data set is realistic as to number of rays and range of incidence angles of teleseismic *P* waves, the quasi-equality of event distribution is idealistic. To achieve a good recovery of the isotropic component of velocity and the anisotropy a good station-event distribution is crucial. For the purpose of analysing directional coverage of a volume by rays in 3-D, we have implemented calculation of so-called ray density tensors (RDT; Appendix B). RDT evaluated for the equally distributed rays with realistic teleseismic incidence angles (Section 5.4) can serve as a benchmark for future comparison with ray geometry of real seismic experiments (Munzarová *et al.* 2018, revision submitted). On the basis of such an analysis, the inversion of real data can be adjusted to actual ray distribution, for example by turning off the inversion for strength of anisotropy and orientation of the symmetry axis at weakly covered parametrization cells. Similarly to our ray density tensors, Huang *et al.* (2015) define normalized length of short axis (NLS) of an ellipse approximating distribution of ray back-azimuth and incidence angles in the case of local-earthquake traveltime inversion for azimuthal and radial anisotropy, respectively. Based on synthetic tests, these authors conclude that inversion at the nodes with NLS parameter as low as 0.3 still yields only a small trade-off between heterogeneities and anisotropy. In this context, our ratios of the two smaller eigenvalues to the largest eigenvalue of the RDT for the synthetic set of purely teleseismic rays (Section 5.4) in a range from 0.1 to 0.2 do seem reasonable. Such ratios of a smaller to the largest eigenvalue describe the strong directional variation of the ray distribution within any subvertical plane as the largest eigenvalue is always subvertical for our set of teleseismic rays. On the contrary, a ratio between the two smaller eigenvalues can be associated with the azimuthal ray coverage, which is, of course, much better in our case as the two smaller eigenvalues are comparable.

Teleseismic *P* waves propagate in the upper mantle at angles between 20° and 50° and thus they can detect very well anisotropy with inclined symmetry axis (e.g. Babuška *et al.* 1984; Grésillaud & Cara 1996). Recovery of a horizontal axis is more difficult with AniTomo as it was confirmed by a synthetic test (not presented in this paper), during which a layer of anisotropy with horizontal symmetry axis was restored only partly by the inversion. For the same reason of limited incidence angles of teleseismic *P* waves, AniTomo can not always distinguish between hexagonal symmetry with inclined high-velocity *a*-axis perpendicular to low-velocity plane (*b*,*c*) and low-velocity *b*-axis perpendicular to high-velocity plane (*a*,*c*) (Fig. S1a). However, both types of hexagonal symmetry are considered in the code because they are physically reasonable and distinguishing between them can be supported by combination of various methods (e.g. Plomerová & Babuška 2010; Plomerová *et al.* 2011). Moreover, allowing for both types of the symmetry (either with *a*- or *b*-axis) increases chance for the model parameters to converge towards one of the solutions, because it is easier to change strength of anisotropy than to rotate the symmetry axis during inversion, and hence to capture the relatively high- and low-velocity directions of anisotropy (Section 5.2).

7 CONCLUSIONS

Widely spread detection of seismic anisotropy of the continental mantle lithosphere called for formulating theory and developing novel tomographic code AniTomo that retrieves 3-D heterogeneous weakly anisotropic structure of the upper mantle. The code iteratively solves the coupled problem of the 3-D anisotropic velocity field by inversion of traveltime residuals of teleseismic *P* waves for parameters describing weak anisotropy with hexagonal symmetry. The model parameters are perturbations of isotropic component of anisotropic velocity, strength of anisotropy and azimuth and inclination of the symmetry axis oriented generally in 3-D. Current version of AniTomo is applicable only to *P* waves and not to *S* waves, for which anisotropic propagation is much more complex.

The main conclusions from the series of realistic synthetic tests that document functionality of code AniTomo as well as effects of inversion setup on the results are:

(1) The coupled anisotropic–isotropic inversion with AniTomo can successfully distinguish isotropic- and anisotropic components of *P*-wave velocity even for complex block-like structures of the upper mantle.

(2) The coupled anisotropic–isotropic inversion does not create anisotropic artefacts when the real structure is purely isotropic.

(3) Isotropic- or anisotropic-velocity artefacts with amplitude mostly of ∼1 per cent might occur in the resulting model, particularly towards the edges of the structures. Strength of anisotropy was 5 per cent in those tests.

(4) Damping factors of all parameters, well-tuned according to synthetic tests, help to achieve a steady convergence towards the correct solution.

(5) Series of inversions with systematically changing initial orientation of anisotropy reduces effects due to a subjective choice of the initial setup.

(6) Similarly to standard isotropic tomography, only signatures consistent over relatively large regions and with similar trends for various initial models should be considered in interpreting of the output parameters.

In the next step, we apply the AniTomo code to data from passive seismic experiment LAPNET to unravel structure of the upper mantle beneath northern Fennoscandia (Munzarová *et al.* 2018, revision submitted) and subsequently to data from other tectonic provinces, for example in the Alpine area, Bohemian Massif or in other parts of Fennoscandia. Tomographic results from AniTomo will contribute to exploration of velocities of anisotropic and heterogeneous upper mantle.

ACKNOWLEDGEMENTS

The research was supported by grant no. M100121201 of the Czech Academy of Sciences, by grant no. 111-10/253101 of the Grant Agency of Charles University and by project CzechGeo/EPOS-Sci, no. CZ.02.1.01/0.0/0.0/16_013/0001800, financed from the Operational Programme Research, Development and Education within ERDF. We would like to thank to Dr Lapo Boschi, Editor of GJI, and to two anonymous reviewers for their thorough review that helped to improve the manuscript. Figures were plotted with the use of the Generic Mapping Tools (Wessel & Smith 1998).

REFERENCES

Aki, K. & Kaminuma, K., 1963. Phase velocity of Love waves in Japan, Part 1. Love waves from Aleutian shock of March 9, 1957, *Bull. Earthq. Res. Inst.,* **41,** 243–259.

Anderson, D.L., 1961. Elastic wave propagation in layered anisotropic media, *J. geophys. Res.,* **82,** 277–296.

Anderson, D.L. & Dziewonski, A.M., 1982. Upper mantle anisotropy: evidence from free oscillations, *Geophys. J. R. astr. Soc.,* **69,** 383–404.

Arlitt, R., Kissling, E. & Ansorge, J., 1999. Three-dimensional crustal structure beneath the TOR array and effects on teleseismic wavefronts, *Tectonophysics,* **314,** 309–319.

Auer, L., Boschi, L., Becker, T.W., Nissen-Meyer, T. & Giardini, D., 2014. Savani: a variable resolution whole-mantle model of anisotropic shear velocity variations based on multiple data sets, *J. geophys. Res.,* **119,** 3006–3034.

Babuška, V. & Cara, M., 1991. *Seismic Anisotropy in the Earth,* Kluwer Academic Publishers.

Babuška, V. & Plomerová, J., 1992. The lithosphere in central Europe—seismological and petrological aspects, *Tectonophysics,* **207,** 141–163.

Babuška, V. & Plomerová, J., 1993. Lithosphere thickness and velocity anisotropy—seismological and geothermal aspects, *Tectonophysics,* **225,** 79–89.

Babuška, V. & Plomerová, J., 2006. European mantle lithosphere assembled from rigid microplates with inherited seismic anisotropy, *Phys. Earth planet. Inter.,* **158,** 264–280.

Babuška, V., Plomerová, J. & Šílený, J., 1984. Spatial variations of Presiduals and deep-structure of the European lithosphere, *Geophys. J. R. astr. Soc.,* **79,** 363–383.

Babuška, V., Plomerová, J. & Šílený, J., 1993. Models of seismic anisotropy in the deep continental lithosphere, *Phys. Earth planet. Inter.,* **78,** 167–191.

Backus, G.E., 1965. Possible forms of seismic anisotropy of the uppermost mantle under oceans, *J. geophys. Res.,* **70,** 3429–3439.

Becker, T.W., Lebedev, S. & Long, M.D., 2012. On the relationship between azimuthal anisotropy from shear wave splitting and surface wave tomography, *J. geophys. Res.,* **117,** B01306, doi:10.1029/2011JB008705.

Ben Ismail, W. & Mainprice, D., 1998. An olivine fabric database: an overview of upper mantle fabrics and mantle anisotropy, *Tectonophysics,* **296,** 145–157.

Bezada, M.J., Faccenda, M. & Toomey, D.R., 2016. Representing anisotropic subduction zones with isotropic velocity models: A characterization of the problem and some steps on a possible path forward, *Geochem. Geophys. Geosyst.,* **17,** 3164–3189.

Bruneton, M., Pedersen, H.A., Farra, V., Arndt, N.T. & Vacher, P. & SVEKALAPKO Seismic Tomography Working Group, 2004. Complex lithospheric structure under the central Baltic Shield from surface wave tomography, *J. geophys. Res.,* **109,** B10303.

Chang, S.J., Ferreira, A.M.G., Ritsema, J., van Heist, H.J. & Woodhouse, J.H., 2015. Joint inversion for global isotropic and radially anisotropic mantle structure including crustal thickness perturbations, *J. geophys. Res.,* **120,** 4278–4300.

Chyba, J., Plomerová, J., Vecsey, L. & Munzarová, H., 2017. Tomography study of the upper mantle around the TESZ based on PASSEQ experiment data, *Phys. Earth planet. Inter.,* **266,** 29–38.

Debayle, E., Dubuffet, F. & Durand, S., 2016. An automatically updated S-wave model of the upper mantle and the depth extent of azimuthal anisotropy, *Geophys. Res. Lett.,* **43**(2), 674–682.

Eberhart-Phillips, D. & Henderson, C.M., 2004. Including anisotropy in 3-D velocity inversion and application to Marlborough, New Zealand, *Geophys. J. Int.,* **156**(2), 237–254.

Eken, T., Shomali, H., Roberts, R. & Bödvarsson, R., 2007. Upper mantle structure of the Baltic Shield below the Swedish National Seismological Network (SNSN) resolved by teleseismic tomography, *Geophys. J. Int.,* **169,** 617–630.

Fichtner, A., Kennet, B.L.N., Igel, H. & Bunge, H.P., 2010. Full waveform tomography for radially anisotropic structure: New insights into present and past states of the Australasian upper mantle, *Earth planet. Sci. Lett.,* **290,** 270–280.

Fichtner, A., Saygin, E., Taymaz, T., Cupillard, P., Capdeville, Y. & Trampert, J., 2013. The deep structure of the North Anatolian fault zone, *Earth planet. Sci. Lett.,* **373,** 109–117.

Fouch, M.J. & Rondenay, S., 2006. Seismic anisotropy beneath stable continental interiors, *Phys. Earth planet. Inter.,* **158,** 292–320.

French, S.W. & Romanowicz, B.A., 2014. Whole-mantle radially anisotropic shear velocity structure from spectral-element waveform tomography, *Geophys. J. Int.,* **199**(3), 1303–1327.

Gou, T., Zhao, D., Huang, Z. & Wang, L., 2018. Anisotropic 3-D ray tracing and its application to Japan subduction zone, *J. geophys. Res.,* **123,** doi:10.1029/2017JB015321.

Grésillaud, A. & Cara, M., 1996. Anisotropy and *P*-wave tomography: a new approach for inverting teleseismic data from a dense array of stations, *Geophys. J. Int.,* **126,** 77–91.

Hirahara, K. & Ishikawa, Y., 1984. Travel time inversion for three-dimensional P-wave velocity anisotropy, *J. Phys. Earth,* **32,** 197–218.

Ho, T., Priestley, K. & Debayle, E., 2016. A global horizontal shear velocity model of the upper mantle from multimode Love wave measurements, *Geophys. J. Int.,* **207**(1), 542–561.

Huang, Z. & Zhao, D., 2013. Mapping P-wave azimuthal anisotropy in the crust and upper mantle beneath the United States, *Phys. Earth planet. Int.,* **225,** 28–40.

Huang, Z., Zhao, D. & Liu, X., 2015. On the trade-off between seismic anisotropy and heterogeneity: numerical simulations and application to Northeast Japan, *J. geophys. Res.,* **120,** 3255–3277.

Hua, Y., Zhao, D. & Xu, Y., 2017. P wave anisotropic tomography of the Alps, *J. geophys. Res.,* **122,** 4509–4528.

Ishise, M., Miyake, H. & Koketsu, K., 2015. Dual subduction tectonics and plate dynamics of central Japan Shown by three-dimensional P-wave anisotropic structure, *Phys. Earth planet. Inter.,* **244,** 49–68.

Ishise, M. & Oda, H., 2005. Three-dimensional structure of P-wave anisotropy beneath the Tohoku district, northeast Japan, *J. geophys. Res.,* **110,** B07304, doi:10.1029/2004JB003599.

Ishise, M. & Oda, H., 2008. Subduction of the Philippine Sea slab in view of *P*-wave anisotropy, *Phys. Earth planet. Inter.,* **166,** 83–96.

Karousová, H., 2013. , Teleseismic Tomography of the Upper Mantle beneath the Bohemian Massif, *PhD thesis*, Department of Geophysics, Faculty of Mathematics and Physics, Charles University, Prague, Czech Republic.

Karousová, H., Plomerová, J. & Babuška, V., 2013. Upper-mantle structure beneath the southern Bohemian Massif and its surroundings imaged by high-resolution tomography, *Geophys. J. Int.,* **194,** 1203–1215.

Karousová, H., Plomerová, J. & Vecsey, L., 2012. Seismic tomography of the upper mantle beneath the north-eastern Bohemian Massif (central Europe), *Tectonophysics,* **564–565,** 1–11.

Kennett, B. & Engdahl, R., 1991. Travel times for global earthquake location and phase identification, *Geophys. J. Int.,* **105,** 429–465.

Kennett, B.L.N., Engdahl, E.R. & Buland, R., 1995. Constraints on seismic velocities in the earth from travel times, *Geophys. J. Int.,* **122,** 108–124

Kissling, E., 1988. Geotomography with local earthquake data, *Rev. Geophys.,* **26,** 659–698.

Kissling, E. & Spakman, W., 1996. Interpretation of tomographic images of uppermost mantle structure: examples from the western and central Alps, *J. Geod.,* **21,** 97–111.

Koulakov, I., Kukarina, E., Fathi, I., Khrepy, S. & Al-Arifi, N., 2015. Anisotropic tomography of Hokkaido reveals delamination-induced flow above a subducting slab, *J. geophys. Res.,* **120,** 3219–3239.

Kustowski, B., Ekström, G. & Dziewoński, A.M., 2008. Anisotropic shear-wave velocity structure of the Earth's mantle: a global model, *J. geophys. Res.,* **113,** B06306, doi:10.1029/2007JB005169.

Lippitsch, R., Kissling, E. & Ansorge, J., 2003. Upper mantle structure beneath the Alpine orogen from high-resolution teleseismic tomography, *J. geophys. Res.,* **108,** B82376, doi:10.1029/2002JB002016.

Liu, X. & Zhao, D., 2016. Seismic velocity azimuthal anisotropy of the Japan subduction zone: constraints from P and S wave traveltimes, *J. geophys. Res.,* **121,** 5086–5115.

Liu, X. & Zhao, D., 2017a. P-wave anisotropy, mantle wedge flow and olivine fabrics beneath Japan, *Geophys. J. Int.,* **210,** 1410–1431.

Liu, X. & Zhao, D., 2017b. Depth-varying azimuthal anisotropy in the Tohoku subduction channel, *Earth planet. Sci. Lett.,* **473,** 33–43.

Long, M.D. & Becker, T.W., 2010. Mantle dynamics and seismic anisotropy, *Earth planet. Sci. Lett.,* **297,** 341–354.

Long, M.D. & Silver, P.G., 2009. Shear-wave splitting and mantle anisotropy: measurements, interpretations, and new directions, *Surv. Geophys.,* **30,** 407–461.

Mainprice, D., 2007. Seismic anisotropy of the deep Earth from a mineral and rock physics perspective, in *Treatise on Geophysics,* pp. 437–491, ed. Schubert, G., Elsevier, Oxford, UK.

Maupin, V. & Park, J., 2007. Theory and observations—wave propagation in anisotropic media, in *Treatise on Geophysics,* Vol. 1: Seismology and the Structure of the Earth, pp. 289–321, eds Romanowicz, B. & Dziewonski, A., Elsevier, doi:10.1016/B978-044452748-6.00007-9.

Menke, W., 1984. *Geophysical Data Analysis: Discrete Inverse Theory,* 1st edn, Academic Press, Inc.

Menke, W., 2015. Equivalent heterogeneity analysis as a tool for understanding the resolving power of anisotropic travel-time tomography, *Bull. seism. Soc. Am.,* **105,** 719–733.

Montagner, J.P., 1994. Can seismology tell us anything about convection in the mantle? *Rev. Geophys.,* **32,** 115–137.

Montagner, J.P., 1998. Where can seismic anisotropy be detected in the Earth's mantle? In boundary layers, *Pure appl. Geophys.,* **151,** 223–256.

Montagner, J.P. & Kennett, B.L.N., 1996. How to reconcile body-wave and normal-mode reference Earth models? *Geophys. J. Int.,* **125,** 229–248.

Montagner, J.P. & Nataf, H.C., 1986. A simple method for inverting the azimuthal anisotropy of surface waves, *J. geophys. Res.,* **91,** 511–520.

Munzarová, H., Plomerová, J., Kissling, E., Vecsey, L. & Babuška, V., 2018. Novel anisotropic teleseismic body-wave tomography code AniTomo to illuminate heterogeneous anisotropic upper mantle: Part II - Application to data of passive seismic experiment LAPNET in northern Fennoscandia, *Geophys. J. Int.,* revision submitted.

Nita, B., Maurya, S. & Montagner, J.P., 2016. Anisotropic tomography of the European lithospheric structure from surface wave studies, *Geochem. Geophys. Geosyst.,* **17,** 2015–2033.

Panning, M. & Romanowicz, B., 2006. A three-dimensional radially anisotropic model of shear velocity in the whole mantle, *Geophys. J. Int.,* **167,** 361–379.

Park, J. & Levin, V., 2002. Seismic anisotropy: Tracing plate dynamics in the mantle, *Science,* **296,** 485–489.

Plomerová, J. & Babuška, V., 2010. Long memory of mantle lithosphere fabric-European LAB constrained from seismic anisotropy, *Lithos,* **120,** 131–143.

Plomerová, J., Munzarová, H., Vecsey, L., Kissling, E., Achauer, U. & Babuška, V., 2016. Cenozoic volcanism in the Bohemian Massif in the context of P-and S-velocity high-resolution teleseismic tomography of the upper mantle, *Geochem. Geophys. Geosyst.,* **17**(8), 3326–3349.

Plomerová, J., Vecsey, L. & Babuška, V. & LAPNET working group, 2011. Domains of Archean mantle lithosphere deciphered by seismic anisotropy—inferences from the LAPNET array in northern Fennoscandia, *Solid Earth,* **2,** 303–313.

Plomerová, J., Vecsey, L. & Babuška, V., 2012. Mapping seismic anisotropy of the lithospheric mantle beneath the northern and eastern Bohemian Massif (central Europe), *Tectonophysics,* **564–565,** 38–53.

Raitt, R.W., Shor , G.G., Francis, T.J.G. & Morris, G.B., 1969. Anisotropy of the Pacific upper mantle, *J. Geophys. Res.,* **74,** 3095–9109.

Sandoval, S., , 2002. , The Lithosphere-Asthenosphere System Beneath Fennoscandia (Baltic shield) by Body-Wave Tomography, *PhD thesis*, Swiss Federal Institute of Technology, Zürich, Switzerland.

Sandoval, S., Kislling, E. & Ansorge, J. & SVEKALAPKO Seismic Tomography working Group, 2004. High-resolution body wave tomography beneath the SVEKALAPKO array - II. Anomalous upper mantle structure beneath the central Baltic Shield, *Geophys. J. Int.,* **157,** 200–214.

Savage, M.K., 1999. Seismic anisotropy and mantle deformation: what have we learned from shear wave splitting? *Rev. Geophys.,* **37,** 65–106.

Shomali, Z.H., Roberts, R.G. & Pedersen, L.B. & the TOR Working Group, 2006. Lithospheric structure of the Tornquist Zone resolved by nonlinear P and S teleseismic tomography along the TOR array, *Tectonophysics,* **416,** 133–149.

Silvennoinen, H., Kozlovskaya, E. & Kissling, E., 2016. POLENET/LAPNET teleseismic P wave travel time tomography model of the upper mantle beneath northern Fennoscandia, *Solid Earth,* **7,** 425–439.

Silver, P.G., 1996. Seismic anisotropy beneath the continents: probing the depths of geology, *Annu. Rev. Earth Planet. Sci.,* **24,** 385–432.

Sobolev, S., Gresillaud, A. & Cara, M., 1999. How robust is isotropic delay time tomography for anisotropic mantle? *Geophys. Res. Lett.,* **26**(4), 509–512.

Spakman, W., Van der Lee, S. & Van der Hilst, R., 1993. Travel-time tomography of the European-Mediterranean mantle down to 1400 km, *Phys. Earth planet. Inter.,* **79,** 3–74.

Tian, Y. & Zhao, D., 2012. Seismic anisotropy and heterogeneity in the Alaska subduction zone, *Geophys. J. Int.,* **190,** 629–649.

Tian, Y. & Zhao, D., 2013. Reactivation and mantle dynamics of North China Craton: insight from *P*-wave anisotropy tomography, *Geophys. J. Int.,* **195,** 1796–1810.

Vecsey, L., Plomerová, J., Kozlovskaya, E. & Babuška, V., 2007. Shear-wave splitting as a diagnostic of varying upper mantle structure beneath south-eastern Fennoscandia, *Tectonophysics,* **438,** 57–77.

Wang, J. & Zhao, D., 2008. *P*-wave anisotropic tomography beneath Northeast Japan, *Phys. Earth planet. Inter.,* **170,** 115–133.

Wang, J. & Zhao, D., 2012. P wave anisotropic tomography of the Nankai subduction zone in Southwest Japan, *Geochem. Geophys. Geosyst.,* **13,** Q05017.

Wang, J. & Zhao, D., 2013. *P*-wave tomography for 3-D radial and azimuthal anisotropy of Tohoku and Kyushu subduction zones, *Geophys. J. Int.,* **193,** 1166–1181.

Weiland, C., Steck, L., Dawson, P. & Korneev, V., 1995. Nonlinear teleseismic tomography at Long Valley caldera, using three-dimensional minimum travel time ray tracing, *J. geophys. Res.,* **100,** 20379–20390.

Wei, W., Zhao, D. & Xu, J., 2013. *P*-wave anisotropic tomography in Southeast Tibet: new insight into the lower crustal flow and seismotectonics, *Phys. Earth planet. Inter.,* **222,** 47–57.

Wessel, P. & Smith, W.H.F., 1998. New, improved version of the generic mapping tools released, *EOS, Trans. Am. Geophys. Un.,* **79,** 579.

Yuan, H., French, S., Cupillard, P. & Romanowicz, B., 2014. Lithospheric expression of geological units in central and eastern North America from full waveform tomography, *Earth planet. Sci. Lett.,* **402,** 176–186.

Yu, D. & Wang, L., 2013. P-wave anisotropy tomography of central Japan: insight into subduction dynamics, *Tectonophysics,* **592,** 14–30.

Zhu, H., Bozdağ, E. & Tromp, J., 2014. Seismic structure of the European upper mantle based on adjoint tomography, *Geophys. J. Int.,* **201,** 18–52.

Šílený, J. & Plomerová, J., 1996. Inversion of shear-wave splitting parameters to retrieve three-dimensional orientation of anisotropy in continental lithosphere, *Phys. Earth planet. Inter.,* **95,** 277–292.

SUPPORTING INFORMATION

Supplementary data are available at *GJI* online.

Figure S1. (a) Scheme of anisotropy with hexagonal symmetry with inclined high-velocity axis *a* or low-velocity axis *b*. Teleseismic *P* waves can hardly distinguish, due to their angles of incidence, between these two types of hexagonal symmetry. (b) Comparison of *P*-wave velocities calculated according to approximate eq. (5) in red and those evaluated as solution of the Christoffel equation, that is exact theoretical values, in black. The elastic coefficients chosen for this example correspond to a hexagonal model of peridotite aggregate (e.g. Ben Ismail & Mainprice 1998; Babuška & Plomerová 2006).

Figure S2. Resulting model parameters corresponding to perturbations of isotropic component of velocity for damping factors of 10 (a) and 100 (b), strength of anisotropy for damping factors of 100 (c) and 1000 (d) and inclination of the symmetry axis for damping

factors of 0.5 (e) and 5 (f). Only one of the four damping factors is always changed and we keep the other three damping factors at their finally selected values during these inversions. Higher damping results in slower convergence towards the correct model parameters. See also caption of Fig. 3.

Figure S3. Diagonal elements of the resolution matrix for all model parameters of testing series I (Section 4). Resolution of the symmetry-axis orientation depends on strength of anisotropy. At nodes with no or low strength of anisotropy, it is irrelevant to look for axis orientation.

Figure S4. Resulting model parameters after four iterations of synthetic inversions with different initial orientations of the symmetry axis from 30 to 180 km depth. See caption of Fig. 2 for description of visualization of the anisotropic parameters.

Figure S5. Resulting model parameters after four iterations of synthetic inversions with different initial orientations of the symmetry axis imaged together in the combined output model. See caption of Fig. 11 for more details.

Figure S6. Model of anisotropic velocities resulting from coupled anisotropic–isotropic inversion of synthetic traveltimes calculated for P waves propagating through the isotropic part of structure imaged in Fig. 9. See caption of Fig. 11 for more details.

Figure S7. Model of anisotropic velocities resulting from coupled anisotropic–isotropic inversion of synthetic traveltimes calculated for P waves propagating through the anisotropic part of the structure imaged in Fig. 9. See caption of Fig. 11 for more details.

Figure S8. Model of isotropic velocities resulting from purely isotropic-velocity inversion of synthetic traveltimes calculated for P waves propagating through the anisotropic part of the synthetic structure imaged in Fig. 9. See caption of Fig. 11 for more details. See caption of Fig. 11 for more details.

Figure S9. Model of anisotropic velocities resulting from inversion for strength of anisotropy and orientation of symmetry axis of synthetic travel times calculated for P waves propagating through the anisotropic part of structure imaged in Fig. 9. The isotropic-velocity component is fixed during the inversion. See caption of Fig. 11 for more details.

Please note: Oxford University Press is not responsible for the content or functionality of any supporting materials supplied by the authors. Any queries (other than missing material) should be directed to the corresponding author for the paper.vicelatc

APPENDIX A

The following demonstration is based on Backus (1965), considering modifications according to our assumptions. The non-zero small variations γ_{ijkl} of elastic coefficients introduced in eq. (2) can be expressed as

$$\begin{aligned}
&\gamma_{1111} = \gamma_{2222} = \tfrac{1}{\rho}\left[A - (\lambda + 2\mu)\right],\\
&\gamma_{3333} = \tfrac{1}{\rho}\left[C - (\lambda + 2\mu)\right],\\
&\gamma_{1122} = \tfrac{1}{\rho}\left[(A - 2N) - \lambda\right],\\
&\gamma_{1133} = \gamma_{2233} = \tfrac{1}{\rho}\left(F - \lambda\right),\\
&\gamma_{1313} = \gamma_{2323} = \tfrac{1}{\rho}\left(L - \mu\right),\\
&\gamma_{1212} = \tfrac{1}{2}\left(\gamma_{1111} - \gamma_{1122}\right) = \tfrac{1}{\rho}\left(N - \mu\right),
\end{aligned} \tag{A1}$$

for a hexagonal anisotropy described by five independent elastic coefficients A, C, F, N and L and for a background isotropic medium represented by Lamé constants λ and μ.

The component of unit propagation vector **n** parallel to the symmetry axis is $n_3 = \cos\alpha$ and the component within plane (n_1, n_2) perpendicular to the symmetry axis equals $\sin\alpha$. Then, we have relation $n_i n_i = 1$. Furthermore, inserting coefficients γ_{ijkl} into eq. (2), we obtain

$$\begin{aligned}
B^{(1)} = {} & \gamma_{1111} + 2\left(\gamma_{1133} + 2\gamma_{1313} - \gamma_{1111}\right)\cos^2\alpha\\
& + \left(\gamma_{1111} + \gamma_{3333} - 2\gamma_{1133} - 4\gamma_{1313}\right)\cos^4\alpha.
\end{aligned} \tag{A2}$$

Formula (A2) can be rewritten without any approximations as a finite Fourier series

$$B^{(1)} = P + Q\cos2\alpha + R\cos4\alpha, \tag{A3}$$

where the coefficients are

$$P = \frac{1}{8\rho}\left[3\left(A + C\right) + 2\left(F + 2L\right)\right] - \frac{\lambda + 2\mu}{\rho}, \tag{A4}$$

$$Q = \frac{1}{2\rho}\left(C - A\right), \tag{A5}$$

$$R = \frac{1}{8\rho}\left[A + C - 2\left(F + 2L\right)\right]. \tag{A6}$$

Then, anisotropic velocity (1) is expressed as

$$v = c + \frac{P}{2c} + \frac{Q}{2c}\cos2\alpha + \frac{R}{2c}\cos4\alpha. \tag{A7}$$

The $\cos 4\alpha$ term is small in comparison with the $\cos 2\alpha$ term in the upper mantle, which is supported by observations of variations of P_n velocity with azimuth (e.g. Raitt *et al.* 1969). Also our evaluation of coefficients Q and R for elastic constants of hexagonal-symmetry approximation of originally orthorhombic aggregate of peridotite (Ben Ismail & Mainprice 1998; Babuška & Plomerová 2006) results in ten times smaller R than Q. Thus we neglect the $\cos 4\alpha$ term

$$v = c + \frac{P}{2c} + \frac{Q}{2c}\cos2\alpha. \tag{A8}$$

The anisotropic velocity can in general be separated into a sum of isotropic ($\bar{v}$) and directional (δv) components

$$v = \bar{v} + \delta v. \tag{A9}$$

Comparing (A8) and (A9), it is obvious that

$$\bar{v} = c + \frac{P}{2c}, \tag{A10}$$

$$\delta v = \frac{Q}{2c}\cos2\alpha. \tag{A11}$$

Raising eq. (A10) to second power, combining it with (A4) and neglecting the P^2 term as $P << c^2$, we get a relation for $\bar{v}^2$

$$\bar{v}^2 = \frac{1}{8\rho}\left[3\left(A + C\right) + 2\left(F + 2L\right)\right]. \tag{A12}$$

Strength of anisotropy commonly defined as

$$k = \frac{v^{\max} - v^{\min}}{\bar{v}} \tag{A13}$$

can in our specific case be expressed as

$$k = \frac{4\left(C - A\right)}{3\left(A + C\right) + 2\left(F + 2L\right)} \tag{A14}$$

taking into account the form of directional component (A11) of the P-wave velocity, substituting c for $\bar{v}$ in the denominator as $P << c^2$ and $Q << c^2$ and including eqs (A5) and (A12).

Thus we may write the anisotropic velocity (A8) with the use of isotropic component of velocity (A12) and strength of anisotropy

(A14) as

$$v = \bar{v} + \frac{\bar{v}k}{2}\cos 2\alpha. \tag{A15}$$

APPENDIX B

Ray density tensor is a tool for assessment of resolution possibilities of a designed tomographic model parameterization along with particular ray geometry (Kissling 1988; Sandoval 2002; Sandoval *et al.* 2004). In addition to the hit-count, the ray density tensor takes into account the length of the ray paths through the cell (similarly as derivative weighted sum) and the ray orientations. To link ray coverage of a cell to a tensor is advantageous since a symmetric tensor can be easily represented by an ellipsoid (Fig. B1), length and orientation of semi-axes of which are defined by tensor eigenvalues and eigenvectors. In the ideal case of the cell being covered equally by the rays from all directions, the ray density tensor becomes an identity tensor and the ellipsoid turns into a sphere. On the other hand, an elongated ellipsoid denotes a direction, along which the rays prevailingly propagate through the cell. To assess the shape of an ellipsoid, it is not even necessary to visualize it. Comparison of the three eigenvalues provides us with the required information about ray coverage quality as well.

How can we transform the geometry of the ray paths within a cell into a tensor?

The part of the ith ray pertaining to the jth cell can be represented by vector $\mathbf{a_{ij}}$ oriented along the ray direction within the cell. Length a_{ij} of the $\mathbf{a_{ij}}$ vector is proportional to length l_{ij} of the ray part normalized by space diagonal L_j of the cell and the vector length may also depend on weight ω_i assigned to the ith arrival time measurement (Sandoval 2002)

$$a_{ij} = \frac{l_{ij}}{L_j}\omega_i. \tag{B1}$$

In a local coordinate system of the ith ray, such that unit vector $\mathbf{x^{loc}}$ parallels the ray within the jth cell, and using 3x3 tensor notation, $\mathbf{a_{ij}}$ gets the form

$$[\boldsymbol{a}_{ij}{}^{loc}] = \begin{pmatrix} a_{ij} & 0 & 0 \\ 0 & 0 & 0 \\ 0 & 0 & 0 \end{pmatrix}. \tag{B2}$$

The square brackets and the italics symbolize that the variable is a 2-D array. Transforming $[\boldsymbol{a}_{ij}{}^{loc}]$ from its local coordinate system to a global coordinate system and summing $[\boldsymbol{a}_{ij}{}^{glob}]$ of all the rays crossing the jth cell, ray density tensor $[\boldsymbol{RDT}_j]$ of the jth cell is obtained

$$[\boldsymbol{RDT}_j] = \sum_{i=1}^{n_{rays}} [\boldsymbol{a}_{ij}{}^{glob}]. \tag{B3}$$

The relation between the local and global coordinate systems is given by orientation of the ray, which is in our case described by the event backazimuth ϕ and ray incidence angle i (Fig. B2).

The transformation of the coordinates of $[\boldsymbol{a}_{ij}]$ from its local to the global coordinate system is according to the tensor transformation law performed as

$$[\boldsymbol{a}_{ij}{}^{glob}] = [\boldsymbol{T}]\,[\boldsymbol{a}_{ij}{}^{loc}]\,[\boldsymbol{T}]^T, \tag{B4}$$

where $[\boldsymbol{T}]$ is the transformation matrix and $[\boldsymbol{T}]^T$ is $[\boldsymbol{T}]$ transposed.

To derive the transformation matrix for our case, the inverse transformation, that is from the global to the local coordinate system

$$[\boldsymbol{a}_{ij}{}^{loc}] = [\boldsymbol{T}]^T\,[\boldsymbol{a}_{ij}{}^{glob}]\,[\boldsymbol{T}], \tag{B5}$$

is more illustrative because the aim of such a transformation is to orient the **x**-axis to become parallel with $\mathbf{a_{ij}}$ in the local coordinate system while **y**- and **z**-axes might be oriented arbitrarily. The transformation of the coordinate system from global to local can be reached by two subsequent rotations (always one axis fixed). First transformation $[\boldsymbol{T}_1]$ of the global coordinate system is a rotation about **z**-axis by angle β (from **x** to **y**) to align **x** with the azimuth of $\mathbf{a_{ij}}$ (Fig. B3). In terms of event backazimuth ϕ, rotation angle β can be expressed as

$$\beta = \frac{\pi}{2} - (\phi - \pi) = \frac{3\pi}{2} - \phi. \tag{B6}$$

Transformation matrix $[\boldsymbol{T}_1]$ is then written as

$$[\boldsymbol{T}_1] = \begin{pmatrix} \cos\beta & \sin\beta & 0 \\ -\sin\beta & \cos\beta & 0 \\ 0 & 0 & 1 \end{pmatrix} = \begin{pmatrix} -\sin\phi & -\cos\phi & 0 \\ \cos\phi & -\sin\phi & 0 \\ 0 & 0 & 1 \end{pmatrix}. \tag{B7}$$

The second transformation $[\boldsymbol{T}_2]$ is a rotation about **y**-axis by angle γ (from **z** to **x**) to tilt **x** up to make it parallel with $\mathbf{a_{ij}}$ (Fig. B4). Expressing γ by ray incidence angle i, we obtain

$$\gamma = \frac{\pi}{2} - i. \tag{B8}$$

And transformation matrix $[\boldsymbol{T}_2]$ can be expressed as

$$[\boldsymbol{T}_2] = \begin{pmatrix} \cos\gamma & 0 & -\sin\gamma \\ 0 & 1 & 0 \\ \sin\gamma & 0 & \cos\gamma \end{pmatrix} = \begin{pmatrix} \sin i & 0 & -\cos i \\ 0 & 1 & 0 \\ \cos i & 0 & \sin i \end{pmatrix}. \tag{B9}$$

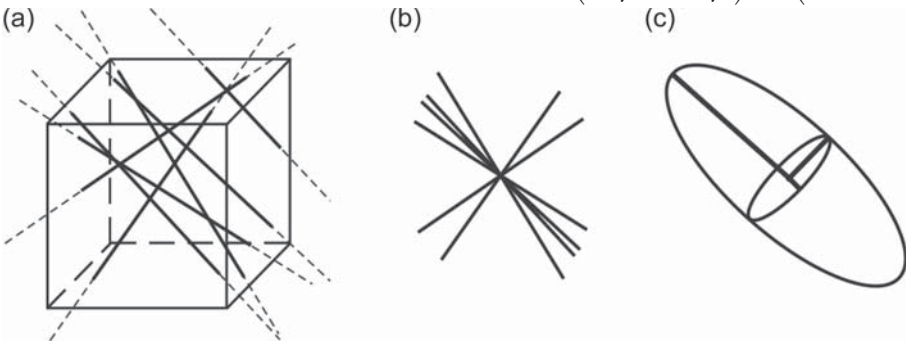

Figure B1. Generation of ray density tensor, after Kissling (1988). (a) Rays crossing a cell of a tomographic model parametrization. (b) Centred ray parts. (c) Ellipsoid best approximating the distribution of the ray parts within the cell.

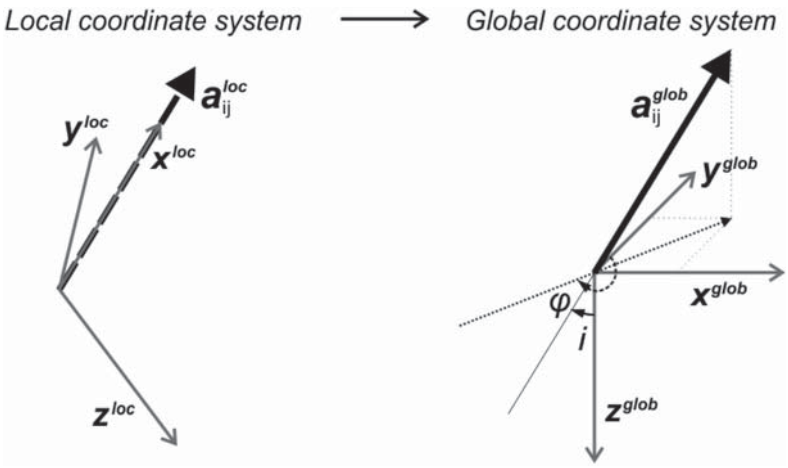

Figure B2. In the coordinate system of the ray part, that is in the local coordinate system, ***x***-axis parallels the ray propagation direction represented by vector $\mathbf{a_{ij}}$. In the global coordinate system, each ray part is defined by its incidence angle i and event backazimuth ϕ.

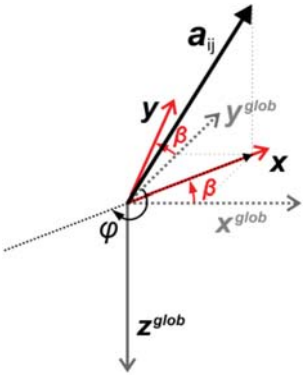

Figure B3. Coordinate system rotated about **z**-axis by angle β so that **x**-axis parallels the ray part azimuth. ϕ is event back-azimuth. See eq. (B6) for relation between rotation angle β and event back-azimuth ϕ.

The transformation of $\mathbf{a_{ij}}$ from the global coordinate system into the local one is then

$$\left[a_{ij}{}^{loc}\right] = [T_2][T_1]\left[a_{ij}{}^{glob}\right][T_1]^T[T_2]^T \tag{B10}$$

and the inverse transformation

$$\left[a_{ij}{}^{glob}\right] = [T_1]^T[T_2]^T\left[a_{ij}{}^{loc}\right][T_2][T_1]\,. \tag{B11}$$

Inserting eqs (B2), (B7) and (B9) into formula (B11), we obtain the relation for tensor $[a_{ij}{}^{glob}]$

$$\left[a_{ij}{}^{glob}\right] = a_{ij}\begin{pmatrix} \sin^2 i \sin^2\phi & \sin^2 i \sin\phi\cos\phi & \sin i\cos i\sin\phi \\ \sin^2 i \sin\phi\cos\phi & \sin^2 i\cos^2\phi & \sin i\cos i\cos\phi \\ \sin i\cos i\sin\phi & \sin i\cos i\cos\phi & \cos^2 i \end{pmatrix}. \tag{B12}$$

Summation of eq. (B12) for all rays crossing the *j*th cell results in ray density tensor (eq. B3). The ray density tensor is obviously symmetric.

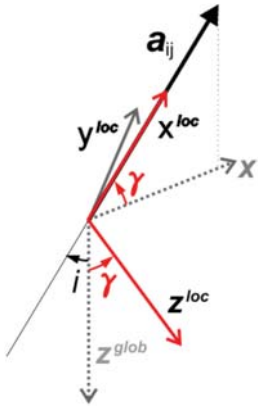

Figure B4. Coordinate system rotated about **y**-axis by angle γ so that **x**-axis points towards the ray propagation. i is ray incidence angle. See eq. (B8) for relation between rotation angle γ and incidence angle i.

Supporting information

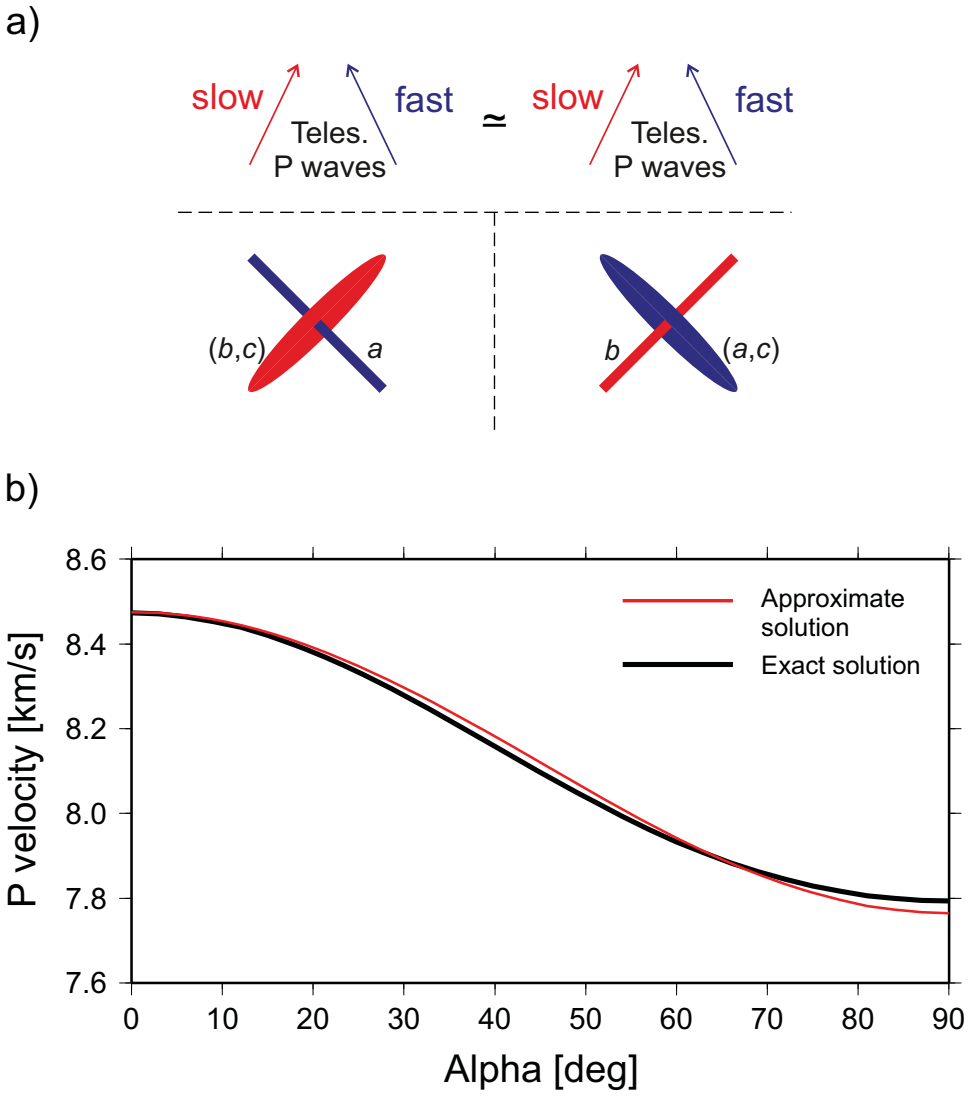

Figure S1. (a) Scheme of anisotropy with hexagonal symmetry with inclined high-velocity axis *a* or low-velocity axis *b*. Teleseismic P waves can hardly distinguish, due to their angles of incidence, between these two types of hexagonal symmetry. (b) Comparison of P-wave velocities calculated according to approximate equation (5) in red and those evaluated as solution of the Christoffel equation, i.e., exact theoretical values, in black. The elastic coefficients chosen for this example correspond to a hexagonal model of peridotite aggregate (e.g., Ben Ismail & Mainprice 1998; Babuška & Plomerová 2006).

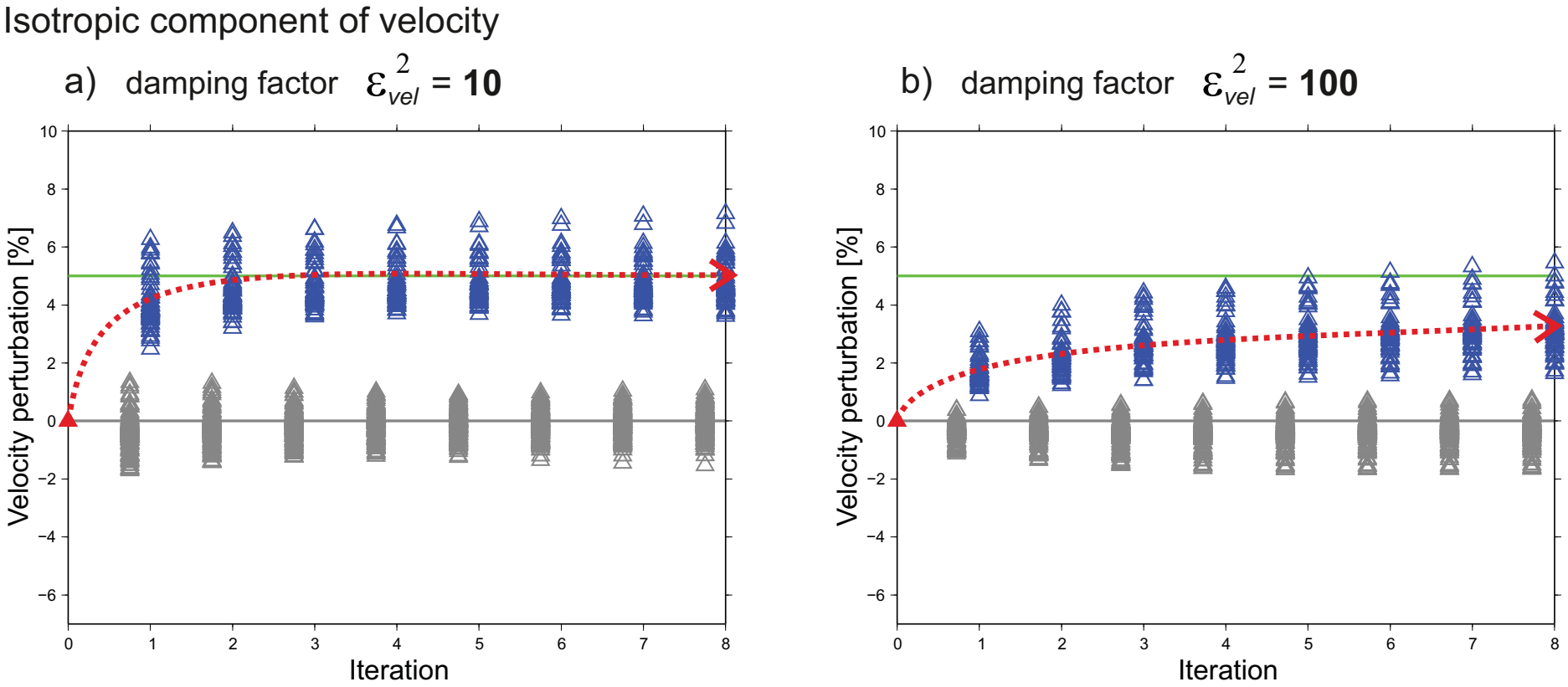

Figure S2. Resulting model parameters corresponding to perturbations of isotropic component of velocity for damping factors of 10 (a) and 100 (b), strength of anisotropy for damping factors of 100 (c) and 1000 (d) and inclination of the symmetry axis for damping factors of 0.5 (e) and 5 (f). Only one of the four damping factors is always changed and we keep the other three damping factors at their finally selected values during these inversions. Higher damping results in slower convergence toward the correct model parameters. See also caption of Fig. 3.

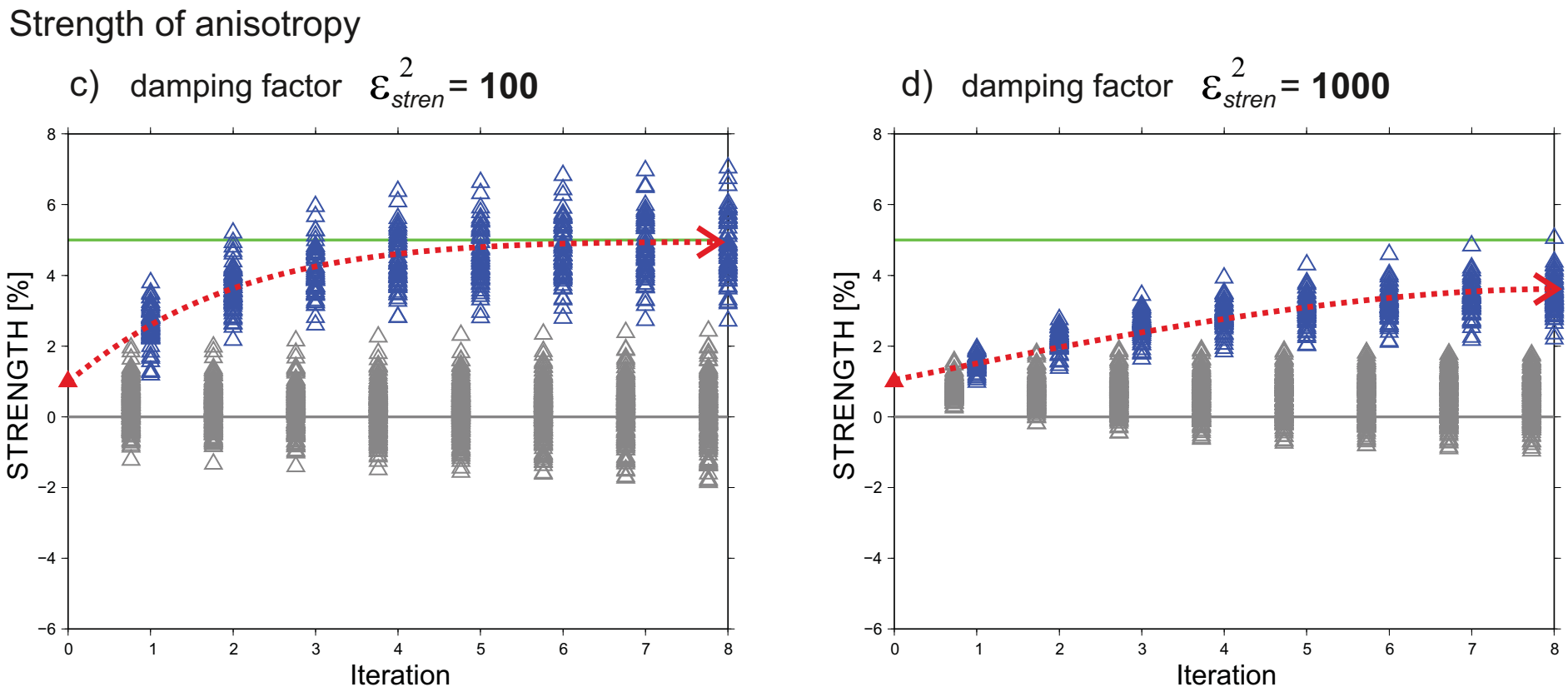

Figure S2. cont.

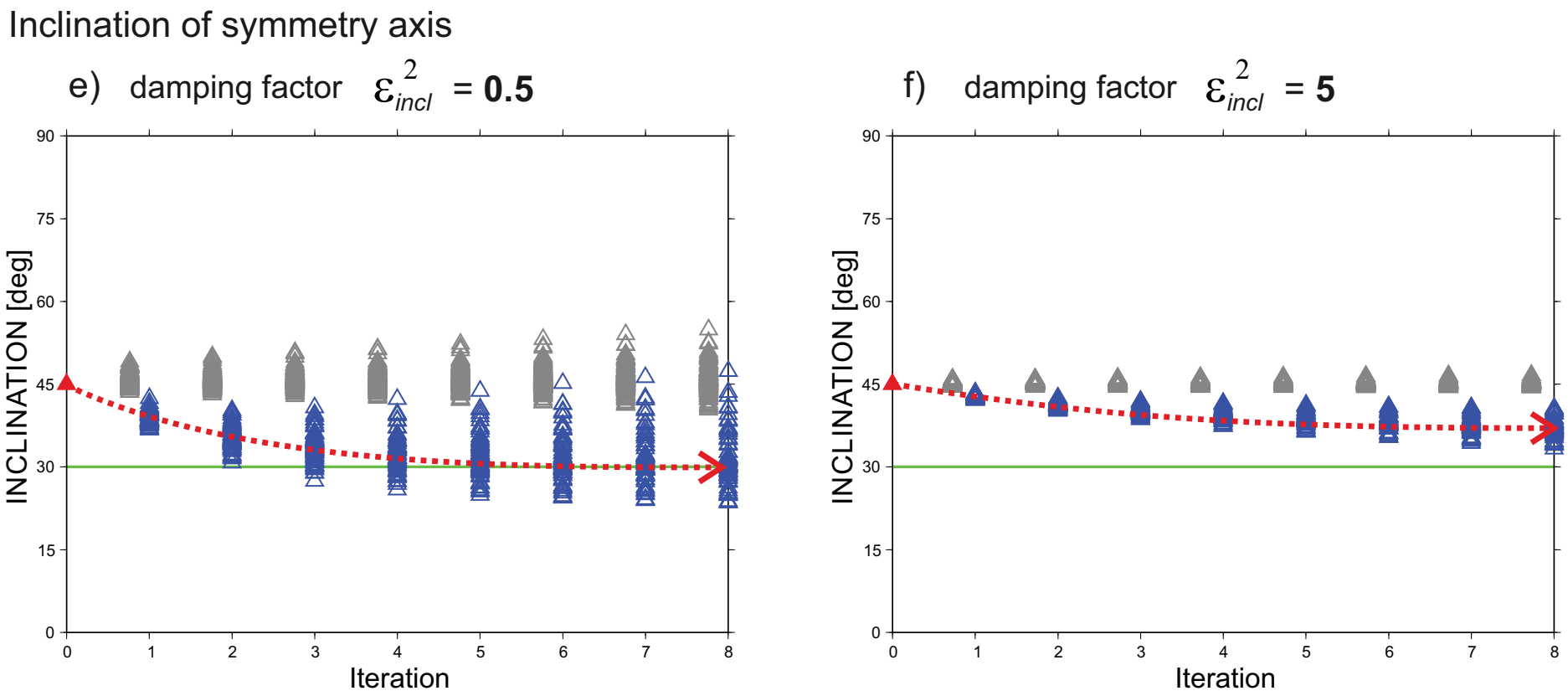

Figure S2. cont.

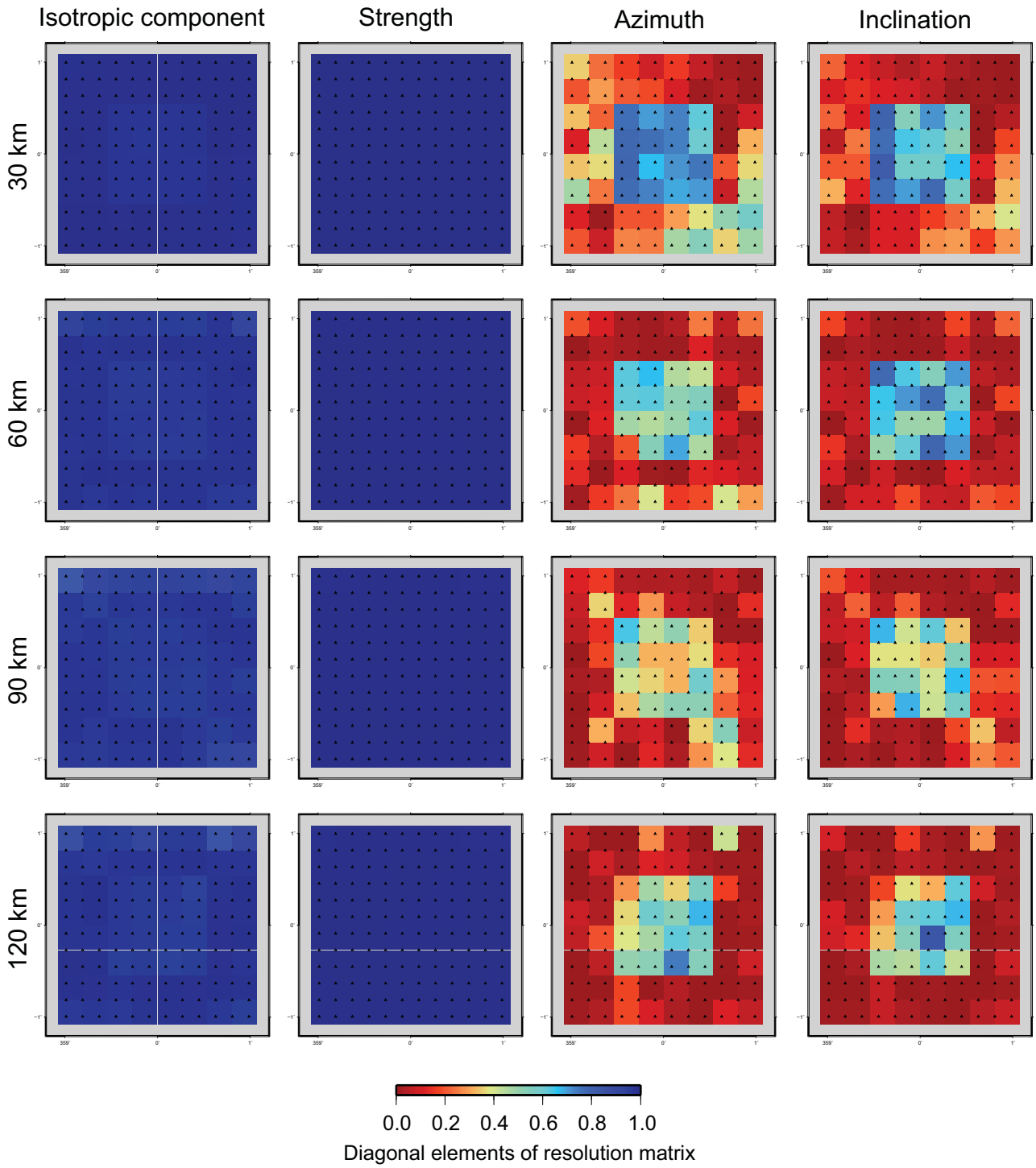

Figure S3. Diagonal elements of the resolution matrix for all model parameters of testing series I (Section 4). Resolution of the symmetry-axis orientation depends on strength of anisotropy. At nodes with no or low strength of anisotropy, it is irrelevant to look for axis orientation.

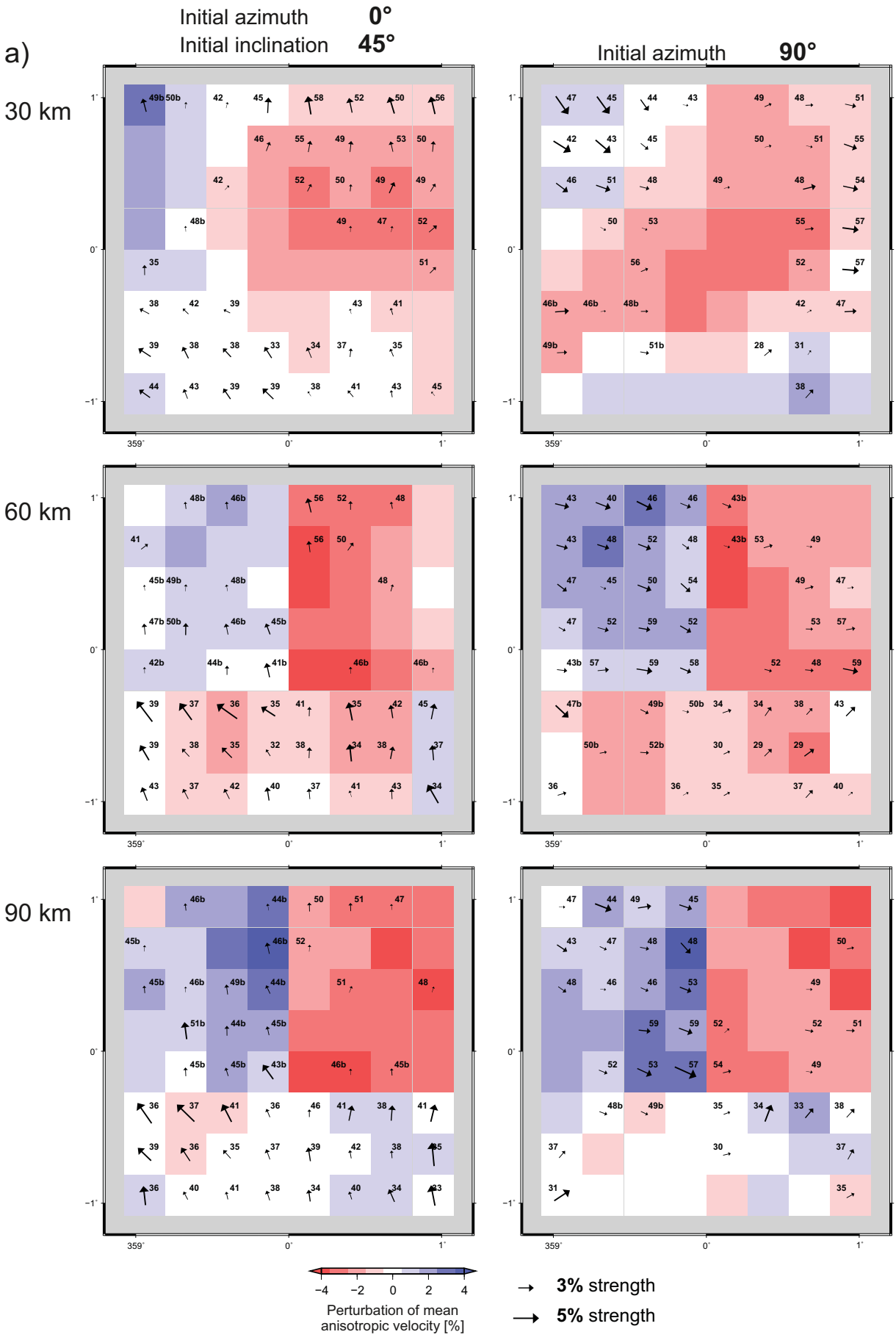

Figure S4. Resulting model parameters after four iterations of synthetic inversions with different initial orientations of the symmetry axis from 30 km to 180 km depth. See caption of Fig. 2 for description of visualization of the anisotropic parameters.

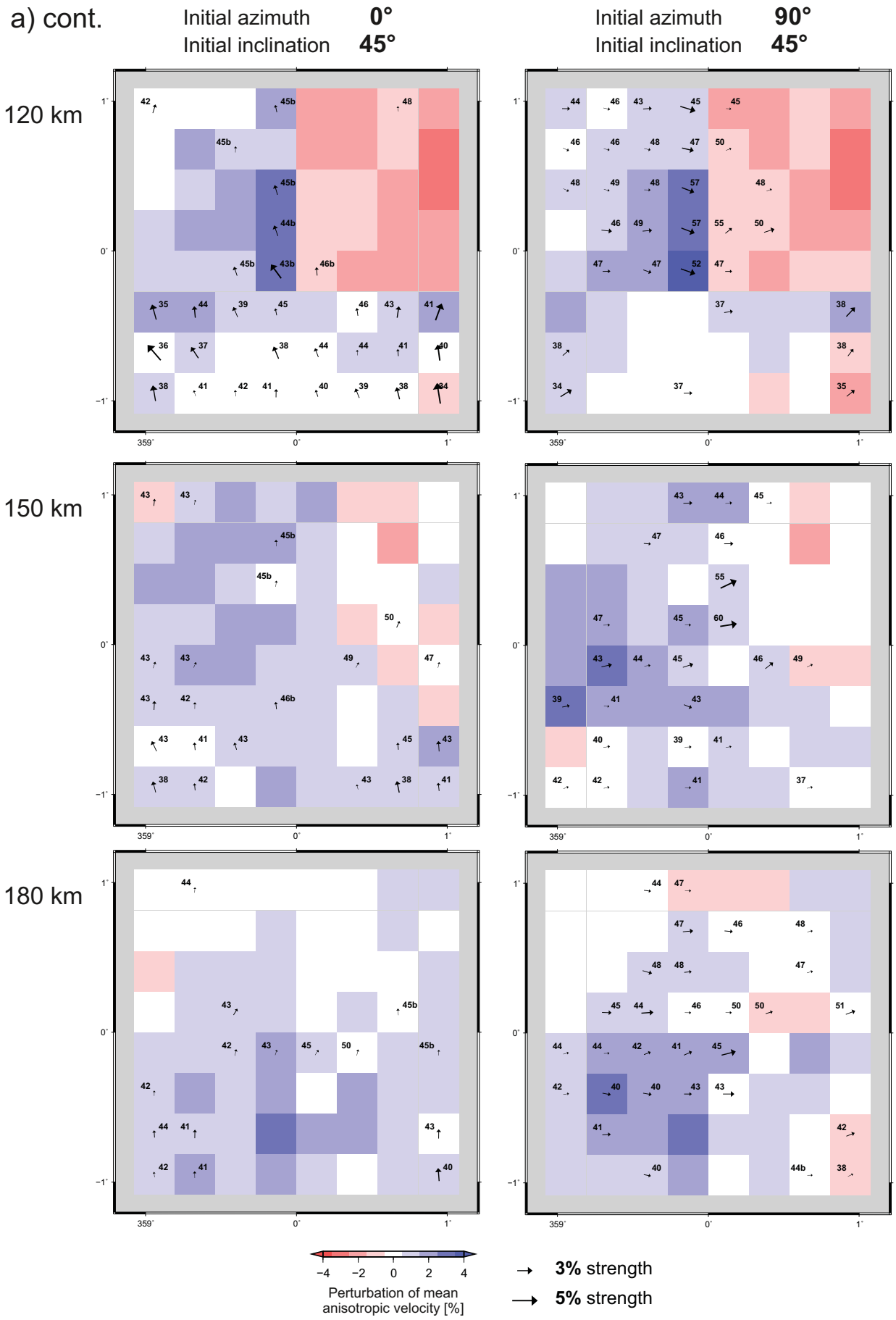

Figure S4. Continue

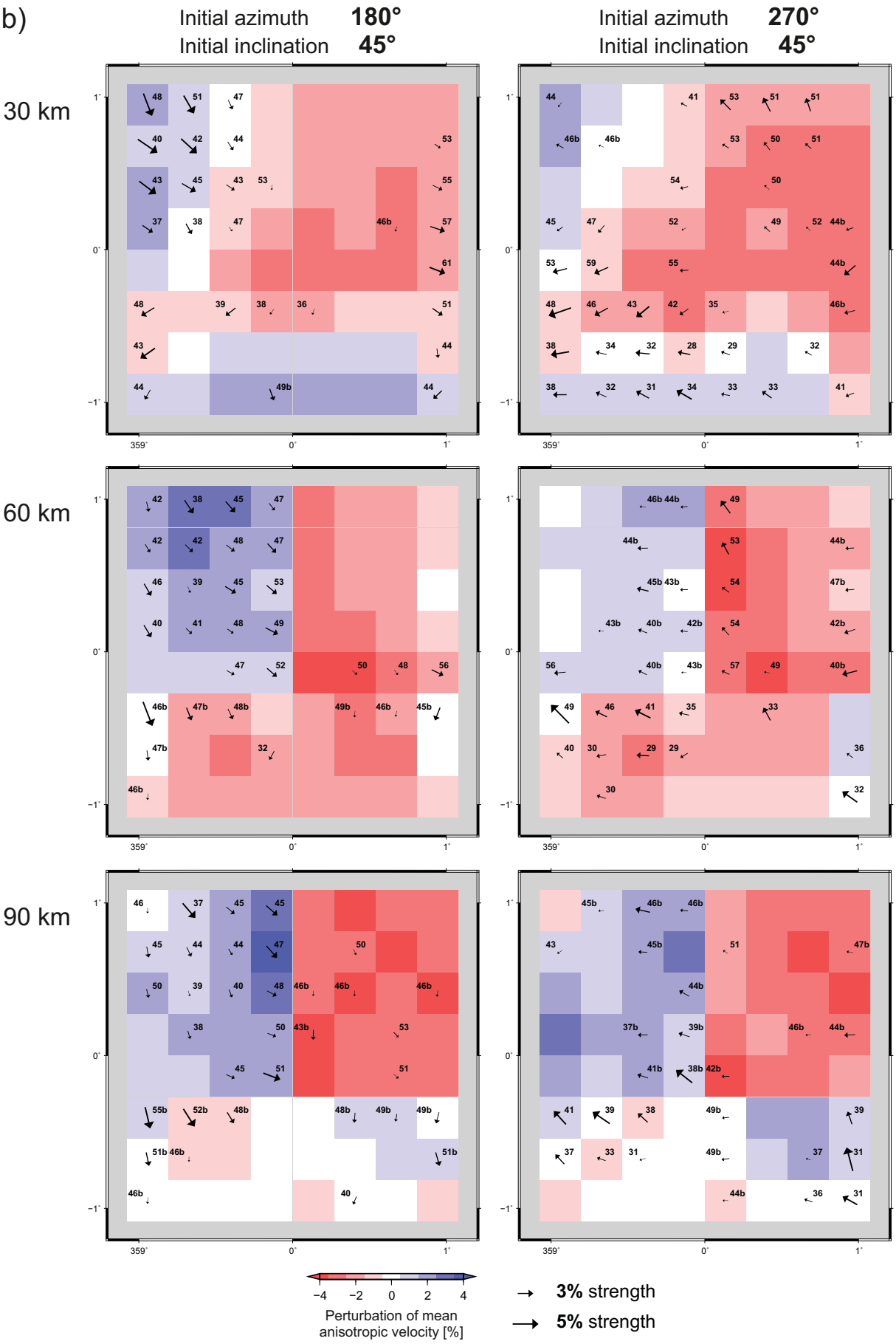

Figure S4. Continue

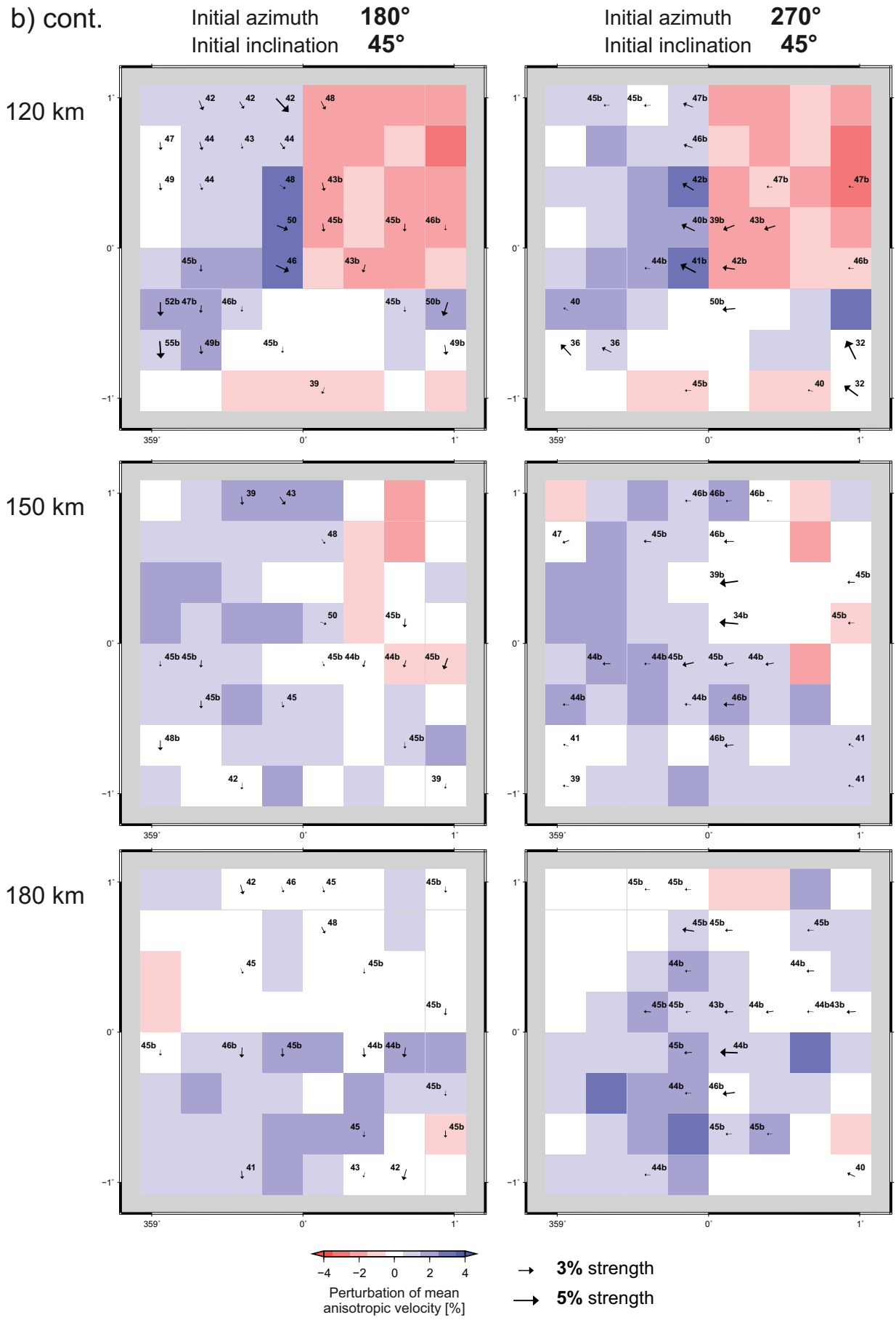

Figure S4. Continue

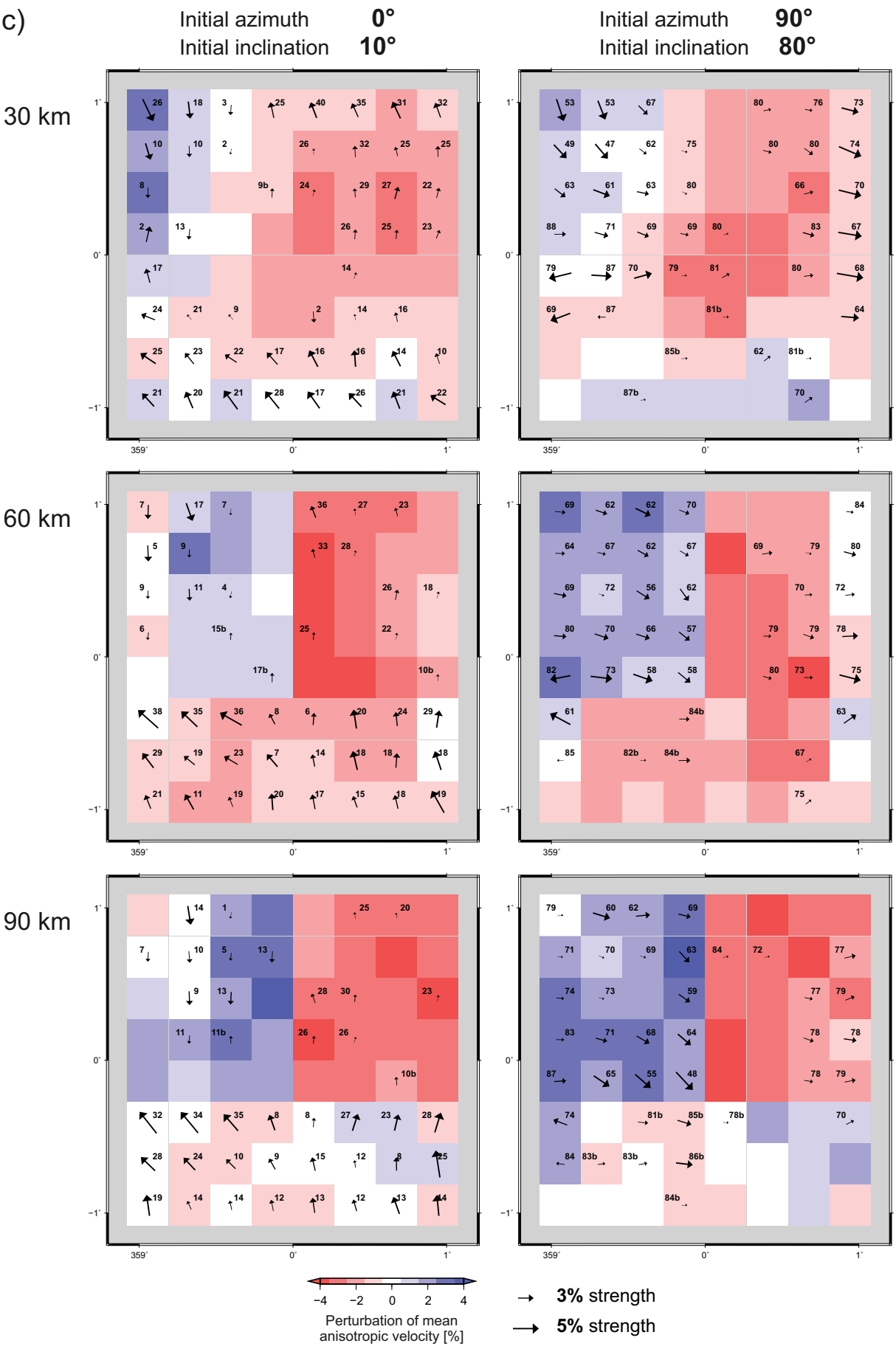

Figure S4. Continue

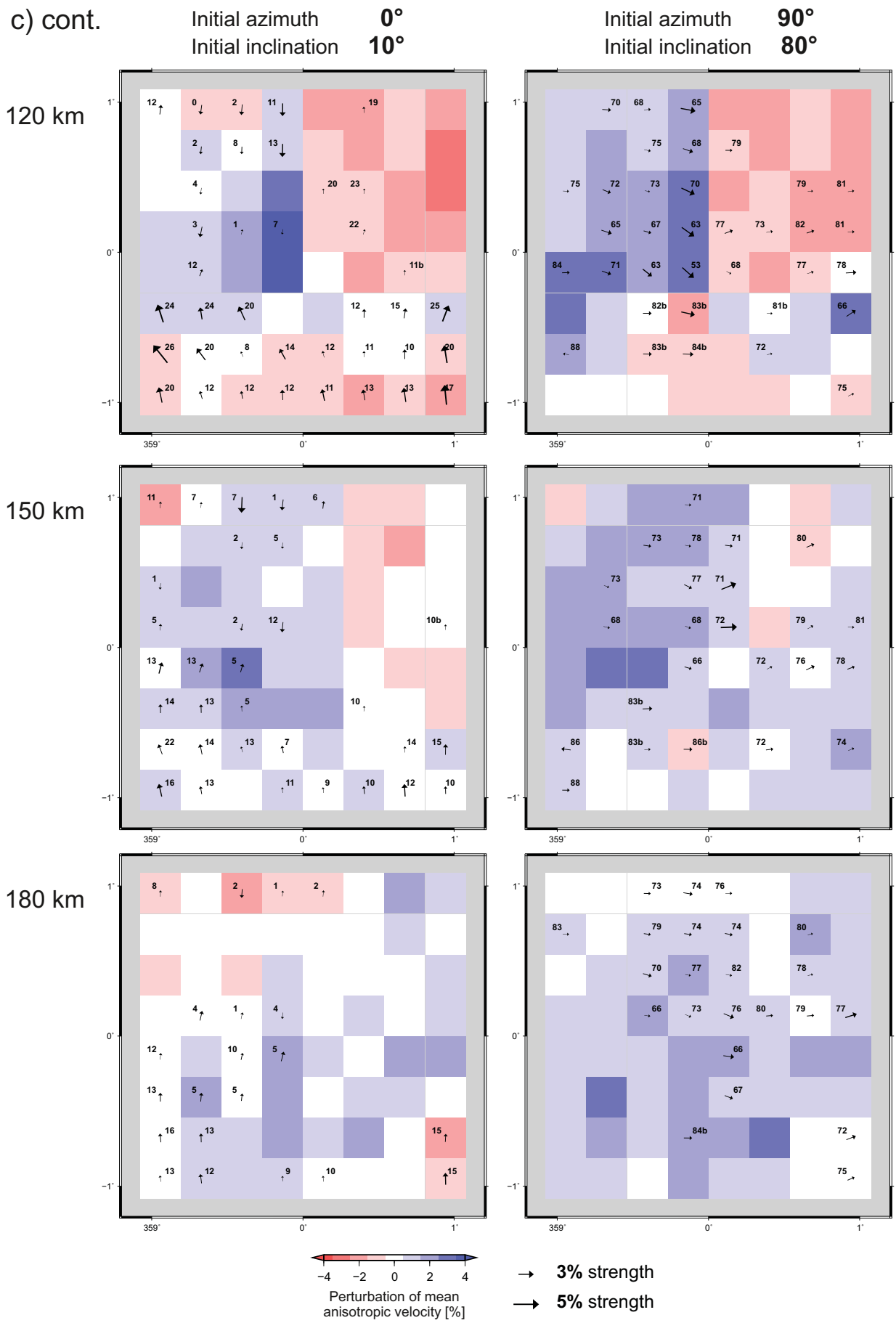

Figure S4. Continue

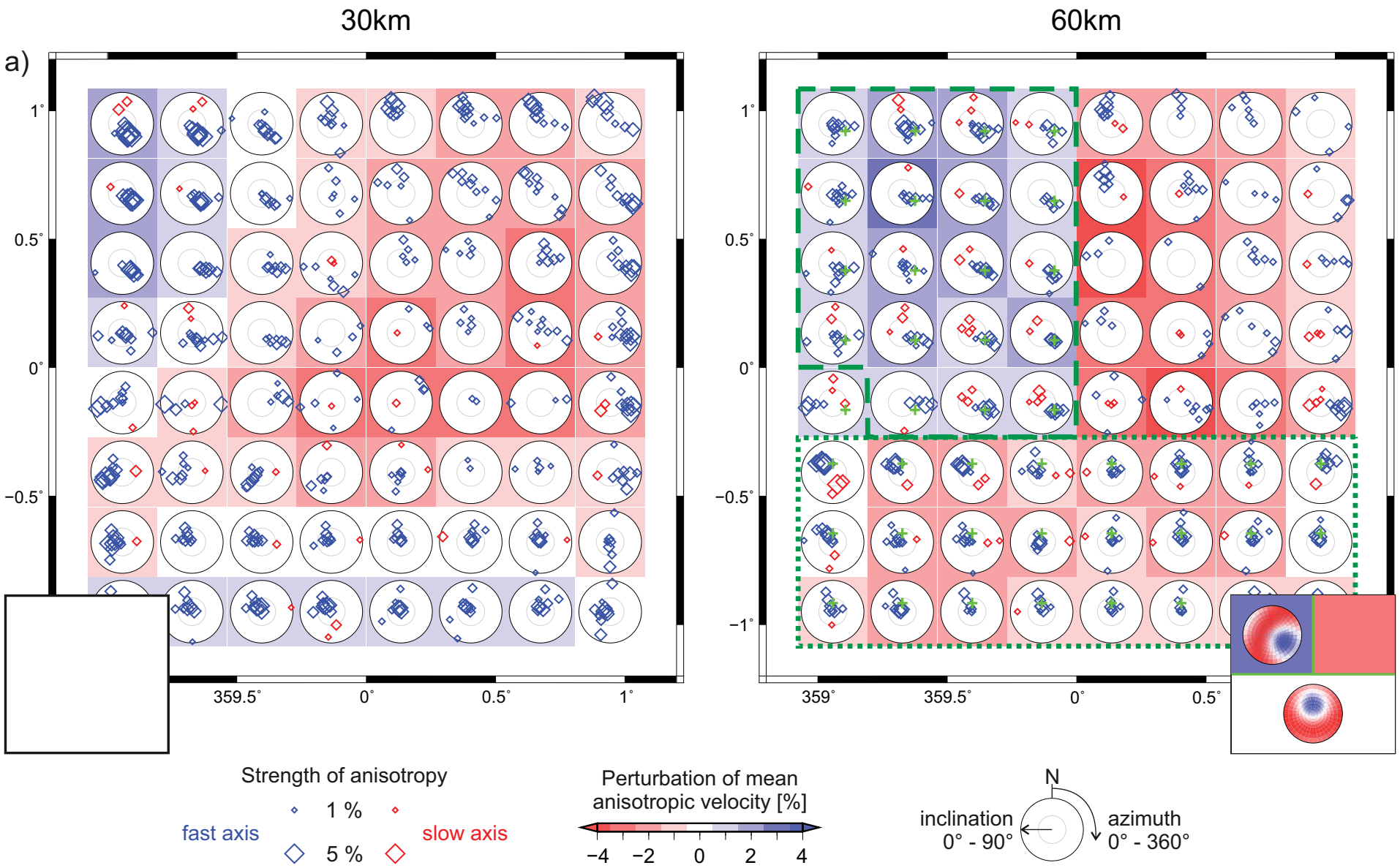

Figure S5. Resulting model parameters after four iterations of synthetic inversions with different initial orientations of the symmetry axis imaged together in the combined output model. See caption of Fig. 11 for more details.

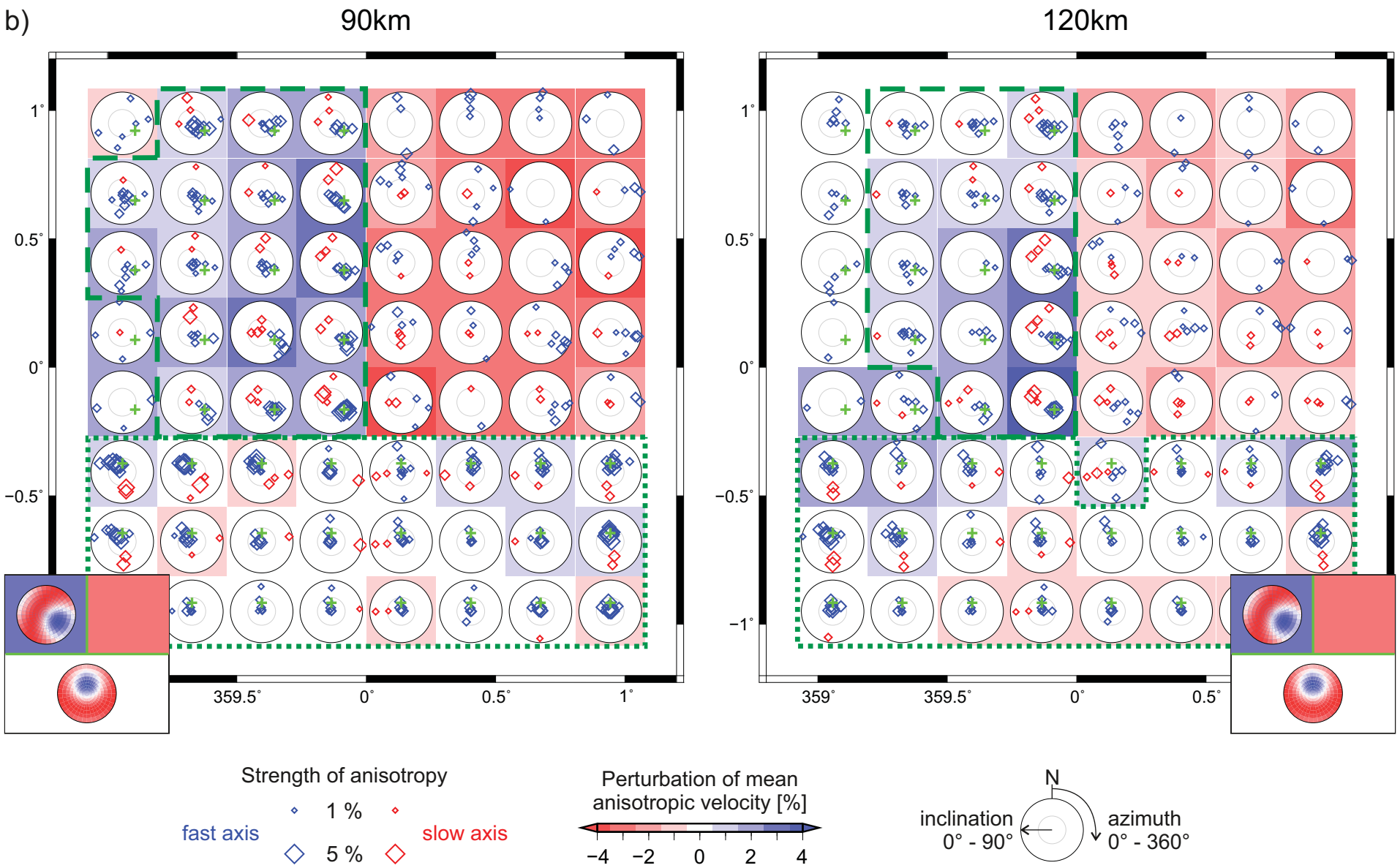

Figure S5. Continue

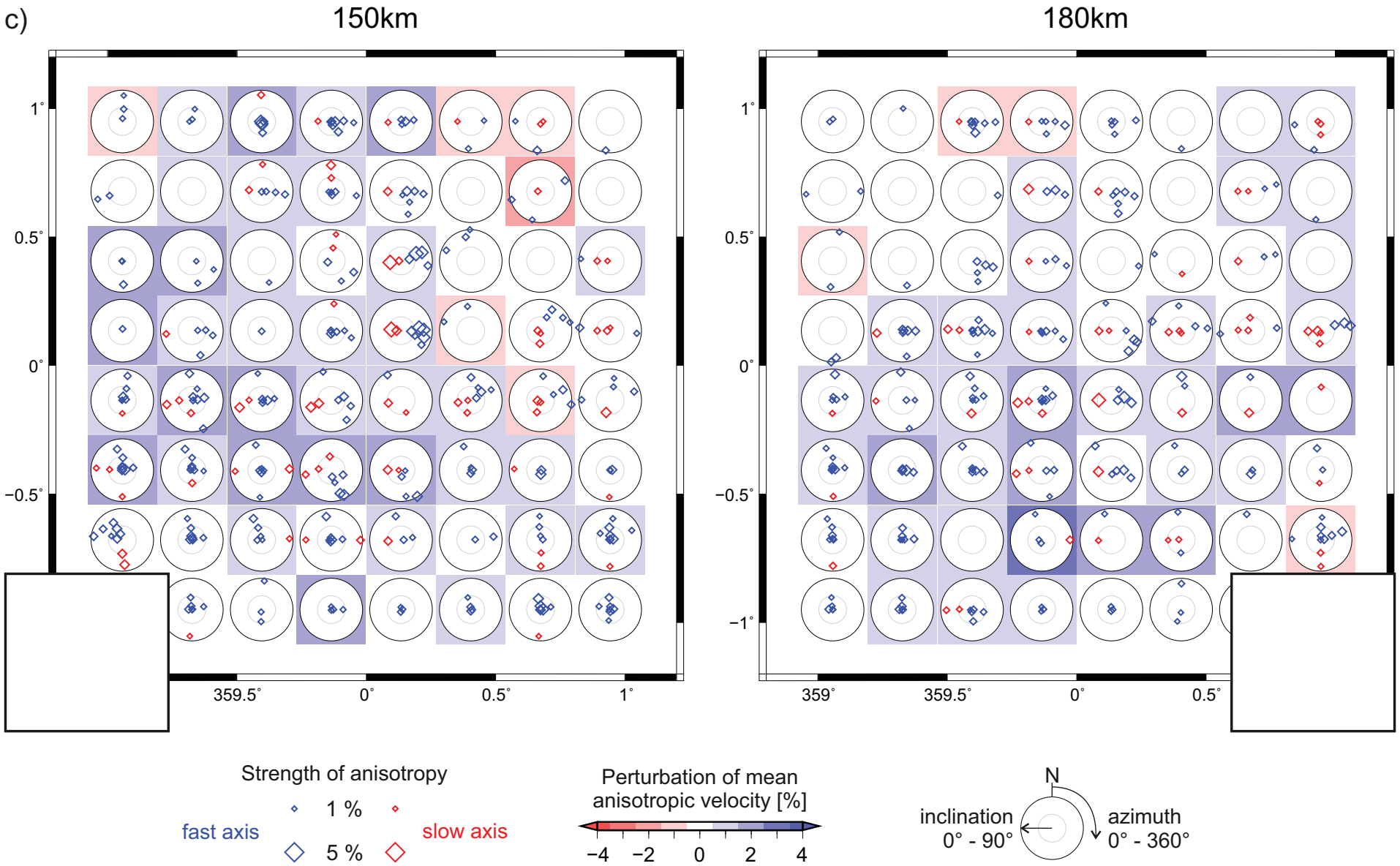

Figure S5. Continue

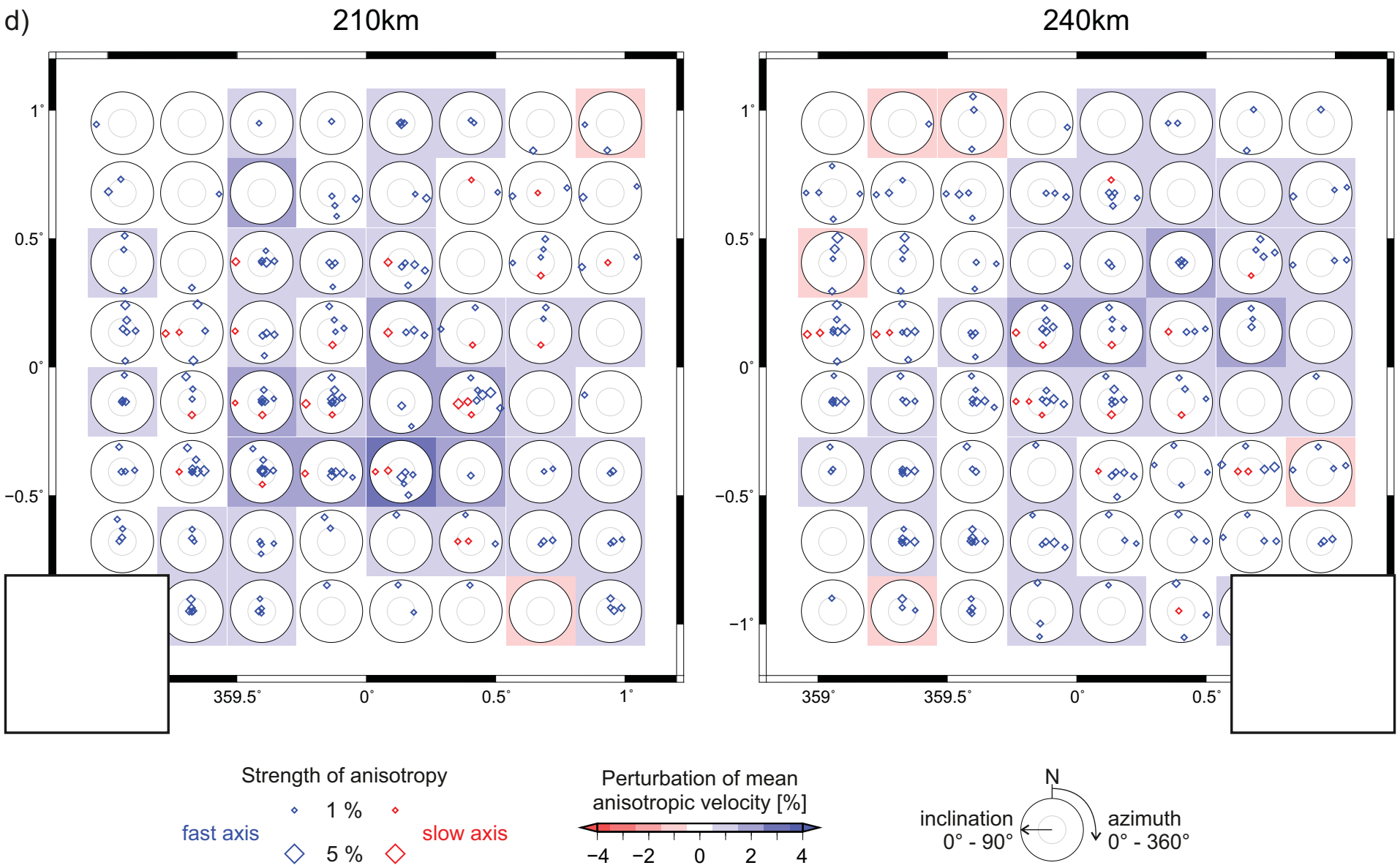

Figure S5. Continue

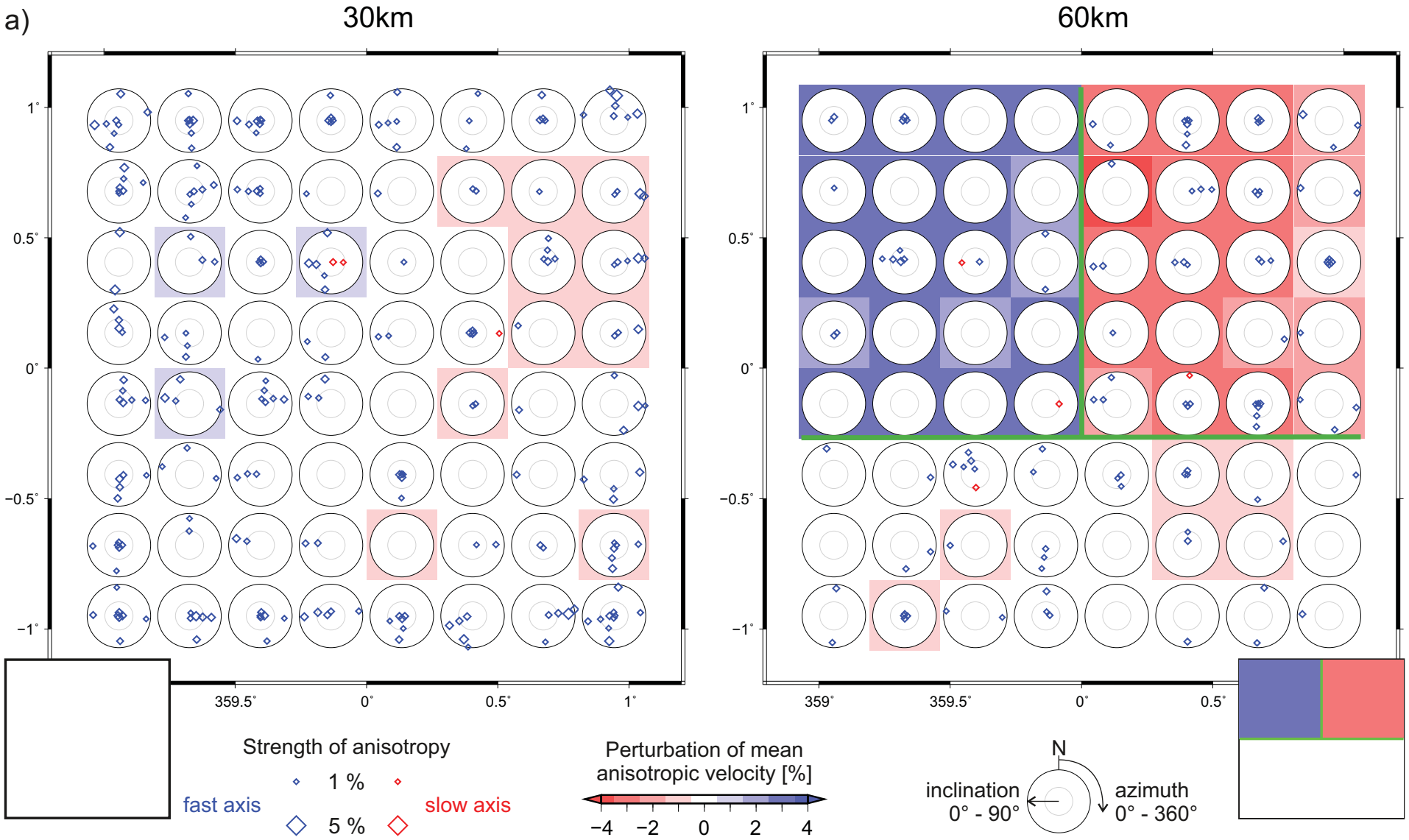

Figure S6. Model of anisotropic velocities resulting from coupled anisotropic-isotropic inversion of synthetic travel times calculated for P waves propagating through the isotropic part of structure imaged in Fig. 9. See caption of Fig. 11 for more details.

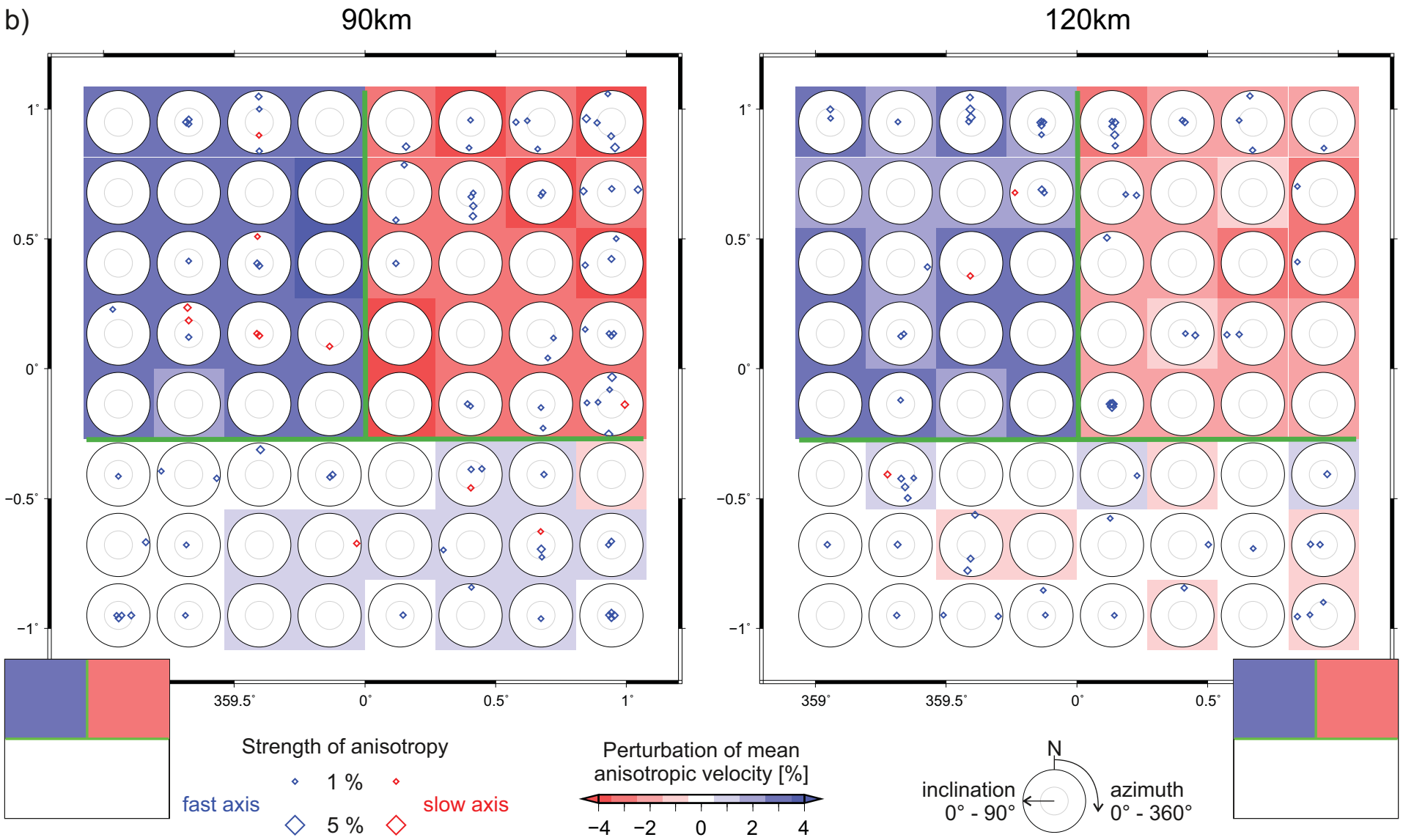

Figure S6. Continue

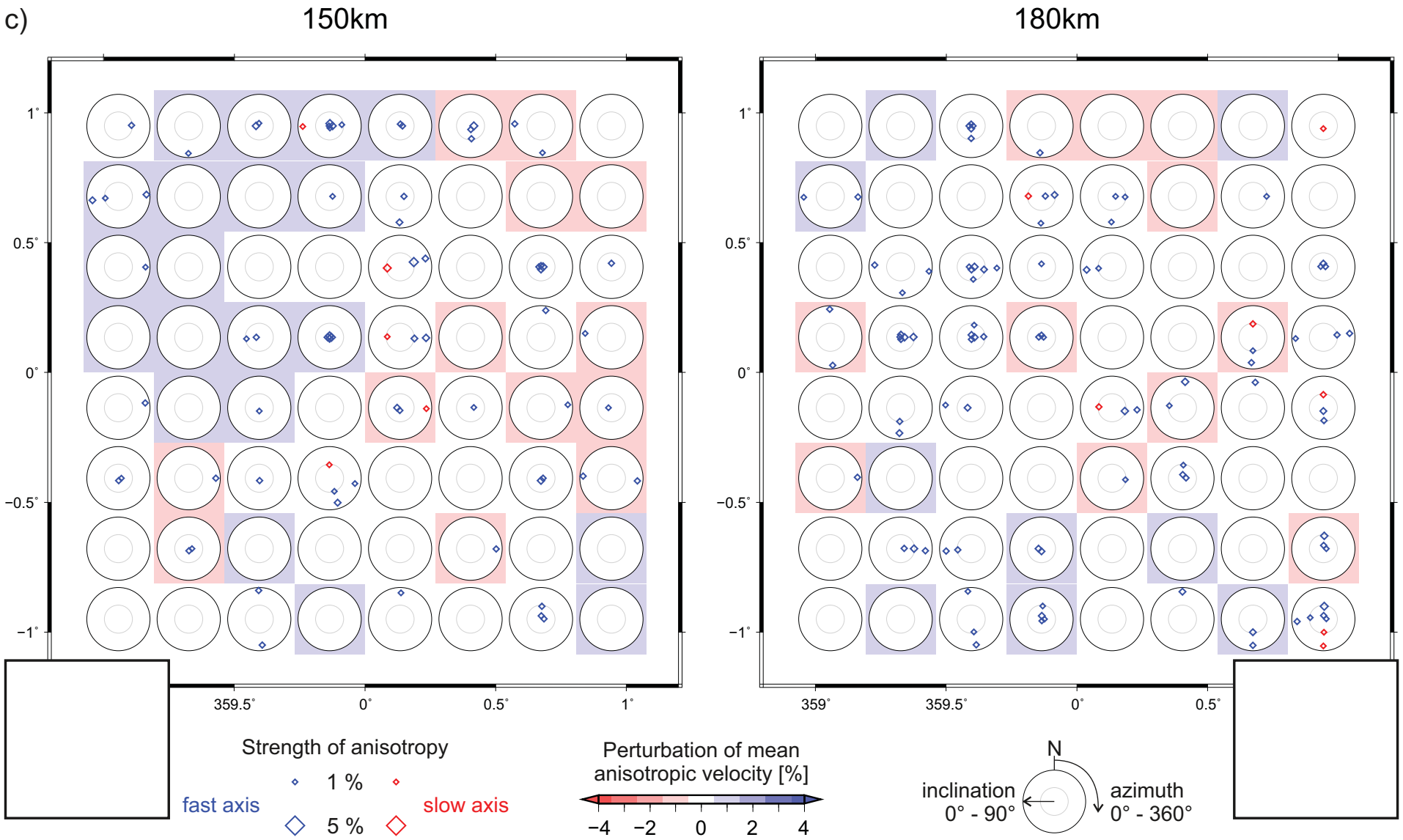

Figure S6. Continue

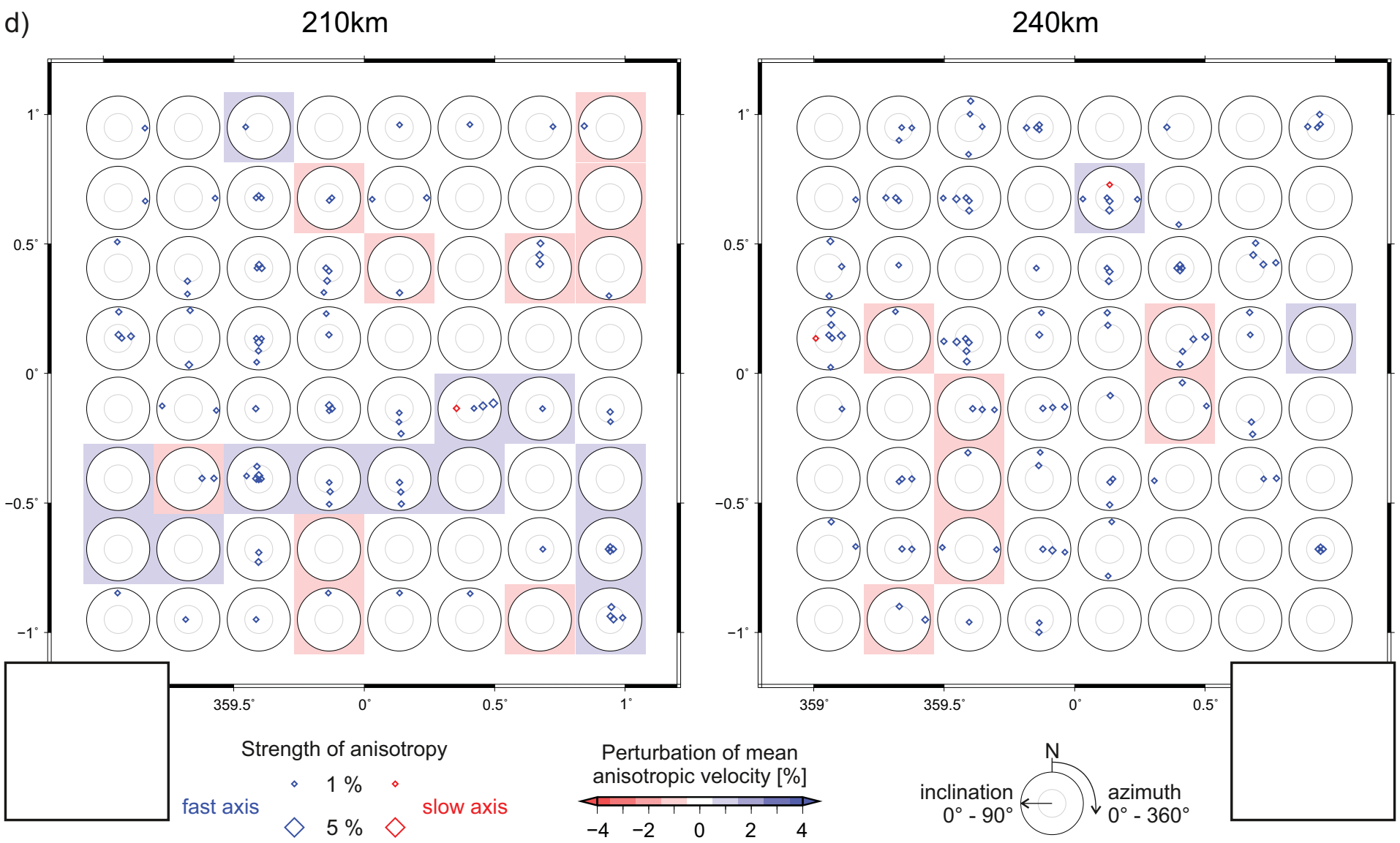

Figure S6. Continue

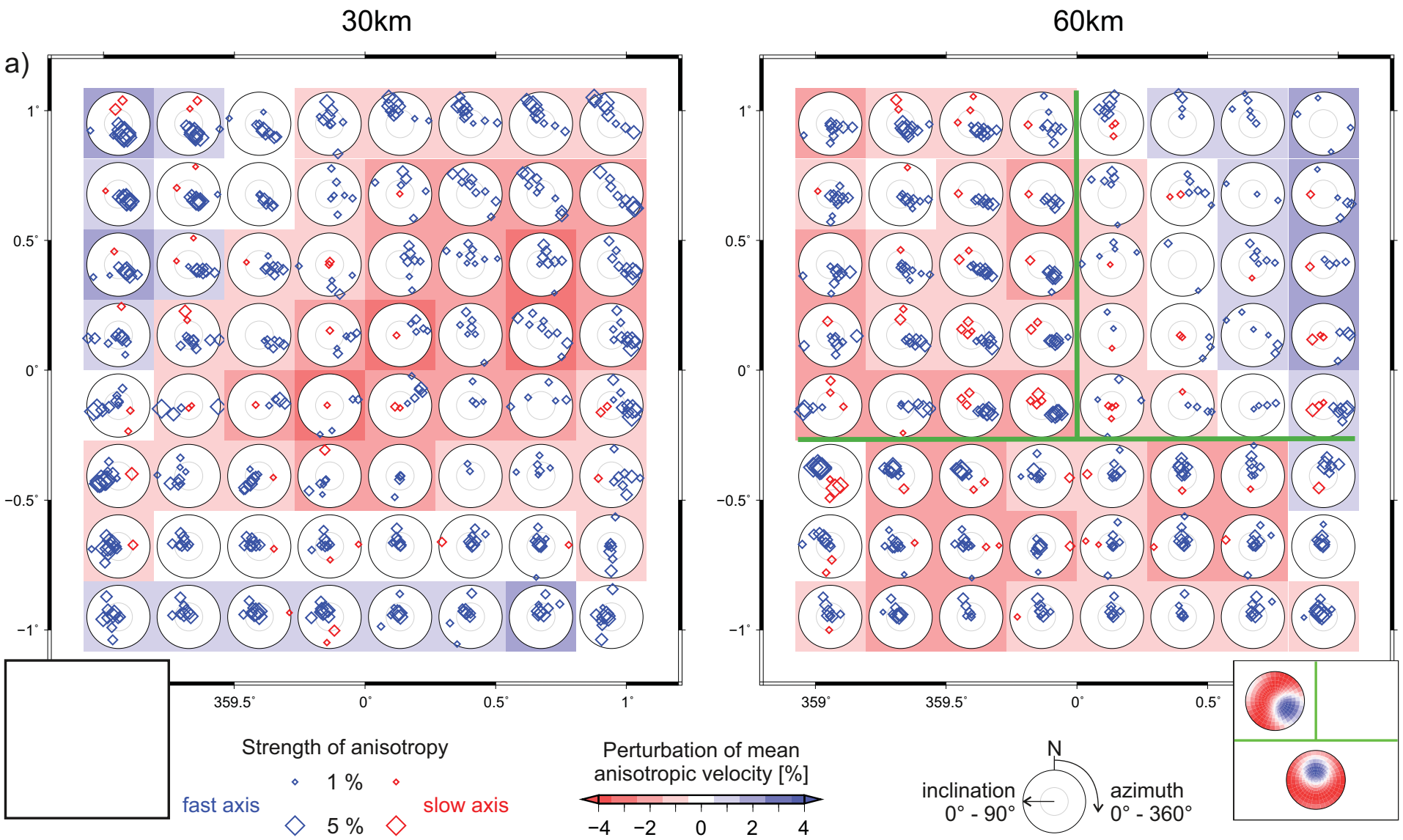

Figure S7. Model of anisotropic velocities resulting from coupled anisotropic-isotropic inversion of synthetic travel times calculated for P waves propagating through the anisotropic part of the structure imaged in Fig. 9. See caption of Fig. 11 for more details.

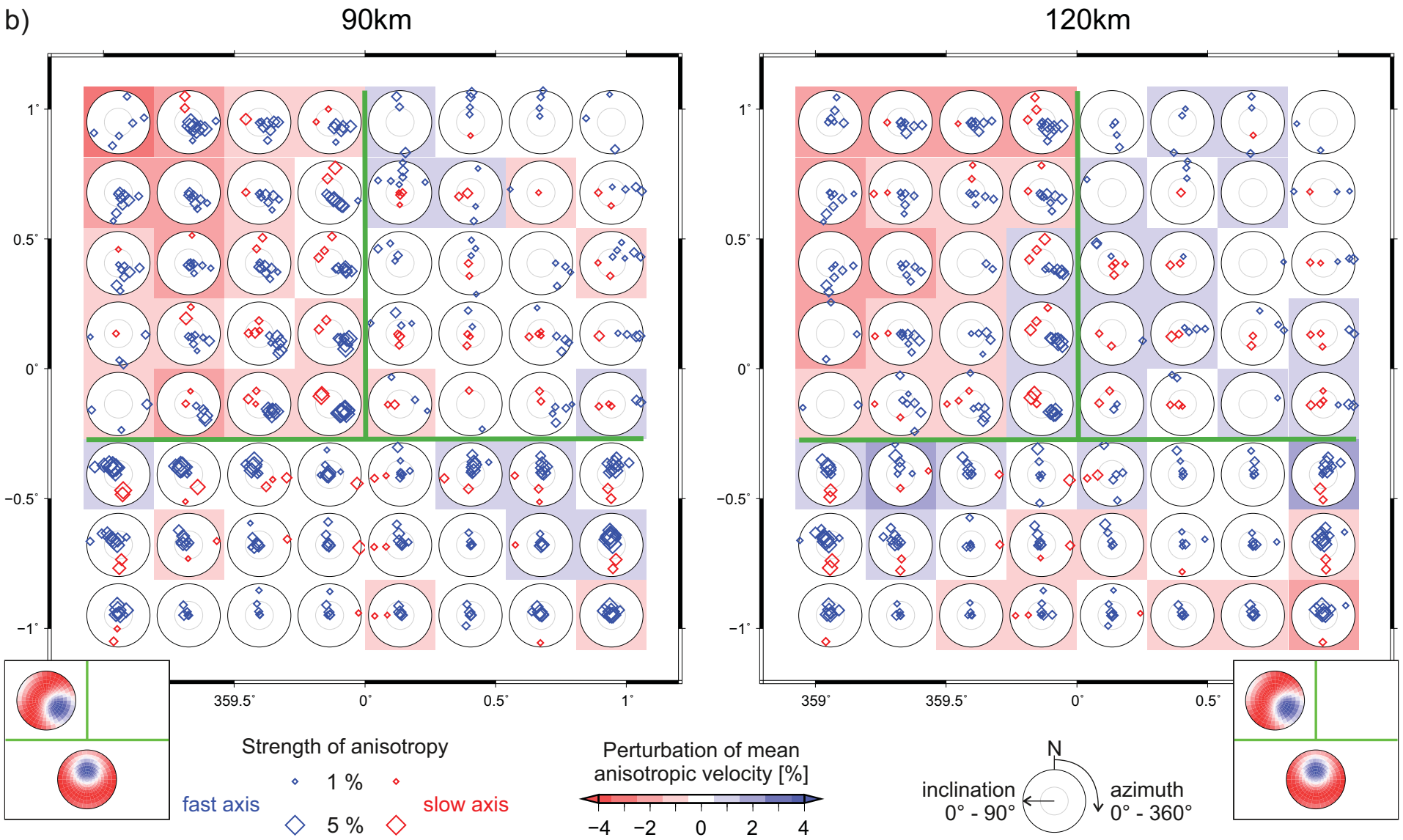

Figure S7. Continue

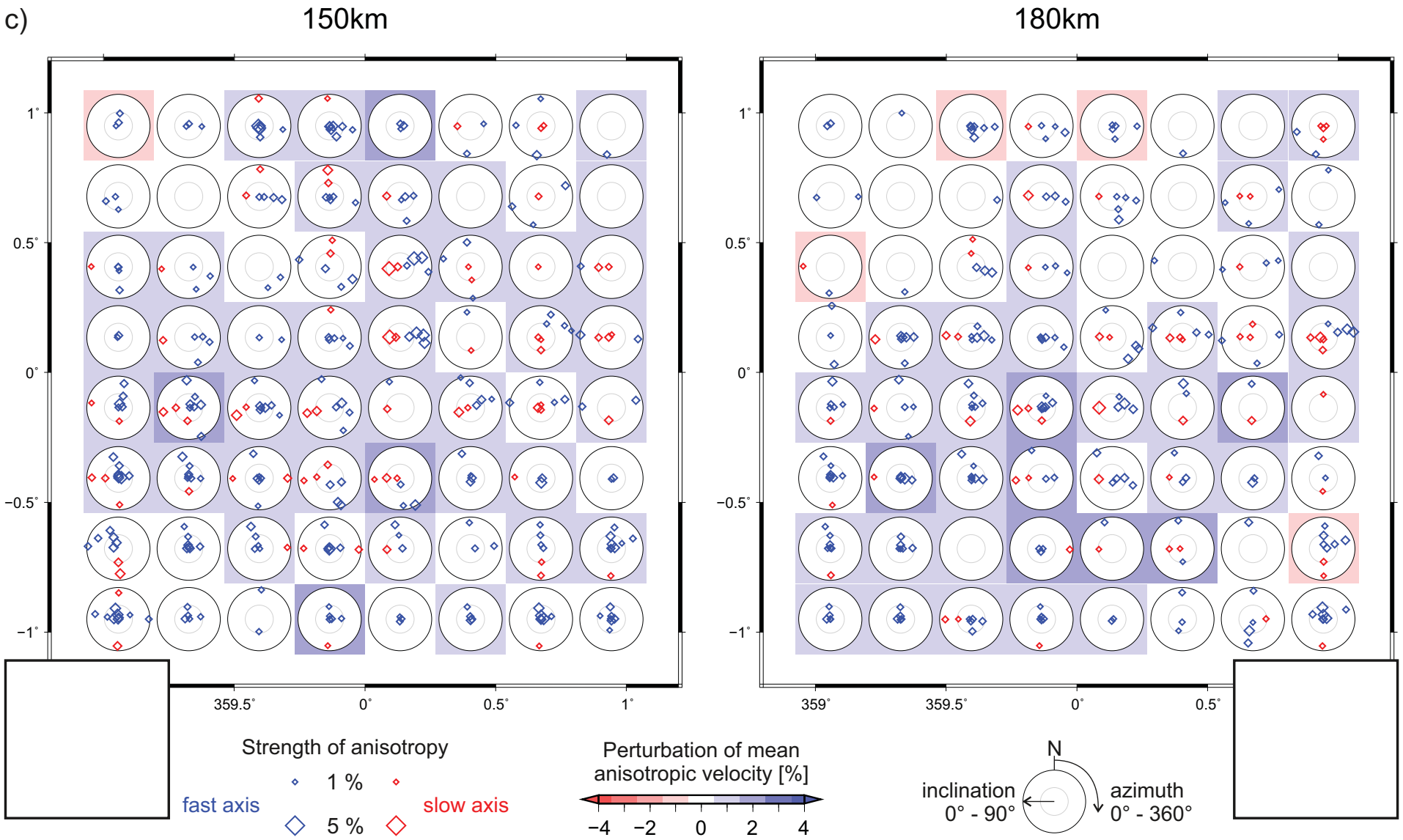

Figure S7. Continue

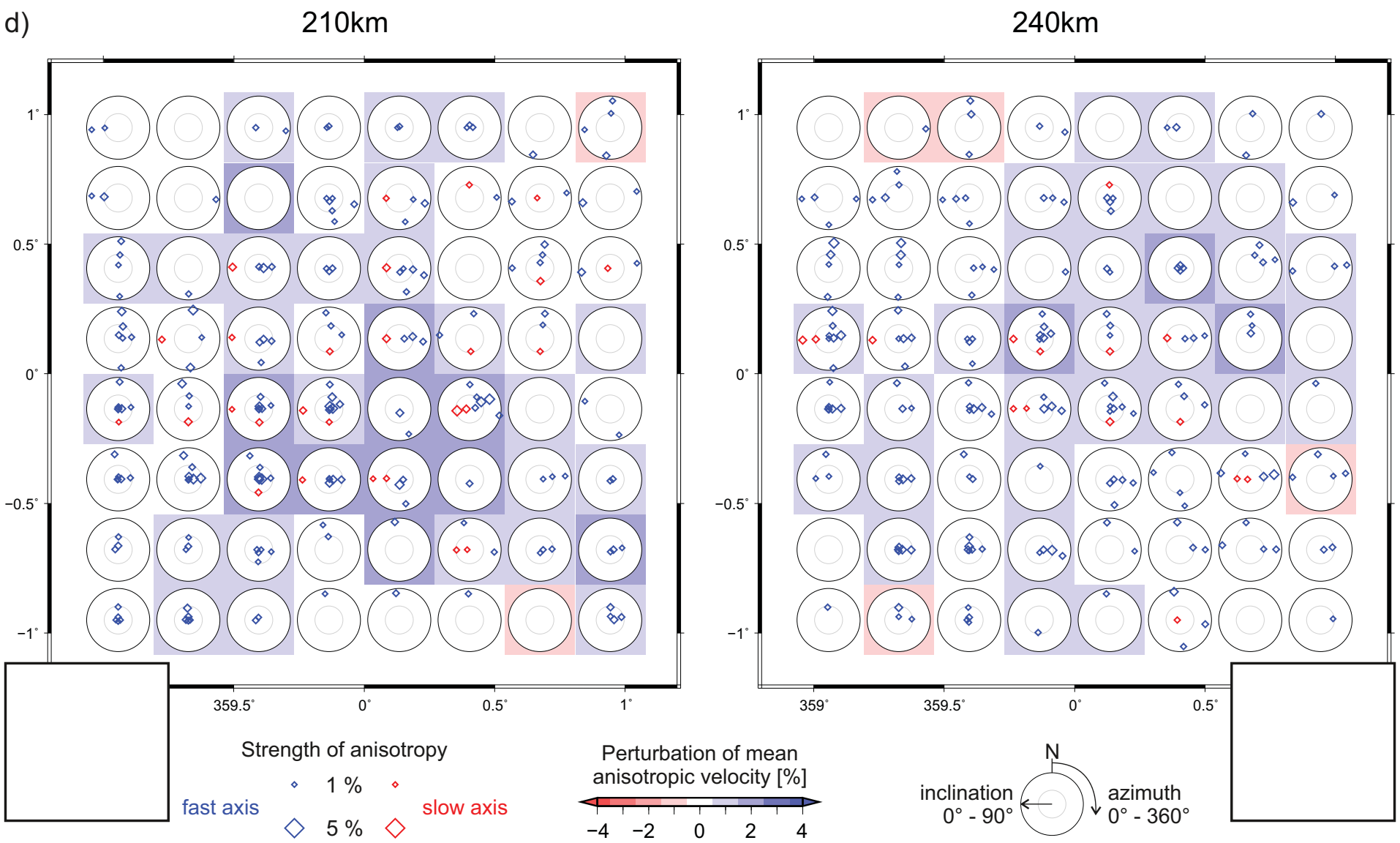

Figure S7. Continue

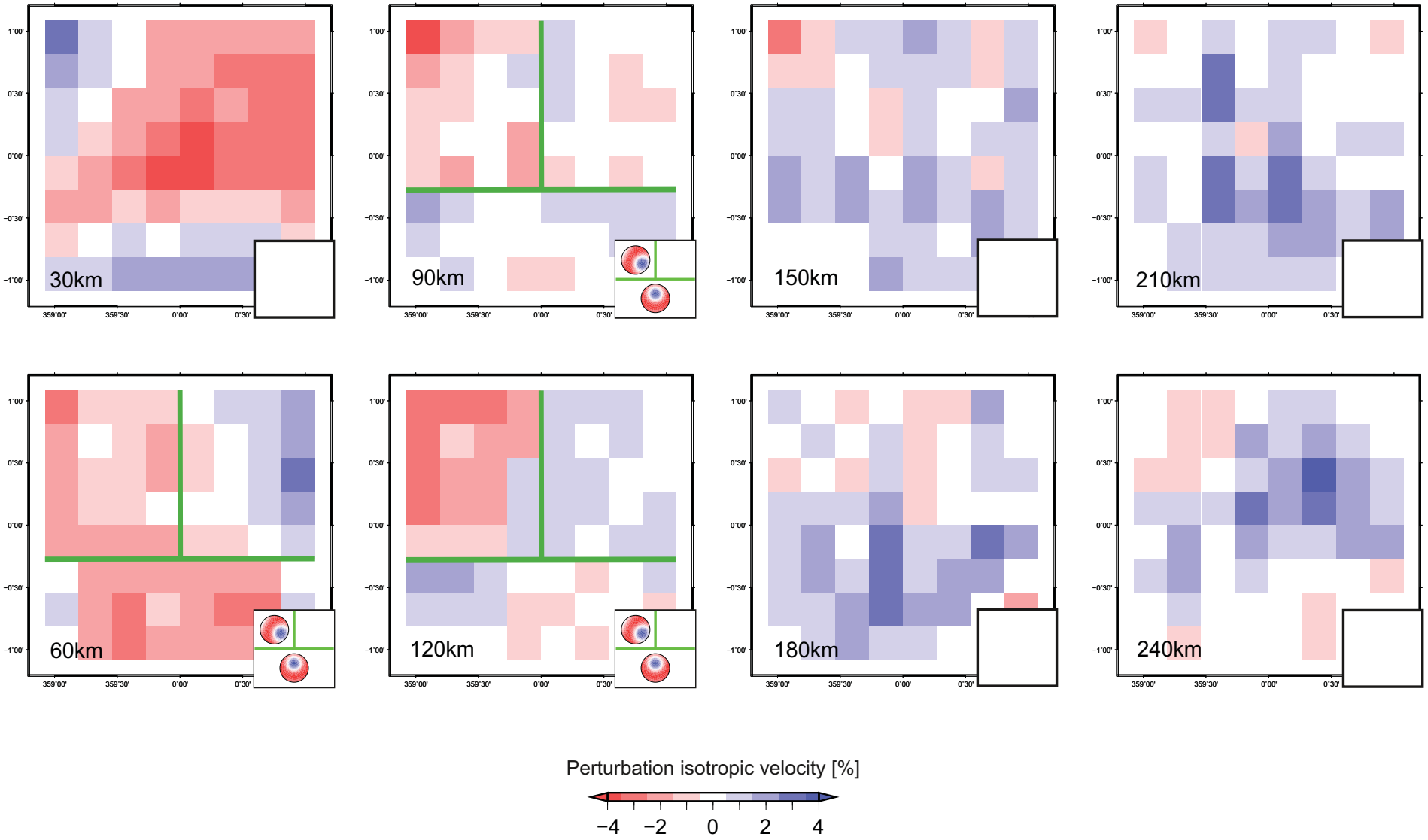

Figure S8. Model of isotropic velocities resulting from purely isotropic-velocity inversion of synthetic travel times calculated for P waves propagating through the anisotropic part of the synthetic structure imaged in Fig. 9. See caption of Fig. 11 for more details.

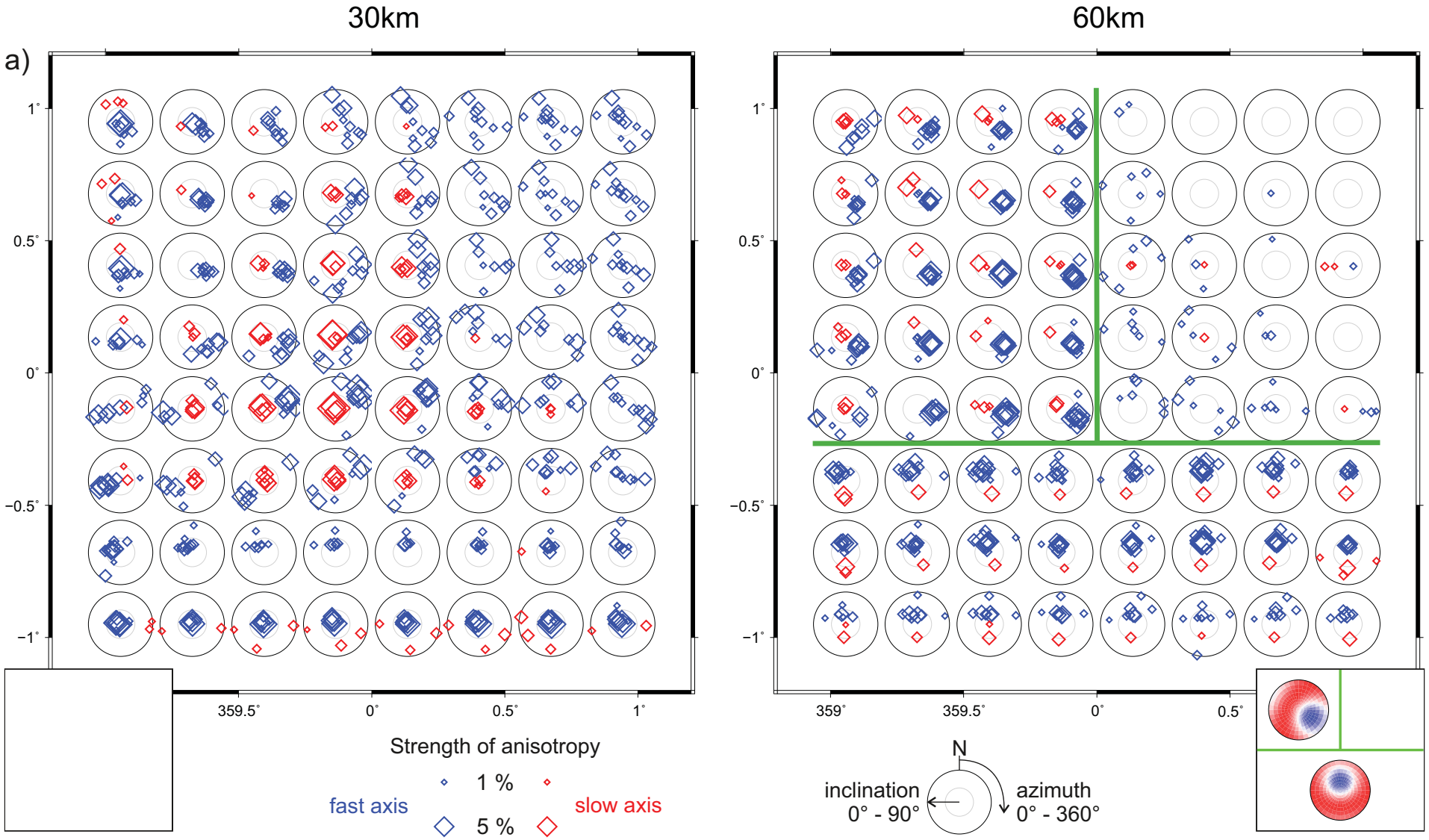

Figure S9. Model of anisotropic velocities resulting from inversion for strength of anisotropy and orientation of symmetry axis of synthetic travel times calculated for P waves propagating through the anisotropic part of structure imaged in Fig. 9. The isotropic-velocity component is fixed during the inversion. See caption of Fig. 11 for more details.

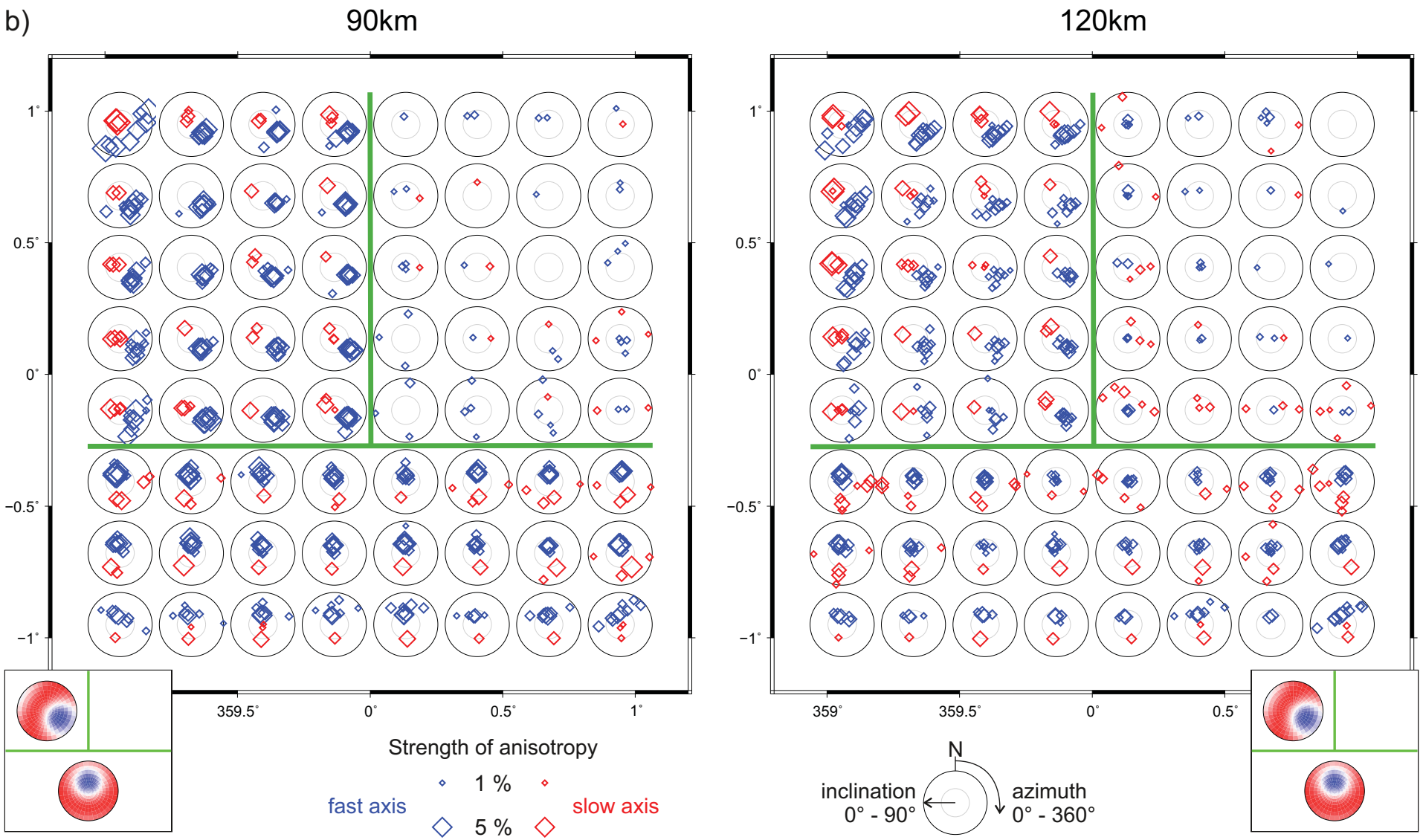

Figure S9. Continue

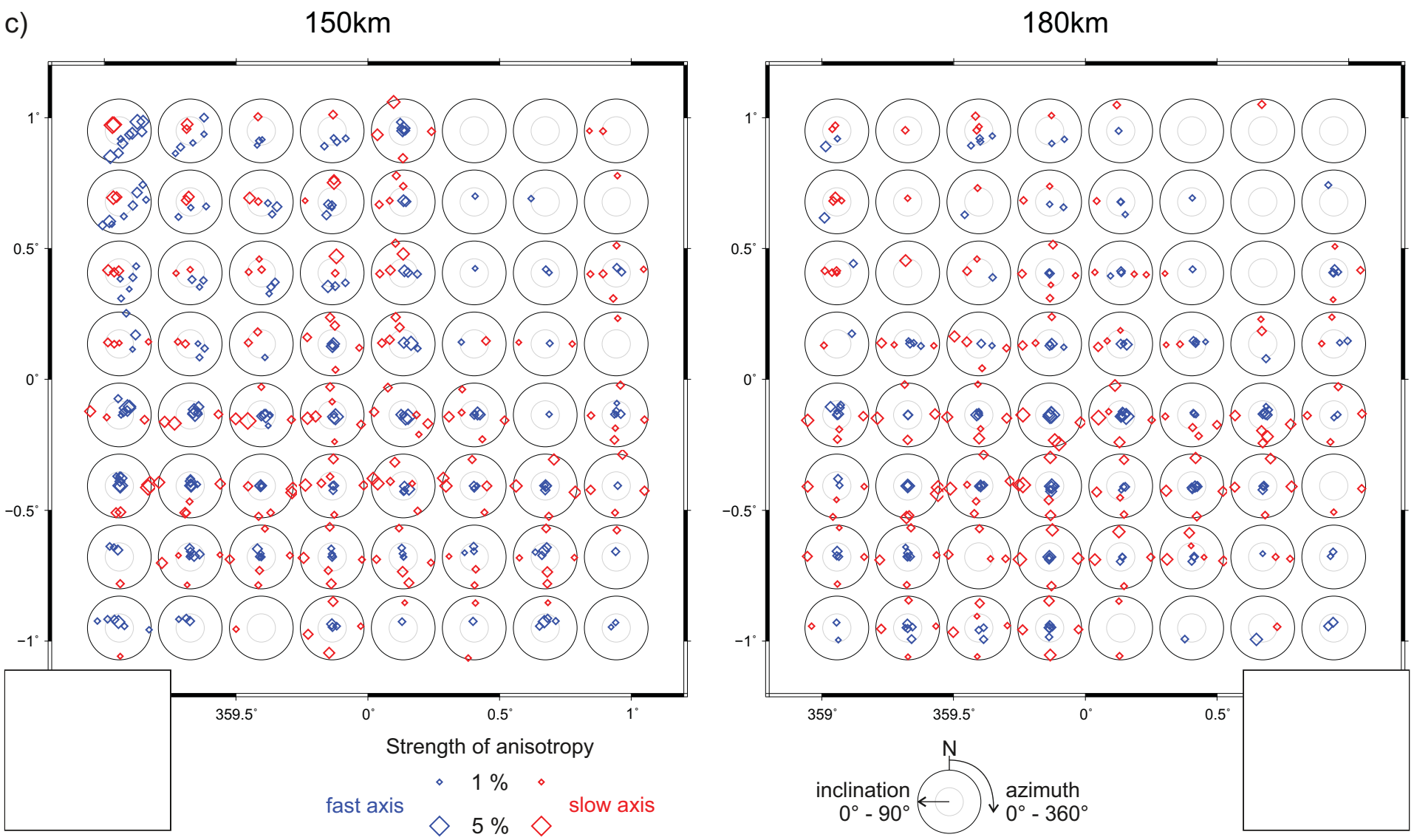

Figure S9. Continue

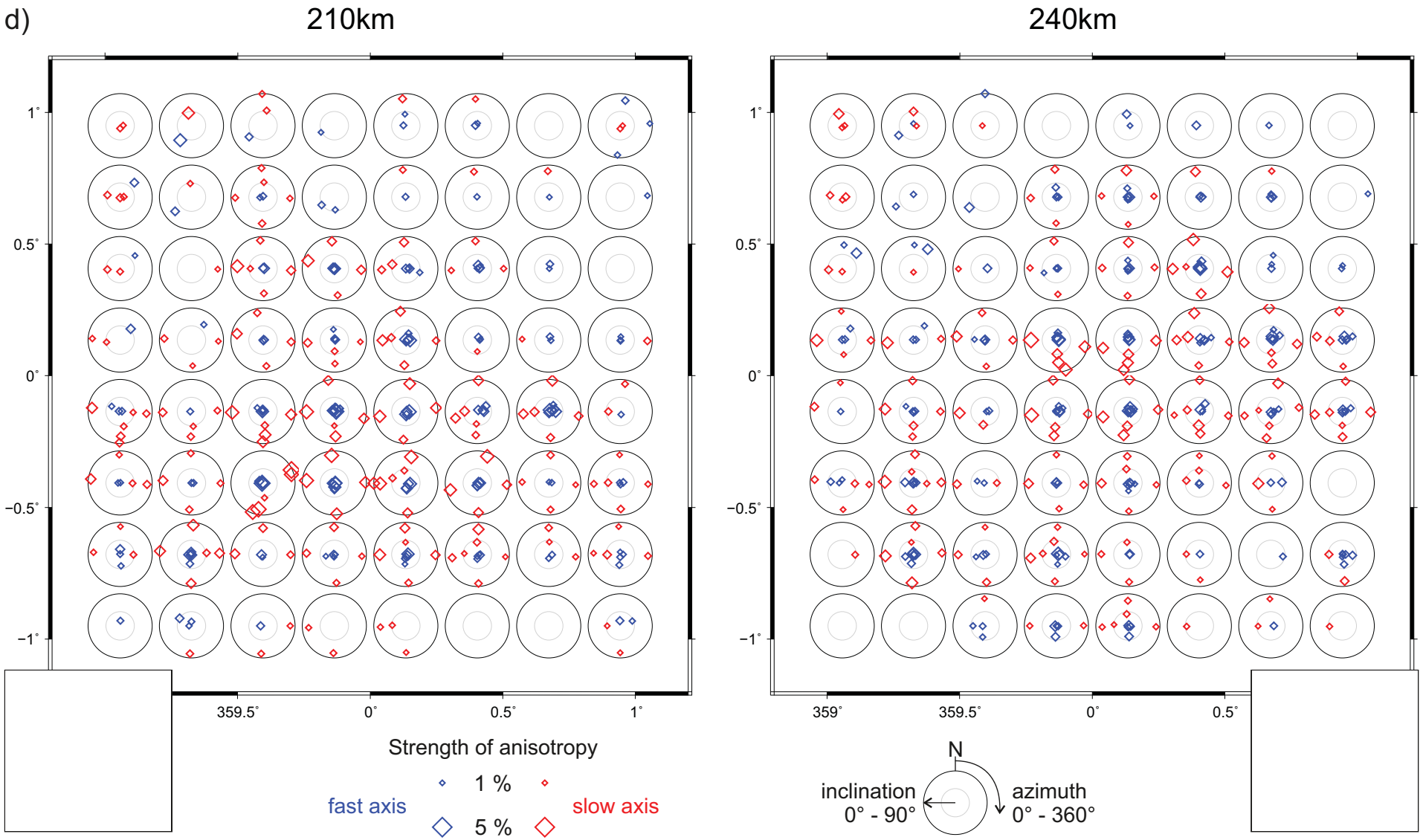

Figure S9. Continue

6. Novel anisotropic teleseismic body-wave tomography code AniTomo to illuminate heterogeneous anisotropic upper mantle: Part II - Application to data of passive seismic experiment LAPNET in northern Fennoscandia

Helena Munzarová[1], Jaroslava Plomerová[1], Eduard Kissling[2], Luděk Vecsey[1], Vladislav Babuška[1]

Geophysical Journal International, Volume **215**, Issue 2, November 2018, Pages 1388-1409, doi:10.1093/gji/ggy327

[1] Institute of Geophysics, Academy of Sciences, Prague, Czech Republic
[2] Institute of Geophysics, Department of Earth Sciences, ETH Zürich, Zürich, Switzerland

Geophysical Journal International

Geophys. J. Int. (2018) **215,** 1388–1409
Advance Access publication 2018 August 06
GJI Seismology

doi: 10.1093/gji/ggy327

Novel anisotropic teleseismic body-wave tomography code AniTomo to illuminate heterogeneous anisotropic upper mantle: Part II – Application to data of passive seismic experiment LAPNET in northern Fennoscandia

Helena Munzarová,[1] Jaroslava Plomerová,[1] Eduard Kissling,[2] Luděk Vecsey[1] and Vladislav Babuška[1]

[1] *Institute of Geophysics, Academy of Sciences, Prague, Czech Republic. E-mail: helena@ig.cas.cz*
[2] *Institute of Geophysics, Department of Earth Sciences, ETH Zürich, Switzerland*

Accepted 2018 August 3. Received 2018 June 27; in original form 2018 February 15

SUMMARY

Seismic anisotropy provides a unique constraint on the past and present dynamics of the lithosphere and sublithospheric mantle. To contribute to studies of large-scale tectonic fabric, we have developed code AniTomo for regional anisotropic tomography. AniTomo allows us to invert simultaneously relative traveltime residuals of teleseismic *P* waves for 3-D distribution of isotropic-velocity perturbations and velocity anisotropy in the upper mantle. Weak hexagonal anisotropy with the symmetry axis oriented generally in 3-D is considered.

The first application of novel code AniTomo to data from passive seismic experiment LAPNET results in a model of anisotropic velocities of the upper mantle beneath northern Fennoscandia. We have opted for northern Fennoscandia for the first application because it is a tectonically stable Precambrian region with a thick anisotropic mantle lithosphere without significant thermal heterogeneities. We carefully analyse the distribution of the rays to limit the fully anisotropic inversion only to the volume with the sufficient directional ray coverage. Capability of the given inversion setup to reveal large-scale anisotropic structures in the upper mantle is documented by a series of synthetic tests.

The strongest anisotropy and the largest velocity perturbations concentrate at depths corresponding to the mantle lithosphere, while in deeper parts of the tomographic model, the lateral variations are insignificant. We delimit regions of laterally and vertically consistent anisotropy in the mantle–lithospheric part of the model. We attribute the retrieved domain-like anisotropic structure of the mantle lithosphere in northern Fennoscandia to preserved fossil fabrics of the Archean microplates, accreted during the Precambrian orogenic processes.

Key words: Body waves; Seismic anisotropy; Seismic tomography; Dynamics of lithosphere and upper mantle.

1 INTRODUCTION

Deciphering fabrics of the upper mantle is an important task for back-in-time reconstruction of development of the continental lithosphere (see for a review of anisotropy, e.g. Babuška & Cara 1991; Šílený & Plomerová 1996; Silver 1996; Savage 1999; Park & Levin 2002; Babuška & Plomerová 2006; Fouch & Rondenay 2006; Mainprice 2007; Maupin & Park 2007; Long & Silver 2009; Long & Becker 2010). Shear and surface waves enable to study smooth and long-wavelength variations of the large-scale velocity anisotropy, resulting in azimuthal- or radial-anisotropy shear-velocity models of the upper mantle (e.g. Panning & Romanowicz 2006; Kustowski *et al.* 2008; Fichtner *et al.* 2010, 2013; Auer *et al.* 2014; French & Romanowicz 2014; Yuan & Beghein 2014; Zhu *et al.* 2014; Chang *et al.* 2015; Debayle *et al.* (2016); Ho *et al.* 2016; Nita *et al.* 2016). On the other hand, teleseismic *P* waves are sensitive to smaller-scale structures due to their shorter wavelengths and they represent independent data. Hammond & Toomey (2003) use teleseismic *P*- and *S*-wave delay times and shear-wave splitting measurements to constrain isotropic and anisotropic heterogeneity in the mantle beneath the southern East Pacific Rise. Systematic studies of seismic anisotropy in various continental provinces document spatial variation of directional terms of relative *P*-wave traveltime residuals and dependence of shear-wave splitting parameters on backazimuth (e.g. Babuška *et al.* 1993; Babuška & Plomerová 2006; Plomerová *et al.* 2011, 2012). The authors interpret such anisotropic signatures

of the body waves by anisotropy with a general orientation of the symmetry axes within blocks, or domains, of mantle lithosphere.

Neglecting seismic anisotropy and considering only isotropic wave propagation in teleseismic body-wave tomography of the upper mantle is a simplification that is incompatible with current understanding of the plate tectonics and upper mantle dynamics. Ignoring seismic anisotropy can potentially bias the resulting isotropic-velocity models (e.g. Bezada *et al.* 2016) and mask true fabrics of the Earth structures. Different approaches of inverting *P*-wave traveltimes or traveltime deviations for anisotropic velocities can be found in various tomographic applications (e.g. Hirahara & Ishikawa 1984; Ishise & Oda 2005; Wang & Zhao 2013), but most of them are limited to the crust, using local-earthquake data sets and searching for azimuthal anisotropy only. On the other hand, for example Liu & Zhao (2017) or Hua *et al.* (2017) evaluate also radial anisotropy from local-earthquake data sets merged with teleseismic data sets, but the separation of radial and azimuthal anisotropy yet represents a significant simplification of the true anisotropic structure of the Earth.

To contribute to studies of large-scale anisotropy of the upper mantle, we have developed a unique code, called AniTomo, for regional anisotropic *P*-wave tomography (Munzarová *et al.* 2018). AniTomo inverts traveltime residuals of teleseismic *P* waves simultaneously for 3-D distribution of isotropic velocity perturbations and anisotropy in the upper mantle. This tomographic code represents a step further from modelling homogeneously anisotropic blocks of mantle lithosphere (e.g. Babuška *et al.* 1993; Šílený & Plomerová 1996; Vecsey *et al.* 2007) towards modelling the upper mantle with arbitrarily varying anisotropy in 3-D. AniTomo assumes a weak anisotropy of the hexagonal symmetry with axes oriented generally in 3-D and it is the first tomographic code that includes inclination of the axes among the model parameters. Allowing for the fully 3-D orientation of the symmetry axes is crucial to model successfully anisotropic fabric of individual domains of the continental mantle lithosphere. The theoretical background of the AniTomo code is presented in a methodological paper by Munzarová *et al.* (2018). The paper also includes many synthetic tests of resolution, separation of the isotropic and anisotropic model parameters, their convergence to the true values and discussion of effects of inversion setup on the results.

For the first application of the AniTomo code to a real data set, we have selected data from international passive seismic experiment POLENET/LAPNET deployed in northern Fennoscandia (2007–2009; e.g. Kozlovskaya 2007). The Fennoscandian Shield is an assemblage of microplate nuclei, island arcs, terranes and mobile belts of prevailingly Archean age in the northeast and of Proterozoic age in the southwest (e.g. Snyder 2002; Korja *et al.* 2006; Lahtinen *et al.* 2015). We focus on the northern part of Fennoscandia, where Archean cratons, that is Karelia, Kola and Norrbotten, accreted together with Belomorian Mobile Belt and various arcs and terranes during the Lapland-Kola and Lapland-Savo oregenies in the Palaeoproterozoic (e.g. Korja *et al.* 2006). At present, northern Fennoscandia is a tectonically stable region with a relatively thick lithosphere (Plomerová & Babuška 2010) and without significant thermal heterogeneities (e.g. Slagstad *et al.* 2009, for a review).

Seismological research of the upper mantle beneath northern Fennoscandia has flourished particularly after the POLENET/LAPNET experiment that complemented sparsely distributed permanent observatories equipped with broad-band seismometers. Various types of data from the experiment, processed by different techniques, provide new information on velocity structure and discontinuities in the upper mantle, for example from inversion of dispersion curves of Rayleigh waves (Pedersen *et al.* 2013) and from joint inversion of *P* and *S* receiver functions (Vinnik *et al.* 2016). Teleseismic *P*-wave traveltimes were analysed to assess thickness of the lithosphere at around 150 km (e.g. Plomerová & Babuška 2010). Silvennoinen *et al.* (2016) evaluated a tomographic model of isotropic-velocity perturbations of the upper mantle (see Section 5.2 for a comparison of the tomographic models). Plomerová *et al.* (2011) delimited domains of uniform large-scale anisotropy with the symmetry axes oriented generally in 3-D within the mantle lithosphere by joint interpretation of *P*- and SKS-wave anisotropic characteristics. Azimuthal anisotropy and its depth dependence within the upper mantle were studied by Vinnik *et al.* (2014) by a joint inversion of SKS splitting parameters and *P* receiver functions.

In this paper, we present a 3-D model of the upper mantle beneath northern Fennoscandia, in which we show *P*-wave isotropic-velocity perturbations and anisotropic parameters retrieved with the novel coupled anisotropic–isotropic tomography code AniTomo. Furthermore, the results are complemented with a series of synthetic inversions to test resolution capability of the LAPNET ray geometry and analysed along with the previous independent findings of anisotropic structure of the region (Plomerová *et al.* 2011).

2 DATA AND THEIR PRE-PROCESSING FOR ANISOTROPIC TOMOGRAPHY

Teleseismic *P*-wave arrival times measured on recordings of the LAPNET array represent a core of the data set for anisotropic tomography of the upper mantle beneath northern Fennoscandia calculated with code AniTomo. POLENET/LAPNET was a subproject of the POLENET-IPY consortium (Cooper *et al.* 2008) related to seismic and geodetic studies in the Arctic regions, which included also tomographic studies of velocity structure of the upper mantle beneath northern Fennoscandia.

Seismic array LAPNET (e.g. Kozlovskaya 2007; http://www.oulu.fi/sgo-oty/lapnet/; http://www.fdsn.org/networks/detail/XK_2007/) was installed on the territory of northern Finland and Finnmark area of Norway, and neighbouring northwestern Russia between May 2007 and September 2009 (see also Plomerová *et al.* 2011). The original array consisted of ∼37 temporary broad-band stations (LP00-LP83) and observatories of the Northern Finland Seismological Network (OUL, SGF, MSF, RNF), the Helsinki University Seismic Network (KU6, VRF, HEF, KEV, KIF) and neighbouring stations in Norway (KTK1). For this study, we enlarge the data set by *P*-wave arrival times measured on ten permanent stations of the Swedish National Seismological Network located westward of the LAPNET array (KUR, NIK, MAS, DUN, LAN, PAJ, ERT, SAL, KAL, HAR; SNSN 1904) and two more stations to the north belonging to the Norwegian seismic networks (ARE0, TRO). This step represents 25 per cent enlargement of the original LAPNET array. The extended array covers an area of about 500 km by 500 km with average interstation spacing of 70 km (Fig. 1).

We select recordings of 90 earthquakes from teleseismic epicentral distances between 20° and 100° (Fig. 2) and measure arrival times of *P* waves on seismograms with 20 Hz sampling simulat-

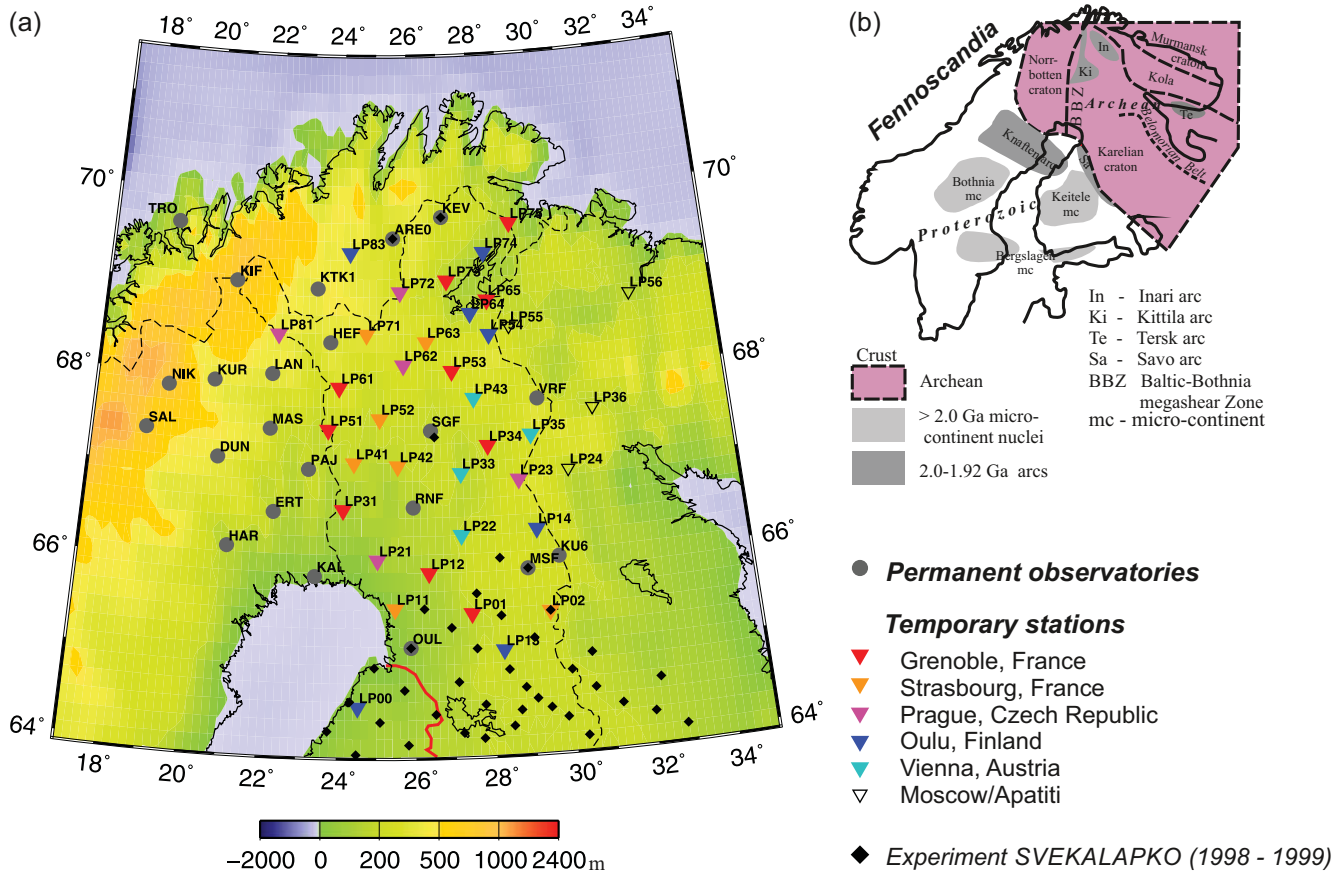

Figure 1. Permanent and temporary seismic stations deployed during passive seismic experiment LAPNET (2007–2009) in northern Fennoscandia (a). Distribution of microcontinental nuclei, island arcs and boundaries of hidden and exposed terranes older than 1.92 Ga in the Fennoscandian Shield (b), redrawn according to Korja *et al.* (2006).

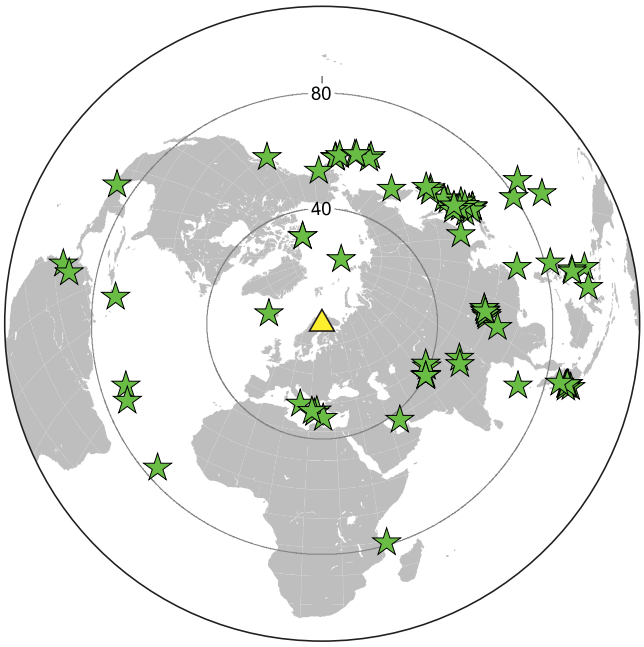

Figure 2. Location of 90 teleseismic events (green stars) recorded by the LAPNET array (yellow triangle) and selected for the teleseismic *P*-wave arrival-time measurements.

ing the WWSSN-SP response with the use of a semi-automatic picker developed by Vecsey (private communication 2010), based on Seismic Handler (Stammler 1993). Because we invert for velocity structure of the upper mantle, we correct the measured traveltimes for differences between a model of the Fennoscandian crust and reference radial velocity model of the Earth IASP'91 (Kennett & Engdahl 1991). We have tested several crustal models and we use a recent model by Silvennoinen *et al.* (2014) for the final calculations.

Data pre-processing for the inversion includes a calculation of absolute traveltime residuals, that is differences between the observed traveltimes and the theoretical traveltimes for reference model IASP'91. To minimize effects originated outside the volume studied, we calculate relative residuals by subtracting an event average residual from the absolute residuals of each event. We also test time stability of the relative residuals to avoid potential operational problems, for example occasional failures of the time synchronization at some of the temporary stations. Finally, the input *P*-wave data set for tomography consists of 3286 relative traveltime residuals, which all lie in an interval of (–2 s; 2 s), out of which 96 per cent are in an interval of (–0.5 s; 0.5 s). Such a low variability of the traveltime residuals excludes a strong large-scale heterogeity in the upper mantle beneath northern Fennoscandia.

3 METHOD

3.1 AniTomo—theoretical background

We use novel anisotropic code AniTomo (Munzarová *et al.* 2018) to invert the relative traveltime residuals of teleseismic *P* waves jointly for both the isotropic-velocity perturbations and velocity anisotropy of the upper mantle beneath northern Fennoscandia. We have developed AniTomo as a modification of code Telinv that is broadly used for standard isotropic-velocity teleseismic tomography (e.g. Weiland *et al.* 1995; Arlitt *et al.* 1999; Lippitsch *et al.* 2003; Sandoval *et al.* 2004; Shomali *et al.* 2006; Eken *et al.* 2007; Karousová *et al.* 2012, 2013; Karousová 2013; Plomerová *et al.* 2016; Silvennoinen *et al.* 2016; Chyba *et al.* 2017). Weak anisotropy models with hexagonal symmetry both with the high-velocity *a*-axis or with the low-velocity *b*-axis, generally oriented in 3-D, are allowed. The medium is described by the isotropic (average) component $\bar{v}$ of the anisotropic velocity v, strength of anisotropy k and two angles for orientation of the symmetry axis—azimuth λ and inclination θ. Then, the formula for *P*-wave velocity v in a weakly anisotropic medium with hexagonal symmetry can be written as

$$v = \bar{v}\left\{1 + k\left[(\sin i\,\sin\theta\,\cos(\varphi - \lambda) + \cos i\,\cos\theta)^2 - \frac{1}{2}\right]\right\}, \quad (1)$$

where ϕ and i are backazimuth and incidence angles defining the propagation of the wave in 3-D. In general, AniTomo is applicable only to *P* waves and not to *S* waves, whose anisotropic propagation is more complex.

We have linearized the relation between the traveltime residual Δt and perturbations of anisotropic parameters $\Delta\bar{v}$, Δk, $\Delta\lambda$ and $\Delta\theta$ at each grid node (indexed with j)

$$\begin{aligned}\Delta t \;&= \sum\nolimits_j \left(\frac{\partial t}{\partial \bar{v}}\right)_j \Delta\bar{v}_j \;+ \sum\nolimits_j \left(\frac{\partial t}{\partial k}\right)_j \Delta k_j \\ &+ \sum\nolimits_j \left(\frac{\partial t}{\partial \lambda}\right)_j \Delta\lambda_j + \sum\nolimits_j \left(\frac{\partial t}{\partial \theta}\right)_j \Delta\theta_j, \end{aligned} \quad (2)$$

which leads to a system of linear equations that we solve with damped least-square method (e.g. Menke 1984)

$$\mathbf{m} = (\boldsymbol{A}^T \boldsymbol{W}_D \boldsymbol{A} + \epsilon^2 \boldsymbol{W}_M)^{-1}\, \boldsymbol{A}^T \boldsymbol{W}_D \mathbf{d}, \quad (3)$$

where $\mathbf{m}$ is vector of model parameters $\Delta\bar{v}$, Δk, $\Delta\lambda$ and $\Delta\theta$ at all nodes. Data vector $\mathbf{d}$ contains traveltime residuals Δt and matrix $\boldsymbol{A}$ stores the partial derivatives from eq. (2). Errors of arrival-time measurements are considered in weighting matrix $\boldsymbol{W_D}$. Damping factor ε^2 stabilizes the ill-posed problem. Independent values of damping must be set for the four types of parameters describing the medium. Horizontal smoothing of model parameters can be achieved via matrix $\boldsymbol{W_M}$. The inverse in eq. (3) is approximated by truncated singular value decomposition. 3-D ray tracing bending technique Simplex (Steck & Prothero 1991), in which ray paths are distorted by sinusoidal signals, is applied. Reliability of the model parameters for a given ray distribution and inversion setup can be assessed with resolution matrix R

$$\mathbf{R} = (\boldsymbol{A}^T \boldsymbol{W}_D \boldsymbol{A} + \epsilon^2 \boldsymbol{W}_M)^{-1}\, \boldsymbol{A}^T \boldsymbol{W}_D \boldsymbol{A}, \quad (4)$$

or, with ray density tensors (see Section 3.2).

3.2 Setup of parameters controlling the inversion

We parametrize the volume studied with an orthogonal 3-D grid of nodes, at which the model parameters are searched during the inversion. After a series of inversion runs, we have selected a regular horizontal grid spacing of 70 km x 70 km. For a smaller spacing between the nodes, the tomographic images disintegrate and they split into single-cell anomalies indicating an overparametrization. Vertical grid nodes are set at 20, 50 and 80 km depth to enhance separation of the mantle lithosphere and the crust. Further down, from 120 to 370 km the spacing is regular with a 50 km step. We do not invert below 370 km because of the decreasing resolution (see, e.g. Figs S1–S3). The ray coverage of the teleseismic data set is not, of course, sufficient to resolve the crustal structure. The Fennoscandian crust is thick and it is quite likely that an effect of the crust and its inner structure need not be fully eliminated by the crustal correction of the relative residuals. Therefore, we invert for isotropic-velocity perturbations at the 20 km depth to compensate the uncorrected crustal effects and to prevent their mapping into the mantle. But of course, we avoid any interpretation of the velocity perturbations at the 20 km depth.

AniTomo enables to invert for arbitrarily selected model parameters at each node. This means that we can search only for isotropic-velocity perturbations at nodes, where the directional distribution of the rays is not sufficient. Purely isotropic inversion in the whole volume is also possible with the code. Diagonal elements of the resolution matrix (RDE; eq. 4; Fig. S1) or ray segments (Fig. S2) show ray coverage at the individual depth layers. Smoothed contours of RDE equal to 0.5 are considered as a limit of the well-resolved part of the volume studied. The relatively small area delimited by the 0.5 contour of RDE at the 50 km depth is caused by smaller vertical spacing between the nodes in this part of the model. For the purpose of anisotropic tomography, we also evaluate so-called ray density tensors (RDT; Kissling 1988; Sandoval *et al.* 2004) to investigate spatial distribution of rays in each cell and according to that we restrict the fully anisotropic inversion only to the well-sampled nodes. Munzarová *et al.* (2018) describe evaluation of the RDT within the AniTomo code in detail.

As an example, Fig. 3 shows orientations of the RDT eigenvectors and sizes of the eigenvalues for nodes at the 120 km depth (see Fig. S3 for all the depth layers). The ray density tensors indicate not only an overall amount of rays within the parametrization cells by size of their eigenvalues, but they also graphically express quality of directional distribution of the rays by orientation of the eigenvectors and ratio between the eigenvalues. The steeper the orientation of the eigenvector belonging to the largest eigenvalue A (green or yellow dots), the more evenly teleseismic rays cover the parametrization cell. The most even distribution of the rays is in the central part of the individual depth layers (Figs 3 and S3), while towards the edges, the eigenvectors with the largest eigenvalue tend to be oriented in direction of prevailing ray orientations. Ratios of the smaller eigenvalues (B1 and B2) with respect to the largest eigenvalue, that is $B1{*}A^{-1}$ and $B2{*}A^{-1}$, express evenness of the directional coverage as well. Synthetic tests with a quasi-equal realistic distribution of stations and teleseismic events show that ratios $B1{*}A^{-1}$ and $B2{*}A^{-1}$ in a range from 0.1 to 0.2 are typical for teleseismic events. The eigenvalue ratios evaluated for the LAPNET data set reach similar values at many grid nodes (background colour in Figs 3 and S3). Though these values seem to be low, they guarantee a good recovery of the anisotropic parameters (Munzarová *et al.* 2018).

To define nodes where we can invert for anisotropy, we need to delimit a subregion with the highest number and the best directional distribution of the rays in each layer. According to the RDT, we define an irregular, but relatively smooth subregion at the 120 km depth, in which the inversion for all the four anisotropic parameters is allowed (space within the red line in Figs 3 and S3). Then, we limit

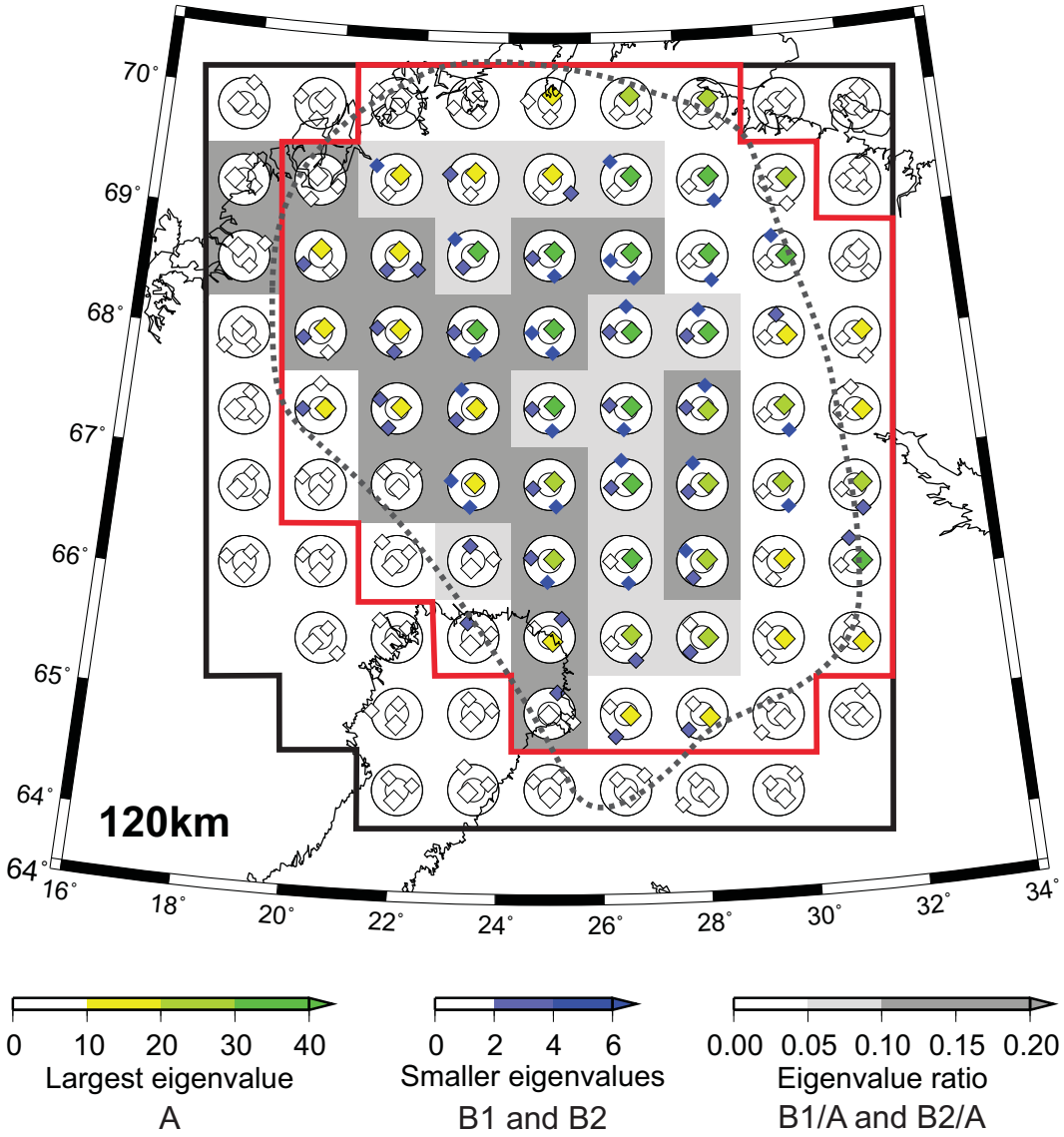

Figure 3. Ray density tensors (RDT) evaluated for the parametrization nodes of the 120 km depth for ray distribution of the LAPNET data set (see Fig. S3 for all the depth layers). We image orientation of three RDT eigenvectors of each node with points in the lower-hemisphere stereographic projection. Size of the largest RDT eigenvalue of a node (marked as A) is displayed with a different colour scale than size of the two smaller eigenvalues (marked as B1 and B2). Ratios between the smaller eigenvalues and the largest eigenvalue at a node, i.e. $B1*A^{-1}$ and $B2*A^{-1}$, are imaged with a background colour. Both the ratios at a node must be larger than the lower limit of a colour band to get the colour. Red line marks the region where inversion for all the four anisotropic parameters is allowed (at depth layers from 50 km down to 270 km). Inversion only for the purely isotropic-velocity perturbations is allowed in between the black and red lines at depths from 50 km to 270 km and within the black line at the 20 km, 320 km and 370 km depths. Smoothed contour of diagonal elements of the resolution matrix equal to 0.5 is imaged with dotted black curves.

the anisotropic inversion only to that subregion at every depth layer from 50 km down to 270 km. At nodes neighbouring the subregion at the 50– 270 km depths (in between the black and red lines in Figs 3 and S3) and at all the nodes of the 20, 320 and 370 km depths (within the black line), we invert only for purely isotropic-velocity perturbations. Thus in total, we invert for 783 perturbations of isotropic-velocity components, 366 perturbations of strength of anisotropy, 366 perturbations of azimuth and 366 perturbations of inclination, that is 1881 unknown model parameters all together.

Well-tuned damping of a mixed-determined problem is also essential for a successful inversion. Damping affects the rate of convergence of the model parameters with number of iterations, their overall amplitude and scatter (for details see Munzarová *et al.* 2018). In the case of azimuth and inclination of the symmetry axis, well-tuned damping factors are essential for stability of the inversion because of non-linearity between the angles and the anisotropic velocity (eq. 1). Perturbations of each of the four anisotropic parameters, that is isotropic component of velocity, strength of anisotropy, azimuth and inclination of the symmetry axis, have their own value of damping in AniTomo, of course, with a different physical meaning. In the case of LAPNET data, we choose value of 3 for damping of the perturbations of isotropic component of the velocity according to the trade-off curve evaluated from the purely isotropic inversions (Fig. 4). We achieve a good compromise between prediction error and solution length and physically reasonable amplitudes of the velocity perturbations for that damping within three iterations. For

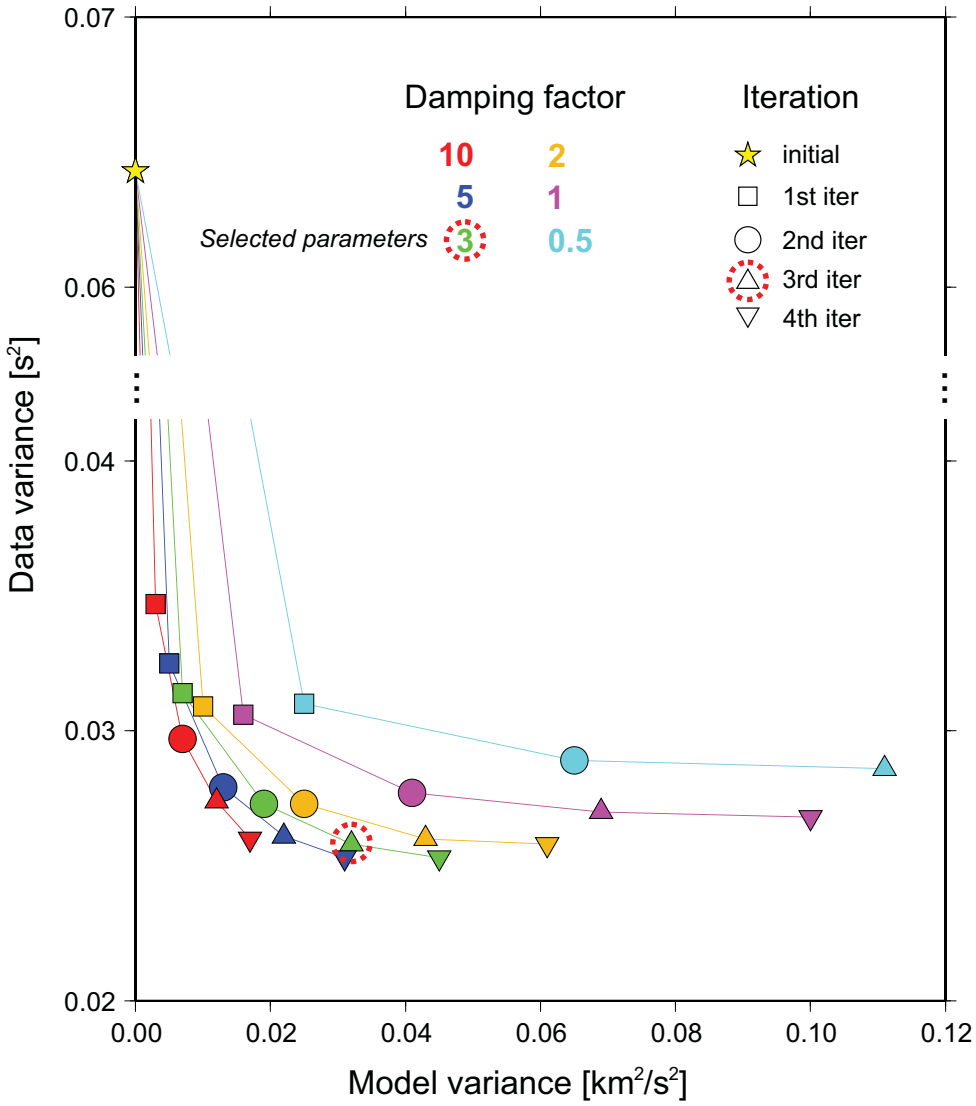

Figure 4. Data and model variance trade-off curve evaluated for various values of damping of the isotropic-velocity perturbations and numbers of iterations from purely isotropic inversions.

damping of perturbations of strength of anisotropy, and perturbations of azimuth and inclination of the symmetry axis, we select 100, 0.1 and 0.5, respectively, after testing various values on synthetic data. These values were chosen already for the series of methodological synthetic tests (Munzarová *et al.* 2018) and they seem to be appropriate also in the case of LAPNET ray geometry. They lead very well to smoothly converging model parameters with limited scatter.

3.3 Anisotropic inversion—initial models and visualization of the results

If the parameters controlling the inversion are well tuned, then purely isotropic-velocity modelling is a single run, including several iterations. On the other hand, evaluation of anisotropy with symmetry axes oriented generally in 3-D consists of a series of single anisotropic inversions that differ in the initial orientation of the symmetry axis (Munzarová *et al.* 2018). This is due to sensitivity of the output anisotropic model to angular deviation between orientation of the symmetry axis of the initial and the target models. In the case of relatively small deviation between the axes (<∼60°), regardless of *a* and *b* model types, the symmetry axis returned by the inversion converges to the correct orientation and the strength of anisotropy increases. But, if the initial axis orientation is approximately perpendicular to the target one, the solution converges to an anisotropic model with the other type of hexagonal symmetry and with the axis approximately perpendicular to the correct orientation. Despite the misinterpretation of the type of hexagonal symmetry, the directions of relatively high and low velocities are well captured when the anisotropy has inclined symmetry axes (Fig. 5a). Based on previous studies of anisotropy with the use of single station method (e.g. Babuška *et al.* 1993; Babuška & Plomerová 2006; Plomerová & Babuška 2010 Plomerová *et al.* 2012), we consider both the *a*-axis and *b*-axis models to approximate the continental mantle lithosphere structure. Discrimination between the models with the high-velocity *a* lineation, and models with the low-velocity *b*-axis

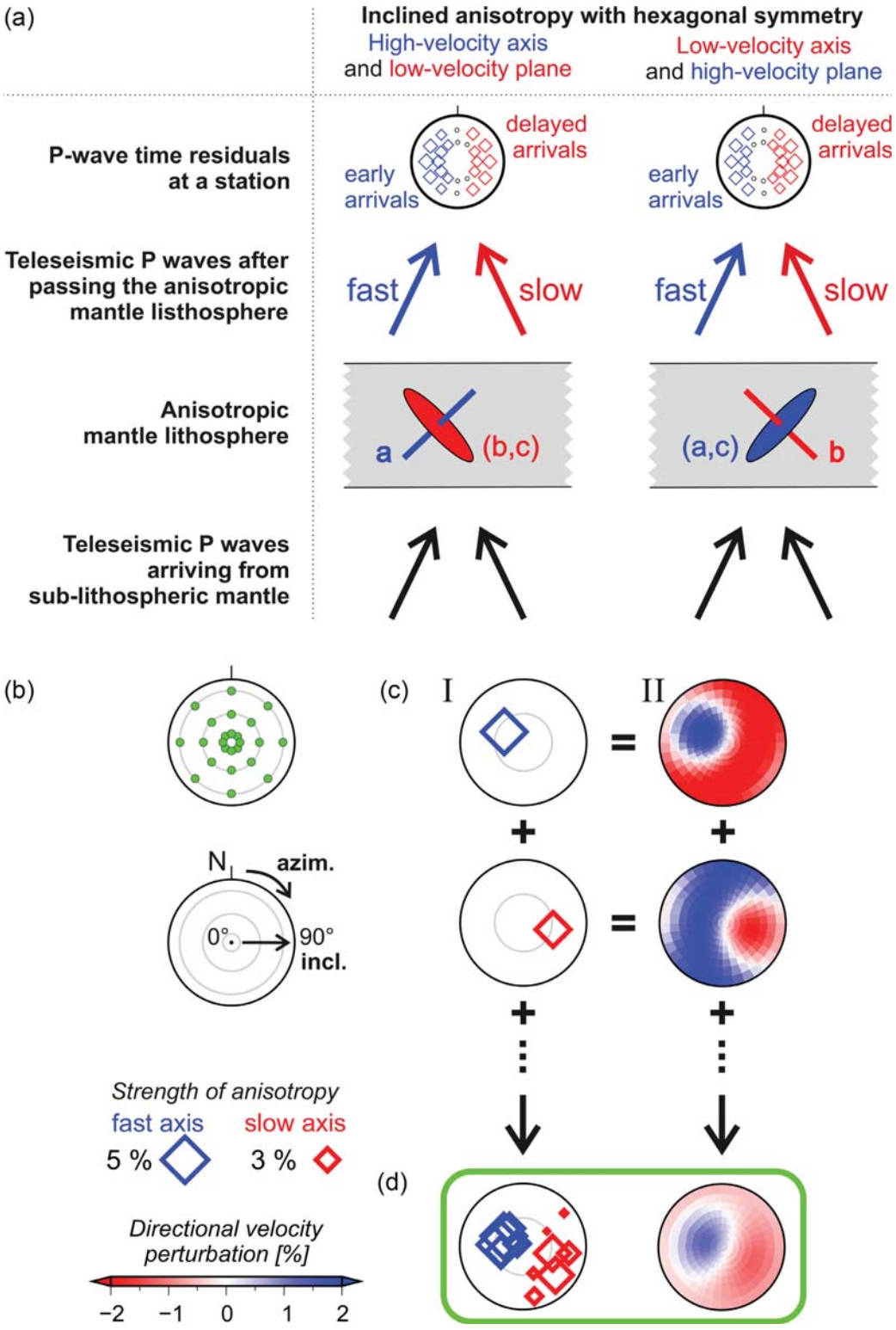

Figure 5. (a) A scheme illustrating influence of anisotropy with inclined symmetry axes on velocity of steeply propagating teleseismic *P* waves. The large-scale anisotropy of a mantle–lithospheric domain is approximated by models with hexagonal symmetry either with the high-velocity *a* axis and the low-velocity (*b*,*c*) plane (lineation), or, with the low-velocity *b*-axis and the high-velocity (*a*,*c*) plane (foliation). The *P*-sphere patterns evaluated for these two types of anisotropy illustrate directional variations of traveltime residuals relative to an isotropic background. (b) A set of 24 initial orientations of symmetry axis displayed in the lower-hemisphere stereographic projection. Azimuth (azim.) covers the 360° range with a step of 45°, while inclination (incl.) acquires values of 10°, 45° and 80°. (c) Two ways of visualization of an individual solution of anisotropy at a parametrization node, i.e. displaying either orientation of its hexagonal-symmetry axis and strength of anisotropy with a single point (I) or its directional distribution of relatively high and low *P*-wave velocities (II). (d) Plotting the individual solutions jointly (I) or averaging their velocity contributions for every direction (II), a final output model of anisotropy is constructed for each node.

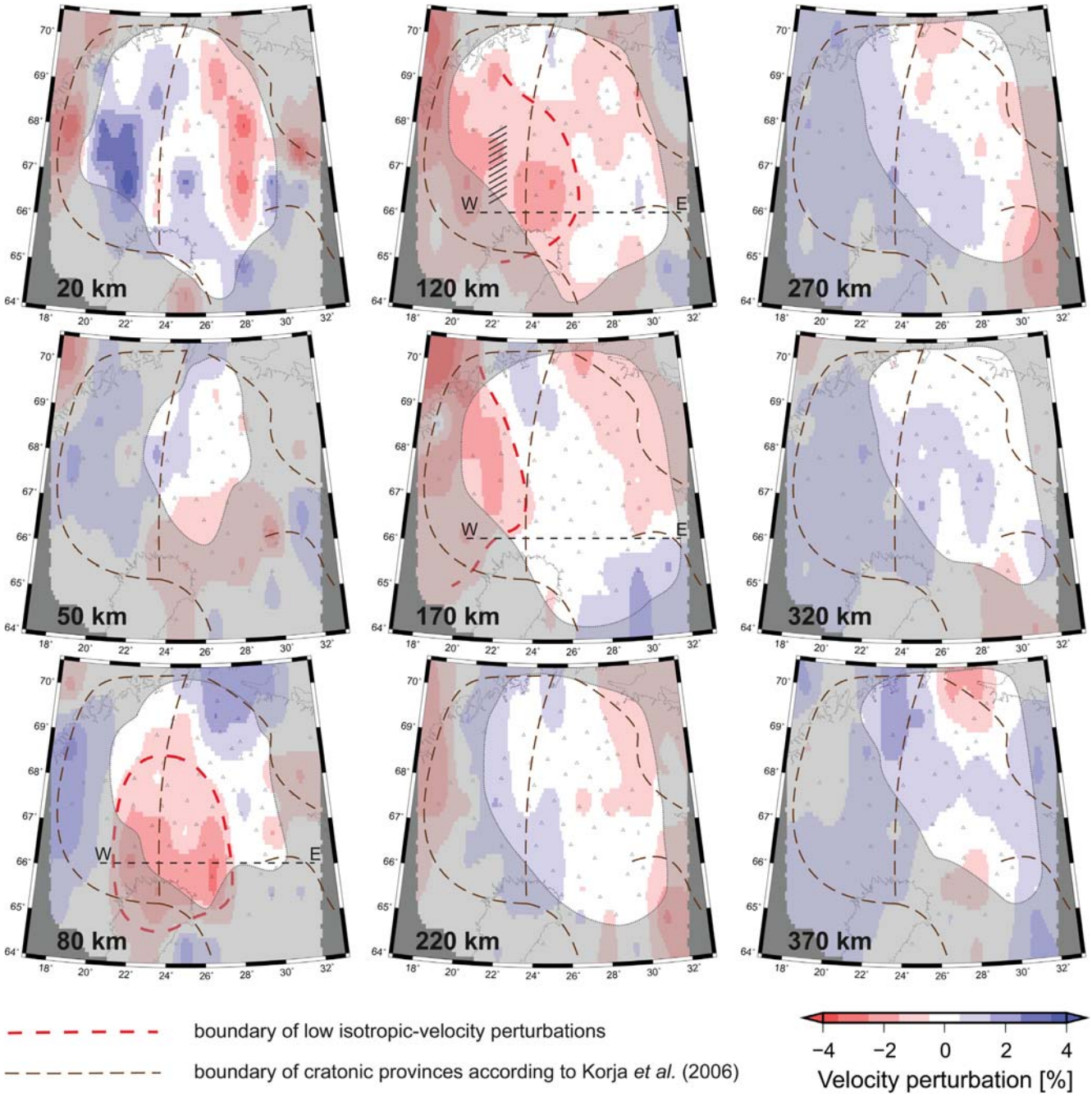

Figure 6. Perturbations of the isotropic velocity calculated as average values of the isotropic-velocity perturbations resulting from the series of the coupled anisotropic–isotropic inversions. See Fig. S11 for a vertical section along the AB profile and Figs R2 and S4 for the anisotropic part of the tomographic model. Part of the model with RDE < 0.5 is shaded. Red dashed line limits the relatively low-velocity perturbations that dominate western and southwestern parts of the model at depths of 80, 120 and 170 km. The hatched area marks a zone of weaker anisotropy and velocity perturbations within Region III at depth of 120 km. The brown dashed curves show boundaries of cratonic provinces after Korja *et al.* (2006); see also Fig. 1. Triangles represent seismic stations of experiment LAPNET together with the nearby permanent stations.

and high-velocity (*a,c*) foliation is in general subtle for the teleseismic *P* waves only. Additional information from independent data, for example shear-wave splitting parameters can help to differentiate between the two types of hexagonal symmetry (e.g. Plomerová *et al.* 2011).

To assure that the anisotropic tomography results in a correct unbiased model, we need to systematically cover the full range of initial orientations of the symmetry axis (Fig. 5b). Therefore, we repeat the inversion 24 times with gridded initial azimuth and inclination within the volume studied. The initial azimuth changes with a step of 45° and the inclination subsequently acquires values of 10°, 45° and 80°. We prefer a successive calculation of eight inversions for the subvertical initial orientations, that is for the inclination of 10° and the different azimuths, to just one inversion with a vertical initial orientation of the symmetry axis. The reason is that despite setting the initial inclination to 0°, the initial azimuth has to be defined as well and its value affects the solution. The initial strength of anisotropy is always 0.1 per cent, the initial 1-D

reference isotropic-velocity model is IASP'91 (Kennett & Engdahl 1991) and all the inversions consist of three iterations. After the calculations, we average the solutions of the eight inversions with a subvertical initial orientation of the axis. Then, we combine the 16 + 1 individual solutions at every parametrization node to obtain the final model, which maps the relatively high- and low-velocity directions of the parametrization cells.

The isotropic part of the final model is evaluated at each node as an average of the velocity perturbations resulting from the series of anisotropic inversions and it is displayed as a background, for example in Figs 6 and 7. Visualization of the anisotropic part of the solution, that is strength of anisotropy together with orientation of the symmetry axis, is more complicated. We either show all the 17 individual solutions for each node (left column in Figs 5c and d), or we calculate directional distribution of relatively high and low velocities by averaging the 17 individual solutions (right column in Figs 5c and d).

3.4 Directional analysis of relative *P*-wave traveltime residuals

The main goal of this paper is to apply AniTomo to real data and to compare the results with independently derived velocity structure of the upper mantle. Plomerová *et al.* (2011) modelled the path-integrated anisotropic structure of the mantle lithosphere of northern Fennoscandia from the LAPNET data. We have reprocessed the LAPNET data set, extended it to the west, and complemented it in the north (Section 2). We evaluate the *P*-residual spheres showing the directional terms of the relative *P*-wave traveltime residuals in the lower-hemisphere stereographic projection. The directional terms at a station express azimuth-incidence angle dependent parts of the relative residuals. We calculate the directional terms from the relative residuals by subtracting the station directional mean, which represents an average velocity beneath the station. To minimize effects of an uneven distribution of the events on the directional mean, we bin the relative residuals by azimuths and incidence angles. Distribution of the negative and positive terms in the *P* spheres, that is early and delayed wave arrivals relatively to a station average (directional mean), exhibits characteristic patterns, from which we can derive the low- and high-velocity directions beneath the stations. The *P*-sphere pattern allows us to derive path-integrated anisotropy beneath each station, while anisotropic tomography (AniTomo) retrieves anisotropy in the individual grid nodes. The stations with a similar pattern of the *P* spheres often cluster and delimit regions of a homogeneous anisotropy, related to large-scale tectonic units. For details of the method, we refer to, for example Babuška & Plomerová (1992, 2006). To verify results of the anisotropic tomography, we also calculate synthetic *P* spheres from synthetic traveltimes evaluated for the final anisotropic model retrieved by the coupled anisotropic–isotropic code.

4 RESULTS

4.1 Anisotropic tomographic model of the upper mantle beneath northern Fennoscandia

We present the final tomographic model of the anisotropic *P*-wave velocity of the upper mantle beneath northern Fennoscandia in two figures. Fig. 6 shows perturbations of the isotropic component of the anisotropic velocity (for simplicity referred further as velocity perturbations) at all depths and Fig. 7 shows the complete solution of the anisotropic inversion at the 80, 120 and 170 km depth layers (see Fig. S4 for all the depth layers). We present the 3-D distribution of relatively high and low velocities averaged over all the individual solutions in each node (Fig. 7, on the left). The stereographic projection on the lower hemisphere makes possible to properly show the resulting 3-D distribution of relatively high- (blue) and low-velocity (red) directions at each grid node. The plots on the right (Fig. 7) show only regions of relatively uniform anisotropy and the characteristic *P*-sphere patterns. The whole set of the individual solutions is imaged in Fig. S4 on the left.

The shallowest layer of the model at the 20 km depth, where only isotropic-velocity perturbations are searched for, is characterized by a great variability of the velocity perturbations with amplitudes larger than 3 per cent (Fig. 6). The crust, of course, cannot be resolved well by the teleseismic tomography, but this layer absorbs heterogeneities of the thick Fennoscandian crust that are not completely compensated by the model of Moho depths used for *a priori* corrections of the travel times (Section 2). When we fix the 20 km depth and run the inversion from 50 km depth (not presented in this paper), the highly variable distribution of the isotropic-velocity perturbations occurs at the 50 km depth. The perturbations at the 50 km depth are similar to those imaged in the 20 km depth when the inversion at 20 km is allowed. This implies that allowing the inversion only from 50 km downward, the perturbations from the shallower crust are mapped into the 50 km depth of the model. When the isotropic-velocity inversion is allowed already at 20 km depth, the amplitudes of the velocity perturbations decrease at the 50 km depth to about 1 per cent, confirming thus separation of the remaining uncorrected crustal structures from the upper mantle. The two models (isotropic inversion allowed at 20 km and no inversion at 20 km) do not differ in the upper mantle from depth of 80 km downwards. At depths of 80 and 120 km, the amplitudes increase to 2 per cent. The strength of anisotropy reaches more than 3 per cent on average per layer down to 170 km. The layers at 80 and 120 km exhibit the strongest anisotropy that can be found in the model (Figs 7 and S4).

The mantle layers at depths of 80–170 km permit a detailed exploration of the results of the anisotropic inversion (Figs 6 and 7), which allows us to delimit regions of consistent anisotropy. For easier orientation, we mark these regions in each layer with numbers I–VI. Negative velocity perturbations of –2 per cent prevail in the western part of these depth layers and they shift towards the west with increasing depth. Strength of anisotropy is 3–4 per cent there and, particularly at depths of 120 and 170 km (Region III), directions of the relatively low velocities dip to the west or northwest, in general. The relatively high velocities lie approximately in a plane steeply dipping to the east or southeast. A sudden change of the anisotropic parameters sharply delimits the eastern boundary of the western region. Region III seems to be split into two subregions at a depth of 120 km by a zone of weaker anisotropy and velocity perturbations (hatched area in Figs 6, 7, S4 and S5). The part of Region III located eastward of this zone might be related to Region IV, delimited at the 80 km depth (Fig. 7a), in which the high-velocity directions dipping to the northeast prevail.

The northeastern part of the volume exhibits a laterally uniform, but depth dependent anisotropy with strength of about 3 per cent (Regions I and II, marked with orange in Figs 7 and S4). At the 50 and 80 km depths, the directions of relatively high velocities tend to dip to the north and the directions of relatively low velocities are perpendicular (Region I), while the anisotropic pattern is different at the 120 and 170 km depths. The directions of relatively low velocities dip to the northeast and the directions of relatively

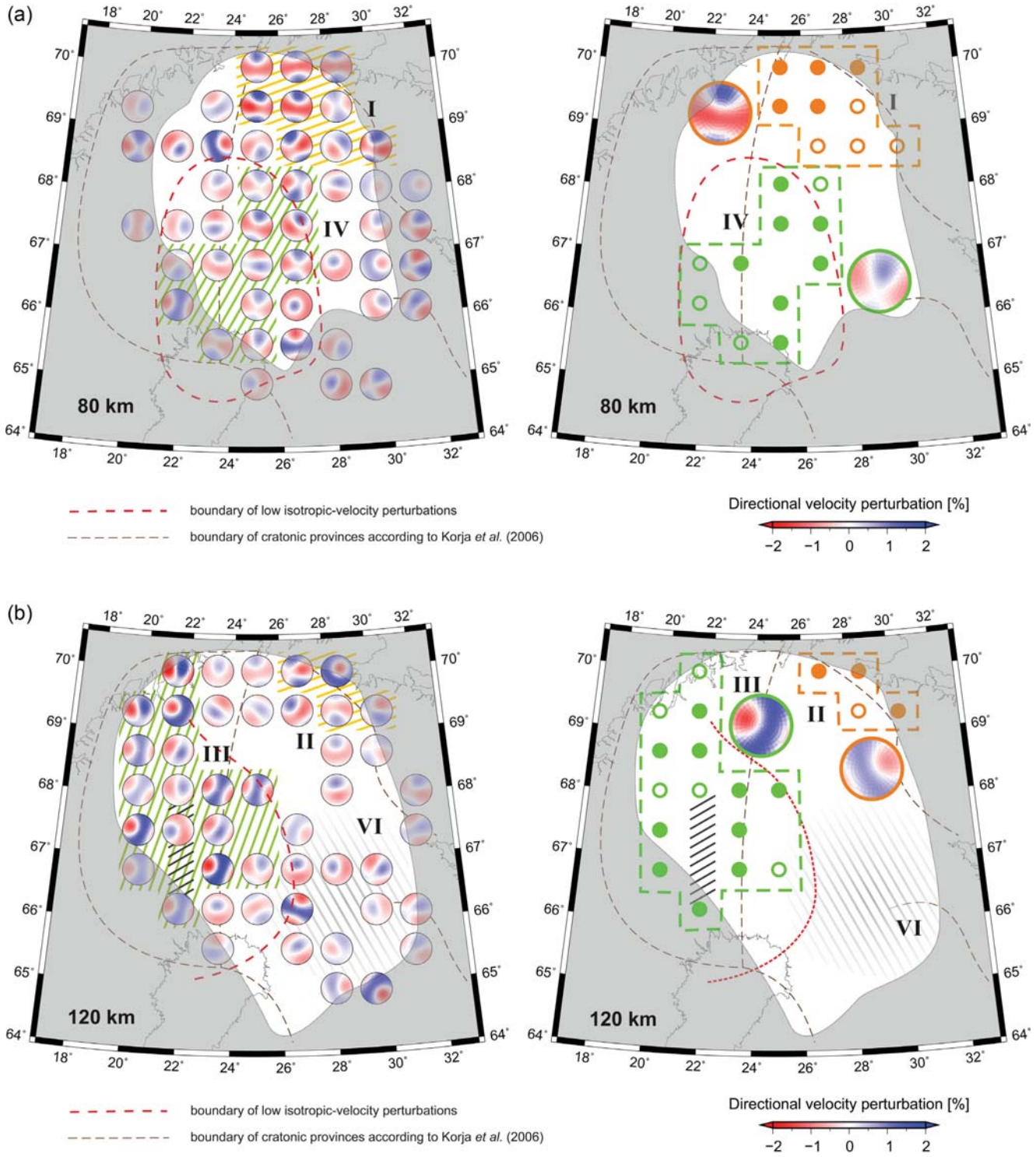

Figure 7. Anisotropic component of *P*-wave velocities at three selected depth layers (see Fig. S4 for all the depth layers). For each grid node we present the anisotropic velocities averaged from the set of individual solutions (left, see Fig. 5 for details). The anisotropic models are shown only for those nodes, for which at least eight individual solutions exhibit strength of anisotropy larger than 1 per cent. Nodes with a similar anisotropic pattern are marked as Regions I–V. A large region with no anisotropy at depth of 120 km is marked as Region VI. The black hatched area locates a zone of weaker anisotropy and velocity perturbations within Region III at depth of 120 km. The typical anisotropic patterns for Regions I–V are shown on the right (see Fig. 5 for details on visualization). Full circles mark nodes, in which the anisotropic pattern matches the typical pattern, while the empty circles mark nodes with only a tendency to the typical pattern. Red dashed curve contours the region with relatively low isotropic-velocity perturbations dominating the model. Part of the model with RDE < 0.5 is shaded. The brown dashed curves show boundaries of cratonic provinces after Korja *et al.* (2006); see also Fig. 1.

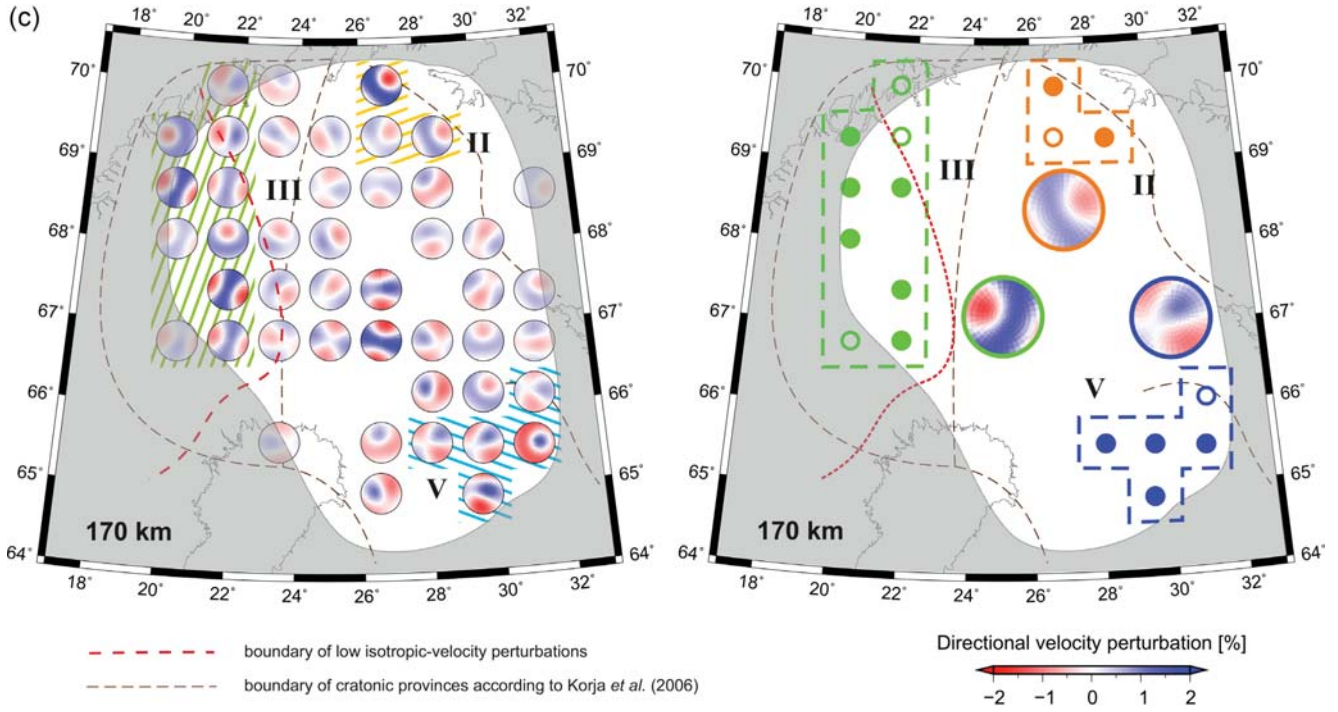

Figure 7. Continued.

high-velocities prevail in a plane dipping to the southwest (Region II).

The very southeastern part of the 170 km depth layer shows positive-velocity perturbations and directions of relatively high velocity dipping towards the northeast (Region V; marked with blue in Figs 7 and S4). The anisotropy retrieved in Region V coincides well with the path-integrated pattern of anisotropy modelled by Plomerová *et al.* (2006, 2011) and it will be discussed later. It is difficult to judge about anisotropy of Region V in shallower depths, where the parameters are not resolved reliably.

The model contains also zones of mostly weak and variable anisotropy among the regions with a consistent anisotropy (e.g. Region VI in Fig. 7b). Single-cell anisotropic patterns occur in these zones. A fragmented anisotropic pattern prevails at the 220 and 270 km depths (Fig. S4). The velocity perturbations below 1 per cent prevail at the depths from 220 km down to 370 km (Fig. 6).

Regarding a consistency among the models of the velocity perturbations coming out from the set of 24 anisotropic inversions, their standard deviation is lower than 1 per cent at all the grid nodes and it is even lower than 0.5 per cent in majority of the nodes (Fig. S6). Such a variation of the individual solutions is reasonably low in terms of teleseismic traveltime tomography and it implies robustness of the average values as well (e.g. Fig. 6). Standard deviations of the velocity perturbations for the LAPNET data set are comparable with those resulting from various synthetic inversions presented in Section 4.2. Focusing on the anisotropic part of the model (the strength of anisotropy and orientation of the high- and low-velocity directions), one can see that the distribution of the individual solutions creates a systematic pattern at each grid node (Fig. S4 on the left). This confirms that the task is well determined and the solution is stable.

To support the results of the anisotropic inversion we compare images of the velocity perturbations from the set of anisotropic inversions (Fig. 6) with those from the purely isotropic inversion (Fig. S5). Distributions of velocity perturbations from both types of the inversion are almost the same. The only difference is that the amplitudes of the velocity perturbations from the isotropic inversion are larger by about 0.2 per cent, on average, than those from the anisotropic inversions, indicating some leakage of velocity perturbations due to the neglected anisotropy in the isotropic images. The leakage is, however, very low and within the resolution limits of the teleseismic tomography, in which steep rays prevail. The resemblance of the velocity perturbations resulting from the purely isotropic inversion and the isotropic part of the anisotropic-velocity model confirms the reliable separation of the isotropic and anisotropic components of the final model.

Reduction of data variance, that is (initial variance—final variance)/initial variance, is 60 per cent for the isotropic-velocity inversion. Evaluation of variance reduction for the coupled anisotropic–isotropic inversion (Figs 7 and S4) is not as straightforward as in the isotropic case, because we can calculate this measure just for each inversion of the set of anisotropic inversions. For the individual anisotropic inversions, the data variance reduction attains values from 61 to 67 per cent, which is not a significantly better fit to the *P*-wave data compared to the fit of the purely isotropic inversion. Nevertheless, the solutions of the individual anisotropic inversions are affected by the initial orientation of the symmetry axis (Section 3.3) and thus, the fit of a single solution cannot be indeed a representative for the whole coupled anisotropic–isotropic model (Figs 6, 7 and S4). Note that the comparison of absolute RMS or variance reduction is a poor measure of the quality of the anisotropic results since the two inverse problems (purely isotropic and anisotropic) are significantly and systematically different. By principle it remains unclear how much of the purely isotropic solution is due to leakage from the ignored anisotropy and for the fully anisotropic solution it needs to be tested how well the parameter separation is working. In our case, the synthetic tests (see also Munzarová *et al.* 2018, and Section 4.2) showed that the coupled inversion of purely isotropic input does not create any artificial anisotropy.

4.2 Synthetic tests

We have designed various synthetic tests to explore capabilities of the LAPNET station-event distribution to resolve laterally and vertically variable heterogeneous anisotropic structure in the upper mantle, sharpness of boundaries, smearing of the input structures and, of course, a trade-off between anisotropy and lateral variations of isotropic velocity. The first synthetic model consists of three blocks with different isotropic components of velocity and anisotropy at depths of 80, 120 and 170 km to mimic a domain-like anisotropic structure in the mantle lithosphere (Figs 8 and S7). One of the blocks is purely isotropic, while the other two exhibit 5 per cent anisotropy with different orientations of the symmetry axes. Amplitude of the velocity perturbations is 3 per cent. We calculate traveltime residuals of *P* waves propagating through the input model with respect to the IASP'91 reference model, considering the ray geometry of the LAPNET data set. Gaussian errors with standard deviation of 0.05 s are added to the calculated traveltimes mimicking the observation errors. For all synthetic tests, the inversion setup and setting of the control parameters is the same as for the inversion of the real data.

The block structure is qualitatively well recovered at the depths of 80, 120 and 170 km, where the synthetic input is assigned (Fig. S7). Nevertheless, the amplitudes of the velocity perturbations and the strength of anisotropy are underestimated at these depths in the retrieved model. The structure is smeared along the ray paths and it leaks to the shallower and deeper parts of the model, which is a typical drawback of any teleseismic tomography. Although the input parameters are homogeneous within each block, the output model parameters tend to vary among the individual nodes, but they correctly capture the general characteristics of the velocity perturbations and the relatively high- or low-velocity directions.

Fig. S8 presents resulting models at the 120 km depth for a set of synthetic tests that always follow the three-block structure (see Fig. S7), but with different isotropic components, as well as with different anisotropic parameters within the blocks. Despite various isotropic and anisotropic velocities of the individual blocks, sharp vertical boundaries between the blocks are well recovered. If the input is purely isotropic (Fig. S8c), no significant artificial anisotropy is generated in the output model. Similarly for the purely anisotropic input structures (Figs S8d–f), false weak velocity perturbations of only ∼1 per cent could appear. The synthetic test in S8f documents that a similarity between an orientation of dominating ray path directions and an orientation of the symmetry axes of anisotropy can create false velocity heterogeneities. This is the case of the northeastern block, where the high-velocity directions dip towards the northeast, that is the azimuths, from which more waves arrive to the northeastern block compared to other azimuths. On the other hand, this is not the case of the northwestern block in the test in Fig. S8e.

We can find an effect similar to the generally observed feature called 'overswinging' of velocity perturbations around strong heterogeneities in the isotropic teleseismic tomography also for the anisotropic parameters in the anisotropic inversion. For example, in the northeastern block, where no anisotropy is prescribed (e.g. Figs S8a and b), a weak false anisotropy is created along the boundary with the other blocks. This effect accentuates the existence of a boundary by enhancing the contrast between the different parameters of the neighbouring blocks. The false anisotropy generated in the northeastern block tends to have a reversed distribution of the relatively high and low velocities compared with the anisotropy in the other blocks. The tests with an idealistic synthetic station-event configuration (Munzarová *et al.* 2018) have also shown that localized artefacts with a size of a few cells may appear close to any boundary, that is either boundaries between heterogeneities within the model or close to the edges of the model itself, including the topmost and the deepest layers, where the inversion for anisotropy is allowed. Thus for the purposes of interpretation of the resulting anisotropic parameters, we consider only distinct signatures consistent over relatively large regions.

4.3 Clustering of path-integrated anisotropy according to *P* spheres

To further complement the information about the large-scale anisotropy of the upper mantle in northern Fennoscandia, we analyse the *P*-residual spheres (Section 3.4) calculated from the final anisotropic tomography model (synthetic spheres) and compare them with the spheres derived directly from the observed residuals (observed spheres).

Fig. 9 presents the observed *P* spheres clustered into several regions according to their pattern (see Fig. S9 for *P* spheres at individual stations). The regions exhibit uniform path-integrated anisotropy, in general. The pattern at stations in the northeast (Domains 1 and 2), in the west (Domain 3) and in the southern part (Domain 4) exhibit bipolar *P*-sphere patterns, which mean that the negative and positive directional terms concentrate in the complementary halves of the sphere. Such a pattern of the *P* spheres indicates that the observed anisotropic signal can be explained by anisotropy with plunging symmetry axes. On the contrary, the majority of the stations in the southeast do not show any systematic distribution of the relatively early and delayed arrivals. An exception is *P*-sphere pattern of stations MSF and KU6 at the very edge of the array (Domain 5). This pattern is in agreement with the *P*-sphere pattern observed at the stations deployed south of the LAPNET array during passive seismic experiment SVEKALAPKO (Plomerová *et al.* 2006, 2011). The division into regions is the same as in Plomerová *et al.* (2011), but the extent of Domain 3 in the northwest is larger due to complementing the data set.

The synthetic *P* spheres (Fig. 10) are evaluated from synthetic traveltimes of *P* waves propagating through the anisotropic part of the final model (on the right in Fig. S4). Comparison of the synthetic and the observed *P* spheres shows a large similarity as to their pattern and geographic distribution. On the other hand, absolute values of the synthetic directional terms are generally lower than those of the observed directional terms due to the probable underestimation of the strength of anisotropy in the averaged anisotropic model.

The synthetic *P* spheres at most of the stations located in the west (e.g. station MAS in Fig. 10) fit the pattern of Domain 3, in which the relatively early arrivals for the waves coming from the east dominate. The synthetic patterns are less distinctive than the observed patterns towards the southwest. Domain 1 and Domain 2, identified in the northeast of the array and characterized by relatively delayed arrivals of the waves coming from the east, are also reproduced very well by the synthetics as to their extent and the observed pattern (e.g. stations LP83 and LP65 in Fig. 10). Domain 4, located in the southern part of the array and characterized by relatively early arrivals of the waves coming from the northeast, can be clearly recognized in the synthetics as well (e.g. station LP41 in Fig. 10). The pattern of Domain 5, however, is only partly reproduced in the synthetic *P* spheres, because the domain is at the very edge of the array. Similarly to the observed *P* spheres, no pattern

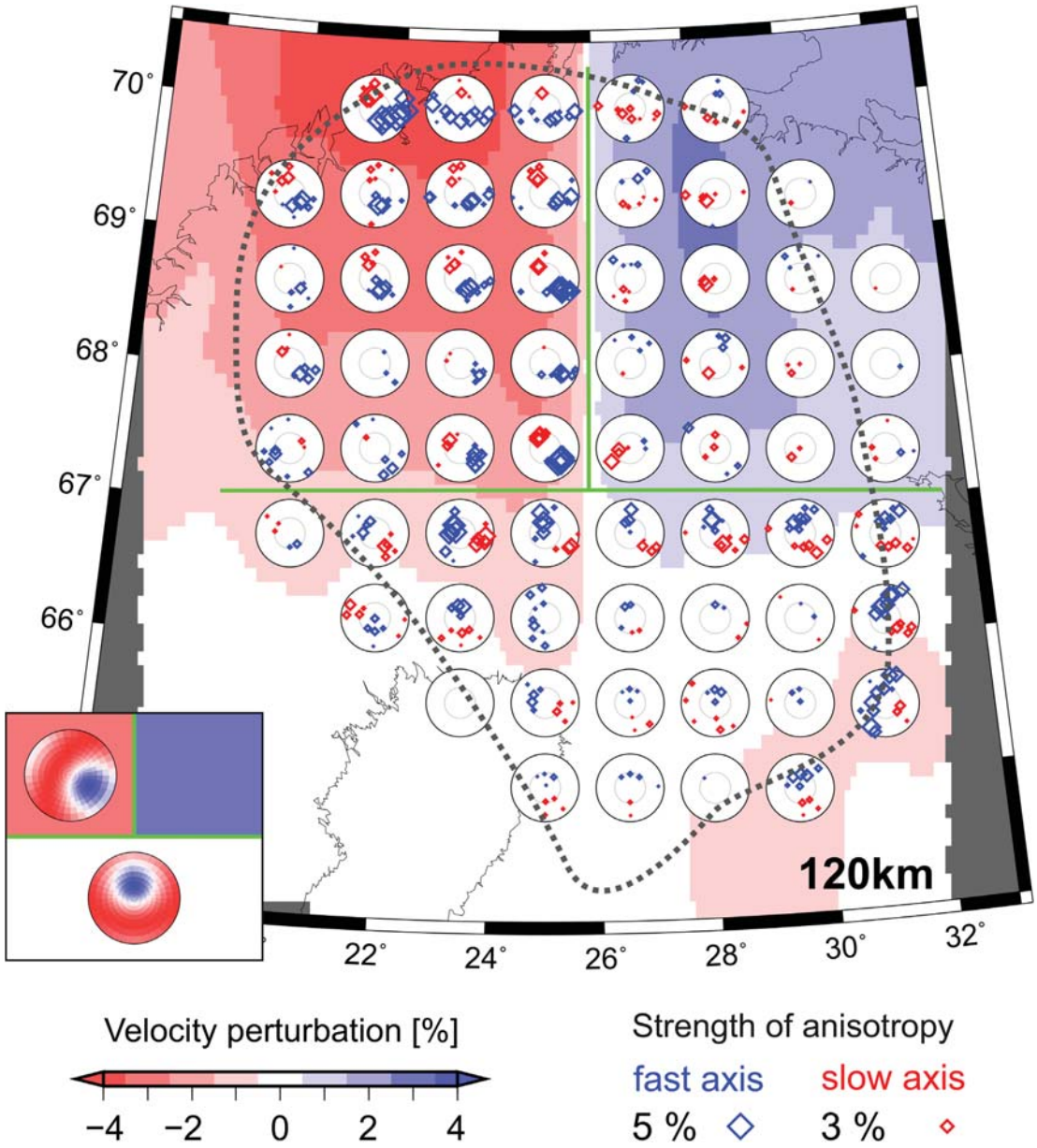

Figure 8. Anisotropic-velocity model at 120 km depth from the synthetic test mimicking a realistic anisotropic structure of the mantle lithosphere (results for all the depth layers are in Fig. S7). The synthetic model consists of three blocks with different isotropic velocities and anisotropy introduced into depths of 80, 120 and 170 km (schematic inset in the lower left-hand corner). Both the northwestern low-velocity and the northeastern high-velocity blocks exhibit 3 per cent amplitude of the isotropic-velocity perturbations relative to the IASP'91 reference model. Strength of anisotropy in the northwestern and in the southern block is 5 per cent. See captions of Figs 7 and 5 for description of plotting the output anisotropic parameters. Dotted black curve marks smoothed contour of RDE equal to 0.5.

prevails in the synthetic *P* spheres in the southeast, where the pattern is indistinctive and laterally variable.

5 DISCUSSION

5.1 Comparison of the anisotropic tomography model with independent inferences on anisotropy in the upper mantle

The AniTomo code is applied for the first time in the region, where anisotropy of the upper mantle has been studied also by different methods. Therefore, we can validate the results of the unique approach of the coupled anisotropic–isotropic tomography with previous results.

Results presented in Section 4 demonstrate the high-degree compatibility between the observed and synthetic *P* spheres, showing the path-integrated anisotropy. The clustering of the two types of *P* spheres according to their patterns is almost identical (Fig. 10), though we compare results from a single-station method, which does not suffer from effects due to model edges, with results from the 3-D anisotropic tomography, in which resolution decreases towards model edges. Moreover, the single-station method, though with limited vertical resolution, is not limited by the grid spacing,

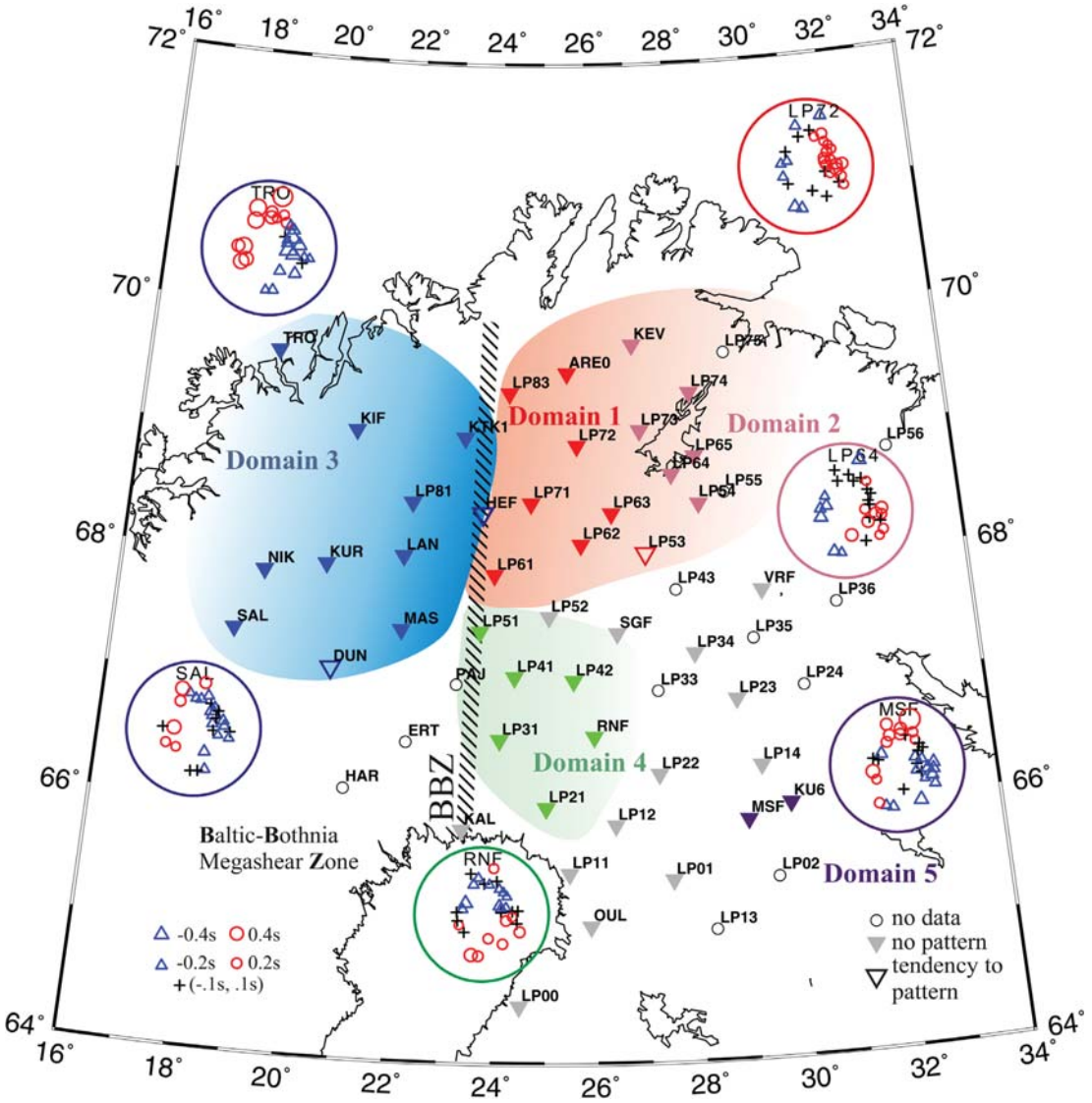

Figure 9. The mantle–lithosphere domains of northern Fennoscandia delimited according to similarity of directional distribution of relatively early and delayed *P*-wave arrival times at the individual stations of the extended LAPNET array (see fig. 2 by Plomerová *et al.* 2011, for the original LAPNET array). Each domain is characterized by a typical *P* sphere showing directional terms of the relative *P*-wave traveltime residuals visualized in the lower-hemisphere stereographic projection. The *P* spheres cover incidence angles from 0° to 50°. Four domains with a distinct bipolar pattern in the west (Domain 3), northeast (Domains 1 and 2) and south (Domain 4) are delimited within the region studied. No distinct *P*-sphere pattern prevails in the southeast, except for the MSF and KU6 stations at the very edge of the array (Domain 5). See Fig. S9 for all the individual observed *P* spheres.

which is in our case 70 km by 70 km, and thus can detect lateral changes on a shorter scale.

Characteristics of the regions with a relatively uniform anisotropy that can be delimited in our tomographic model are compared in Tab. 1 with inferences on the path-integrated anisotropy modelled for individual domains of the mantle lithosphere by inversion of body-wave anisotropic parameters by Plomerová *et al.* (2011) and Vecsey *et al.* (2007). Distribution of the regions with a consistent anisotropy within the mantle lithosphere coming from both methods is in accord, in general, but, the tomographic model provides on top of that a vertical resolution.

Completely independent, though path-integrated as well, information on anisotropic structure of the upper mantle comes from the shear-wave splitting. Therefore, we superimpose the polarization azimuths of the fast split SKS waves (Plomerová *et al.* 2011) on dip directions of the high-velocity lineation or strikes of the dipping high-velocity foliations retrieved within Regions I–V of our final *P*-wave anisotropic velocity model (Fig. 11). In the case of plunging symmetry axis *b*, the fast *S* polarizations vary around the strike of the dipping foliation plane in dependence on the back-azimuth. This leads to a seeming discrepancy between the average fast shear-wave polarization and the dipping high-velocity directions from the *P*-wave anisotropy, especially when the average fast *S* polarizations are associated with the fast velocity directions (see also Plomerová *et al.* 2011). On the other hand, in case of the models with dipping lineation, the fast *S* polarization azimuth and the azimuth of dipping high-velocities from *P*-wave anisotropy coincide. Despite the different wavelengths of the *P* and SKS waves analysed, the high-velocity directions of anisotropy of Regions I–V retrieved by the tomography and the fast-polarization azimuths correlate (Fig. 11). At nodes, where we show strikes of the dipping foliations of anisotropy retrieved by the coupled tomography, the

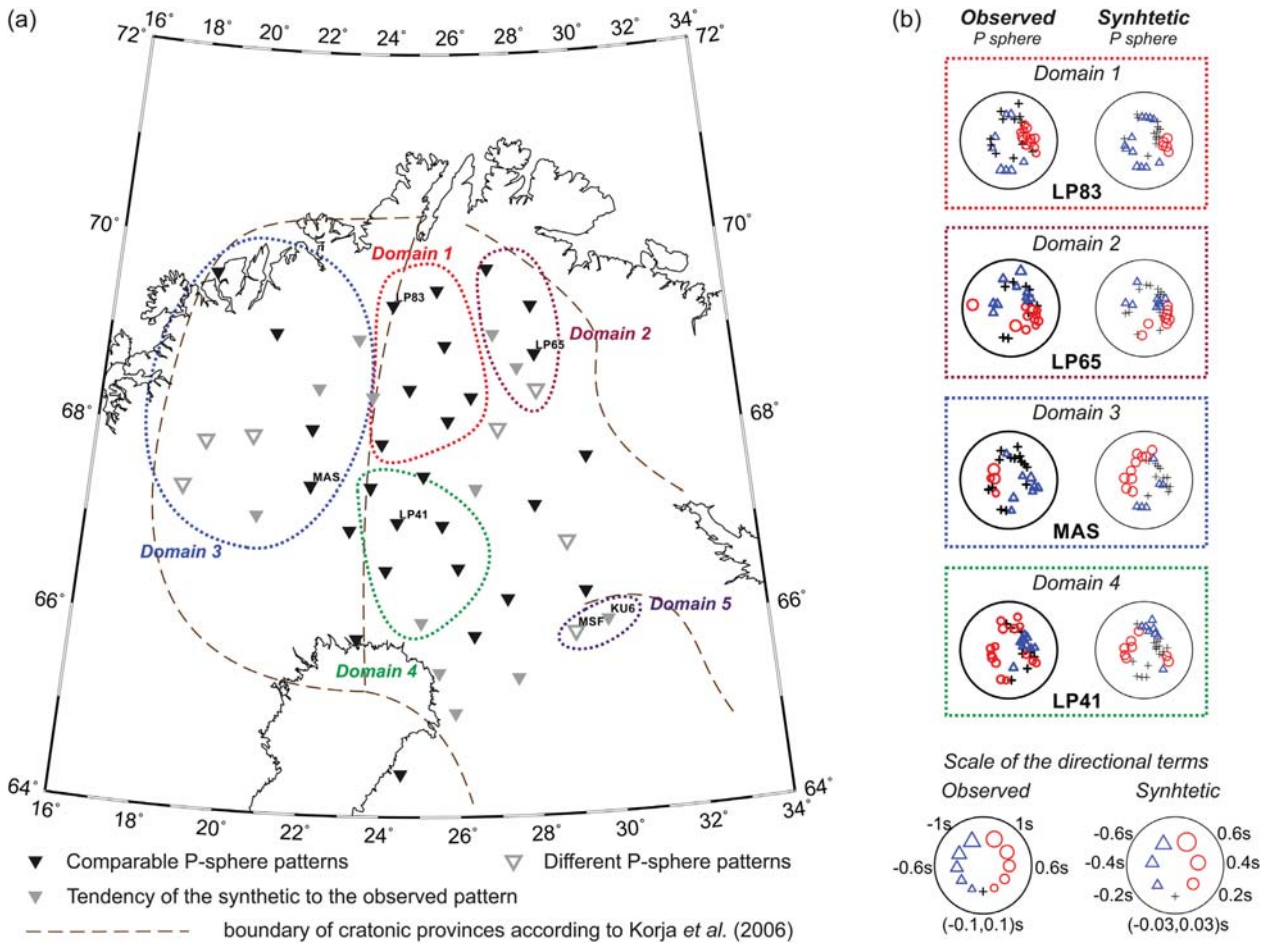

Figure 10. (a) Comparison of the observed *P* spheres (Fig. 9) and those calculated for the anisotropic model from the coupled anisotropic–isotropic tomography (Figs 7 and S4). Dotted curves group stations with a similar observed *P*-sphere pattern. (b) Examples of the synthetic and the observed *P* spheres for Domains 1–4. Stations with a sparse directional distribution of the rays are not considered in the analysis. For details about visualization of directional terms at a station, see caption of Fig. 9.

Table 1. Anisotropic characteristics of regions (left) and domains (right) in the upper mantle beneath northern Fennoscandia resulting from anisotropic tomography (this study, see also Fig. R2) and from a single-station study of path-integrated anisotropy (Plomerová *et al.* 2011).

Anisotropy from *P*-wave tomography (this study)					Path-integrated anisotropy from body-waves (Plomerová *et al.* 2011)					
							P		***P*** **+** ***SKS***	
Region	Axis	θ (°)	λ (°)	Depth (km)	Domain	Axis	θ (°)	λ (°)	θ (°)	λ (°)
I	***a***	**80**	**0**	50, 80	**1**	***b***	25	80	**80**	**80**
II	***b***	**60**	**70**	120, 170	**2**	***b***	30	105	**80**	**105**
III	***b***	**60**	**300**	120, 170	**3**	***b***	60	275	**60**	**280**
IV	***a***	**60**	**30**	80, (120)	**4**	***a***	15	55	**70**	**55**
V	***a***	**60**	**40**	170	∗	***a***	70	60	**60**	**30**
VI	**no consistent anisotropy**			120	**5**		**no P pattern, but SKS splitting**			

∗NW Archean (Vecsey *et al.* 2007).
Angles θ and λ represent inclination (measured from vertical) and, azimuth (measured clockwise from the north) of the hexagonal-symmetry axis.

azimuth of the fast *S* polarizations (evaluated in 3-D) vary along the strikes (e.g. the western part of the region). Whereas, in the north-east, where models with the *a*-axes prevail, the fast *S* polarization azimuths parallel the azimuth of dipping lineation.

Similarly to, for example Plomerová *et al.* (2006, 2011, 2012), Eken *et al.* (2010) and Munzarová *et al.* (2013), we relate the regional variations of the anisotropic velocity structure from the coupled tomography to domains of the mantle lithosphere preserving the fossil fabrics, because at depths below the lithosphere bottom the anisotropy is weak in general. The only discrepancy between the single station analysis of path-integrated anisotropic characteristics of *P* and *S* waves was detected in the southeastern part of the LAPNET array (Plomerová *et al.* 2011), in which *P* waves do not detect any anisotropy (no P pattern; see Figs 9 and S9), whereas the shear waves show significant splitting (see, e.g. Fig. 11). Though the final tomographic model (Fig. S4) shows only very weak and variable anisotropy at depth of 220 km and deeper in general, it localizes some anisotropy at depth of 270 km around 67°–68°N and

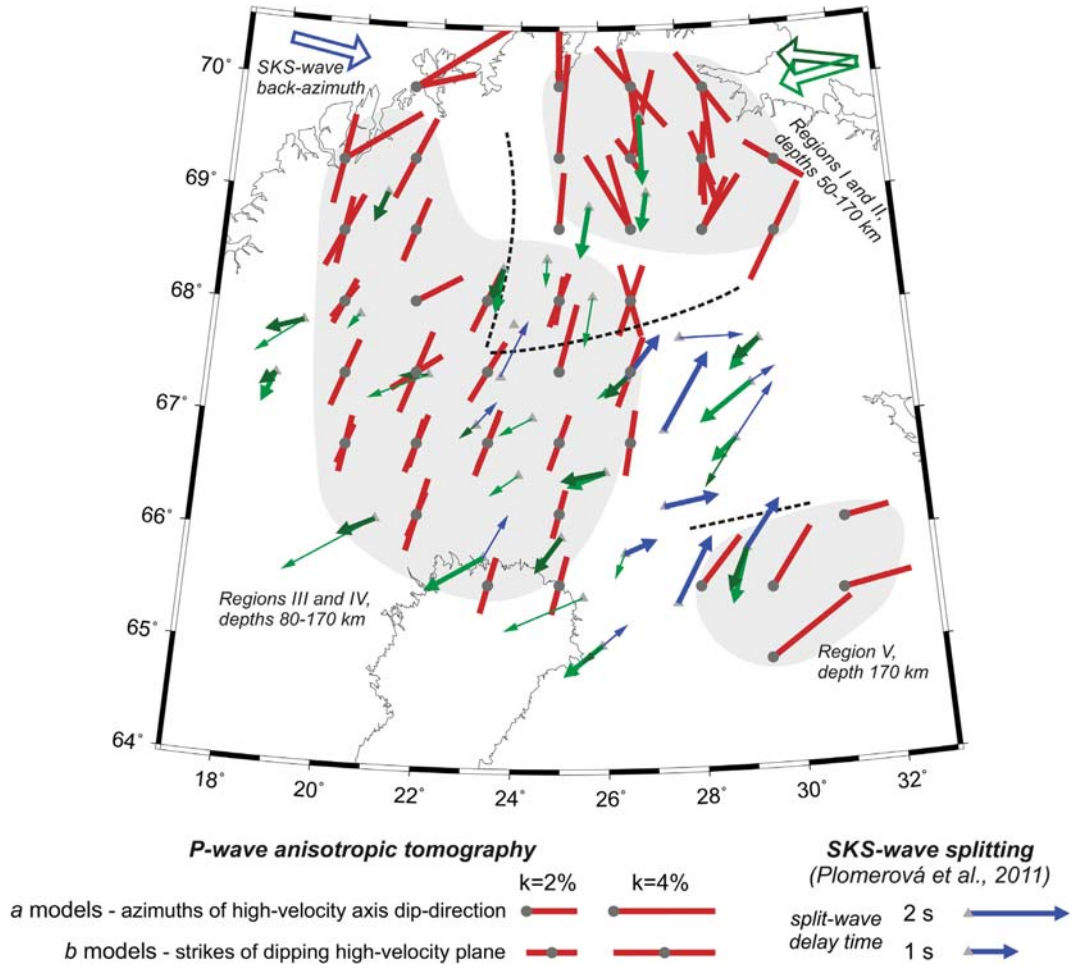

Figure 11. Polarization azimuths of the fast split shear waves evaluated at the LAPNET stations for three teleseismic events (Plomerová *et al.* 2011) plotted together with the azimuths of dip directions of the high-velocity *a*-axis models or the azimuth of strikes of the dipping high-velocity plane for the b models resulting from the *P*-wave coupled anisotropic–isotropic velocity tomography. We plot the anisotropy from the tomography only for Regions I–V jointly for all the depth layers of the model where those regions are located (grey background delimits Regions I–V; see Figs 7 and S4). The line segments representing the *a*-axis azimuths start in the parametrization nodes (coloured crosses), while the line segments marking the strikes of dipping (*a,c*) foliations are centred in the corresponding nodes. Good and firm splitting measurements (thick and thin arrows, respectively) and domain boundaries (black dashed curves) according to Plomerová *et al.* (2011). The azimuths of the fast *S* polarizations (evaluated in 3-D) vary along the strikes of the dipping foliations retrieved by the tomography, or, parallel the dipping lineation and document thus compatibility of the two independent inferences on the upper mantle anisotropy.

26°–29°E (Fig. S4). This region of deep anisotropy correlates with the area of large split delay times and does not have any anisotropic equivalent in the P spheres.

5.2 Comparison of velocity perturbations from anisotropic and isotropic tomography models

For simplicity of the discussion, we denote *P*-wave velocity perturbations retrieved by the coupled anisotropic–isotropic inversion with AniTomo as Model 1 (Fig. 6), those from purely isotropic inversion by AniTomo as Model 2 (Fig. S5) and perturbations from isotropic inversion by Telinv as Model 3 (Silvennoinen *et al.* 2016). The recently published Model 3 for the upper mantle beneath northern Fennoscandia was calculated with standard isotropic inversion code Telinv (Section 3). Silvennoinen *et al.* (2016) evaluated the *P* wave traveltime residuals for the LAPNET network independently. In the south of the region they complemented the data set with measurements from seismic array SVEKALAPKO (e.g. Sandoval *et al.* 2004; Hjelt *et al.* 2006). The velocity perturbations of anisotropic Model 1 and isotropic Model 2, calculated with AniTomo, are almost identical as to distribution of relative perturbations. They both show similar gross features as the isotropic Model 3, particularly at depths of 120 and 170 km (180 km in Model 3 by Silvennoinen *et al.* 2016), where the relatively low-velocity heterogeneity dominates the well-resolved central part of the region. However, in Model 1 and Model 2, the low-velocity heterogeneity shifts towards the west with increasing depth, while in the isotropic Model 3, this heterogeneity splits and surrounds the central unperturbed part of the model.

Compared to anisotropic Model 1, higher amplitudes of the velocity perturbations prevail in the isotropic Model 3 (Silvennoinen *et al.* 2016). However, the amplitudes of the velocity perturbations resulting from teleseismic traveltime tomography are very sensitive to a setup of the inversion (e.g. Foulger *et al.* 2013; Munzarová *et al.* 2018), for example damping factor of velocity perturbations. Model 3 is calculated with a relatively low damping factor and a higher number of iterations compared to the anisotropic Model 1, which both contribute to larger amplitudes of the resulting

velocity perturbations, in general. Lateral variations of the velocity perturbations in Model 1 and Model 2 considerably decrease with depth. At 220 km and deeper , they hardly exceed 2 per cent in the well-resolved parts. On the contrary, in the highly heterogeneous Model 3, the lateral variations of the velocity perturbations reach 7 per cent at almost all the parametrization layers and they do not decrease with depth. It is a general characteristic of teleseismic tomography that unresolved parts of the residuals are mapped into the deepest parts of the models.

Reversed positive and negative perturbations at 80 km depth result from differences in the model parametrizations at shallower depths. The 80 km depth is the first layer, at which the velocity perturbations are searched in Model 3, while in Model 1 and Model 2 we start inverting for velocity at 20 and 50 km depths to accommodate crustal structures uncompensated by the *a priori* assumed model of the Moho (Silvennoinen *et al.* 2014). Therefore, the first layers in Model 1 or Model 2, that is 20 km (Figs 6 and S5), and 80 km in Model 3, resemble each other. The 80 km depth of Model 3 might be biased by the leakage of the shallow structures into greater depths (Karousová *et al.* 2012).

5.3 Trade-off between anisotropy and lateral variations of isotropic velocity

The anisotropic tomographic inversion of *P*-wave traveltime residuals, performed by novel code AniTomo, is a unique approach to study heterogeneous anisotropic structure of the upper mantle. Our work covers also investigation of a potential trade-off between anisotropy and spatial variations of isotropic velocity, which might play a significant role not only in the coupled anisotropic–isotropic tomography, but also in the standard approach of isotropic interpretation of seismic-wave traveltimes. We have performed a large series of synthetic tests of the new code, showing that for a quasi-even realistic distribution of stations and teleseismic events, the upper-mantle anisotropy can be sufficiently separated from lateral variations of the isotropic velocities by the simultaneous inversion (Munzarová *et al.* 2018).

Regarding the LAPNET data set, exhibiting, as any real data set, an unequal distribution of rays, we have carefully studied the resolution capability of its station-event configuration before the inversion. Based on analysis of the ray density tensors (Section 3.2), we allow the fully anisotropic inversion only in a limited volume within the depths layers from 50 km down to 270 km (Fig. 3). Results of the inversions with different settings, that is from purely isotropic to anisotropic ones, the second one with various initial orientations of the symmetry axis, exhibit a stable consistency among the individual anisotropic solutions and a very low variability of the velocity perturbations (Section 4.1).

The results of the extensive series of synthetic tests (Section 4.2) demonstrate that the inversion setup together with the LAPNET ray geometry can detect anisotropic structures of the upper mantle with a limited trade-off between isotropy and anisotropy. Boundaries between various synthetic blocks are recovered reliably in the output models, confirming thus plausibility of, for example westward inclination of the eastern boundary of Region III (Fig. 7). On the other hand, we cannot avoid some undesirable effects that are typical of teleseismic tomography, such as underestimated output amplitudes or vertical smearing of the structures. The resulting amplitudes of the velocity perturbations (up to 2 per cent at 80 and 120 km depths) and the strength of anisotropy (up to 3–4 per cent at 80 and 120 km depths) of the final tomographic model might be considered as the lower limit of the real parameters. We would like to note that the synthetic tests presented in this publication are focused particularly on the mantle lithosphere and the upper mantle beneath relatively stable continental regions without extremal heterogeneities in the mantle, for example subduction zones. The main target of this study is the application of the novel coupled tomography on real data and therefore, we chose Fennoscandia as a representative of such a region. For studies of active regions, for example active subduction zones, which include strongly variable heterogeneities and complex anisotropy in the asthenosphere, further testing of new code AniTomo would be appropriate.

5.4 LAB in northern Fennoscandia

The lithosphere–asthenosphere boundary (LAB) in northern Fennoscandia is modelled mostly at depths of ∼150 km by applying different techniques with the use of the LAPNET array data (Plomerová & Babuška 2010; Pedersen *et al.* 2013; Vinnik *et al.* 2014). The LAB deepens towards southcentral Finland, where the Karelian craton root extends below 200 km (Artemieva 2006; Plomerová *et al.* 2008). Pedersen *et al.* (2013) reveal a decrease of *S*-wave velocity at 150 km depth by inverting the dispersion curve of Rayleigh waves recorded during the LAPNET experiment. Vinnik *et al.* (2016) estimate the depth of LAB at 160 km by analysis of *S* receiver functions. All these results comply well with the decrease of variations of the isotropic velocities accompanied by reduction of the anisotropy at the depth layer of 220 km compared to the 170 km layer of our tomographic model. This can be related to a structural change from lithosphere to asthenosphere at depth around 170 km (Figs 6 and S4). To document that anisotropy potentially located below the 170 km depth can be, in principle, detected by our tomographic setup, we design a synthetic model with two anisotropic blocks lying one above the other (Fig. S10). The results of the synthetic test show that the tomographic inversion is able to resolve correctly a vertically variable anisotropic structure down to 220 km depth. However, if anisotropy with a subhorizontal preferred orientation of the symmetry axis prevails in the asthenosphere, which is modelled, for example by Vinnik *et al.* (2014), it might remain partly undetected by our tomographic inversion because of the limited range of angles of propagation of the teleseismic *P* waves from 20° to 50°.

5.5 The anisotropic tomographic model in light of tectonic settings

The results of anisotropic tomography of the upper mantle beneath northern Fennoscandia presented in this paper are in accord with the domain-like anisotropic structure of the mantle lithosphere inferred from path-integrated anisotropic parameters of *P*- and SKS-waves (Plomerová *et al.* 2011). The anisotropic tomography allows us to follow structural changes in the volume studied not only laterally, but also with depth. The lithosphere of northern Fennoscandia preserves fossil fabrics (e.g. Babuška *et al.* 1993; Plomerová & Babuška 2010) of Archean microplate nuclei assembled during Palaeoproterozoic orogenic processes (e.g. Lahtinen *et al.* 2005; Weihed *et al.* 2005; Korja *et al.* 2006). The individual microplate nuclei are separated by accreted mixtures of island arcs, terranes and mobile belts, such as Inari and Kittilä arcs or Belomorian mobile belt (see Fig. 1b).

In light of the large-scale tectonics, we associate western Region III marked in slices at depth 120 and 170 km (Fig. 7) mostly

with the mantle lithosphere of the Norrbotten craton, accreted to the Karelian and Kola provinces (Fig. 1b). Following the westward shift of the anisotropic pattern as well as the low-velocity perturbations with increasing depth (Figs 6 and 7), Region III seems to thrust over the provinces to the east (Fig. S11). The tomography images the Norrbotten craton down to ∼170 km depth. The low-velocity perturbations within the Norrbotten mantle lithosphere were also modelled by teleseismic *P*-wave isotropic-velocity tomography of the upper mantle below the Swedish national seismological network by Eken *et al.* (2007) and in anisotropy-corrected tomography (Eken *et al*. 2012). The margins of the Norrbotten craton could have undergone modification during the accretion process, but the inherited pre-collisional fabric of the rigid mantle lithosphere survived. Anisotropy in this region is approximated by low-velocity axis *b* plunging towards northwest by both the coupled tomography as well as by inversion of the *P*- and SKS-wave anisotropic parameters (Domain 3 in Table 1; Plomerová *et al.* 2011).

The pattern characteristic for Region III at depth of 120 and 170 km diminishes at depth of 80 km, where we see Region IV above the southeastern part of Region III. It is approximated by anisotropy with the high-velocity symmetry *a* axis dipping towards the northeast (see also model of Domain 4, Table 1). At the 120 km depth, roughly along 22°E latitude, there is a zone of weaker anisotropy and velocity perturbations within Region III (hatched area in Figs 6, 7, S4 and S5). Admitting the existence of such a zone, the subregion located eastward might be related to a potential downward continuation of Region IV. Azimuths of the high-velocity directions due to the fabrics of Regions III and IV are close, though the models of anisotropy differ. The geographical location of the zone of weaker anisotropy roughly correlates with the Baltic-Bothnia megashear Zone at the surface (BBZ; Fig. 1b), a suture zone between the Norrbotten and Karelian cratons. Moreover, the fabric of Region IV, revealed in the coupled tomography, coincides with the fabric of the Karelian domain modelled from the SVEKALAPKO experiment data (Plomerová *et al.* 2006; Vecsey *et al.* 2007).

From the tectonic point of view, the eastern part of the target region is more complex. The complexity of the tomographic model in the northeast probably mirrors deep structure of the various accreted arcs mapped at the surface (Korja *et al.* 2006) and intervening the Kola and Norrbotten cratons (Fig. 1). The coupled tomography images two regions in the northeast. Region II located in the northeast at the 120 and 170 km depths is shifted by ∼100 km northeastward with respect to Region I, which is delimited at the 50 and 80 km depths (Figs 7 and S4). Although we are discussing the very edge of the tomographic model, the results are supported by the path-integrated anisotropy modelled by Plomerová *et al.* (2011), who identified narrow Domain 1 and Domain 2 in the mantle lithosphere (see also Table 1). The anisotropy revealed in Region I differs, at first glance, from path-integrated anisotropy suggested for either Domain 1 or Domain 2 by Plomerová *et al.* (2011). A depth-variable anisotropy, which can be detected in the coupled tomography, can contribute to that. Nevertheless, the similarity of the synthetic and observed *P* spheres (Figs 10 and 11) documents that the 3-D distribution of anisotropy modelled by the coupled tomography in the upper mantle comply with the path-integrated *P*-sphere patterns evaluated for the individual stations.

Southward of the northeastern Region I and Region II, where the Belomorian mobile belt separates the Kola and Karelian cratons, no large-scale regionally consistent anisotropy appears in our tomographic model of *P*-wave anisotropic velocities. Similarly, no anisotropic signal is identified in the observed *P*-spheres (Fig. 9). However, strong splitting of SKS waves was evaluated there (Plomerová *et al.* 2011). If none of the methods employing teleseismic *P* waves detects anisotropic signal, but shear waves split, then the symmetry axis is probably horizontal. Because dipping fabrics prevail in the continental domains of the mantle lithosphere investigated up to now (e.g. Babuška & Plomerová 2006; Plomerová *et al.* 2012), the anisotropic signal detected by the SKS waves probably originates at depths below ∼250 km. These depths assign the anisotropy into the sublithospheric upper mantle, which allows us to relate the anisotropy to the present-day flow in the asthenosphere.

In the very southeastern margin of the model the tomography detects anisotropic signal yet at depth of 170 km. Keeping in mind that resolution of any tomography at its edges is low, we would not rely on the results. However, the anisotropic model with high-velocity *a*-axis plunging to the northeast is identical with the fabric derived from both the LAPNET and the SVEKALAPKO data for the Karelian lithosphere, whose thickness attains about 200–220 km in the southcentral Finland (Plomerová *et al.* 2006; Vecsey *et al.* 2007).

6 CONCLUSIONS

We present a tomographic model of coupled *P*-wave isotropic-velocity perturbations and velocity anisotropy of the upper mantle beneath northern Fennoscandia. The anisotropic tomography is based on our new code AniTomo (Munzarová *et al.* 2018) applied on 3286 relative traveltime residuals of teleseismic *P* waves recorded during passive seismic experiment LAPNET. AniTomo is a novel and unique code considering weak anisotropy with symmetry axes oriented generally in 3-D, that is including axes inclination. The model parameters, iteratively searched at nodes of a 3-D parametrization grid, are perturbations of isotropic component of velocity, strength of anisotropy and orientation of the hexagonal-symmetry axis defined by an azimuth and inclination. After an extensive testing of the code on realistic synthetic data sets and structures (Munzarová *et al.* 2018), we apply the code (this issue) for the first time on a real data recorded in the Archean part of Fennoscandia. We carry out a careful analysis of the ray distribution and document ability of the code to resolve large-scale anisotropic structures in the upper mantle of Fennoscandia by a series of specifically designed synthetic tests.

Images of isotropic component of the anisotropic-velocity perturbations show gross features similar to images of velocity perturbations from the purely isotropic inversion. This means that for the setup of our inversions, there is only a small leakage of anisotropic perturbations into the isotropic model, when anisotropy is neglected. Thus, the isotropic and anisotropic parts of the model resulting from the anisotropic inversion are sufficiently separated.

The largest velocity perturbations and the strongest anisotropy concentrate at depth of 80–170 km, that is in the mantle lithosphere. Below these depths, the lateral velocity variations decrease significantly.

According to the modelled anisotropy, which varies both laterally and vertically, the mantle lithosphere of northern Fennoscandia can be divided into several regions exhibiting consistent fabrics. The delimited regions correlate with the tectonic units and their boundaries often correlate with prominent sutures in the crust. The Baltic-Bothnia megashear Zone, the most significant suture zone in the region, seems to have its imprint in the mantle–lithosphere as well.

We identify mantle lithosphere domain associated withthe Norrbotten craton, characterized by a distinct anisotropy of about 3–4

per cent strength down to ∼170 km depth. A relatively complex depth-varying anisotropy in the northeast of the model likely reflects deep structure of various arcs accreted in between the Kola and Norrbotten cratons. The southeastern part of the tomographic model shows a less consistent large-scale *P*-wave anisotropy. A small region in the very southeast margin exhibits a fabric similar not only to that revealed by single-station methods from the LAPNET data (Plomerová *et al.* 2011), but also to that in the Karelian mantle lithosphere from data of experiment SVEKALAPKO in southcentral Finland (Plomerová *et al.* 2006; Vecsey *et al.* 2007).

Anisotropic tomography retrieves individual regions characterized by consistent, but differently oriented fabrics. The regions are compatible with the domains delimited by joint studies of path-integrated anisotropy from directional analysis of *P*-wave traveltime residuals and SKS-wave splitting parameters (Plomerová *et al.* 2011). We relate the domain-like anisotropic structure to blocks of Archean mantle lithosphere, which probably preserve their original fossil fabrics. The fabrics mostly survived various tectonic events including the lithosphere domain accretion, as well as the Palaeoproterozoic orogenic processes when northern Fennoscandia was formed.

LAPNET WORKING GROUP

Elena Kozlovskaya[1], Helle Pedersen[3], Jaroslava Plomerová[6], Ulrich Achauer[4], Eduard Kissling[7], Irina Sanina[8], Teppo Jämsen[1], Hanna Silvennoinen[1], Catherine Pequegnat[3], Riitta Hurskainen[1], Robert Guiguet[3], Helmut Hausmann[5], Petr Jedlička[6], Igor Aleshin[10], Ekaterina Bourova[3], Reynir Bodvarsson[11], Evald Brückl[10], Tuna Eken[6], Pekka Heikkinen[2], Gregory Houseman[14], Helge Johnsen[12], Elena Kremenetskaya[9], Kari Komminaho[2], Helena Munzarová[12], Roland Roberts[11], Bohuslav Růžek[6], Hossein Shomali[11], Johannes Schweitzer[13], Artem Shaumyan[8], Luděk Vecsey[6], Sergei Volosov[8]

Institutions participating in the creation of the data set

1. Sodankylä Geophysical Observatory of the University of Oulu, Finland
2. Institute of Seismology of the University of Helsinki, Finland
3. University of Grenoble, France
4. University of Strasbourg, France
5. Institute of Geodesy and Geophysics, Vienna University of Technology, Austria
6. Geophysical Institute of the Czech Academy of Sciences, Prague, Czech Republic
7. Institute of Geophysics ETH Zürich, Switzerland
8. Institute of Geospheres Dynamics of the Russian Academy of Sciences, Moscow, Russia
9. The Kola Regional Seismological Centre, of the Russian Academy of Sciences, Russia
10. Geophysical Centre of the Russian Academy of Sciences, Schmidt Institute of Physics of the Earth of the Russian Academy of Sciences, Russia
11. Swedish National Seismological Network, University of Uppsala, Sweden
12. Institute of Solid Earth Physics, University of Bergen, Norway
13. NORSAR, Norway
14. University of Leeds, UK

ACKNOWLEDGEMENTS

The research was supported by grant no. 210/12/2381 of the Grant Agency of the Czech Republic and by project CzechGeo/EPOS-Sci, no. CZ.02.1.01/0.0/0.0/16_013/0001800, financed from the Operational Programme Research, Development and Education within ERDF. We would like to thank to Dr Lapo Boschi for his editorial work and to two anonymous reviewers for their thorough reviews that helped to improve the manuscript. Contributions of all members of the LAPNET Working Group are greatly appreciated. Figures were plotted with the use of the Generic Mapping Tools (Wessel & Smith 1998).

REFERENCES

Arlitt, R., Kissling, E. & Ansorge, J., 1999. Three-dimensional crustal structure beneath the TOR array and effects on teleseismic wavefronts, *Tectonophysics,* **314,** 309–319.

Artemieva, I.M., 2006. Global 1° × 1° thermal model TC1 for the continental lithosphere: implications for lithosphere secular evolution, *Tectonophysics,* **416,** 245–277.

Auer, L., Boschi, L., Becker, T.W., Nissen-Meyer, T. & Giardini, D., 2014. Savani: a variable resolution whole-mantle model of anisotropic shear velocity variations based on multiple data sets, *J. geophys. Res.: Solid Earth,* **119,** 3006–3034.

Babuška, V. & Cara, M., 1991. *Seismic Anisotropy in the Earth,* Kluwer Academic Publishers.

Babuška, V. & Plomerová, J., 1992. The lithosphere in central Europe—seismological and petrological aspects, *Tectonophysics,* **207,** 141–163.

Babuška, V. & Plomerová, J., 2006. European mantle lithosphere assembled from rigid microplates with inherited seismic anisotropy, *Phys. Earth. planet. Inter.* **158,** 264–280.

Babuška, V., Plomerová, J. & Šílený, J., 1993. Models of seismic anisotropy in the deep continental lithosphere, *Phys. Earth. planet. Inter.,* **78,** 167–191.

Bezada, M.J., Faccenda, M. & Toomey, D.R., 2016. Representing anisotropic subduction zones with isotropic velocity models: a characterization of the problem and some steps on a possible path forward, *Geochem. Geophys. Geosyst.,* **17,** 3164–3189.

Chang, S.J., Ferreira, A.M.G., Ritsema, J., van Heist, H.J. & Woodhouse, J.H., 2015. Joint inversion for global isotropic and radially anisotropic mantle structure including crustal thickness perturbations, *J. geophys. Res.,* **120,** 4278–4300.

Chyba, J., Plomerová, J., Vecsey, L. & Munzarová, H., 2017. Tomography study of the upper mantle around the TESZ based on PASSEQ experiment data, *Phys. Earth planet. Inter.,* **266,** 29–38.

Cooper, A.K., Barrett, P.J., Stagg, H., Storey, B., Stump, E. & Wise, W., the 10th ISAES editorial team, eds., 2008. Antarctica: a Keystone in a Changing World. *Proceedings of the 10th International Symposium on Antarctic Earth Sciences,* National Academic Press, Washington, DC.

Debayle, E., Dubuffet, F. & Durand, S., 2016. An automatically updated S-wave model of the upper mantle and the depth extent of azimuthal anisotropy, *Geophys. Res. Lett.,* **43**(2), 674–682.

Eken, T., Shomali, H., Roberts, R. & Bödvarsson, R., 2007. Upper mantle structure of the Baltic Shield below the Swedish National Seismological Network (SNSN) resolved by teleseismic tomography, *Geophys. J. Int.,* **169,** 617–630.

Eken, T., Plomerová, J., Roberts, R., Vecsey, L., Babuška, V., Shomali, H. & Bodvarsson, R., 2010. Seismic anisotropy of the mantle lithosphere beneath the Swedish National Seismological Network (SNSN), *Tectonophysics,* **480,** 241–258.

Eken, T., Plomerová, J., Vecsey, L., Babuška, V., Roberts, R., Shomali, H. & Bodvarsson, R., 2012. Effects of seismic anisotropy on P-velocity of the Baltic Shield, *Geophys. J. Int.,* **188,** 600–612.

Fichtner, A., Kennet, B.L.N., Igel, H. & Bunge, H.P., 2010. Full waveform tomography for radially anisotropic structure: new insights into present and past states of the Australasian upper mantle, *Earth planet. Sci. Lett.,* **290,** 270–280.

Fichtner, A., Saygin, E., Taymaz, T., Cupillard, P., Capdeville, Y. & Trampert, J., 2013. The deep structure of the North Anatolian fault zone, *Earth planet. Sci. Lett.,* **373,** 109–117.

Fouch, M.J. & Rondenay, S., 2006. Seismic anisotropy beneath stable continental interiors, *Phys. Earth planet. Inter.,* **158,** 292–320.

Foulger, G.R. *et al.*, 2013. Caveats on tomographic images, *Terra Nova,* **0,** 1–23.

French, S.W. & Romanowicz, B.A., 2014. Whole-mantle radially anisotropic shear velocity structure from spectral-element waveform tomography, *Geophys. J. Int.,* **199**(3), 1303–1327.

Hammond, W.C. & Toomey, D.R., 2003. Seismic velocity anisotropy and heterogeneity beneath the Mantle Electromagnetic and Tomography Experiment (MELT) region of the East Pacific Rise from analysis of P and S body waves, *J. geophys. Res.,* **108**(B4), 2176.

Hirahara, K. & Ishikawa, Y., 1984. Travel time inversion for three-dimensional P-wave velocity anisotropy, *J. Phys. Earth,* **32,** 197–218.

Hjelt, S.-E., Korja, T., Kozlovskaya, E., Lahti, I. & Yliniemi, J., & BEAR and SVEKALAPKO Working Groups, 2006. Electrical conductivity and seismic velocity structures of the lithosphere beneath the Fennoscandian Shield, in *European Lithosphere Dynamics,* Vol. **32,** pp. 541–559, eds Gee, D. & & Stephenson, R., Geol. Soc. London, Mem. Ser.

Ho, T., Priestley, K. & Debayle, E., 2016. A global horizontal shear velocity model of the upper mantle from multimode Love wave measurements, *Geophys. J. Int.,* **207**(1), 542–561.

Hua, Y., Zhao, D. & Xu, Y., 2017. P wave anisotropic tomography of the Alps, *J. geophys. Res.: Solid Earth,* **122,** 4509–4528.

Ishise, M. & Oda, H., 2005. Three-dimensional structure of P-wave anisotropy beneath the Tohoku district, northeast Japan, *J. geophys. Res.,* **110,** B07304.

Karousová, H., Plomerová, J. & Babuška, V., 2012. A three-dimensional velocity model of the crust of the Bohemian Massif, *Stud. Geophys. Geod.,* **56,** 249–267.

Karousová, H., 2013. Teleseismic tomography of the upper mantle beneath the bohemian massif, *PhD thesis*, Department of Geophysics, Faculty of Mathematics and Physics, Charles University, Prague, Czech Republic.

Karousová, H., Plomerová, J. & Babuška, V., 2013. Upper-mantle structure beneath the southern Bohemian Massif and its surroundings imaged by high-resolution tomography, *Geophys. J. Int.,* **194,** 1203–1215.

Kennett, B. & Engdahl, R., 1991. Travel times for global earthquake location and phase identification, *Geophys. J. Int.,* **105,** 429–465.

Kissling, E., 1988. Geotomography with local earthquake data, *Rev. Geophys.,* **26,** 659–698.

Korja, A., Lahtinen, R. & Nironen, M., 2006. The Svekofennian orogen: a collage of microcontinents and island arcs, in *European Lithosphere Dynamics,* **Vol. 32,** pp. 561–578, eds Gee, D.G. & Stephenson, R.A., Geol. Soc. London, Memoirs.

Kozlovskaya, E., 2007. Seismic network XK: LAPNET/POLENET seismic temporary array (RESIF-SISMOB). RESIF - Réseau Sismologique et géodésique Français.

Kustowski, B., Ekström, G. & Dziewoński, A.M., 2008. Anisotropic shear-wave velocity structure of the Earth's mantle: a global model, *J. geophys. Res.,* **113,** B06306.

Lahtinen, R., Korja, A. & Nironen, M., 2005. Palaeoproterozoic tectonic evolution, in *The Precambrian Geology of Finland—Key to the Evolution of the Fennoscandian Shield,* pp. 418–532, eds Lehtinen, M., Nurmi, P.A. & Rämö, O.T., Elsevier.

Lahtinen, R., Huhmaa, H., Lahayea, Y., Kousa, J. & Luukas, J., 2015. Archean–Proterozoic collision boundary in central Fennoscandia: revisited, *Precambrian Res.,* **261,** 127–165.

Lippitsch, R., Kissling, E. & Ansorge, J., 2003. Upper mantle structure beneath the Alpine orogen from high-resolution teleseismic tomography, *J. geophys. Res.,* **108,** B82376,

Liu, X. & Zhao, D., 2017. P-wave anisotropy, mantle wedge flow and olivine fabrics beneath Japan, *Geophys. J. Int.,* **210,** 1410–1431.

Long, M.D. & Becker, T.W., 2010. Mantle dynamics and seismic anisotropy, *Earth planet. Sci. Lett.,* **297,** 341–354.

Long, M.D. & Silver, P.G., 2009. Shear-wave splitting and mantle anisotropy: measurements, interpretations, and new directions, *Surv. Geophys.,* **30,** 407–461.

Mainprice, D., 2007. Seismic anisotropy of the deep Earth from a mineral and rock physics perspective, in *Treatise on Geophysics,* pp. 437–491, ed Schubert, G., Elsevier.

Maupin, V. & Park, J., 2007. Theory and observations–Wave propagation in anisotropic media, in *Treatise on Geophysics,* Vol. **1**: Seismology and the Structure of the Earth, pp. 289–321, eds Romanowicz, B. & Dziewonski, A., Elsevier.

Menke, W., 1984. *Geophysical Data Analysis: Discrete Inverse Theory,* 1st edn, Academic Press, Inc.

Munzarová, H., Plomerová, J., Babuška, V. & Vecsey, L., 2013. Upper-mantle fabrics beneath the Northern Apennines revealed by seismic anisotropy, *Geochem.Geophys. Geosyst.,* **14,** 1156–1181.

Munzarová, H., , Plomerová, J. & Kissling, E., 2018. Novel anisotropic teleseismic body-wave tomography code AniTomo to illuminate heterogeneous anisotropic upper mantle. Part I - Theory and inversion tuning with realistic synthetic data, *Geophys. J. Int.,* **215,** 524–545, .

Nita, B., Maurya, S. & Montagner, J.P., 2016. Anisotropic tomography of the European lithospheric structure from surface wave studies, *Geochem. Geophys. Geosyst.,* **17,** 2015–2033.

Panning, M. & Romanowicz, B., 2006. A three-dimensional radially anisotropic model of shear velocity in the whole mantle, *Geophys. J. Int.,* **167,** 361–379.

Park, J. & Levin, V., 2002. Seismic anisotropy: Tracing plate dynamics in the mantle, *Science,* **296,** 485–489.

Pedersen, H., Debayle, E. & Maupin, V., the POLENET/LAPNET Working Group, 2013. Strong lateral variations of lithospheric mantle beneath cratons—example from the Baltic Shield, *Earth planet Sci. Lett.,* **383,** 164–172.

Plomerová, J. & Babuška, V., 2010. Long memory of mantle lithosphere fabric-European LAB constrained from seismic anisotropy, *Lithos,* **120,** 131–143.

Plomerová, J., Babuška, V., Kozlovskaya, E., Vecsey, L. & Hyvonen, L.T., 2008. Seismic anisotropy—a key to resolve fabrics of mantle lithosphere of Fennoscandia, *Tectonophysics,* **462,** 125–136.

Plomerová, J., Babuška, V., Vecsey, L., Kozlovskaya, E. & Raita, T., SSTWG, 2006. Proterozoic-Archean boundary in the upper mantle of eastern Fennoscandia as seen by seismic anisotropy, *J. Geodyn.,* **41,** 400–410.

Plomerová, J., Munzarová, H., Vecsey, L., Kissling, E., Achauer, U. & Babuška, V., 2016. Cenozoic volcanism in the Bohemian Massif in the context of P-and S-velocity high-resolution teleseismic tomography of the upper mantle, *Geochem. Geophys. Geosyst.,* **17**(8), 3326–3349.

Plomerová, J., Vecsey, L. & Babuška, V., 2012. Mapping seismic anisotropy of the lithospheric mantle beneath the northern and eastern Bohemian Massif (central Europe), *Tectonophysics,* **564–565,** 38–53.

Plomerová, J., Vecsey, L. & Babuška, V., LAPNET working group, 2011. Domains of Archean mantle lithosphere deciphered by seismic anisotropy—inferences from the LAPNET array in northern Fennoscandia, *Solid Earth,* **2,** 303–313.

Sandoval, S., Kislling, E. & Ansorge, J., SVEKALAPKO Seismic Tomography working Group, 2004. High-resolution body wave tomography beneath the SVEKALAPKO array—II. Anomalous upper mantle structure beneath the central Baltic Shield, *Geophys. J. Int.,* **157,** 200–214.

Savage, M.K., 1999. Seismic anisotropy and mantle deformation: what have we learned from shear wave splitting?, *Rev. Geophys.,* **37,** 65–106.

Shomali, Z.H., Roberts, R.G. & Pedersen, L.B., the TOR Working Group, 2006. Lithospheric structure of the Tornquist Zone resolved by nonlinear P and S teleseismic tomography along the TOR array, *Tectonophysics,* **416,** 133–149.

Šílený, J. & Plomerová, J., 1996. Inversion of shear-wave splitting parameters to retrieve three-dimensional orientation of anisotropy in continental lithosphere, *Phys. Earth planet. Inter.,* **95,** 277–292.

Silvennoinen, H., Kozlovskaya, E. & Kissling, E., 2016. POLENET/LAPNET teleseismic *P* wave travel time tomography model of the upper mantle beneath northern Fennoscandia, *Solid Earth,* **7,** 425–439.

Silvennoinen, H., Kozlovskaya, E., Kissling, E. & Kosarev, G., POLENET/LAPNET working group, 2014. A new Moho boundary map

for northern Fennoscandian shield based on combined controlled-source seismic and receiver function data, *Geophys. Res. J.,* **1/2,** 19–32.

Silver, P.G., 1996. Seismic anisotropy beneath the continents: probing the depths of geology, *Annu. Rev. Earth planet. Sci.,* **24,** 385–432.

Slagstad, T., Balling, N., Elvebakk, H., Midttømme, K., Olesen, O., Olsen, L. & Pascal, C., 2009. Heat-flow measurements in Late Palaeoproterozoic to Permian geological provinces in south and central Norway and a new heat-flow map of Fennoscandia and the Norwegian "Greenland Sea", *Tectonophysics,* **473,** 341–361.

SNSN, 1904. Swedish National Seismic Network. Uppsala University, Uppsala, Sweden. Other/Seismic network.

Snyder, D.B., 2002. Lithospheric growth at margins of cratons, *Tectonophysics,* **355,** 7–22.

Stammler, K., 1993. Seismic handler programmable multichannel data handler for interactive and automatic processing of seismological analyses, *Comput. Geosci.,* **19,** 135–140.

Steck, L.K. & Prothero, W.A., 1991. A 3-D raytracer for teleseismic body-wave arrival times, *Bull. seism. Soc. Am.,* **81,** 1332–1339.

Vecsey, L., Plomerová, J., Kozlovskaya, E. & Babuška, V., 2007. Shear-wave splitting as a diagnostic of varying upper mantle structure beneath south-eastern Fennoscandia, *Tectonophysics,* **438,** 57–77.

Vinnik, L., Kozlovskaya, E., Oreshin, S., Kosarev, G., Piiponen, K. & Silvennoinen, H., 2016. The lithosphere, LAB, LVZ and Lehmann discontinuity under central Fennoscandia from receiver functions, *Tectonophysics,* **667,** 189–198.

Vinnik, L., Oreshin, S., Makeyeva, L. & Kozlovskaya, E., POLENET/LAPNET Working Group, 2014. Anisotropic lithosphere below Fennoscandia from receiver functions and SKS waveforms of POLENET/LAPNET array, *Tectonophysics,* **628,** 45–54.

Wang, J. & Zhao, D., 2013. P-wave tomography for 3-D radial and azimuthal anisotropy of Tohoku and Kyushu subduction zones, *Geophys. J. Int.,* **193,** 1166–1181.

Wessel, P. & Smith, W.H.F., 1998. New, improved version of the generic mapping tools released, *EOS, Trans. Am. Geophys. Un.,* **79,** 579.

Weihed, P., Arndt, N., Billström, K., Duchesne, J.C., Eilu, P., Martinsson, O., Papunen, H. & Lahtinen, R., 2005. 8: Precambrian geodynamics and ore formation: the Fennoscandian Shield, *Ore Geol. Rev.,* **27,** 273–322.

Weiland, C.M., Steck, L.K., Dawson, P.B. & Korneev, V.A., 1995. Nonlinear teleseismic tomography at Long Valley caldera, using three-dimensional minimum travel time ray tracing, *J. geophys. Res.,* **100,** 20379–20390.

Yuan, K. & Beghein, C., 2014. Three-dimensional variations in Love and Rayleigh wave azimuthal anisotropy for the upper 800 km of the mantle, *J. geophys. Res.: Solid Earth,* **119,** 3232–3255.

Zhu, H., Bozdağ, E. & Tromp, J., 2014. Seismic structure of the European upper mantle based on adjoint tomography, *Geophys. J. Int.,* **201,** 18–52.

SUPPORTING INFORMATION

Supplementary data are available at *GJI* online.

Figure S1. Diagonal elements of resolution matrix evaluated according to eq. (4) for the ray geometry of the LAPNET data set and the final parametrization of the volume studied with a denser vertical spacing at the top part. Dotted white curve marks smoothed contour of RDE equal to 0.5. The relatively small area delimited by the 0.5 contour at the 50 km depth is caused by denser vertical grid spacing in this part of the model. Red line delimits a region where inversion for all four anisotropic parameters is allowed, while inversion just for the purely isotropic-velocity perturbations is allowed within volume contoured by black line (see Figs 3 and S3). Triangles represent seismic stations of experiment LAPNET.

Figure S2. Ray paths at the individual depth layers of model parametrization. Dashed black curve marks smoothed contour of RDE equal to 0.5. Red line delimits a region where inversion for all the four anisotropic parameters is allowed, while inversion just for the purely isotropic-velocity perturbations is allowed in a larger region, marked by blue line (see Figs 3 and S3). Triangles represent seismic stations of experiment LAPNET.

Figure S3. Ray density tensors (RDT) evaluated at the parametrization nodes of all the depths for the ray distribution of the LAPNET data set. See caption of Fig. 3 for details.

Figure S4. Anisotropic-velocity model retrieved by the coupled anisotropic-isotropic tomography. On the left, there are all individual solutions of the anisotropic part of the model displayed at each parametrization node (see Fig. 5 for details). Only individual solutions with strength of anisotropy larger than 1 per cent at nodes with at least eight individual solutions larger than 1 per cent are plotted. On the background, the isotropic-velocity perturbations as in Fig. 6 are displayed. On the right, we present the anisotropic velocities averaged from the set of individual solutions. See Figs 5 and 7 for details.

Figure S5. *P*-wave isotropic-velocity perturbations retrieved by the isotropic version of the AniTomo code. Part of the model with RDE < 0.5 is shaded. Red dashed line marks the region with relatively low-velocity perturbations that dominates the model at depths of 80, 120 and 170 km. The hatched area locates a zone of weaker anisotropy and velocity perturbations within Region III at depth of 120 km. Distribution of the isotropic-velocity perturbations from the purely isotropic inversion and from the set of the coupled anisotropic–isotropic inversions (Fig. 6) are the same, in general. The brown dashed curves mark boundaries of cratonic provinces after Korja *et al.* (2006); see also Fig. 1.

Figure S6. Standard deviations of the isotropic-velocity perturbations evaluated at each grid node from the set of 24 coupled anisotropic-isotropic inversions with different initial orientations of the symmetry axis. The standard deviations are lower than 1 per cent at almost all the grid nodes and they are even lower than 0.5 per cent in majority of the nodes. Triangles represent seismic stations of experiment LAPNET together with the nearby permanent stations.

Figure S7. Anisotropic-velocity model retrieved by the coupled anisotropic-isotropic tomography code for the synthetic test mimicking a realistic anisotropic structure of the mantle lithosphere. See caption of Fig. 8 for details.

Figure S8. Anisotropic-velocity model at 120 km depth from a set of synthetic tests that follows the three-block structure (see Fig. S7), but with different characteristics of the blocks (schematic insets in the lower left corners). Perturbations of the isotropic velocities in the blocks with non-zero deviation from the IASP'91 model are set to 3 per cent amplitude. Strength of anisotropy in the anisotropic blocks is always 5 per cent. See captions of Figs 7 and 5 for description of plotting the output anisotropic parameters. Dotted black curve marks smoothed contour of RDE equal to 0.5.

Figure S9. *P* spheres showing directional distribution of relatively early and delayed *P*-wave arrival times at the individual stations of the extended LAPNET array. The stations are clustered into the domains according to similarity of their *P*-sphere patterns (see Fig. 9 for details). The *P* spheres exhibiting only a tendency to the typical pattern of the corresponding domain are marked by a dashed frame.

Figure S10. Anisotropic-velocity model from a synthetic test designed to investigate capability of the LAPNET ray geometry to resolve a vertically variable anisotropy. The synthetic model includes two 5 per cent anisotropic blocks with different orientation of symmetry axes. The upper one is at depths of 80 and 120 km with axis azimuth of 300° and inclination of 40°. The lower block is at depths of 170 and 220 km with axis azimuth of 60° and inclination of 60°. See caption of Figs 5 and 7 for description of plotting the

output anisotropic parameters. Dotted black curve marks smoothed contour of RDE equal to 0.5.

Figure S11. Vertical cross-section through the model of the isotropic-velocity perturbations from the coupled anisotropic-isotropic tomography along the 66°N latitude. Parts of the model with RDE < 0.5 and the depths corresponding to the crust are shaded. Red dashed line marks the westward dipping boundary of the relatively low-velocity perturbations dominating the western part of the model at depths of 80, 120 and 170 km (see also Figs 6 and 7).

Supporting information

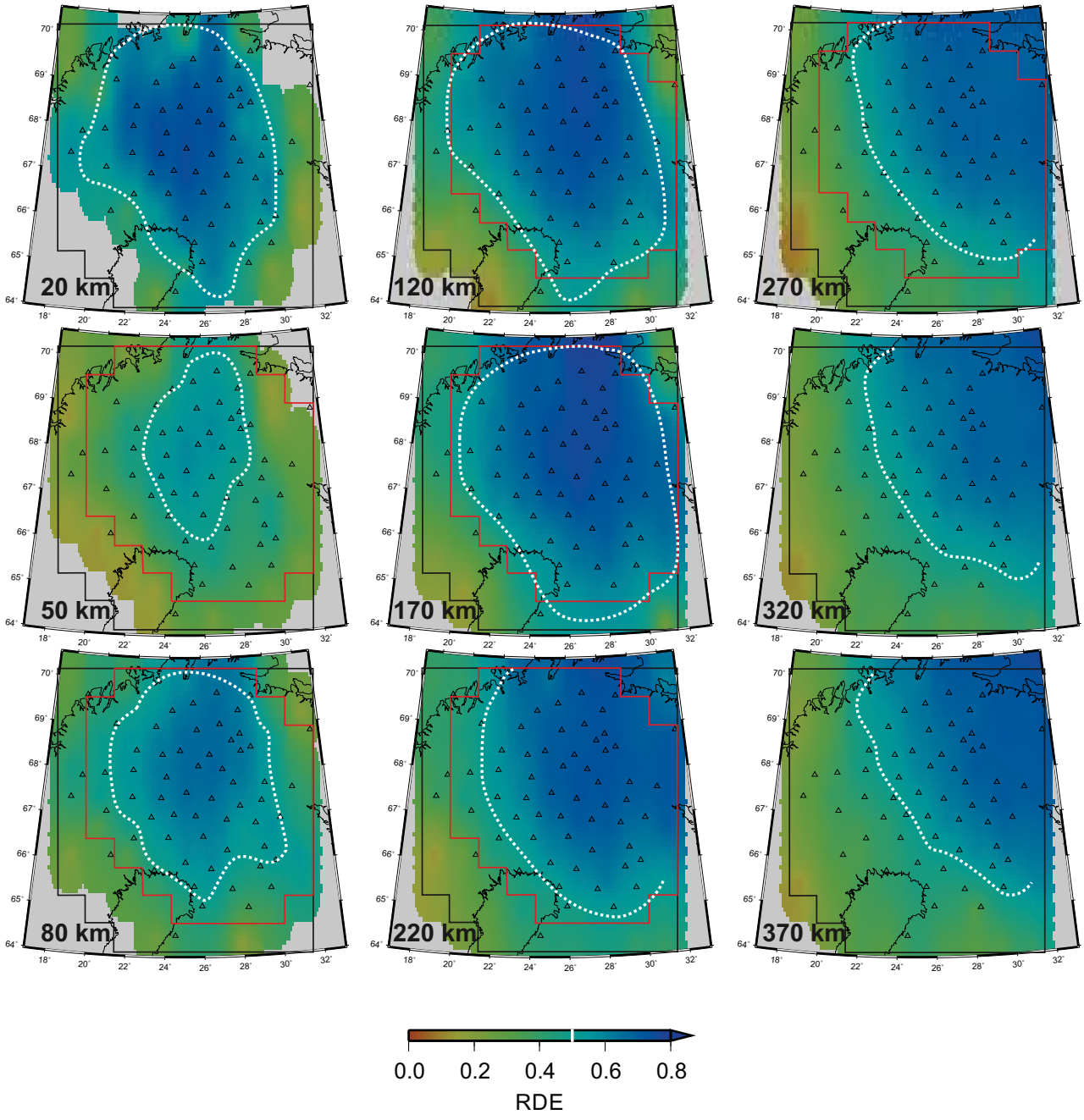

Figure S1. Diagonal elements of resolution matrix evaluated according to equation (4) for the ray geometry of the LAPNET dataset and the final parameterization of the volume studied with a denser vertical spacing at the top part. Dotted white curve marks smoothed contour of RDE equal to 0.5. The relatively small area delimited by the 0.5 contour at the 50 km depth is caused by denser vertical grid spacing in this part of the model. Red line delimits a region where inversion for all four anisotropic parameters is allowed, while inversion just for the purely isotropic-velocity perturbations is allowed within volume contoured by black line (see Figs 3 and S3). Triangles represent seismic stations of experiment LAPNET.

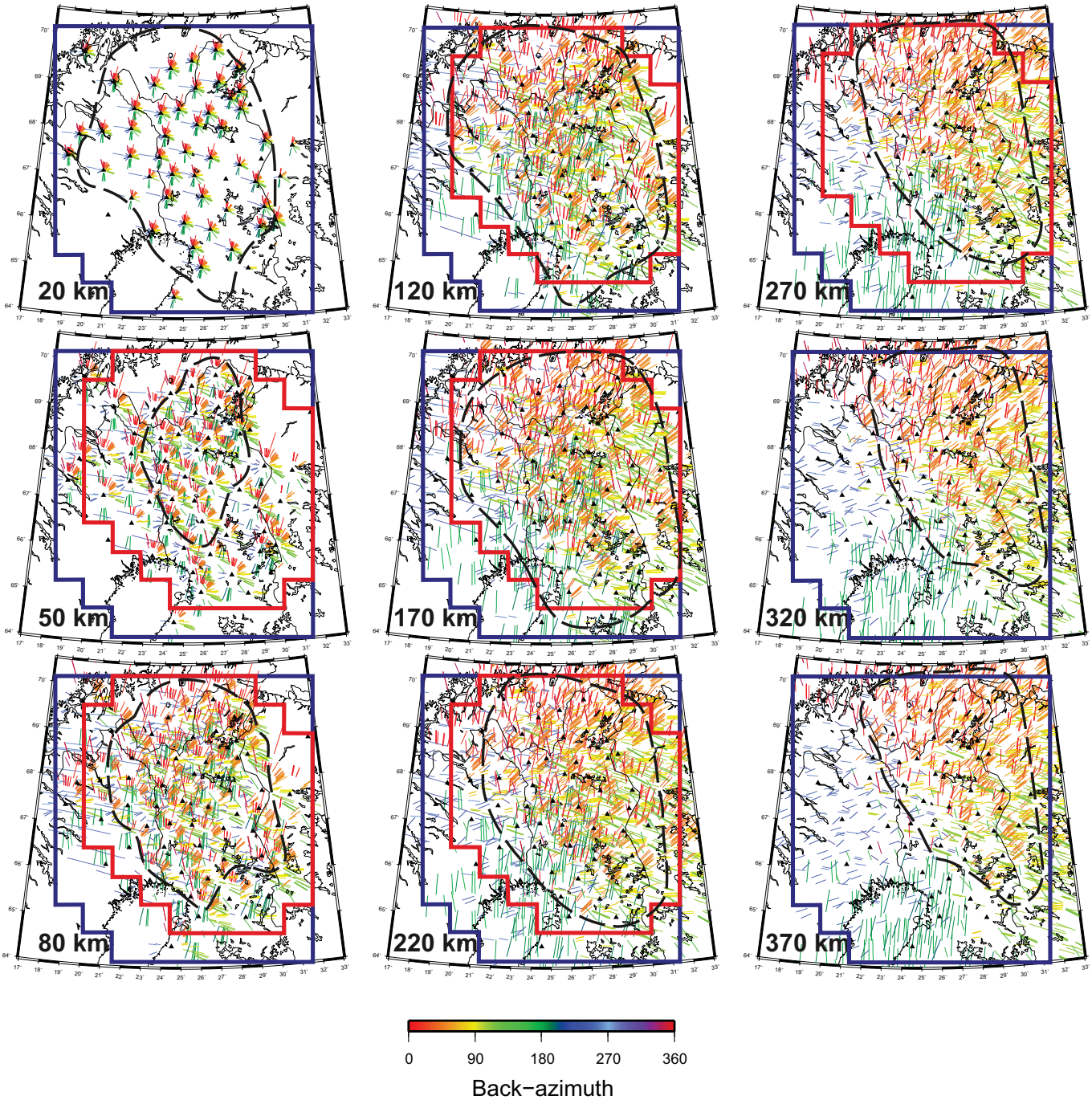

Figure S2. Ray paths at the individual depth layers of model parameterization. Dashed black curve marks smoothed contour of RDE equal to 0.5. Red line delimits a region where inversion for all the four anisotropic parameters is allowed, while inversion just for the purely isotropic-velocity perturbations is allowed in a larger region, marked by blue line (see Figs 3 and S3). Triangles represent seismic stations of experiment LAPNET.

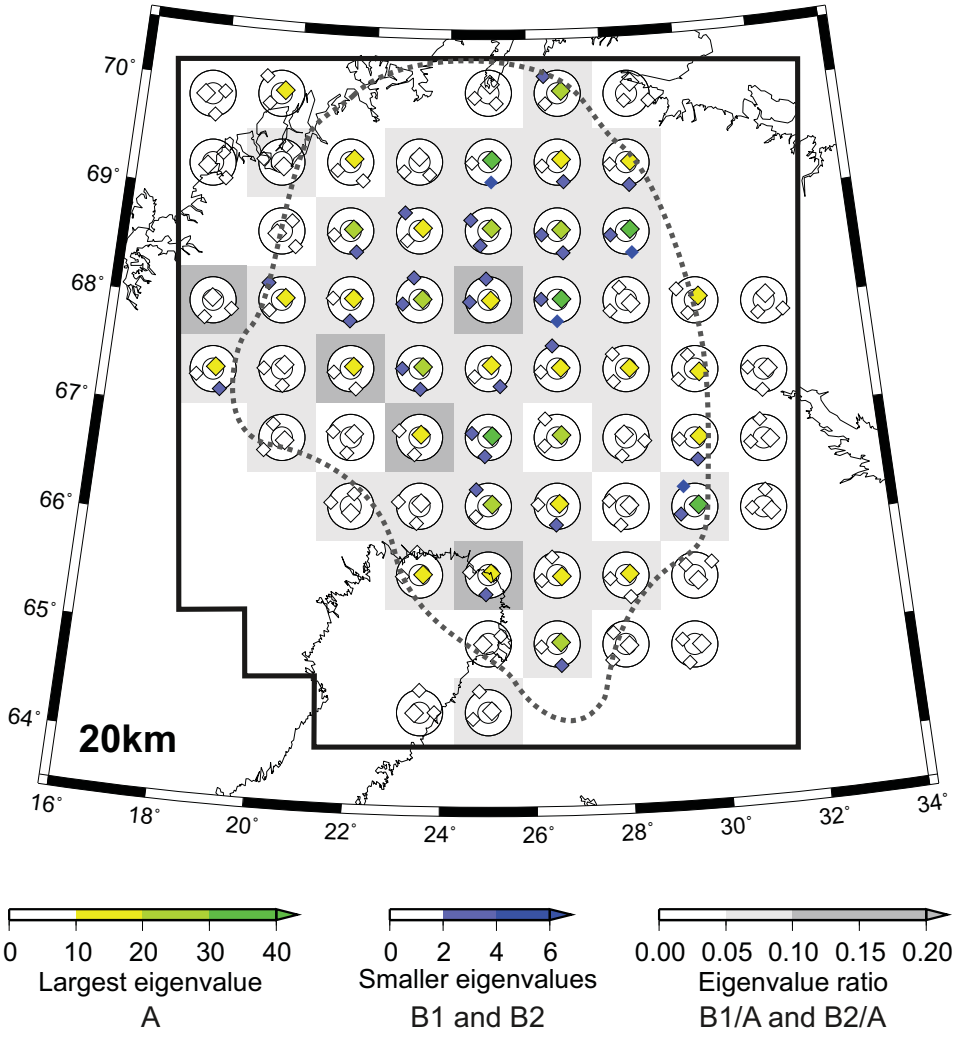

Figure S3. Ray density tensors (RDT) evaluated at the parameterization nodes of all the depths for the ray distribution of the LAPNET dataset. See caption of Fig. 3 for details.

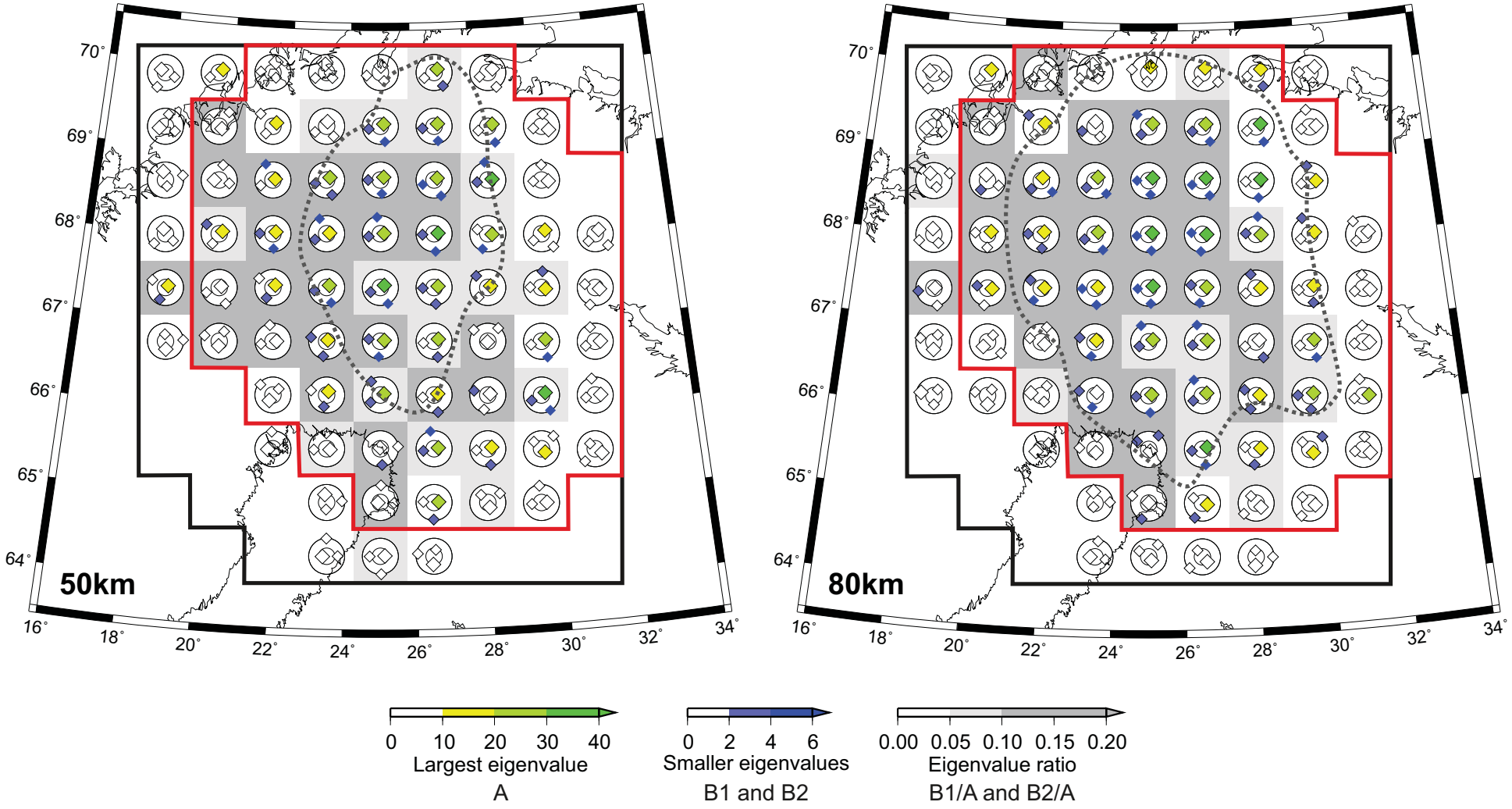

Figure S3. Continue

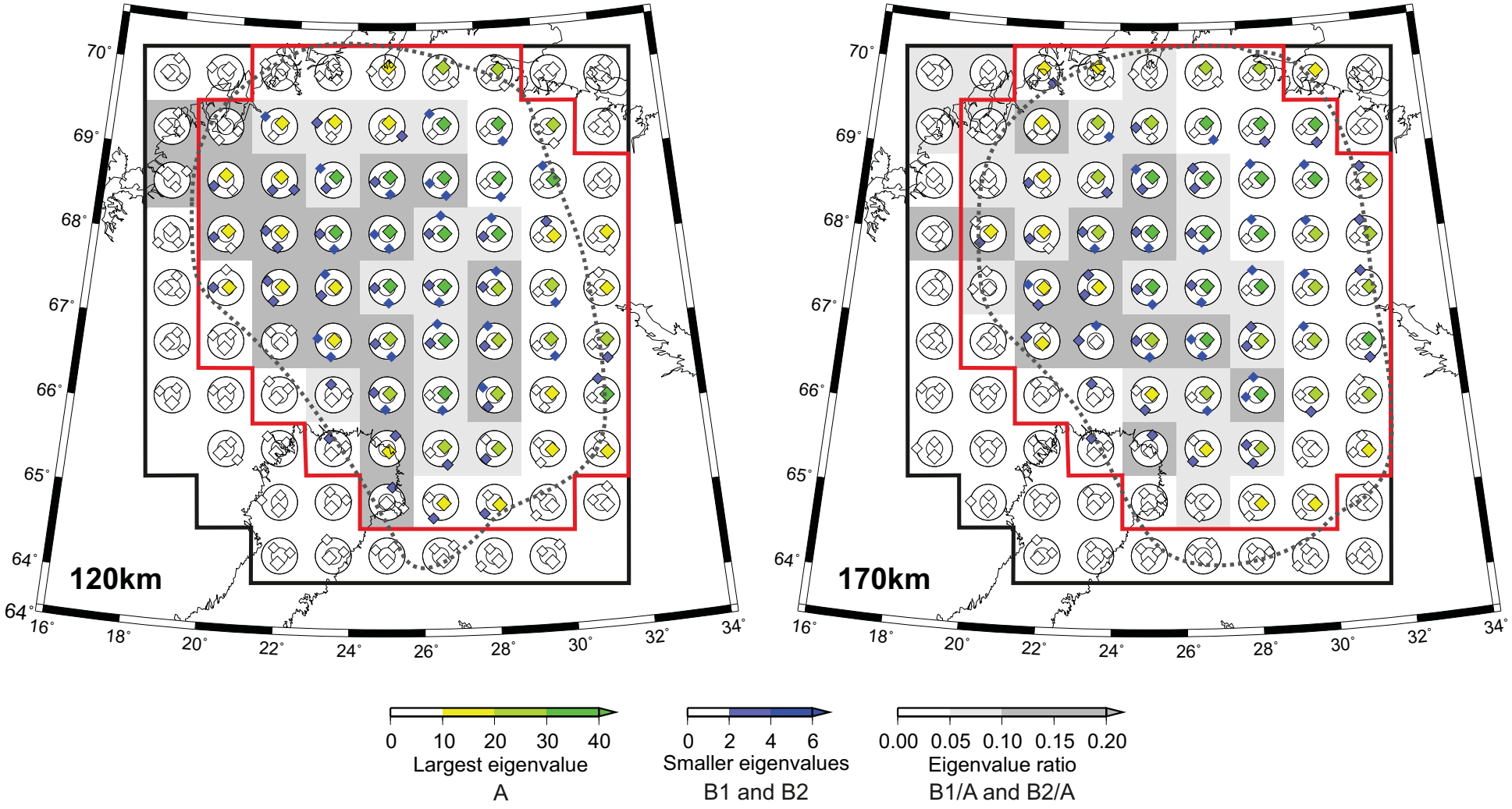

Figure S3. Continue

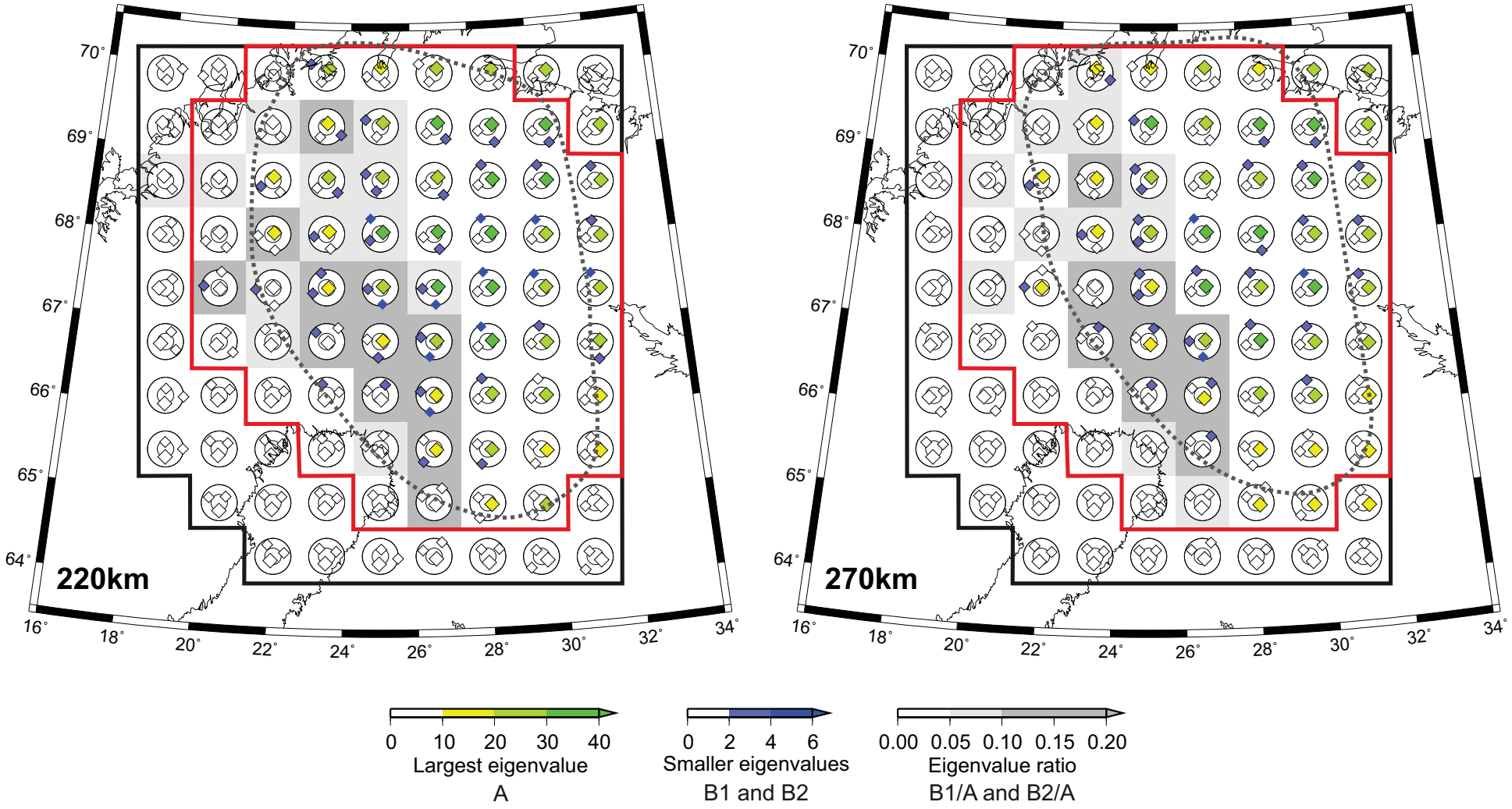

Figure S3. Continue

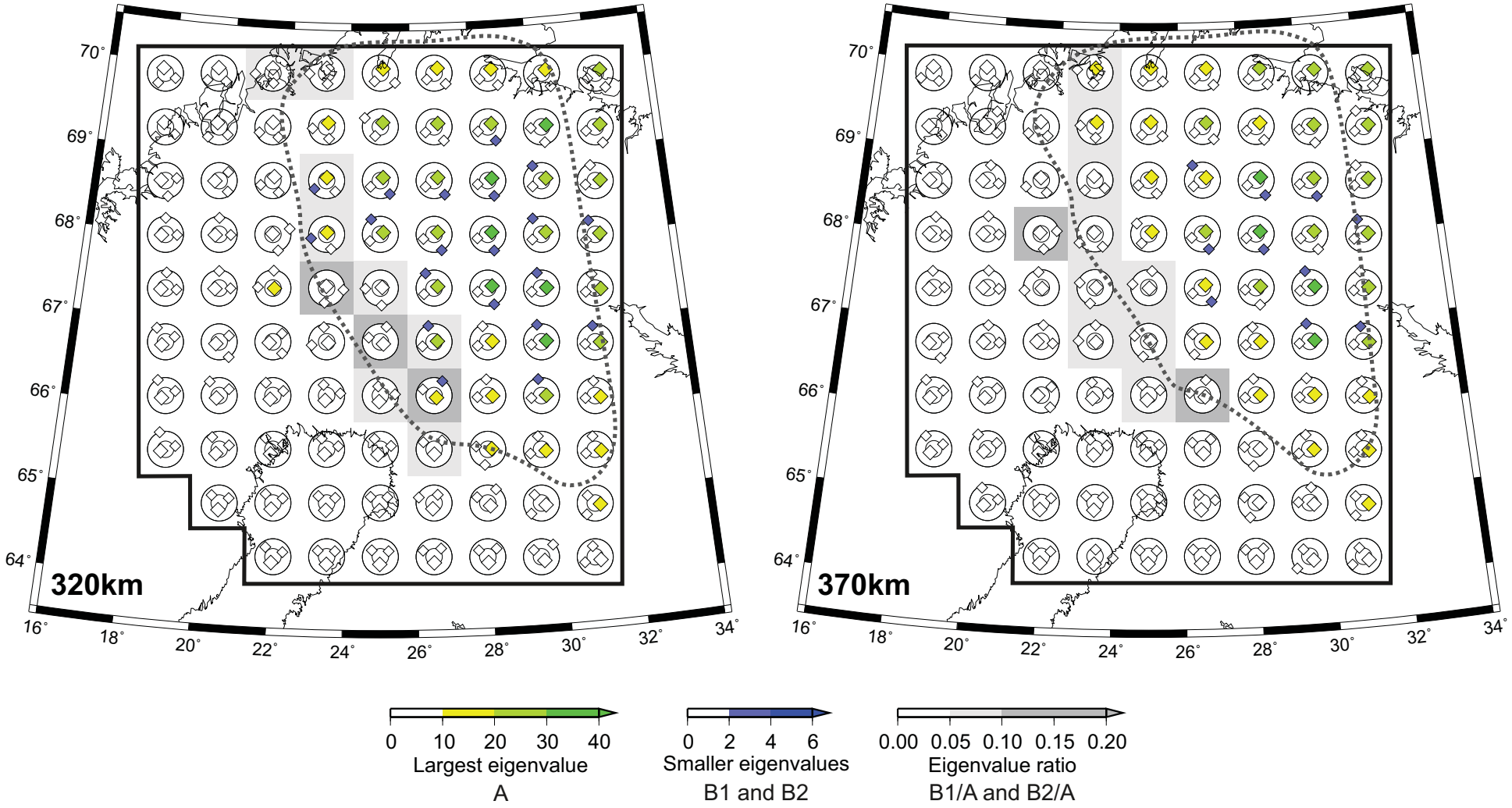

Figure S3. Continue

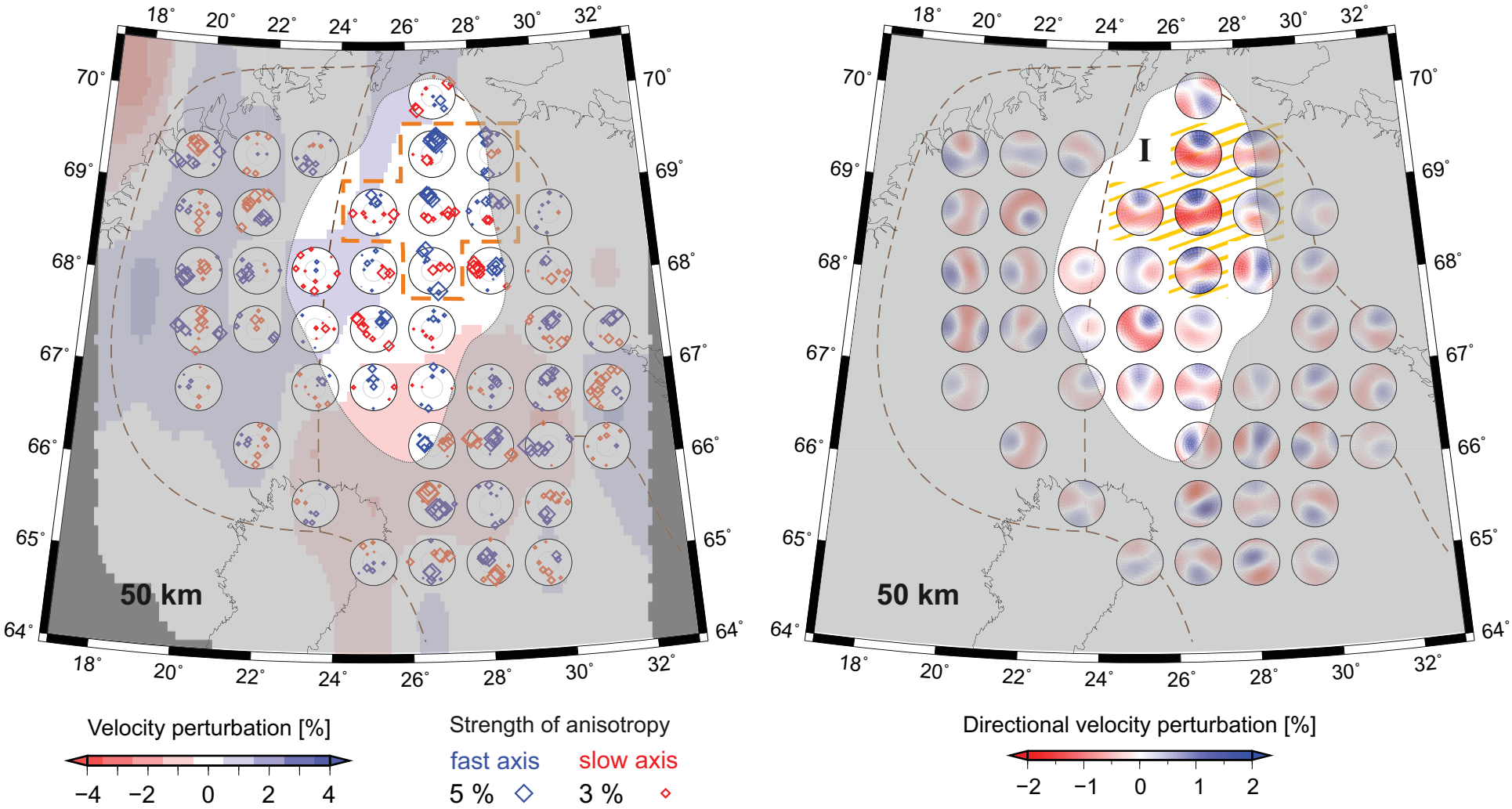

Figure S4. Anisotropic-velocity model retrieved by the coupled anisotropic-isotropic tomography. On the left, there are all individual solutions of the anisotropic part of the model displayed at each parameterization node (see Fig. 5 for details). Only individual solutions with strength of anisotropy larger than 1 % at nodes with at least 8 individual solutions larger than 1 % are plotted. On the background, the isotropic-velocity perturbations as in Fig. 6 are displayed. On the right, we present the anisotropic velocities averaged from the set of individual solutions. See Figs 5 and 7 for details.

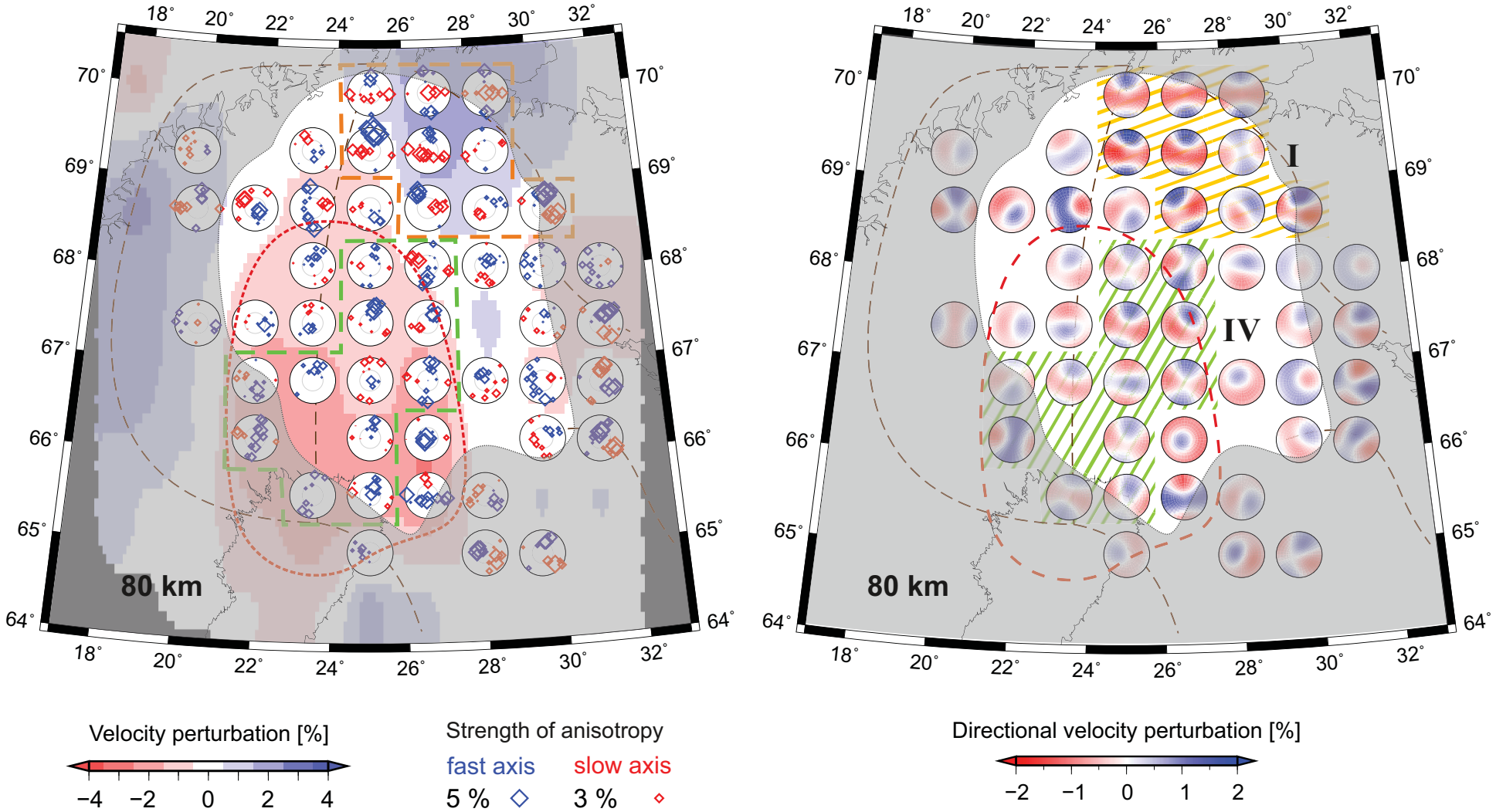

Figure S4. Continue

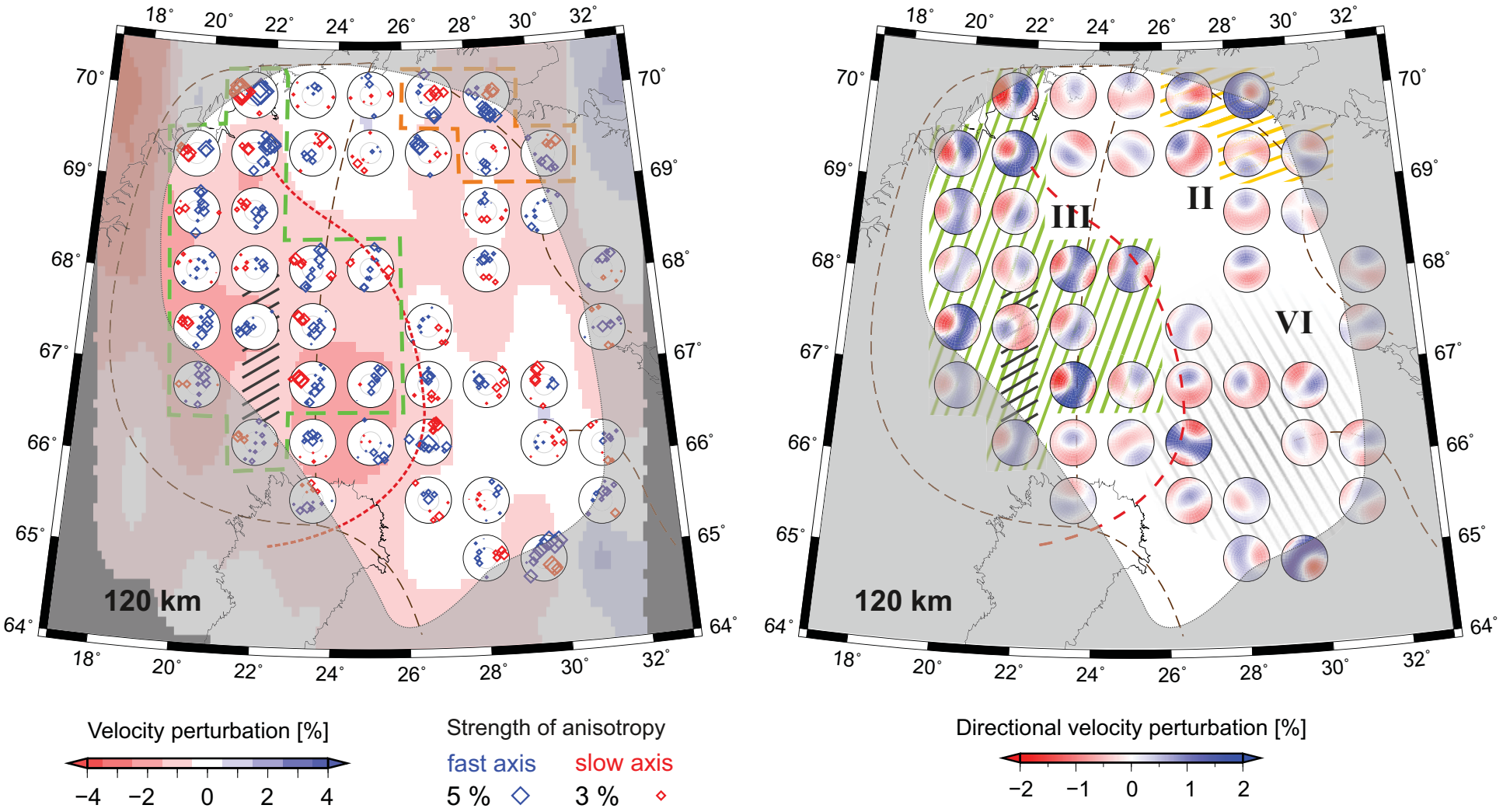

Figure S4. Continue

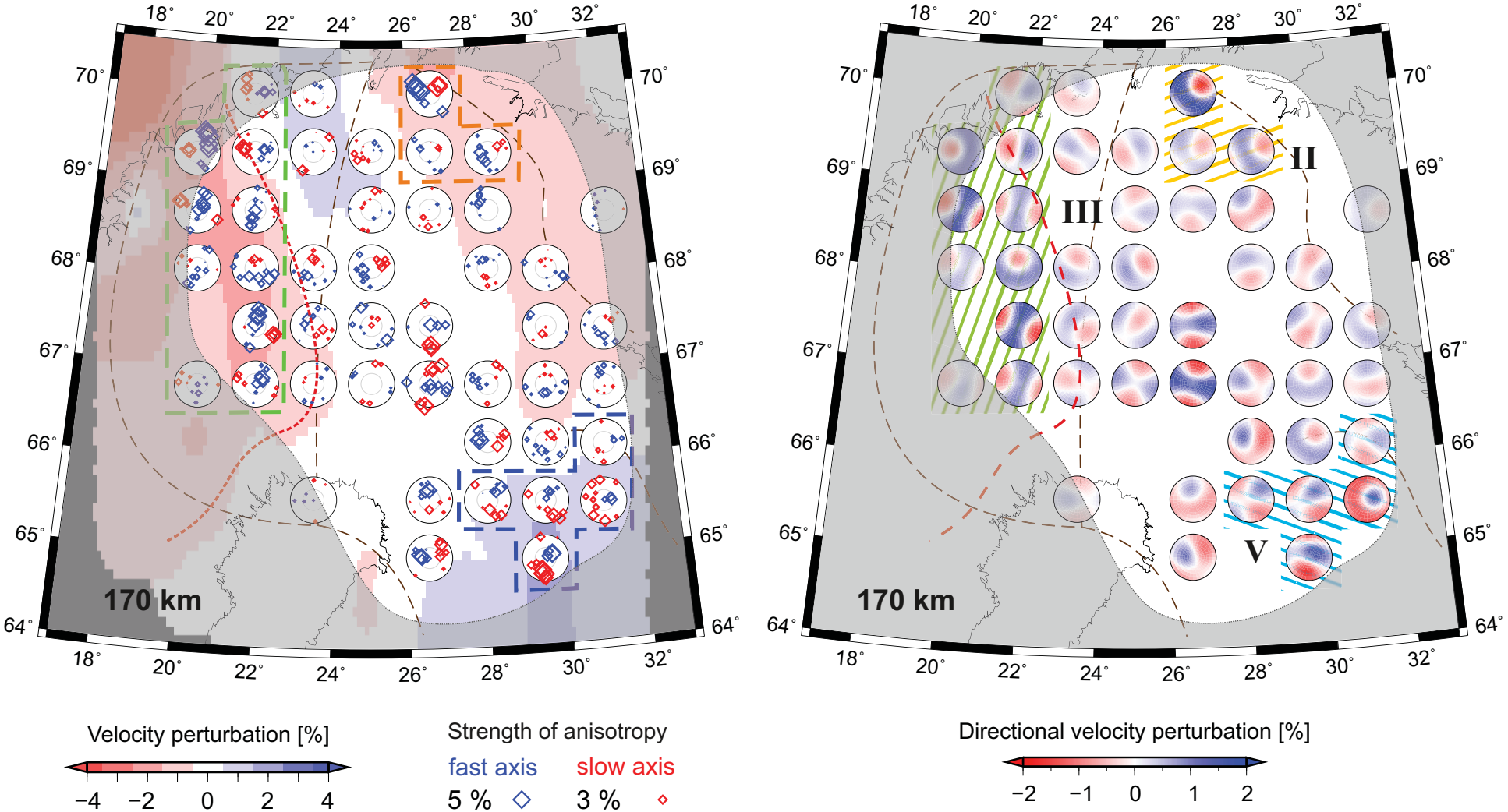

Figure S4. Continue

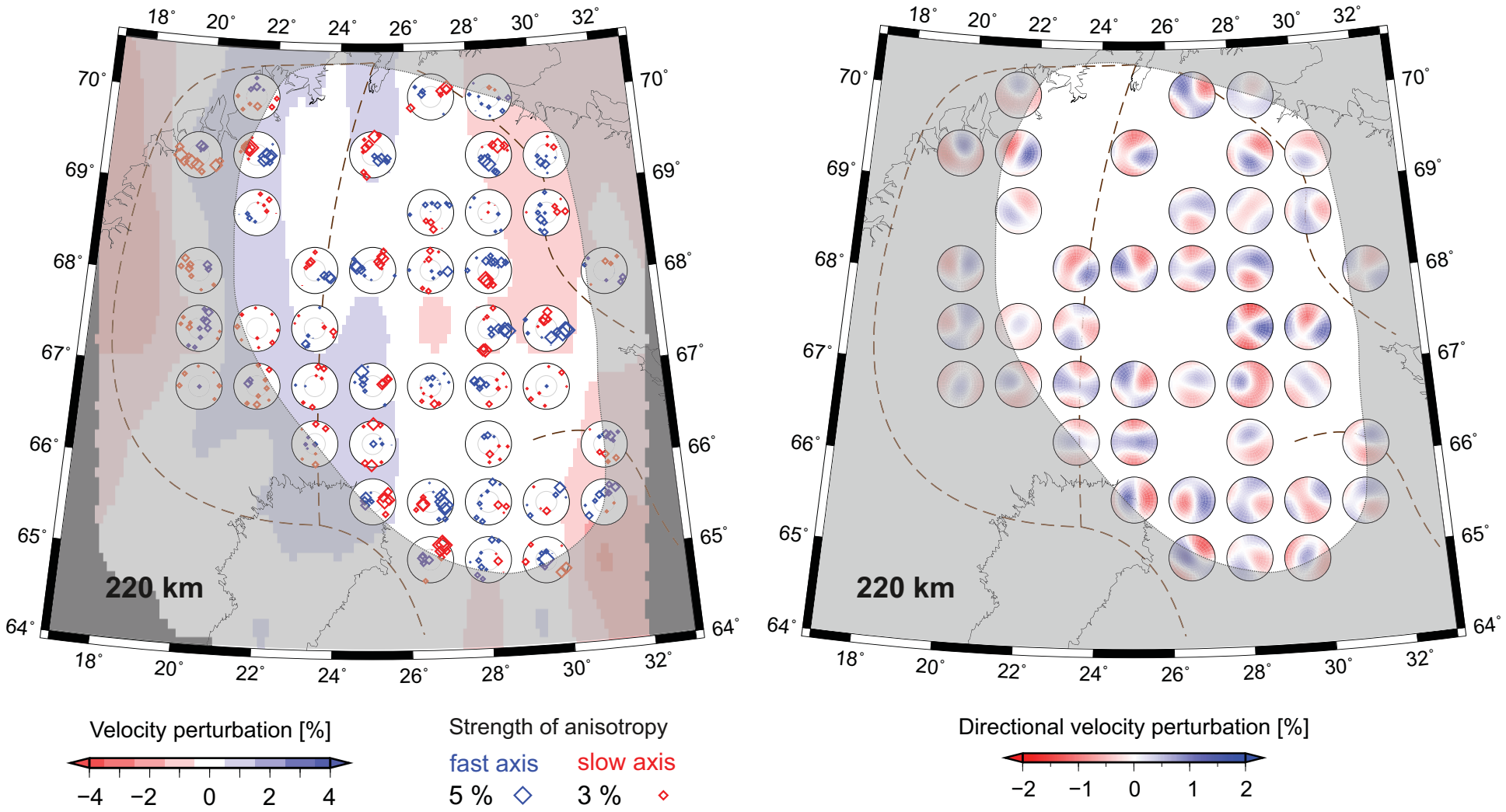

Figure S4. Continue

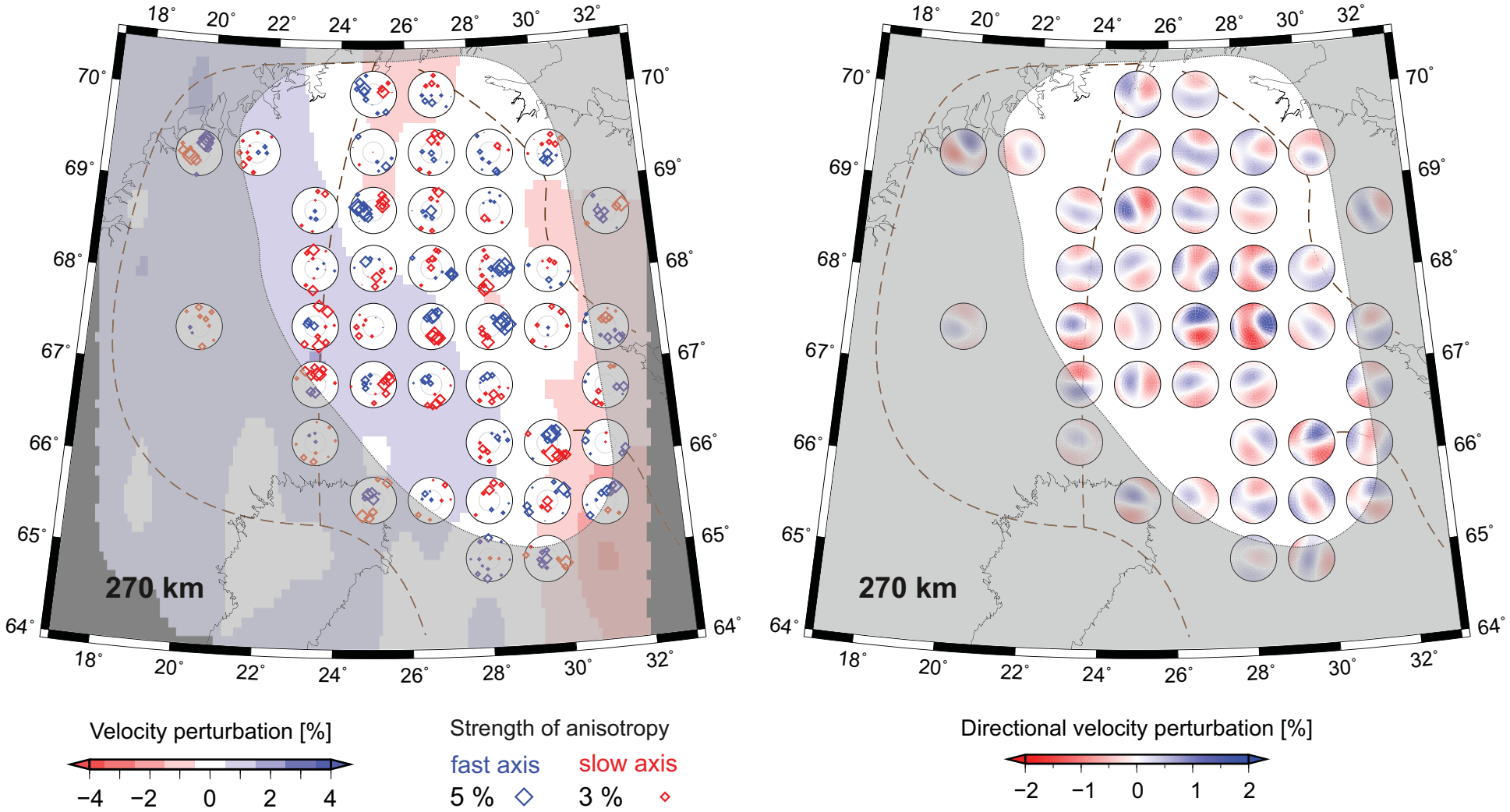

Figure S4. Continue

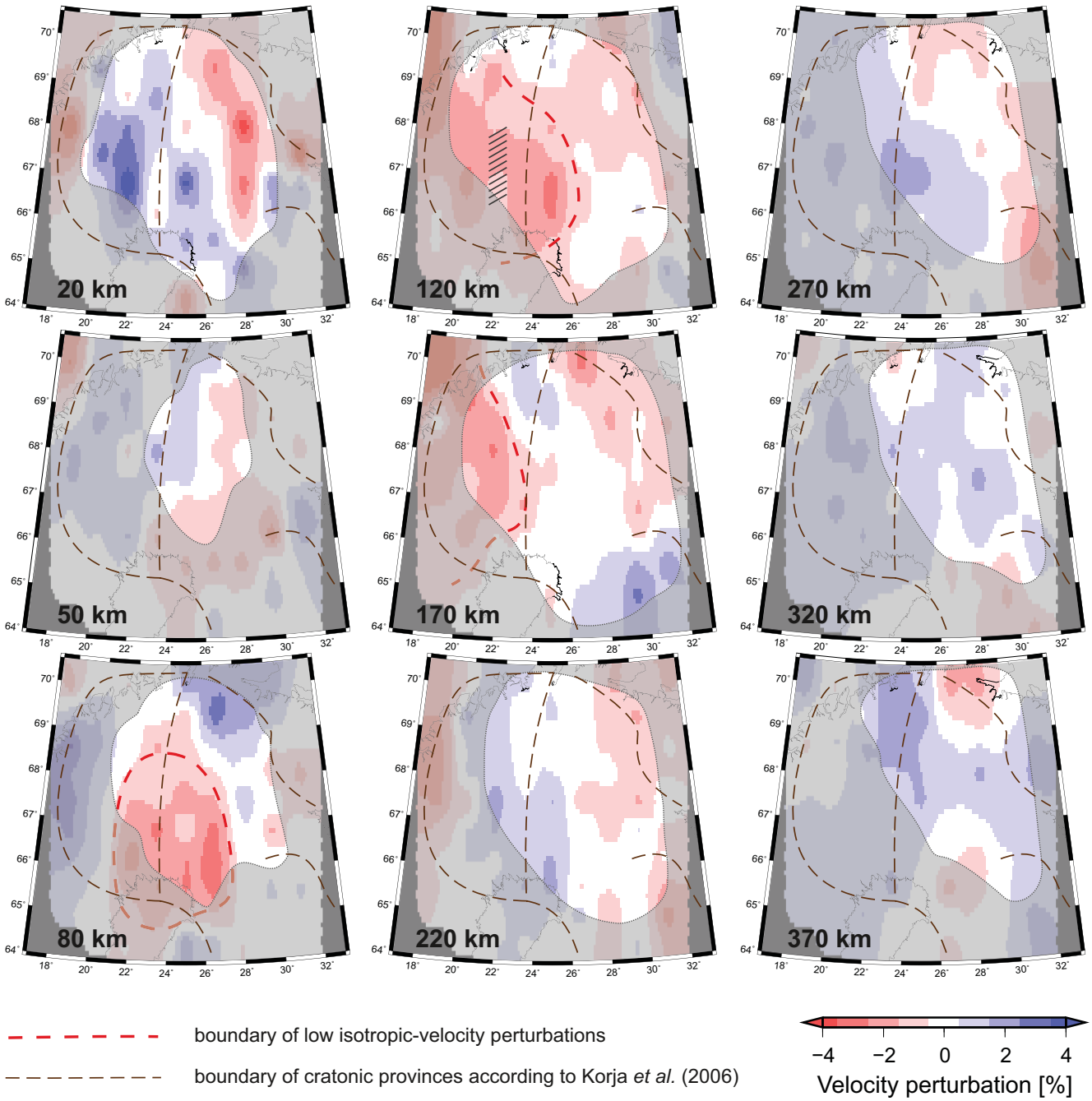

Figure S5. P-wave isotropic-velocity perturbations retrieved by the isotropic version of the AniTomo code. Part of the model with RDE < 0.5 is shaded. Red dashed line marks the region with relatively low-velocity perturbations that dominates the model at depths of 80 km, 120 km and 170 km. The hatched area locates a zone of weaker anisotropy and velocity perturbations within Region III at depth of 120 km. Distribution of the isotropic-velocity perturbations from the purely isotropic inversion and from the set of the coupled anisotropic-isotropic inversions (Fig. 6) are the same, in general. The brown dashed curves mark boundaries of cratonic provinces after Korja *et al.* (2006); see also Fig. 1.

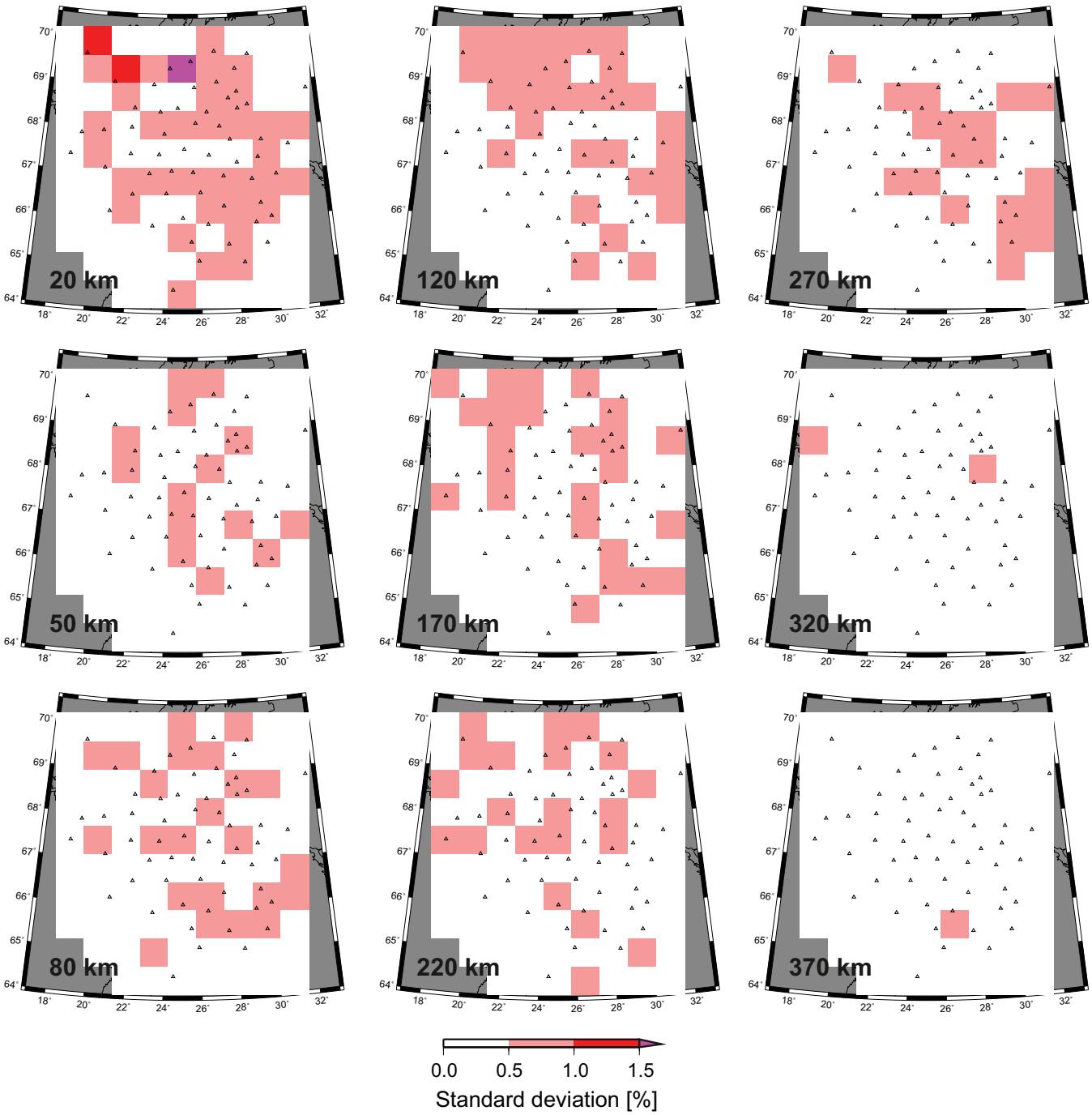

Figure S6. Standard deviations of the isotropic-velocity perturbations evaluated at each grid node from the set of 24 coupled anisotropic-isotropic inversions with different initial orientations of the symmetry axis. The standard deviations are lower than 1 % at almost all the grid nodes and they are even lower than 0.5 % in majority of the nodes. Triangles represent seismic stations of experiment LAPNET together with the nearby permanent stations.

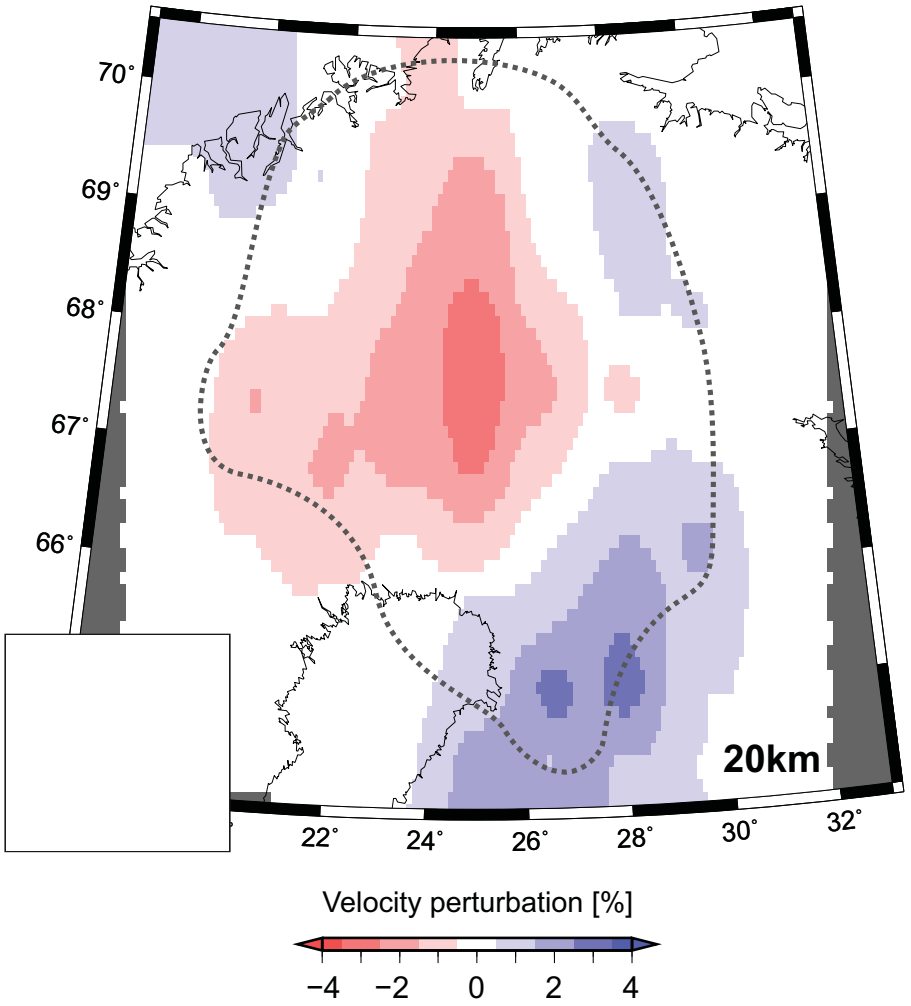

Figure S7. Anisotropic-velocity model retrieved by the coupled anisotropic-isotropic tomography code for the synthetic test mimicking a realistic anisotropic structure of the mantle lithosphere. See caption of Fig. 8 for details.

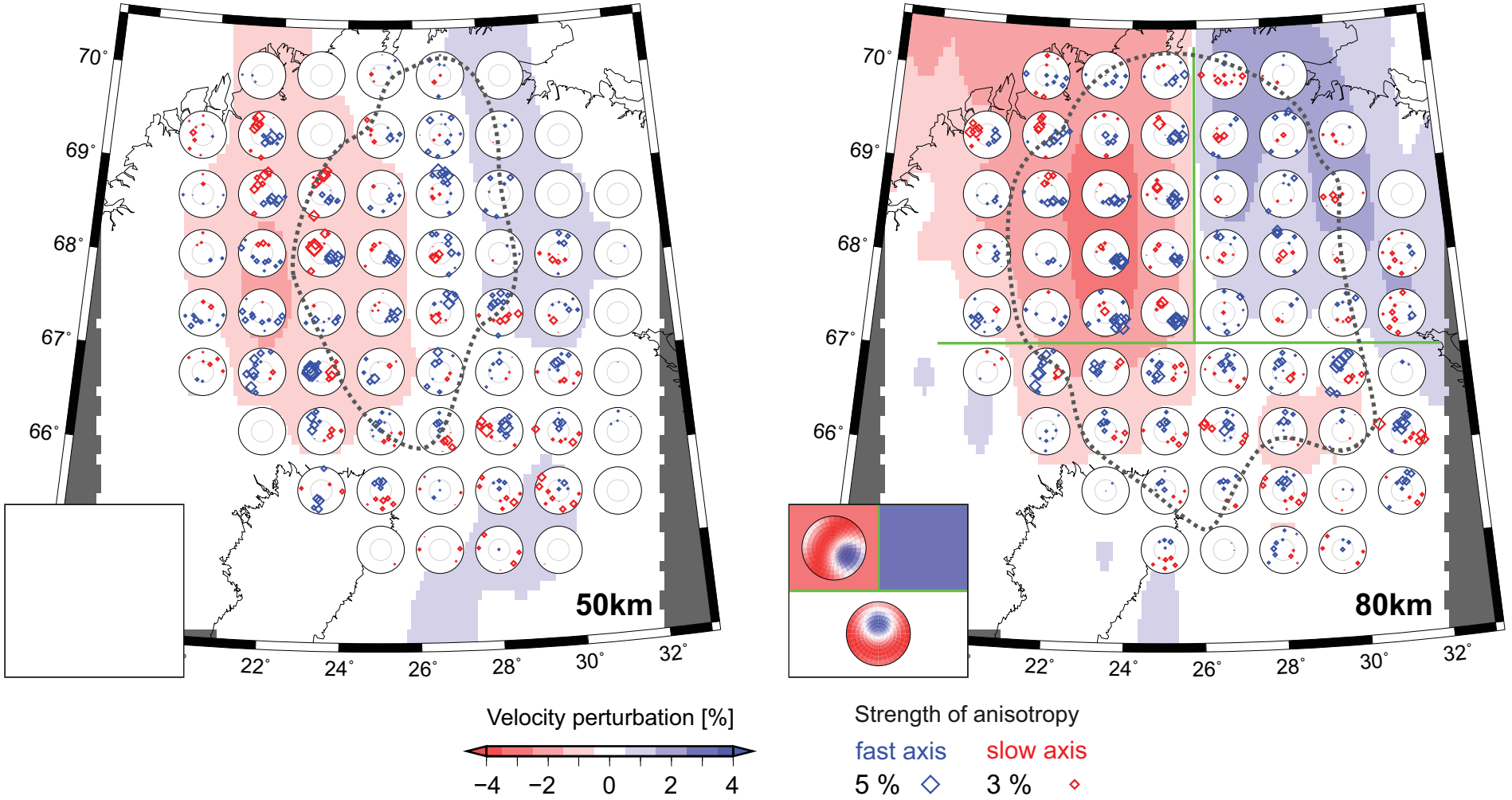

Figure S7. Continue

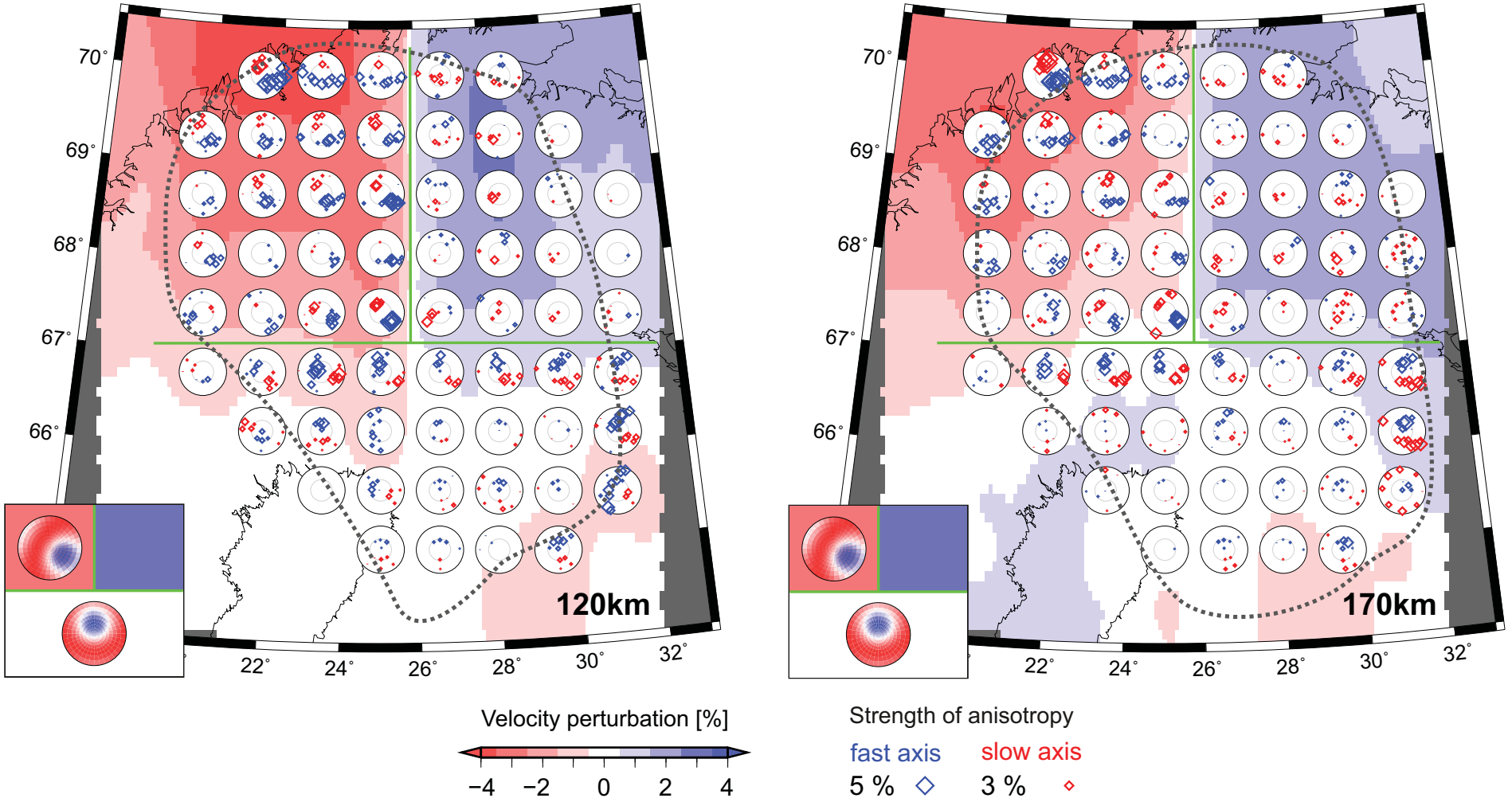

Figure S7. Continue

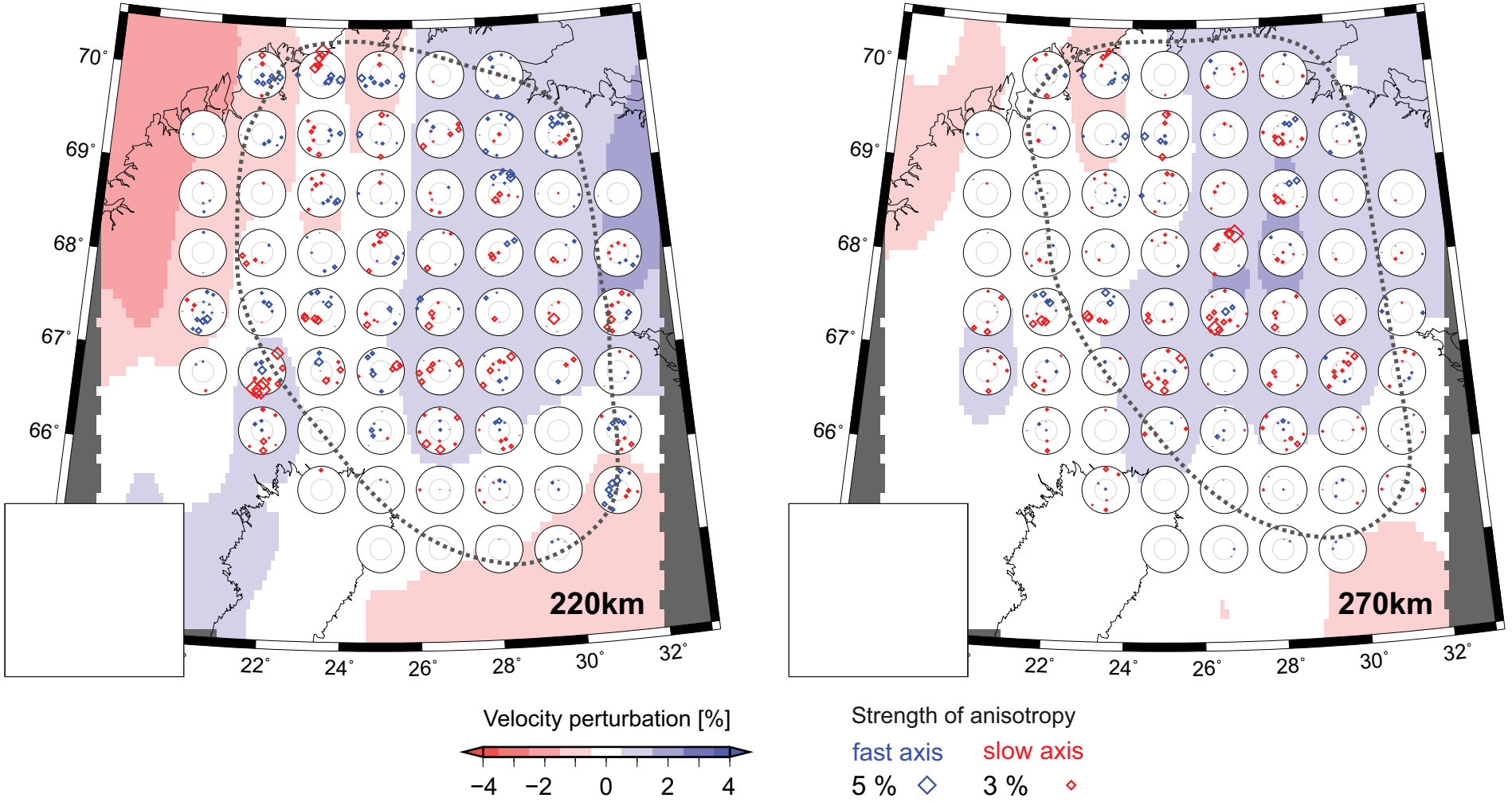

Figure S7. Continue

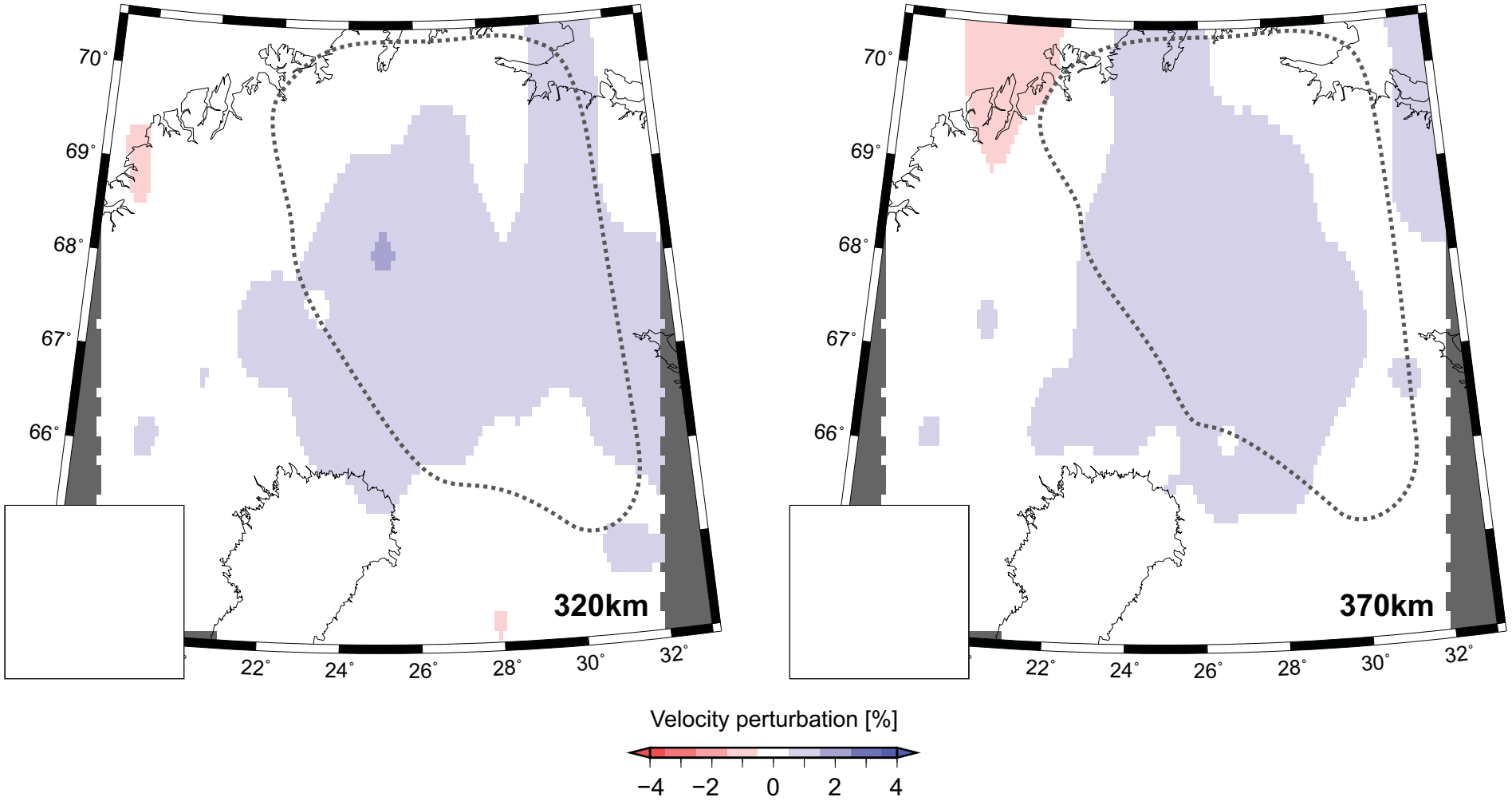

Figure S7. Continue

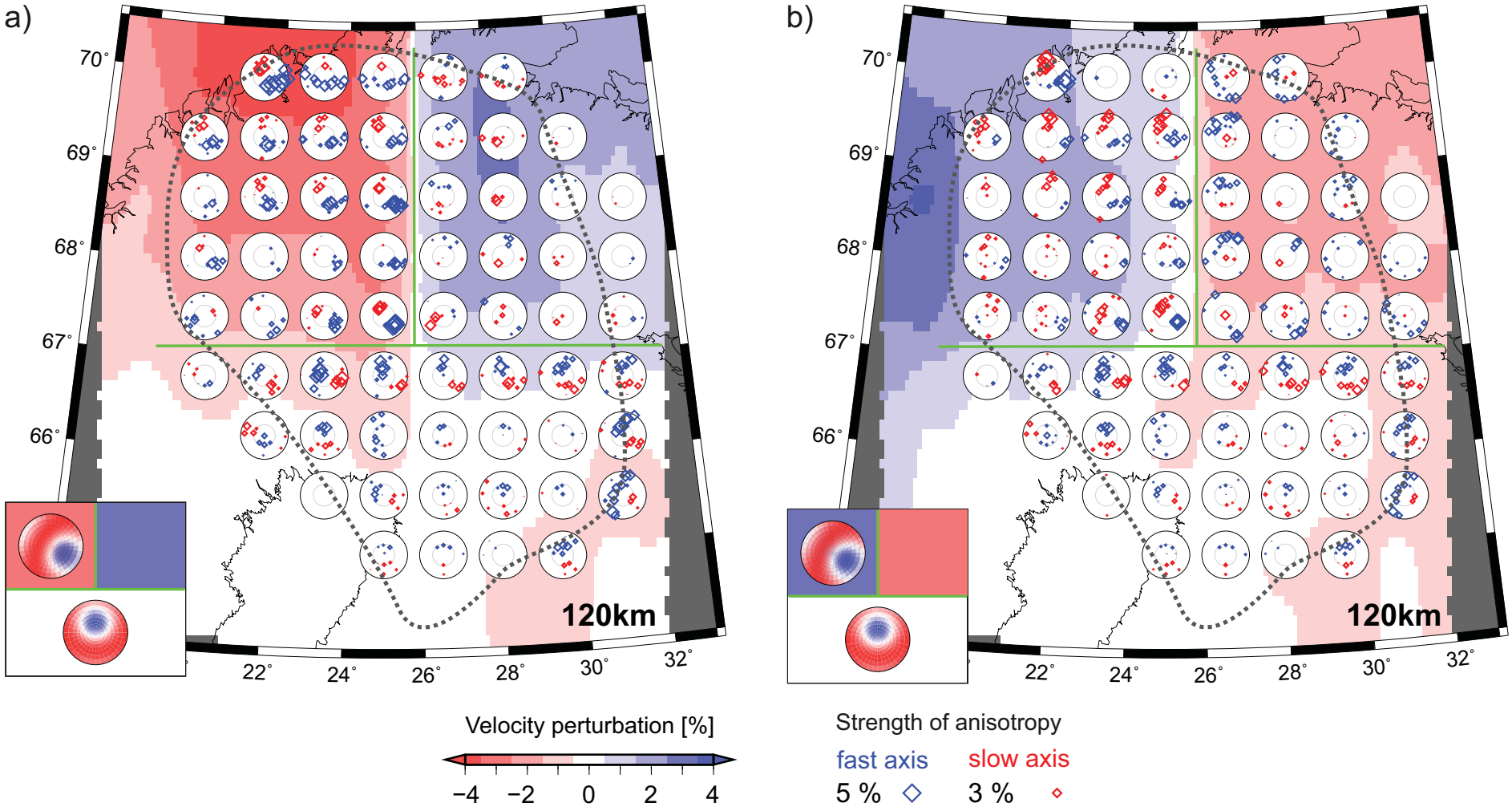

Figure S8. Anisotropic-velocity model at 120 km depth from a set of synthetic tests that follows the three-block structure (see Fig. S7), but with different characteristics of the blocks (schematic insets in the lower left corners). Perturbations of the isotropic velocities in the blocks with non-zero deviation from the IASP'91 model are set to 3% amplitude. Strength of anisotropy in the anisotropic blocks is always 5 %. See captions of Figs 7 and 5 for description of plotting the output anisotropic parameters. Dotted black curve marks smoothed contour of RDE equal to 0.5.

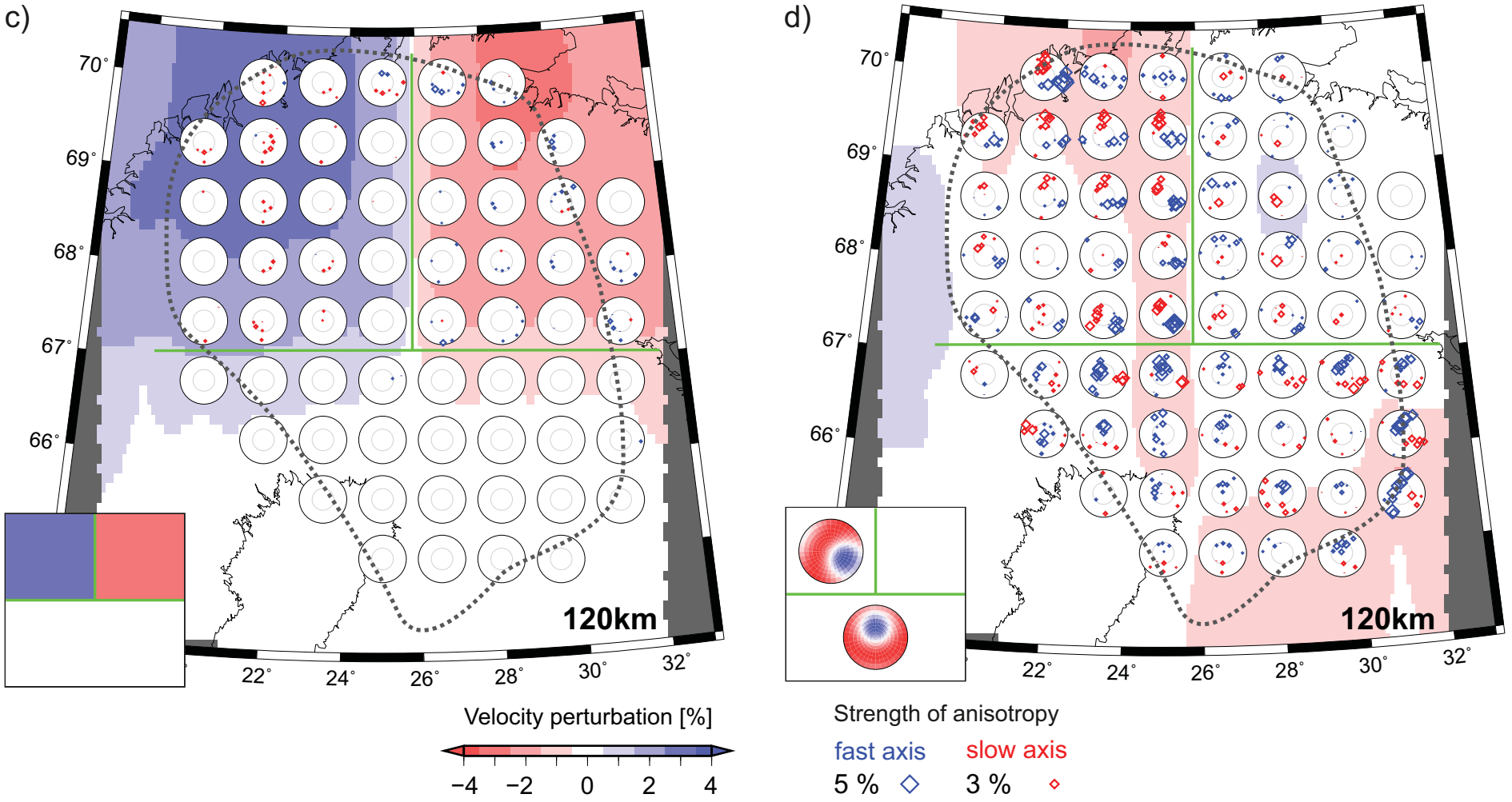

Figure S8. Continue

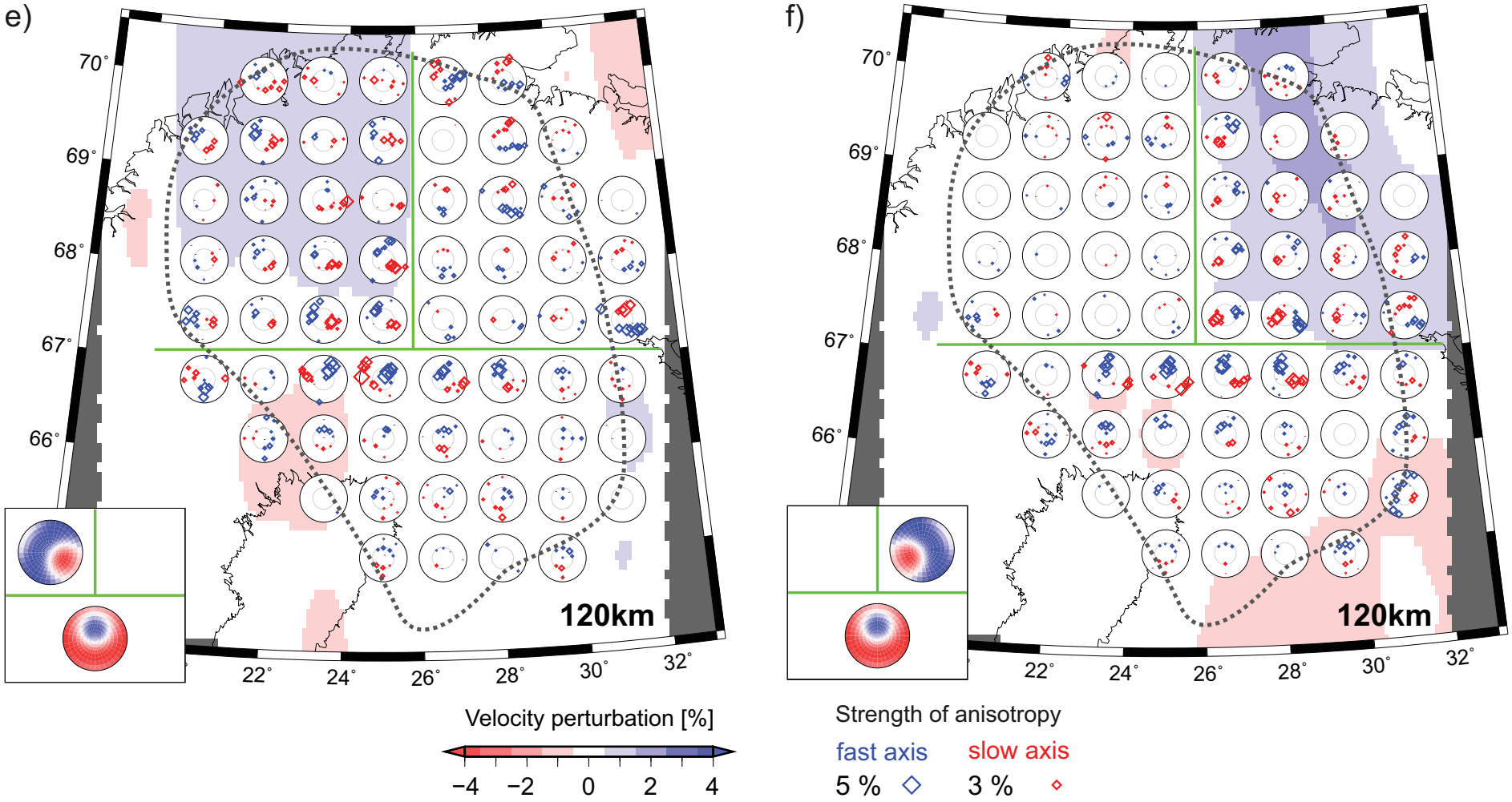

Figure S8. Continue

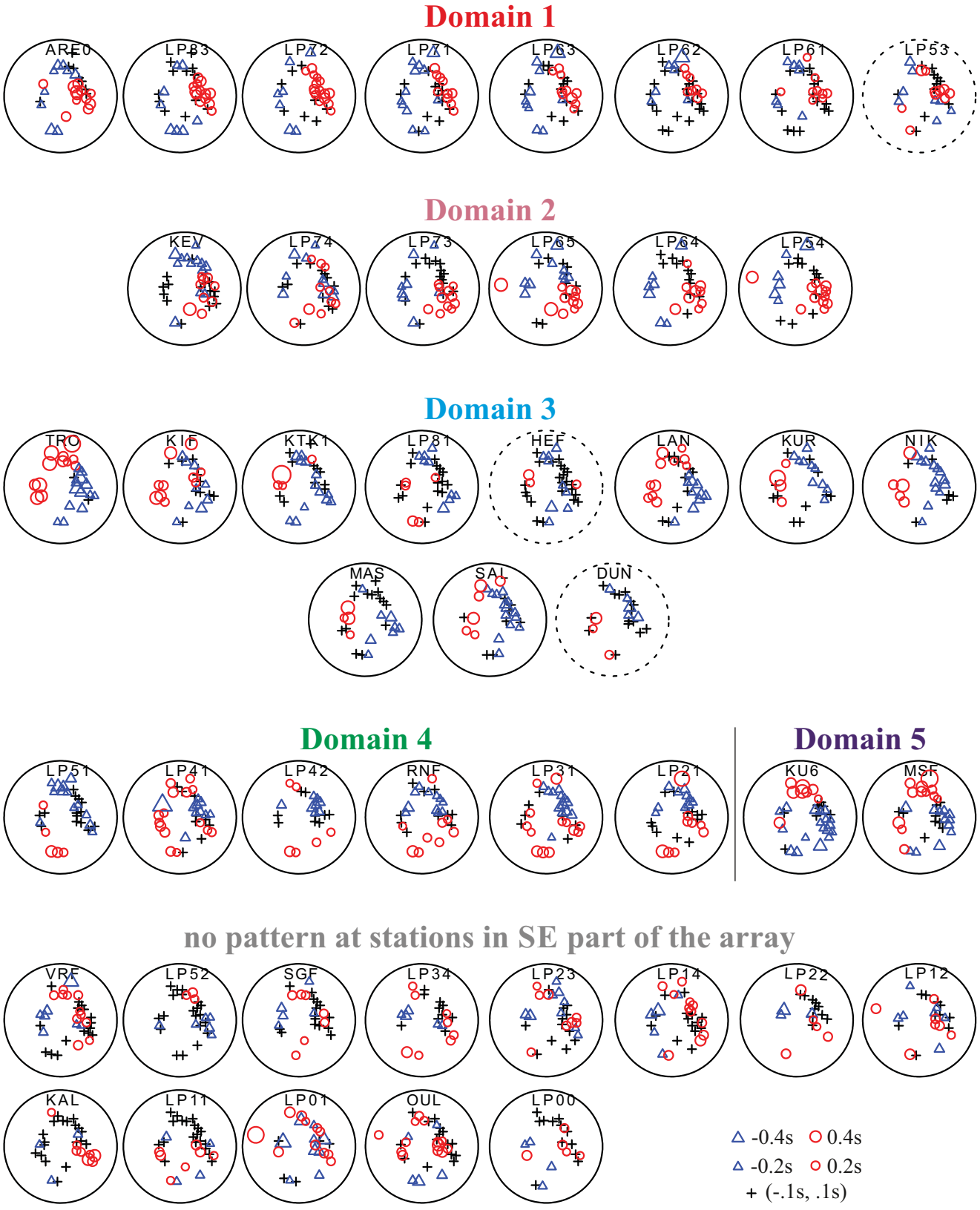

Figure S9. P spheres showing directional distribution of relatively early and delayed P-wave arrival times at the individual stations of the extended LAPNET array. The stations are clustered into the domains according to similarity of their P-sphere patterns (see Fig. 9 for details). The P spheres exhibiting only a tendency to the typical pattern of the corresponding domain are marked by a dashed frame.

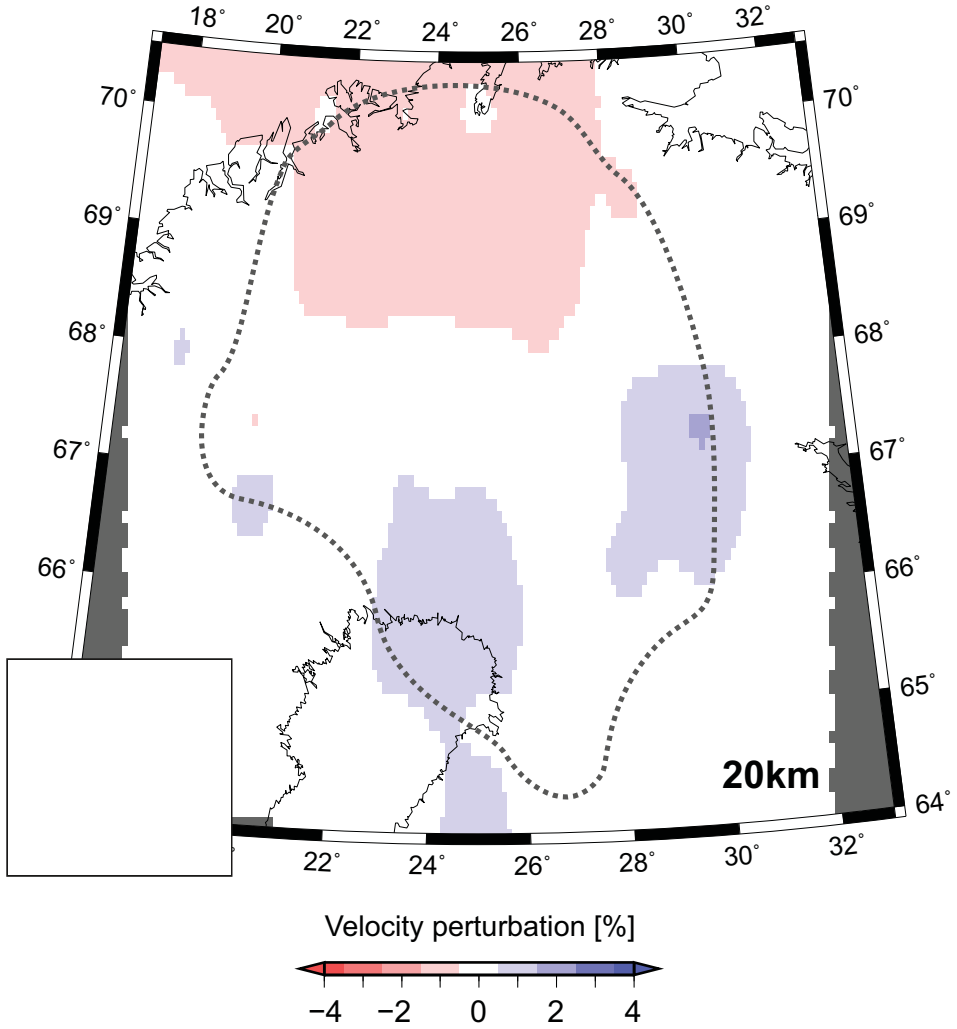

Figure S10. Anisotropic-velocity model from a synthetic test designed to investigate capability of the LAPNET ray geometry to resolve a vertically variable anisotropy. The synthetic model includes two 5 % anisotropic blocks with different orientation of symmetry axes. The upper one is at depths of 80 km and 120 km with axis azimuth of 300º and inclination of 40º. The lower block is at depths of 170 km and 220 km with axis azimuth of 60º and inclination of 60º. See caption of Figs 5 and 7 for description of plotting the output anisotropic parameters. Dotted black curve marks smoothed contour of RDE equal to 0.5.

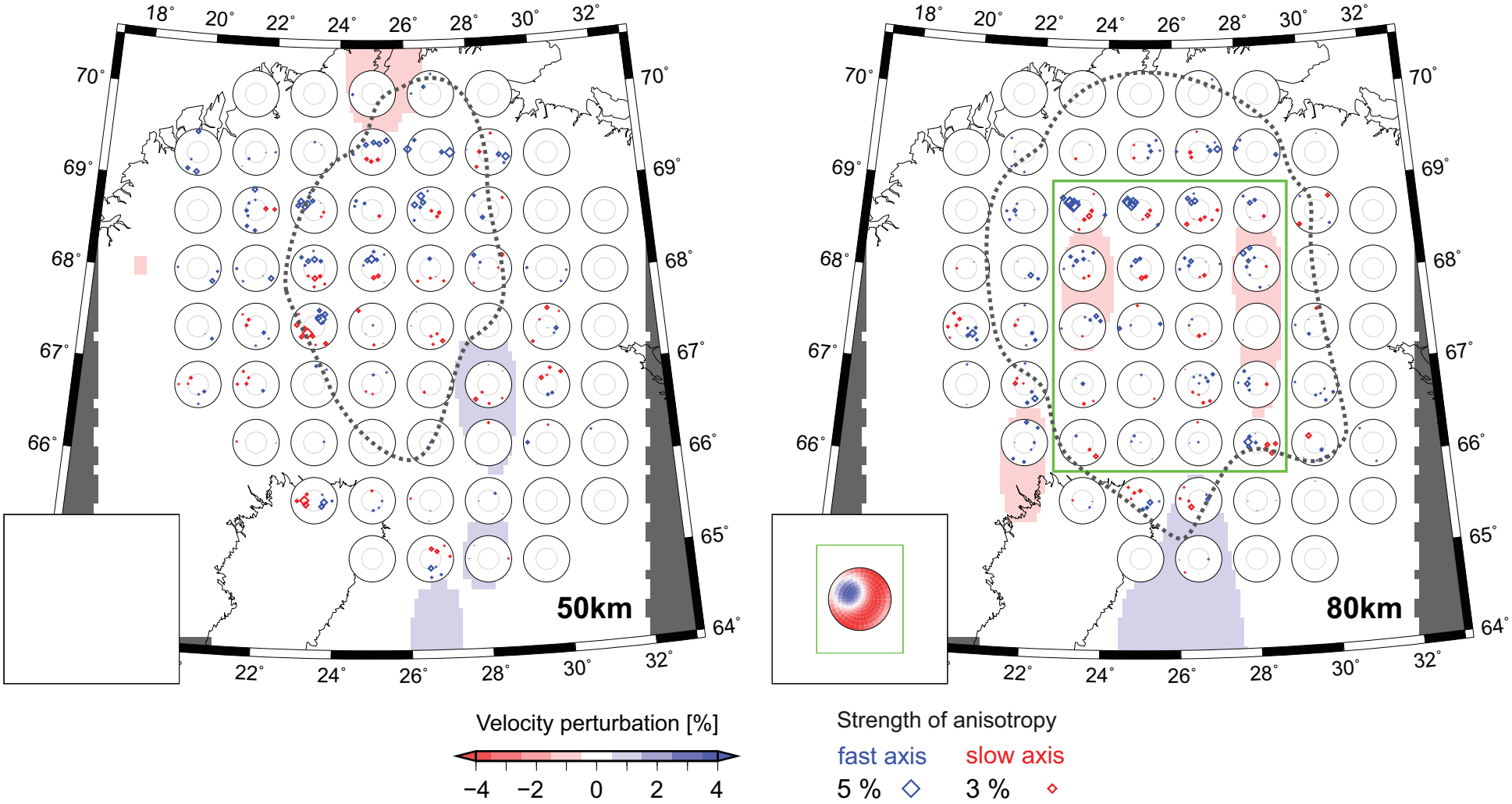

Figure S10. Continue

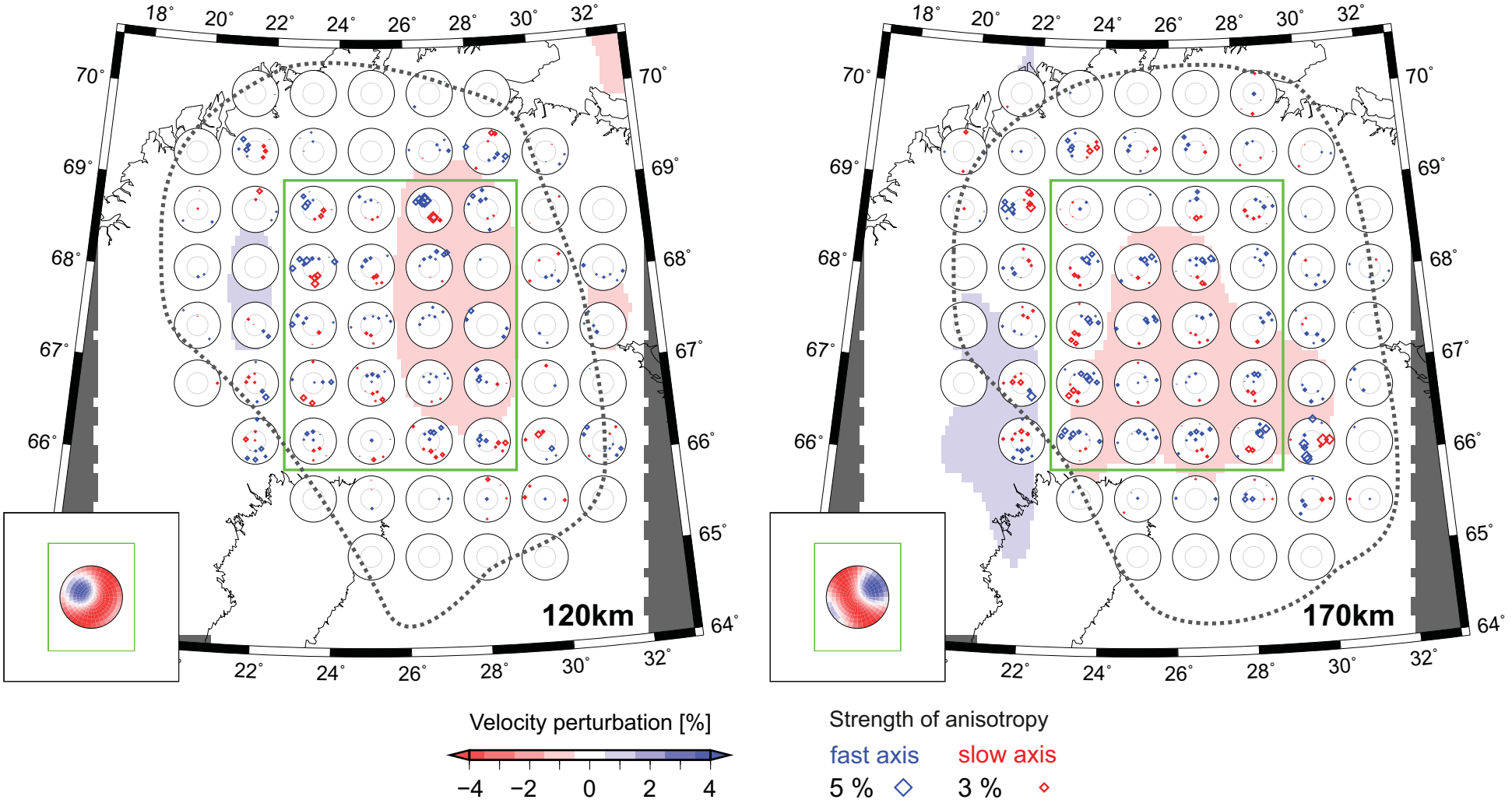

Figure S10. Continue

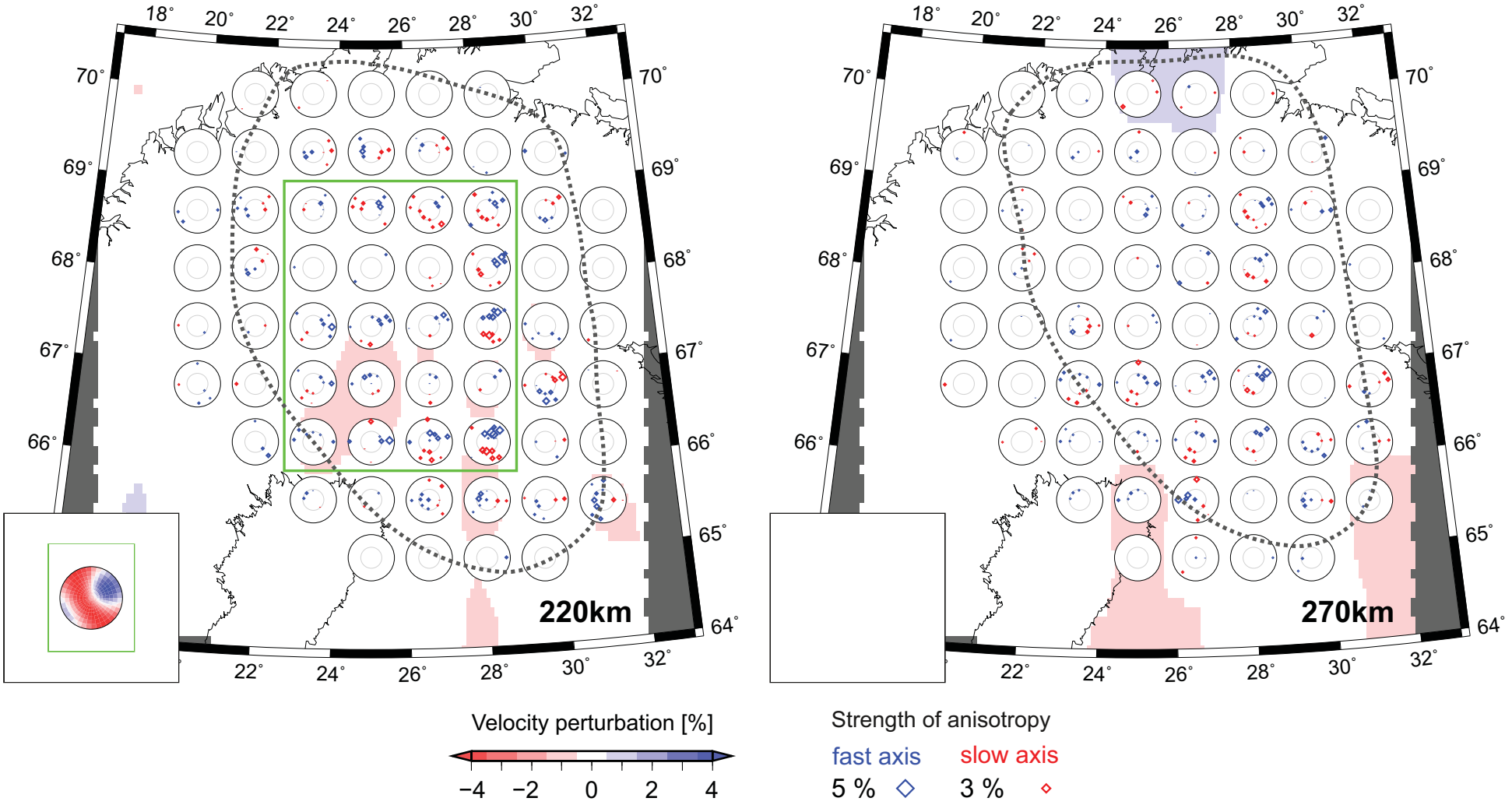

Figure S10. Continue

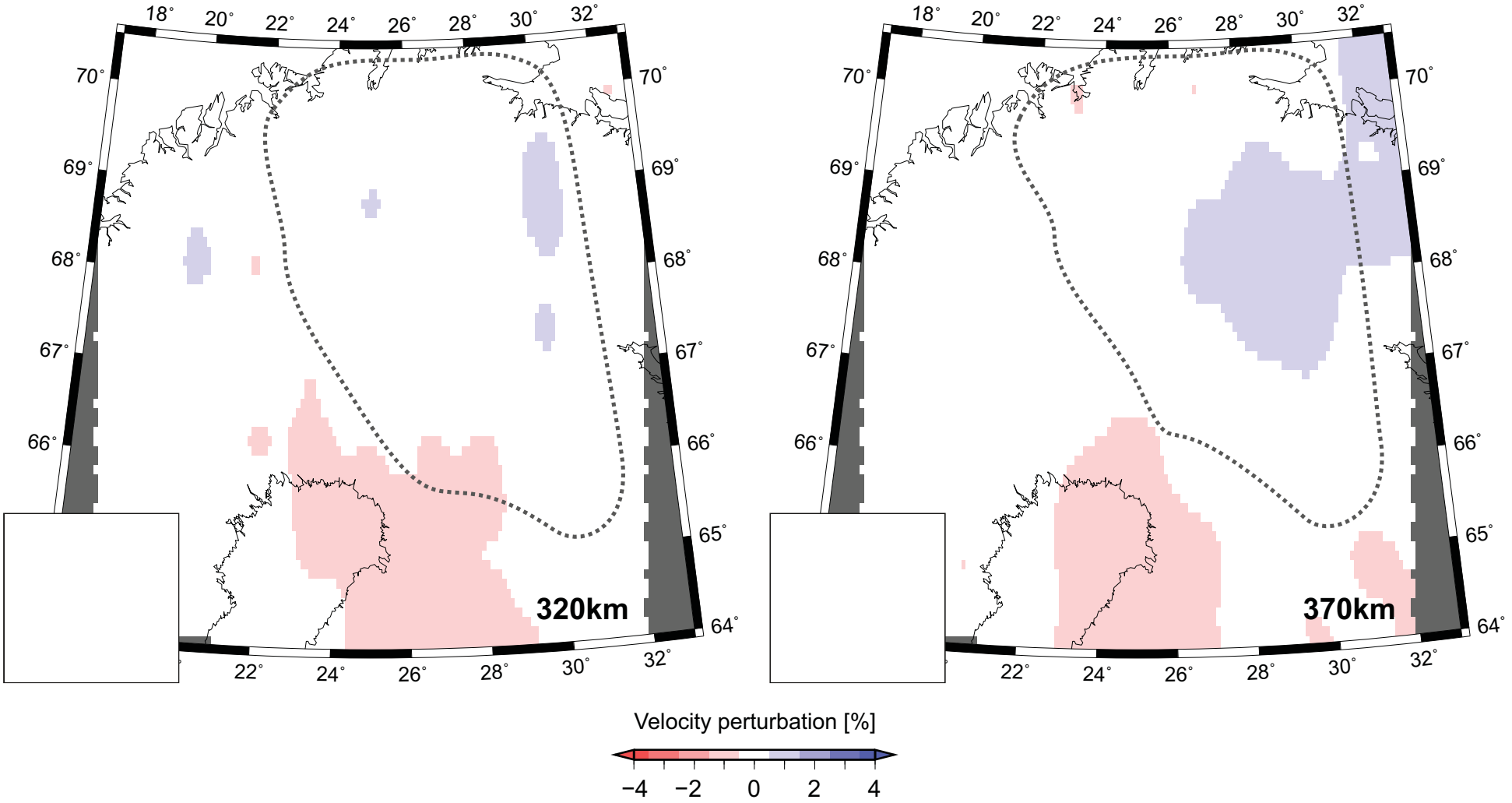

Figure S10. Continue

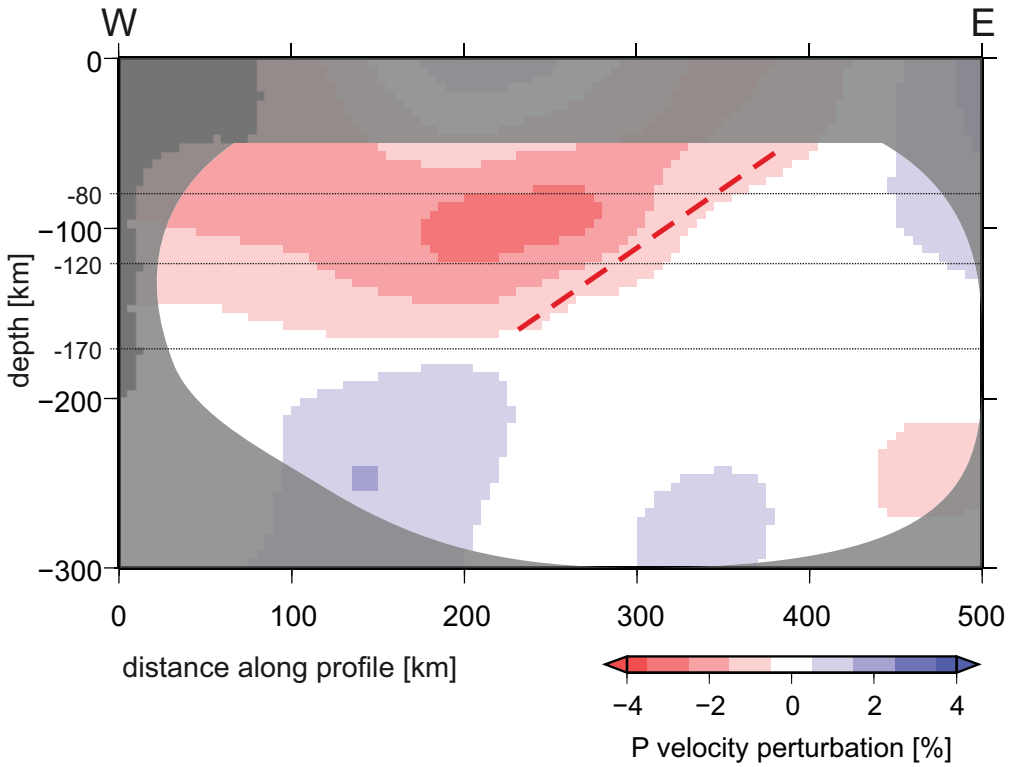

Figure S11. Vertical cross-section through the model of the isotropic-velocity perturbations from the coupled anisotropic-isotropic tomography along the 66°N latitude. Parts of the model with RDE < 0.5 and the depths corresponding to the crust are shaded. Red dashed line marks the westward dipping boundary of the relatively low-velocity perturbations dominating the western part of the model at depths of 80 km, 120 km and 170 km (see also Figs 6 and 7).

7. Concluding remarks

The motivation for this doctoral research was a widely spread detection of seismic anisotropy of the continental mantle lithosphere that called for a formulation of theory and development of a novel tomographic code that would allow for anisotropic velocities in the upper mantle considering a general orientation of the symmetry axes. In the Thesis, we formulate equations for the coupled anisotropic-isotropic tomography, perform various synthetic tests and apply the new code to data from northern Fennoscandia.

The **main outcomes** of our research, contributing to exploration of the heterogeneous and anisotropic Earth's upper mantle, are as follows:

1) Novel code AniTomo for coupled anisotropic-isotropic regional tomography. The code retrieves 3D heterogeneous weakly anisotropic velocity structure of the upper mantle by an iterative inversion of travel-time residuals of teleseismic P waves for parameters describing weak anisotropy with hexagonal symmetry with either the high-velocity *a* axis or the low-velocity *b* axis. The model parameters are perturbations of isotropic component of the anisotropic velocity, strength of anisotropy, and azimuth and inclination of the symmetry axis. Any of the four model parameters can be fixed during the inversion at any node of a parameterization grid. Our approach of searching for orientation of the symmetry axes freely in 3D is unique and more general in comparison with the published methods that usually assume only horizontal or vertical orientation of the high-velocity symmetry axis. The code represents a step further from modelling homogeneously anisotropic blocks of the mantle lithosphere (e.g., Plomerová *et al.* 2002; Vecsey *et al.* 2007; Plomerová *et al*. 2011) towards modelling anisotropy arbitrarily varying in 3D.

2) Illustrative documentation of convergence of the model parameters in dependence on the inversion setup. We carefully investigate and document with synthetics the influence of various parameters controlling the inversion. The tests confirm that well-tuned damping factors lead to a steady convergence of model parameters toward the correct solution. Regarding an initial model, series of inversions with systematically changing initial orientation of anisotropy reduces effects due to a subjective choice of the initial model and leads to a robust model of anisotropic velocities. In general, the synthetic tests are a powerful tool and should be routinely used to tune the setup of any inversion.

3) Synthetic tests focused on trade-off between anisotropy and isotropic heterogeneities. The synthetic tests confirm that code AniTomo can successfully distinguish between the isotropic and anisotropic components of the P-wave velocity. We show that the method does not create anisotropic artefacts when the target structure is purely isotropic. In the case of purely anisotropic structure, the situation is more complex and a part of the anisotropic velocity might be misinterpreted either as an isotropic component or as a localized and usually weaker anisotropy smeared into the isotropic part. Nevertheless, regions of distinct anisotropy and isotropic-velocity heterogeneities are identified correctly, which is a great benefit of the coupled anisotropic-isotropic inversion compared to a purely isotropic inversion that misinterprets the anisotropic signal completely.

4) Synthetic tests of a real station-event distribution. A high-quality dataset, in terms of precise measurements of travel-time residuals from a dense regional array of seismic stations and a broad range of event back-azimuths and epicentral distances, is of course, a prerequisite to obtain a reliable model of anisotropic velocities. As an example of a real case, we carefully investigate capability of the dataset from passive seismic experiment LAPNET to resolve large-scale anisotropic structures of the upper mantle. The investigation includes synthetic tests and a directional analysis of the ray paths, which allows us to limit the fully anisotropic inversion only to a well-resolved part of the volume studied.

5) Tomographic model of P-wave isotropic-velocity perturbations and velocity anisotropy of the upper mantle beneath northern Fennoscandia. For the first time, we apply novel code AniTomo to relative travel-time residuals of teleseismic P waves recorded during seismic experiment LAPNET in northern Fennoscandia. The largest velocity perturbations and the strongest anisotropy concentrate at the mantle-lithospheric depths, while deeper the lateral velocity variations decrease significantly. We identify regions of consistent anisotropy that probably reflects fossil fabric of individual blocks of the Archean mantle lithosphere.

6) Validation of the coupled anisotropic-isotropic tomographic model by independent inferences. The regions of consistent anisotropy derived from the tomography are compatible with the mantle-lithosphere domains delimited by joint investigations of path-integrated anisotropy from directional analysis of P-wave travel-time residuals and SKS-wave splitting parameters (Plomerová *et al.* 2011). The tomographic model provides us with a vertical resolution on top of that.

7) Example P spheres for various heterogeneous anisotropic structures of the upper mantle. The forward mode of code AniTomo enables evaluation of synthetic P-wave travel times. Therefore, it is now possible to compare directional terms of relative P-wave travel-time residuals observed at a station (P spheres) with those evaluated for a suggested model of anisotropic velocities. On a series of synthetic P spheres, we show how different anisotropic upper-mantle structures, e.g., a model of the Eger Rift and the adjacent tectonic units, influence directional terms of the P-wave travel-time residuals. Such comparisons validate interpretations of real data.

Outlook

After the first successful application of the novel coupled anisotropic-isotropic tomography code to a real LAPNET dataset, we will continue modelling the P-wave anisotropic velocities of the upper mantle also in other tectonic provinces, where sufficiently dense and large regional arrays of seismic stations have been deployed. We will concentrate particularly on the Bohemian Massif (BM), for which separate studies on seismic anisotropy and isotropic-velocity tomography have already been carried out from data of various passive seismic experiments covering the BM, e.g., BOHEMA (e.g., Plomerová *et al.* 2007; 2016; Karousová *et al.* 2012; 2013) or PASSEQ (e.g., Vecsey *et al.* 2014; Chyba *et al.* 2017). To improve resolution of the tomography images, the datasets of all the recent experiments will be merged. Currently, international co-operative experiment AlpArray covering the greater Alpine region and including a large part of the BM is in operation (e.g., Hetényi *et al.* 2018). Tomographic images from the novel AniTomo code will contribute to understanding the complex deep structure of the Alpine orogen.

Another possible future development of the anisotropic tomography is an inclusion of shear-wave data into the inversion. Shear waves can provide us with independent information on the upper-mantle structures as they have longer wavelengths, their propagations can broaden the range of incidence angles and they are sensitive to the elastic parameters in a different way compared to the P waves.

References

Chyba, J., Plomerová, J., Vecsey, L. & Munzarová, H., 2017. Tomography study of the upper mantle around the TESZ based on PASSEQ experiment data, *Phys. Earth planet. Inter.*, **266**, 29-38. doi.org/10.1016/j.pepi.2017.01.002

Hetényi, G., Molinari, I., Clinton, J., Bokelmann, G., Bondár, I., Crawford, W.C., Dessa, J.X., Doubre, C., Friederich, W., Fuchs, F., Giardini, D., Gráczer, Z., Handy, M.R., Herak, M., Jia, Y., Kissling, E., Kopp, H., Korn, M., Margheriti, L., Meier, T., Mucciarelli, M., Paul, A., Pesaresi, D., Piromallo, C., Plenefisch,

T., Plomerová, J., Ritter, J., Rümpker, G. Šipka, V., Spallarossa, D., Thomas, C., Tilmann, F., Wassermann, J., Weber, M., Wéber, Z., Wesztergom, V., Živčić, M., AlpArray Seismic Network Team, AlpArray OBS Cruise Crew &·AlpArray Working Group, 2018. The AlpArray Seismic Network – a large-scale European experiment to image the Alpine orogen, *Surv. Geoph.*, **39(5)**, 1009-1033. https://doi.org/10.1007/s10712-018-9472-4

Karousová, H., Plomerová, J., & Babuška, V., 2013. Upper-mantle structure beneath the southern Bohemian Massif and its surroundings imaged by high-resolution tomography, *Geophys. J. Int.*, **194**, 1203–1215, doi:10.1093/gji/ggt159.

Karousová, H., Plomerová, J. & Vecsey, L., 2012. Seismic tomography of the upper mantle beneath the north-eastern Bohemian Massif (central Europe), *Tectonophysics,* **564–565,** 1–11.

Plomerová, J., Achauer, U., Babuška, V. & Vecsey, L., 2007. Upper mantle beneath the Eger Rift (Central Europe): plume or asthenosphere upwelling?, *Geophys. J. Int.*, **169(2)**, 675-682.

Plomerová, J., Babuška, V., Vecsey, L., Kouba, D. & TOR working group, 2002. Seismic anisotropy of the lithosphere around the Trans-European Suture Zone (TESZ) based on teleseismic body-wave data of the Tor experiment, *Tectonophysics*, **360**, 89-114.

Plomerová, J., Munzarová, H., Vecsey, L., Kissling, E., Achauer, U. & Babuška, V., 2016. Cenozoic volcanism in the Bohemian Massif in the context of P-and S-velocity high-resolution teleseismic tomography of the upper mantle, *Geochem. Geophys. Geosyst.*, **17** (8), 3326–3349. http://dx.doi.org/10.1002/2016GC006318

Plomerová, J., Vecsey, L., Babuška, V. & LAPNET working group, 2011. Domains of Archean mantle lithosphere deciphered by seismic anisotropy – Inferences from the LAPNET array in northern Fennoscandia, *Solid Earth*, **2**, 303–313, doi:10.5194/se-2-303-2011.

Vecsey, L., Plomerová, J. & Babuška, V., 2014. Mantle lithosphere transition from the East European Craton to the Variscan Bohemian Massif imaged by shear-wave splitting, *Solid Earth*, **5**, 779–792.

Vecsey, L., Plomerová, J., Kozlovskaya, E. & Babuška, V., 2007. Shear-wave splitting as a diagnostic of varying upper mantle structure beneath south-eastern Fennoscandia, *Tectonophysics*, **438**, 57–77, doi:10.1016/j.tecto.2007.02.017.

List of publications

1) Publications forming the core of the Thesis

Chapter 5

Munzarová, H., Plomerová, J. & Kissling, E., 2018. Novel anisotropic teleseismic body-wave tomography code AniTomo to illuminate heterogeneous anisotropic upper mantle: Part I – Theory and inversion tuning with realistic synthetic data, *Geophys. J. Int.*, **215** (1), 524-545, doi:10.1093/gji/ggy296.

Chapter 6

Munzarová, H., Plomerová, J., Kissling, E., Vecsey, L. & Babuška, V., 2018. Novel anisotropic teleseismic body-wave tomography code AniTomo to illuminate heterogeneous anisotropic upper mantle: Part II - Application to data of passive seismic experiment LAPNET in northern Fennoscandia, *Geophys. J. Int.*, 215 (2), 1388-1409, doi:10.1093/gji/ggy327.

2) Publications supplementary to the subject

Supplement 1

Munzarová, H., Plomerová, J., Babuška, V. & Vecsey, L., 2013. Upper-mantle fabrics beneath the Northern Apennines revealed by seismic anisotropy, *Geochem. Geophys. Geosyst.*, **14**, 1156–1181, doi:10.1002/ggge.20092.

Supplement 2

Plomerová, J., **Munzarová, H.**, Vecsey, L., Kissling, E., Achauer, U. & Babuška, V., 2016. Cenozoic volcanism in the Bohemian Massif in the context of P-and S-velocity high-resolution teleseismic tomography of the upper mantle, *Geochem. Geophys. Geosyst.*, **17** (8), 3326–3349, doi:10.1002/2016GC006318.

Vecsey, L., Plomerová, J., Jedlička, P., **Munzarová, H.** & Babuška, V., 2017. Data quality control and tools in passive seismic experiments exemplified on the Czech broadband seismic pool MOBNET in the AlpArray collaborative project, *Geosci. Instrum. Method. Data Syst.*, **6**, 505-521, doi:10.5194/gi-6-505-2017.

Chyba, J., Plomerová, J., Vecsey, L. & **Munzarová, H.**, 2017. Tomography study of the upper mantle around the TESZ based on PASSEQ experiment data, *Phys. Earth Planet. Int.*, **266**, 29-38, doi:10.1016/j.pepi.2017.01.002.

Supplement 1

Upper-mantle fabrics beneath the Northern Apennines revealed by seismic anisotropy

Helena Munzarová[1], Jaroslava Plomerová[1], Vladislav Babuška[1], Luděk Vecsey[1]

Geochemistry, Geophysics, Geosystems, Volume **14**, Issue 4, April 2013, Pages 1156–1181, doi:10.1002/ggge.20092

[1] Institute of Geophysics, Academy of Sciences, Prague, Czech Republic

Geochemistry Geophysics Geosystems G3

Published by AGU and the Geochemical Society

Article
Volume 14, Number 4
29 April 2013
doi:10.1002/ggge.20092
ISSN: 1525-2027

Upper-mantle fabrics beneath the Northern Apennines revealed by seismic anisotropy

Helena Munzarová
Geophysical Institute, Academy of Sciences of the Czech Republic, Boční II/1401, 141 31 Prague 4 Czech Republic (helena@ig.cas.cz)

Department of Geophysics, Faculty of Mathematics and Physics, Charles University, Prague, Czech Republic

Jaroslava Plomerová, Vladislav Babuška, and Luděk Vecsey
Geophysical Institute, Academy of Sciences of the Czech Republic, Prague Czech Republic

[1] We image anisotropic structure of the upper mantle beneath the Northern Apennines based on body-wave data collected during the RETREAT experiment (2003–2006). Joint analysis of anisotropic parameters evaluated from independent data sets—teleseismic P-wave travel times and shear-wave splitting—allows us to identify regions of different fabrics both in the mantle lithosphere and in the sublithospheric mantle. We recognize three regions—the Tyrrhenian, Adriatic, and Transition—with their own anisotropic characteristics. The slab-parallel flow prevails in the sublithospheric mantle beneath the thin Tyrrhenian plate, while nearly slab-perpendicular orientation of the high velocities dominates on the Adriatic side of the region. The asthenospheric-flow pattern excludes a simple corner-flow model to fit the fabric of the upper mantle in the syn-convergent extensional tectonics and suggests the end of the subduction roll-back. We map fossil anisotropy with inclined symmetry axes within two domains of the thick continental Adriatic lithosphere. We estimate the lithosphere thickness of the Tyrrhenian and Adriatic plates at ~50 km and ~80 km, respectively, the latter being subducted down to no more than ~200 km with indications of inherited frozen-in anisotropic fabric. If a potential detachment at the northern end of the Apennine slab exists, then it would have to be narrow and in its initial stage. Synthetic tests of the well-known trade-off between isotropic heterogeneity and evaluated anisotropic parameters, along with combining independent data sets, document a sufficient separation of both effects.

Components: 14,900 words, 14 figures, 2 tables.

Keywords: body-wave anisotropy; Northern Apennines; upper mantle.

Index Terms: 8120 Tectonophysics: Dynamics of lithosphere and mantle: general (1213); 7203 Seismology: Body waves; 7240 Seismology: Subduction zones (1207, 1219, 1240).

Received 13 November 2012; **Revised** 8 February 2013; **Accepted** 9 February 2013; **Published** 29 April 2013.

Munzarová, H., J. Plomerová, V. Babuška, and L. Vecsey (2013), Upper-mantle fabrics beneath the Northern Apennines revealed by seismic anisotropy, *Geochem. Geophys. Geosyst.*, *14*, 1156–1181, doi:10.1002/ggge.20092.

Geochemistry Geophysics Geosystems G3 MUNZAROVÁ ET AL.: MANTLE FABRICS BENEATH THE N. APENNINES 10.1002/ggge.20092

1. Introduction

[2] The north-west/south-east trending Apennine orogenic belt, located in the central Mediterranean region, is separated into two geodynamical different arcs—the Northern Apennine (NA) arc and the arc-shaped region beginning in the Southern Apennines, continuing to the Calabrian Arc and ending in Sicily (Figure 1). The Calabrian Arc exhibits characteristics of an active subduction zone, e.g., the volcanism in Aeolian Islands and seismicity down to several hundreds of kilometers, while none of these two features is present in the NA. In comparison with the southern part, there is only shallow seismicity possibly related to an eastward retreating subduction zone beneath the NA [e.g., *Malinverno and Ryan*, 1986; *Chiarabba et al.*, 2005; *Pondrelli et al.*, 2006]. Different geodynamic development of the two tectonic arcs of the Apennine belt is also evident in GPS measurements [e.g., *Serpelloni et al.*, 2005]. While Sicily and southern Italy move northward at speed as much as 10 mm/yr, the velocities of the northern part of Italy are one order smaller or even statistically insignificant [*Oldow et al.*, 2002].

[3] The Apennine mountain belt started developing in the Late Cretaceous due to slow collision of the African and European plates [*Stampfli and Borel*, 2002]. The collision led to westward subductions of the Adriatic and Ionian microplates beneath the European plate [*Dewey et al.*, 1989; *Doglioni*, 1991; *Rosenbaum and Lister*, 2004; *Vignaroli et al.*, 2008; *Handy et al.*, 2010]. It is estimated that rates as large as 5 cm/yr occurred in the Apennine convergence zone in isolated periods during the last 30 My [*Faccenna et al.*, 2003]. Evolution of the region was controlled by processes of syn-convergent extension related to a roll-back of the Adriatic slab and extension of the Tyrrhenian back-arc basin. As a consequence of these processes, an eastward retreat of the subducting slab started to form the geometry of the Apennine trench in the Late Miocene. The Apennine orogeny was thus moved to its present-day position, i.e., the north-west/south-east orientation.

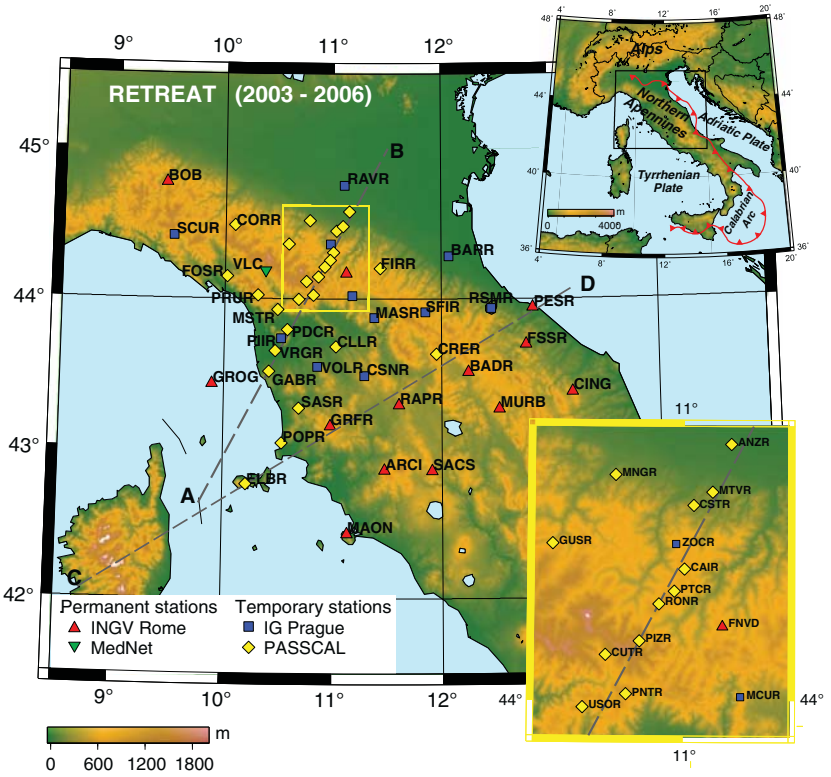

Figure 1. Map of the RETREAT array along with the main thrust front in the Italian peninsula associated with the convergence of the Adriatic and Tyrrhenian plates (red curve; upper right inset). Region of the RETREAT experiment is marked. Lower right inset: a detailed map of densely deployed stations (yellow rectangle).

Geochemistry Geophysics Geosystems G3 MUNZAROVÁ ET AL.: MANTLE FABRICS BENEATH THE N. APENNINES 10.1002/ggge.20092

Serpelloni et al. [2005] estimate the present-day convergent movement in the NA of less than 1 mm/yr. According to *Wortel and Spakman* [2000], such low rates might indicate either that the subduction stopped there, or that some portions of the Apennine slab begun to detach from the surface plate. The end of subduction in the NA is also inferred from observations of quasi-Love (QL) waves from the great 2004 Sumatra-Andaman earthquake [*Levin et al*., 2007] and the recent teleseismic tomography of *Benoit et al*. [2011].

[4] To bring new information on the lithosphere-asthenosphere structure beneath the NA and on tectonic development of the region, international multidisciplinary project RETREAT was organized between 2003 and 2006 [*Margheriti et al*., 2006]. The RETREAT project aimed at developing a self-consistent dynamic model of the syn-convergent-extension in the NA. Results of seismological investigations indicated significant lateral differences in the upper-mantle structure (for a review, see http://www.rci.rutgers.edu/~vlevin/vadims-research/RETREAT-research.html). Studies of seismic anisotropy that constitute a strong research component of the project clearly identified different structures of the upper mantle on the opposite sides of the Apennines [*Plomerová et al*., 2006; *Salimbeni et al*., 2008]. Measurements along the NA Profile passive experiment (NAP) show orogen-parallel polarizations of the fast split shear waves in the mountain crest, on average, that tend to change to orogen-normal further south-west in the Tyrrhenian zone [*Margheriti et al*., 1996]. Such results could imply a 2D orogen-parallel sublithospheric flow beneath the Adriatic plate due to the slab roll-back and orogen-normal flow beneath the Tyrrhenian plate associated with the extension in the back-arc basin [*Park and Levin*, 2002]. However, results of the shear-wave splitting from the RETREAT data in an area northward of the NAP profile indicate more complex structures beneath the NA [*Plomerová et al*., 2006; *Salimbeni et al*., 2008]. Geographical variations of polarization azimuths both in the Adriatic and Tyrrhenian plates along with a convincing dependence on back-azimuth do not permit the simple explanation of the observed anisotropy exclusively by the mantle flow. The authors relate the variations of shear-wave splitting also to a fossil anisotropy in the mantle lithosphere with generally inclined symmetry axes, or to a combination of both the effects.

[5] Though the splitting of teleseismic shear waves clearly evidences anisotropic structure of the upper mantle, complementary information on the upper-mantle fabrics can be exploited from variations of directional terms of relative P-wave travel-time residuals [e.g., *Babuška and Plomerová*, 1992]. P waves illuminate the upper-mantle volume at broader fans of incidences and azimuths than core-mantle refracted shear waves (SKS), which allows us to retrieve orientation of symmetry axes more reliably. Particularly anisotropy with symmetry axes of inclination between 30º and 60º is usually explicitly manifested in the so-called "bipolar" pattern of directional variations of P-wave travel-time residuals at a station [*Babuška et al*., 1993]. Due to their shorter wavelength in comparison with shear waves, the P waves also can detect boundaries of the mantle lithosphere domains with different fabrics in a greater detail than shear waves [*Plomerová et al*., 2011].

[6] Several tomographic models of velocity perturbations in the upper mantle beneath the NA image the steeply inclined Adriatic slab [e.g., *Amato et al*., 1993; *Babuška and Plomerová*, 1990; *Lucente et al*., 1999; *Piromallo and Morelli*, 2003; *Spakman and Wortel*, 2004; *Cimini and Marchetti*, 2006; *Koulakov et al*., 2009; *Benoit et al*., 2011] The slab represents a high-velocity subvertical heterogeneity which contributes to the directional variations of the P-wave travel-time residuals and thus might complicate the interpretation of regional changes in patterns of directional terms of relative P residuals. On the other hand, neglecting anisotropic propagation in isotropic tomography might cause misinterpretations of parts of the travel-time residuals generated by anisotropic structures. Therefore, we try to carefully consider the well-known effects related to the trade-off between anisotropy and velocity heterogeneities.

[7] This paper is a follow-up of *Plomerová et al*. [2006] where the results of P-wave travel-time residuals from several regional arrays and from the national network in Italy [*Plomerová*, 1997] were summarized and where the shear-wave splitting parameters evaluated from data collected during the initial stage of the RETREAT experiment were analyzed. Our aim is to present a more detailed image of anisotropic structure of the lithosphere and the sublithospheric mantle beneath the NA based on an enhanced set of body-wave data collected during the RETREAT experiment. We jointly analyzed P-wave velocity variations and shear-wave splitting and discuss the effects caused by seismic anisotropy and heterogeneity. The joint interpretation of body-wave anisotropic parameters allows us to image individual domains of the mantle lithosphere characterized by their own fabrics generally oriented in 3D. We discuss our results in the context of the up-to-date published

Geochemistry Geophysics Geosystems G3 MUNZAROVÁ ET AL.: MANTLE FABRICS BENEATH THE N. APENNINES 10.1002/ggge.20092

results on the crustal structure [*Di Stefano et al*., 2011], the isotropic tomography [*Benoit et al*., 2011], and other recent findings on the large-scale tectonics of the region [*Levin et al*., 2007; *Salimbeni et al*., 2008; *Piccinini et al*., 2010; *Miller and Piana Agostinetti*, 2012].

2. Data and Methods

[8] Permanent stations of the Italian National Network (INGV Roma) and a MedNet station (VLC) together with 10 temporary stations from the Institute of Geophysics of the Czech Academy of Sciences (IG Prague) formed a backbone of the RETREAT array during its three-year operation. Additional 25 stations of the IRIS PASSCAL Instrument Center were installed on a profile perpendicular to the NA mountain belt. In total, 50 stations (Table S1, Supporting Information)[1] provided data for the passive seismic experiment oriented towards studying the upper-mantle structure [*Plomerová et al*., 2006; *Margheriti et al*., 2006].

[9] Propagation of both shear and longitudinal (P) waves are affected by anisotropic structures of the upper mantle. In the case of P waves, large-scale anisotropy in the upper mantle is well expressed in patterns of P-residual spheres showing azimuth-incidence angle-dependent terms of relative residuals at individual stations [e.g., *Babuška et al*., 1993]. Polarizations of the fast split-shear waves and delay times of the slow split waves measure orientation and strength of anisotropy. Joint interpretation of the shear-wave splitting parameters and directional terms of P-wave travel-time residuals allows us to infer 3D self-consistent anisotropic models of the upper mantle [*Šílený and Plomerová*, 1996].

[10] To analyze directional dependences of P-wave travel-time residuals at individual stations [e.g., *Babuška et al*., 1992], we measured arrival times of teleseismic P waves from epicentral distances between 20° and 100°. We picked the P-wave arrival times on recordings from the RETREAT event-oriented database sampled with 20 Hz. To gain as much as possible arrival-time measurements at highest accuracy (+/− 0.05 s) and to process huge amount of seismograms effectively, first we tested on a subset of seismograms arrival times measured manually with three semi-automatic pickers [*Munzarová*, 2011]. A picker developed by F.P. Lucente and D. Piccinini (personal communication within the RETREAT-experiment cooperation) and another one based on the adaptive-stacking method designed by *Rawlinson and Kennett* [2004] were found unsatisfactory for the RETREAT data. Therefore, a new semi-automatic picking procedure based on Seismic Handler software by *Stammler* [1993] complemented with several shell scripts [*L. Vecsey*, personal communication] was finally assessed to be the most precise and reliable of the tested pickers.

[11] High accuracy of the measurements was reached by a new two-step picking procedure, in which: (1) a selected part of a reference P-wave seismogram (Figure S3a, Supporting Information) is automatically cross-correlated with the waveforms at other stations in order to find time differences between them. Then, the traces are shifted to become aligned (Figure S3b, Supporting Information); (2) in an arbitrary seismogram, we select a distinct extreme which can be traced across all the waveforms and which is the closest to the first P-wave onset. Time of this extreme, called the relative P-wave arrival time, is then automatically picked in all seismograms of the event (Figure S3c, Supporting Information). We also measure the absolute arrival time for each event on at least one seismogram, where the first onset is clear. Then, we recalculate the absolute arrival times from the relative ones at all stations.

[12] We measured P-wave arrival times on recordings of 312 teleseismic events (see upper right inset of Figure 2 and Table S2, Supporting Information), which provided 7378 measurements at individual stations. Total number of measurements gives us also an estimate of approximately 150 arrival times per station on average. Station SFIR exhibits the highest number of 302 observations for a single station. We checked the time stability of the travel-time residuals computed according to radial reference Earth model IASP91 [*Kennett*, 1991] (the so-called absolute residuals) to prevent including incorrect data due to technical problems at some stations, e.g., due to temporary failure of time synchronization.

[13] As our study is focused on the upper-mantle structure, we corrected the P-wave travel times for effects originated in the crust with the use of *Di Stefano et al*. [2011] crustal model. For stations located above the transition between the thin Tyrrhenian and thick Adriatic lithosphere [see also *Bianchi et al*., 2010], where a distinct step in Moho depths of about 20 km exists, we considered azimuths of arriving waves and applied appropriate corrections according to the two different crusts. Effects originated outside the volume studied, e.g., due to foci

[1] Additional supporting information may be found in the online version of this article.

Geochemistry Geophysics Geosystems G3 MUNZAROVÁ ET AL.: MANTLE FABRICS BENEATH THE N. APENNINES 10.1002/ggge.20092

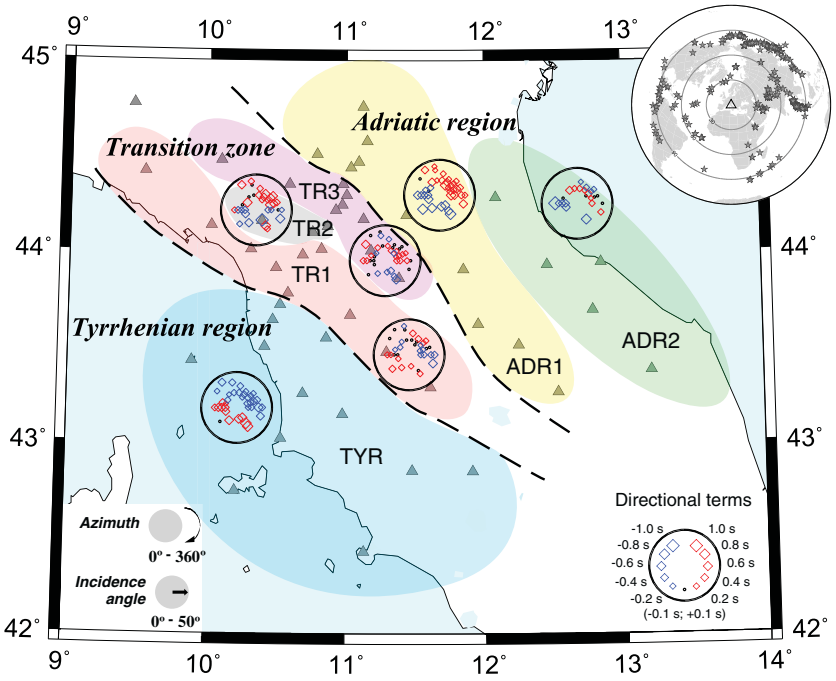

Figure 2. Six regions defined according to the similarity of the P-sphere patterns at individual stations (see Figure S4, Supporting Information). Each subregion is characterized by an average P sphere (lower-hemisphere stereographic projection of average directional terms—azimuth-incidence angle-dependent terms). Each of the directional terms of the P sphere is calculated as an average from appropriate directional terms at all stations (gray triangles) in the corresponding subregion. The boundaries between the Tyrrhenian region, the Transition zone, and the Adriatic region are marked with black dashed lines. Upper right inset: locations of 312 teleseismic earthquakes used in the P-wave study.

mislocations, source-region structures, or reflecting heterogeneities along deep-mantle paths, are minimized by calculating relative residuals. An event mean calculated from residuals of all stations which recorded the event was subtracted from individual measurements. The procedure allows us to separate the relative travel-time residuals into a station directional mean, i.e., an average of relative residuals at a station, and into directional terms, which represent azimuth-incidence angle-dependent components of the relative residuals [e.g., *Babuška and Plomerová*, 1992]. Data binning according to source regions is used to balance uneven foci distribution (see upper right inset of Figure 2). The directional terms at a station are visualized in the lower hemisphere stereographic projection as a function of azimuth, from 0° to 360°, and angle of propagation within the mantle lithosphere—from 15° and 45° measured from vertical, called "P spheres" (see lower right inset of Figure 2). Positive directional terms, i.e., delayed arrivals relative to the station directional mean, indicate low-velocity directions, while negative values, relatively early arrivals, signify high-velocity directions beneath a station.

[14] To better constrain the well-known trade-off between the effects of anisotropy and heterogeneities in P-wave propagation, we also analyze results of shear-wave splitting [*Plomerová et al.*, 2006; *Salimbeni et al.*, 2008], which is considered as indisputable evidence of anisotropy. Shear waves entering an anisotropic medium split into two quasi-shear waves, each propagating with a different velocity and with mutually perpendicular polarizations. *Salimbeni et al.* [2008] studied splitting of the core-mantle refracted shear waves (SKS), i.e., the delay times between the fast and slow split waves and the polarization directions of the fast waves, for 27 teleseismic earthquakes recorded during the RETREAT experiment (see upper right inset of Figure 4). For each station-event pair, they determined the splitting parameters according to the method of minimizing energy on the transverse component [*Vecsey et al.*, 2008], using computer code SPLITshear available at http://www.ig.cas.cz/en/personal-pages/ludek-vecsey/split. The method used is a 3D modification of procedure designed by *Silver and Chan* [1991]. The splitting parameters—the fast polarization directions ψ and split

Geochemistry Geophysics Geosystems G3 MUNZAROVÁ ET AL.: MANTLE FABRICS BENEATH THE N. APENNINES 10.1002/ggge.20092

delay time δt—are sought in the LQT ray-parameter coordinate system in the modified version.

[15] We search for individual groups of stations characterized by similar patterns of the P spheres and/or exhibiting similar variations of the SKS splitting parameters with back-azimuth, which indicates regions with similar structure of the upper mantle. Sharp changes of the P-sphere patterns and the shear-wave splitting parameters mark boundaries of domains with consistent fossil anisotropy in the mantle lithosphere. Anisotropy related to a present-day flow in the sublithospheric upper mantle usually relates to large regions and changes are smooth.

[16] Stations with similar P-sphere pattern approximately delimit a lateral extent of the upper-mantle domains with consistent anisotropy. To estimate thickness of the mantle lithosphere, we employ, with some modifications, the method of evaluating the lithosphere-asthenosphere boundary (LAB) depths beneath the stations from static terms of relative P-wave travel-time residuals in central Europe [*Babuška and Plomerová*, 1992]. There, the static terms are calculated from steep waves approaching a station from all back-azimuth ranges. However, having in mind the Adriatic subduction, we modified the method and separated waves approaching the stations into two azimuthal segments (from −45° to 135°; and from 135° to 315°). The separation of the azimuthal segments is governed by a strike of ~135° of the NA mountain range. We model the LAB relief according to the empirical residual-depth relation with a gradient of 9.4 km/0.1 s [*Babuška and Plomerová*, 1992]. A reference level for the residual-depth estimates is set by linking the RETREAT relative residuals with the European and Italian data sets [*Plomerová and Babuška*, 2010]. We plot the LAB depths at piercing points of the rays and the LAB boundary.

3. Results

3.1. Directional Dependence of P-wave Travel-time Residuals

[17] Areas with consistent P-sphere patterns at stations deployed in different tectonic settings indicate uniform anisotropic structures in a volume of the upper mantle beneath the stations [e.g., *Babuška and Plomerová*, 2006]. Stations with similar P-sphere patterns form groups in the NA region and divide it into three major parts—the Tyrrhenian and the Adriatic, and a Transition zone in between—and into six subregions altogether (Figure 2 and Figure S4, Supporting Information). In order to demonstrate characteristic P-sphere patterns, we show an average P sphere for each subregion (Figure 2) where each directional term is calculated as an average of respective directional terms from all stations in a subregion. P spheres of individual stations are shown in Figure S4 (Supporting Information) of the electronic supplement.

[18] Waves arriving to the stations in the Tyrrhenian region (TYR) from the south-west are delayed (positive terms, red diamonds in Figure 2) relatively to a directional mean at the station, while waves coming from the north-east arrive earlier (negative terms, blue diamonds). Such a type of P-sphere pattern—one half positive and the other negative—is called a "bipolar pattern" [e.g., *Babuška and Plomerová*, 1992].

[19] Stations east of the NA crest, in the Adriatic region (ADR), exhibit characteristic bipolar P pattern, but reversed in comparison with the TYR pattern (Figure 2 and Figure S4, Supporting Information). The ADR region can be divided into two subregions (ADR1 and ADR2), which slightly differ for waves propagating from the north-east—positive terms dominate in the ADR1 subregion for all angles of incidence, while negative directional terms (faster directions) occur at shallow angles in the ADR2.

[20] Approximately a half of the RETREAT stations were located in the NA mountain range, above the Tyrrhenian- and Adriatic-plate contact. Abrupt changes of the P patterns at these stations relative to the TYR and ADR regions delimit the Transition zone (TR). Additional changes of the P-sphere patterns in the TR allowed us to divide the zone into three subregions (TR1, TR2, and TR3 in Figure 2). The directional terms of waves arriving from south-west and north-east azimuths at shallow angles are positive at stations of the TR1 group thus indicating relatively low-velocity directions, while negative terms (relatively high-velocity directions) are evaluated for the north-west and south-east azimuths, regardless of incidences. The TR3 pattern tends to be a reversed TR1 pattern, and absolute values of the directional terms in both the TR1 and TR3 regions are lower than that in the small region TR2 (Figure 2 and Figure S4, Supporting Information) which contains only three stations. Their P patterns, with larger values, tend to the bipolar ADR1 pattern. The TR2 thus seems to form a separate region within the heterogeneous TR. In comparison with the consistent P patterns in the TYR and ADR regions, the P pattern above the

Geochemistry Geophysics Geosystems G3 MUNZAROVÁ ET AL.: MANTLE FABRICS BENEATH THE N. APENNINES 10.1002/ggge.20092

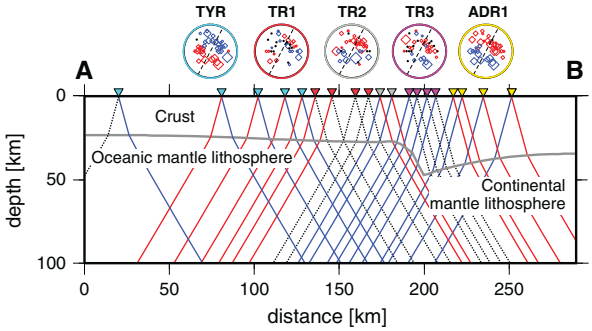

Figure 3. Vertical cross section along profile AB (see Figure 1 for its location) with the P spheres representing each subregion along the profile and with schematic rays of the P waves to the stations from epicentral distances of 60°. The stations along the profile (triangles) are colored according to the corresponding subregions (see Figure 2). Thickness of the crust is according to *Di Stefano et al*. [2011]. Colors of the rays in the cross section represent values of the directional terms (blue - negative; red - positive; dotted black - close to zero) at stations from the opposite directions along the profile (orientation of the profile is marked in the P spheres by dashed lines).

transition of both plates is less consistent internally (see Figure S4, Supporting Information). However, we admit that the P pattern of the TR region reflects a complex structure of the contact of the Tyrrhenian and Adriatic crusts, and the applied crustal corrections can hardly eliminate all effects of the real structure of the crust.

[21] To show clearly lateral changes of the P-sphere patterns at densely spaced stations located along profile AB crossing the NA (see Figure 1), we plot a vertical cross section down to a depth of ~100 km (Figure 3). The P spheres represent each subregion along the profile. To what extent this overall P-velocity pattern reflects anisotropy of the lithosphere-asthenosphere system, or, is affected by the subducted slab or inaccuracies of the crustal model, will be discussed in Chapter 4.

3.2. Regional and Directional Variations of SKS Splitting Parameters

[22] As the shear-wave splitting is considered as an indisputable proof of anisotropy, we also analyze characteristic features of SKS splitting parameters evaluated by *Salimbeni et al*. [2008] from the RETREAT station seismograms in combination with the P-wave travel-time residuals that form the core data in this paper. The SKS splitting parameters were evaluated by the method of minimizing energy on the transverse component [*Silver and Chan*, 1991; *Vecsey et al*., 2008]. We plot the fast shear-wave polarization azimuths and split delay times in piercing points at depth of 80 km (Figure 4) as main sources of the anisotropy are in the upper mantle, and we expect its lateral changes around this depth. We examine the geographical distribution of the splitting parameters and how much they vary with back-azimuth at individual stations. For that purpose, we plot the splitting parameters in different colors assigned according to their back-azimuth [see also *Plomerová* et al., 2006].

[23] Considering the fast shear-wave polarization azimuths, the whole area of the RETREAT experiment can be roughly divided into two main regions: the Tyrrhenian and the Adriatic (see the black dashed line in Figure 4). The TYR is characterized by highly consistent polarization azimuths regardless of back-azimuths of the steeply incident SKS waves. Polarizations in the ADR exhibit both a distinct dependence on back-azimuth and different regional characteristics, according to which *Plomerová et al*. [2006] delimited three additional subregions in the Adriatic plate (dotted black curves in Figure 4). Clustering the stations with similar splitting parameters leads to regionalization of the NA area into regions which differ, at a first glance, from the six subregions identified in compliance with the P-residual analysis (Figure 2).

[24] To appraise variability of polarization azimuths at individual regions, we plot rose diagrams, which illustrate a frequency of occurrence of the fast shear-wave polarization azimuths in 18° wide fans. First, we plot the diagrams for the six subregions delimited according to the P-sphere patterns (Figure 5). To emphasize the azimuthal dependence of the splitting parameters, we consider the full azimuth range, i.e., the φ from 0° to 360° (retrieved from the polarization directions ψ in the LQT ray-parameter system) and plot rose diagrams of the fast shear-wave polarization azimuths for the south-western back-azimuths (from 135° to 315°) separately from those

Geochemistry Geophysics Geosystems G3

10.1002/ggge.20092

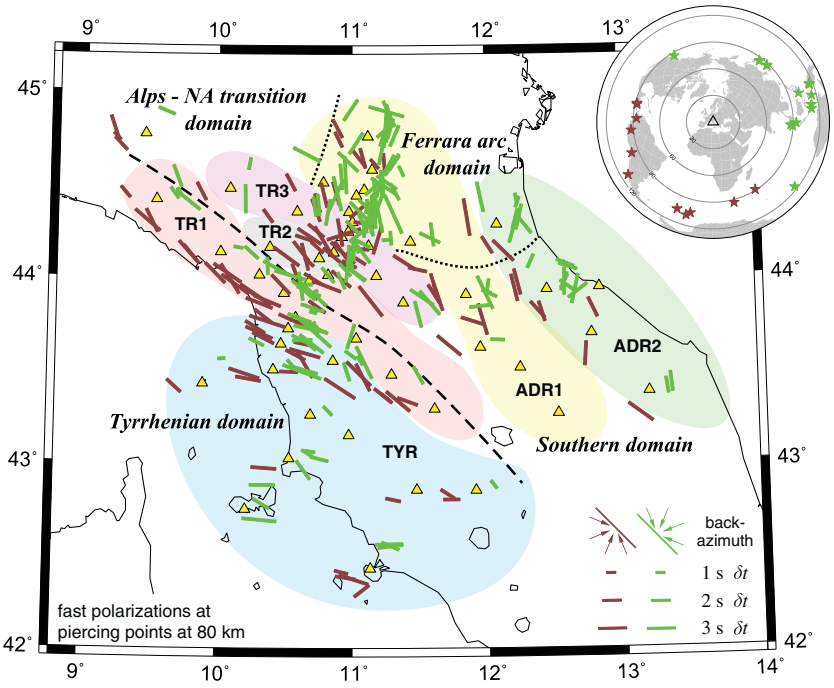

Figure 4. Shear-wave splitting parameters (fast S polarization azimuth φ and split delay time δt; *Salimbeni et al.* [2008]) plotted separately for the north-eastern (green - back-azimuth in a range from −45° to 135°) and the south-western (brown - back-azimuth in a range from 135° to 315°) back-azimuths. Individual measurements are represented by a bar oriented in the fast-polarization azimuth and scaled with the delay time. The measurements are projected into piercing points at a depth of 80 km. Six subregions delimited according to similarity of the P-sphere patterns (see Figure 2) are colored. The black dashed and dotted lines separate regions with different characteristics of the shear-wave splitting parameters (see also *Plomerová et al.* [2006]). Yellow triangles stand for stations. Upper-right inset: locations of 27 teleseismic earthquakes used for evaluation of SKS splitting parameters by *Salimbeni et al.* [2008] distinguished with color according to their back-azimuth.

for the north-eastern back-azimuths (from −45° to 135°). Such separation of the polarization azimuth is related to the strike of the subduction zone beneath the NA (see also Figure 4). To be compatible with the commonly used presentations and to emphasize differences in the variations of the splitting azimuths, we also present the opposite azimuths in the rose diagrams (light colors). Behavior of the polarizations indicates a complex anisotropic structure of the upper mantle beneath the NA region (Figure 5). We observe both distinct regional variations of the polarization azimuths and different characteristics of the back-azimuth dependences in individual subregions.

[25] There is only a weak dependence on back-azimuth in the westernmost region (TYR). The fast S polarization azimuths are almost independent of the two back-azimuth intervals, (left and right columns in Figure 5). Further to the north-east, in the TR1 region, the rose diagram for the north-eastern back-azimuths splits into two dominant polarizations. One of them coincides with the dominant polarizations in the rose diagram for the south-western back-azimuths, which are slightly clockwise rotated relative to the TYR region. The TR2 region contains only few data, but with the same trend. The back-azimuth dependence of polarizations becomes significant in the diagrams of the TR3, ADR1, and ADR2 subregions, in which the distinct polarization azimuths for the waves coming from the north-east do not correspond to the most frequent polarization azimuths for the south-west (Figure 5). Moreover, moving from the Tyrrhenian coast through the TR to the Adriatic coast, a general clock-wise rotation of the polarization azimuths is observed (Figures 4 and 5).

[26] Particularly, the diffuse pattern of the fast S polarizations in the ADR1 for waves from the north-east led us to regroup the splitting parameters in accordance with the clustering introduced by *Plomerová et al.* [2006]. According to the geographical variations of the shear-wave splitting parameters, the authors identified the Tyrrhenian domain and three subregions in the ADR—the Southern domain of the NA (SD),

Geochemistry Geophysics Geosystems G3 MUNZAROVÁ ET AL.: MANTLE FABRICS BENEATH THE N. APENNINES 10.1002/ggge.20092

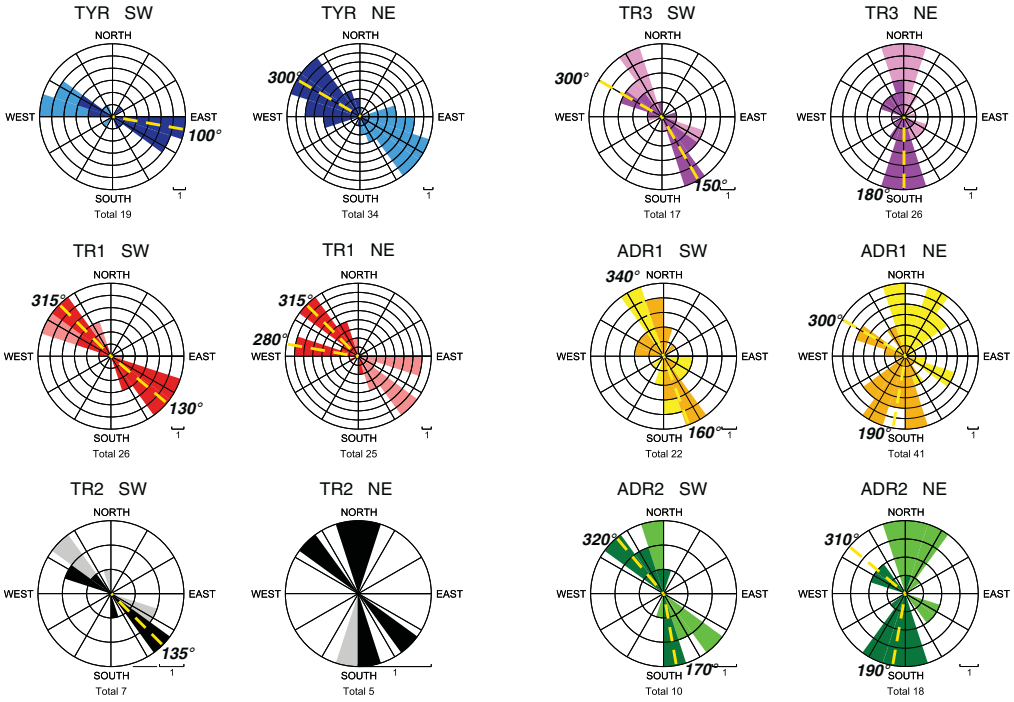

Figure 5. Rose diagrams of the fast shear-wave polarization azimuths φ (dark colors - azimuths recalculated from down-oriented angle ψ in the LQT coordinate system [*Vecsey et al*., 2007]) at subregions delimited according to the P-sphere patterns for the south-western back-azimuths (SW, from 135° to 315°, left diagrams) and for the north-eastern back-azimuths (NE, from −45° to 135°, right diagrams). Opposite polarization azimuths are shown in light colors. Scale in the bottom right part of each diagram shows the radius scale of one measurement. The most frequent polarization azimuths (yellow dashed lines) and total number of measurements for each diagram are given. Colors of the diagrams follow the colors of respective subregions as they have been introduced in Figure 2.

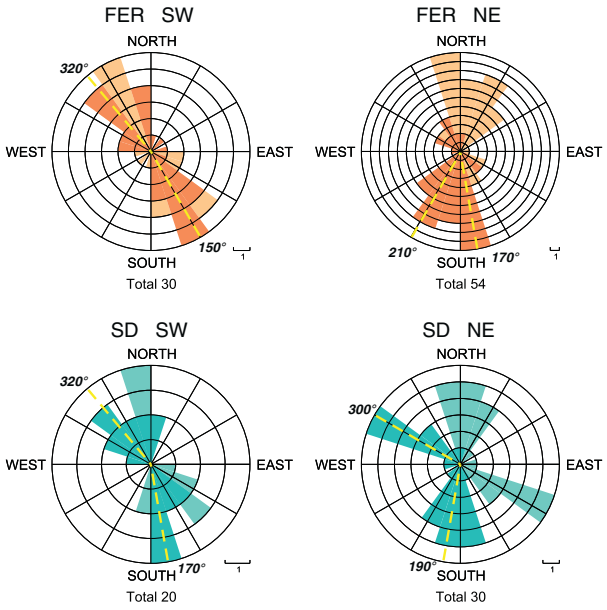

Figure 6. Rose diagrams of the fast shear-wave polarization azimuths for clusters of stations in the Adriatic region regrouped according to *Plomerová et al*. [2006] shown separately for the south-western, resp. north-eastern, back-azimuths (left, resp. right, diagrams). FER - Ferrara arc domain, SD - Southern domain of the Northern Apennines. For more details, see also caption of Figure 5.

Geochemistry Geophysics Geosystems G3 MUNZAROVÁ ET AL.: MANTLE FABRICS BENEATH THE N. APENNINES 10.1002/ggge.20092

the Ferrara arc domain (FER) in the central part of the region, and the Alps-Apennines Transition domain in the north characterized with null splitting (see limits of these regions in Figure 4). We regrouped the stations in the ADR1, ADR2, and a part of the TR3 regions similarly to that and searched whether the new rose diagrams differ distinctly for the FER and SD regions (Figure 6). Indeed, the shear-wave polarization azimuths differ, both regionally and in their back-azimuth dependences. Two components of the anisotropic signal are clearly evident, particularly in the SD domain. The north-south component of the apparent fast polarizations occurs in both regions (FER, SD) with only a weak back-azimuth dependence in FER (see Figure 6). On the other hand, the second component in the diagrams differs substantially in both regions. Polarizations at ~300° prevail in the SD domain, while the second component in the FER rose diagram is perpendicular (~210°) to that direction. Distinct back-azimuth variations of the polarizations in the ADR indicate non-negligible contributions reflecting anisotropy of individual domains comprising the continental Adriatic mantle lithosphere. The observed apparent upper-mantle anisotropy thus likely consists of an anisotropic signal from the mantle lithosphere superimposed on an anisotropic signal related to a sublithospheric mantle flow.

[27] With the use of the standard double-layer formula of *Savage and Silver* [1993] for fitting back-azimuth variations of the apparent polarizations of SKS phases, we grid searched for a double-layer model by varying azimuths $\varphi_{1,2}$ of horizontal fast symmetry axes $\boldsymbol{a}$ and time delays $\delta t_{1,2}$ for the lower and upper layer, respectively. The main task was to fit the rose diagrams of the FER and SD regions for the polarization azimuths of waves propagating through the Adriatic plate domains (see Figure 6). We show results of the modeling for waves from the north-eastern back-azimuths (7), for which the propagations are not affected by structure of the subducting slab. The solution is not unique. The two components to the apparent anisotropic signal in the FER and SD subregions can be simulated best by about three four models of two anisotropic layers (Table 1 and Figure 7). The best solution for the FER region was obtained for the high velocities in azimuths of 80° and 20° and in the SD region in 60° and 0° for the lower and upper layer, respectively. Three of the four suitable models for the FER subregion require larger contributions from the lower layer than from the upper, which means either a thicker lower layer or a stronger anisotropy, or both. The preferable model for FER (Table 1, in bold) with $\delta t_2 = 0.6$ s is compatible with ~5 % anisotropy of the mantle lithosphere and a thickness of ~50 km [*Silver*, 1996]. In the SD region, the synthetic polarizations are less scattered, but fitting the two components of the observed polarizations is more difficult. The north-western polarizations prevail in the observed diagrams, while the northward polarizations dominate in the synthetics calculated for the same set of waves.

3.3. Comparison of Observed and Synthetic P-residual Spheres Generated for Isotropic Tomography to Evaluate Effects of Subducted Slab on the Directional Dependence of Relative P Residuals

[28] The NA lie in an active tectonic region of the subducted Adriatic plate and assumed retreating trench accompanied by horizontal flows in the sublithospheric mantle [e.g., *Margheriti et al*., 2003]. Both the upper-mantle anisotropy and velocity heterogeneities, manifested mainly by the subduction, affect propagation of seismic waves. Standard methods of imaging velocities or velocity perturbations in the upper mantle consider only isotropic propagations. It is generally accepted that velocity perturbations due to heterogeneities and due to anisotropy are comparable in their amplitudes, though difficult to separate. However, neglecting anisotropy can cause false or distorted artifacts in the isotropic tomography, e.g., wrong amplitudes of heterogeneities, or, false heterogeneities [*Eken et al*., 2012]. On the other hand, also the P-residual spheres, which bear information about anisotropy, might be affected by uncorrected heterogeneities.

[29] To estimate possible effects of the major velocity heterogeneity in the upper mantle beneath the NA on the directional terms in the P spheres, we computed synthetic travel times for P waves with event-station locations of our measurements propagating through the recent tomographic model of the subducted Adriatic slab by *Benoit et al*. [2011]. Comparison of the synthetic directional terms plotted in the P spheres (Figure 8 and Figure S5, Supporting Information) with the observed P spheres (Figure 2 and Figure S4, Supporting Information) reveals significant differences in the geographical distribution of the P-sphere patterns from both methods. The spheres differ both in the distribution pattern of the negative and positive terms, as well as in their absolute values.

[30] According to the distribution of the P-wave directional terms in the synthetic P spheres, the stations form only two distinct groups, each of them with its own "synthetic" P pattern (Figure 8 and Figure S5, Supporting Information). Stations

Geochemistry Geophysics Geosystems G3

10.1002/ggge.20092

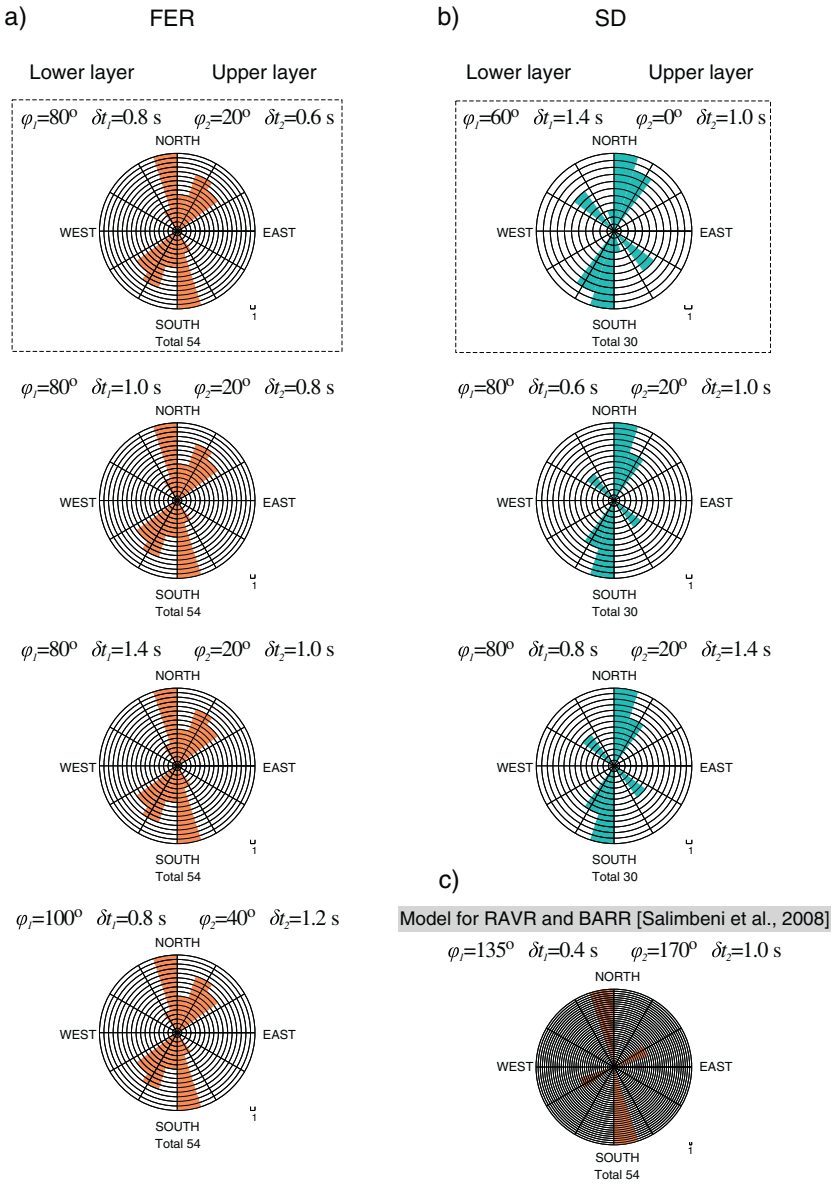

Figure 7. Synthetic rose diagrams for selected double-layer models that fit best the observed rose diagrams (a) in FER (orange diagrams) and (b) SD (turquoise diagrams) domains calculated for waves arriving from the north-eastern back-azimuths (compare with respective diagrams in Figure 6). Dashed frames mark preferred models. (c) Synthetic rose diagram for a double-layer model proposed by *Salimbeni et al.* [2008] to fit best the splitting parameters of the RAVR and BARR stations in the Po Plain (located in the FER domain). For more details, see caption of Figure 5.

clustered into the pattern Synthetic 1 are located in the TYR. With exception of station PIIR, the lateral extent of the Synthetic 1 subregion is the same as for the TYR subregion defined according to the "observed" P-sphere pattern. However, there are differences in characteristics of both types of the P-patterns. The "observed" pattern is clearly bipolar (Figure 2), while the "synthetic" pattern only weakly tends to that. Moreover, the "synthetic" P-pattern is less consistent than the observed one, and the absolute values of the synthetic terms gradually decrease with increasing distance south-westward from the boundary between the Synthetic 1 and Synthetic 2 regions, which is not the case of the "observed" P patterns in the TYR subregion (Figures S4 and S5, Supporting Information).

[31] Other stations form one large group—Synthetic 2 (Figures 8 and S5, Supporting Information) with a clear bipolar synthetic P pattern with negative terms

Geochemistry Geophysics Geosystems G3 MUNZAROVÁ ET AL.: MANTLE FABRICS BENEATH THE N. APENNINES 10.1002/ggge.20092

Table 1. Parameters of Double-layer Models Fitting the Rose Diagrams of the FER and SD Subregions (See Figure 4 for their Location)

Station	Double-layer Models for FER				Double-layer Models for SD				One-layer Models	
	Lower Layer		Upper Layer		Lower Layer		Upper Layer			
	φ_1 (°)	δt_1 (s)	φ_2 (°)	δt_2 (s)	φ_1 (°)	δt_1 (s)	φ_2 (°)	δt_2 (s)	φ (°)	δt (s)
	80	**0.8**	**20**	**0.6**	**60**	**1.4**	**0**	**1.0**	-	-
	80	1.0	20	0.8	80	0.6	20	1.0	-	-
	80	1.4	20	1.0	80	0.8	20	1.4	-	-
	100	0.8	40	1.2	-	-	-	-	-	-
BARR[a]	135	0.4	170	1.0	-	-	-	-	-	-
RAVR[a]	135	0.4	170	1.0	-	-	-	-	-	-
RAVR[b]	30	?	145	?	-	-	-	-	15	1.6
RSMR[b]	-	-	-	-	35	?	135	?	25	1.2
ZOCR[b]	90–120	1.3	20–40	2–3	-	-	-	-	28	1.55

[a]*Salimbeni et al.* [2008].
[b]According to *Menke and Levin* [2003] method (personal communication).

from the south-western directions and positive terms from the north-eastern directions. This is, however, different from the observed P-sphere patterns, clustered into the five subregions (see TR1, TR2, TR3, ADR1, and ADR2 in Figure 2). The synthetic P-spheres thus do not allow any detailed delimitation of the TR and the ADR.

[32] To demonstrate quantitatively the differences between the synthetic and the observed P spheres, we have calculated average directional terms

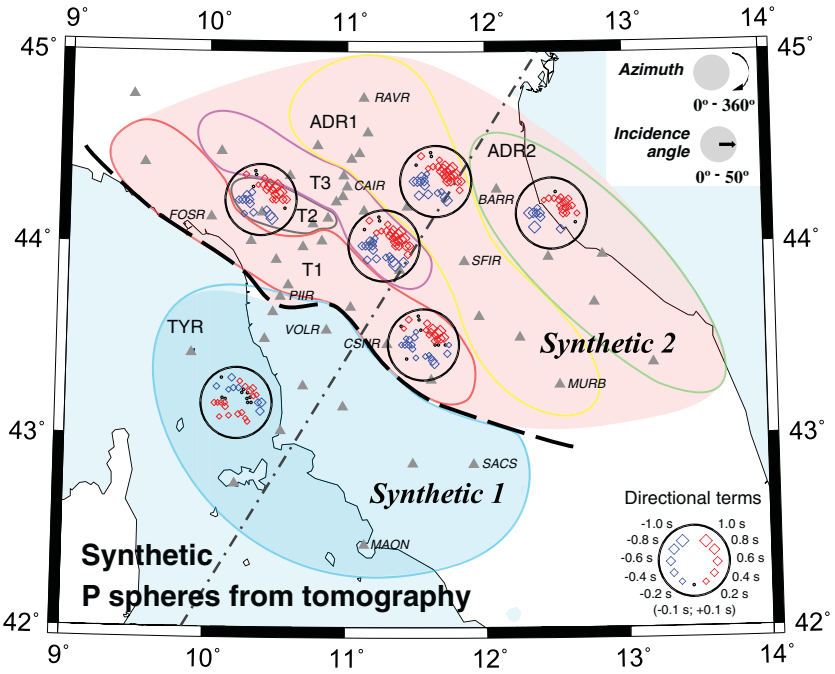

Figure 8. Synthetic P-sphere patterns calculated for the isotropic tomographic model of *Benoit et al.* [2011]. Two groups of stations inferred from similarity of the synthetic P-sphere patterns are marked with differently colored backgrounds and separated by a black dashed curve. An average synthetic P sphere (for more details see Figure 2) is plotted for each of the six subregions derived from the observed travel-time residuals (contoured in different colors; see Figures 2 and S4, Supporting Information) in order to show differences between the synthetics (Figure S5), which remain unchanged across the area covering the Transition zone and the Adriatic region, and the observed P pattern (see also Figure S4, Supporting Information). Several stations mentioned later in the text are labeled. Dot-dashed line locates the vertical cross section in Figure 10.

Geochemistry Geophysics Geosystems G3

10.1002/ggge.20092

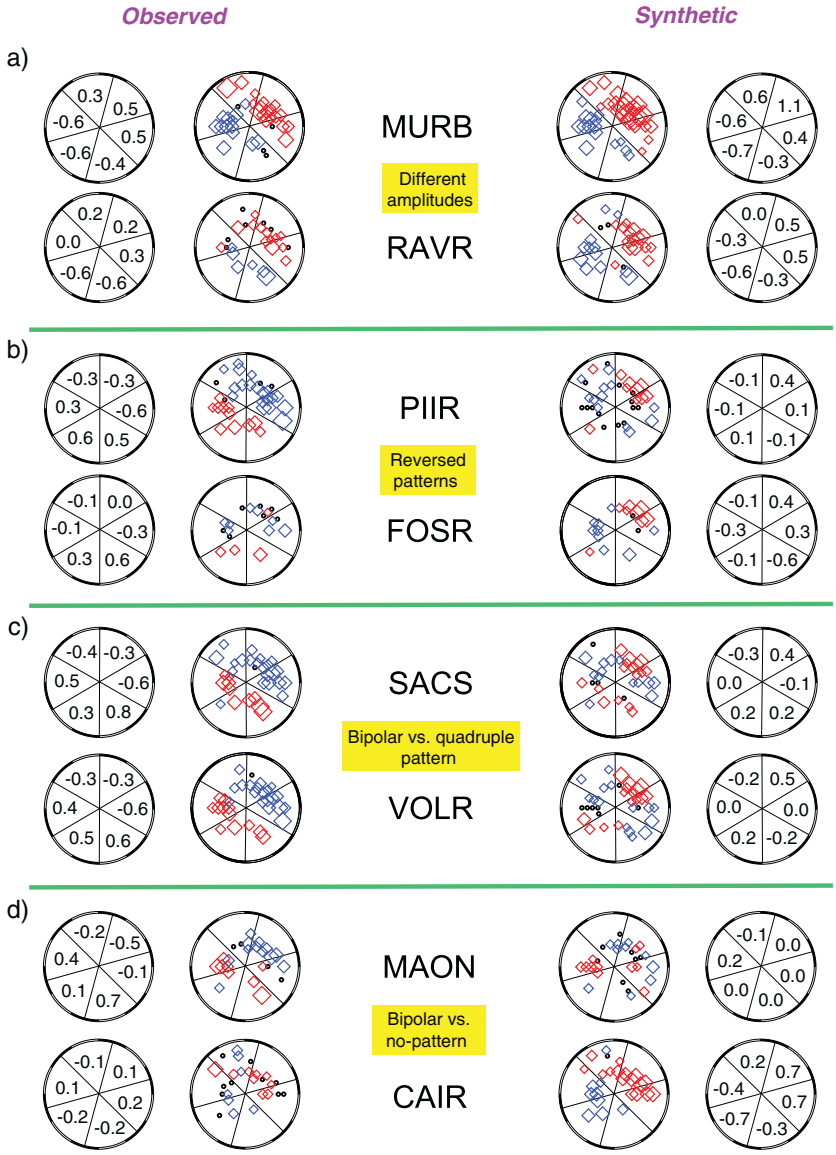

Figure 9. Comparison of the observed and the synthetic P spheres at selected stations representing differences between the patterns. Directional terms (in seconds) are calculated in 60° azimuth bins. To avoid smoothing of the pattern, always one of the segment boundaries in each P sphere follows the azimuth separating the early and delayed arrivals.

in six azimuth bins, for which we show characteristic examples (Figure 9). To avoid additional smoothing of the pattern, always one of the segment boundaries in each P sphere follows the azimuth separating the early and delayed arrivals.

[33] Some of the observed and synthetic P spheres, e.g., those at stations MURB and RAVR, seem to be similar, but the amplitudes of the directional terms are much larger in the synthetics (Figure 9a). On the other hand, at some stations, the observed and synthetic patterns are completely reversed (station PIIR in Figure 9b), or tend to be reversed (station in FOSR Figure 9b). A clear bipolar pattern from the observed data might also change into a quadruple pattern in the synthetics (see SACS and VOLR Figure 9c). Finally, a bipolar pattern turned into "no pattern" in some cases (Figure 9d). The "no pattern" is well reflected in the bin values of the directional terms close to zero for the synthetics of MAON and the observed pattern at CAIR, while the differences of the bin values attain ~1 s in the case of the observed bipolar pattern at MAON and the synthetics of CAIR.

Geochemistry Geophysics Geosystems G3 MUNZAROVÁ ET AL.: MANTLE FABRICS BENEATH THE N. APENNINES 10.1002/ggge.20092

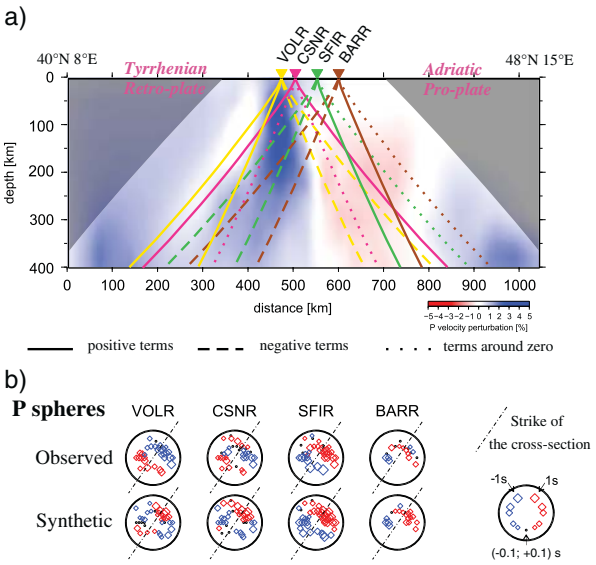

Figure 10. (a) Vertical cross section (for location see Figure 8) through the P-velocity tomographic model of *Benoit et al*. [2011] and rays from epicentral distances of 40° and 80° to four selected stations. For details, see also Figure 2. (b) Observed and synthetic P-residual spheres at the selected stations.

[34] Schematic ray tracing with the use of TauP [*Crotwell et al*., 1999] from the epicentral distances of 40° and 80° to four RETREAT stations is imaged against a vertical cross section through the tomography (Figure 10; for location of the profile see Figure 8). Station VOLR is located just above the high-velocity heterogeneity imaged by tomography, which results in the quadruple pattern of the synthetic P sphere, while the "observed" pattern is clearly bipolar. Stations CSNR and SFIR further to the north-east show similar bipolar patterns in the synthetics, but observed and synthetic patterns for the CSNR station differ. Less data at station BARR located in the north-easternmost part of the profile resulted in similar patterns.

3.4. Lithosphere Thickness

[35] Figures 11 and 12 show the LAB depths estimated from the modified static terms calculated from the relative P-wave residuals recorded during the RETRAT experiment. The LAB relief is smooth and indicates a depth of the NA subduction. The LAB estimates contour the most prominent high-velocity perturbations in the tomography by *Benoit et al*. [2011] along both profiles (Figures 11 and 12). The Adriatic slab probably sinks no more than to 200 km. The lithosphere of the over-riding Tyrrhenian plate is thinner (e.g., Figure 12). A thinning of the Adriatic plate occurs also towards the Po Plain (cf. the Adriatic LAB in Figures 11 and 12).

[36] The LAB models strongly depend on our knowledge of the crust structure. To correct for crustal effects, we used the Moho-depth model by *Di Stefano et al*. [2011] and incorporated also corrections for sediments [*Vuan et al*., 2011]. Good knowledge of the Moho depth around the contact of the Tyrrhenian and Adriatic crusts is crucial. Our results, calculated with the model characterized by a simple step at the Moho, did not fit results from surrounding stations (Figure 11). Therefore, we modified the crustal model around the contact in analogy with the model of *Finetti et al*. [2001] and the recent results from harmonic decomposition of receiver functions by *Bianchi et al*. [2010]. Instead of a simple step we considered an under-thrusting of the Adriatic crust beneath the Tyrrhenian plate. Under-thrusting of the ~16 km thick crustal material near the step in Moho depths deepens the anomalous values of the LAB by ~60 km and matches them with surrounding LAB depths.

4. Discussion

[37] Seismic anisotropy provides key information for understanding the tectonic fabric of the whole lithosphere-asthenosphere system. Mapping structural changes through both geographical and directional variations of anisotropic parameters evaluated in 3D represents a powerful tool, especially in continental provinces, where relatively thick mantle lithosphere consists of domains with their own fossil structure [*Babuška and Plomerová*, 2006]. Moreover, in regions of colliding plates accompanied by a plate

Geochemistry Geophysics Geosystems G3

10.1002/ggge.20092

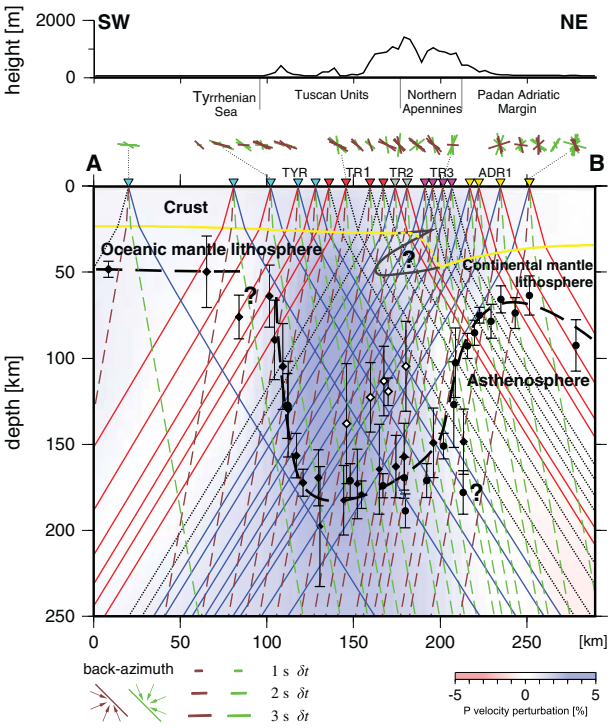

Figure 11. Lithospheric cross section along profile AB (see Figures 1 or 13 for its location) drawn over the tomography section [*Benoit et al.*, 2011]. Estimates of the LAB depths calculated from the static terms of relative P residuals (only steep incidences considered; e.g., *Plomerová and Babuška* [2010]) separately for the north-eastern (circles) and south-western (diamonds) back-azimuths are plotted into the piercing points of the rays and the LAB. Moho-depth model by *Di Stefano et al.* [2011] (in yellow), and its necessary modification (in black) to fit the LAB values in the central part of the slab (white diamonds) are shown. Stations along the profile (triangles) are colored according to the subregions derived from the P-sphere patterns (see Figures 2 and 3). Schematic P-wave ray paths from epicentral distances of 60° (solid and dotted curves) are the same as in Figure 3. Above each station, the respective shear-wave splitting parameters are imaged as bars aligned with fast polarization azimuths and scaled with delay times (see also Figure 4). Corresponding SKS ray paths for the south-western and north-eastern back-azimuths (dashed brown and green curves, respectively) are shown as well. Characteristics of the splitting parameters change along the profile similarly to the P pattern, though less expressively.

subduction, distinct anisotropy related to a present-day flow in the sublithospheric mantle can mask the lithospheric contribution to the observed apparent anisotropy, particularly if only azimuthal anisotropy is searched for. The NA result from intermittently independent motion of up to five microplates between a collision of the major plates of Eurasia and Africa [*Handy et al.*, 2010]. At present, the collision is expressed by a south-westward subduction of the Adriatic plate, and the region can serve as a natural laboratory to test the upper-mantle structure, its formation, and evolution [e.g., *Faccenna et al.*, 2001; *Lucente et al.*, 2006].

4.1. Heterogeneity Versus Anisotropy

[38] Three main regions, the TYR, the TR, and the ADR, delimited according to body-wave anisotropy, form bands approximately parallel to the mountain range (see Figure 2). The bipolar P-sphere patterns in the TYR and ADR regions are mutually reversed, each with negative terms from the directions where the subducted slab is located. This feature naturally leads to a possibility that the observed bipolar signal might be significantly controlled by the high-velocity heterogeneity represented by the subvertical slab.

[39] The synthetic P spheres (see Figure 8) calculated for waves propagating through the isotropic velocity model of the upper mantle from the RETREAT data [*Benoit et al.*, 2011] differ from the observed P spheres associated mainly with anisotropic structure of the mantle lithosphere (see Figures 9 and 10). Though an imprint of the high-velocity slab can remain in the P spheres even after the careful P-residual processing, the slab effect is weaker in comparison with effects of the plate fabrics at majority of stations (see Figure 8). Moreover, the shear-wave

Geochemistry Geophysics Geosystems G3

10.1002/ggge.20092

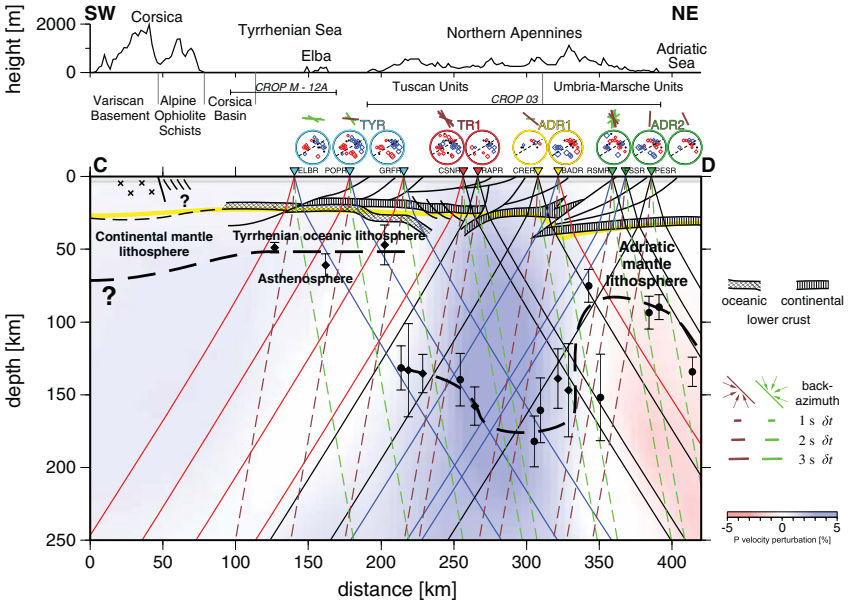

Figure 12. Lithospheric cross section along profile CD (see Figures 1 or 13 for its location) drawn over the tomography section [*Benoit et al.*, 2011]. Moho-depth model by *Di Stefano et al.* [2011] (in yellow) and schematic crustal cross-section simplified from *Finetti et al.* [2001] are shown. Stations along the profile (triangles) are colored according to the subregions derived from the P spheres, also shown above the stations (see Figure 2). For information about the estimates of the lithosphere-asthenosphere boundary (LAB), shear-wave splitting parameters, and the P and SKS ray paths, see captions of Figures 3 and 11.

splitting exhibits similar geographical variations (see Figures 11 and 12) and thus indicates that also in this tectonically complex region, we are able to detect the P-wave anisotropy and relate it to the mantle lithosphere. Tiny differences in delimiting the regions of similar characteristics of anisotropic parameters determined from the SKS splitting and P residuals are restricted to the margins of individual domains (see Figures 4 and 11). We explain this "discrepancy" by differences in wavelengths and ray paths of both types of waves. P waves, having only about ¼ of the SKS wavelength, are more sensitive to lateral structural changes than the SKS waves.

[40] There are differences in tomographic models of the subducted Adriatic slab [e.g., *Amato et al.*, 1993; *Lucente et al.*, 1999; *Piromallo and Morelli*, 2003; *Spakman and Wortel*, 2004; *Giacomuzzi et al.*, 2011; *Benoit et al.*, 2011]. A question how exactly the position of the steep high-velocity slab is imaged by seismic tomography remains open, as well as the depth extent of the subduction. Most of the tomography studies detect high velocities down to about 200–400 km. However, *Benoit et al.* [2011] admit ~100–150 km depth smearing of the steep heterogeneity. Nevertheless, extent of the positive perturbations, related to the subduction, is also in accord with our estimates of the depth of the slab bottom to be around 200 km (see Figures 11, 12, and 13). *Piromallo and Morelli* [2003] included into their tomography also regional events, which broadened the fan of P-wave ray paths and resulted in modeling a less steep Adriatic subduction. However, neither the broadening, nor the deepening of the high-velocity heterogeneity can alternatively explain the anisotropic signal retrieved from body waves [*Plomerová et al.*, 2006].

[41] One has to admit that real slab geometry is more complex than that retrieved from any tomography, which might also lead to differences between the synthetic and observed P-spheres. This is also evident in the TR zone, where the heterogeneity effect of the slab is combined with the fabric of the flat-lying mantle lithosphere. Having in mind the complex crustal structure, effects due to the significant (~20 km) step of Moho depths could explain the weak P patterns in the TR. However, the heterogeneous signal observed in the TR should not be assigned solely to the complex Moho geometry, because (1) we corrected the travel times for propagation of the P waves through the crust [*Di Stefano et al.*, 2011] and (2) the step in Moho depths located beneath the TR3 (Figure 11) would make the hypothetical bipolar pattern caused by

Geochemistry Geophysics Geosystems G3

10.1002/ggge.20092

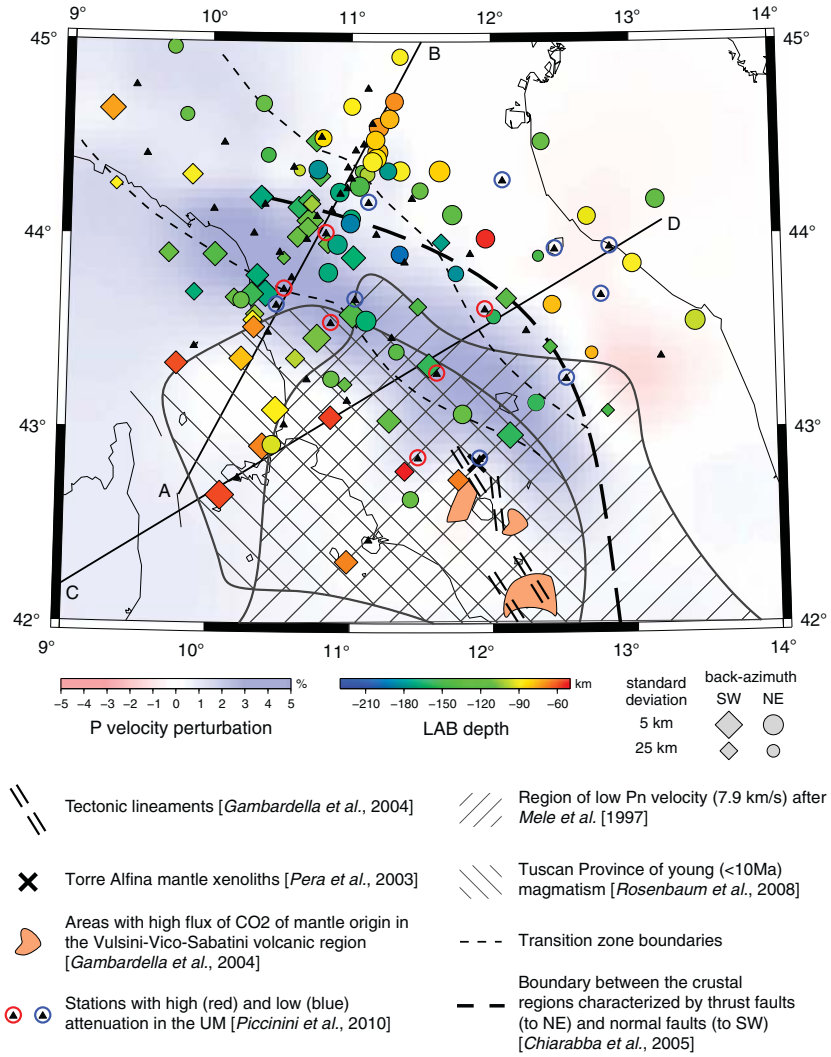

Figure 13. Slice section through tomographic model by *Benoit et al*. [2011] at depth of 75 km. The region of high-velocity perturbations corresponds to the deepest estimates of the lithosphere-asthenosphere boundary (LAB) beneath the Northern Apennines. The LAB depth marks are sized according to their standard deviations. Stations with high attenuation [*Piccinini et al*., 2010], regions of low Pn velocity [*Mele et al*., 1997], and young magmatism [*Rosenbaum et al*., 2008] concentrate on the Tyrrhenian side of the Northern Apennines, while stations with low attenuation are mostly on the Adriatic side.

the slab heterogeneity even stronger. Nevertheless, the bipolarity of the observed P-sphere pattern is suppressed in this region. Therefore, a source of the observed directional dependences of the P-wave residuals in the TR must be located deeper below the crust, i.e., in the upper mantle. We consider this heterogeneous zone to be formed by blocks of mantle lithosphere with frozen anisotropy. The blocks might have been sheared during the movement of the Adriatic promontory to the north, at the contact zone with the European plate, before the opening of the Tyrrhenian Sea [e.g., *Handy et al*., 2010].

4.2. Lithospheric and/or Sublithospheric Upper-Mantle Anisotropy

[42] The shear-wave splitting evaluated in the region attains more than 1 s at the most of the stations [*Margheriti et al*., 1996; *Plomerová et al*., 2006; *Salimbeni et al*., 2008]. Average value of ~1 s is typical for most of tectonically different continental regions [*Wuestefeld et al*., 2009]. The heterogeneous crust, with schistose metamorphic rocks and imbricated layers like those in the Adriatic upper crust [*Finetti et al*., 2001] representing anisotropic media, can only locally affect the observed splitting delays

Geochemistry Geophysics Geosystems G3 MUNZAROVÁ ET AL.: MANTLE FABRICS BENEATH THE N. APENNINES 10.1002/ggge.20092

by a weak contribution at values below a detectable limit of teleseismic shear-wave splitting, for which usually 0.3 s is accepted.

[43] An intrinsic anisotropy of the upper mantle, caused mainly by systematic lattice preferred orientation of olivine crystals, is at least partly constrained by anisotropy of mantle xenoliths [e.g., *Ben-Ismail and Mainprice*, 1998]. Formation of frozen-in anisotropic fabric can be related to the stress field of the last mantle-lithosphere deformation [*Silver and Chan*, 1991; *Savage*, 1999], or, the fabric has preserved information about the olivine preferred orientation formed in the stress field in time of the lithosphere origin [*Babuška and Plomerová*, 1989]. The overall percentage of the preferred orientation of olivine crystals in an anisotropic volume is decisive for the apparent large-scale anisotropy detected through the shear-wave splitting. Surface-wave studies [e.g., *Montagner*, 1994] detect significant decrease of anisotropy below 200 km. Similarly, characteristic changes of both the P- and S-wave anisotropic parameters and their relation to distinct tectonic features represent independent arguments for locating sources of anisotropic signal in the lithospheric part of the upper mantle in stable continental regions. We may thus ask, which of the potential anisotropic sources—the lithospheric mantle, the sublithospheric mantle (asthenospheric flow), or even the subducted slab—dominates the apparent anisotropic signal observed in the province around convergent plate margins, or, what is the mutual proportionality of these sources.

[44] *Babuška et al*. [1993] showed that anisotropic signal detected in the P spheres, i.e., in distribution of the negative and positive directional terms extracted from relative residuals, can be modeled in the continental lithosphere by peridotite aggregates with plunging symmetry axes. 3D self-consistent anisotropic models of individual domains of mantle lithosphere result from joint inversion/interpretation of both the P- and S-wave anisotropic parameters [*Babuška and Plomerová*, 2006]. While a cumulative character dominates in the P-wave travel times, shear-wave splitting characteristics are more complex in the case that waves propagate through a more complicated medium than a single anisotropic "layer". Inclination of symmetry axes in the lithospheric domains causes a dependence of evaluated splitting parameters on initial polarization (back-azimuth). Then, the characteristic π-modality, a priori assumed in the case of horizontal symmetry axes, disappears. Modeling variations of apparent splitting parameters (often from 2D evaluation of azimuthal anisotropy), by double-layer models with horizontal symmetry axes, leads to an additional reduction of the back-azimuth variations to π/2 periodicity [*Savage and Silver*, 1993]. Moreover, these models do not generate the observed bipolar P pattern.

[45] Subcrustal lithosphere beneath the TYR region is too thin (~30 km, see Figures 11 and 12, and, e.g., *Miller and Piana Agostinetti* [2012]) to generate the distinct bipolar pattern of the P residuals and the ~1 s split delay time (see Figures 3 and 11). Moreover, fabrics of oceanic lithosphere tend to be of a flat-sandwiched structure with subhorizontal high velocities coupled with the sublithospheric flow. Thickness of this layer is comparable with wavelength of the teleseismic shear waves recorded by broad-band seismometers, thus at a limit of "visibility". Dominating trench-parallel fast S polarizations in the TYR region and also in the western rim of the TR1 zone allow us to associate most of the anisotropic signal westward of the NA range with a slab-parallel flow in the asthenosphere. The fast shear-wave polarizations only slightly rotate to ~45° of the trench-perpendicular direction in the southern TYR region. No distinct dependence of the polarizations on back-azimuth also supports the interpretation by a subhorizontal flow. Nevertheless, the fast S polarization azimuths at the stations in the TYR for waves from the north-east become to be partly controlled also by the anisotropy of the Adriatic slab; see the SKS ray paths and greater variations of the splitting parameters in Figure 11. However, slab-parallel orientation of the fast S polarizations dominated at the TYR region, is not in agreement with a trench-perpendicular flow that would be expected for an extensional region related to a slab retreat, as was already pointed out in *Plomerová et al*. [2006] and *Salimbeni et al*. [2008]. Further to the south of the NA, the fast S polarizations evaluated by *Margheriti et al*. [1996] tend to be closer to the standard trench-perpendicular model, but this orientation might be related to a slab "window" between the NA and the Southern Apennines [*Lucente et al*., 2006].

[46] How then to explain the strong bipolar P-sphere pattern attaining up to 0.9 s difference in the extremes of the directional terms in the TYR region, if the lithosphere is thin and of oceanic type with a flat fabric and assuming the recent tomographic velocity model of *Benoit et al*. [2011] is correct? Contribution from the fast isotropic heterogeneity to the P pattern appears negligible (cf. observed and synthetic P spheres, Figures 2, S4, 8, and S5). However, we have to

Geochemistry Geophysics Geosystems G3 MUNZAROVÁ ET AL.: MANTLE FABRICS BENEATH THE N. APENNINES 10.1002/ggge.20092

consider that the thick continental Adriatic lithosphere exhibits clear signs of anisotropy (see Figure 5 and discussion below). Assuming orientation of anisotropy within the slab remained unchanged relative to the plate boundaries, the rays to the stations in the TYR region propagate from the north-east along the high-velocity directions relative to those from the south-west (see Figure 2). Ray paths within the short but thick subducted slab (see Figures 11 and 13) are long enough to create the observed P-pattern. This finding can be considered as an independent indication that a former oceanic subduction resulting from the Europe-Africa-plate collision was followed by a steep short subduction of the thicker continental Adriatic plate [*Handy et al*., 2010].

[47] Differences in distributions of shear-wave polarizations expressed in the rose diagrams (see Figure 5) evidence complex structure of the upper mantle. Similar to other continental regions [e.g., *Babuška and Plomerová*, 2006, 2012], including those of Archean ages [*Plomerová et al*., 2011], the observed changes in anisotropic signals of body waves allow us to delimit boundaries of domains of the upper mantle with consistent fabrics. On the basis of geographical and back-azimuth variations of shear-wave polarization, *Plomerová et al*. [2006] proposed a domain-like structure of the Adriatic plate (ADR). In the FER, the NA orogen-perpendicular fast S polarizations prevail, whereas in the SD, the apparent polarizations tend to orientate orogen parallel (see Figure 4). Distributions of polarization azimuths determined for the waves propagating from the south-west differ from those characterizing propagations from the north-east (see Figure 6). This finding and the different polarizations within the two domains testify thus for different mantle structures of both regions. Diffuse structure of the rose diagrams of ADR1 and ADR2 for waves propagating from the north-east (see Figure 5; see also Figure 6 of *Salimbeni et al*. [2008]) turns to clearly bimodal distributions in the circular diagrams constructed for the FER and SD separately. We associate these two contributions in the apparent polarizations with the shear-wave propagation through anisotropic sublithospheric mantle and then through different blocks of the thick Adriatic lithosphere with their own fabric. One can hardly expect sudden and distinct changes of the asthenosphere flow along the NA slab, but sudden fabric changes of individual blocks/domains of the continental mantle lithosphere have been well documented [*Babuška and Plomerová*, 2006].

[48] *Salimbeni et al*. [2008] prefer a double-layer model with a horizontal "fast" axis at 170° in the upper layer and 135° in the lower layer for the BARR and RAVR stations. A contribution to the apparent split delay time δt from the upper (lithosphere) layer of this model doubles that from the lower (asthenospheric) layer. Both stations belong to our FER domain. We constructed a synthetic rose diagram (see Figure 7c) for the double-layer model of *Salimbeni et al*. [2008] and compared it with the rose diagram of the FER domain for the same back-azimuths (see upper right diagram in Figure 6). However, there is only a little correlation between the rose diagrams, probably due to a low number of waves coming from different back-azimuths to characterize the structure beneath single stations as *Salimbeni et al*. [2008] also admit.

[49] Having a better distribution of rays is not only a question of a length of period of an array registration. Ray-path limitation is a reality, because waves arrive only from earthquakes, whose locations are restricted to specific regions. Therefore, interpreting jointly independent sets of body-wave anisotropic parameters broadens fan of ray paths sampling the upper-mantle volume, and it is challenging to retrieve more realistic self-consistent models of the upper mantle. In the case of modeling, the mantle lithosphere in stable continental regions, the bipolar pattern of the P spheres can be modeled by peridotite aggregates with plunging symmetry axis ***a*** in the case that azimuth of the fast S polarizations and dip direction from the P-spheres agree, or, with plunging symmetry axis ***b***, i.e., dipping (***a***,***c***) foliation plane, if the fast S polarizations parallel the strike of the (***a***,***c***) plane [*Babuška et al*., 1993]. Following this rule and interpreting directly the fast S polarizations (see Figure 6), one could relate the relatively stable north-south component to the anisotropy reflecting the slab-parallel flow in the sublithospheric upper mantle on the Adriatic side. In such a case, the lithosphere fabric of the FER could be approximated by an anisotropic model with the ***a*** axis dipping at azimuth ~210° and that of SD by an anisotropic model with the ***b*** axis of symmetry and the southward dipping (***a***,***c***) foliation striking at ~300°. However, these models, approximated by two anisotropic layers with horizontal symmetry axes [*Savage and Silver*, 1993], did not accommodate the visualized apparent polarizations.

[50] In the case of a grid search through double-layer anisotropic models of the upper mantle beneath the ADR, we found an azimuth of high velocities and a delay time for each of the layers in both the FER and SD regions (see Figure 7 and Table 1) to fit the observed rose diagrams (see Figure 6). The thickness of upper layer beneath the FER corresponds to

Geochemistry Geophysics Geosystems G3 MUNZAROVÁ ET AL.: MANTLE FABRICS BENEATH THE N. APENNINES 10.1002/ggge.20092

the thickness of the mantle lithosphere of ~50 km (Po Plain basin) resulting from the static terms of P-wave travel-time residuals (see Figure 11). The models show high velocities at azimuth 80° and 60° in the lower layers (sublithospheric upper mantle) of the FER and SD domains, respectively, far from the slab-parallel orientation predicted due to the suggested slab roll-back [e.g., *Faccena et al*., 2003]. Fast velocity orientations in the upper layers at 20° (200°) and 0° (180°) in the FER and SD lithosphere, respectively, correlate well with the south-south-west azimuths of the dipping high velocities inferred from the P-spheres (see Figures 2 and S4).

[51] *Menke and Levin* [2003] developed a waveform fitting technique that allows testing radial-horizontal and tangential-horizontal components of shear waves for splitting as predicted by one- and double-layer anisotropic models with horizontal high-velocity directions. Without the necessity of fitting the apparent parameters, the method yields consistent results and provides additional information on statistical significance of the double-layer solution. However, in the case of the NA, the double-layer solutions for the upper mantle proposed by this method for some stations (Table 1) differ from solutions by the method fitting the apparent splitting parameters [*Savage and Silver*, 1993]. It is surprising that for two nearby stations ZOCR and RAVR, both located in the FER domain of the Adriatic plate, the fast-velocity directions in the upper and lower layers result in mutually interchanged azimuths (Table 1). Since the waveform fitting method searches for azimuth anisotropy only, it is not suitable for regions with complex structure and especially for retrieving mantle lithosphere fabric, for which there are independent indications on fabric inclination. *Menke and Levin* [2003] admit that some processes, other than those producing the double-layer flat anisotropy, affect the shear-wave splitting. Fabric inclinations, either in the continental lithosphere or due to complex nonhorizontal flow in the sublithospheric mantle, can be the sources.

[52] Similar regionalization of the NA province into three regions—the Tyrrhenian, Adriatic, and Overlapping domains, the last one coinciding with our TR—comes from the harmonic decomposition of migrated radial and transverse receiver functions [*Bianchi et al*., 2010]. The procedure takes into consideration anisotropy in the uppermost mantle. The authors associate the revealed symmetry directions of anisotropy with characteristics of the mantle material at depths of 40–70 km, i.e., with fabrics of the mantle lithosphere, particularly of the thick Adriatic plate. Prevailing north-north-east to north-east directions are in agreement with axis orientations we derive in this study, as well as the distinct regionalization according to lateral changes of the anisotropic parameters [*Plomerová et al*., 2006].

[53] Simple estimate on a depth source of anisotropy below a dense array is usually based on calculating Fresnel zones [e.g., *Alsina and Snieder*, 1995], assuming horizontal fast velocities in the upper mantle. *Salimbeni et al*. [2008] estimated the depth interval of anisotropic layers and concluded that both the double-layer models with a horizontal axis of symmetry and the Fresnel-zone estimate suggest a lithospheric contribution [see also *Plomerová et al*., 2006].

4.3. Lithosphere thickness around the steep Adriatic subduction

[54] Differences in estimates of the lithosphere thickness beneath the northern Italy stem from independent data and methods [surface waves—*Panza et al*., 1980; S-wave receiver functions (SRF)—*Miller and Piana Agostinetti*, 2012; P-wave travel-time residuals—*Babuška and Plomerová*, 1990]. All of the estimates are consistent in showing a shallow LAB beneath the TYR westward of the NA and a thicker continental Adriatic lithosphere eastward of the NA (Figure 13). The modification of the method presented by *Babuška and Plomerová* [1992], i.e., separation of the static terms according to the wave azimuth relative to the strike of the NA mountain range and plotting the LAB depths at piercing points of the rays and the LAB boundary, results in a smooth model of LAB relief (see Figures 11 and 12) in contrast to LAB estimates averaged for all back-azimuth ranges and plotted directly beneath each station [e.g., *Miller and Piana Agostinetti*, 2012]. We relate the banana shape of the deep LAB relief beneath the NA with the Adriatic slab subduction (Figure 13).

[55] The model width of the Adriatic subduction is of ~80–100 km (see Figures 11 and 12) can be an independent sign of the continental plate subduction [*Bianchi et al*., 2010]. Diffuse values of the LAB estimates located at the north-eastern edge of the slab probably reflect the wave propagation along the high-velocity directions within the anisotropic slab. Less well-defined LAB beneath the Adriatic slab along the southern profile (see Figure 12) can be an independent indication of a fragmentation of the slab, whose continuation south of 43°N is questioned by results of independent methods [*Benoit et al*., 2011; *Spakman and Wortel*, 2004].

Geochemistry Geophysics Geosystems G3 MUNZAROVÁ ET AL.: MANTLE FABRICS BENEATH THE N. APENNINES 10.1002/ggge.20092

[56] *Piccinini et al*. [2010] calculated the P- and S-wave spectra to infer attenuation in the Earth mantle and to analyze its variations beneath the NA and surroundings. Stations located south-westward of the 700 m elevation isoline of the Apennine chain above the steep subduction (Tyrrhenian side of the NA) exhibit high attenuation, while a low attenuation prevails on the Adriatic side of the NA orogen (Figure 13). Subvertical orientation of the Adriatic slab imaged by tomography [e.g., *Benoit et al*., 2011] excludes a presence of a standard asthenosphere wedge above a less steep subduction. *Thomson et al*. [2010] state from measurements of low-temperature thermochronometers (apatite (U-Th)/He and fission track) that "no single model of wedge kinematics is likely appropriate for the NA over the long term" and that "different lithospheric geodynamic processes have acted at different times in different lateral segments of the orogen". To explain the high attenuation evaluated above the subducting continental Adriatic lithosphere relative to its flat part leads us to refresh the idea of the slab detachment [*Levin et al*., 2007]. The potential detachment filled with the low-velocity asthenospheric material would have to be narrow, with width below the teleseismic shear-wave length (~40 km), and in its initial stage.

4.4. Seismic Anisotropy and Tectonics

[57] Seismic anisotropy measured by means of shear-wave splitting, detection of QL waves or evaluating transverse components of receiver functions shed light on the lithospheric and sublithospheric parts of the upper-mantle fabrics, their past and present deformation, and lateral/vertical changes of their structures. The main results of anisotropy studies evidence a complex structure of the region, in which none of the basic models, e.g., a slab roll-back or a slab detachment, works within the whole province [*Plomerová et al*., 2006; *Levin et al*., 2007]. Shear-wave anisotropy recognizes different mantle fabrics westward and eastward of the north-west/south-east oriented NA orogen [*Salimbeni et al*., 2008], with additional subregions, particularly in the Adriatic domain [*Plomerová et al*., 2006], while the QL waves differentiate the mantle structure north and south of the 44°N latitude [*Levin et al*., 2007].

[58] Results of this study are in agreement with previous investigations mentioned above, distinguishing regions with principal mantle tectonics: (1) the TYR with the thin oceanic lithosphere and distinct north-west/south-east oriented flow in the sublithospheric mantle, (2) two regions with relatively thicker continental lithosphere belonging to the Adriatic plate

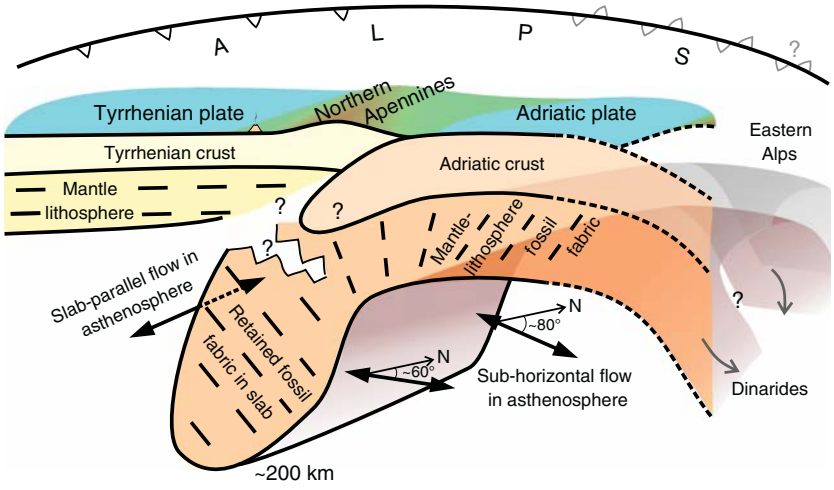

Figure 14. Cartoon of the lithosphere-asthenosphere system beneath the Northern Apennines and surrounding area. The front of the cartoon is approximately orogen perpendicular. Fossil olivine fabrics, both in the Adriatic mantle lithosphere and in the subducted slab, in combination with the asthenospheric flow, are interpreted as sources of the evaluated anisotropic signal in seismic body waves. The slab-parallel flow in the sublithospheric mantle beneath the Tyrrhenian plate and almost slab-orthogonal flow on the Adriatic side indicate a ceased slab roll-back. The north-eastern flow beneath the Adriatic plate might result from its blocking within a limited space by surrounding subductions. Volcanism above the southern tip of the Northern Apennine slab (see also Figure 13) might relate to a slab detachment, or, to a slab tear in the central part of the Apennines.

Geochemistry Geophysics Geosystems G3

10.1002/ggge.20092

Table 2. Summary of the Upper-mantle Anisotropic Models in the Northern Apennine Region

Region		Anisotropic Layer	Symmetry Axes: Azimuth φ (°)	Symmetry Axes: Inclination α (°)	Thickness of Anisotropic Layer (km) [d]	Thickness of Anisotropic Layer (km) [e]	LAB Depth (km) [f]
Adriatic	Tyrrhenian domain	Upper	-	0	30	-	50
		Lower	140 [a]	0	-	-	
	Ferrara arc domain	Upper	210 (*a* axis) [b]	30–60 [b]	50	54	80
		Lower	80 [c]	0	-	72	
	Southern domain	Upper	30 (*b* axis) [b]	30–60 [b]	60	90	90
		Lower	60 [c]	0	-	126	
	Transition zone		Maximum P velocity (°)		Slab width (km)		Depth of slab sink (km)
	Adriatic slab		Azimuth φ (°)	Inclination α (°)			
			~30	30–60	80–100 [f]		200 [f]

Upper layer ~ Mantle lithosphere.
Lower layer ~ Sublithospheric mantle.
[a]Slab-parallel azimuths of the fast shear-wave polarizations (see Figure 4; *Salimbeni et al*. [2008]).
[b]Azimuths and inclinations of symmetry axis inferred from joint interpretation of P-residual directional terms and shear-wave splitting parameters (see section 4.2.).
[c]Azimuths inferred from modeling of split shear-wave polarizations by double-layer anisotropy with horizontal symmetry axis *a* (see Table 1; *Savage and Silver* [1993]).
[d]Thicknesses from the LAB depth estimates from P-wave static terms (see section 3.4.).
[e]Thickness calculated according to formula $L = \delta t \frac{\beta_0}{\delta\beta}$, where $\frac{\beta_0}{\delta\beta} = \frac{4.5km/s}{0.05} = 90km/s$ [*Silver*, 1996] and δt from modeling of split shear-wave polarizations by double-layer anisotropy (see Table 1; *Savage and Silver* [1993]).
[f]LAB evaluated from static terms of P-wave travel-time residuals (see section 3.4.).

underlain by the mantle, which is deformed inconsistently with the retreat-related subduction-zone parallel flow, and (3) the approximately 80 km wide TR in between the Tyrrhenian and ADRs and above the steeply subducted part of the Adriatic plate (Figure 14 and Table 2). The steep high-velocity heterogeneity [*Benoit et al*., 2011] makes evaluation of particularly P-wave anisotropy difficult, and we admit that small remnant effects could be preserved in the overall anisotropy patterns. Proposed geologic models of the NA region are derived mostly from shallow observations; however, teleseismic measurements focus on deeper processes which take place in the upper mantle and drive the shallow tectonics. Evaluation of seismic anisotropy can thus help to differentiate especially between subduction with or without a slab roll-back or a slab break-off, lateral extent of these phenomena, including a slab continuity, or its fragmentation.

[59] *Lucente et al*. [2006] map a long route of the progressive eastward retreat of a regional-scale subduction zone (trapped between two continents) through the west-central Mediterranean mantle in the last 30 My. At present, the upper-mantle fabrics resulting from seismic anisotropy do not show the simple deformation pattern in the upper mantle either due to a slab roll-back, i.e., the trench perpendicular in the supra-slab region and the orogen-parallel in the subslab region, or, due to a slab break-off resulting in the sublithospheric mantle flow towards the site of the detachment. Variability of the anisotropy as to its orientation evidences a complex structure of the NA and fragmentation of the Apennine chain [*Lucente et al*., 2005; *Miller and Piana Agostinetti*, 2012].

[60] Though, e.g., *Pondrelli et al*. [2006] and *Miller and Piana Agostinetti* [2012] assume that the Adriatic plate subduction beneath the NA is still active, results from body-wave anisotropy presented in this paper as well as those from surface-wave study of QL waves by *Levin et al*. [2007] suggest that the subduction-zone retreat has ceased. Formerly eastward dominated asthenospheric flow due to the slab roll-back seems to be deflected on the Tyrrhenian side to the north-west/south-east direction along the short steep slab [*Benoit et al*., 2012; for the most recent velocity tomography image]. Then, the north-western movement of the Tyrrhenian crust, detected north of ~41°N from GPS measurements [*Serpelloni et al*., 2005], appears coherent with the upper-mantle flow. The flow slightly turns clockwise towards the NA chain. The same rotation can be observed along the NA in direction from south to the north (see Figures 4 and 5, and Table 1). The recent isotropic tomography from the RETREAT data [*Benoit et al*., 2011] as well as the tomography from data of permanent stations only [*Lucente et al*., 1999] do not show a continuous slab along the whole collision zone in the Italian peninsula [*Wortel and Spakman*, 2000; *Piromallo and Morelli*, 2003]. The authors limit the high-velocity heterogeneity in the upper mantle related to the NA subduction to latitudes north of ~42°, being separated from the

Geochemistry Geophysics Geosystems G3 MUNZAROVÁ ET AL.: MANTLE FABRICS BENEATH THE N. APENNINES 10.1002/ggge.20092

Southern Apennines by a tear beneath the Central Apennines. The separation is visible also in mapping of the LAB by SRF [*Miller and Piana Agostinetti*, 2012] and in a distinct change of size and direction of residual geodetic velocities [*Serpelloni et al*., 2005]. Low Pn velocities [*Mele et al*., 1997] and young magmatism [*Rosenbaum et al*., 2008] surrounding 43°N, together with high flux of CO_2 [*Gambardella et al*., 2004] southward of 43°N also indicate presence of hot asthenosphere in shallow mantle depths (Figure 13). Up to now, there is no convincing anisotropy measurement indicating a mantle material flow related to a tearing associated to the ending part of the NA subduction [see also *Levin et al*., 2007; *Margheriti et al*., 2003].

[61] Structure of the upper mantle on the Adriatic side of the NA is complex, reflecting the mantle-lithosphere structure of ~80 km thick continental Adriatic plate (see Figures 11, 12, and 13) as well as deformation in the sublithospheric mantle constricted by nearby subductions beneath the Western and Eastern Alps, and Dinarides [*Babuška et al*., 1990; *Piromallo and Morelli*, 2003; *Lippitsch et al*., 2003; *Koulakov et al*., 2009]. However, due to the lack of well distributed shear-wave polarization measurements, none of the techniques used resulted in a unique double-layer anisotropic model of the mantle beneath the FER and SD Adriatic domains (Table 1; see also *Menke and Levin* [2003]; *Plomerová et al*. [2006]; *Salimbeni et al*. [2008]). Nevertheless, the models agree with a change of the asthenospheric flow from the north-eastern towards the east-north-eastern (60° in SD of the Adria, and 80° in the FER). Alternatively, *Levin et al*. [2007] hypothesize that the mantle flow towards the site of the subducted slab detachment from the surface lithosphere north of 44°N, originally proposed by *Wortel and Spakman* [2000], would explain the apparent north/south trending SKS fast polarizations and the lack of QL scattering. However, the subduction zone parallel polarizations in the Tyrrhenian domain and prevailingly null or very week split measurements in the Alps-NA transition domain (see Figure 4; see also *Plomerová et al*. [2006]) most probably reflect the fact that the broad-band shear waves sample multistructures at scales of their wavelength. Nearby subductions beneath the Western and Eastern Alps, as well as beneath the Dinarides (Figure 14), might block a mantle flow expected in the case of a broader NA slab break-off, similarly as in the case of a noticeable subduction-zone retreat. Seismicity in the NA is mostly limited to the crust [*Chiarabba et al*., 2005]. Normal faults prevail in the crust above the slab and reverse faults in the crust north-easterly from the NA mountain range [*Pondrelli et al*., 2006]. This is in accord with a continuing extension along the NA and an active compression of the crust above the Adriatic lithosphere (Figure 13) and can reflect a possible pull of the sinking Adriatic lithosphere.

5. Conclusions

[62] In the upper mantle beneath the NA, we recognize regions of different fabrics in the mantle lithosphere and also in the sublithospheric mantle. Based on joint analysis of directional terms of relative P-wave travel-time residuals and shear-wave splitting evidencing anisotropy in the upper mantle, we model the upper-mantle fabric in the Tyrrhenian, Transition, and ADRs. The last one comprises two subregions with distinct anisotropy of the continental lithosphere. The TR between the Adriatic and TYRs is about 80 km wide. Joint analysis of the two different and independent data sets (P-wave travel-time residuals and shear-wave splitting) allows us to infer anisotropic structures of the mantle lithosphere oriented generally in 3D with inclined symmetry axes. Tests of the well-known trade-off between the heterogeneity and anisotropy showed differences between the synthetic P spheres calculated for the standard tomographic model of isotropic velocity perturbations [*Benoit et al*., 2011] and the observed P spheres implying that we succeeded in detecting anisotropy in both types of body waves.

[63] Back-azimuth dependence of body-wave anisotropic parameters along with their geographical variability require double-layer models and anisotropy with inclined symmetry axes, particularly in the upper layer associated with the continental mantle lithosphere of the Adriatic plate. Slab-parallel fast shear-wave polarizations reflect predominantly sublithospheric flow beneath the Tyrrhenian plate. Anisotropic signal expressed in the P-spheres at stations located above the thin and flat oceanic-type Tyrrhenian lithosphere reflects most probably the inherited anisotropy of the subducted slab itself. Anisotropy evaluated in two Adriatic subregions indicates combined effects of fossil anisotropy with a dipping symmetry axis in the mantle lithosphere domains and anisotropy due to the north-easterly oriented flow in the asthenosphere. Fabric of the upper mantle in the TR between both major regions is complex. The region might be composed of slices

Geochemistry Geophysics Geosystems G3

10.1002/ggge.20092

of the Adriatic mantle lithosphere sheared off during the collision with the European plate.

[64] Static terms of relative P-wave travel-time residuals, divided according to the strike of the subduction zone (~135°), provided first detailed depth estimate of the LAB in the region of the NA. We estimate thickness of the thin Tyrrhenian lithosphere at ~50 km and of the thicker continental Adriatic lithosphere at ~80 km. We model a depth of the subduction of the Adriatic plate down to no more than 200 km.

[65] Generally accepted model of the subduction roll-back does not work in the current stage of the NA evolution. Slab-parallel flow in the sublithospheric mantle on the Tyrrhenian side and a north-easterly oriented flow on the Adriatic side support the idea of the ending subduction-zone retreat. Mass transfer in the sublithospheric mantle might be blocked in the upper 200 km by the frame of the surrounding subductions—the Alps to the north and the Dinarides to the east, both formed as a result of independent motions of the microplates between the colliding Europe and Africa.

Acknowledgments

[66] We thank all members of the Retreat Seismic Working Group, particularly to L. Margheriti, S. Pondrelli, N. Piana Agostinetti, F. P. Lucente, D. Piccinini (INGV Roma), to J. Park and V. Levin (Yale University, USA), and to B. Růžek, P. Jedlička (IG Prague) for their cooperation during the field work and data processing. To draw most of the figures, we used the GMT plotting software [*Wessel and Smith*, 1998]. The research was partly supported by grants No. IAA300120709 of the Grant Agency of the Academy of Sciences of the Czech Republic, No. P210/12/2381 of the Grant Agency of the Czech Republic, No. 111-10/253101 of the Grant Agency of Charles University, and No. SVV-2013-267308 of the Ministry of Education, Youth, and Sports of the Czech Republic. We greatly appreciate the thoughtful review comments provided by Francesco Pio Lucente, an anonymous reviewer and Thorsten Becker, Editor-in-Chief, which have improved substantially the manuscript.

References

Alsina, D., and R. Snieder (1995), Small-scale sublithospheric continental mantle deformations: constraints from SKS splitting observations, *Geophys. J. Int.*, *123*, 431–448, doi:10.1111/j.1365-246X.1995.tb06864.x.

Amato, A., B. Alessandrini, and G. B. Cimini (1993), Teleseismic wave tomography of Italy, in *Seismic Tomography: Theory and Practice*, edited by H. M. Iyer and K. Hirahara, pp. 361–397, Chapman and Hall, London.

Babuška, V., and J. Plomerová (1989), Seismic anisotropy of the subcrustal lithosphere in Europe: another clue to recognition of accreted terranes?, in *Deep Structure and Past Kinematics of Accreted Terranes*, edited by J. W. Hillhouse, pp. 209–217, Geophys. Monograph 50, IUGG 5, Washington, D. C.

Babuška V., and J. Plomerová (1990), Tomographic studies of the upper mantle beneath Italian region, *Terra Nova*, *2*, 569–576, doi:10.1111/j.1365-3121.1990.tb00122.x.

Babuška, V., and J. Plomerová (1992), The lithosphere in central Europe - Seismological and petrological aspects, *Tectonophysics*, *207*, 141–163, doi: 10.1016/0040-1951(92)90475-L.

Babuška, V., and J. Plomerová (1993), Lithosphere thickness and velocity anisotropy - Seismological and geothermal aspects, *Tectonophysics*, *225*, 79–89, doi:10.1016/0040-1951(93)90250-N.

Babuška, V., and J. Plomerová (2006), European mantle lithosphere assembled from rigid microplates with inherited seismic anisotropy, *Phys. Earth Planet. Inter.*, *158*, 264–280, doi:10.1016/j.pepi.2006.01.010.

Babuška, V., and J. Plomerová (2012), Boundaries of mantle-lithosphere domains in the Bohemian Massif as extinct exhumation channels for high-pressure rocks, *Gondwana Res.*, doi:10.1016/j.gr.2012.07.005, online.

Babuška, V., J. Plomerová, and J. Šílený (1993), Models of seismic anisotropy in deep continental lithosphere, *Phys. Earth Planet. Inter.*, *78*, 167–191, doi:10.1016/0031-9201(93)90154-2.

Ben-Ismail, W., and D. Mainprice (1998), An olivine fabric database: An overview of upper mantle fabrics and seismic anisotropy, *Tectonophysics*, *296*, 145–157.

Benoit, M. H., M. Torpey, K. Liszewski, V. Levin, and J. Park (2011), P and S wave upper mantle seismic velocity structure beneath the northern Apennines: New evidence for the end of subduction, *Geochem. Geophys. Geosyst.*, *12*, Q06004, doi:10.1029/2010GC003428.

Bianchi, I., J. Park, N. Piana Agostinetti, and V. Levin (2010), Mapping seismic anisotropy using harmonic decomposition of receiver functions: An application to Northern Apennines, Italy, *J. Geophys. Res.*, *115*, B12317, 1–14, doi:10.1029/2009JB007061.

Chiarabba, C., L. Jovane, and R. DiStefano (2005), A new view of Italian seismicity using 20 years of instrumental recordings, *Tectonophysics*, *395*, 251–268, doi:10.1016/j.tecto.2004.09.013.

Cimini, G. B., and A. Marchetti (2006), Deep structure of peninsular Italy from seismic tomography and subcrustal seismicity, *Ann. Geophys.*, *49*, 331–345.

Crotwell, H. P., T. J. Owens, and J. Ritsema (1999), The TauP Toolkit: Flexible seismic travel-time and ray-path utilities, *Seismol. Res. Lett.*, *70*, 154–160.

Dewey, J. F., M. L. Helman, E. Turco, D. H. W. Hutton, and S. D. Knott (1989). Kinematics of the western Mediterranean, in *Alpine Tectonics, Special Publication* No. 45, edited by M. P. Coward, D. Dietrich, and R. G. Park, pp. 265-283, Geological Society, London.

Di Stefano, R., I. Bianchi, M. G. Ciaccio, G. Carrara, and E. Kissling (2011), Three-dimensional Moho topography in Italy: New constraints from receiver functions and controlled source seismology, *Geochem. Geophys. Geosyst.*, *12*, Q09006, doi:10.1029/2011GsC003649.

Doglioni, C. (1991), A proposal of kinematic modelling for W-dipping subductions possible applications to the Tyrrhenian–Apennines system, *Terra Nova*, *3*, 423–434, doi:10.1111/j.1365-3121.1991.tb00172.x.

Eken, T., J. Plomerová, L. Vecsey, V. Babuška, R. Roberts, H. Shomali, and R. Bodvarsson (2012), Effects of seismic anisotropy on P-velocity tomography of the Baltic Shield,

Geophys. J. Int., *188*, 600–612, doi:10.1111/j.1365-246X.2011.05280.x.

Faccenna, C., T. W. Becker, F. P. Lucente, L. Jolivet, and F. Rossetti (2001), History of subduction and back-arc extension in the central Mediterranean, *Geophys. J. Int.*, *145*, 809–820, doi:10.1046/j.0956-540x.2001.01435.x.

Faccenna, C., L. Jolivet, C. Piromallo, and A. Morelli (2003), Subduction and the depth of convection in the Mediterranean mantle, *J. Geophys. Res.*, *108*(B2), 2099, doi:10.1029/2001JB001690.

Finetti, I. R., M. Boccaletti, M. Bonini, A. Del Ben, R. Geletti, M. Pipan, and F. Sani(2001), Crustal section based on CROP seismic data across the North Tyrrhenian-Northern Apennines-Adriatic Sea, *Tectonophysics*, *343*, 135–163, doi:10.1016/S0040-1951(01)00141-X.

Gambardella, B., C. Cardellini, G. Chiodini, F. Frondini, L. Marini, G. Ottonello, and M. V. Zuccolini (2004), Fluxes of deep CO2 in the volcanic areas of central-southern Italy, *J. Vol. Geo. Res.*, *136*, 31–52, doi: 10.1016/j.jvolgeores.2004.03.018.

Giacomuzzi, G., C. Chiarabba, and P. De Gori (2011), Linking the Alps and Apennines subduction systems: New constraints revealed by high-resolution teleseismic tomography,*Earth Planet. Sci. Lett.*, *301*, 531–543, doi:10.1016/j.epsl.2010.11.033.

Handy, R., S. M. Schmid, R. Bousquet, E. Kissling, and D. Bernoulli (2010), Reconciling plate-tectonic reconstructions of Alpine Tethys with the geological-geophysical record of spreading and subduction in the Alps, *Earth Sci. Rev.*, *102*, 121–158, doi:10.1016/j.earscirev.2010.06.002.

Kennett, B.L.N. (1991), *IASPEI 1991 Seismological Tables*, *Research School of Sci*., Australian National University, Canberra.

Koulakov, I., M. K. Kaban, M. Tesauro, and S. Cloetingh (2009), P- and S-velocity anomalies in the upper mantle beneath Europe from tomographic inversion of ISC data, *Geophys. J. Int.*, *179*, 345–366, doi:10.1111/j.1365-246X.2009.04279.x.

Levin, V., D. Okaya, and J. Park (2007), Shear wave birefringence in wedge-shaped anisotropic regions, *Geophys. J. Int.*, *168*, 275–286, doi: 10.1111/j.1365-246X.2006.03224.x.

Lippitsch, R., E. Kissling, and J. Ansorge (2003), Upper mantle structure beneath the Alpine orogen from high-resolution teleseismic tomography, *J. Geophys. Res.*, *108*(B8), 2376, doi:10.1029/2002JB002016.

Lucente, F. P., G. B. Chiarabba, and D. Giardini (1999), Tomographic constraints on the geodynamic evolution of the Italian region, *J. Geophys. Res.*, *104*, 20307–20327, doi:10.1111/j.1365-246X.2009.04279.x.

Lucente, F. P., L. Margheriti, C. Piromallo, and G. Barruol (2006), Seismic anisotropy reveals the long route of the slab through the western–central Mediterranean mantle, *Earth Planet. Sci. Lett*, *241*, 517–529, doi:10.1016/j.epsl.2005.10.041.

Malinverno, A., and W. B. F. Ryan (1986), Extension in the Tyrrhenian Sea and shortening in the Apennines as result of arc migration driven by sinking of the lithosphere, *Tectonics*, *5*, 227–245, doi:10.1029/TC005i002p00227.

Margheriti, L., C. Nostro, M. Cocco, and A. Amato (1996), Seismic anisotropy beneath the Northern Apennines (Italy) and its tectonic implications, *Geophys. Res. Lett.*, *23*, 2721–2724, doi:10.1029/96GL02519.

Margheriti, L., F. P. Lucente, and S. Pondrelli (2003), SKS splitting measurements in the Apenninic-Tyrrhenian domain (Italy) and their relation with lithospheric subduction and mantle convection, *J. Geophys. Res.*, *108*(B4), 2218, doi:10.1029/2002JB001793.

Margheriti, L., et al., (2006), The subduction structure of the Nothern Apennines: Results from the RETREAT seismic deployment, *Ann. Geophys.*, *49*, 1119-1131.

Mele, G., A. Rovelli, D. Seber, and M. Barazangi (1997), Shear wave attenuation in the lithosphere beneath Italy and surrounding regions: Tectonic implications, *J. Geophys. Res.*, *102*, 11863–11875, doi:10.1029/97JB00262.

Menke, W., and V. Levin (2003), The cross-convolution method for interpreting SKS splitting observations, with application to one and two layer anisotropic Earth models, *Geophys. J. Int.*, *154*, 379–392, doi:10.1046/j.1365-246X.2003.01937.x.

Miller, M. S., and N. Piana Agostinetti (2012), Insights into the evolution of the Italian lithospheric structure from S receiver function analysis, *Earth Planet. Sci. Lett.*, *345-348*, 49–59, doi:10.1016/j.epsl.2012.06.028.

Montagner, J.-P. (1994), Can seismology tell us anything about convection in the mantle?, *Rev. Geophys.*, *32*, 115–137, doi:10.1029/94RG00099.

Munzarová, H. (2011), Anisotropy of the upper mantle under the Northern Apennines based on data from the international experiment RETREAT (Italy), M.S. thesis, Dep. of Geophys., Charles Univ., Prague, Czech Republic.

Oldow, J. S., L. Ferranti, D. S. Lewis, J. K. Campbell, B. D'Argenio, R. Catalano, G. Pappone, L. Carmignani, P. Conti, and C. L. V. Aiken (2002), Active fragmentation of Adria, the north African promontory, central Mediterranean orogen, *Geology*, *30*, 779–782, doi:10.1130/0091-7613(2002)030.

Panza, G., S. Mueller, and G. Calcagnile (1980), The gross features of the lithosphere-asthenosphere system in Europe from seismic surface waves and body waves, *Pure Appl. Geophys.*, *118*, 1209–1213, doi:10.1007/BF01593061.

Park, J., and V. Levin (2002), Seismic anisotropy: Tracing plate dynamics in the mantle, *Science*, *296*, 485-489, doi:10.1126/science.1067319.

Piccinini, D., M. Di Bona, F. P. Lucente, V. Levin, and J. Park (2010), Seismic attenuation and mantle wedge temperature in the northern Apennines subduction zone (Italy) from teleseismic body wave spectra, *J. Geophys. Res.*, *115*, B09309, doi:10.1029/2009JB007180.

Piromallo, C., and A. Morelli (2003), P wave tomography of the mantle under the Alpine-Mediterranean area, *J. Geophys. Res.*, *108*(B2), 2065, doi:10.1029/2002JB001757.

Plomerová, J. (1997), Seismic anisotropy in tomographic studies of the upper mantle beneath southern Europe, Annali di Geofisica, XL, 111–121.

Plomerová, J., and V. Babuška (2010), Long memory of mantle lithosphere fabric - European LAB constrained from seismic anisotropy, *Lithos*, *120*, 131–143, doi:10.1016-j.lithos.2010.01.008.

Plomerová, J., L. Margheriti, J. Park, V. Babuška, S. Pondrelli, L. Vecsey, D. Piccinini, V. Levin, P. Baccheschi, and S. Salimbeni (2006), Seismic anisotropy beneath the Northern Apennines (Italy): Mantle flow or lithosphere fabric?, *Earth Planet. Sci. Lett.*, *247*, 157–170, doi:10.1016/j.epsl.2006.04.023.

Plomerová, J., L. Vecsey, V. Babuška, and LAPNET working group (2011), Domains of Archean mantle lithosphere deciphered by seismic anisotropy – Inferences from the LAPNET array in northern Fennoscandia, *Solid Earth*, *2*, 303–313, doi:10.5194/se-2-303-2011.

Pondrelli, S., S. Salimbeni, G. Ekstrom, A. Morelli, P. Gasperini, and G. Vannucci (2006), Seismic anisotropy beneath the northern Apennines (Italy): Mantle flow or lithosphere fabric?, *Earth Planet. Sci. Lett.*, *247*, 157–170, doi:10.1016/j.epsl.2006.04.023.

Rawlinson, N., and B. L. N. Kennett (2004), Rapid estimation of relative and absolute delay times across a network by Adaptive Stacking, *Geophys. J. Inter.*, *157*, 332-340, doi:10.1111/j.1365-246X.2004.02188.x.

Rosenbaum, G., and G. S. Lister (2004), Neogene and Quaternary rollback evolution of the Tyrrhenian Sea, the Apennines, and the Sicilian Maghrebides. *Tectonics*, *23*, TC1013, doi:10.1029/2003TC001518.

Rosenbaum, G., M. Gasparon, F. P. Lucente, A. Peccerillo, and M. S. Miller (2008), Kinematics of slab tear faults during subduction segmentation and implications for Italian magmatism, *Tectonics*, *27*, TC2008, doi:10.1029/2007TC002143.

Salimbeni, S., S. Pondrelli, L. Margheriti, J. Park, and V. Levin (2008), SKS splitting measurements beneath Northern Apennines region: A case of oblique trench-retreat, *Tectonophysics*, *462*, 68–82, doi:10.1016/j.tecto.2007.11.075.

Savage, M. K. (1999), Seismic anisotropy and mantle deformation: What have we learned from shear wave splitting?, *Rev. Geophys.*, *37*, 65–106, doi:10.1029/98RG02075.

Savage, M. K., and P. G. Silver (1993), Mantle deformation and tectonics: Constraints from seismic anisotropy in western United States, *Phys. Earth Planet. Inter.*, *78*, 207–227.

Serpelloni, E., M. Anzidei, P. Baldi, G. Casula, and A. Galvani (2005), Crustal velocity and strain-rate fields in Italy and surrounding regions: New results from the `analysis of permanent and non-permanent GPS networks, *Geophys. J. Int.*, *161*, 861–880, doi:10.1111/j.1365-246X.2005.02618.x.

Šílený, J., and J. Plomerová (1996), Inversion of shear-wave splitting parameters to retrieve three-dimensional orientation of anisotropy in continental lithosphere, *Phys. Earth Planet. Inter.*, *95*, 277–292, doi:10.1016/0031-9201(95)03121-9.

Silver, P. G. (1996), Seismic anisotropy beneath the continents: probing the depths of geology, *Annu. Rev. Earth Planet. Sci.*, *24*, 385–432, doi:10.1146/annurev.earth.24.1.385.

Silver, P. G., and W. W. Chan (1991), Shear wave splitting and subcontinental mantle deformation, *J. Geophys. Res.*, *96*, 16429–16454, doi:10.1029/91JB00899.

Spakman, W., and M. J. R. Wortel (2004), A tomographic view on Western Mediterranean Geodynamics, in The TRANSMED Atlas, The Mediterranean Region from Crust to Mantle, edited by W. Cavazza, F. M. Roure, W. Spakman, G. M. Stampfli and P. A. Ziegler, pp. 31-52, Springer, Berlin.

Stammler, K. (1993), Seismichandler programmable multichannel data handler for interactive and automatic processing of seismological analyses, *Comput. Geosci.*, *19*, 135–140, doi:10.1016/0098-3004(93)90110-Q.

Stampfli, G., G. and Borel (2002), A plate tectonic model for the Paleozoic and Mesozoic constrained by dynamic plate boundaries and restored synthetic oceanic isochrones, *Earth Planet. Sci. Lett.*, *196*, 17–33, doi:10.1016/S0012-821X(01)00588-X.

Thomson, S. N., M. T. Brandon, P. W. Reiners, M. Zattin, P. J. Isaacson. and M. L. Balestrieri (2010), Thermochronologic evidence for orogen-parallel variability in wedge kinematics during extending convergent orogenesis of the northern Apennines, Italy, *Geol. Soc. Am. Bull.*, *122*, 1160–1179, doi:10.1130/B26573.1.

Vecsey, L., J. Plomerová, and V. Babuška (2008), Shear-wave splitting measurements - Problems and solutions, *Tectonophysics*, *462*, 178–196, doi:10.1016/j.tecto.2008.01.021.

Vignaroli, G., C. Faccenna, L. Jolivet, C. Piromallo, and F. Rossetti (2008), Subduction polarity reversal at the junction between the Western Alps and the Northern Apennines, Italy, *Tectonophysics*, *450*, 34–35, doi:10.1016/j.tecto.2007.12.012.

Vuan, A., P. Klin, G. Laurenzano, and E. Priolo (2011), Far-source long-period displacement response spectra in the Po and Venetian plains (Italy) from 3D wavefield simulations, *Bull. Seismol. Soc. Am.*, *101*, 1055–1072, doi:10.1785/0120090371.

Wessel, P., and W. H. F. Smith (1998), New, improved version of the Generic Mapping Tools released, *EOS Trans. AGU*, *79*, 579, doi:10.1029/98EO00426.

Wortel, M. J. R., and W. Spakman (2000), Subduction and slab detachment in the Mediterranean-Carpathian region, *Science*, *290*, 1910–1917, doi:10.1126/science.290.5498.1910.

Wuestefeld, A., G. Bokelmann, G. Barruol, and J.-P. Montagner (2009), Identifying global seismic anisotropy patterns by correlating shear-wave splitting and surface-wave data, *Phys. Earth Planet. Inter.*, *176*, 198–212, doi:10.1016/j.pepi.2009.05.006.

Auxiliary material for Paper 2012GC004537

Upper-mantle fabrics beneath the Northern Apennines revealed by seismic anisotropy

Helena Munzarová

Geophysical Institute, Academy of Sciences of the Czech Republic,
Boční II/1401,
141 31 Prague 4, Czech Republic

Jaroslava Plomerová
Geophysical Institute, Academy of Sciences of the Czech Republic

Vladislav Babuška
Geophysical Institute, Academy of Sciences of the Czech Republic

Luděk Vecsey
Geophysical Institute, Academy of Sciences of the Czech Republic

Geochem. Geophys. Geosyst., doi:10.1029/2012GC004537

Introduction

The auxiliary material consists of the station list (table "2012GC004537-Table_S1.doc"), the event list (table "2012GC004537-Table_S2.doc"), of a figure accompanying the semi-automatic picking procedure (figure "2012GC004537-Fig_S3.pdf"), and of two figures that present the results of P-wave anisotropy and of the synthetic tests in a greater detail (figures "2012GC004537-Fig_S4.pdf" and "2012GC004537-Fig_S5.pdf") than the Figures 2 and 8 created for the printed version.

1. 2012GC004537-Table_S1.doc List of seismic stations involved in experiment RETREAT.
1.1 Column "STA", station code.
1.2 Column "LAT", degrees, latitude of the station, north of equator.
1.3 Column "LON", degrees, longitude of the station, east of Greenwich.
1.4 Column "ALT", km, altitude of the station.

2. 2012GC004537-Table_S2.doc List of events used for P-wave directional term analysis.
2.1 Column "DAY", number of days from the start of recording.
2.2 Column "EVENT", event code compiled of the origin date and time.
2.3 Column "DATE", origin date [yy/mm/dd].
2.4 Column "OT", origin time [hhmmss.ss].
2.5 Column "LAT", degrees, latitude of the earthquake, north of equator.
2.6 Column "LON", degrees, longitude of the earthquake, east of Greenwich.
2.7 Column "D", km, depth of the earthquake.
2.8 Column "MAG", moment magnitude of the earthquake.
2.9 Column "BACK", degrees, back-azimuth of the earthquake.
2.10 Column "DIST", degrees, epicentral distance of the earthquake from the station array.

3. 2012GC004537-Fig_S3.pdf
Example of measuring teleseismic P-wave arrival times with semi-automatic picking software Autopick; (a) Original seismograms simulated to WWSSN-SP response; Setting cross-correlation window (blue rectangle) containing the initial part of a reference seismogram; (b) Seismograms aligned by the time shifts derived from the cross-correlations; Blue rectangle delimits a time interval around the selected distinct extreme which can be traced across all the waveforms and which is the closest to the first P-wave onset; (c) Relative P-wave arrival times (P) at all stations and three manually measured absolute P-wave arrival times (P_abs).

4. 2012GC004537-Fig_S4.pdf
P-residual spheres at individual stations for the whole RETREAT array (a) and for two parts of the array with densely spaced stations (b, c; green and blue rectangles, respectively). Stations with similar P-sphere pattern form groups (colored regions). For more details see also caption of Figure 2.

5. 2012GC004537-Fig_S5.pdf
Synthetic P-residual spheres at individual stations derived from the tomography model of Benoit et al. [2011] for the whole RETREAT array (a) and for two parts of the array with densely spaced stations (b, c; green and blue rectangles, respectively). Stations with similar synthetic P-sphere pattern form groups (colored regions). The domains according to the observed P spheres (Figs. 2 and S3) are delineated with colored lines. Dot-dashed line indicates location of the vertical cross-section in Figure 10.

Table S1. List of seismic stations involved in experiment RETREAT[a]

STA	LAT	LON	ALT	STA	LAT	LON	ALT
ANZR	44.5760	11.1500	0.039	MNGR	44.5070	10.7850	0.404
ARCI	42.8519	11.4754	1.080	MSTR	43.9130	10.4920	0.230
BADR	43.5100	12.2440	0.441	MTVR	44.4680	11.0910	0.274
BARR	44.2828	12.0797	0.079	MURB	43.2630	12.5246	0.845
BOB	44.7679	9.4478	0.910	PDCR	43.7810	10.5800	0.083
CAIR	44.2940	11.0030	0.848	PESR	43.9410	12.8400	0.152
CING	43.3756	13.1954	0.626	PIIR	43.7219	10.5250	0.066
CLLR	43.6680	11.0300	0.220	PIZR	44.1310	10.8620	1.236
CORR	44.4760	10.0890	0.702	PNTR	44.0110	10.8200	0.827
CRER	43.6190	11.9520	1.246	POPR	43.0220	10.5340	0.016
CSNR	43.4731	11.2902	0.636	PRUR	44.0100	10.3090	0.479
CSTR	44.4380	11.0320	0.310	PTCR	44.2440	10.9710	0.901
CUTR	44.1000	10.7560	0.691	RAPR	43.2890	11.6090	0.337
ELBR	42.7470	10.2110	0.146	RAVR	44.7559	11.1188	0.015
FIRR	44.1890	11.4340	0.721	RONR	44.2150	10.9230	1.048
FNVD	44.1678	11.1229	0.950	RSMR	43.9303	12.4497	0.645
FOSR	44.1350	10.0200	0.520	SACS	42.8491	11.9097	0.845
FSSR	43.6930	12.7770	0.480	SASR	43.2570	10.6900	0.431
GABR	43.5000	10.4130	0.246	SCUR	44.4156	9.5361	0.817
GRFR	43.1470	10.9760	0.741	SFIR	43.9048	11.8469	0.548
GROG	43.4262	9.8920	0.118	USOR	43.9810	10.6850	0.864
GUSR	44.3510	10.5880	0.666	VLC	44.1594	10.3864	0.562
MAON	42.4283	11.1309	0.237	VOLR	43.5478	10.8572	0.325
MASR	43.8611	11.3808	0.500	VRGR	43.6400	10.4700	0.011
MCUR	44.0050	11.1797	0.726	ZOCR	44.3508	10.9765	0.700

[a]STA – station code; LAT – latitude [º]; LON – longitude [º]; ALT – altitude [km]

Table S2. List of events used for P-wave directional term analysis[a]

DAY	EVENT	DATE	OT	LAT	LON	D	MAG	BAZ	DIST
1	0310231054	03/10/23	105439.68	51.40	176.69	33	5.6	8.6	84.1
3	0310251241	03/10/25	124135.25	38.40	100.95	10	5.8	60.0	64.8
3	0310251247	03/10/25	124758.83	38.38	100.97	10	5.8	60.0	64.9
6	0310282148	03/10/28	214821.02	43.84	147.75	65	6.1	29.5	84.5
9	0310310106	03/10/31	010628.28	37.81	142.62	10	7.0	35.9	87.7
11	0311021335	03/11/02	133531.09	44.58	150.33	33	5.5	27.5	84.7
14	0311050058	03/11/05	005851.11	4.97	-77.77	33	6.0	272.4	85.3
18	0311091952	03/11/09	195236.81	-0.67	-19.69	10	6.6	219.7	51.9
21	0311120826	03/11/12	082643.74	33.17	137.07	384	6.4	42.3	89.0
23	0311141843	03/11/14	184351.14	36.40	141.07	41	5.7	37.7	88.2
26	0311170643	03/11/17	064306.80	51.15	178.65	33	7.8	7.5	84.6
26	0311170712	03/11/17	071242.55	51.28	177.61	33	5.8	8.1	84.3
27	0311180212	03/11/18	021222.57	51.10	178.12	33	5.5	7.8	84.6
27	0311180750	03/11/18	075010.66	51.04	178.89	33	5.8	7.3	84.7
35	0311261925	03/11/26	192507.34	28.52	-43.73	10	5.6	269.2	45.5
40	0312010138	03/12/01	013831.96	42.90	80.51	10	6.0	65.2	49.3
44	0312052126	03/12/05	212609.48	55.54	165.78	10	6.7	14.0	78.6
48	0312091244	03/12/09	124401.68	51.33	-179.27	33	6.2	6.1	84.6
58	0312190011	03/12/19	001158.23	19.85	95.70	10	5.6	78.5	73.0
60	0312210740	03/12/21	074045.83	-0.77	-20.60	10	6.6	220.7	52.5
61	0312220847	03/12/22	084707.35	42.28	144.60	37	5.8	32.3	84.7
62	0312230558	03/12/23	055837.19	-0.70	-20.33	10	5.8	220.4	52.3
65	0312260156	03/12/26	015652.44	29.00	58.31	10	6.8	94.9	40.6
68	0312290130	03/12/29	013054.70	42.42	144.61	33	6.1	32.2	84.5
81	0401110432	04/01/11	043247.79	-36.70	53.35	5	6.2	147.0	89.3
81	0401111931	04/01/11	193132.81	55.60	165.68	21	5.5	14.0	78.5
86	0401161807	04/01/16	180755.66	7.64	-37.70	10	6.2	244.0	55.3
89	0401190722	04/01/19	072252.91	84.47	105.21	10	5.6	7.5	47.0
94	0401241301	04/01/24	130145.70	52.12	-30.18	10	5.9	301.8	28.1
96	0401261027	04/01/26	102707.65	51.13	178.08	36	5.6	7.8	84.5
97	0401270950	04/01/27	095052.17	56.81	-156.76	75	5.6	352.9	78.9
100	0401301751	04/01/30	175144.81	44.73	150.06	30	5.5	27.6	84.5
111	0402102033	04/02/10	203351.27	59.37	-152.03	65	5.6	350.9	75.9
115	0402141030	04/02/14	103022.18	34.77	73.22	11	5.5	78.3	48.2
123	0402220646	04/02/22	064627.04	-1.56	100.49	42	6.3	91.2	91.1
126	0402250856	04/02/25	085606.50	54.62	162.81	19	5.5	15.9	78.9
138	0403082339	04/03/08	233911.34	10.48	-43.92	10	6.0	251.8	57.4
142	0403122245	04/03/12	224519.00	36.40	70.77	218	5.8	77.7	45.7
146	0403162123	04/03/16	212319.86	37.56	96.67	14	5.5	63.0	62.6
147	0403170321	04/03/17	032107.91	-21.12	-65.59	289	6.1	245.4	95.0
149	0403192042	04/03/19	204200.31	-34.50	55.28	10	5.7	144.5	88.2
150	0403200853	04/03/20	085315.11	53.83	160.47	52	5.8	17.5	79.1
156	0403261520	04/03/26	152006.62	41.86	144.21	22	5.8	32.7	84.9
157	0403271847	04/03/27	184729.20	33.95	89.18	8	6.0	70.3	59.7
166	0404052124	04/04/05	212404.00	36.51	71.03	187	6.6	77.4	45.8
170	0404090155	04/04/09	015550.71	-1.55	100.54	65	5.5	91.1	91.1
175	0404140154	04/04/14	015409.22	55.23	162.66	51	6.2	15.8	78.3
175	0404142307	04/04/14	230739.94	71.07	-7.75	12	6.0	347.8	28.8
197	0405061343	04/05/06	134312.89	42.53	145.02	28	5.6	31.9	84.6
202	0405110828	04/05/11	082848.28	0.41	97.82	21	6.2	91.6	87.8
202	0405112358	04/05/11	235854.41	12.70	-44.49	10	5.5	254.1	56.2

219	0405281238	04/05/28	123844.47	36.29	51.61	17	6.3	89.2	32.0
220	0405290347	04/05/29	034710.77	37.75	141.88	29	5.8	36.5	87.4
226	0406040148	04/06/04	014803.17	54.46	-163.85	72	5.6	356.7	81.7
232	0406101519	04/06/10	151957.75	55.68	160.00	188	6.9	17.1	77.3
249	0406271251	04/06/27	125150.35	-40.92	43.31	10	5.6	155.8	89.6
250	0406280949	04/06/28	094947.00	54.80	-134.25	20	6.8	340.1	77.0
251	0406290701	04/06/29	070130.90	10.74	-87.04	9	6.3	283.0	88.0
253	0407010920	04/07/01	092044.14	54.13	-35.26	10	5.6	305.8	31.2
260	0407081030	04/07/08	103049.16	47.20	151.30	128	6.4	25.7	82.7
269	0407170610	04/07/17	061018.07	34.75	140.22	46	5.6	39.2	89.2
271	0407190801	04/07/19	080149.46	49.62	-126.97	23	6.4	333.6	79.6
273	0407210011	04/07/21	001129.78	40.97	143.08	30	5.5	33.9	85.2
274	0407220945	04/07/22	094514.90	26.49	128.89	20	6.1	52.0	89.9
277	0407251435	04/07/25	143519.06	-2.43	103.98	582	7.3	89.4	94.2
281	0407290144	04/07/29	014406.91	12.45	95.00	22	5.9	84.7	77.5
281	0407291323	04/07/29	132303.28	12.44	95.00	24	5.6	84.7	77.5
290	0408070930	04/08/07	093016.94	51.75	-166.31	8	6.3	358.0	84.5
290	0408071418	04/08/07	141835.23	-6.24	95.67	20	5.8	97.9	90.8
293	0408100147	04/08/10	014732.81	36.44	70.80	207	6.0	77.6	45.7
293	0408100613	04/08/10	061333.24	39.63	141.96	69	5.7	35.4	85.8
307	0408241005	04/08/24	100534.47	32.54	92.19	10	5.7	70.0	62.6
313	0408301223	04/08/30	122321.60	49.54	157.28	11	5.7	21.0	82.3
319	0409051007	04/09/05	100707.82	33.07	136.62	14	7.2	42.6	88.8
319	0409051457	04/09/05	145718.61	33.18	137.07	10	7.4	42.3	89.0
320	0409062329	04/09/06	232935.09	33.21	137.23	10	6.6	42.1	89.0
321	0409071836	04/09/07	183620.27	33.24	137.09	10	5.6	42.2	88.9
322	0409081458	04/09/08	145825.83	33.14	137.20	21	6.2	42.2	89.1
323	0409091633	04/09/09	163321.73	17.76	-81.55	25	6.0	284.4	79.3
327	0409130300	04/09/13	030012.85	44.00	151.41	8	6.1	27.1	85.6
329	0409151910	04/09/15	191050.59	14.22	120.41	115	6.0	66.0	93.9
332	0409180707	04/09/18	070748.43	23.11	-67.61	10	5.7	279.6	65.9
333	0409192026	04/09/19	202604.09	52.21	174.03	25	6.2	10.1	83.0
350	0410061440	04/10/06	144039.92	35.95	139.92	64	5.8	38.8	88.0
351	0410072146	04/10/07	214620.30	37.12	54.48	34	5.6	85.9	33.7
352	0410081436	04/10/08	143606.11	13.93	120.53	105	6.5	66.1	94.2
359	0410150408	04/10/15	040850.24	24.53	122.69	94	6.7	57.5	87.8
366	0410221200	04/10/22	120012.43	14.17	40.30	10	5.5	130.1	39.0
367	0410230856	04/10/23	085600.86	37.23	138.78	16	6.6	38.8	86.5
367	0410230903	04/10/23	090312.53	37.32	138.82	10	6.1	38.7	86.4
367	0410230911	04/10/23	091157.42	37.24	138.61	18	5.8	38.9	86.4
367	0410230934	04/10/23	093404.99	37.32	138.81	10	6.3	38.7	86.4
368	0410242104	04/10/24	210457.06	37.31	138.70	11	6.0	38.8	86.4
370	0410260211	04/10/26	021133.44	31.02	81.15	10	6.0	77.7	55.8
371	0410270140	04/10/27	014050.26	37.28	138.88	14	6.0	38.7	86.5
379	0411041403	04/11/04	140311.67	43.62	146.81	61	5.9	30.2	84.3
383	0411081555	04/11/08	155501.16	24.10	122.54	29	6.3	57.9	88.0
386	0411111002	04/11/11	100247.33	42.14	144.34	32	6.1	32.5	84.7
390	0411150906	04/11/15	090656.56	4.70	-77.51	15	7.2	272.0	85.3
391	0411161157	04/11/16	115728.14	53.06	160.13	48	5.5	18.0	79.8
392	0411172058	04/11/17	205822.31	39.19	71.86	20	5.8	73.6	45.1
395	0411200807	04/11/20	080722.08	9.60	-84.17	16	6.4	280.2	86.7
396	0411211141	04/11/21	114107.76	15.68	-61.71	14	6.3	269.5	66.5
401	0411262242	04/11/26	224237.31	42.38	142.90	58	5.7	33.3	83.9
403	0411281832	04/11/28	183214.12	43.01	145.12	39	7.0	31.6	84.2
411	0412061415	04/12/06	141511.89	42.90	145.23	35	6.8	31.5	84.4

419	0412140556	04/12/14	055610.04	44.12	141.79	10	5.8	33.0	82.0
419	0412142320	04/12/14	232013.36	18.96	-81.41	10	6.8	285.2	78.4
426	0412211534	04/12/21	153428.12	42.96	145.41	37	5.7	31.4	84.4
431	0412260308	04/12/26	030844.21	13.74	93.01	30	5.9	85.0	75.2
431	0412260324	04/12/26	032454.94	4.47	94.07	26	5.8	91.2	82.2
431	0412261019	04/12/26	101931.73	13.46	92.74	26	6.3	85.4	75.2
431	0412261448	04/12/26	144844.27	13.59	92.91	30	5.8	85.2	75.2
432	0412270032	04/12/27	003216.48	5.48	94.47	33	6.1	90.2	81.8
432	0412270049	04/12/27	004928.59	12.98	92.39	23	6.1	86.0	75.2
432	0412270939	04/12/27	093906.80	5.35	94.65	35	6.2	90.2	82.1
432	0412271446	04/12/27	144646.48	12.35	92.47	19	5.8	86.5	75.7
433	0412281117	04/12/28	111743.87	4.73	95.21	36	5.8	90.2	82.9
434	0412290139	04/12/29	013941.24	8.38	93.16	34	5.9	89.0	78.9
434	0412290150	04/12/29	015052.57	9.11	93.76	8	6.1	88.0	78.8
434	0412290556	04/12/29	055647.54	8.79	93.20	12	6.2	88.6	78.7
434	0412292112	04/12/29	211259.47	5.23	94.62	29	5.7	90.3	82.1
435	0412301758	04/12/30	175811.19	12.24	92.51	30	5.8	86.5	75.8
436	0412311438	04/12/31	143846.62	5.11	94.86	49	5.6	90.2	82.4
437	0501010403	05/01/01	040310.99	5.47	94.40	36	5.8	90.3	81.8
437	0501010625	05/01/01	062544.82	5.10	92.30	11	6.7	92.0	80.5
437	0501011908	05/01/01	190807.80	7.34	94.46	55	6.1	88.8	80.6
437	0501012228	05/01/01	222813.78	7.19	92.76	10	5.5	90.1	79.4
438	0501020827	05/01/02	082741.89	3.24	95.46	8	5.9	91.2	84.1
438	0501021535	05/01/02	153556.72	6.36	92.79	30	6.4	90.7	80.0
440	0501040913	05/01/04	091312.25	10.67	92.36	23	6.1	87.8	76.8
441	0501051454	05/01/05	145404.81	5.49	94.39	48	5.9	90.3	81.8
442	0501060011	05/01/06	001117.10	5.60	93.25	30	5.5	91.0	80.9
442	0501060056	05/01/06	005629.91	5.32	94.83	49	6.1	90.1	82.2
443	0501071049	05/01/07	104914.33	8.77	93.56	30	5.5	88.4	78.9
445	0501092212	05/01/09	221256.52	4.93	95.11	40	6.1	90.2	82.7
448	0501120840	05/01/12	084003.65	-0.88	-21.19	10	6.8	221.3	52.8
454	0501180659	05/01/18	065903.74	57.05	-33.81	10	5.7	311.6	30.6
454	0501181409	05/01/18	140906.22	42.95	144.87	42	6.3	31.7	84.2
456	0501200259	05/01/20	025910.50	49.83	156.18	38	5.5	21.6	81.8
460	0501240416	05/01/24	041647.44	7.33	92.48	30	6.3	90.2	79.1
463	0501272009	05/01/27	200952.16	5.51	94.31	30	5.6	90.3	81.7
473	0502060424	05/02/06	042418.63	13.85	93.58	35	5.6	84.6	75.5
480	0502130122	05/02/13	012209.31	5.08	94.79	48	5.7	90.3	82.3
481	0502142338	05/02/14	233808.66	41.73	79.44	22	6.2	67.0	49.1
483	0502162027	05/02/16	202752.48	-36.32	-16.56	10	6.6	201.7	83.7
484	0502170531	05/02/17	053128.08	4.70	95.16	47	5.9	90.3	82.9
485	0502181933	05/02/18	193346.41	5.45	94.42	48	5.8	90.3	81.8
489	0502220225	05/02/22	022522.92	30.75	56.82	14	6.5	93.8	38.5
492	0502252304	05/02/25	230404.02	38.11	72.71	114	6.1	74.6	46.2
493	0502261237	05/02/26	123740.69	40.73	142.38	68	5.8	34.5	85.1
493	0502261256	05/02/26	125652.62	2.91	95.59	36	6.8	91.3	84.4
501	0503060521	05/03/06	052143.43	84.95	99.39	10	6.3	7.0	46.4
505	0503100028	05/03/10	002826.36	85.25	92.89	10	5.5	6.6	45.8
508	0503130331	05/03/13	033123.08	27.09	61.89	54	6.0	94.5	44.2
508	0503132212	05/03/13	221245.81	5.49	94.60	52	5.5	90.1	81.9
511	0503161323	05/03/16	132332.56	43.47	146.89	39	5.6	30.2	84.5
512	0503171337	05/03/17	133737.11	15.14	-91.38	197	6.1	289.1	87.9
512	0503172320	05/03/17	232049.34	4.86	95.09	60	5.7	90.2	82.7
515	0503200153	05/03/20	015341.83	33.81	130.13	10	6.7	46.5	85.0
520	0503250104	05/03/25	010452.96	5.49	94.37	39	5.9	90.3	81.8

523	0503281609	05/03/28	160936.53	2.09	97.11	30	8.6	90.8	86.1
523	0503281830	05/03/28	183044.56	0.92	97.87	36	6.1	91.2	87.4
523	0503281902	05/03/28	190219.91	1.01	97.82	30	5.8	91.1	87.3
523	0503282313	05/03/28	231300.95	0.17	97.04	38	5.7	92.3	87.4
526	0503310723	05/03/31	072353.79	1.70	97.12	22	5.8	91.1	86.4
528	0504021252	05/04/02	125236.59	78.61	6.10	10	6.1	358.5	34.9
529	0504030059	05/04/03	005921.42	0.37	98.32	30	6.0	91.3	88.2
529	0504030310	05/04/03	031056.47	2.02	97.94	36	6.3	90.3	86.7
533	0504072004	05/04/07	200441.06	30.49	83.66	11	6.3	76.8	57.9
535	0504091516	05/04/09	151627.89	56.17	-154.52	14	6.0	351.6	79.3
536	0504101114	05/04/10	111419.62	-1.71	99.78	30	6.5	91.8	90.6
536	0504102222	05/04/10	222215.70	35.60	140.40	43	6.1	38.6	88.5
540	0504141129	05/04/14	112952.55	-1.91	99.95	33	5.8	91.8	90.9
543	0504172123	05/04/17	212350.83	-1.63	99.62	21	5.8	91.8	90.5
570	0505140505	05/05/14	050518.48	0.59	98.46	34	6.8	91.0	88.1
570	0505141804	05/05/14	180455.06	30.69	56.86	10	5.5	93.8	38.6
577	0505210511	05/05/21	051135.39	-3.29	-80.99	39	6.3	268.7	93.4
577	0505212301	05/05/21	230116.05	5.28	94.80	55	5.9	90.1	82.2
587	0505310229	05/05/31	022931.29	5.24	94.43	30	5.5	90.4	82.0
588	0506012006	05/06/01	200641.45	28.88	94.63	25	6.1	71.8	66.5
597	0506100350	05/06/10	035007.88	51.19	179.55	40	5.6	6.9	84.6
599	0506120417	05/06/12	041713.49	52.79	143.87	10	5.6	27.0	75.5
600	0506132244	05/06/13	224433.91	-19.99	-69.20	115	7.8	248.6	96.6
601	0506141710	05/06/14	171012.28	51.24	179.31	17	6.8	7.0	84.5
601	0506142249	05/06/14	224917.81	50.98	179.43	27	5.6	7.0	84.8
602	0506150250	05/06/15	025054.19	41.29	-125.95	16	7.2	328.8	86.4
604	0506170621	05/06/17	062142.59	40.77	-126.57	12	6.6	328.9	87.1
606	0506191615	05/06/19	161515.23	35.61	140.48	48	5.7	38.6	88.6
614	0506271135	05/06/27	113545.60	18.78	-107.30	20	6.2	302.7	95.6
618	0507010348	05/07/01	034828.69	36.57	71.32	63	5.6	77.2	46.0
621	0507041136	05/07/04	113605.65	-42.28	42.37	10	6.3	157.0	90.6
622	0507050152	05/07/05	015202.95	1.82	97.08	21	6.8	91.1	86.3
623	0507060824	05/07/06	082441.95	69.00	-16.64	10	5.6	340.2	28.9
626	0507092337	05/07/09	233711.14	33.42	140.82	55	5.8	39.5	90.5
637	0507202154	05/07/20	215405.72	43.07	109.02	6	5.5	51.8	66.8
640	0507230734	05/07/23	073456.77	35.50	139.98	61	6.1	39.0	88.4
640	0507231440	05/07/23	144025.02	36.39	70.72	209	5.5	77.7	45.6
640	0507232253	05/07/23	225335.08	5.11	94.80	48	5.6	90.2	82.3
641	0507241542	05/07/24	154206.20	7.92	92.19	16	7.5	90.0	78.5
642	0507251602	05/07/25	160207.56	71.11	-7.43	10	5.5	348.0	28.8
643	0507260408	05/07/26	040837.16	45.37	-112.61	12	5.7	323.0	77.6
643	0507261217	05/07/26	121714.27	52.87	160.10	27	5.8	18.1	79.9
643	0507261411	05/07/26	141136.39	-15.35	-72.96	110	5.9	254.4	96.0
644	0507270239	05/07/27	023922.57	33.26	142.32	33	5.5	38.6	91.4
646	0507290500	05/07/29	050030.09	52.91	-168.65	50	5.6	359.5	83.4
646	0507292033	05/07/29	203340.03	2.86	93.56	32	5.8	92.8	83.0
647	0507301513	05/07/30	151320.12	5.18	94.48	38	5.8	90.4	82.1
651	0508031103	05/08/03	110315.13	11.25	-85.54	14	6.5	282.3	86.6
653	0508050056	05/08/05	005653.72	51.24	-178.25	23	5.8	5.5	84.7
654	0508060402	05/08/06	040232.96	85.26	97.16	10	5.5	6.6	46.2
655	0508070217	05/08/07	021746.04	-47.09	33.62	10	6.2	164.5	93.1
664	0508160246	05/08/16	024628.40	38.28	142.04	36	7.2	36.1	87.0
673	0508252108	05/08/25	210813.03	36.94	79.17	17	5.5	72.6	51.3
685	0509060116	05/09/06	011602.35	24.08	122.19	32	6.1	58.1	87.8
689	0509101657	05/09/10	165747.27	4.86	95.04	41	5.8	90.3	82.7

692	0509131432	05/09/13	143257.81	8.07	91.91	30	5.5	90.1	78.2
699	0509202123	05/09/20	212337.56	12.71	40.53	10	5.5	131.1	40.3
700	0509210225	05/09/21	022508.11	43.89	146.15	103	6.1	30.5	83.9
702	0509231348	05/09/23	134831.41	16.13	-87.49	29	5.9	287.1	84.5
703	0509241924	05/09/24	192402.66	12.47	40.63	11	5.6	131.1	40.6
705	0509260155	05/09/26	015537.67	-5.68	-76.40	115	7.5	263.8	91.7
710	0510012154	05/10/01	215409.34	-23.61	-63.63	547	5.7	242.3	95.5
717	0510080350	05/10/08	035040.80	34.54	73.59	26	7.7	78.3	48.6
717	0510081046	05/10/08	104628.79	34.73	73.10	8	6.4	78.4	48.1
717	0510081225	05/10/08	122520.18	34.77	73.12	10	5.8	78.3	48.1
717	0510082113	05/10/08	211331.86	34.73	73.18	10	5.9	78.3	48.2
718	0510091920	05/10/09	192037.44	34.35	73.70	10	5.5	78.5	48.8
720	0510111505	05/10/11	150539.66	4.82	95.10	30	6.0	90.3	82.8
721	0510122023	05/10/12	202338.23	34.86	73.11	10	5.6	78.2	48.1
724	0510151006	05/10/15	100617.01	46.82	154.11	42	6.1	24.1	83.9
724	0510151551	05/10/15	155107.20	25.32	123.36	183	6.5	56.5	87.6
726	0510171923	05/10/17	192302.20	-17.77	-69.49	123	5.8	250.4	95.3
728	0510190233	05/10/19	023328.31	34.75	73.04	5	5.6	78.4	48.1
728	0510191144	05/10/19	114442.79	36.40	140.84	32	6.5	37.9	88.1
729	0510201526	05/10/20	152631.95	52.21	-169.04	35	5.7	359.7	84.1
731	0510221312	05/10/22	131247.81	37.15	140.93	53	5.6	37.4	87.5
732	0510231008	05/10/23	100814.74	37.38	134.56	380	6.0	41.4	84.4
732	0510231504	05/10/23	150420.89	34.85	73.04	10	5.6	78.3	48.0
737	0510282230	05/10/28	223058.23	11.07	-62.04	64	5.5	266.1	69.8
749	0511091133	05/11/09	113313.19	-1.02	-76.94	248	5.9	267.5	88.9
750	0511101929	05/11/10	192954.14	57.47	120.59	6	5.9	34.4	63.3
754	0511142138	05/11/14	213851.42	38.11	144.90	11	7.0	34.2	88.3
760	0511201253	05/11/20	125302.95	53.84	-164.09	30	6.2	356.8	82.3
761	0511211536	05/11/21	153630.98	31.02	130.00	145	6.2	48.3	87.1
767	0511271022	05/11/27	102219.19	26.77	55.86	10	6.1	99.7	40.1
767	0511271630	05/11/27	163037.56	26.84	55.81	10	5.5	99.6	40.0
772	0512021313	05/12/02	131309.52	38.09	142.12	29	6.5	36.1	87.2
775	0512051219	05/12/05	121956.62	-6.22	29.83	22	7.2	155.7	52.9
781	0512111554	05/12/11	155413.91	57.44	120.76	10	5.7	34.4	63.4
782	0512122101	05/12/12	210140.62	43.21	139.33	26	5.7	35.0	81.8
782	0512122147	05/12/12	214746.06	36.36	71.09	224	6.5	77.5	45.9
791	0512211432	05/12/21	143239.30	6.62	-82.75	10	6.0	277.0	87.8
793	0512232147	05/12/23	214728.00	-1.39	-77.52	192	6.1	267.6	89.5
800	0512301826	05/12/30	182643.91	7.53	-82.27	10	6.1	277.4	86.8
802	0601010847	06/01/01	084713.35	4.74	95.14	51	5.7	90.3	82.8
808	0601070223	06/01/07	022343.59	52.42	173.61	30	5.7	10.3	82.8
821	0601200853	06/01/20	085352.94	31.07	-41.42	10	5.7	270.7	42.4
822	0601210407	06/01/21	040704.74	13.03	93.27	52	5.8	85.4	75.8
824	0601232050	06/01/23	205044.98	6.86	-77.79	14	6.2	273.8	84.1
854	0602222219	06/02/22	221907.80	-21.32	33.58	11	7.5	156.9	68.4
860	0602280731	06/02/28	073102.65	28.12	56.87	18	6.2	97.2	40.0
875	0603151419	06/03/15	141948.69	-21.14	33.72	10	5.6	156.7	68.3
880	0603201740	06/03/20	174044.52	34.76	73.75	10	5.6	78.0	48.6
885	0603250728	06/03/25	072857.65	27.57	55.69	18	5.9	98.8	39.5
885	0603250955	06/03/25	095512.38	27.54	55.78	10	5.5	98.8	39.6
885	0603251000	06/03/25	100036.60	27.47	55.80	15	5.5	98.9	39.6
891	0603310117	06/03/31	011700.96	33.50	48.78	7	6.1	95.9	31.3
892	0604011002	06/04/01	100219.57	22.87	121.28	9	6.2	59.5	88.1
906	0604152240	06/04/15	224054.09	22.80	121.36	17	5.9	59.5	88.2
911	0604202325	06/04/20	232502.16	60.95	167.09	22	7.6	11.6	73.6

912	0604210432	06/04/21	043243.82	60.53	165.82	9	6.3	12.4	73.8
912	0604211114	06/04/21	111415.33	61.35	167.52	12	6.1	11.3	73.3
913	0604220721	06/04/22	072157.95	61.20	167.32	10	5.8	11.4	73.4
916	0604251826	06/04/25	182617.16	1.99	97.00	21	6.3	91.0	86.1
920	0604291658	06/04/29	165806.31	60.49	167.52	11	6.6	11.5	74.1
921	0604300043	06/04/30	004310.59	44.50	102.39	10	5.7	53.8	62.1
931	0605100242	06/05/10	024251.03	52.51	-169.26	18	6.4	359.9	83.8
932	0605111722	06/05/11	172254.14	23.31	94.32	48	5.7	76.6	69.8
934	0605130311	06/05/13	031142.94	5.51	94.44	45	5.9	90.2	81.8
937	0605161528	06/05/16	152825.92	0.09	97.05	12	6.8	92.3	87.4
943	0605221112	06/05/22	111200.38	60.77	165.74	16	6.7	12.3	73.6
943	0605221308	06/05/22	130801.67	54.28	158.43	184	6.2	18.5	78.2
949	0605280900	06/05/28	090012.45	19.16	121.18	23	5.6	62.1	90.8
957	0606050627	06/06/05	062707.96	1.17	-28.07	10	6.0	229.9	54.6
957	0606050634	06/06/05	063431.80	1.02	-28.16	10	5.6	229.9	54.8
961	0606092317	06/06/09	231727.88	-47.75	32.61	22	5.9	165.3	93.5
963	0606112001	06/06/11	200126.31	33.13	131.14	139	6.3	46.3	86.0
966	0606140418	06/06/14	041842.51	51.75	177.08	14	6.4	8.3	83.8
967	0606150649	06/06/15	064948.83	45.39	97.35	9	5.8	55.2	58.7
968	0606161710	06/06/16	171040.30	40.35	143.71	30	5.6	33.9	86.0
970	0606181828	06/06/18	182802.25	33.03	-39.70	10	5.9	272.1	40.1
974	0606221053	06/06/22	105311.57	45.42	149.34	95	6.1	27.7	83.7
979	0606271807	06/06/27	180722.73	6.50	92.79	28	6.2	90.6	79.9
980	0606282102	06/06/28	210209.20	26.82	55.90	10	5.8	99.6	40.1
983	0607011934	06/07/01	193439.61	51.06	-179.31	41	5.5	6.2	84.8
984	0607021720	06/07/02	172025.78	51.10	-179.36	49	5.6	6.2	84.8
990	0607082040	06/07/08	204000.98	51.21	-179.31	22	6.6	6.2	84.7
991	0607090416	06/07/09	041620.11	51.04	-179.17	19	5.5	6.1	84.9
1011	0607291953	06/07/29	195343.05	23.59	-63.92	10	5.8	277.7	63.0
1019	0608061816	06/08/06	181640.17	26.12	144.01	23	6.0	41.2	98.2
1024	0608111430	06/08/11	143040.69	18.56	-101.06	60	6.1	298.1	91.8
1029	0608161839	06/08/16	183900.38	-28.82	61.74	13	5.9	136.8	86.4
1030	0608171111	06/08/17	111135.54	55.62	161.69	55	6.1	16.2	77.7
1037	0608242150	06/08/24	215036.66	51.15	157.52	43	6.5	20.2	80.9
1039	0608262340	06/08/26	234039.47	51.33	-179.57	35	5.8	6.3	84.5
1039	0608262346	06/08/26	234618.52	51.38	-179.54	35	5.7	6.3	84.5
1044	0608312258	06/08/31	225825.80	28.80	130.03	33	5.6	49.7	88.8
1045	0609011025	06/09/01	102517.13	53.26	159.70	51	5.7	18.2	79.5
1045	0609011204	06/09/01	120422.17	53.97	-166.39	75	5.9	358.2	82.3
1061	0609170730	06/09/17	073011.10	-17.69	41.83	10	5.5	147.7	67.8
1062	0609180346	06/09/18	034601.54	51.64	-173.90	53	5.8	2.8	84.6

[a]DAY – number of days from the start of recording; EVENT – event code compiled of the origin date and time; DATE – origin date [yy/mm/dd]; OT – origin time [hhmmss.ss]; LAT – latitude [º]; LON – longitude [º]; D – depth [km]; MAG – moment magnitude; BACK – back-azimuth [º]; DIST – epicentral distance [º]

Fig. S3

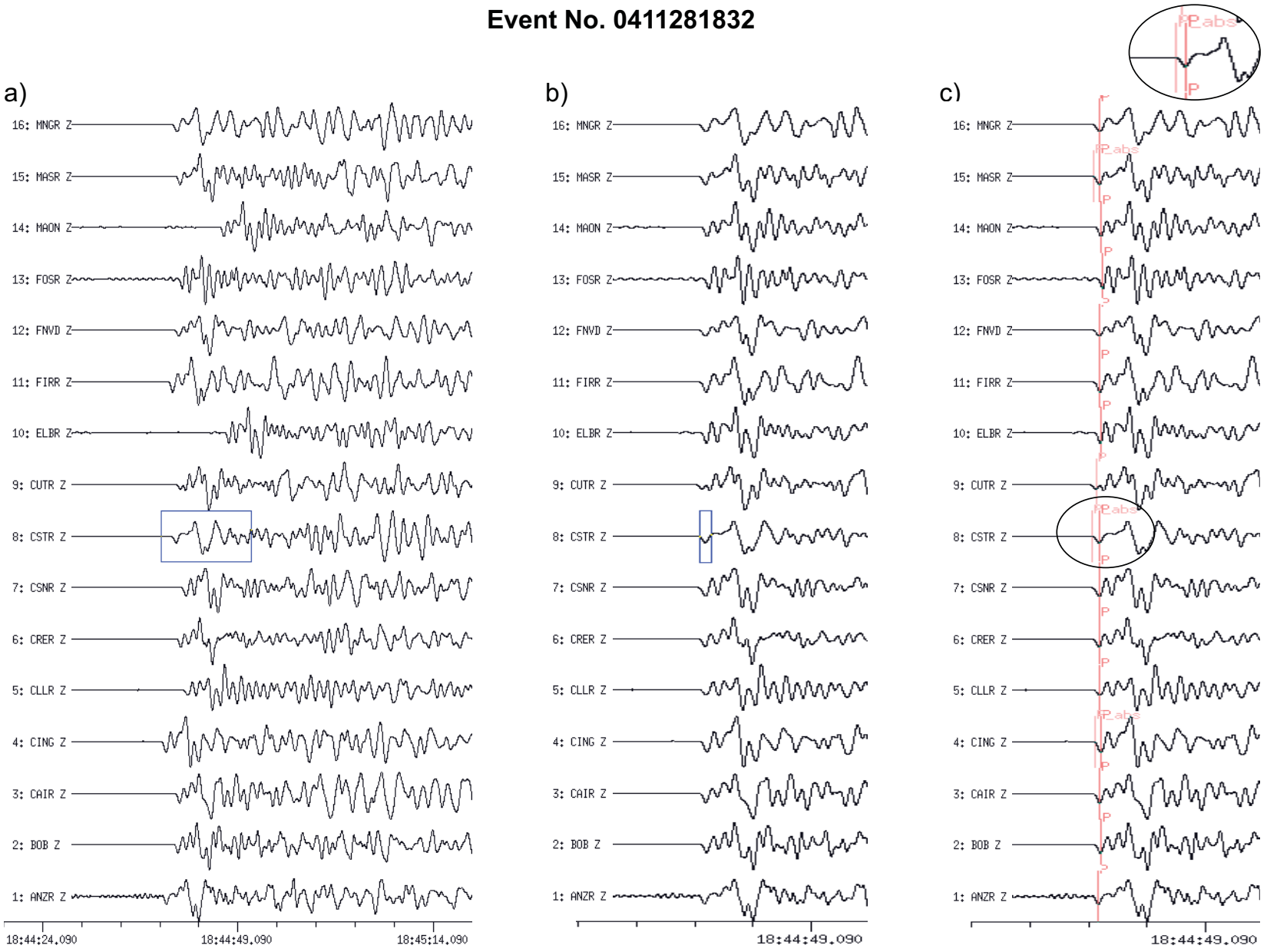
Event No. 0411281832
a)
b)
c)
16: MNGR Z
15: MASR Z
14: MAON Z
13: FOSR Z
12: FNVD Z
11: FIRR Z
10: ELBR Z
9: CUTR Z
8: CSTR Z
7: CSNR Z
6: CRER Z
5: CLLR Z
4: CING Z
3: CAIR Z
2: BOB Z
1: ANZR Z
18:44:24.090
18:44:49.090
18:45:14.090
18:44:49.090
18:44:49.090
P
S
Pabs

Fig. S4

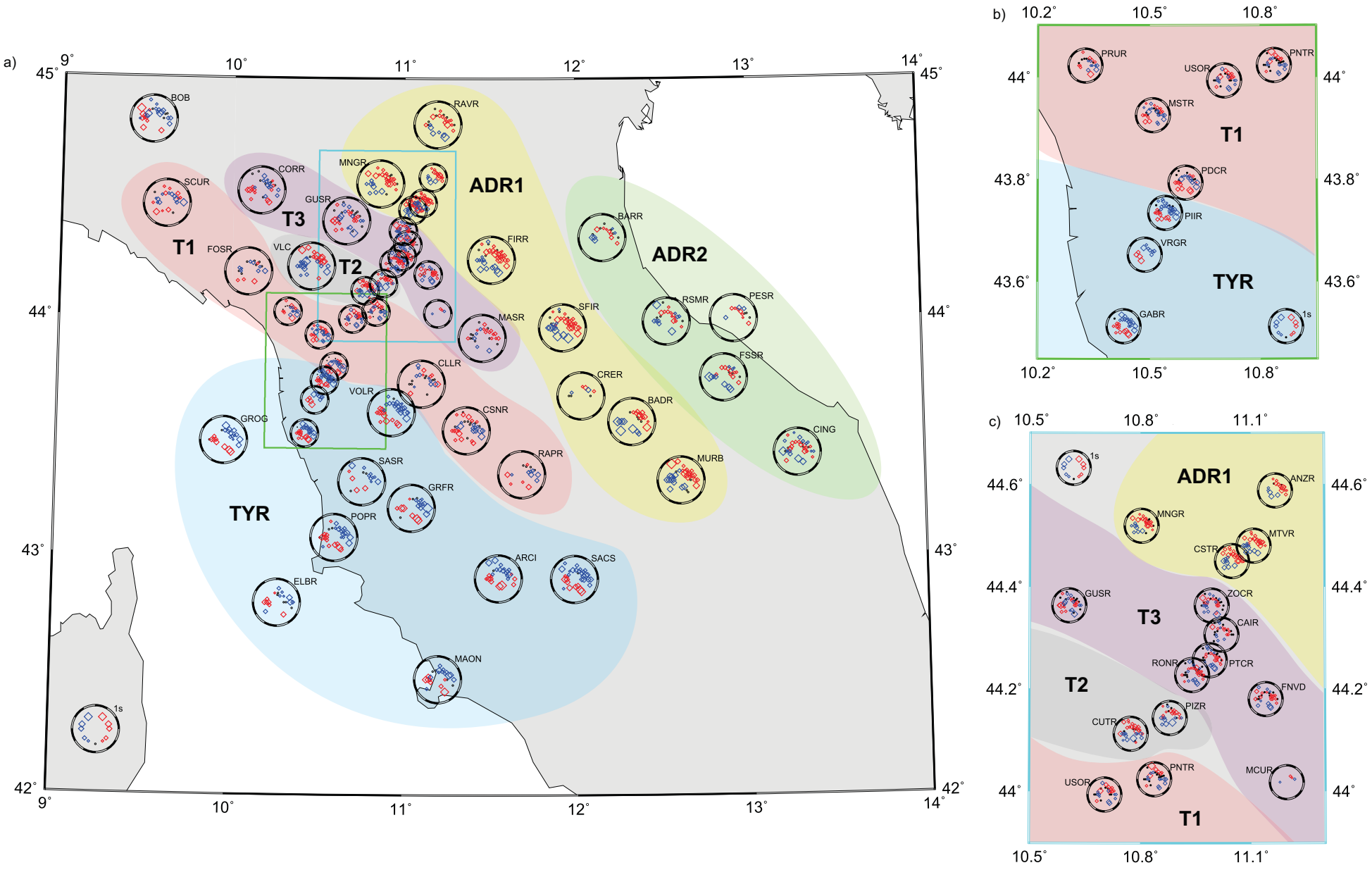
a)
9°
10°
11°
12°
13°
14°
45°
44°
43°
42°
BOB
RAVR
MNGR
CORR
SCUR
GUSR
T3
T1
FOSR
VLC
T2
FIRR
ADR1
BARR
ADR2
SFIR
MASR
RSMR
PESR
FSSR
CLLR
CRER
VOLR
BADR
CSNR
GROG
CING
RAPR
MURB
SASR
GRFR
TYR
POPR
ARCI
SACS
ELBR
MAON
1s
b)
10.2°
10.5°
10.8°
44°
43.8°
43.6°
PRUR
USOR
PNTR
MSTR
T1
PDCR
PIIR
VRGR
TYR
GABR
1s
c)
10.5°
10.8°
11.1°
44.6°
44.4°
44.2°
44°
1s
ADR1
ANZR
MNGR
MTVR
CSTR
GUSR
ZOCR
T3
CAIR
RONR
PTCR
T2
FNVD
PIZR
CUTR
PNTR
MCUR
USOR
T1

Fig. S5

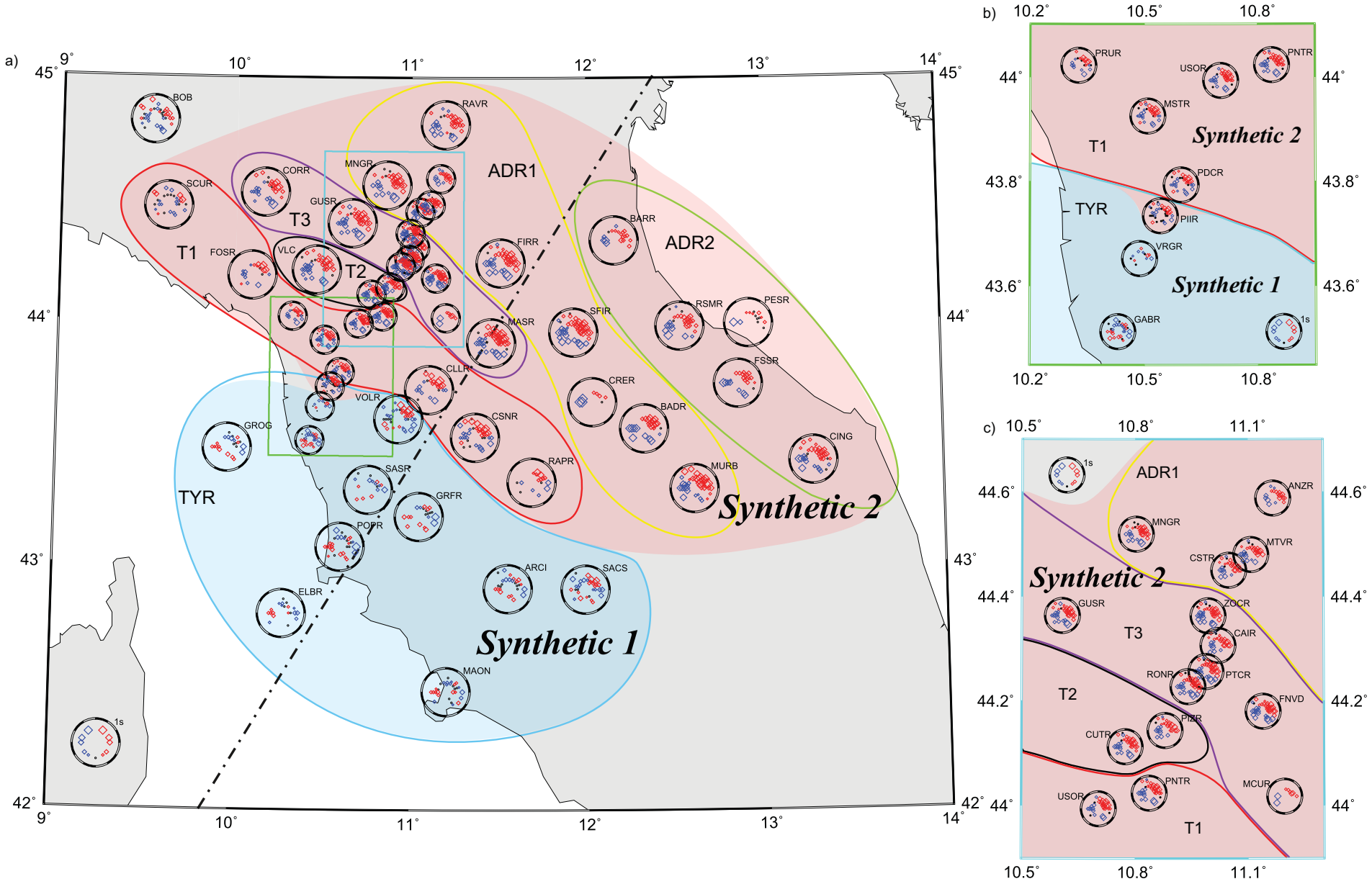
a)
b)
c)
ADR1
ADR2
T1
T2
T3
TYR
Synthetic 1
Synthetic 2
BOB
RAVR
CORR
MNGR
SCUR
GUSR
FOSR
VLC
FIRR
BARR
MASR
SFIR
RSMR
PESR
FSSR
CLLR
CRER
BADR
CING
VOLR
CSNR
GROG
RAPR
MURB
SASR
GRFR
PODR
ARCI
SACS
ELBR
MAON
1s
PRUR
USOR
PNTR
MSTR
PDCR
PIIR
VRGR
GABR
ANZR
MTVR
CSTR
ZOCR
CAIR
PTCR
RONR
FNVD
PIZR
CUTR
MCUR

Supplement 2

Cenozoic volcanism in the Bohemian Massif in the context of P-and S-velocity high-resolution teleseismic tomography of the upper mantle

Jaroslava Plomerová[1], Helena Munzarová[1], Luděk Vecsey[1], Eduard Kissling[2], Ulrich Achauer[3], Vladislav Babuška[1]

Geochemistry, Geophysics, Geosystems, Volume **17**, Issue 8, August 2016, Pages 3326–3349, doi:10.1002/2016GC006318

[1] Institute of Geophysics, Academy of Sciences, Prague, Czech Republic
[2] Institute of Geophysics, Department of Earth Sciences, ETH Zürich, Zürich, Switzerland
[3] Institute of Earth Physics, University of Strasbourg, Strasbourg, France

AGU PUBLICATIONS

Geochemistry, Geophysics, Geosystems

RESEARCH ARTICLE
10.1002/2016GC006318

Key Points:
- Velocity-perturbation patterns in the P- and S-wave models exhibit similar features
- None of the models display a clear narrow "plume-like" structure
- Broad shape of heterogeneity and no evident connection with deeper parts support interpretation by lithosphere thinning along Eger Rift

Supporting Information:
- Supporting Information S1

Correspondence to:
J. Plomerová,
jpl@ig.cas.cz

Citation:
Plomerová, J., H. Munzarová, L. Vecsey, E. Kissling, U. Achauer, and V. Babuška (2016), Cenozoic volcanism in the Bohemian Massif in the context of P- and S-velocity high-resolution teleseismic tomography of the upper mantle, *Geochem. Geophys. Geosyst.*, *17*, 3326–3349, doi:10.1002/2016GC006318.

Received 23 FEB 2016
Accepted 22 JUL 2016
Accepted article online 2 AUG 2016
Published online 19 AUG 2016

The copyright line for this article was changed on 12 OCT 2016 after original online publication.

Cenozoic volcanism in the Bohemian Massif in the context of P- and S-velocity high-resolution teleseismic tomography of the upper mantle

Jaroslava Plomerová[1], Helena Munzarová[1], Luděk Vecsey[1], Eduard Kissling[2], Ulrich Achauer[3], and Vladislav Babuška[1]

[1]Institute of Geophysics, Academy of Sciences of the Czech Republic, Prague, Czech Republic, [2]Institute of Geophysics, Swiss Federal Institute of Technology, Zürich, Switzerland, [3]Institute of Earth Physics, University of Strasbourg, Strasbourg, France

Abstract New high-resolution tomographic models of P- and S-wave isotropic-velocity perturbations for the Bohemian upper mantle are estimated from carefully preprocessed travel-time residuals of teleseismic P, PKP and S waves recorded during the BOHEMA passive seismic experiment. The new data resolve anomalies with scale lengths 30–50 km. The models address whether a small mantle plume in the western Bohemian Massif is responsible for this geodynamically active region in central Europe, as expressed in recurrent earthquake swarms. Velocity-perturbations of the P- and S-wave models show similar features, though their resolutions are different. No model resolves a narrow subvertical low-velocity anomaly, which would validate the "baby-plume" concept. The new tomographic inferences complement previous studies of the upper mantle beneath the Bohemian Massif, in a broader context of the European Cenozoic Rift System (ECRIS) and of other Variscan Massifs in Europe. The low-velocity perturbations beneath the Eger Rift, observed in about 200km-broad zone, agree with shear-velocity models from full-waveform inversion, which also did not identify a mantle plume beneath the ECRIS. Boundaries between mantle domains of three tectonic units that comprise the region, determined from studies of seismic anisotropy, represent weak zones in the otherwise rigid continental mantle lithosphere. In the past, such zones could have channeled upwelling of hot mantle material, which on its way could have modified the mantle domain boundaries and locally thinned the lithosphere.

1. Introduction

The western Bohemian Massif belongs to one of the most geodynamically active regions in central Europe. The BOHEMA passive seismic experiment [*Plomerová et al*., 2003] was designed to confirm or to reject the existence of a small mantle plume as a possible cause of this activity and the Cenozoic volcanism. Tomography of the upper mantle is a powerful tool to image structures of Earth's interior. Velocity perturbations to a simple background model provide essential information on the deep structures. The upper mantle beneath the Bohemian Massif (BM) appears as a part of an extensive low-velocity region beneath central Europe detected in various large-scale tomographic studies of Europe [e.g., *Goes et al*., 1999; *Wortel and Spakman*, 2000; *Piromallo and Morelli*, 2003; *Amaru*, 2007; *Koulakov et al*., 2009]. However, the resolution of such tomographic images, based on travel times of body waves measured at permanent observatories in the area, is not sufficient to infer upper-mantle structures at scales less than ~100 km.

Temporary arrays of seismic stations, which were deployed in Europe during the last two decades (e.g., Eifel [*Ritter et al*., 2001]; SVEKALAPKO [*Sandoval et al*., 2004]; TransAlp [*Lippitsch et al*., 2003; *Kissling et al*., 2006]; CALIXTO [*Weidle et al*., 2005]; TOR [*Shomali et al*., 2006]; BOHEMA [*Plomerová et al*., 2007]; PASSEQ [*Wilde-Piórko et al*., 2008]; TOPOIBERIA [*Díaz et al*., 2015]), recorded data for a more-detailed regional research, as well as for a comprehensive model beneath all Europe, down to the lower mantle [*Amaru*, 2007]. Two recent teleseismic tomography studies based on body waves recorded by temporary arrays in the Carpathians-Pannonian region (Carpathian Basin Project) [*Dando et al*., 2011] and the Eastern Alps (ALPASS) [*Mitterbauer et al*., 2011] presented detailed velocity models of the upper mantle south-eastward and southward of the BM, respectively, but improved only marginally the resolution of the BM, due to the large spacing of the permanent observatories and low resolution at the spatial boundaries of the models.

AGU Geochemistry, Geophysics, Geosystems 10.1002/2016GC006318

Our long-term research of the BM upper-mantle structure has been based on data from several temporary arrays, which step-by-step covered the massif (MOSAIC, BOHEMA I-III) [*Plomerová et al*., 2005, 2007, 2012; *Babuška et al*., 2008; *Karousová et al*., 2012b, 2013]. In these deployments we focused both on isotropic P velocity in the upper mantle and on detecting seismic velocity anisotropy. The research resulted in 3D models of the mantle lithosphere fabrics consistent with mapped boundaries of the lithospheric domains, as well as estimates of the lithosphere-asthenosphere boundary by different methods [*Plomerová et al*., 2012; *Geissler et al*., 2012; *Babuška and Plomerová*, 2013].

The Bohemian Massif is the largest of the Variscan Massifs with one of the smallest rifts of the European Cenozoic Rift System (ECRIS) and the most wide-spread Cenozoic volcanism within the massif. *Granet et al*. [1995] hypothesized that there are several "baby-plumes," that is, narrow subvertical low-velocity anomalies in the European upper mantle, associated with regions of the Tertiary-Quaternary volcanism. The low-velocity material feeding the "baby plumes" was commonly assumed to lie deeper in the mantle. According to the "baby plume" hypothesis, such low-velocity anomalies are suggested in the mantle beneath five regions of the ECRIS, namely the French Massif Central, Rhenish Massif, Rhine Graben, Bohemian Massif and the Pannonian Basin. However, such tube-like low-velocity anomalies have been imaged in teleseismic P-wave tomography only beneath the first two of the five, i.e., beneath the French Massif Central (MC) [*Granet et al*., 1995] and the Rhenish Massif (RM) [*Ritter et al*., 2001]. The RM anomaly was also interpreted to cause variations in the shear-wave splitting above the Eifel hotspot [*Walker et al*., 2005]. However, up to now, no baby plume has been found beneath other rifts of the ECRIS, such as beneath the Rhine Graben in the Vosges-Black Forest region [*Achauer and Masson*, 2002], or, in preliminary P-wave tomography beneath the Eger Rift in the western BM [*Plomerová et al*., 2007]. Similarly, no "baby plume" was identified in the tomographic models beneath the Pannonian Basin [*Chang et al*., 2010; *Dando et al*., 2011], a region with extensive Cenozoic volcanism, comparable with that of the MC.

This paper aims at presenting the most detailed images of P- and S-velocity perturbations to date of the western BM upper mantle down to ~350 km. In this region, where the existence of one of the "baby plume" structures was suggested, a temporary regional network of densely spaced stations was installed within the framework of the Czech-French-German project BOHEMA [*Plomerová et al*., 2003]. Our high-resolution P-velocity perturbation model is computed from a new set of carefully picked PKP arrival times combined with an extended set of previously processed P-wave data that provided the first insight into the upper-mantle velocities [*Plomerová et al*., 2007]. The new extended data set underwent independent preprocessing compared to the previous study. We used a new update of the inversion code [*Karousová et al*., 2013] with different model parameterization. Moreover, *a priori* crustal corrections were used to minimize the leakage of crustal velocity perturbations into the upper-mantle images [*Karousová et al*., 2012a]. To get independent information, we measured also S-wave arrivals, because S waves are even more sensitive to a potential velocity decrease due to an increase of temperature or a decrease of viscosity in the upper-mantle material. To minimize potential effects of inclined anisotropic structures in the mantle lithosphere domains on isotropic tomographic images [e.g., *Babuška and Plomerová*, 2013, and references therein], we measure separately S-arrivals on the T (transverse) and the Q (perpendicular to T in the ray plane) components, without any intention to judge an anisotropic structure of the upper mantle from standard isotropic tomography. The new tomographic images have the highest resolution in the western part of the BM, where a hypothetical "baby-plume" was anticipated in analogy with the concept of *Granet et al*. [1995]. Tomographic studies combining independent data sets could shed new light on architecture of the upper mantle also in other regions where small-size plumes were suggested.

2. Tectonic Background

2.1. Variscan Massifs and ECRIS

Variscan massifs in Phanerozoic Europe vary in size, amount and extent of rifts and the Cenozoic volcanism (Figure 1). The Bohemian Massif (BM) represents the easternmost and the most prominent relic of the Late Paleozoic collisional belt of the Variscides in central Europe [*Franke*, 2006; *Linnemann et al*., 2008]. The BM unit assemblage was created during the Variscan cycle resulting from the collision of two major continents–Gondwana to the south and Laurentia-Baltica to the north [*Matte*, 1986]. Between these two continents, small microplates, separated by ocean basins, drifted during the early Paleozoic. Some of them collided to

AGU Geochemistry, Geophysics, Geosystems 10.1002/2016GC006318

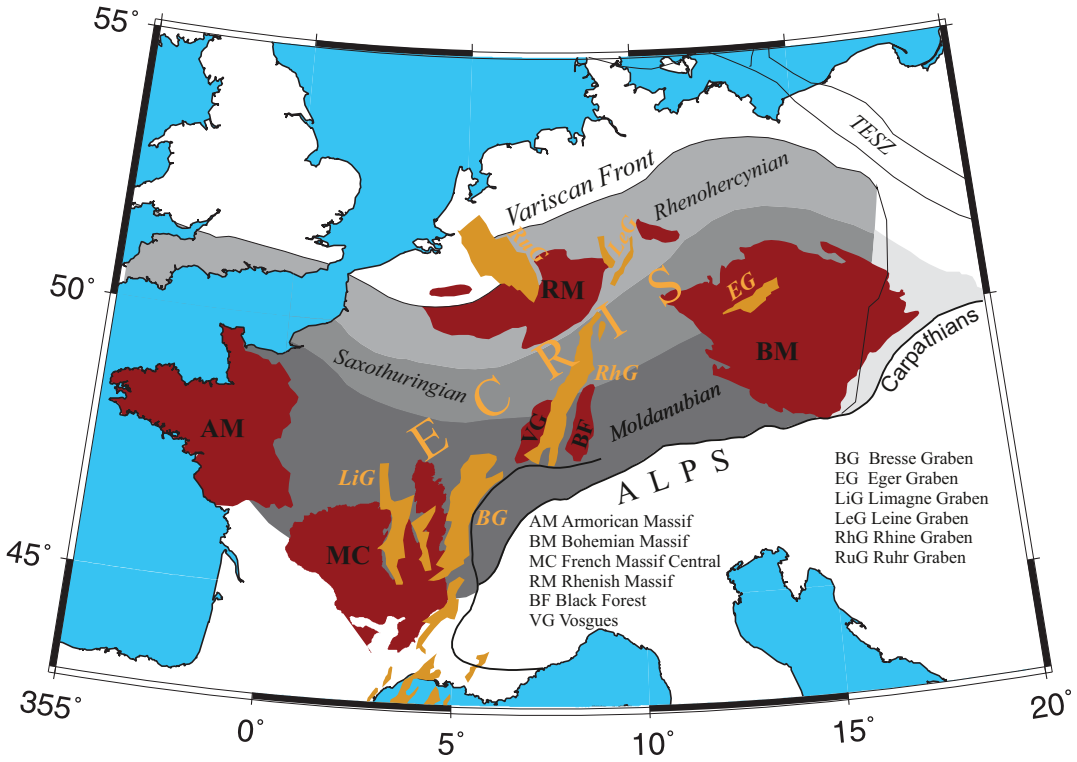

Figure 1. Variscan orogenic belt, massifs and European Cenozoic Rift System (ECRIS).

form the BM from the Silurian to the Permian. In the Mesozoic and Cenozoic eras, the BM formed the northern foreland of the Alpine orogen. Stresses within the European lithosphere caused by the Atlantic opening and the Alpine orogeny resulted in rifting and alkaline volcanism in central and western Europe [e.g., *Ziegler and Dezes*, 2006; *Ziegler et al.*, 2006].

The European Cenozoic Rift System (ECRIS) [*Ziegler*, 1992] extends from the Dutch North Sea coast southward to the Western Mediterranean and spans from western Europe far into its central/eastern part (Figure 1). Graben structures of the rift system are linked through transfer zones or transform fault systems. The Tertiary Eger (Ohře) Rift (ER) is an ENE-WSW striking structure, exhibiting a slightly enhanced heat flow [*Čermák*, 1994] and wide-spread Cenozoic volcanism [*Ulrych et al.*, 2000]. The rift structure developed in the western part of the BM, where three major tectonic units - the Saxothuringian (ST) in the north and the Teplá-Barrandian (TB) and the Moldanubian (MD) units in the south have converged (Figure 2a). The distinct ~120 km long graben structure in the ER developed above the steep ST-TB mantle-lithosphere boundary. From the large extent of volcanism we can assume the rift structure (ER) continues in the mantle lithosphere to the southwest and to the northeast on both ends of the Eger Graben (EG), i.e., beyond the Mariánské-Lázně Fault (MLF) and Elbe Fault Zone (EFZ) zones that limit the graben (EG; Figure 2).

The ER represents an integral part of the European Cenozoic Rift System, which evolved in response to passive rifting related to compressional stresses during the Alpine and Pyrenean collisions [*Ziegler*, 1992; *Dezes et al.*, 2004]. Though mantle-plume activity is not considered to drive the rifting, evolution of the ECRIS was accompanied by the development of major volcanic centers in the French Massif Central and in the Rhenish and Bohemian Massifs [*Ziegler and Dezes*, 2006]. This led to the hypothesis, supported by results of seismic tomography [*Goes et al.*, 1999; *Ritter et al.*, 2001; *Amaru*, 2007], that the ECRIS may have a common source of "plume-like" volcanism in the mantle, manifested by "baby-plumes" beneath the Variscan massifs [*Granet et al.*, 1995; *Ritter et al.*, 2001].

From the geodynamical point of view, the western BM is the most active part of the massif. Recent tectonic activity is primarily associated with Cenozoic volcanism [*Ulrych et al.*, 2000], gas emanations containing high

AGU Geochemistry, Geophysics, Geosystems 10.1002/2016GC006318

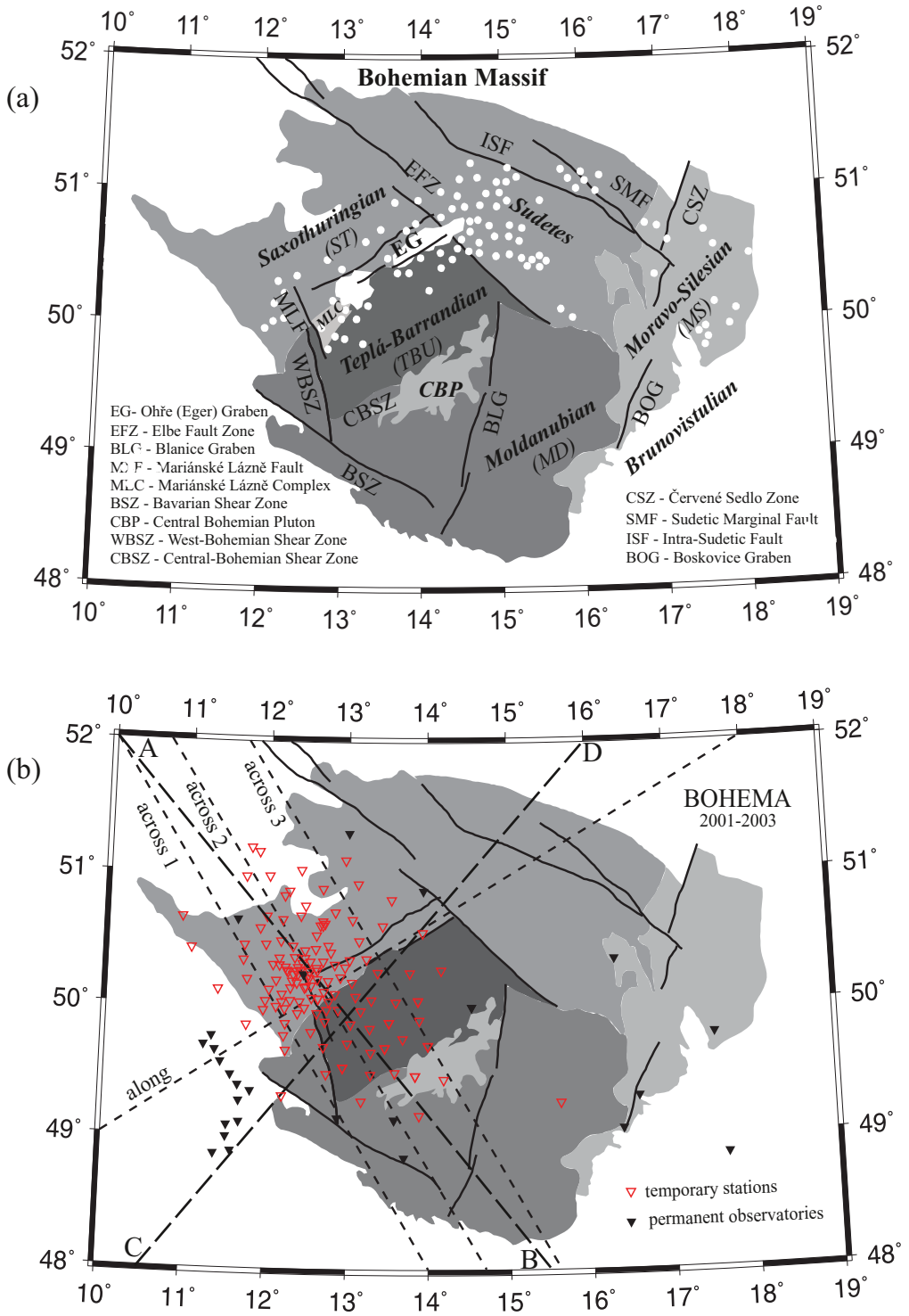

Figure 2. Simplified tectonic map of the Bohemian Massif showing (a) major units, faults and volcanism (white), and (b) seismic stations of the BOHEMA passive experiment. Dashed lines locate the cross sections through tomography images of velocity perturbations presented in Figures 8 and 10; supporting information Figure S5.

AGU Geochemistry, Geophysics, Geosystems 10.1002/2016GC006318

proportions of mantle-derived CO_2 and ^3He [*Kämpf et al*., 2013], as well as by episodic shallow earthquake swarms [*Horálek and Fischer*, 2008] and neotectonic crustal movements [*Bankwitz et al*., 2003; *Peterek et al*., 2011]. The question of a possible source of mantle fluids is important, namely in relation to the increase of $^3He/^4He$ ratios observed by *Bräuer et al*. [2005]. The authors interpret primitive helium as evidence for ascending mantle-derived melt and as an indication of a possible volcanic activity.

2.2. BM Crust and Lithosphere-Asthenosphere Boundary

The structure of the western-BM lower lithosphere and the depth of the lithosphere-asthenosphere boundary (LAB) have been subjects of several studies since the early 80s [e.g., *Babuška et al*., 1987]. The lithosphere thins to 80–90 km along the ER [*Plomerová et al*., 1998] in models which exploit the increased velocity contrast across the LAB, caused by orientation differences in seismic anisotropy within the lower lithosphere and the sublithosphere mantle [e.g., *Plomerová and Babuška*, 2010]. Lithosphere thinning up to about 65 km has been identified by the S-receiver function method [*Heuer et al*., 2007] in the western part of the ER. Preliminary results of the teleseismic P-wave travel-time tomography down to a depth of about 270 km by *Plomerová et al*. [2007] did not recognize any "tube-like" low-velocity anomaly which could be interpreted as a mantle plume beneath the western part of the ER.

The average thickness of the BM crust is about 33 km, but Moho depth varies between 26 and 40 km on relatively short distances. The crust is thinner around the junction of the Saxothuringian/Teplá Barradian/Moldanubian tectonic units in the western part of the massif. According to the refraction model of *Hrubcová et al*. [2005], the thinnest crust of about 30 km is characteristic for the ST-TB transition. Moreover, the authors identified the top of a highly reflective lower-crustal layer up to 9 km thick at ~26 km depth beneath the ST unit, whereas beneath the TB and MD units the Moho appears as a sharp velocity discontinuity. With the use of the Ps receiver functions, *Geissler et al*. [2005] and *Heuer et al*. [2006] interpret Moho depths as shallow as 24 km beneath the junction of the three tectonic units. Differences in the Moho depths modeled by the two methods are 5–6 km in the Saxothuringian, while in the TB unit and further in the Moldanubian, the results of both methods are consistent [*Karousová et al*., 2012a]. The authors attribute the different Moho depths from the controlled-source seismics and receiver-function method to a much larger sensitivity to the sharpness of the velocity contrast of the latter method. *Hrubcová and Geissler* [2009] admit that an unclear reflection from the weakly reflective Moho 30–32 km can be masked by a strong reflection from the top of the reflective transition zone at about 28 km and thus can lead to the different Moho depths in the ST. Average P velocities in the west Bohemian crust vary between 6.1 and 6.3 km, with the highest values in the Mariánské-Lázně Complex (MLC), an exhumed block of the lower crust [*Jelínek et al*., 1997]

3. Data

Shear waves are strongly sensitive to a velocity decrease, particularly in the presence of melt or mantle fluids. Therefore, we measured shear-wave arrival times on recordings of the BOHEMA array (Figure 2b) operated during the 2001–2003 to complement results of the preliminary P-wave tomography [*Plomerová et al*., 2007], which reflected gross features of P-velocity variation without any detailed tectonic correlations.

We have evaluated manually arrival times on the broad-band recordings of direct S, core-mantle refracted SKS, SKKS or PKS waves as well as several reflected phases, e.g., sS, ScS, SS of events with magnitudes at least 5 from epicentral distances 30°–145° (Figure 3). To avoid an additional bias into isotropic tomography coming from upper-mantle anisotropic structure beneath the western BM (average shear-wave split-delay time $\delta t = 1.2$ s [*Babuška et al*., 2008]), we rotated the Z, N, E geographical components of the shear-wave recordings into the L, Q, T ray-parameter coordinate system, in which the L and Q axes lie in the ray planes and L is oriented in the ray direction and, the T axis is perpendicular to the (L,Q) plane. Then we picked the arrival times of shear waves with SH and SV polarizations (denoted here as ST and SQ phases) separately on the T and Q components for 60 and 83 teleseismic events, respectively. The input files for the tomography consist of 1464 and 1943 travel times of ST and SQ shear phases measured at 77 broad-band temporary stations of the BOHEMA array and seismological observatories in the region. The stations were equipped mostly with STS2 and several Guralp CMG-3T, CMG-3ESP and CMG-T40 seismometers, and various data acquisition systems (http://www.ig.cas.cz/en/structure/observatories/mobile-seismic-stations/map-stations).

AGU Geochemistry, Geophysics, Geosystems 10.1002/2016GC006318

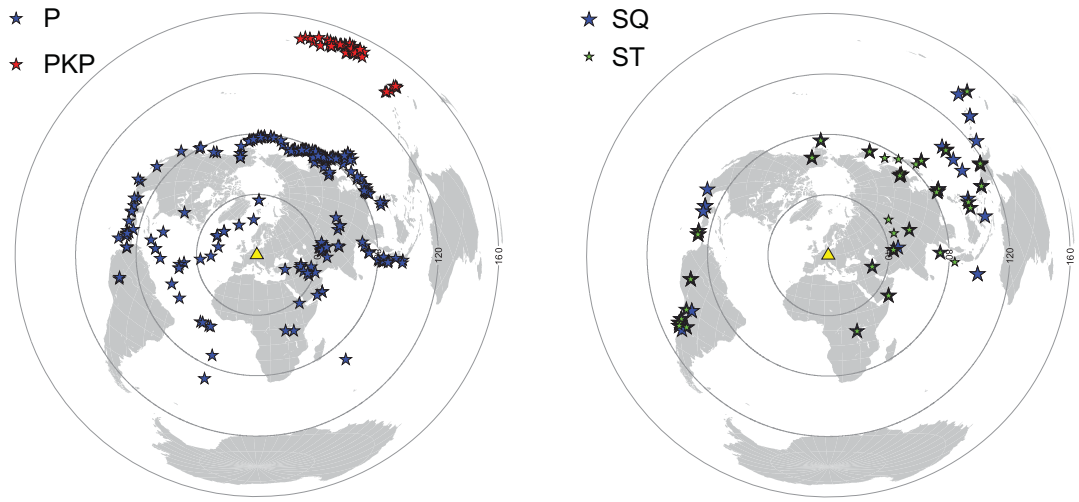

Figure 3. Distribution of earthquake foci from which travel times of P, PKP and shear waves are analyzed.

Dominant periods of shear waves are 6–10 s, i.e., in flat parts of seismic sensor responses, thus without a need to correct for instrument response.

We picked the shear-wave arrival times in a standard way, i.e., by the first clear extremes of the shear waveforms correlated across the array (Figure 4) with the use of Seismic Handler software [*Stammler*, 1993]. A quality factor of each measurement was set according to the uncertainty of the picking and used in the weighting matrix during the tomography inversion. We recalculated the correlated picks of an event into absolute arrival times according to one or several clear phase onsets of the event. Absolute travel-time residuals were calculated relative to the IASP'91 model [*Kennett and Engdahl*, 1991] and their time stability of relative residual was tested to avoid any instrumental effects, e.g., due to occasional failures of time synchronization at some of the temporary stations.

To reduce effects of the heterogeneous crust with variable Moho depth and to prevent their mapping into velocity-perturbation images of the upper mantle, the absolute residuals were corrected for differences between the crust velocities of the reference IASP'91 model and the smooth velocity model of the BM crust [*Karousová et al*., 2012a]. Travel times in the upper crust can be affected locally by thick sediments. Therefore, we applied corrections for sediments, where sedimentary layer was thick enough to slow down the teleseismic P waves by at least 0.1s. Applying the deterministic crustal corrections in a tomographic inversion leads to smoother perturbations at shallow mantle depths (see supporting information Figure S6) compared with those [*Plomerová et al*., 2007, Figure 2] calculated from travel times corrected by "layer-stripping" approach [*Evans and Achauer*, 1993].

The same rules were applied in careful estimation of arrival times for different branches of the PKP phases from recordings of 58 earthquakes (Figure 3). The correlated times were picked on Z components of both the short-period and broad-band stations of the BOHEMA array, all corrected for the WWSSN responses. Most of the measurements were of the highest quality, i.e., with measurement accuracy of one sample ($\pm$ 0.05 s on recordings with 20 Hz sampling). The 3763 PKP travel times augmented a new set of 14013 high-quality P-wave arrivals. The new set of P-wave arrival times includes measurements made for the inversion of *Plomerová et al*. [2007], complemented by P arrivals mostly from the less well-covered SW quadrant.

Tomographic images of the P- and S-velocity perturbations are calculated from relative residuals of both the P+PKP and S waves, respectively. Event residual means were subtracted from measurements at individual stations to suppress heterogeneities out of the region. 98% of 17776 relative residuals in the P+PKP tomography input lie in interval (−1 s, 1 s) out of which 96% are in interval (−0.7 s, 0.7 s), the residual range of the 2007 inversion [*Plomerová et al*., 2007]. Number of intersecting rays increases in the new input for P-velocity perturbation model, which represents significant improvement for tomography resolution.

AGU Geochemistry, Geophysics, Geosystems 10.1002/2016GC006318

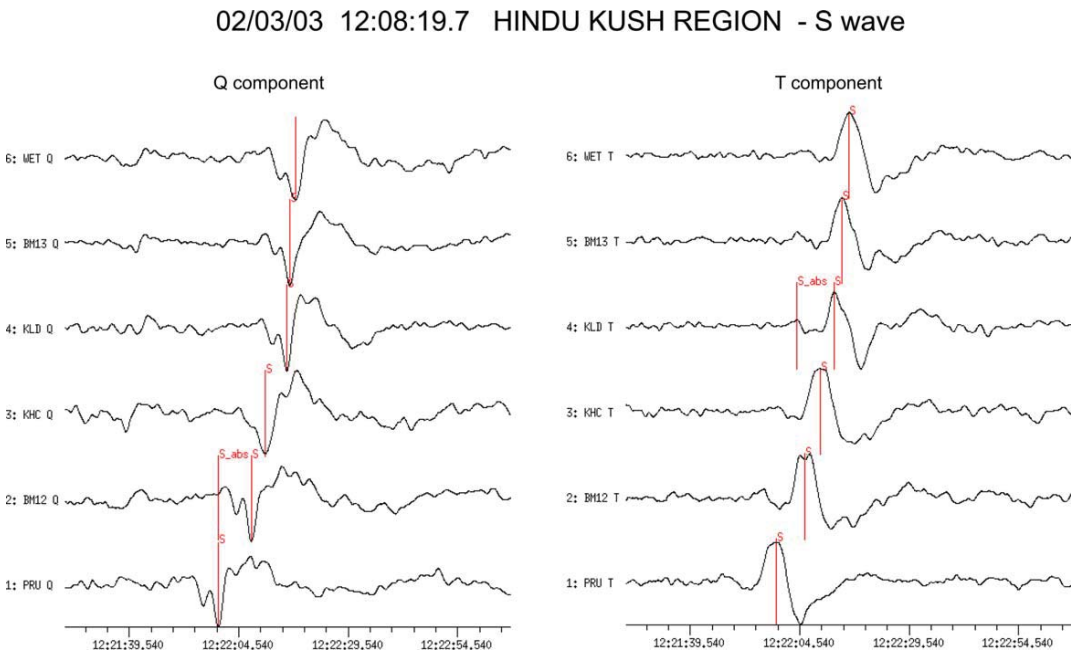

Figure 4. Examples of shear-wave picking on the Q and T components of several stations of the BOHEMA array.

4. Seismic Tomography–Method and Model Parameterization

Teleseismic tomography images spatial distribution and magnitude of velocity perturbations estimated by back-projection of relative travel-time residuals into the target volume, which is, in case of regional tomography, the upper mantle beneath the array of seismic stations. We have updated the frequently used TELINV tomographic code (http://www.ig.cas.cz/en/research-teaching/software-download/), which is based on a modified nonlinear inversion scheme known as the ACH method [*Aki et al.*, 1977; *Evans and Achauer*, 1993]. During the tomography calculation, a starting reference velocity model, in our case the IASP'91 radial Earth model [*Kennett and Engdahl*, 1991], is iteratively adjusted by solving a system of linearized travel-time equations which relate the relative travel-time residuals Δt to the velocity perturbations Δv^i along the ray path, composed of segments s_i,

$$\Delta t = \sum_i \left(\frac{\partial t}{\partial v}\right)_i \Delta v^i = \sum_i -\frac{s_i}{v_i^2}\Delta v^i. \quad (1)$$

The task is solved by a weighted damped least-square method [*Menke*, 1984]

$$m = \left(A^T W_D A + \varepsilon^2 W_M\right)^{-1} A^T W_D d \quad (2)$$

where m is vector of unknown velocity perturbations, d is data vector containing travel-time residuals Δt. The partial derivatives in (1) are stored in matrix A. Weighting matrix W_D contains errors of arrival-time measurements. The ill-posed problem is stabilized by damping factor ε^2 and smoothing matrix W_M. The matrix inverse is approximated by truncated singular value decomposition. The 3D ray-tracing bending technique Simplex [*Steck and Prothero*, 1991], in which ray paths are distorted by sinusoidal signals, is applied. Though the starting model is arbitrary, it should be close to the real velocity distribution, to satisfy the assumption of linearization of the travel-time equations. The velocity perturbations evaluated from relative residuals express velocity variations within each horizontal layer and should not be converted into the absolute velocities.

The velocity perturbations are calculated at nodes of an orthogonal 3D grid, parameterizing velocities of the model volume. Off the nodes, the perturbations are linearly interpolated considering velocities of the surrounding nodes. The grid spacing depends on ray geometry, given by the station-event distribution, and on a dominant wavelength of teleseismic body waves. We chose horizontal grid spacing of 30 km, from the

AGU Geochemistry, Geophysics, Geosystems 10.1002/2016GC006318

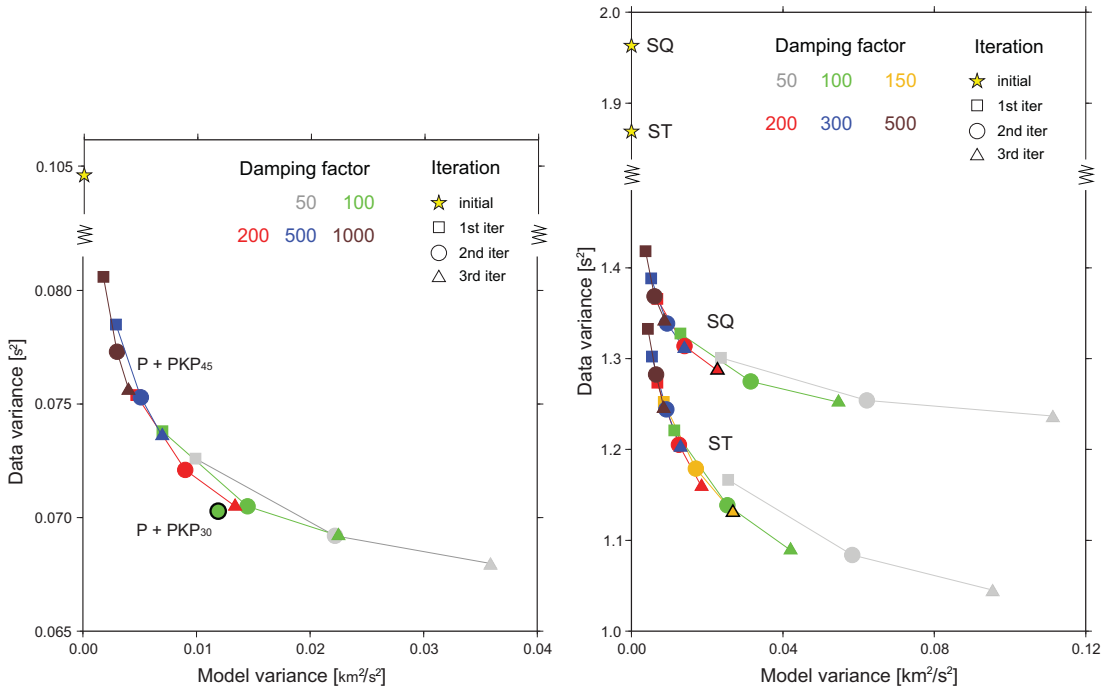

Figure 5. Data and Model variance trade-off curves for different damping factors and number of iterations. The final parameters are black contoured.

30, 45, 60 km tested, as it provided the most stable results for both the P- and S-wave data sets. The selected spacing reflects the relatively small size of individual tectonic units within the BM. Apart from influence of the spacing on the results, we tested the effect of grid position in relation to the known mantle block boundaries [e.g., *Babuška and Plomerová*, 2013] by shifting the grid in different directions.

The initial vertical spacing of the nodes between depths of 35 km and 350 km was 45 km for both P and S waves. However, the large number of the P and PKP arrivals allowed refinement to 30km starting from 20 km depth (Figure 5). Note that the P+PKP$_{30}$ model (i.e., the model with the 30km vertical grid spacing calculated from the P and PKP relative residuals) variance is lower than for P+PKP$_{45}$ (the same but with the 45km vertical grid spacing) at approximately the same data variance level. Total number of inverted nodes was 1144 for two S-velocity perturbation models, and 2176 and 3264 for the P$_{45}$- and refined P$_{30}$-velocity perturbation models, respectively. The perturbations at the first inverted depths are resolved less reliably due to the ray steepness and the resulting lack of ray intersections. Perturbations at nodes at crustal levels tend to absorb imperfect crustal corrections and data errors, which would otherwise project into deeper parts of the model.

The damping parameters, smoothing and number of iterations control stability and complexity of the solution [*Lippitsch et al.*, 2003]. We selected these parameters according to the trade-off curves (Figure 5) with a criterion that velocity perturbations must have a physical meaning, i.e., amplitudes of perturbations should be consistent with the velocity range of upper-mantle rocks. Damping parameters of 100, 200 and 150 were selected for P, SQ and ST waves, respectively, by estimating the inflection points of the trade-off curves between data and model variances. Less damping and fewer inversion iterations can result in the same data- and model-variance pairs as the higher parameters in the trade-off curves without visible changes of the velocity-perturbation pattern. The main features of the tomographic images after the second and third iterations remain unchanged, which argues for the stability of the solution. Considering the inversion computational burden with the large amount of the P+PKP data, we chose velocity perturbations after the second iterations. The difference between the estimate of data error and standard deviation of the final residuals (~0.2 s) can be explained by well-known limitations of the isotropic teleseismic travel-time tomography, e.g., imperfect crustal corrections, velocity-model simplification or the neglect of anisotropy.

AGU Geochemistry, Geophysics, Geosystems 10.1002/2016GC006318

There are several options to measure and visualize the velocity perturbations and assess their reliability. A very common and simple way is to count rays passing through each grid cell, i.e. "hit-count" (Nhit). A better alternative is a "derivative weighted sum," which considers lengths of the ray segments in each cell. Furthermore, diagonal elements of the resolution matrix (RDE)

$$R=\left(A^T W_D A+\varepsilon^2 W_M\right)^{-1} A^T W_D A \tag{3}$$

also incorporate the spatial orientation of the rays and are thus represent comprehensively how closely a particular estimate of the model parameters fits the true solution [*Menke*, 1984]. For qualitative insight into the ray distribution, which emphasizes the importance of how the rays intersect within grid cells, we also display the rays in depth-slices with color-coded back-azimuths (see Figure 7b in next section).

5. Results

Figure 6 shows velocity perturbations in horizontal slices at different depths of the P+PKP$_{30}$ velocity model. Hit counts and diagonal elements of the resolution matrix are shown in supporting information Figure S1. Variance reduction of the model is 33%. Only the nodes hit by more than 30 rays (supporting information Figure S1) are visualized in the plots. Based on synthetic tests, regions with RDE $>$0.7 and sufficient number of intersecting rays are considered as well-resolved.

All layers show smooth lateral variations of the velocity perturbations without taking fluctuations of positive-to-negative values at cell-size scale. Moving the center of the grid node does not affect the pattern of perturbations. Perturbations at 20 km depths reflect some uncompensated velocity heterogeneities in the crust and uncorrected variations of Moho depths. Perturbations at 50 km depth represent velocity variations in the topmost upper mantle (35–65 km). The ER separates the low-velocity perturbations beneath the ST on one side and the high-velocity perturbations beneath the TB and MD on the other side.

To verify the existence of a plume-like structure, we map expected low-velocity perturbations at the upper-mantle depths. The low-velocity perturbations cover a broad vicinity of the ER (Figure 6) at the 80 km depth, being the most significantly low south of the EG structure, beneath which the LAB shallows at least to ~80 km [*Plomerová and Babuška*, 2010]. The high-velocity perturbations beneath the southern BM correspond to a thicker lithospheric domain of the MD mantle, thrust beneath the TB [e.g., *Babuška and Plomerová*, 2013]. In slices at 110 and 140 km depths, the low-velocity perturbations concentrate around the southwestern end of the EG (~12.5E 50N) and the western part of the TB unit. Below these depths, the low-velocity perturbations shift to the NE and weaken. The high-velocity perturbations in the southern BM, distinct between 80 and 140 km node depths, continue deeper. The high-velocity perturbations prevail in the lowermost three layers of the model also in the western part of the BM, but partly lying out of the contoured well-resolved region which shifts toward the NE due to prevailing number of rays from the NE (Japan, Kuriles). Amplitudes of the velocity perturbations decrease with increasing depth, in general, and the negative perturbations do not exhibit a distinct concentration solely beneath the south-western end of the EG. If a plume-like structure is present, then the low-velocity perturbations should continue through all the depth slices, which is not the case.

Gross features imaged in shear-velocity perturbations, retrieved separately from the Q and T components of shear-waves are similar to those retrieved from the P+PKP waves (Figure 6; supporting information Figures S2 and S3). The relatively broad region of lower velocities around the center of the array (50N 12.5E) can be traced without interruption down to ~125 km and ~170 km in the SQ and ST models, respectively. The differences in perturbations between the two shear-wave models can be attributed to differences in ray-path distribution as well as to the lower number of rays (~10% each compared to number of P+PKP rays), and also to effects due to neglect of anisotropy. To constrain the shear isotropic velocity-perturbation models by the largest amount of data and improved azimuthal coverage, we inverted the combined SQ and ST data sets with the same parameters that were used for the separate ST and SQ inversions. Thanks to better coverage the area of well-resolved cells is slightly larger in the resulting SQ+ST model, but distribution of velocity perturbations does not change (supporting information Figure S4). This means that the isotropic velocities are resolved well in the shear models. No tube-like low-velocity anomaly appears to be required by the data.

AGU Geochemistry, Geophysics, Geosystems 10.1002/2016GC006318

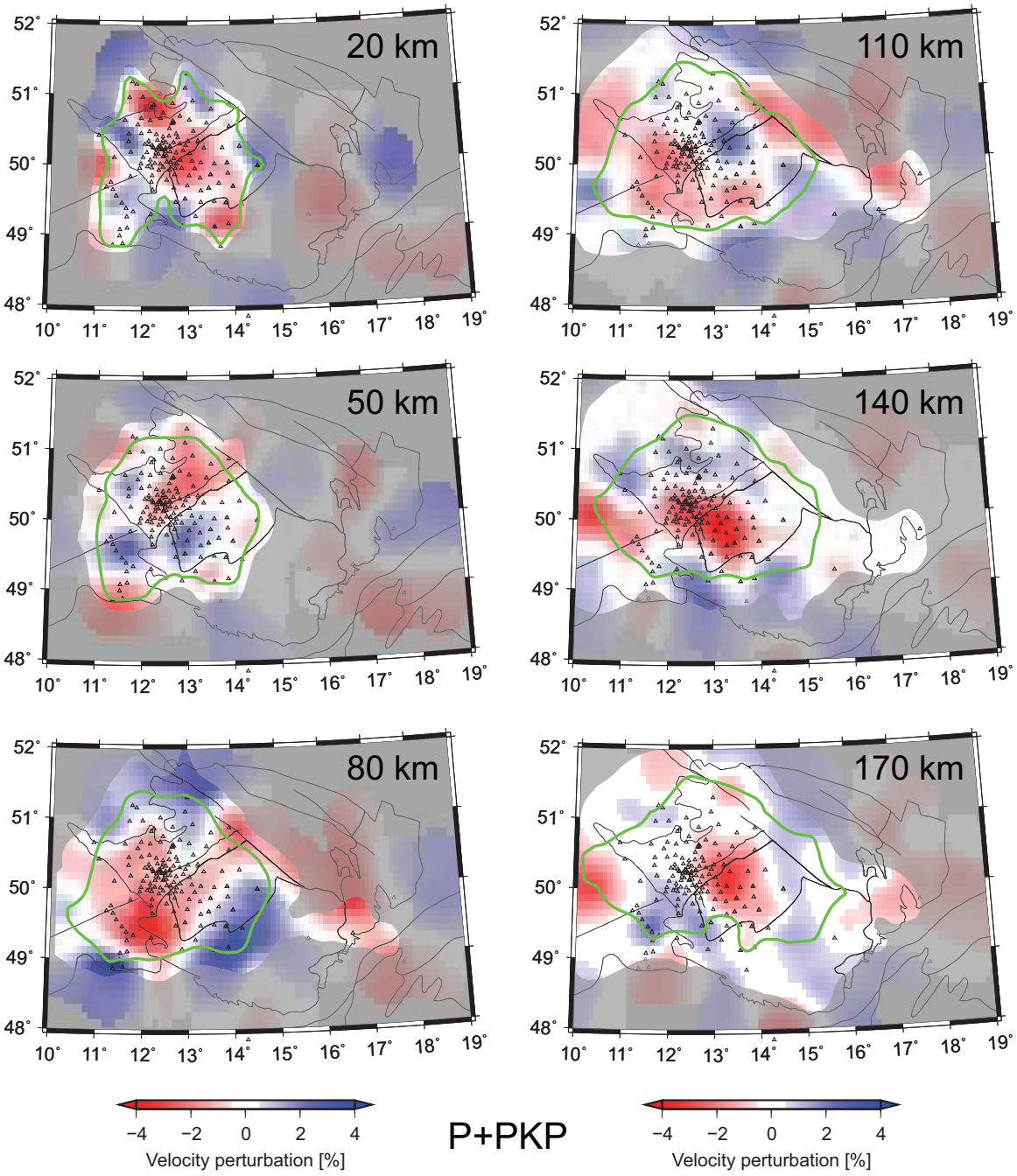

Figure 6. Plane views of v_P velocity perturbations down to 350 km in a model with 30 km vertical node spacing. Well-resolved regions with RDE $\geq$ 0.7 are contoured (green), regions with RDE $\leq$ 0.5 are shaded. See also supporting information Figure S1.

To assess similarities and/or differences between the velocity-perturbation models in the well-resolved parts, we show jointly the perturbations at three slices in the upper mantle along with ray-path distribution (Figure 7). We use the same scales to compare P and S tomography, though perturbation amplitudes in S tomography are larger. Assuming the same damping parameters and constant Poisson's ratio, one can expect that the relative velocity perturbations are of the same level in both the P and S-wave tomography. Then theoretically, travel-time residuals of S waves should approximately double the residuals of P waves. However in practice, the S-wave residuals are about ~3 times larger than the P residuals. The remaining

AGU Geochemistry, Geophysics, Geosystems 10.1002/2016GC006318

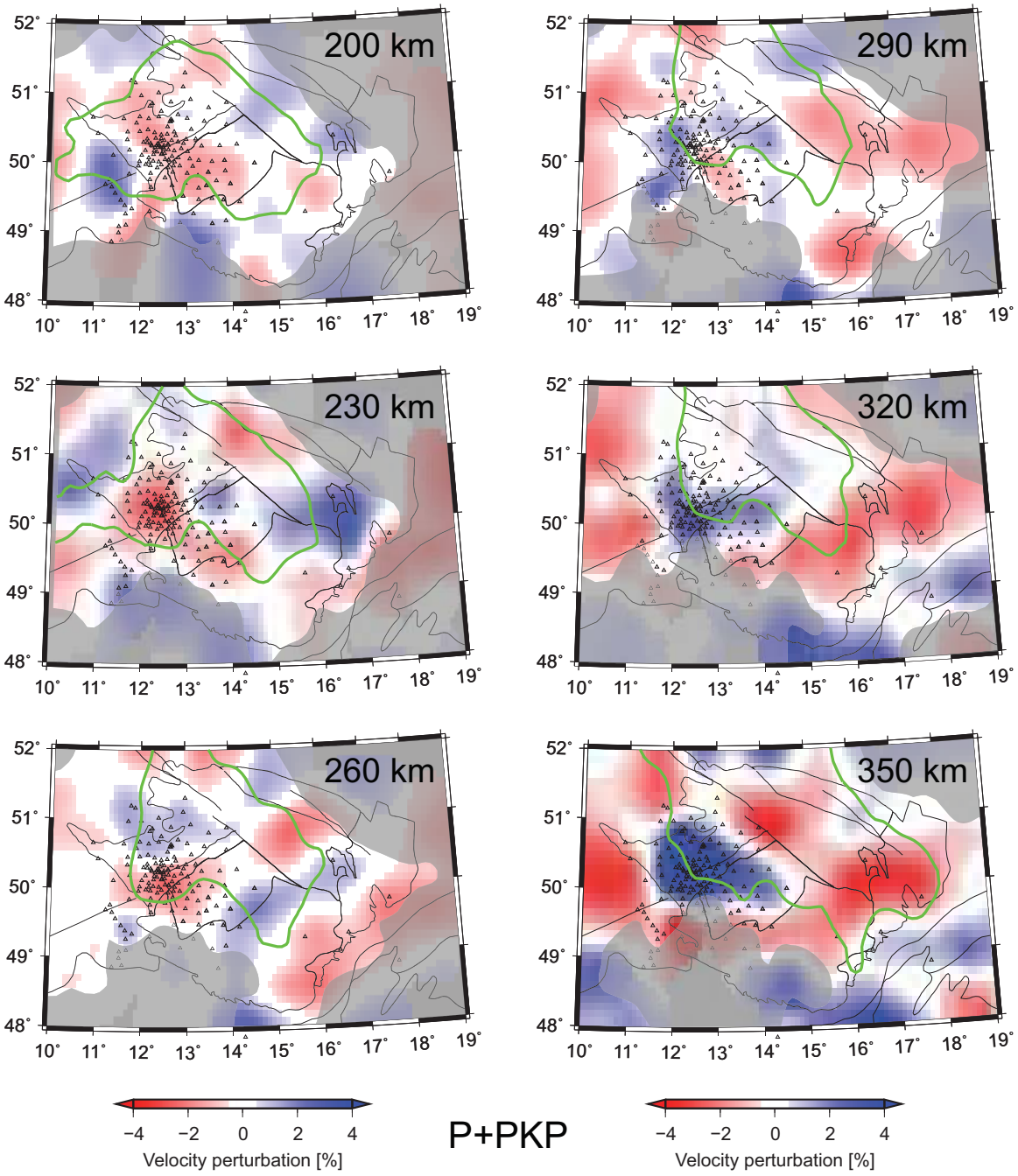

Figure 6. (continued)

~1/3 of the unexplained S residuals might relate to, e.g., larger picking errors, different ray paths, neglecting anisotropy, and variations in Poisson ratio.

A broad area of lower velocities around the center of the array at 12.5E 50N appears in all three types of tomography images in the 80 km depth slices. Differences between the P and S results appear at 125 km depth, but the general features persist. The low-velocity perturbations below the central part of the array, around the ER and MLF crossing (SW end of the EG), can be traced in all the models. The low-velocity

AGU Geochemistry, Geophysics, Geosystems 10.1002/2016GC006318

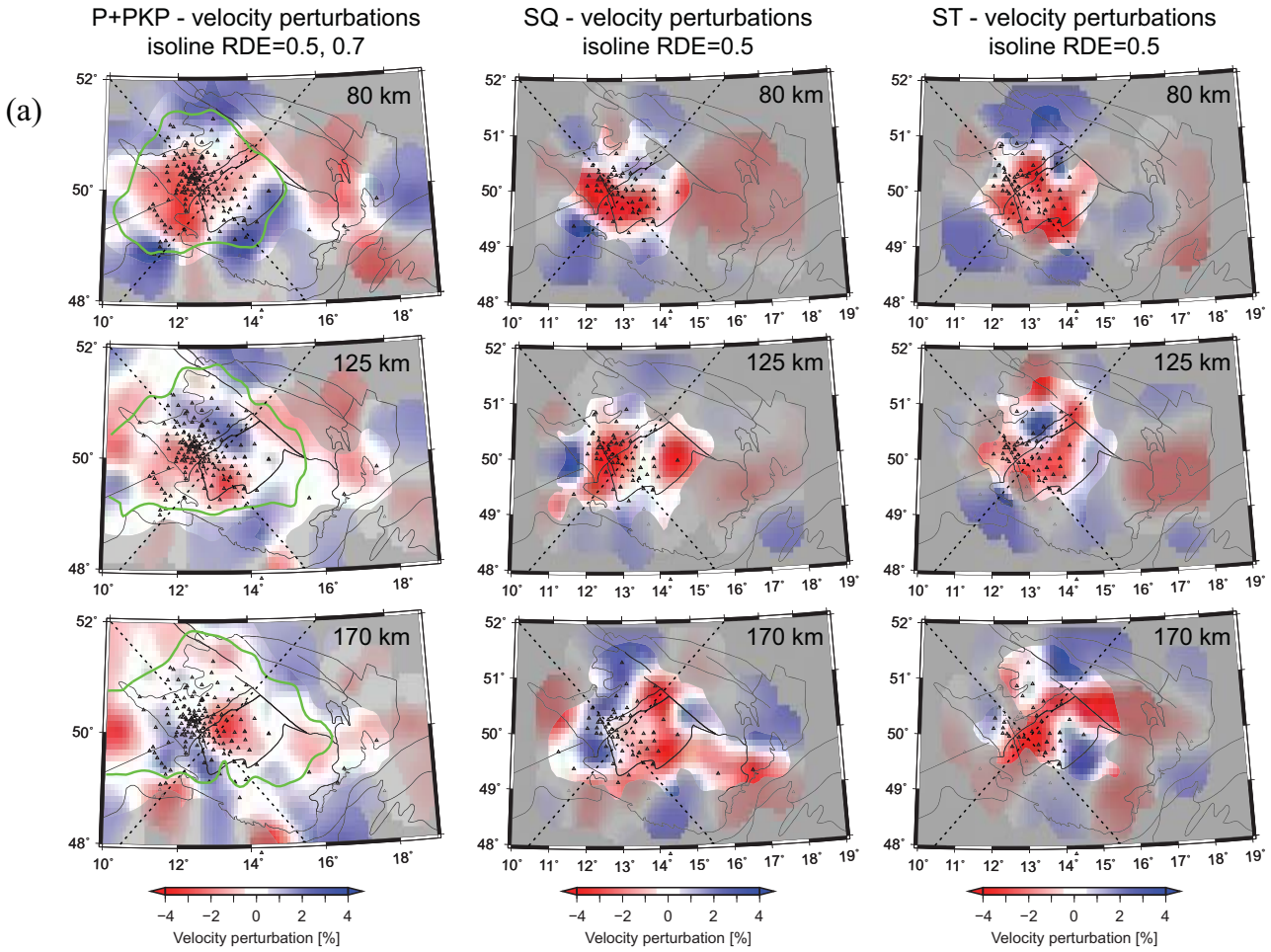

Figure 7. Comparison of v_P and v_S velocity perturbations in (a) three depth slices in models with 45 km vertical node spacing derived from three data sets: P+PKP, SQ and ST waves (b) along with ray-path distribution. Well-resolved regions of P+PKP model are contoured (RDE $\geq$ 0.7; green), less well-resolved ones are shaded (RDE $\leq$ 0.5). Dashed lines mark cross sections shown in Figure 8.

perturbations are larger in extent and amplitude in the central parts of the SQ and ST models. The NE shift of the low-velocity anomalies, i.e., toward the center of the BM, is evident both in the P+PKP$_{45}$ and SQ tomographic images at depths of 170 km. The anomalies occupy a large portion of the mantle beneath the TB unit, particularly in the SQ images. Perturbations in the P-wave tomographic model are less distinct in comparison with the upper layers, while both in the SQ and ST models the amplitudes of perturbations are similar.

Two cross sections through the three velocity-perturbation models are drawn along profiles, which cut the major low-velocity anomaly and image its depth extent (Figure 8, see also Figures 2 and 7). The anomaly is 150–250 km wide and it can be traced without interruption down to ~200 km in the S tomography. In the P+PKP tomography the region of the velocity decrease seems to be thinner (150–200 km), but it can be traced deeper (down to ~300 km). Steeper incidence for the rays in the P tomography can result in larger vertical smearing in comparison with the S tomography, but tomography based on ST shows a deeper extent of low-velocity perturbations. The region with low-velocity perturbations extends down to the same depth beneath the crossing of both profiles in all three tomography outputs (see squares in Figure 8). The low-velocity anomaly appears narrower beneath profile AB, while it is fragmented and broad beneath profile CD.

We performed several synthetic tests to assess resolution capability of the BOHEMA network (Figure 9, see also Figure 10b). Positive and negative perturbations alternate in the synthetic velocity model we test

AGU Geochemistry, Geophysics, Geosystems 10.1002/2016GC006318

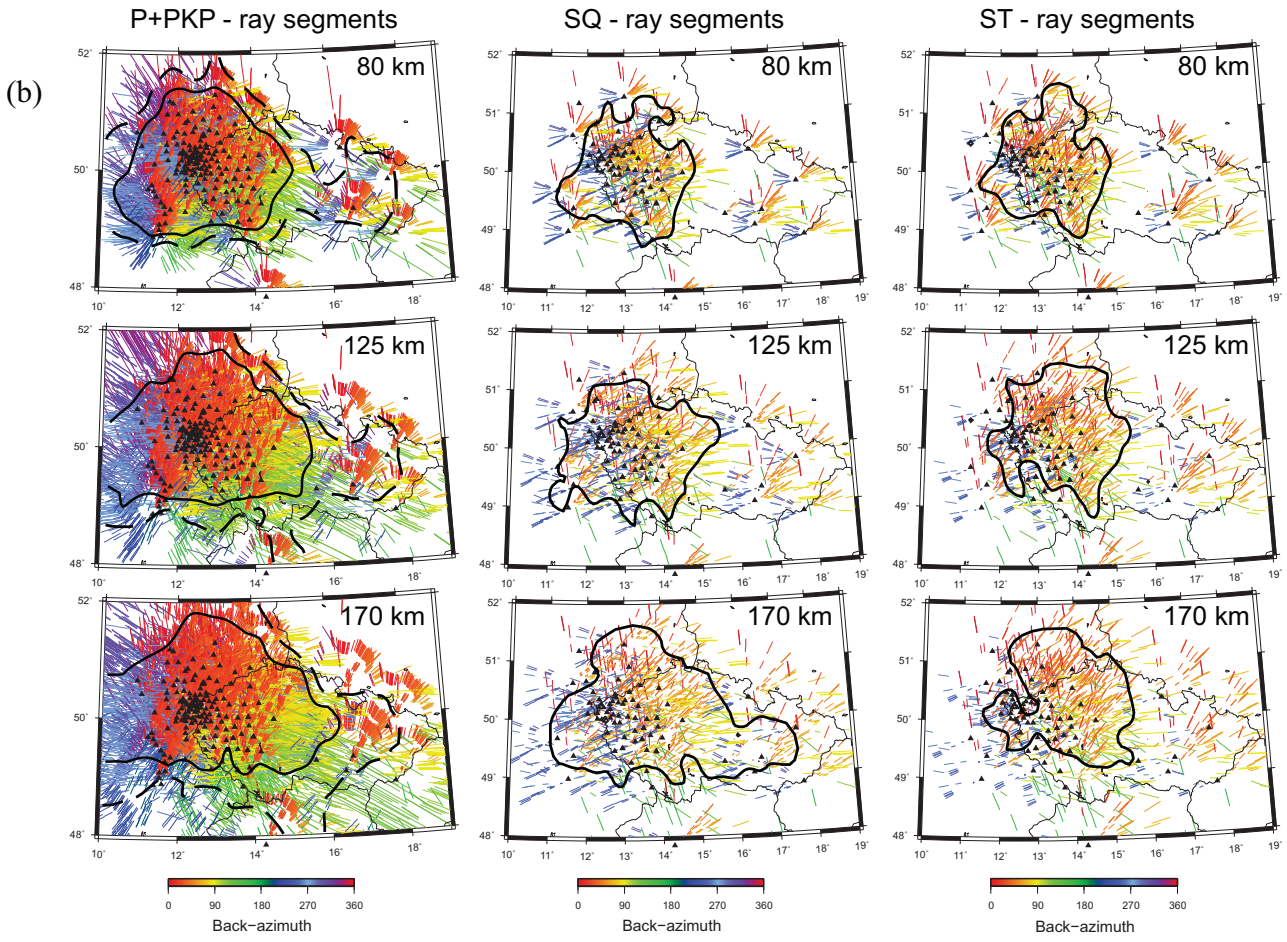

Figure 7. (continued)

(A and B velocity-perturbation patterns, Figure 9). Results for the P+PKP$_{30}$ station-event distribution show that tomography returns the synthetic perturbations reliably within well-sampled parts of the model (see also supporting information Figure S1). A slight smearing of the perturbations into depth levels without prescribed synthetic anomalies reflects the typical characteristic of teleseismic body-wave tomography.

6. Discussion

6.1. Plume or Asthenosphere Upwelling?

There are two competing scenarios to explain the upper mantle structure beneath the western BM: (1) existence of a "baby-plume," similar to those modeled beneath the French Massif Central (MC) [*Granet et al*., 1995] and Rhenish Massif (RM) [*Ritter et al*., 2001] and (2) the lithosphere thinning, i.e., asthenosphere upwelling beneath the Eger Rift in the western BM [*Plomerová et al*., 1998, 2007]. Low-velocity perturbations imaged in the P- and S-wave tomography of the upper mantle can help to answer which of the two scenarios is more probable.

Exploring the low-velocity perturbations in the western BM with the aim to support or to exclude the existence of a potential baby plume, we concentrate on detecting a narrow subvertical low-velocity anomaly having a diameter about 50 km. We have constructed several "tectonic" cross sections along and across the ER, to visualize in 3D the velocity perturbations in the P and S models and compared them with images of a

AGU Geochemistry, Geophysics, Geosystems 10.1002/2016GC006318

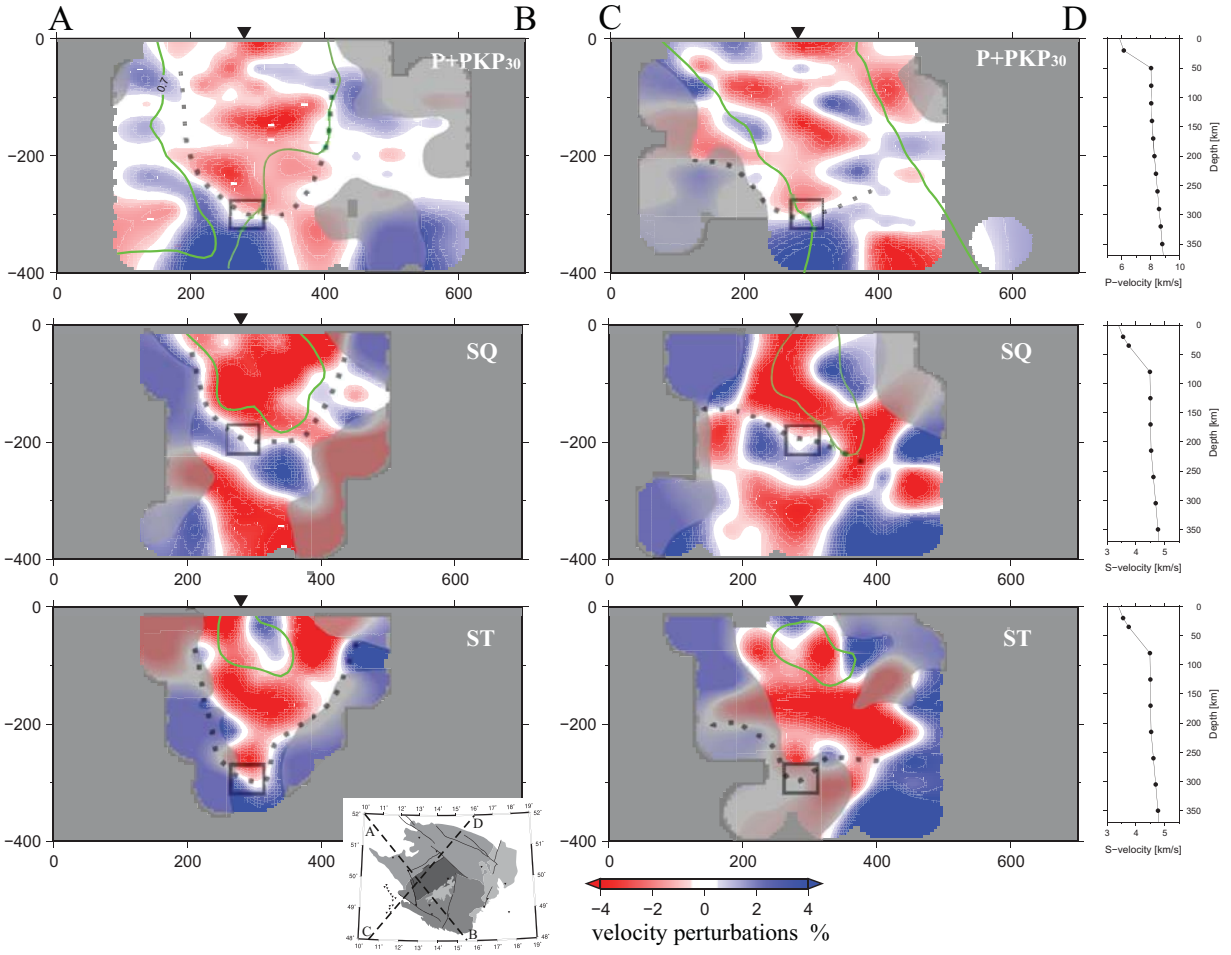

Figure 8. Cross sections through the velocity perturbation models along the AB and CD profiles (for locations see also Figures 2b and 7) cutting the most distinct anomalies. Perturbations with "hit-count" Nhit $\geq$ 30 and Nhit $\geq$ 10 are plotted in the P and S tomography, respectively. Regions with RDE $\leq$ 0.5 are dimmed, regions with RDE $\geq$ 0.7 are contoured (green). Region of continuous lower velocities is schematically marked by dotted curves. Rectangles mark its depth extend beneath point of profile crossing (triangles).

synthetic plume (Figure 10 and supporting information Figure S4). Though resolutions of the P and S models differ, the images show similar features (see also Figure 7). They display a ~200 km zone of low-velocity perturbations interrupted at depths near 150–200 km. The zone is most distinct beneath the central sections (Figure 10a), crossing the western ER. It is fragmented in the other two cross sections (supporting information Figure S4). The upper boundary of the low-velocity perturbations can be related to the shallow LAB, modeled below the western ER at ~80 km [e.g., *Plomerová and Babuška*, 2010].

Figure 10b shows a cross section through a synthetic model mimicking a low-velocity plume designed in analogy with those imaged by teleseismic body-wave tomography beneath the French Massif Central [*Granet et al.*, 1995] or Rhenish Massif [*Ritter et al.*, 2001]. The inversion was calculated from synthetics for the P+PKP station-event configuration and assumes a 2% velocity reduction relative to the IASP'91 reference model in a 60 km wide vertical column. The low-velocity perturbations from the synthetics occupy a narrow vertical volume identified only in the middle section crossing the triple junction of the ST/TB/MD units in the western end of the ER. In contrast to that, the observed low-velocity perturbations occupy about four times broader fragmented volume without a clear and indisputable link to deeper parts of the mantle, where a common source feeding the "baby plumes" was suggested [*Granet et al.*, 1995; *Goes et al.*, 1999]. An interpretation of the lower velocities in the upper mantle beneath the western BM as reflecting a "baby plume" thus seems unlikely.

AGU Geochemistry, Geophysics, Geosystems 10.1002/2016GC006318

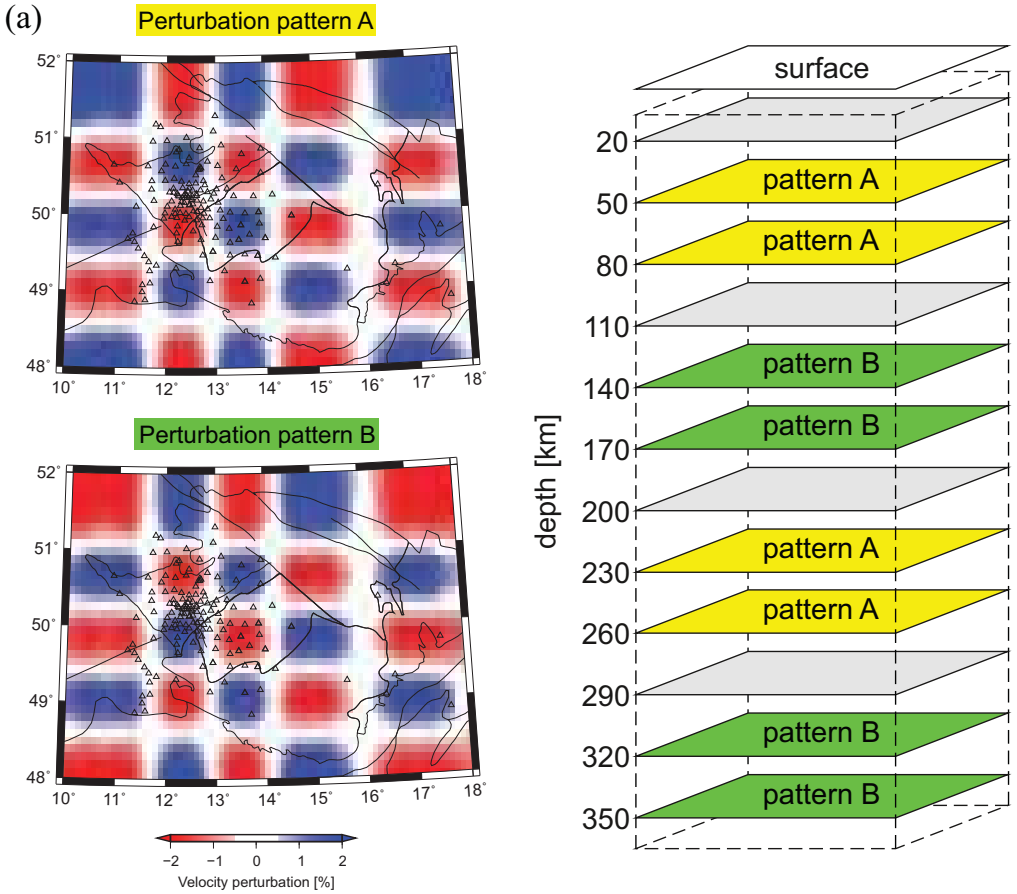

Figure 9. Checkerboard test of the array resolution for (a) synthetic model and (b) recovered velocity perturbations.

Already initial regional inversions for P-velocity structure [*Plomerová et al*., 2007] did not show any narrow subvertical low-velocity anomaly in the upper mantle beneath the western BM. That preliminary tomography used 90% of the P-wave arrival times of the present P-wave set (without the PKP phases) with residuals in a range of (−0.7 s, 0.7 s). At first glance, the resulting models presented in this study differ from the preliminary 2007 model (supporting information Figure S5), though they both effect 33% data-variance reduction. However, if we restrict the comparison to the well-resolved parts of the new model and take into consideration differences in the residual preprocessing, the crustal corrections applied, the model parameterizations and inversion regularization, as well as the graphical visualizations [*Plomerová et al*., 2007], the general features of both models are similar (supporting information Figure S6). We attribute the diffuse pattern of small alternating negative and positive perturbations in the shallow layers of the preliminary model mainly to shortcomings of the "layer-stripping" approach [*Evans and Achauer*, 1993] used to correct for crustal effects and to the narrower travel-time-residual range. Uncorrected remnants of crustal heterogeneities might be mapped into the upper mantle [*Karousová et al*., 2012a] in the earlier model. The broad low-velocity anomaly around the ER and higher velocities beneath the Moldanubian unit are clearly visible in both models, though they are more fragmented in the 2007 model. At 110 km depth, the separation of negative and positive perturbations in the SW and NE of the ER is less evident in the 2007 model. Perturbations in the deeper layers of the 2007 model with larger cells are smoother and exhibit high coherence with large-scale features of the model presented in this paper. The perturbation pattern (this paper) reflects the complex structure of the upper mantle in the western BM, whose mantle lithosphere is composed of several domains with differently oriented fabrics [e.g., *Babuška and Plomerová*, 2013].

AGU Geochemistry, Geophysics, Geosystems 10.1002/2016GC006318

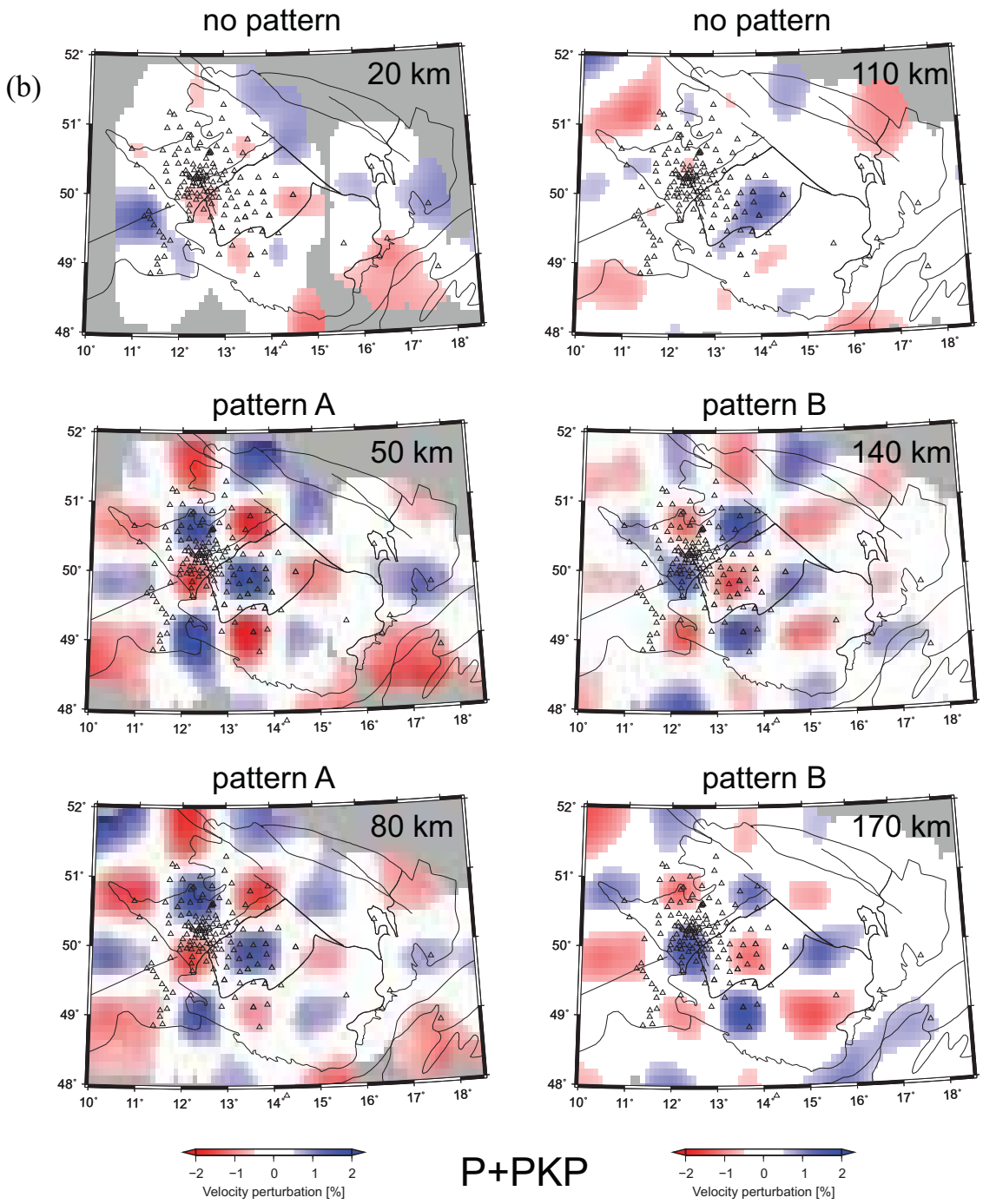

Figure 9. (continued)

The full-waveform tomographic velocity model of the European mantle by *Fichtner and Villaseñor* [2015] has much less vertical smearing than the body-wave teleseismic tomography. This model images several localized low-velocity anomalies that can be related to the ECRIS. The low-velocitie regions, including one beneath the BM, are confined to the upper 200 km of the mantle, with distinct velocity minima beneath centers of tectonic and volcanic activity. If plumes existed below the 300 km depth, then their diameters

AGU Geochemistry, Geophysics, Geosystems 10.1002/2016GC006318

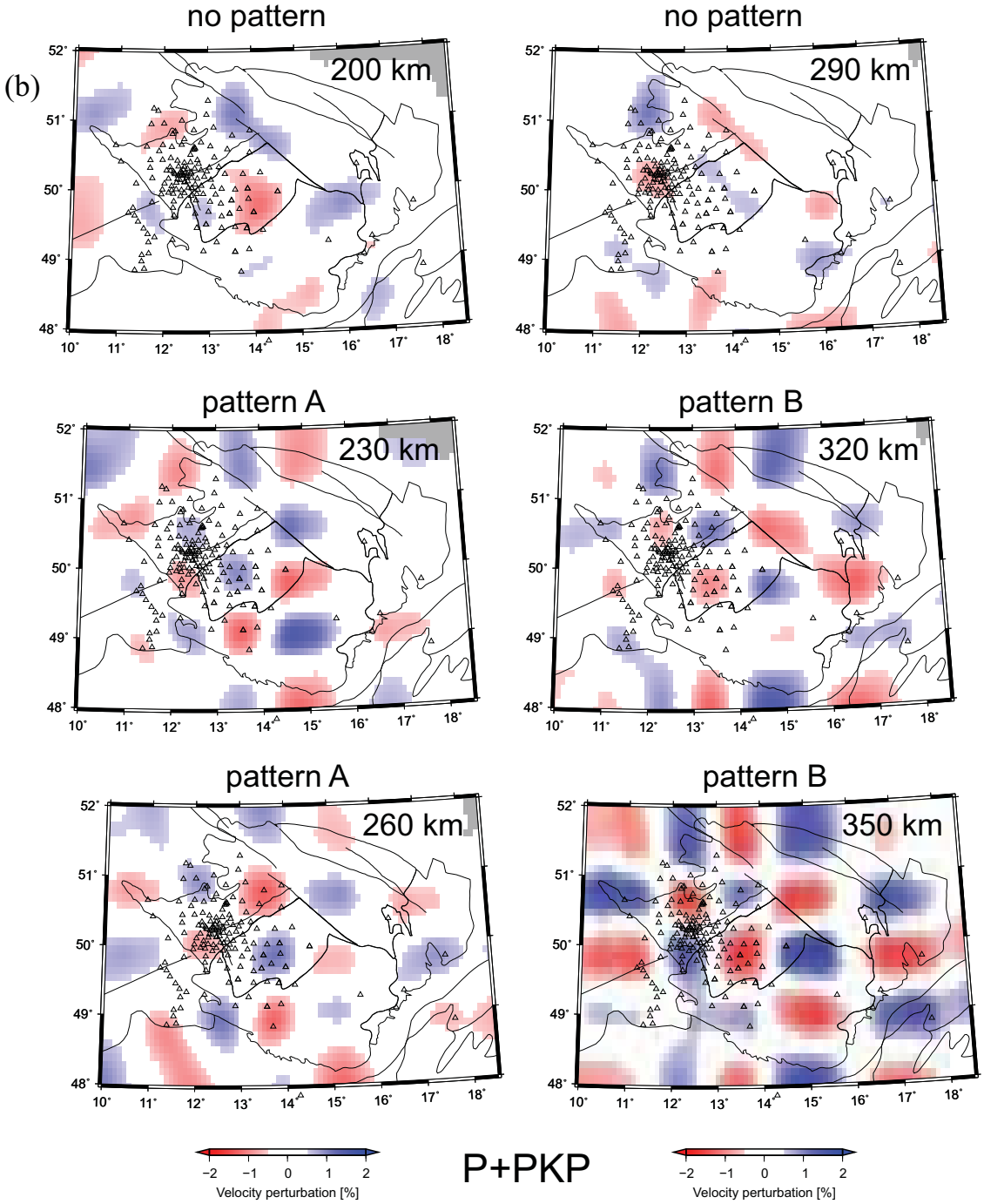

Figure 9. (continued)

would have to be smaller than ~100 km to remain seismically invisible. Because full-waveform inversions do not show clear evidence for mantle plume beneath central and western Europe, a common deep-mantle source of volcanism along the ECRIS seems to be implausible.

The results of the P and S tomography presented in this paper thus support the alternative explanation of the lower velocities detected beneath the western part of the BM, i.e., by the shallowing the lithosphere-

AGU Geochemistry, Geophysics, Geosystems 10.1002/2016GC006318

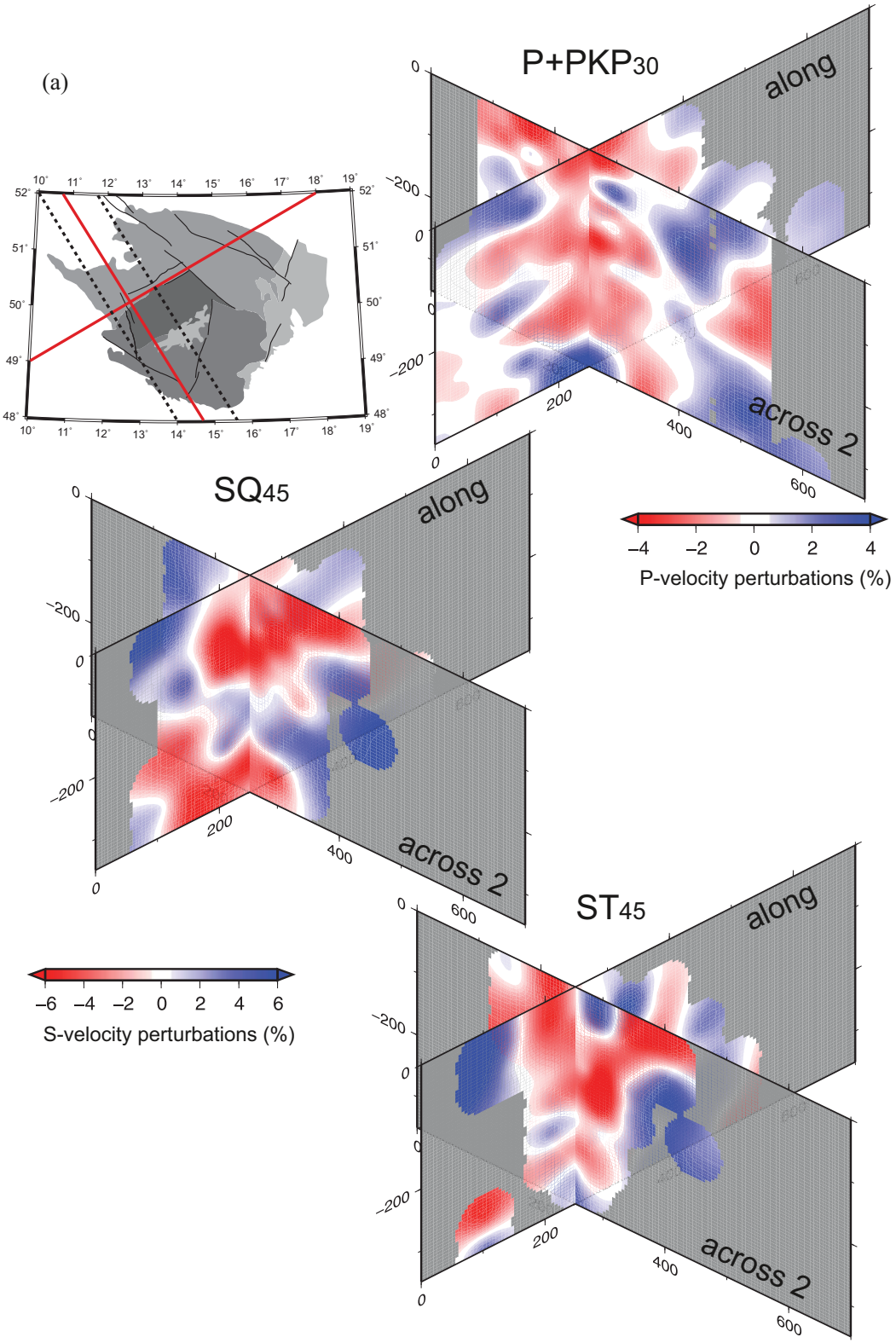

Figure 10. Cross sections through the velocity perturbation models along "tectonic" profiles (a) oriented parallel and across the Eger Rift (see also supporting information Figure S5); (b) cross section cutting the model of a synthetic plume modeled as 2% low-velocity anomaly of 60 km width in analogy with the plumes in the French Massif Central and Eiffel.

AGU Geochemistry, Geophysics, Geosystems 10.1002/2016GC006318

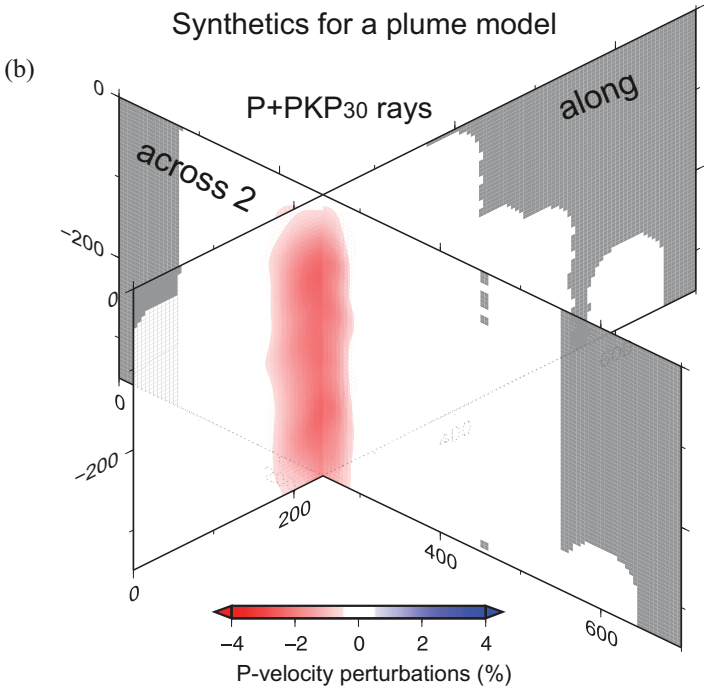

Figure 10. (continued)

asthenosphere boundary beneath the ER [*Plomerová et al*., 1998, 2007]. The corresponding LAB updoming was also modeled by different techniques [e.g., *Heuer et al*., 2007; *Geissler et al*., 2007; *Plomerová and Babuška*, 2010]. Based on results of P receiver functions, *Heuer et al*. [2011] accepted the proposed plume-like structure in the upper mantle below the western Bohemia earthquake region [*Granet et al*., 1995], but with no or only weak imprint on the 410 km discontinuity. On the other hand, the boundaries between mantle domains of the three tectonic units forming the lower lithosphere in the region, determined from studies of seismic anisotropy, represent weak zones in the otherwise rigid mantle lithosphere. In the past, such zones probably served as paths for upward flow of hot mantle material, which could modify the mantle domain boundaries and locally thinned their lithosphere.

The general distribution of positive and negative velocity perturbations in the upper mantle tomography in this paper correlates well with the depth-variations of the LAB reported by *Plomerová and Babuška* [2010]. The tomographic images show the asthenosphere upwelling along the ER and the southward thickening of the high-velocity lithosphere beneath the MD part of the BM, detectable down to 80–140 km depths (e.g., Figure 6). The detected lithosphere thinning along the WSW-ENE-trending ER fits the general orientation of the Variscan orogen in central Europe and parallels the boundaries between the ST, MD and TB lithospheric domains in the upper mantle [*Babuška and Plomerová*, 2006]. We interpret the mantle-lithosphere domains with consistent anisotropy fabrics as representatives of originally separated microplates, which were assembled during the Gondwana and Laurentia-Baltica collision and created the BM [*Babuška and Plomerová*, 2013]. Gradual stabilization of the bottom of the lithosphere took place as a result of slab break-off episodes and the erosion of the lithosphere-asthenosphere boundary by mantle flow. This erosion likely affected the weakened suture zones as well. Such process could have led to the observed LAB upwelling related to the ST and TB/MD mantle-domain contacts.

6.2. Results of BOHEMA Tomography in Light of Other Studies

Long-term seismological research, carried out in the western BM, supplied new inferences on the upper-mantle structure, especially its velocities, anisotropy, domain-like structure, discontinuities etc., and calls for a reassessment of the "baby-plume" concept suggested for Variscan Europe.

AGU Geochemistry, Geophysics, Geosystems 10.1002/2016GC006318

High-resolution velocity images from the BOHEMA P and S arrivals did not identify a narrow "baby-plume" beneath the BM. In the absence of the clear magma conduit that would be detectable in the present-day upper-mantle velocities it is prudent to ask why abundant volcanism spreads along the ER and from where it was fed in the past. *Amaru* [2007] combined data from permanent observatories and several temporary arrays [*Amaru et al*., 2008], and imaged velocities down to the lower mantle. Low velocities dominate beneath central Europe at depths down to 400–600 km. Moreover, the tomography of the authors above shows a distinct vertical low-velocity zone extending from the bottom of the lower mantle to the Transition Zone. Because the perturbation weakens both in its extent and amplitude at the lower boundary of the Transition Zone, its connection with the upper mantle low-velocities is less evident. In spite of that, *Amaru* [2007] accepts the *Goes et al*. [1999] interpretation that this lower mantle upwelling is a source for the MC, RM and BM volcanism. The Bohemian Massif is the thickest of the Variscan Massifs [*Plomerová and Babuška*, 2010] and may as such have the "strongest" lithosphere which would not allow a plume of small scale and force to penetrate through the compact block. This process might end in accumulating the upwelling material at the base of the lithosphere as a kind of underplating, followed by gradual erosion of the basal lithosphere into the shape of a broadly updoming mantle anomaly.

Concentration of the low-velocity material in the sublithospheric upper mantle beneath central Europe is a striking feature in the tomography by *Amaru* [2007]. Existence of weakened zones in the lithosphere appears as a necessary condition for transport of hot molten material to the surface [*Babuška et al*., 2002], as its transport upward through an intact rigid mantle-lithosphere block would be difficult. Boundaries between mantle-lithosphere domains, delimited from large-scale seismic anisotropy, have often matched the boundaries of crustal terranes. *Babuška et al*. [2002] modeled fabrics of three sharply bounded mantle lithosphere domains beneath the MC and proposed that magmas feeding the Cenozoic volcanism, which developed on two peripheral parts of the southern thinned domain, were channeled to the Cantal and Mont Dore volcanoes by the reactivated Variscan suture hidden in the mantle.

Wilson and Downes [2006] deduce from distribution of the low-velocity anomalies beneath the MC and RM [*Granet et al*., 1995; *Ritter et al*., 2001] that they do not seem to be rooted in the lower mantle, though they might extend down to the Transition Zone. A positive thermal anomaly at the Transition Zone depths, which could be related to the hotter low-velocity material reservoir in the mantle, is absent. Instead, the location of the plume-like structure actually correlates with a zone of high-velocity material within the Transition Zone reflecting accumulation of subducted slabs. The authors proposed the low-velocity anomalies could be products of localized fluid streaming from the top of the Transition Zone.

Walker et al. [2005] interpret shear-wave splitting in the Rhenish Massif by a parabolic asthenospheric flow and use optimum model parameters to calculate Eurasian plate speed at 12 km/Ma. Their model is consistent with geological, tomographic, receiver function, electrical conductivity anisotropy and geochemical findings in the Eifel region, as well as with global absolute plate motion, whose speed is estimated at 19 $\pm$ 14 km/Ma in the HS3-NUVEL1A [*Gripp and Gordon*, 2002]. Indeed, ages of volcanic centers are very different. Volcanism is dated back to 28 Ma on the east (the southern Leine Graben), while it is much younger (from 2.7 Ma to recent) in the central part of the RM (the southern Ruhr Graben). The plume structure manifested clearly in tomography by *Ritter et al*. [2001] down to the top of the Transition Zone splits at depths of around 50 km. The eastern shallow anomaly, without an evident connection to the deeper parts, may represent remnants of the older volcanism terminated about 5 Ma ago. Extension related to the Leine Graben rifting weakened further the contact of the Rhenohercynian (RH) and ST mantle lithosphere domains and enabled sublithospheric mantle upwelling along the Rheic Suture. The younger volcanism further to the west is fed with the hot mantle material transported to the surface most probably along the same suture opened (weakened) by the extension related to the rifting below the Ruhr Graben.

6.3. Rifts, Sutures, and Volcanism Distribution

In general, the centers of the Tertiary to Quaternary volcanism linked to the ECRIS concentrate mostly at the ends of the rifts, close to distinct tectonic sutures cutting the rifts at high angles, e.g., the Limagne Graben (LiG) in the Massif Central (MC) and the Moldanubian Suture (MD), or, the Ruhr (RhG) and Leine (LeG) Grabens in the Rhenish Massif (RM) and the Rheic Suture (Figure 11a). In the Eger Rift (ER), the volcanism is not restricted to the graben structure (EG) which is parallel the Saxothuringian/Teplá-Barrandian Suture. It extends to the southwest, beyond the Mariánské-Lázně Fault (MLF), and to the northeast, beyond the Elbe

AGU Geochemistry, Geophysics, Geosystems 10.1002/2016GC006318

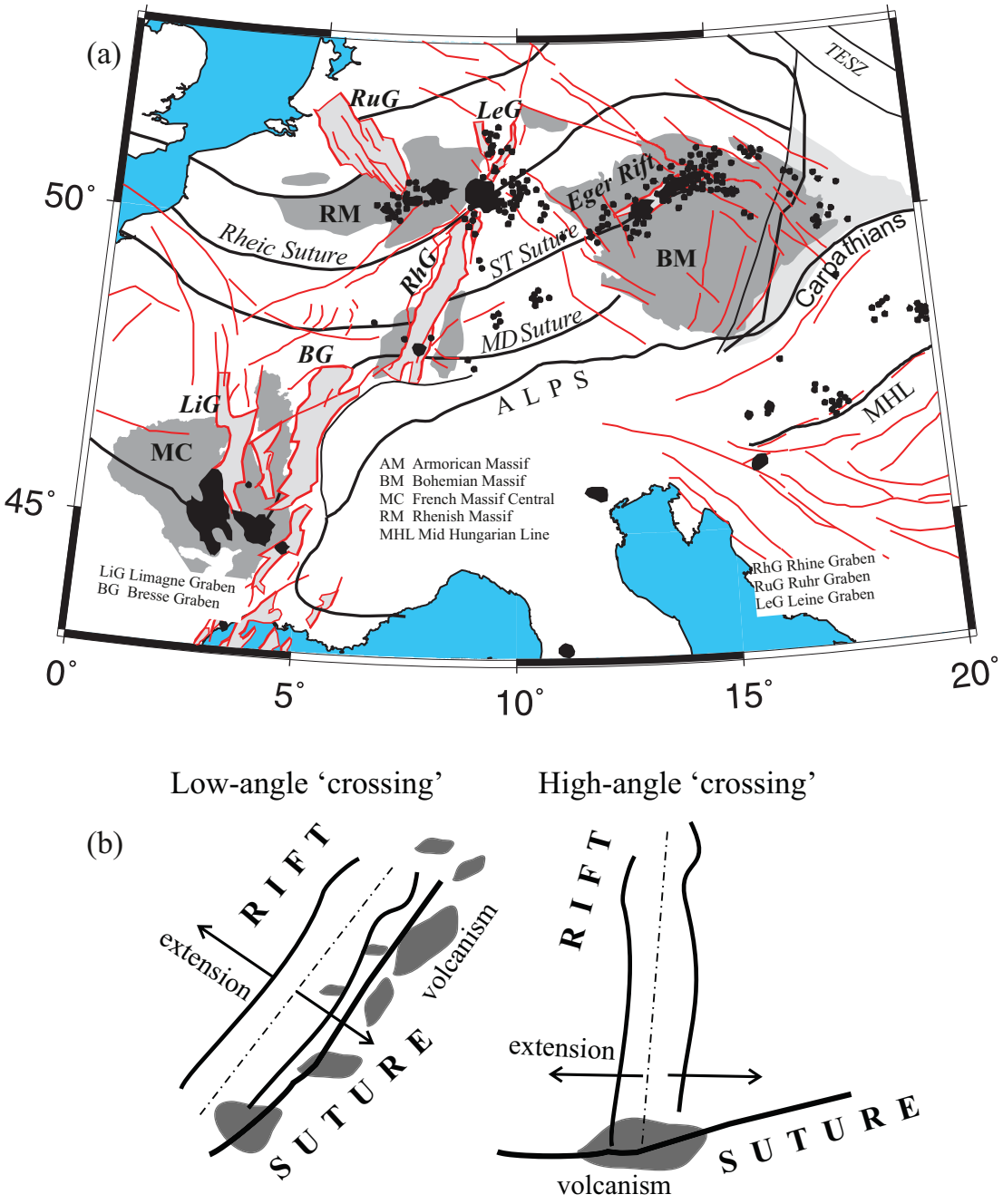

Figure 11. (a) ECRIS and related Cenozoic volcanism and (b) schematic presentation of the low- and high-angle rift and suture "crossing."

Fault Zone (EFZ). Both fault zones limit the graben structure (EG) of the presumably longer Eger Rift (Figure 2). The EFZ and the Sudetic faults (ISF, SMF) seem to be responsible for volcanism taking place in the northern part of the BM.

The broadly spread volcanism along the ER might reflect differences in orientation of the structures and acting extensional stresses (Figure 11b). Alignment of the rift elongation axis (perpendicular to the rift extension) and the deep mantle lithosphere suture between the ST and TB/MD resulted in weakening of a longer segment of the ST Suture and thus in opening of a larger portion of the rift for ascent of the hot volcanic

AGU Geochemistry, Geophysics, Geosystems 10.1002/2016GC006318

mantle material to the surface. The orientation of the rift axis and the suture in the mantle lithosphere seems to be responsible for either a widely distributed volcanism (in case of subparallel orientation) or for creating a localized volcanic center (in case of a high-angle orientation). This may explain why no narrow and steep, finger-like low-velocity anomaly similar to those modeled beneath the MC and RM has been imaged beneath the ER in the western BM. Only short segments of the RH/ST and MD sutures were likely weakened by extensional stresses of the rifts in the MC and RM (Figure 11). These two short segments of the sutures might thus be apt to appear as "circular" conduits for hot material escaping episodically from the mantle to the surface.

Babuška and Plomerová [2010] suggested that the sublithospheric mantle beneath the western BM acted as a major source for heat and partial melts. Variscan boundaries in the brittle lithospheric-mantle domains served as magma conduits for the late-orogenic granitic magmatism and, after rejuvenation of some of them, also for the Cenozoic volcanism. It is likely that some of the so-called intra-plate phenomena can be related to partly healed, and later rejuvenated, micro-plate boundaries. The upward flow of the hot mantle material could penetrate along the boundaries from deeper parts to the surface, modify the domain boundaries and/or thin the domains. Orientation of lithosphere domain boundaries in the mantle and extensional forces in the rifts seems to play important role in distribution of volcanism. Mantle processes in general, appear to be decisive for various near-surface features or geological characteristics observed on the surface.

7. Conclusions

By inverting body-wave travel-time residuals we have shed light on the question regarding the general validity of the well-known "baby-plume" concept in central European provinces with Cenozoic volcanism, particularly in the western Bohemian Massif. High-resolution P- and S-wave velocity tomography based on data recorded during the BOHEMA passive seismic experiment show that velocity-perturbation patterns in the P- and S-wave models exhibit similar features, in general, though their resolutions are different. None of the models display a clear "plume-like" structure, i.e., a narrow subvertical low-velocity anomaly, neither below the western Eger Rift, nor below other parts of the BM. This finding is in accord with results of the full-waveform inversion which did not image mantle plumes beneath Europe, that could be responsible for the ECRIS [*Fichtner and Villaseñor*, 2015].

A 200 km wide zone of low-velocity perturbations beneath the western BM seems to be interrupted in the velocity models of present-day upper mantle at depths of ~150–200 km, indicating no or a very weak connection of the zone with a potential magma reservoir at greater depths. The low-velocity zone is most distinct beneath the western end of the graben structure of the ER and it is fragmented in the remaining segments of the rift. The broad shape of the anomaly and the lack of evident connection with deeper parts of the mantle support our interpretation of such low-velocity anomaly in the western BM by a lithosphere thinning along the Eger Rift. An upward flow of hot mantle material could penetrate in the past along boundaries of the mantle lithosphere domains from the sublithospheric mantle to the surface, modify the domain boundaries and/or thinned the lithosphere. Upper boundary of the low-velocity perturbations can be related to the shallow LAB, modeled below the western ER at ~80 km [e.g., *Plomerová and Babuška*, 2010].

Results of several seismic velocity-tomography studies indicate broadly dispersed low-velocities, indicative of hot buoyant upper mantle beneath central Europe. Processes that transported the hot material actively, either in the past, or at present, hardly could "drill" upward through the compact rigid block of the mantle lithosphere. More likely, an episodic transport of the material happened along weakened zones between the blocks. Boundaries of the mantle lithosphere domains, manifested at the surface as distinct sutures can serve as paths for the mantle material transport to the volcanic centers, particularly, if the collisional zone between the domains was weakened due to extensional processes. The rift extension at a high angle to a suture might allow extrusion of the volcanic material along the entire rift, whereas extension subparallel to the suture opens only a short segment of the rift. The rifts in the French Massif Central and in the Rhenish Massif can serve as examples of the latter and the Eger Rift in the western part of the BM for the former rift-suture configuration.

AGU Geochemistry, Geophysics, Geosystems 10.1002/2016GC006318

Acknowledgments
Suggestions of A. Fichtner and an anonymous reviewer improved the manuscript. Special thanks go to Jeffrey Park for a critical reading of the manuscript for style and clarity. The Grant Agency of the Czech Republic supported the research by grant P210-12-2381 and the BOHEMA array operation during 2001-2003 by grant 205/01/1154. We greatly appreciate operation of five broad-band stations provided by the ETH Zürich at the early stage of the experiment, whose seismograms substantially enlarge the data sets. Data acquisition from permanent observatories was supported by the project of large research infrastructure CzechGeo/EPOS, grant LM2010008 and LM2015079. Waveforms of the events used in this study are accessible via the Institute of Geophysics, Czech Academy of Sciences seismological archive upon request.

References

Achauer, U., and F. Masson (2002), Seismic tomography of continental rifts revisited: From relative to absolute heterogeneities, *Tectonophysics*, *358*, 17–37, doi:10.1016/S0040-1951(02)00415-8.

Aki, K., A. Christoffersson, and E. S. Husebye (1977), Determination of the three dimensional seismic structure of the lithosphere, *J. Geophys. Res.*, *82*, 277–296, doi:10.1029/JB082i002p00277.

Amaru, M. L. (2007), Global travel time tomography with 3-D reference models, PhD thesis, Utrecht Univ., Utrecht, Netherlands.

Amaru, M. L., W. Spakman, A. Villaseñor, S. Sandoval, and E. Kissling (2008), A new absolute arrival time data set for Europe, *Geophys. J. Int.*, *173*, 465–472, doi:10.1111/j.1365-246X.2008.03704.x.

Babuška, V., and J. Plomerová (2006), European mantle lithosphere assembled from rigid microplates with inherited seismic anisotropy, *Phys. Earth Planet. Inter.*, *158*, 264–280, doi:10.1016/j.pepi.2006.01.010.

Babuška, V., and J. Plomerová (2010), Mantle lithosphere control of crustal tectonics and magmatism of the western Ohře (Eger) Rift, *J. Geosci.*, *55*, 171–186, doi:10.3190/jgeosci.070.

Babuška, V., and J. Plomerová (2013), Boundaries of mantle-lithosphere domains in the Bohemian Massif as extinct exhumation channels for high-pressure rocks, *Gondwana Res.*, *23*, 973–987, doi:10.1016/j.gr.2012.07.005.

Babuška, V., J. Plomerová, and J. Šílený (1987), Structural model of the subcrustal lithosphere in central Europe, in *The Composition, Structure and Dynamics of the lithosphere-Asthenosphere System, Geophys. Ser.*, edited by C. Froidevaux and K. Fuchs, pp. 239–251, AGU, Washington, D. C.

Babuška, V., J. Plomerová, L. Vecsey, M. Granet, and U. Achauer (2002), Seismic anisotropy of the French Massif Central and predisposition of Cenozoic rifting and volcanism by Variscan suture hidden in the mantle lithosphere, *Tectonics*, *21*(4), 1029, doi:10.1029/2001TC901035.

Babuška, V., J. Plomerová, and L. Vecsey (2008), Mantle fabric of western Bohemian Massif (central Europe) constrained by 3D seismic P and S anisotropy, *Tectonophysics*, *462*, 149–163, doi:10.1016/j.tecto.2008.01.020.

Bankwitz, P., G. Schneider, H. Kämpf, and E. Bankwitz (2003), Structural characteristics of epicentral areas in Central Europe: Study case Cheb Basin (Czech Republic), *J. Geodyn.*, *35*, 5–32, doi:10.1016/S0264-3707(02)00051-0.

Bräuer, K., H. Kämpf, S. Niedermann, and G. Strauch (2005), Evidence for ascending upper mantle-derived melt beneath the Cheb basin, central Europe, *Geophys. Res. Lett.*, *32*, L08303, doi:10.1029/2004GL022205.

Čermák, V. (1994), Results of heat flow studies in Czechoslovakia, in *Crustal Structure of the Bohemain Massif and the West Carpathians*, edited by V. Bucha and M. Blížkovský, pp. 85–120, Springer, Berlin.

Chang, S. J., S. van der Lee, M. P. Flanagan, H. Bedle, F. Marone, E. M. Matzel, M. E. Pasyanos, A. J. Rodgers, B. Romanowicz, and Ch. Schmid (2010), Joint inversion for three-dimensional S velocity mantle structure along the Tethyanmargin, *J. Geophys. Res.*, *115*, B08309, doi:10.1029/2009JB007204.

Dando, B. D. E., G. W. Stuart, G. A. Houseman, E. Heged, E. Brückl, and S. Radovanovi (2011), Teleseismic tomography of the mantle in the Carpathian–Pannonian region of central Europe, *Geophys. J. Int.*, *186*, 11–31, doi:10.1111/j.1365-246X.2011.04998.x.

Dezes, P., S. M. Schmid, and P. A. Ziegler (2004), Evolution of the European Cenozoic Rift System: Interaction of the Alpine and Pyrenean orogens with their foreland lithosphere, *Tectonophysics*, *389*, 1–33, doi:10.1016/j.tecto.2004.06.011.

Díaz, J., J. Gallart, I. Morais, G. Silveira, D. Pedreira, J.A. Pulgar, N.A. Dias, M. Ruiz, and J.M. González-Cortina (2015), From the Bay of Biscay to the High Atlas: Completing the anisotropic characterization of the upper mantle beneath the westernmost Mediterranean region, *Tectonophysics*, *663*, 192–202.

Evans, J. R., and U. Achauer (1993), Teleseismic velocity tomography using the ACH method: Theory and application to continental scale studies, in *Seismic Tomography*, edited by H. M. Iyer and K. Hirahara, pp. 319–360, Chapman and Hall, London, U. K.

Fichtner, A., and A. Villaseñor (2015), Crust and upper mantle of the western Mediterranean–Constraints from full-waveform inversion, *Earth Planet. Sci. Lett.*, *428*, 52–62, doi:10.1016/j.epsl.2015.07.038.

Franke, W. (2006), The Variscan rogeny in Central Europe: Construction and collapse, in *European Lithosphere Dynamics, Memoirs*, vol. 32, edited by D. G. Gee and R. A. Stephenson, pp. 333–343, Geol. Soc., London, doi:10.1144/GSL.MEM.2006.032.01.20.

Geissler, W. H., H. Kämpf, R. Kind, K. Bräuer, K. Klinge, T. Plenefisch, J. Horálek, J. Zedník, and V. Nehybka (2005), Seismic structure and location of a CO2 source in the upper mantle of the western Eger Rift, central Europe, *Tectonics*, *24*, TC5001, doi:10.1029/2004TC001672.

Geissler, W. H., H. Kämpf, W. Seifert, and P. Dulski (2007), Petrological and seismic studies of the lithosphere in the earthquake swarm region Vogtland/NW Bohemia, central Europe, *J. Volcanol. Geotherm. Res.*, *159*, 33–69, doi:10.1016/j.jvolgeores.2006.06.011.

Geissler, W. H., H. Kämpf, Z. Skácelová, J. Plomerová, V. Babuška, and R. Kind (2012), Lithosphere structure of the NE Bohemian Massif (Sudetes)–A teleseismic receiver function study, *Tectonophysics*, *564-565*, 12–37, doi:10.1016/j.tecto.2012.05.005.

Goes, S., W. Spakman, and H. Bijwaard (1999), A lower mantle source for central European volcanism, *Science*, *286*, 1928–1931, doi:10.1126/science.286.5446.1928.

Granet, M., M. Wilson, and U. Achauer (1995), Imaging a mantle plume beneath the French Massif Central, *Earth Planet. Sci. Lett.*, *136*, 281–96, doi:10.1016/0012-821X(95)00174-B.

Gripp, A. E., and R. G. Gordon (2002), Young tracks of hotspots and current plate velocities, *Geophys. J. Int.*, *150*, 321–361, doi:10.1046/j.1365-246X.2002.01627.x.

Heuer, B., W. H. Geissler, R. Kind, and H. Kämpf (2006), Seismic evidence for asthenospheric updoming beneath the western Bohemian Massif, central Europe, *Geophys. Res. Lett.*, *33*, L05311, doi:10.1029/2005GL025158.

Heuer, B., H. Kampf, R. Kind, and W. H. Geissler (2007), Seismic evidence for whole lithosphere separation between Saxothuringian and Moldanubian tectonic units in central Europe, *Geophys. Res. Lett.*, *34*, L09304, doi:10.1029/2006GL029188.

Heuer, B., W. H. Geissler, R. Kind, and BOHEMA Working Group (2011), Receiver function search for a baby plume in the mantle transition zone beneath the Bohemian Massif, *Geophys. J. Int.*, *187*, 577–594, doi:10.1111/j.1365-246X.2011.05155.x.

Horálek, J., and T. Fischer (2008), Role of crustal fluids in triggering the West Bohemia/Vogtland earthquake swarms: Just what we know (a review), *Stud. Geophys. Geod.*, *52*, 455–478, doi:10.1007/s11200-008-0032-0.

Hrubcová, P., and W. H. Geissler (2009), The crust-mantle transition and the Moho beneath the Vogtland/west Bohemian region in the light of different seismic methods, *Stud. Geophys. Geod.*, *53*, 275–294, doi:10.1007/s11200-009-0018-6.

Hrubcová, P., P. Środa, A. Špičák, A. Guterch, M. Grad, G. R. Keller, E. Brueckl, and H. Thybo (2005), Crustal and uppermost mantle structure of the Bohemian Massif based on CELEBRATION 2000 data, *J. Geophys. Res.*, *110*, B11305, doi:10.1029/2004JB003080.

Jelínek, E., V. Štědrá, and J. Cháb (1997), The Mariánské Lázně complex, in *Geological Model of Western Bohemia Related to the KTB Borehole in Germany*, vol.47, edited by S. Vrána and V. Štědrá, pp. 61–70, Czech Geol. Surv., Prague.

AGU Geochemistry, Geophysics, Geosystems 10.1002/2016GC006318

Kämpf, H., K. Bräuer, J. Schumann, K. Hahne, and G. Strauch (2013), CO2 discharge in an active, non-volcanic continental rift area (Czech Republic): Characterisation (δ13C, 3He/4He) and quantification of diffuse and vent CO2 emissions, *Chem. Geol.*, *339*, 71–83, doi:10.1016/j.chemgeo.2012.08.005.

Karousová, H., J. Plomerová, and V. Babuška (2012a), Three-dimensional velocity model of the crust of the Bohemian Massif and its effects on seismic tomography of the upper mantle, *Stud. Geophys. Geod.*, *56*, 249–267, doi:10.1007/s11200-010-0065-z.

Karousová, H., J. Plomerová, and L. Vecsey (2012b), Seismic tomography of the upper mantle velocity structure beneath the north-eastern Bohemian Massif (central Europe), *Tectonophysics*, *564-565*, 1–11, doi:10.1016/j.tecto.2012.06.031.

Karousová, H., J. Plomerová, and V. Babuška (2013), Upper mantle structure beneath the southern Bohemian Massif and its surroundings imaged by high-resolution tomography, *Geophys. J. Int.*, *194*(2), 1203–1215, doi:10.1093/gji/ggt159.

Kennett, B. L. N., and E. R. Engdahl (1991), Traveltimes for global earthquake location and phase identification, *Geophys. J. Int.*, *105*, 429–465, doi:10.1111/j.1365-246X.1991.tb06724.x.

Kissling, E., S. M. Schmid, R. Lippitsch, J. Ansorge, and B. Fügenschuh (2006), Lithosphere structure and tectonic evolution of the Alpine arc: New evidence from high-resolution teleseismic tomography, in *European Lithosphere Dynamics, Memoirs*, vol. 32, edited by D. G. Gee and R. A. Stephenson, pp. 129–145, Geol. Soc., London, doi:10.1144/GSL.MEM.2006.032.01.08.

Koulakov, I., M. K. Kaban, M. Tesauro, and S. Cloetingh (2009), P- and S- velocity anomalies in the upper mantle beneath Europe from tomographic inversion of ISC data, *Geophys. J. Int.*, *179*, 345–366, doi:10.1111/j.1365-246X.2009.04279.x.

Linnemann, U., et al. (2008), Precambrian, in *The Geology of Central Europe*, edited by T. McCann, pp. 21–101, Geol. Soc., London, U. K.

Lippitsch, R., E. Kissling, and J. Ansorge (2003), Upper mantle structure beneath the Alpine orogen from high-resolution teleseismic tomography, *J. Geophys. Res.*, *108*(B8), 2376, doi:10.1029/2002JB002016.

Matte, P. (1986), Tectonics and plate-tectonics model for the variscan belt of Europe, *Tectonophysics*, *126*, 329–374, doi:10.1016/0040-1951(86)90237-4.

Menke, W. (1984), *Geophysical Data Analysis: Discrete Inverse Theory*, Academic, Orlando, Fla.

Mitterbauer, U., M. Behm, E. Brückl, R. Lippitsch, A. Guterch, G. R. Keller, E. Kozlovskaya, E. M. Rumpfhuber, and F. Šumanovac (2011), Shape and origin of the East-Alpine slab constrained by the ALPASS teleseismic model, *Tectonophysics*, *510*, 195–206, doi:10.1016/j.tecto.2011.07.001.

Peterek, A., C. D. Reuther, and R. Schunk (2011), Neotectonic evolution of the Cheb Basin (Northwestern Bohemia, Czech Republic) and its implications for the late Pliocene to recent crustal deformation in the western part of the Eger Rift, *Z. Geol. Wiss.*, *39*(5/6), 335–365.

Piromallo, C., and A. Morelli (2003), P wave tomography of the mantle under the Alpine-Mediterranean area, *J. Geophys. Res.*, *108*(B2), 2065, doi:10.1029/2002JB001757.

Plomerová, J., and V. Babuška (2010), Long memory of mantle lithosphere fabric–European LAB constrained from seismic anisotropy, *Lithos*, *120*, 131–143, doi:10.1016/j.lithos.2010.01.008.

Plomerová, J., V. Babuška, J. Šílený, and J. Horálek (1998), Seismic anisotropy and velocity variations in the mantle beneath the Saxothuringicum-Moldanubicum contact in central Europe, *Pure Appl. Geophys.*, *151*, 365–394, doi:10.1007/s000240050118.

Plomerová, J., U. Achauer, V. Babuška, M. Granet, and Bohema Working Group (2003), BOHEMA 2001-2003–Passive seismic experiment to study lithosphere-asthenosphere system in the western part of the Bohemian Massif, *Stud. Geophys. Geod.*, *47*, 691–701, doi:10.1023/A:1024784223048.

Plomerová, J., L. Vecsey, V. Babuška, M. Granet, and U. Achauer (2005), Passive seismic experiment MOSAIC – a pilote study of mantle lithosphere anisotropy of the Bohemian Massif, *Stud. Geophys. Geod.*, *49*, 541–560, doi:10.1007/s11200-005-0026-0.

Plomerová, J., U. Achauer, V. Babuška, and L. Vecsey (2007), Upper mantle beneath the Eger Rift (Central Europe): Plume or asthenosphere upwelling?, *Geophys. J. Int.*, *169*(2), 675–682, doi:10.1111/j.1365-246X.2007.03361.x.

Plomerová, J., L. Vecsey, and V. Babuška (2012), Mapping seismic anisotropy of the lithospheric mantle beneath the northern and eastern Bohemian Massif (central Europe), *Tectonophysics*, *564-565*, 38–53, doi:10.1016/j.tecto.2011.08.

Ritter, J. R. R., M. Jordan, U. R. Christensen, and U. Achauer (2001), A mantle plume below the Eifel volcanic fields, Germany, *Earth Planet. Sci. Lett.*, *186*, 7–14, doi:10.1016/S0012-821X(01)00226-6.

Sandoval, S., E. Kisslling, J. Ansorge, and SVEKALAKO Seismic Tomography Working Group (2004), High-resolution body wave tomography beneath the SVEKALAPKO array–II. Anomalous upper mantle structure beneath the central Baltic Shield, *Geophys. J. Int.*, *157*, 200–214, doi:10.1111/j.1365-246X.2004.02131.x.

Shomali, Z. H., R. G. Roberts, L. B. Pedersen, and the TOR Working Group (2006), Lithospheric structure of the Tornquist Zone resolved by nonlinear P and S teleseismic tomography along the TOR array, *Tectonophysics*, *416*, 133–149, doi:10.1016/j.tecto.2005.11.019.

Stammler, K. (1993), Seismic Handler–Programable multichannel data handler for interactive and automatic processing of seismological analyses, *Comput. Geosci.*, *19*, 135–140, doi:10.1016/0098-3004(93)90110-Q.

Steck, L. K., W. A. Prothero (1991), A 3-D ray-tracer for teleseismic body-wave arrival-times, *Bull. Seismol. Soc. Am.*, *81*, 1332–1339.

Ulrych, J., V. Cajz, E. Pivec, J. K. Novák, and Č. Nekovařík (2000), Cenozoic intraplate alkaline volcanism of western Bohemia, *Stud. Geophys. Geod.*, *44*, 346–351, doi:10.1023/A:1022131413783.

Walker, K. T., G. H. R. Bokelmann, S. L. Klemperer, and G. Bock (2005), Shear-wave splitting around the Eifel hotspot: Evidence for a mantle upwelling, *Geophys. J. Int.*, *163*, 962–980, doi:10.1111/j.1365-246X.2005.02636.x.

Weidle, C., S. Widiyantoro, and CALIXTO Working Group (2005), Improving depth resolution of teleseismic tomography by simultaneous inversion of teleseismic and global P-wave traveltime data–Application to the Vrancea region in Southeastern Europe, *Geophys. J. Int.*, *162*, 811–823, doi:10.1111/j.1365-246X.2005.02649.x.

Wilde-Piórko, M., et al. (2008), PASSEQ 2006-2008: Passive seismic experiment in Trans-European Suture Zone, *Stud. Geophys. Geod.*, *52*, 439–448, doi:10.1007/s11200-008-0030-2.

Wilson, M., and H. Downes (2006), Tertiary-Quaternary intra-plate magmatism in Europe and its relationship to mantle dynamics, in *European lithosphere dynamics, Memoirs*, vol. 32, edited by D. G. Gee and R. A. Stephenson, pp. 147–166, Geol. Soc., London, doi:10.1144/GSL.MEM.2006.032.01.09.

Wortel, M. J. R., and W. Spakman (2000), Subduction and slab detachment in the Mediterranean-Carpathian region, *Science*, *290*, 910–917.

Ziegler, P. A. (1992), European Cenozoic rift system, *Tectonophysics*, *208*, 91–111, doi:10.1016/0040-1951(92)90338-7.

Ziegler, P. A., and P. Dezes (2006), Crustal evolution of Western and Central Europe, in *European Lithosphere Dynamics, Memoirs*, vol. 32, edited by D. G. Gee and R. A. Stephenson, pp. 43–56, Geol. Soc., London, doi:10.1144/GSL.MEM.2006.032.01.03.

Ziegler, P. A., M. E. Schumacher, P. Dezes, J. D. Van Wees, and S. Cloetingh (2006), Post-Variscan evolution of the lithosphere in the area of the European Cenozoic Rift System, in *European Lithosphere Dynamics, Memoirs*, vol. 32, edited by D. G. Gee and R. A. Stephenson, pp. 97–112, Geol. Soc., London, doi:10.1144/GSL.MEM.2006.032.01.06.

Geochemistry, Geophysics, Geosystems

Supporting Information for

Cenozoic volcanism in the Bohemian Massif in the context of P- and S-velocity high-resolution teleseismic tomography of the upper mantle

Jaroslava Plomerová[1], Helena Munzarová[1], Luděk Vecsey[1], Eduard Kissling[2], Ulrich Achauer[3], Vladislav Babuška[1]

[1]Institute of Geophysics, Academy of Sciences of the Czech Republic, Boční II/1401, 14131 Prague 4, Czech Republic, [2]Institute of Geophysics, Swiss Federal Institute of Technology, Sonneggstrasse 5, 8092 Zürich, Switzerland, [3]Institute of Earth Physics, University of Strasbourg, 5 rue René Descartes, 67084 Strasbourg, France

Contents of this file

Introduction

This supporting information provides figures complementing the main article.

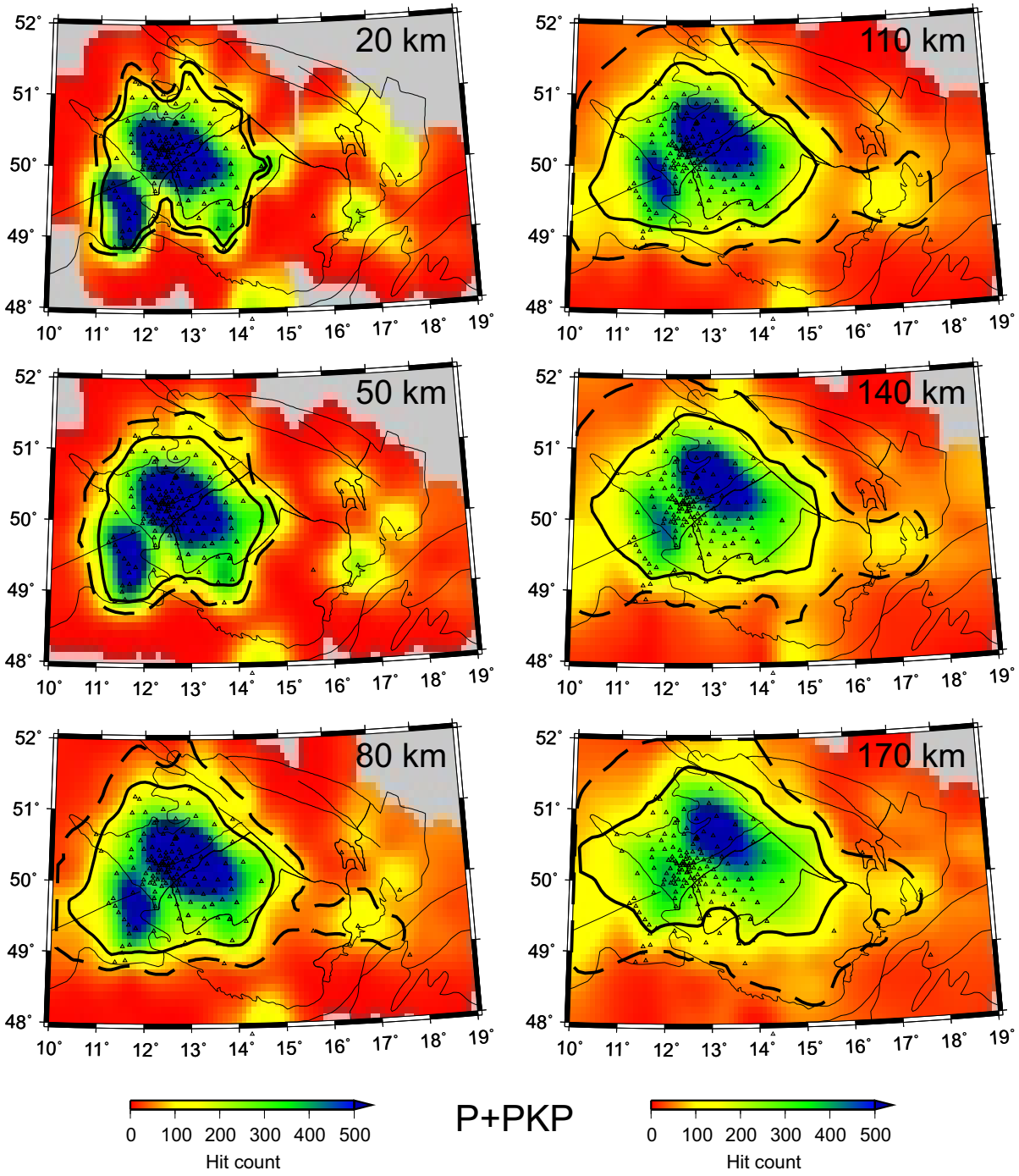

Figure S1. Hit-counts with contours of RDE = 0.7 (solid black) and RDE = 0.5 (dashed) for the P+PKP30 velocity perturbation model in Fig. 6.

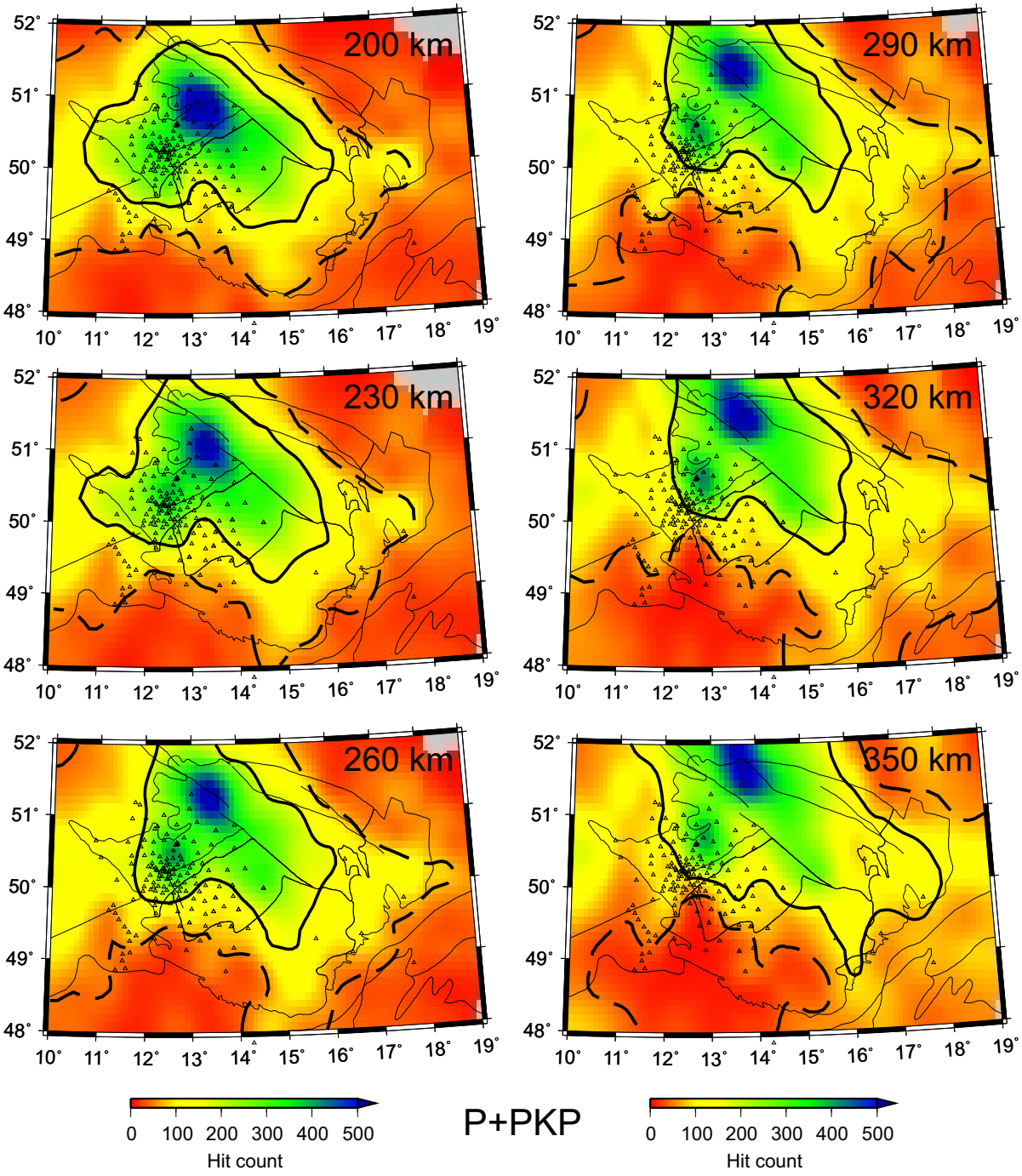

Figure S1. continuation

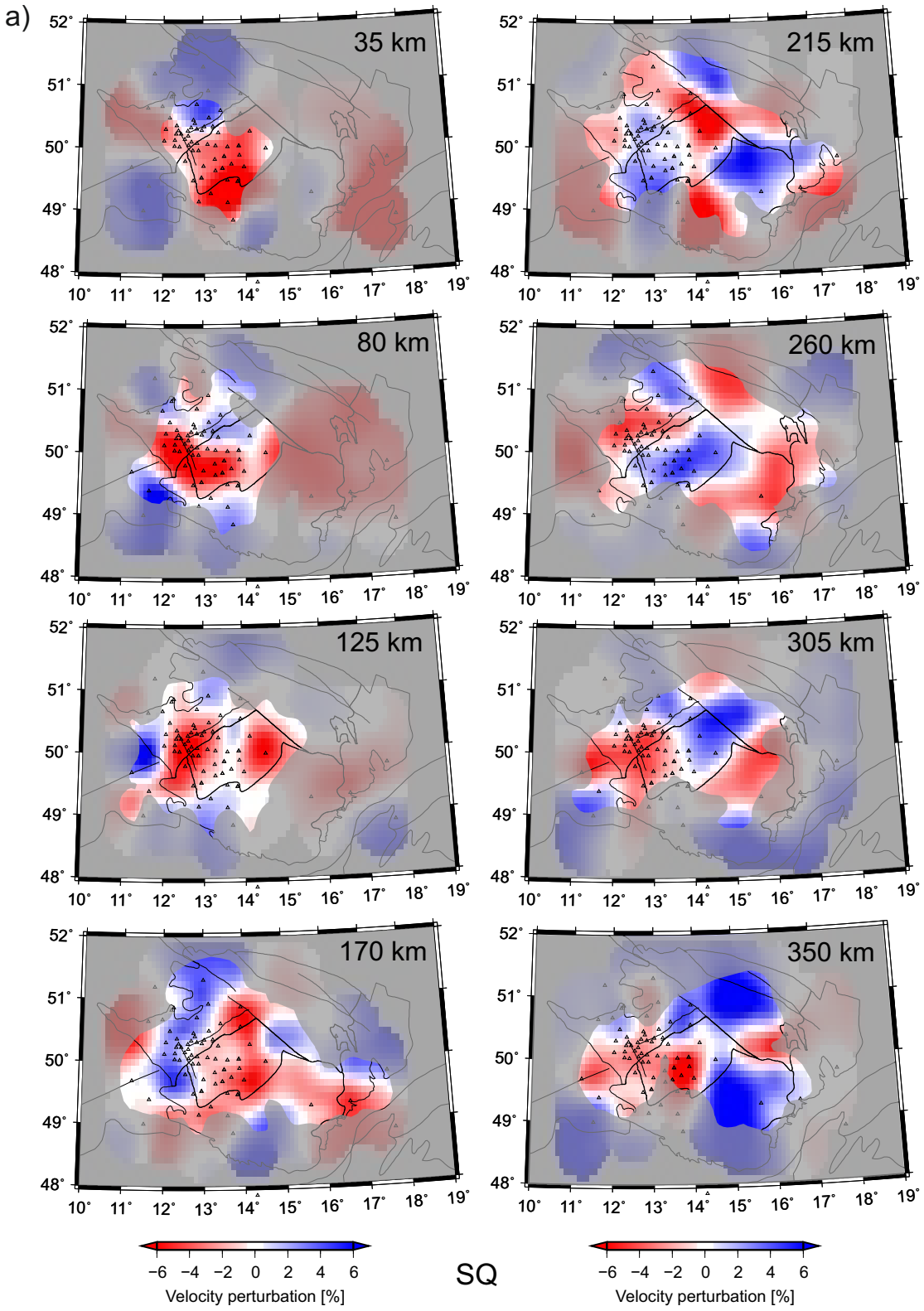

Figure S2. Velocity-perturbation model SQ45 where regions with RDE ≤ 0.5 are shaded (a) and hit-counts with contour of RDE = 0.5 (b).

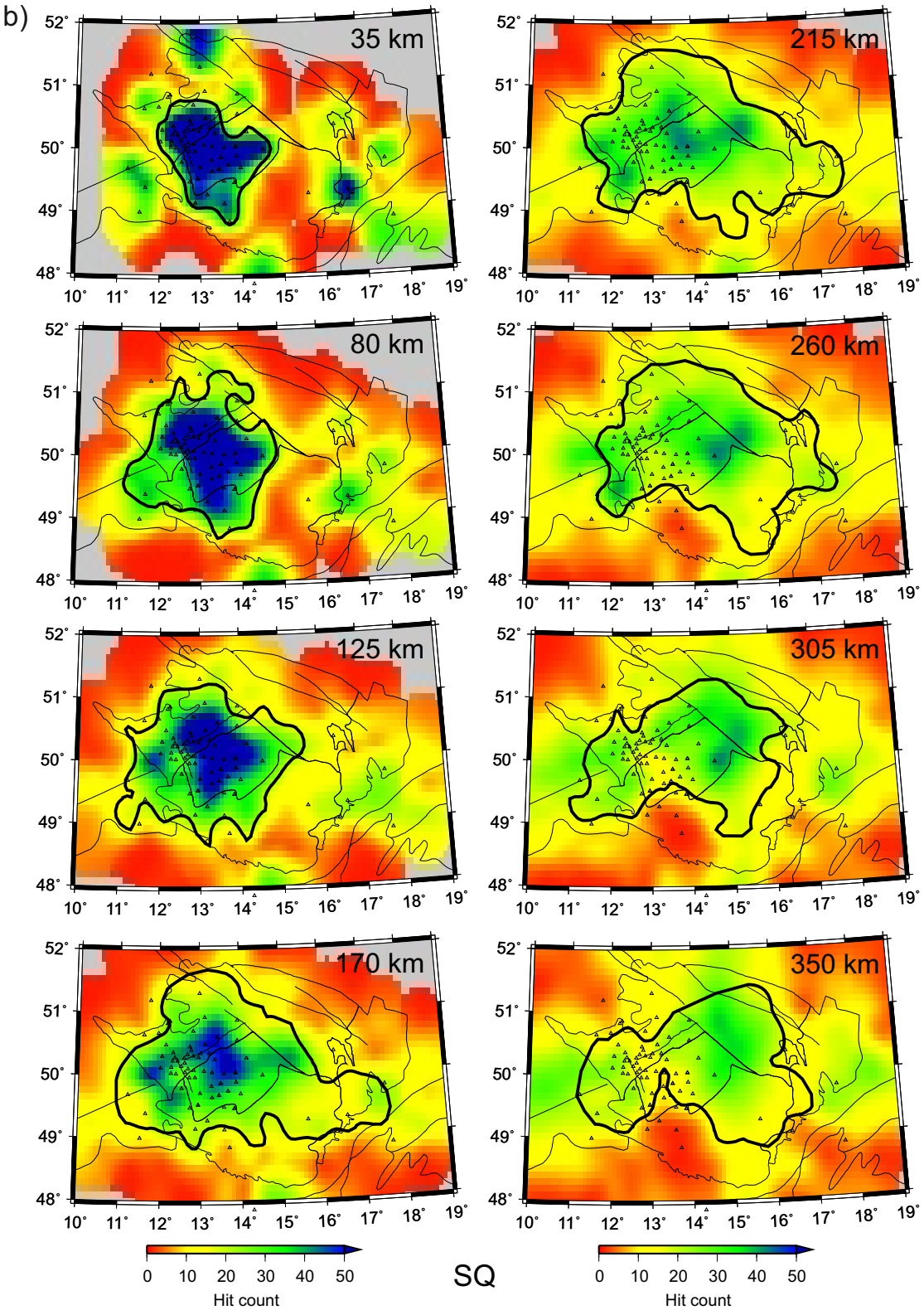

Figure S2. continuation

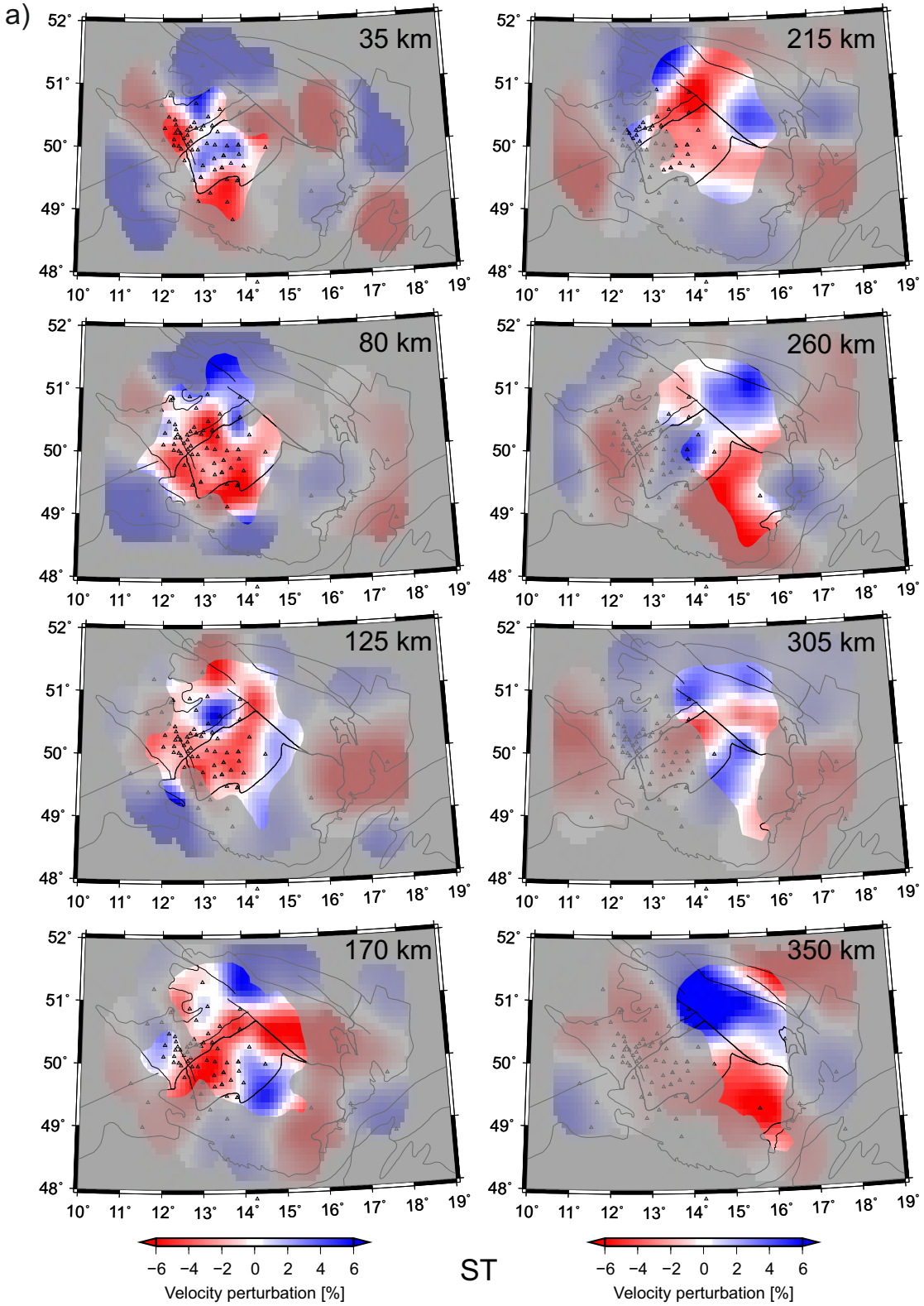

Figure S3. Velocity-perturbation model ST45 where regions with RDE ≤ 0.5 are shaded (a) and hit-counts with a contour of RDE = 0.5 (b).

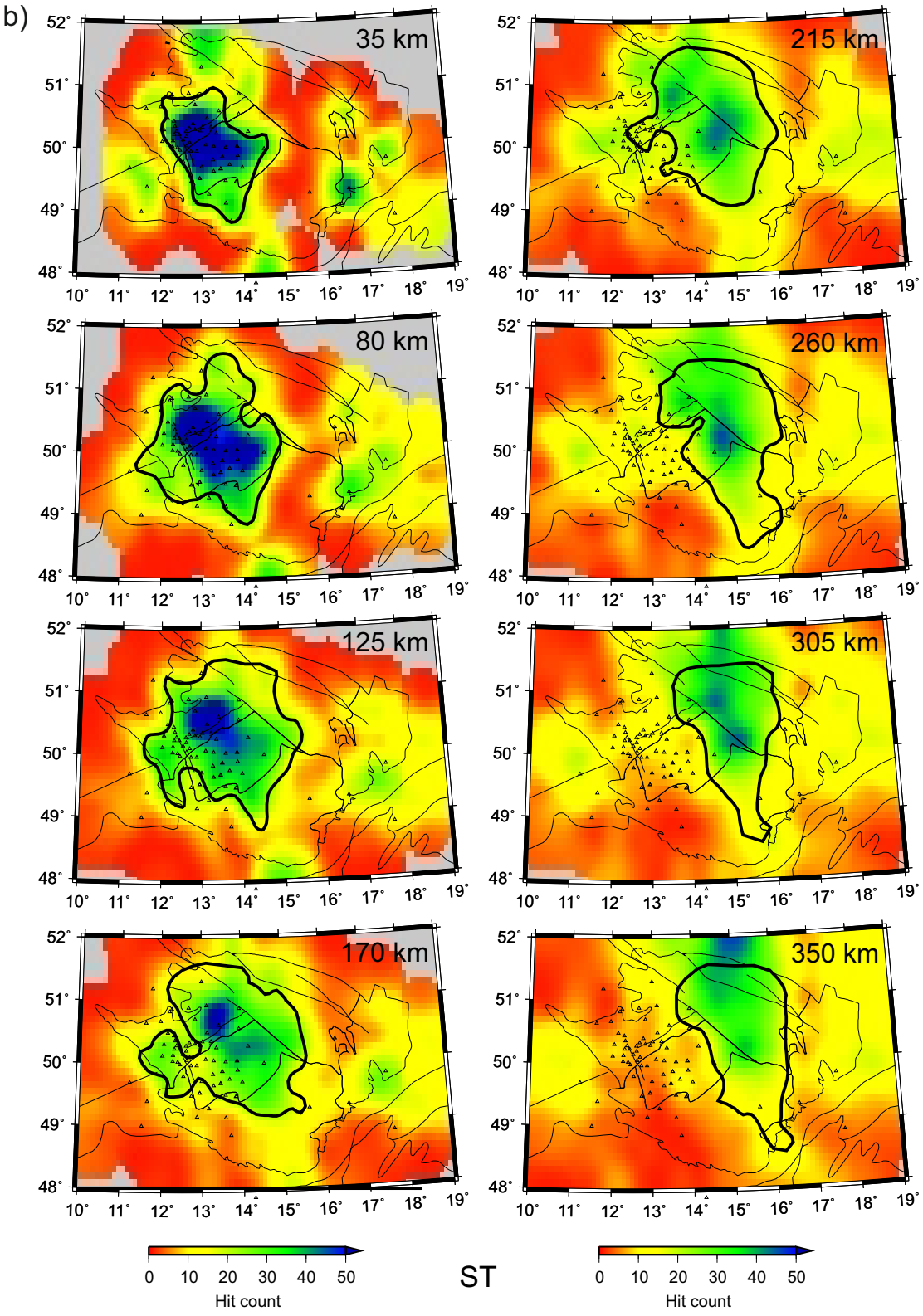

Figure S3. continuation

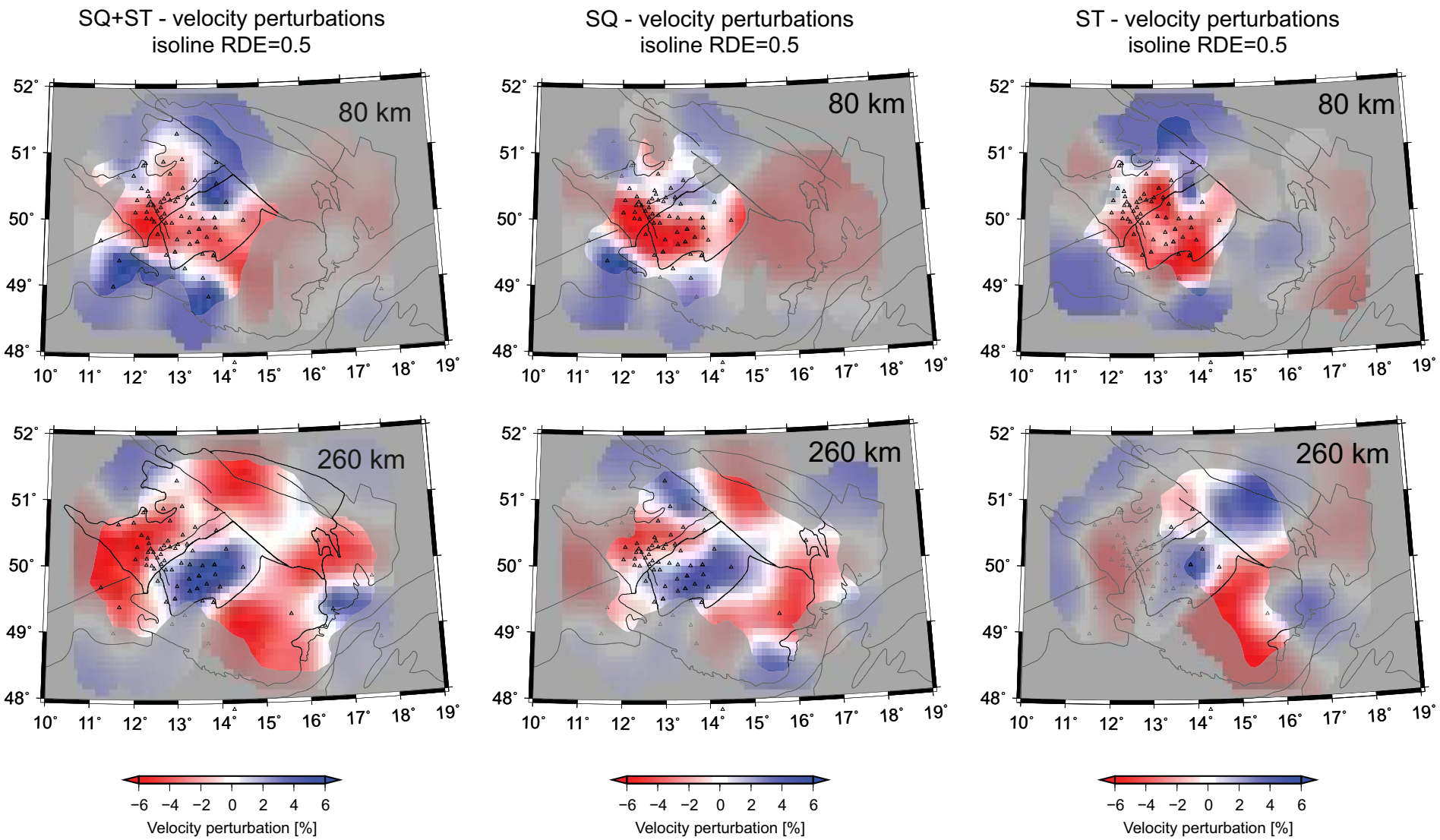

Figure S4. Shear-velocity perturbations at lithospheric (80 km) and sub-lithospheric (260 km) slices for three models calculated from all shear-wave residuals together (SQ+ST) and from travel-time residuals for shear waves measured separately on the Q and T components (SQ, ST). Regions with RDE ≤ 0.5 are shaded.

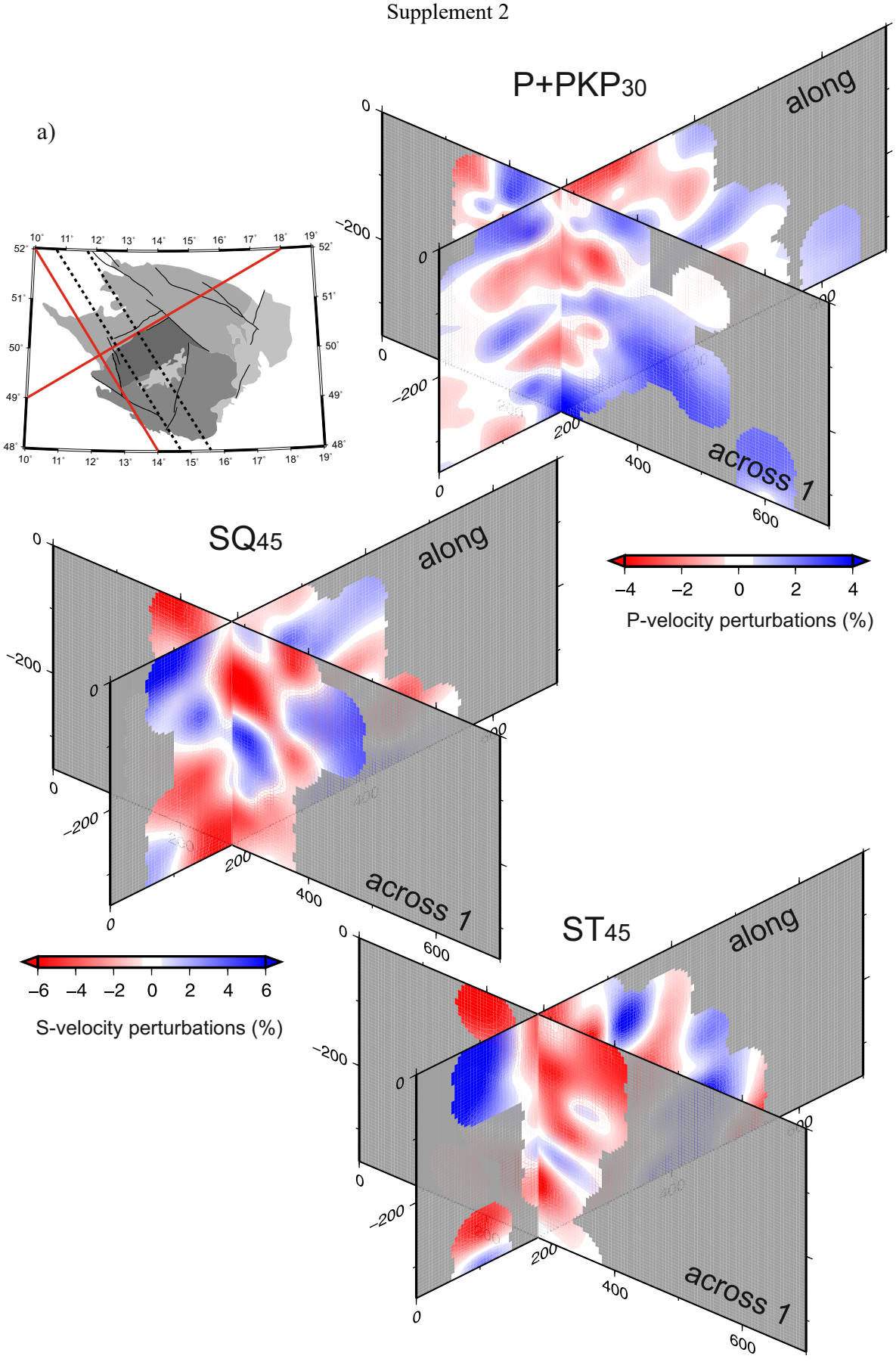

Figure S5. Cross-sections through the velocity perturbation models along additional 'tectonic' profiles oriented parallel and across the Eger Rift (see also Fig. 10).

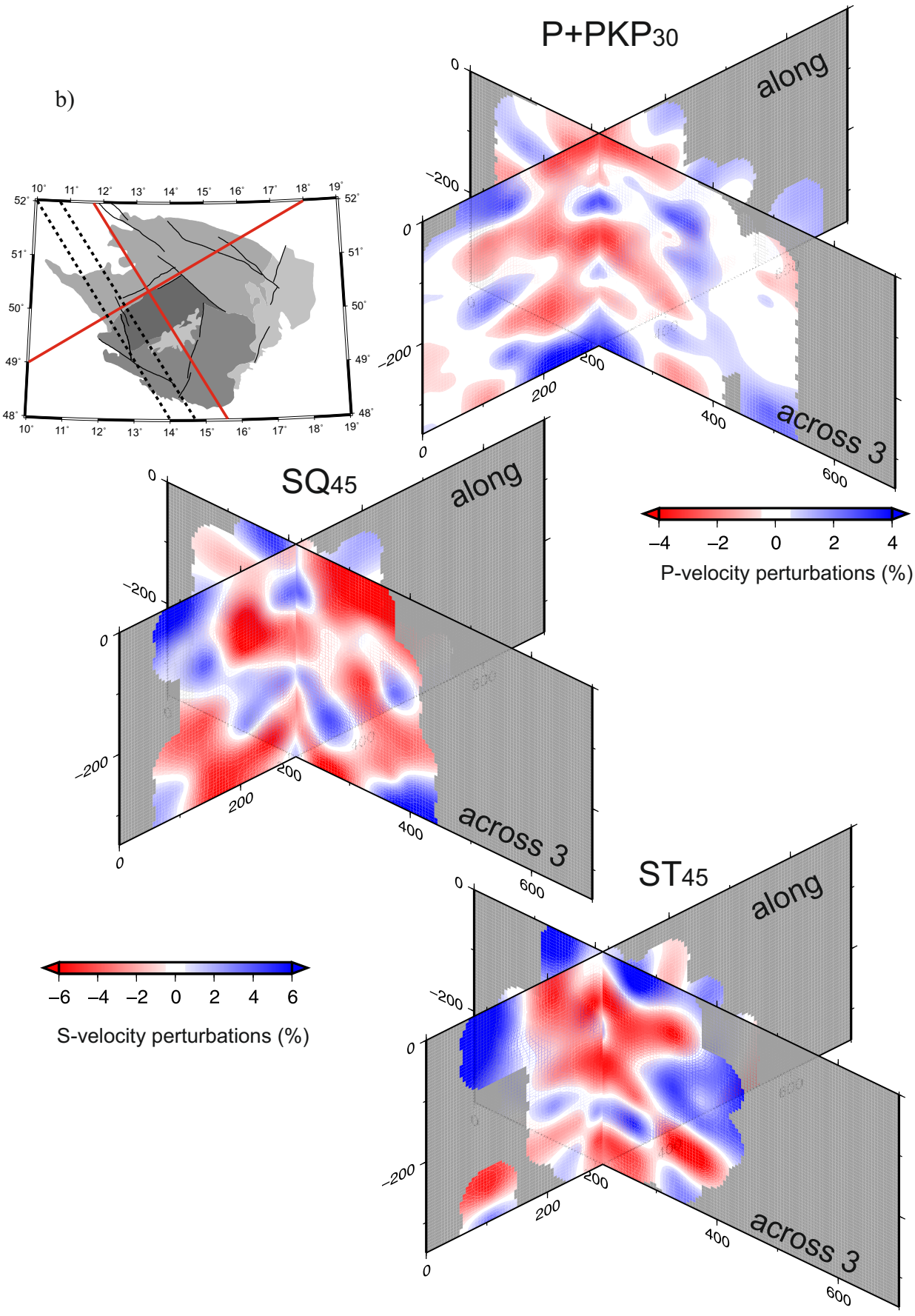

Figure S5. continuation

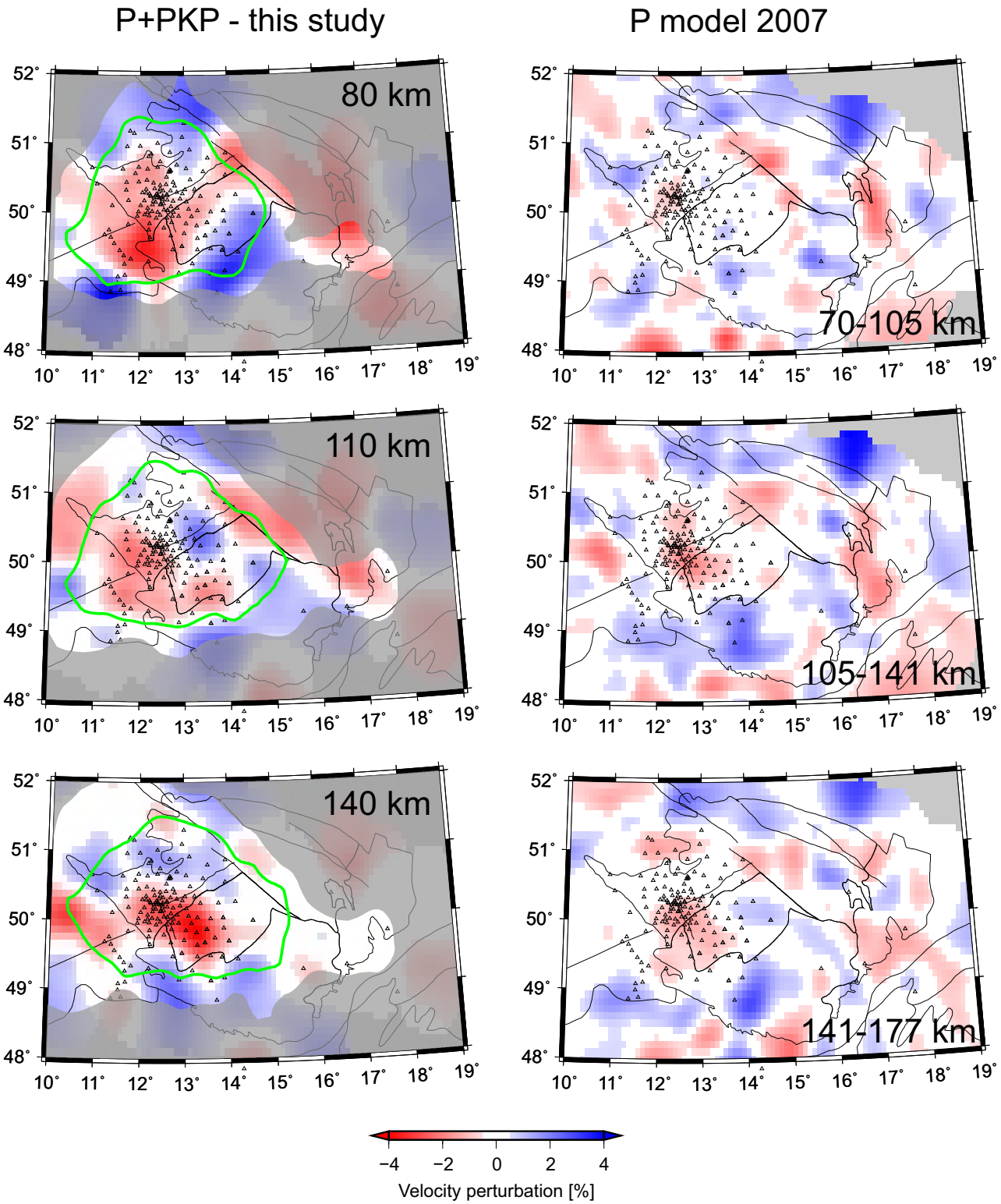

Figure S6. Selected layers of vP velocity perturbations in the P+PKP model presented in this paper and in the 2007 model [Plomerová et al. 2007].